

Subhas Chandra Mukhopadhyay *Editor*

Next Generation Sensors and Systems

Smart Sensors, Measurement and Instrumentation

Volume 16

Series editor

Subhas Chandra Mukhopadhyay
School of Engineering and Advanced Technology (SEAT)
Massey University (Manawatu)
Palmerston North
New Zealand
E-mail: S.C.Mukhopadhyay@massey.ac.nz

More information about this series at <http://www.springer.com/series/10617>

Subhas Chandra Mukhopadhyay
Editor

Next Generation Sensors and Systems

 Springer

Editor

Subhas Chandra Mukhopadhyay
School of Engineering and Advanced
Technology (SEAT)
Massey University
Palmerston North
New Zealand

ISSN 2194-8402 ISSN 2194-8410 (electronic)
Smart Sensors, Measurement and Instrumentation
ISBN 978-3-319-21670-6 ISBN 978-3-319-21671-3 (eBook)
DOI 10.1007/978-3-319-21671-3

Library of Congress Control Number: 2015944456

Springer Cham Heidelberg New York Dordrecht London
© Springer International Publishing Switzerland 2016

This work is subject to copyright. All rights are reserved by the Publisher, whether the whole or part of the material is concerned, specifically the rights of translation, reprinting, reuse of illustrations, recitation, broadcasting, reproduction on microfilms or in any other physical way, and transmission or information storage and retrieval, electronic adaptation, computer software, or by similar or dissimilar methodology now known or hereafter developed.

The use of general descriptive names, registered names, trademarks, service marks, etc. in this publication does not imply, even in the absence of a specific statement, that such names are exempt from the relevant protective laws and regulations and therefore free for general use.

The publisher, the authors and the editors are safe to assume that the advice and information in this book are believed to be true and accurate at the date of publication. Neither the publisher nor the authors or the editors give a warranty, express or implied, with respect to the material contained herein or for any errors or omissions that may have been made.

Printed on acid-free paper

Springer International Publishing AG Switzerland is part of Springer Science+Business Media
(www.springer.com)

Preface

Sensors are the most important component in any system and understanding the fundamentals of operation, integration into a system and the selection are very useful. There is a continuous advancement of sensing technology, embedded system, wireless communication technology, nano-technology and miniaturization which make it possible to develop smart wireless electronic systems to monitor many phenomenon around us continuously.

This Special Issue titled “Next Generation Sensors and Systems” in the book series of “Smart Sensors, Measurement and Instrumentation” contains the invited papers from renowned experts working in the field. A total of 14 chapters have described the advancement in the area of Sensors and Sensing Technologies, Signal processing, Wireless Sensors and Sensor Networks, Protocols, Topologies, Instrumentation architectures, Measurement Techniques, Energy Harvesting and Scavenging, Design and Prototyping in recent times.

The first chapter by Mohamed Serry describes the new nanostructured Schottky junctions based on graphene/platinum grown on different substrates which are fabricated and investigated for sensing applications. The uniqueness of the research is based on the process for growing the graphene layer on the M-S junction.

The design of a planar interdigital micro-sensor for the characterization of biological mediums by impedance spectroscopy is presented in “[Design and Realization of a Planar Interdigital Microsensor for Biological Medium Characterization](#)” by T.-T. Ngo, A. Bourjilat, J. Claudel, D. Kourtiche and M. Nadi. A theoretical optimization of the geometrical parameters of the sensor is proposed allowing the extension of the measurement frequency range by reducing the polarization effect manifested by a double layer.

In “[Molecularly Imprinted Impedimetric Sensing of Phthalates: A Real-Time Assay Technique](#)”, a real-time, non-invasive detection of phthalates was performed employing electrochemical impedance spectroscopy technique incorporating an enhanced penetration depth interdigital capacitive transducer by A.I. Zia, Apeksha Rao and S.C. Mukhopadhyay. The research was conducted to investigate the application of pre-concentration extraction polymer with molecular imprinted

recognition sites as an analyte sensitive coating for the sensor to introduce molecular selectivity for di (2-ethylhexyl) phthalate molecules.

A. Zhukov, M. Ipatov, J.J. del Val, M. Ilyn, A. Granovsky and V. Zhukova have developed a novel functional materials exhibiting giant magnetoresistance (GMR) and reported on magnetic, transport and structural properties of $\text{Co}_x\text{-Cu}_{100-x}$ ($5 \leq x \leq 30$) and $\text{Fe}_{37}\text{Cu}_{63}$ glass-coated microwires prepared by the Taylor-Ulitovsky method in “[Magnetic and Transport Properties of M-Cu \(M = Co, Fe\) Microwires](#)”. In the next chapter the correlation of “[Giant Magnetoimpedance Effect of Amorphous and Nanocrystalline Glass-Coated Microwires](#)” by A. Zhukov, A. Talaat, M. Ipatov, J.J. del Val, L. Gonzalez-Legarreta, B. Hernando and V. Zhukova. The outcomes of the research lead to the development of magnetically soft thin wires for applications in magnetic field sensors.

Non-Faradaic Electrochemical Modification of Catalytic Activity (NEMCA) was investigated for the first time for the activation and reactivation of the industrial potentiometric oxygen sensor based on stabilized zirconia solid electrolyte, which was reported in “[Aged Zirconia Electrochemical Oxygen Sensor Activation and Re-activation Using NEMCA](#)” by P. Shuk and R. Jantz. The NEMCA has improved the sensor response, impedance and stability.

In “[A New Scheme for Determination of Respiration Rate in Human Being Using MEMS Based Capacitive Pressure Sensor](#)”, the development of a MEMS-based capacitive nasal sensor system for measuring Respiration Rate (RR) of humans has been reported by Madhurima Chattopadhyay and Deborshi Chakraborty. Two identical arrays of diaphragms based MEMS capacitive nasal sensors have been designed and fabricated. In the proposed scheme, the two identical sensor arrays are mounted below Right Nostril (RN) and Left Nostril (LN), in such a way that the nasal airflow during inspiration and expiration impinge on the sensor diaphragms. A Finite Element Method based simulation study for monitoring the condition of lungs and heart of acute respiratory distress syndrome (ARDS) patients for monitoring their conditions ranging from dynamic shifting of body fluids to lung aeration has been reported in “[Monitoring of the Lung Fluid Movement and Estimation of Lung Area Using Electrical Impedance Tomography](#)” by Deborshi Chakraborty and Madhurima Chattopadhyay. The chapter has presented a brief overview on application of EIT for monitoring of the lung fluid movement and estimation of lung area in a human being along with physical and mathematical aspect with a goal to achieve a system having higher potential to cater medical challenges in lung oriented diseases.

A smart home’s monitoring system incorporating wellness’s context based on daily activities of human beings will be very useful to predict future’s event for pro-active medical treatment. The “[Activity and Anomaly Detection in Smart Home: A Survey](#)” by U.A.B.U.A. Bakar, H. Ghayvat, S.F. Hasan and S.C. Mukhopadhyay have reviewed the state-of-the-art dense sensing paradigm and anomaly detection approaches including sensors, data, analysis, algorithms and comparison of techniques.

In “[Real-Time Monitoring of Meat Drying Process Using Electromagnetic Wave Sensors](#)”, Magomed Muradov, Jeff Cullen and Alex Mason have investigated use an electromagnetic (EM) wave sensor to monitor the meat drying process and determine its suitability as a non-destructive and non-contact technique. The sensor has been modelled using High Frequency Structure Simulation Software (HFSS) and then constructed. Experimental work was conducted involving measurement of meat weight and EM signature (namely the S11 parameter in the frequency range 1–6 GHz) over a period of approximately one week, with measurements recorded every hour. The change in EM signature and weight loss has been analysed and correlations drawn from the resultant data.

Arijit Chowdhury, Avik Ghose, Tapas Chakravarty and P. Balamuralidhar have investigated the noise performance of a few smartphone based accelerometers in “[An Improved Fusion Algorithm For Estimating Speed From Smartphone’s Ins/Gps Sensors](#)”. The noise analysis has been used for improving the estimation of the speed of moving vehicle, as captured by GPS. A number of experiments were carried out to capture the vehicle’s position and speed from On Board Diagnosis V2 (OBD2), GPS as well as 3-axes accelerometer. The authors have also demonstrated a method by which the phone’s orientation is compensated for while calculating speed from the measured acceleration. A new method of INS/GPS fusion has been proposed to enhance the accuracy of speed estimation. It is envisaged that with increasing estimation accuracy, the application of multi-sensor fusion in autonomous vehicles will be greatly enhanced.

The “[Monitoring Water in Treatment and Distribution System](#)” by Joyanta Kumar Roy and Subhas Chandra Mukhopadhyay has reviewed and explained the importance of water quality monitoring and its technology from generation to the distribution. They have reported a SCADA-based intelligence sensing system which is utilising the Internet of Things to improve easy access to monitor water quality, treatment process and plant health in real time. Internet of Things is a new era of computing technology and a smart connect, machine to machine, machine to infrastructure, machine to environment intelligent system, which can talk to each other and make operational functions in universal network in the cloud.

A novel way for the recognition and classification of objects inside a scene, inspired by the well-known frame theory is described in “[An Application of the Frame Theory for Signature Extraction in the Analysis of 3D Point Clouds](#)” by F. Martino, C. Patruno, R. Marani and E. Stella. Three-dimensional (3D) point clouds have been obtained using a laser triangulation system of high resolution to achieve low noise datasets for the validation.

The last chapter by K. Tashiro, A. Ikegami, S. Shimada, H. Kojima and H. Wakiwaka presents the design of self-generating component powered by magnetic energy harvesting. A magnetic field alarm has been developed to demonstrate the devices. It consists of an energy harvesting module, Cockcroft-Walton circuit and piezo buzzer. The energy harvesting module is composed of coil and magnetic flux concentration core. It can generate 200 μW from an environmental magnetic field of 200 μT at 60 Hz.

I do sincerely hope that the readers will find this special issue interesting and useful in their research as well as in practical engineering systems. We are very happy to be able to offer the readers such a diverse special issue, both in terms of its topical coverage and geographic representation.

Finally, I would like to wholeheartedly thank all the authors for their contribution to this special issue.

Subhas Chandra Mukhopadhyay

Contents

Graphene Based Physical and Chemical Sensors	1
Mohamed Serry	
Design and Realization of a Planar Interdigital Microsensor for Biological Medium Characterization	23
T.-T. Ngo, A. Bourjilat, J. Claudel, D. Kourtiche and M. Nadi	
Molecularly Imprinted Impedimetric Sensing of Phthalates: A Real-Time Assay Technique	55
A.I. Zia, Apeksha Rao and S.C. Mukhopadhyay	
Magnetic and Transport Properties of M-Cu (M = Co, Fe) Microwires	81
A. Zhukov, M. Ipatov, J.J. del Val, M. Ilyn, A. Granovsky and V. Zhukova	
Giant Magnetoimpedance Effect of Amorphous and Nanocrystalline Glass-Coated Microwires	103
A. Zhukov, A. Talaat, M. Ipatov, J.J. del Val, L. Gonzalez-Legarreta, B. Hernando and V. Zhukova	
Aged Zirconia Electrochemical Oxygen Sensor Activation and Re-activation Using NEMCA	131
P. Shuk and R. Jantz	
A New Scheme for Determination of Respiration Rate in Human Being Using MEMS Based Capacitive Pressure Sensor	143
Madhurima Chattopadhyay and Deborshi Chakraborty	

Monitoring of the Lung Fluid Movement and Estimation of Lung Area Using Electrical Impedance Tomography.	161
Deborshi Chakraborty and Madhurima Chattopadhyay	
Activity and Anomaly Detection in Smart Home: A Survey.	191
U.A.B.U.A. Bakar, Hemant Ghayvat, S.F. Hasanm and S.C. Mukhopadhyay	
Real-Time Monitoring of Meat Drying Process Using Electromagnetic Wave Sensors.	221
Maged Muradov, Jeff Cullen and Alex Mason	
An Improved Fusion Algorithm For Estimating Speed From Smartphone's Ins/Gps Sensors.	235
Arijit Chowdhury, Avik Ghose, Tapas Chakravarty and P. Balamuralidhar	
Monitoring Water in Treatment and Distribution System.	257
Joyanta Kumar Roy and Subhas Chandra Mukhopadhyay	
An Application of the Frame Theory for Signature Extraction in the Analysis of 3D Point Clouds.	289
F. Martino, C. Patruno, R. Marani and E. Stella	
Design of Self-generating Component Powered by Magnetic Energy Harvesting—Magnetic Field Alarm.	311
K. Tashiro, A. Ikegami, S. Shimada, H. Kojima and H. Wakiwaka	

About the Editor



Dr. Subhas Chandra Mukhopadhyay (M'97, SM'02, F'11) graduated from the Department of Electrical Engineering, Jadavpur University, Calcutta, India with a **Gold medal** and received the Master of Electrical Engineering degree from **Indian Institute of Science**, Bangalore, India. He has a **Ph.D. (Eng.)** degree from Jadavpur University, India and a **Doctor of Engineering** degree from Kanazawa University, Japan.

Currently, he is working as a **Professor of Sensing Technology** with the School of Engineering and Advanced Technology, Massey University, Palmerston North, New Zealand. He has over 25 years of teaching

and research experiences.

His fields of interest include Sensors and Sensing Technology, Instrumentation, Wireless sensor networks, Electromagnetics, control, electrical machines and numerical field calculation, etc.

He has authored/co-authored four books and over **300** papers in different international journals, conferences, and book chapter. He has edited **12** conference proceedings. He has also edited **11** special issues of international journals as lead guest editor and **19** books out of which **17** are with Springer-Verlag. He has delivered **229** seminars as keynote, invited, tutorial and special lectures in **24** countries.

He was awarded numerous awards throughout his career and attracted over NZ \$4.1 M on different research projects.

He is a **Fellow** of IEEE (USA), a **Fellow** of IET (UK) and a **Fellow** of IETE (India). He is a **Topical Editor** of IEEE Sensors journal, an **Associate Editor** of IEEE Transactions on Instrumentation and Measurements and a **Technical Editor** of IEEE Transactions on Mechatronics. He is the co-editor-in-chief of the International Journal on Smart Sensing and Intelligent Systems (www.s2is.org). He was the Technical Programme Chair of ICARA 2004, ICARA 2006 and ICARA 2009. He was the General chair/Co-chair of ICST 2005, ICST 2007, IEEE ROSE 2007, IEEE EPSA 2008, ICST 2008, IEEE Sensors 2008, ICST 2010, IEEE Sensors 2010, ICST 2011,

ICST 2012, ICST 2013 and ICST 2014. He has organized the IEEE Sensors conference 2009 at Christchurch, New Zealand during 25–28 October 2009 as General Chair. He is planning to organize the Ninth ICST in Auckland, New Zealand during 8–10 December 2015.

He was a Distinguished Lecturer of IEEE Sensors council from 2010 to 2013. He is the Founding and Ex-**Chair** of the IEEE Instrumentation and Measurement Society New Zealand Chapter. He chairs the IEEE IMS Technical Committee 18 on Environmental Measurements.

Graphene Based Physical and Chemical Sensors

Mohamed Serry

Abstract New nanostructured Schottky junctions based on graphene/platinum grown on different substrates are fabricated and investigated for sensing applications. The integration of graphene layer (s) on regular M-S junctions was only possible by using an ALD-grown platinum thin film (~ 40 nm) and then growing graphene in PECVD at temperatures lower than platinum silicide formation temperature (i.e., <700 °C). The electrochemical and radiation sensing behaviors were investigated using two different substrate types. The first is a moderately-doped n-type (e^- conc. $\approx 2 \times 10^{15}$ cm^{-3}) silicon substrate in which a Schottky rectifier response with different threshold voltages was observed. An order of magnitude increase in generated current was observed with the use of high-resistivity silicon substrates ($\rho \geq 10,000$ Ωcm). By adding a dielectric layer to form a graphene-metal-insulator-semiconductor junction (Graphene-MIS) a linear ohmic response was observed. The obtained responses were explained by studying the band diagrams for the different processes with the aid of XPS and Raman analyses that clearly indicated the p-doping of the graphene layer in response to γ -ray radiations, which resulted in a strong reversed current tunneled through the ultrathin platinum layer. In the case of high-resistivity silicon substrates, the reversed current is much stronger due to the weak forward current from the substrate, which resulted in a stronger reverse response and, ultimately, higher sensitivity. The uniqueness of the research is based on the process for growing the graphene layer on the M-S junction. Exfoliated graphene results in increased contact resistance and low e^- mobility, which will not yield the desired effects.

M. Serry (✉)

The American University in Cairo, New Cairo, Egypt
e-mail: mserry@aucegypt.edu

1 Introduction

Nanostructured materials on MEMS-integrated devices could replace most current conventional sensors. They provide the advantages of utilizing nanostructured materials' surface-to-volume ratio and the materials can be engineered for increased selectivity. MEMS provides an integrated platform for detection, signal processing and sample handling. Combined, the distinct advantages of nanomaterials could potentially overcome the limited detection range, low sensitivity, and large sample size of conventional sensors.

MEMS-integrated nanotmaterials, including carbon nanotubes, silicon nanowires, and metal oxide nanowires, have been successfully implemented in several sensor applications including gas sensors [1–4], infrared detectors [5, 6], temperature sensors [7, 8], pressure sensor [9], humidity sensor [10], and chemical and biochemical sensors [11–14]. However the monolithic integration of graphene on MEMS platforms is currently facing several challenges due to the high temperatures required to grow graphene layers (more than 1000 °C on a Cu catalyst layer) and the difficulty of aligning exfoliated graphene on a specific device site. Therefore, practical application and optimal use of nanomaterials will require a process that facilitates the integration of graphene layers on MEMS leading to enhanced sensor functionality, sensitivity, and selectivity.

2 Motivation

In past decades, scaling down of solid-state sensors resulted in improved device efficiency and capacity. However, along with the ability to scale down devices come challenges with designing and developing nanostructures that must operate properly in an increasingly smaller environment. Schottky diodes can replace conventional PN junctions and bipolar transistors in scaled down solid-state sensors, offering faster response and lower threshold voltages as shown in Fig. 1. Schottky diode-based sensors generally consist of a metal-semiconductor (M-S) junction. The most common choices of metals are catalytic type noble metals (e.g., Au, Pt, and Pd) [15–18]. Schottky diodes have been implemented for developing highly efficient sensors, solar cells and electrochromic devices [19–23]. Graphene ultrathin sheets are emerging as ideal candidates for thin-film devices and combination with other semiconductor materials such as silicon. They have been produced in the form of ultrathin sheets consisting of one or a few atomic layers directly grown by chemical vapor deposition (CVD) [24–26] or by solution processing [27, 28] and then transferred to various substrates.

In this work, we have implemented a direct, simple, reusable, isotropic, wide range, and ultrahigh sensitive range of physical and chemical sensors based on graphene-Schottky junctions. The sensor is based on a nanostructured array of graphene grown on a platinum/n-Si substrate. The new sensor structure (Fig. 2) is a Schottky barrier diode based on forming an M-S junction of n-type silicon substrate

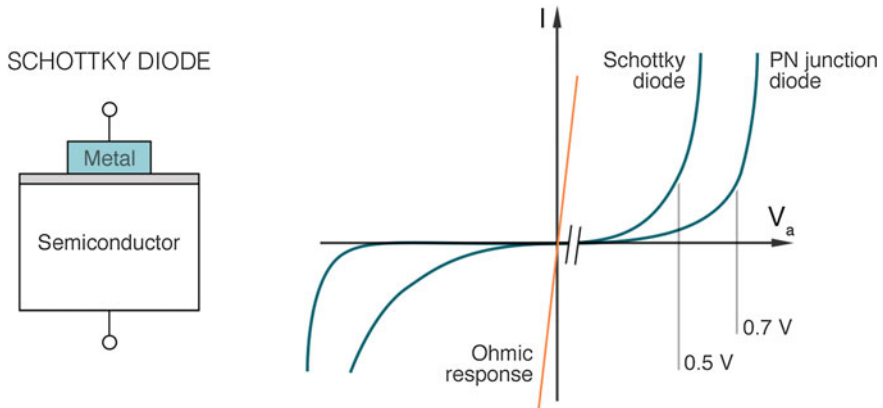


Fig. 1 Comparing the IV response of PN versus M-S junctions

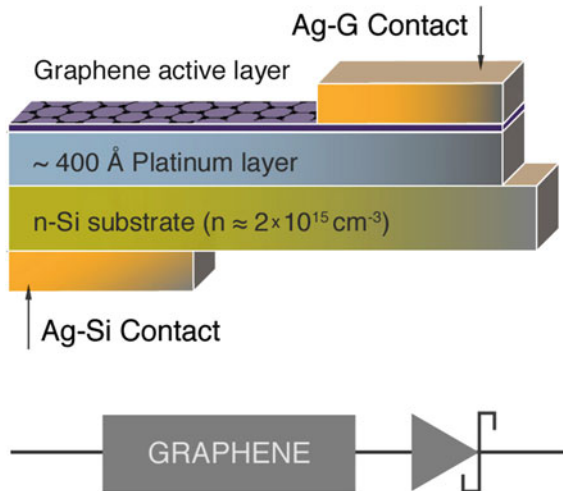


Fig. 2 Schematic of the developed sensor

and ultrathin film platinum integrated with a graphene layer. In this chapter, two examples covering the physical and chemical aspects of our proposed structure will be presented. The first is related to a gamma-photon sensor and the second is a label free glucose sensor [29–32]. Enhanced performance of both sensors is demonstrated mainly due to the band interaction at the graphene-platinum-silicon junctions, which yields stronger forward/reverse currents in response to stimulus. An added feature of the glucose sensor is the increased surface-to-volume ratio at the graphene surface, which enhances sensitivity and allows for direct interaction between the glucose OH groups and graphene surface without the need for surface functionalization (e.g., glucose oxidase as commonly used in glucose sensors [33–36]).

3 Operating Principle of Graphene-Schottky Sensors

The working principle of our new device design is based on the interaction of γ -photons with the graphene layer, which changes the local electric field distribution and thus the variation of the Schottky barrier's height (SBH) and width, resulting in a detectable current change. We refer to it as a Graphene-Schottky junction. As schematically shown in Fig. 3, as graphene is positively biased and in contact with Pt it becomes p-doped and its Fermi level (E_f) is lowered. Therefore, as γ -photons penetrate through the bulk of the whole device, there are no graphene electrons available for interband transition, especially at lower radiation doses (Fig. 3a). Meanwhile, at the Pt/n-Si interface, when a forward-bias voltage is applied to the Schottky diode depicted in Fig. 4, the work function of Pt ($\sim 5.7\text{--}5.98$ eV) is greater than that of the n-Si (4.5 eV), therefore the contact potential is reduced. Thus, the electrons move from the conduction band across the depletion region to the metal, creating a forward current (I_{fwd}) through the junction (Fig. 5).

The current across a Pt/n-Si junction is mainly due to majority carriers. Moreover, there are three mechanisms by which current can flow: (1) diffusion of carriers, (2) thermionic emission, and (3) quantum mechanical tunneling. According to the thermionic emission theory of Schottky diodes, the dependence of forward current on the applied voltage is given by the expression [37]:

$$I = I_s \left\{ \exp\left(\frac{qV}{kT}\right) - 1 \right\}, \quad (1)$$

where q is the charge of one electron, V the applied voltage, T the absolute temperature in Kelvin, k is the Boltzmann's constant, and I_s is the saturation current as defined by:

$$I_s = AA^{**}T^2 \exp\left(-\frac{q\Phi}{kT}\right), \quad (2)$$

in which A is the junction's surface area, A^{**} the Richardson constant and Φ is the zero bias Schottky barrier height in eV. Therefore, the Schottky barrier height (SBH) can be extracted from Eq. (2) as:

$$\Phi = \frac{kT}{q} \ln\left(\frac{AA^{**}T^2}{I_s}\right), \quad (3)$$

where, I_s can be obtained from the current density at the zero voltage. As the Pt/n-Si junction is exposed to γ -photons, more bonds are broken in the Si lattice, which results in the freeing of more electrons and shifts the Fermi level up. The flowing current is increased as a result of two main effects: (i) an increase in thermionic emissions due to excess electrons in the conduction band, and (ii) an increase of the

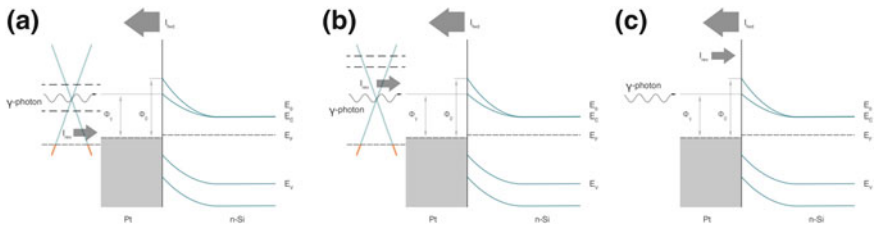


Fig. 3 Schematic of the energy band diagram at the interface of the Schottky junction showing the interactions between gamma-photons and the sensor. **a** The graphene-Schottky device at low doses, when graphene is positively charged, the Fermi level (E_f) is lowered. Upon gamma irradiation, e-h pair is formed in Si lowering the SBH, while in graphene there is no electron available for the interband transition, a strong forward current will flow from Si to Graphene. **b** at higher doses graphene electrons are excited to higher states increasing the reverse current and therefore reduce the overall net current, **c** for the conventional Pt/n-Si Schottky junction, forward current is induced at lower doses but the response is saturated at higher doses due to the counterbalancing induced reverse current

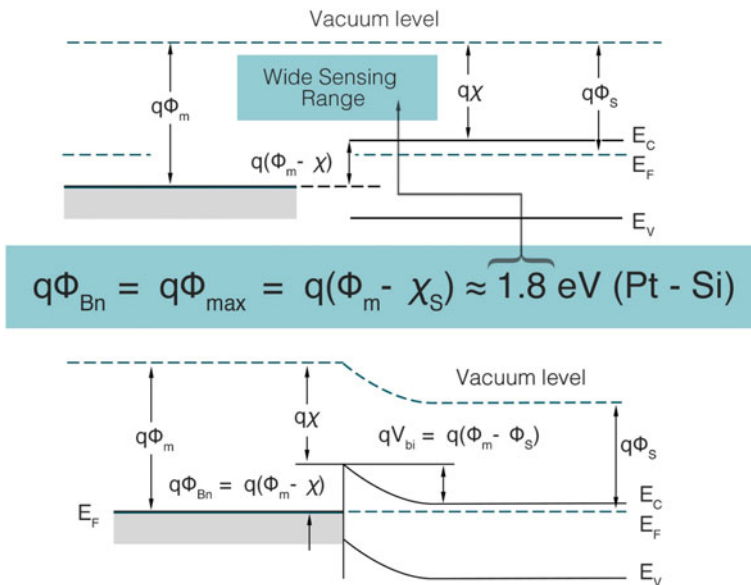


Fig. 4 Schematic of the energy bands at the Pt-Si junction

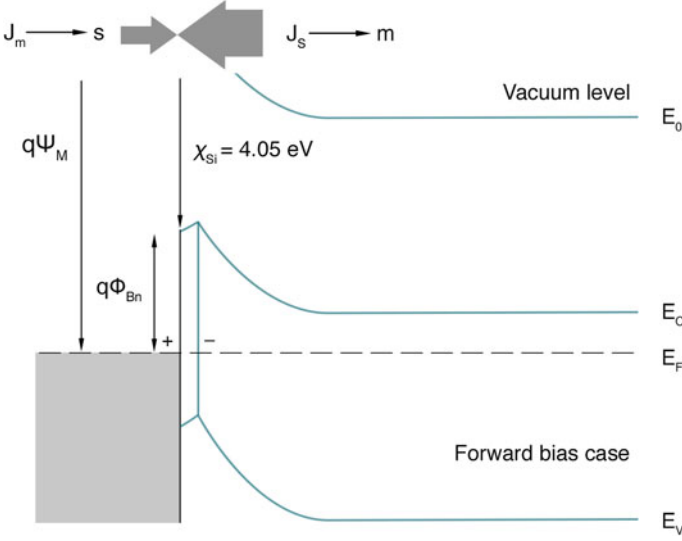


Fig. 5 Schematic of the forward and reverse currents at Pt-Si junction

tunneling current due to a decrease in the depletion layer thickness (i.e., barrier's width). Consequently, the change in SBH can be determined from the following equation:

$$\Delta\Phi = (\Phi_\gamma - \Phi_0), \quad (4)$$

where Φ_γ and Φ_0 are SBH before and after exposure to γ -irradiation. Therefore, the intimate junction with the p-doped graphene layer coupled with interaction with γ -photons results in shifting the SBH down as expressed in Eq. (4). As a result, a forward current (I_{fwd}) is induced in the Si-G direction thermionically and by diffusion through the thin Pt layer. Using Eqs. (1)–(4) the SBH differences of the sensor with graphene layer towards γ -photons exposure were calculated and presented in Table 1. As can be seen in the table, the Graphene-Schottky junction (i.e., G/Pt/n-Si) gives the largest change in barrier height especially at low doses (as explained earlier), as compared to conventional junctions (i.e., Pt/n-Si). Meanwhile, the released electrons reduce the thickness of the depletion region resulting reverse current (I_{rev}) induced in the G-Si direction (Fig. 3a, b). The net current flow can be determined according to:

$$I_{net} = I_{fwd} - I_{rev}. \quad (5)$$

At low radiation doses, the forward current is much larger than the reverse current because half of the photon energy excites most graphene electrons to states lower than the Si conduction band (E_C). However, at higher radiation doses,

Table 1 SBH change under different irradiation doses for the three devices

Device structure	SBH ^a (eV) versus Raditaion dose				
	3 kGy	15 kGy	25 kGy	30 kGy	60 kGy
G/Pt/n-type Si	-0.0161	-0.0534	-0.0740	-0.0327	-0.0381
G/Pt/high resistivity Si	-0.2666	-0.2828	-0.2858	0.0166	0.0405
Pt/n-type Si	-0.0219	-0.0043	-0.0544	-0.0278	0.0925

^aSchottky Barrier Height

half-photon energy excites electrons to higher levels, resulting in a stronger reverse current and reducing the SBH change (Table 1) and lowers device's sensitivity.

The sensing behavior at low and high radiation doses can be summarized with the aid of Figs. 3a, b as follows: Graphene layer is p-doped as contact is established with Pt, in addition to further lowering of the graphene's Fermi level due to positive biasing. Both effects combined result in further lowering of the SBH of the junction, which results in a stronger forward current as compared to the conventional junction. In response to γ -irradiations, SBH is reduced further, resulting in a stronger forward current, whereas at the graphene interface, the half γ -photon energy is insufficient to excite the graphene electrons for interband transition, which results in a weak reverse current.

This phenomenon is also responsible for the increase in the detection range of graphene-based devices as compared to their conventional counterparts due to an increase in vacant states for the source electrons, which get saturated faster in conventional junctions under very high radiation doses (Fig. 3c).

The effect of radiation dose on the SBH for the Graphene-Schottky device at low and high doses is shown in Fig. 6. The figure clearly shows that at lower radiation doses, change in SBH is more pronounced. Further, the figure clearly shows that the change in SBH ($\Delta\Phi$) can be linearized as:

$$\Delta\Phi = \Delta\Phi_{\max}D_{\gamma}. \quad (6)$$

where, $\Delta\Phi_{\max}$ is the maximum barrier height before excitation and D_{γ} is the normalized parameter that is the function of radiation dosage, which is equal to -292×10^{-6} eV/kGy in case of low radiation doses and -1.67×10^{-4} eV/kGy in case of high radiation doses. This linear relationship between the stimulus and the change in SBH is hardly observed in conventional Schottky sensors, which adds to the advantages of the sensor described here.

It should be noted that in the set of devices in which high-resistivity (i.e., low-doped) silicon substrates ($\rho \geq 10,000 \Omega\text{cm}$) were used, the forward current became significantly lower due to the low carrier concentration. Therefore, the net current in the reverse direction is larger than in the case of a low-resistivity silicon substrate, which was verified experimentally. The authors are currently investigating new devices that incorporate graphene on lowly doped Si substrates, which will be the subject of future reports.

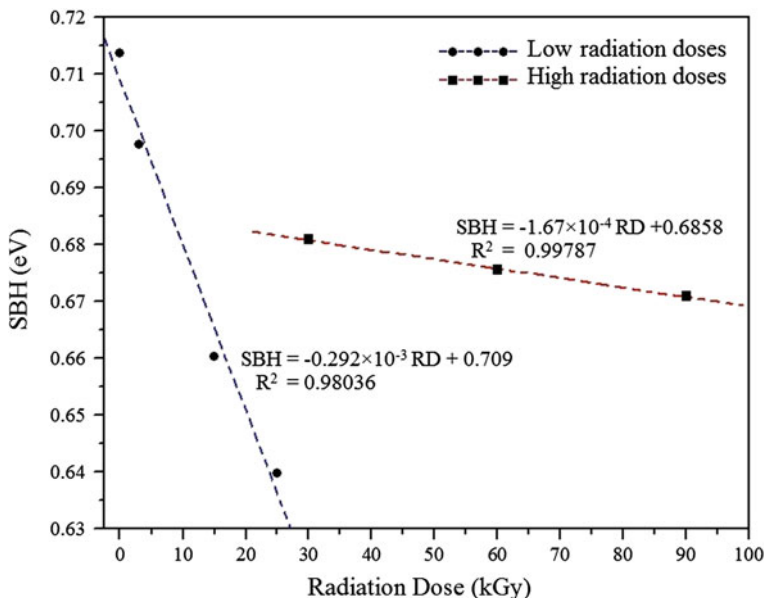


Fig. 6 Effect of Radiation Dose (RD) on Schottky Barrier Height (SBH) in low and high irradiation regimes

In the case of glucose chemical sensing, when a forward-bias voltage is applied to the Schottky diode depicted earlier, i.e., an n-type Si where the work function of Pt (i.e., 5.98 eV) is greater than that of the n-Si (4.5 eV), the contact potential is reduced. Thus, the electrons move from the conduction band across the depletion region to the metal, creating a forward current (metal to semiconductor) through the junction. The current across a Pt-n-Si junction is mainly due to majority carriers. As noted above, there are three mechanisms by which current can flow: (1) diffusion of carriers, (2) thermionic emission, and (3) quantum mechanical tunneling.

As the junction is exposed to more radiation, more bonds are broken in the Si lattice, which results in the freeing of more electrons and shifts the Fermi level up. The flowing current is increased as a result of two main effects: (i) an increase in thermionic emissions due to excess electrons in the conduction band, and (ii) an increase of the tunneling current due to a decrease in the depletion layer thickness. The sensing mechanism can be summarized as follows (Fig. 7):

As glucose molecules are adsorbed at the graphene surface, OH^- molecules adsorb on graphene surface. OH^- p-dopes graphene layer, shifting Dirac point to positive potential. OH^- molecules diffuse into the bulk of Pt metal and land on Pt/Si interface and form thin dipole layer. The barrier height is reduced by the formation of thin dipoles:

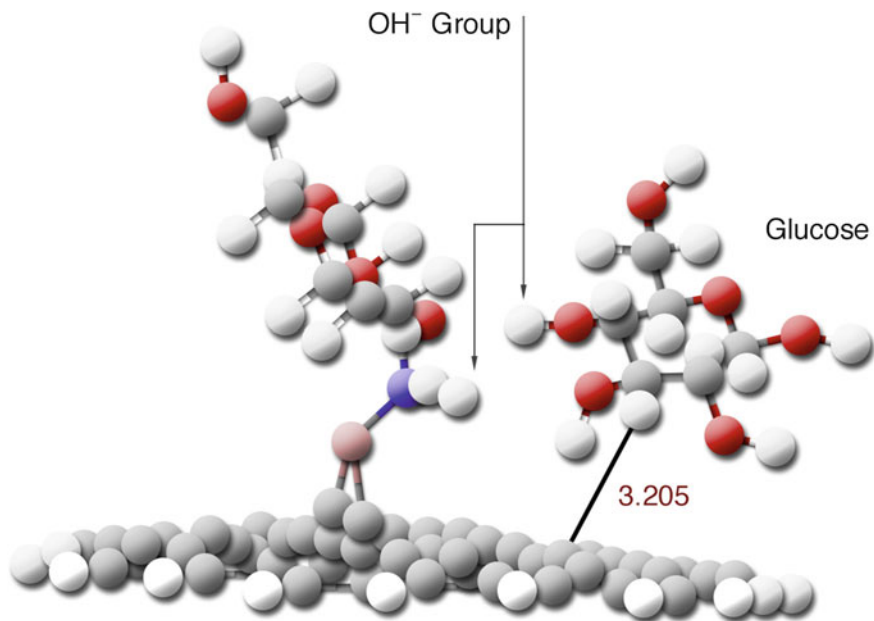


Fig. 7 Adsorption of glucose molecules on graphene surface

$$\Delta\Phi_b = \Delta\Phi_{b_{\max}} C_G. \quad (7)$$

where, $\Delta\Phi_b$ is the new barrier height, $\Delta\Phi_{b_{\max}}$ is the maximum barrier height before excitation (i.e., ~ 5.98 eV in case of Pt/n-Si), and C_G is the normalized parameter that is a function in glucose concentration, which can be determined experimentally. As a result, a net current flow can be determined according to Eq. 5, where, I_{fwd} is the forward current from the substrate to graphene direction mainly due to the thermionic effect, and I_{rev} is the reverse current flow in the direction from graphene to substrate due to electrons tunneled through the ultrathin platinum layer to the conduction band of the substrate.

In devices where low-resistivity n-type silicon were used (e^- conc. $\approx 2 \times 10^{15} \text{ cm}^{-3}$), the forward current is higher than the reverse current due to the p-doping of the graphene layer and the high mobility of the graphene holes (up to 200,000 ms/V), which results in a net current in the forward direction that is proportional to the glucose concentration, which was verified experimentally.

4 Material Development and Characterization

Three device variations were fabricated to compare their different responses (Fig. 8). Graphene high-uniformity film with small flake size embedded with platinum particles was synthesized using two deposition steps. The first deposition step of the platinum catalysis was performed in Atomic Layer Deposition (ALD) using Cambridge NanoTech Savannah ALD deposition system. The precursor used was Trimethyl (methylcyclopentadienyl) platinum (IV) with high purity O_2 used as an oxidizing agent. Deposition temperature was $275\text{ }^\circ\text{C}$ for 50–300 cycles to produce the catalysis Pt thin film of around 40–300 Å in thickness. The second deposition step utilized Plasma-Enhanced Chemical Vapor deposition (PECVD) using an Oxford Instruments Plasma Lab 100 PECVD System at $600\text{ }^\circ\text{C}$. The pressure was maintained at 1500 m Torr and the chamber was heated to $600\text{ }^\circ\text{C}$ in a methane (CH_4) rich environment.

X-ray Photo-electron Spectroscopy (XPS) characterization data were performed on a K-Alpha XPS from Thermo Scientific in the range of 1–1350 eV to inspect the surface chemistry of the Graphene. Raman spectra of the graphene thin film were obtained by Enwave Optorionics Raman Spectroscopy ($\lambda_{\text{ex}} = 532\text{ nm}$, $P = 500\text{ mW}$, acquisition time = 10 s). Atomic Force Microscopy (AFM) from Bruker, and Field Emission Scanning Electron Microscopy (FE-SEM) from Zeiss were used for structural and morphological characterizations.

The SEM images of the top view of Pt catalysis layer after ALD deposition is presented in Fig. 9b. The thickness of the film in this figure is $\sim 120\text{ \AA}$. From Fig. 9b it is observed that the Pt film is made of fairly organized hexagonal close-packed particles with diameters ranging from 30 to 40 nm. Figure 9a shows the top view image of the graphene film. It is observed from the figure that the film is made of a highly packed columnar nanostructured network close to the structure of the underlying Pt catalysis layer.

Figure 9c shows the AFM image of the graphene layer with a maximum height of 5 nm above the surface. The XPS analysis was carried out in order to investigate the elemental composition of the film. As depicted in Fig. 10a XPS survey spectra of the graphene surface shows the presence of C, with very little O_2 as a contaminant. This is evident by the C1 s peak at a binding energy of 285.11 eV and the

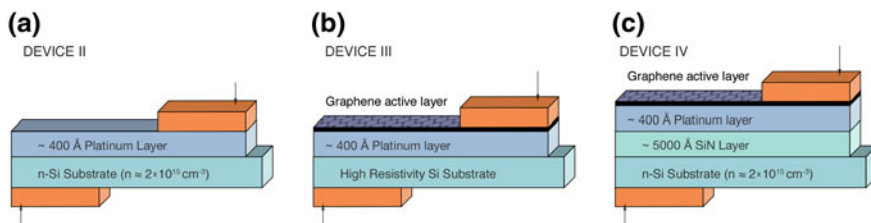


Fig. 8 Schematic of the three types of devices fabricated for comparison **a** the conventional Schottky device; **b** the high resistivity Si substrate device; and **c** graphene-platinum-SiN-Si junctions

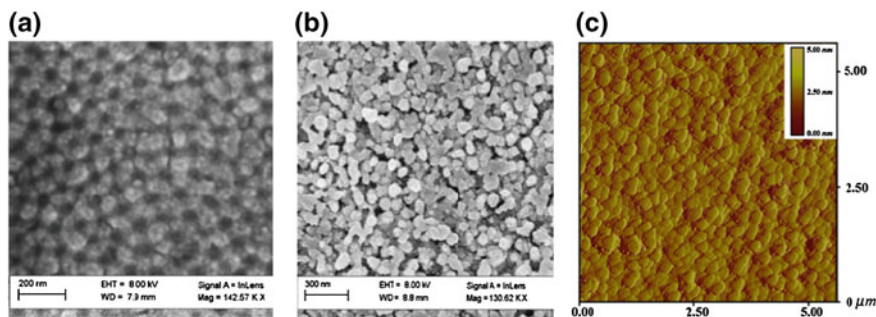


Fig. 9 **a** SEM image of graphene layer, **b** SEM image of the platinum layer, **c** AFM images of the graphene surface

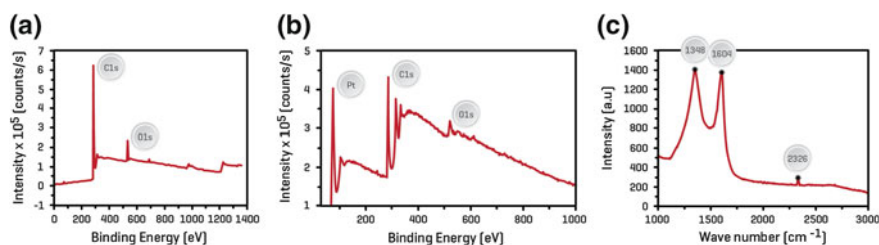


Fig. 10 **a** XPS survey of the surface, **b** XPS survey after 10 s etching, **c** Raman spectrum of the graphene surface

O1 s at a binding energy of 533 eV. It is observed that the peaks obtained were in agreement with previous reports, indicating that the film consists of graphene. Figure 10b depicts the XPS survey after etching the surface for 10 s. The peaks in this figure can be resolved into three main peaks with binding energies of 75.08 eV for Pt, 285.08 eV for C, and 520.08 eV for O₂ contaminants, respectively. The presence of Pt within the layer is the main source of p-doping of the graphene layer. Figure 10c shows the Raman spectrum of the graphene surface.

The figure displays the graphene's D, G, D+D' bands, and a slightly flat 2D band. The shift in the G band can be attributed to the doping of the graphene with the platinum layer [38, 39].

5 Experimental Setup

All the fabricated samples were subsequently irradiated with γ -photons from a cobalt 60 (Co⁶⁰) source; the irradiation dosages were adjusted through exposure times at an approximate rate of 25 min per 1 kGy. The samples were connected according to the circuit show in Fig. 11 and the I–V characteristics for different samples were

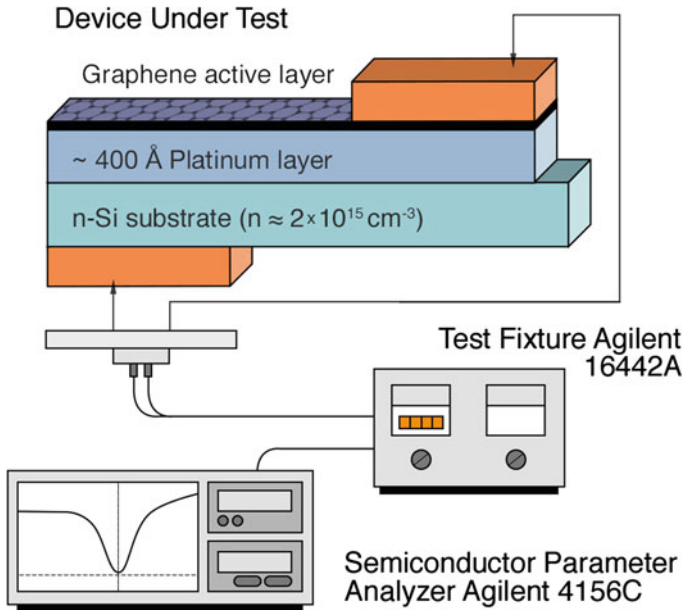


Fig. 11 Schematic of the forward and reverse currents at Pt-Si junction

measured using the 4156C high-precision semiconductor parameter analyzer before and after irradiation. All samples were irradiated with 2–5 kGy dose, then measured for their I–V characteristic and re-irradiated with another 5 kGy dose. This process was repeated several times up to a cumulative dose of 120 kGy.

6 Gamma Irradiations Sensing Behaviors

Figure 12 shows the I–V characteristics of the Graphene-Schottky device at room temperature after exposure to low (Fig. 12a) and high (Fig. 12b) radiation doses, respectively. In order to exhibit the role of the proposed structure more clearly, devices with a conventional contact were also irradiated simultaneously for comparison. These devices are referred to as Pt/n-Si devices. Comparison between the I–V curves at room temperature for the Graphene-Schottky and Pt/n-Si devices at different radiation doses are demonstrated in Fig. 13.

From the figure, it is observed that the sensors with conventional Pt/n-Si contact gave the lowest forward current value at all voltages in comparison to Graphene-Schottky contact. This is due to the high Schottky barrier height (SBH) for Pt/n-Si device and stresses the fact that the current is mainly governed by the SBH. Figure 13 clearly illustrates the advantage of our proposed device as up to an order of magnitude increase in the output current could be obtained as

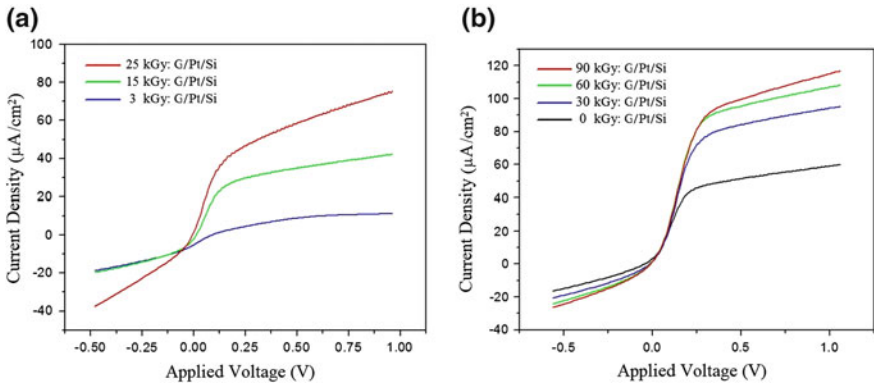
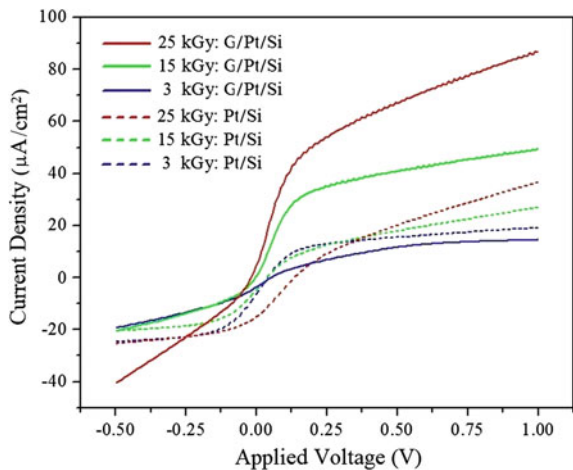


Fig. 12 I–V characteristics of Graphene-Schottky device at room temperature in response to **a** low radiation doses; **b** high radiation doses [31]

Fig. 13 Comparison of the I–V characteristics of the proposed Graphene-Schottky versus a conventional Schottky junction in response to different radiation doses clearly indicating higher output current for the proposed device [31]



compared to the conventional Pt/n-Si junction. The responses of the sensors with high resistivity Si devices after being exposed to 5 and 10 kGy of γ -irradiations are demonstrated in Fig. 14. The sensors exhibit higher output current but a significant drop in sensitivity. It is estimated that reverse current is more significant in this class of sensors.

Figure 15 shows the output current versus irradiation dose at different bias voltages for Graphene-Schottky (Fig. 15a), and Pt/n-Si (Fig. 15b) devices, respectively. The curves in Fig. 15a clearly indicate higher response at lower doses while the curves flatten at higher doses due to the increased reverse current, as discussed in the previous section. Conversely, for the conventional Pt/n-Si devices a significant drop in the current is observed at higher doses, which can be attributed to the saturation of the forward current, as described above.

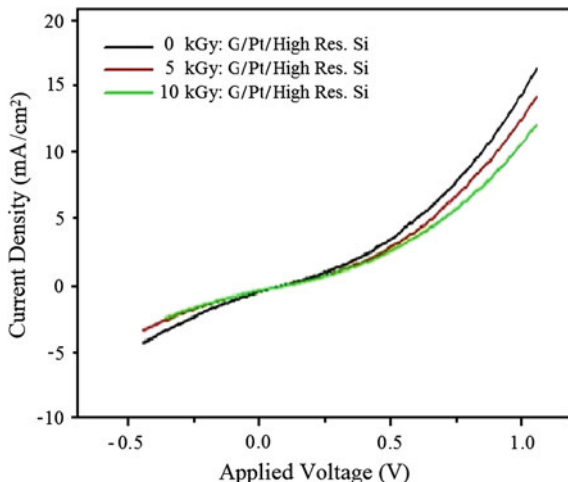


Fig. 14 I-V characteristics of the high resistivity Si substrate device at room temperature

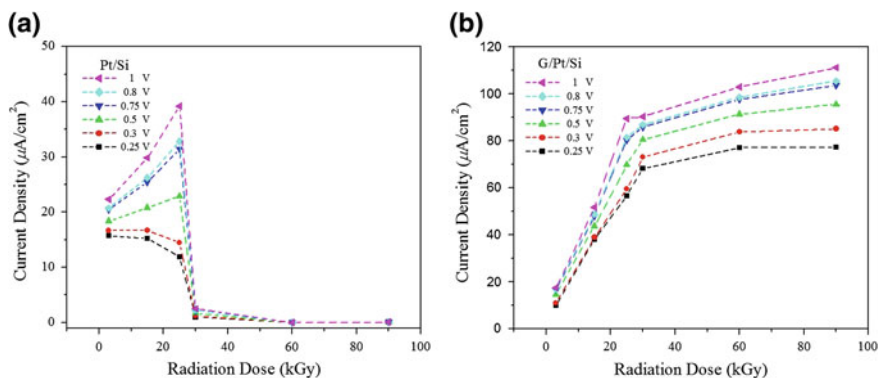


Fig. 15 Effect of radiation dose on current density at different bias voltages for **a** conventional Pt/n-Si Schottky junction, indicating insensitive response at higher radiation doses; and, **b** Graphene-Schottky devices indicating high sensitivity at higher doses [31]

Figures 16a–d demonstrate the sensitivity of the Graphene-Schottky device at low and high doses. Figures 16a, b show that a sensitivity of up to $3.259 \mu\text{A}/\text{kGy cm}^2$ at 1 V bias can be realized at low irradiation doses, while the devices are not comparably sensitive at higher doses. As shown in Figs. 16c, d, a drop in sensitivity to $0.3463 \mu\text{A}/\text{kGy cm}^2$ at 1 V bias is observed at higher radiation doses. It was demonstrated that sensitivity of the device can be linearized with respect to the applied voltage at both higher and lower doses, which is inline with the linearization in SBH that was noted earlier.

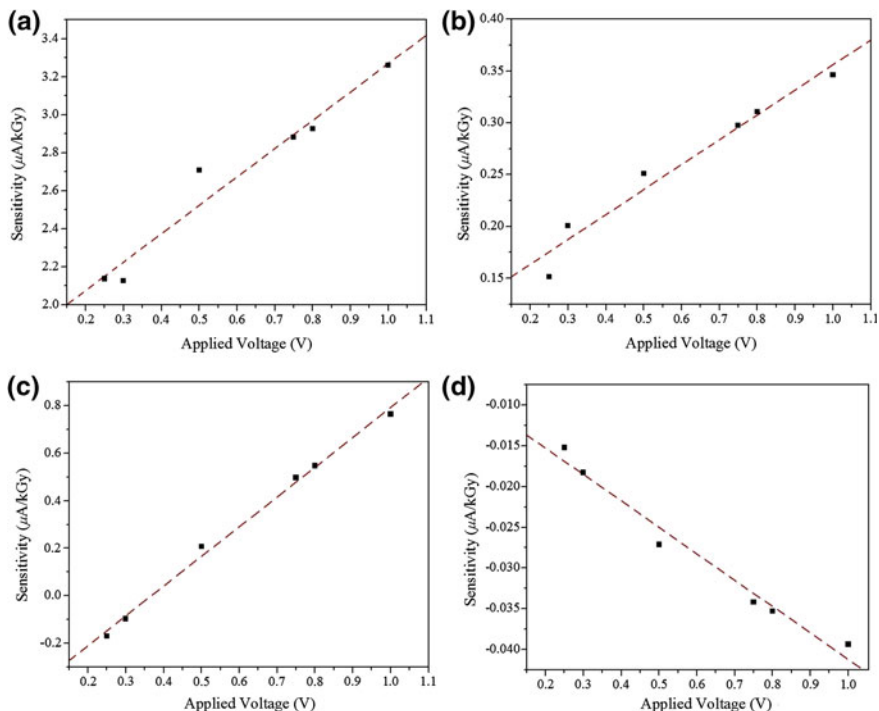


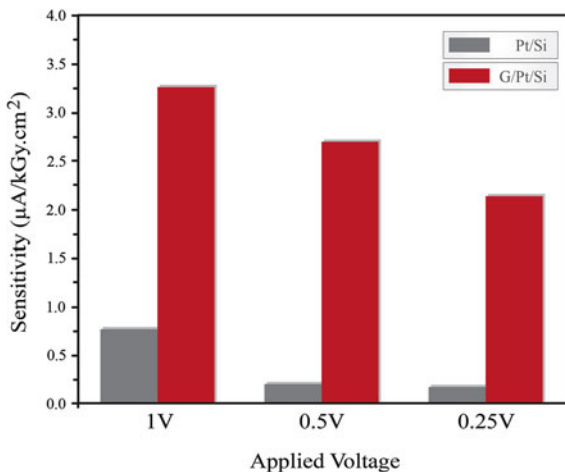
Fig. 16 Effect of Radiation Dose on output current at bias of **a** 0.25 V, low doses, **b** 1 V, low doses, **c** 0.25 V, high doses, **d** 1 V, high doses. The curves indicate Sensitivity up to 3.259 $\mu\text{A/kGy}$ in case of low radiation doses at 1 V bias voltage [31]

Several samples of each device were irradiated and re-irradiated, Fig. 17 summarizes the sensitivity of conventional schottky and graphene based schottky devices at low and high radiation doses. Study of the I–V characteristics of the devices revealed acceptable drifts that are estimated at an average of $\pm 0.2422 \mu\text{A/kGy cm}^2$ at 0.25 V and low radiation doses which is equivalent to $\sim 10.8 \%$ of the device's sensitivity at that specific bias. The average drift is estimated to be $\pm 0.2156 \mu\text{A/kGy cm}^2$ at 1 V bias, which is equivalent to $\sim 6.61 \%$ of the device's sensitivity at that specific bias. The drift can be attributed to variations in CVD and ALD processes, deposition uniformity across the Si wafer, temperature variations, and Co60 source variations.

7 Glucose Sensing Behaviors

By investigating the bonding attachment of glucose on a graphene surface, we will find that by rotating the carbon-carbon bonds to make the ring resemble a beach chair in shape, all of the carbon-carbon bonds are able to assume tetrahedral

Fig. 17 Comparing the Sensitivity of the Graphene-Schottky devices versus Pt/n-Si indicating up to 11 times enhancement of sensitivity at 0.5 and 0.25 V bias



bonding angles. This ‘chair’ conformation provides the lowest possible energy conformation for cyclohexane and other six-membered rings. Moreover, as stated in [40]: “As a general rule, the most stable chair conformation of a six-membered ring will be that in which the bulkier groups are in the equatorial position.”

The predominant solution form is shown on the right, β -D-glucopyranose (Fig. 18). The tetrahydropyran structure is common in nature, showing up most frequently in the form of sugars such as glucose. Glucose has a number of different forms that exist in equilibrium, the predominant form in aqueous solution being β -D-glucopyranose [41].

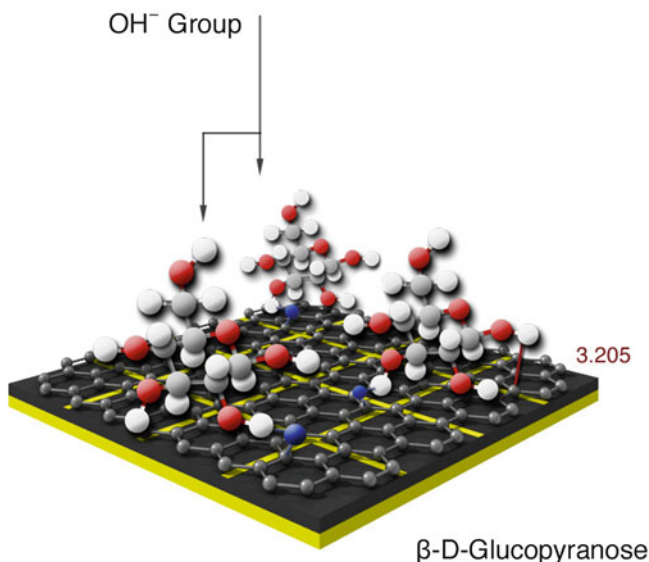


Fig. 18 Schematic of bonding between β -D-glucopyranose and the graphene surface

The anomeric effect was initially defined as the preference for an electronegative substituent, at the anomeric carbon in a carbohydrate, to be in an axial rather than equatorial orientation. A more modern definition of the anomeric effect has come to include not only carbohydrates, but also saturated heterocycles and acyclic systems containing heteroatoms. In cyclohexane, it is well known that substituents attached to the ring tend to prefer the equatorial position over the axial position due to unfavorable steric interactions in the axial conformer. However, contrary to steric predictions, electronegative substituents at the anomeric position of carbohydrates and other heterocycles have been observed to exist predominantly as the axial conformer. This phenomenon is known as the anomeric effect. In 1955, Chu and Lemieux discovered the first example of the anomeric effect. ⁴ They determined that in aldohexopyranoses the conformation with the axial orientation of the acetoxy group at position C(2) is favored.

The equilibrium between the axial and equatorial conformers lies in favor of the axial position (Fig. 19). Calculations of ΔG (kcal/mol) confirmed the equilibrium shift toward the axial position. Since the equilibrium lies opposite of the outcome predicted by sterics, researchers have used stereoelectronic arguments to rationalize the apparent anomaly in conformational selectivity. Two rationales exist that explain the origin of the anomeric effect, the electrostatic model (also known as the rabbit ear and dipole-dipole model) and the molecular orbital model (also known as the double-bond/no-bond model and hyperconjugative model) [42].

The output of the graphene schottky sensor is used as an input to the active area of an SAW device, which can be used as a wireless transmitter to a nearby central mobile device. The device continuously reports glucose blood levels. However, appropriate passive unique device identification techniques are essential. A possible

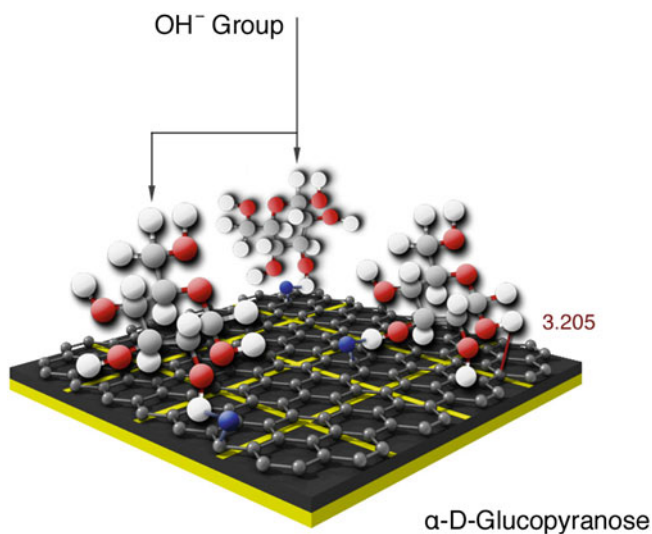


Fig. 19 Schematic of the bonding between alpha-d-glycopyranose and the graphene surface

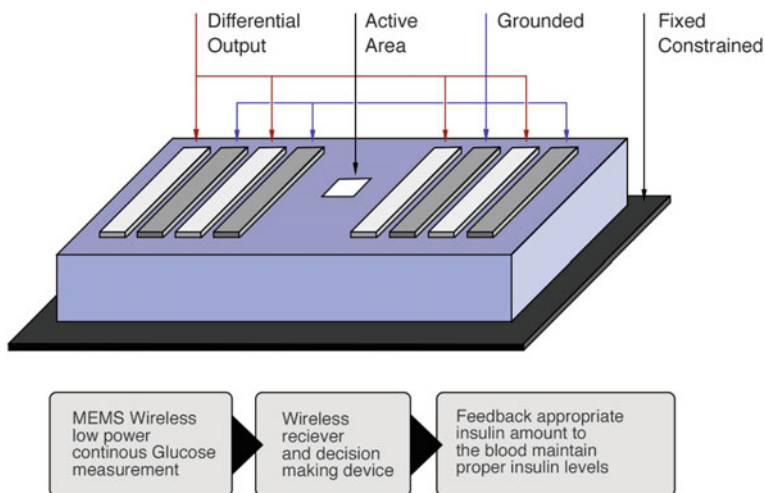


Fig. 20 Top Schematic of the Surface Acoustic Wave (SAW) device showing the active sensing area containing Graphene-SBD structure active sensing material, Bottom Autonomous insulin feedback system scheme adopted in this research

technique would be using uniquely spaced reflector slots for each device, thus forming a unique code via decoding received RF wave phase differences [43]. The SAW platform was numerically simulated using COMSOL™ with a Lithium Niobate (LiNbO_3) substrate as the piezoelectric substrate (Fig. 20). LiNbO_3 was chosen for the piezoelectric substrate because of its high SAW propagation velocity of 4792 m/s and large electromechanical coupling factor. The experimental measurements of the Graphene/PT response to Glucose are shown in Figs. 21a, b, the

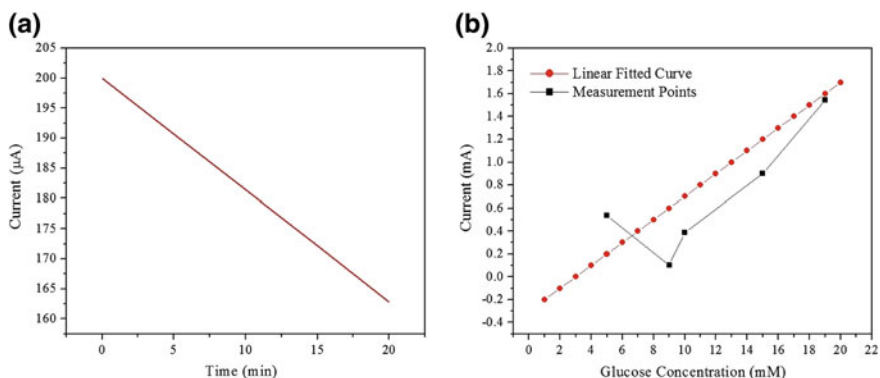
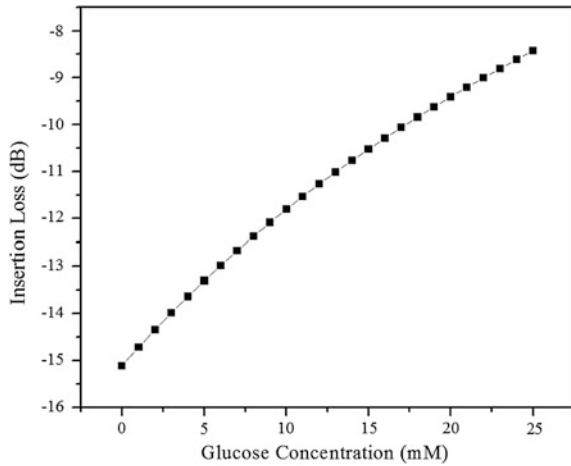


Fig. 21 a Graphene-SBD transient response (current difference) to 25 mM glucose concentration at room temperature, b Graphene-SBD current versus glucose concentration response at room temperature after 5 min

Fig. 22 Device sensitivity (SAW Insertion loss vs. Glucose Concentration), Average Sensitivity = 0.268 dB/m



linear fit equation of electrical current versus glucose concentration was used as the input to the simulation model. The measurement output of Graphene/Pt response to glucose drops of different concentrations was fitted into a linear Equation (Eq. 7).

The final Sensitivity of the graphene/PT device coupled with the SAW platform is demonstrated in Fig. 22. Average Sensitivity = 0.268 dB/mM for the range of 0–25 mM of Glucose concentrations.

8 Conclusion

In this chapter, we have described and demonstrated two examples of graphene-based physical and chemical sensors with numerous practical applications. A new device concept has been demonstrated for achieving highly sensitive and wide detection range nanostructured radiation sensors by integrating Graphene to a Schottky junction. The key idea is that the current flowing through the Schottky junction is dominantly controlled by the junction's characteristics (i.e., SBH, and barrier's width), which is highly sensitive to the stimuli around the junction, such as γ -photons in our case. We have demonstrated an overall enhancement in sensitivity of up to 11 times and detection range of more than 5 times as compared to conventional Schottky junctions. It was further demonstrated that our proposed device's SBH modulation could be linearized as a function in the radiation dose unlike conventional junctions, which further demonstrates that this sensing principle can be effective in sensing other sorts of radiations or other biochemical species. The proposed sensor operates on low power, is isotropic (i.e., independent of the radiation exposure angle), easy to fabricate, can operate wirelessly, and can be seamlessly integrated in wearable detection devices for ultrahigh sensitivity online monitoring of γ -radiations. Finally, a new set of devices based on Graphene-MIS

(i.e., Metal-Insulator-Semiconductor) and Graphene/Pt/high resistivity Si are currently under investigation by the authors and will be the subjects of further reports. The sensing methodology introduced here, together with ongoing research and further development, will result in devices that can be used in a wide range of applications, including biochemical, gas, infrared, and temperature sensors.

References

1. J.F. Creemer, S. Helveg, P.J. Kooyman, A.M. Molenbroek, H.W. Zandbergen, P.M. Sarro, A MEMS Reactor For Atomic-Scale Microscopy Of Nanomaterials Under Industrially Relevant Conditions. *J. Microelectromech. Syst.* **16**(2), 254–264 (2010)
2. X. Zang, Q. Zhou, J. Chang, Y. Liu, L. Lin, Graphene and carbon nanotube (CNT) in MEMS/NEMS applications. *Microelectron. Eng.* **132**, 192–206 (2015)
3. L.F. Velasquez-Garcia, B.L.P. Gassend, A.I. Akinwande, CNT-Based MEMS/NEMS gas ionizers for portable mass spectrometry applications. *J. Microelectromech. Syst.* **16**(3), 484–493 (2010)
4. Z. Hou, J. Wu, W. Zhou, X. Wei, D. Xu, Y. Zhang, B. Cai, A MEMS-based ionization gas sensor using carbon nanotubes. *IEEE Trans. Electron. Devices* **54**(6), 1545–1548 (2007)
5. H. Chen, N. Xi, B. Song, L. Chen, J. Zhao, K.W.C. Lai, R. Yang, Infrared camera using a single nano-photodetector. *IEEE Sens. J.* **13**(3), 949–958 (2013)
6. M. Lapisa, G. Stemme, F. Niklaus, Skolan för elektro- och systemteknik (EES), KTH & Mikrosystemteknik (Bytt namn 20121201), “Wafer-level heterogeneous integration for MOEMS, MEMS, and NEMS”. *IEEE J. Sel. Top. Quantum Electron.* **3**(3), 629–644 (2011)
7. J. Han, P. Cheng, H. Wang, C. Zhang, J. Zhang, Y. Wang, L. Duan, G. Ding, MEMS-based Pt film temperature sensor on an alumina substrate. *Mater. Lett.* **125**, 224–226 (2014)
8. C. Hierold, A. Jungen, C. Stampfer, T. Helbling, Nano electromechanical sensors based on carbon nanotubes. *Sens. Actuators, A* **136**(1), 51–61 (2007)
9. J. Pekarek, R. Vrba, J. Prasek, O. Jasek, P. Majzlikova, J. Pekarkova, L. Zajickova, MEMS carbon nanotubes field emission pressure sensor with simplified design: performance and field emission properties study. *IEEE Sens. J.* **15**(3), 1430–1436 (2015)
10. S. Wang, C. Hsiao, S. Chang, K. Lam, K. Wen, S. Young, S. Hung, B. Huang, CuO nanowire-based humidity sensor. *IEEE Sens. J.* **12**(6), 1884–1888 (2012)
11. E. Comini, C. Baratto, G. Faglia, M. Ferroni, A. Ponzoni, D. Zappa, G. Sberveglieri, Metal oxide nanowire chemical and biochemical sensors. *J. Mater. Res.* **28**(21), 2911 (2013)
12. S. Xi, T. Shi, D. Liu, L. Xu, H. Long, W. Lai, Z. Tang, Integration of carbon nanotubes to three-dimensional C-MEMS for glucose sensors. *Sens. Actuators, A* **198**, 15 (2013)
13. R. MacKenzie, C. Fraschina, T. Sannomiya, V. Auzelyte, J. Vörös, Optical sensing with simultaneous electrochemical control in metal nanowire arrays. *Sens. (Basel, Switz.)* **10**(11), 9808–9830 (2010)
14. S.J. Patil, A. Zajac, T. Zhukov, S. Bhansali, Ultrasensitive electrochemical detection of cytokeratin-7, using Au nanowires based biosensor. *Sens. Actuators: B. Chem.* **129**(2), 859–865 (2008)
15. L. Wang, H. Dou, Z. Lou, T. Zhang, Encapsulated nanoreactors (Au@SnO₂): a new sensing material for chemical sensors. *Nanoscale* **5**(7), 2686 (2013)
16. A. Lajn, H.v. Wenckstern, Z. Zhang, C. Czekalla, G. Biehne, J. Lenzner, H. Hochmuth, M. Lorenz, M. Grundmann, S. Wickert, C. Vogt, R. Denecke, Properties of reactively sputtered Ag, Au, Pd, and Pt Schottky contacts on n-type ZnO. *J. Vac. Sci. Technol. B* **27**, 1769–1773 (2009)
17. I. Weber, Influence of noble metals on the structural and catalytic properties of Ce-doped SnO₂ systems. *Sens. Actuators B: Chem.* **97**(1), 31–38 (2004)

18. L. Wang, Z. Lou, R. Wang, T. Fei, T. Zhang, Ring-like PdO-decorated NiO with lamellar structures and their application in gas sensor. *Sens. Actuators B: Chem.* **171–172**, 1180–1185 (2012)
19. A. Rani, A.S. Zoofakar, J.Z. Ou, R. Ab Kadir, H. Nili, K. Latham, S. Sriram, M. Bhaskaran, S. Zhuiykov, R.B. Kaner, K. Kalantar-zadeh, Reduced impurity-driven defect states in anodized nanoporous Nb₂O₅: the possibility of improving performance of photoanodes. *Chem. Commun.* **49**, 6349–6351 (2013)
20. G. Ramírez, S.E. Rodil, S. Muhl, D. Turcio-Ortega, J.J. Olaya, M. Rivera, E. Camps, L. Escobar-Alarcón, Amorphous niobium oxide thin films. *J. Non-Cryst. Solids* **356(50)**, 2714–2721 (2010)
21. M. Lopez-Garcia, Y.-L.D. Ho, M.P.C. Taverne, L.-F. Chen, M.M. Murshidy, A.P. Edwards, M.Y. Serry, A.M. Adawi, J.G. Rarity, R. Oulton, Efficient out-coupling and beaming of Tamm optical states via surface plasmon polariton excitation. *Appl Phys Lett* **104(23)**, 231116 (2014)
22. X. Fang, L. Hu, K. Huo, B. Gao, L. Zhao, M. Liao, P.K. Chu, Y. Bando, D. Golberg, New ultraviolet photodetector based on individual Nb₂O₅ nanobelts. *Adv. Funct. Mater.* **21**, 3907–3915 (2011)
23. J.Z. Ou, R.A. Rani, M.-H. Ham, M.R. Field, Y. Zhang, H. Zheng, P. Reece, S. Zhuiykov, S. Sriram, M. Bhaskaran, R.B. Kaner, K. Kalantar-zadeh, Elevated temperature anodized Nb₂O₅: a photoanode material with exceptionally large photoconversion efficiencies. *ACS Nano* **6**, 4045–4053 (2012)
24. A. Reina, X.T. Jia, J. Ho, D. Nezich, H. Son, V. Bulovic, M.S. Dresselhaus, J. Kong, Large-scale arrays of single layer graphene resonators. *Nano Lett.* **9(8)**, 3087 (2009)
25. K. Keun Soo, Y. Zhao, H. Jang, S.Y. Lee, J.M. Kim, K.S. Kim, J.-H. Ahn, P. Kim, J.-Y. Choi, B.H. Hong, Large-scale pattern growth of graphene films for stretchable transparent electrodes. *Nature* **457(7230)**, 706–710 (2009)
26. X.S. Li, W.W. Cai, J.H. An, S. Kim, J. Nah, D.X. Yang, R. Piner, A. Velamakanni, I. Jung, I. E. Tutuc, S. K. Banerjee, L. Colombo, R. S. Ruoff. *Science* **324(1312)**, 14 (2009)
27. X. Li, G. Zhang, X. Bai, X. Sun, X. Wang, E. Wang, H. Dai, Highly conducting graphene sheets and Langmuir-Blodgett films. *Nat. Nanotechnol.* **3(9)**, 538–542 (2008)
28. Y. Hernandez, V. Nicolosi, M. Lotya, F. Blighe, Z. Sun, De Sukanta, I.T. McGovern et al., High-yield production of graphene by liquid-phase exfoliation of graphite. *Nat. Nanotechnol.* **3(9)**, 563–568 (2008)
29. A. Sharaf, A. Gamal, M. Serry, New nanostructured Schottky diode gamma-ray radiation sensor. *Procedia Eng.* **87**, 1184–1189 (2014)
30. M. Serry, A. Gamal, M. Shaban, A. Sharaf, High sensitivity optochemical and electrochemical metal ion sensor. *Micro & Nano Lett* **8(11)**, 775–778 (2013)
31. M. Serry, A. Sharaf, A. Emira, A. Abdul-Wahed, A. Gamal, Nanostructured graphene-Schottky junction low-bias radiation sensors. *Sens. Actuators A: Phys.* (2015). [10.1016/j.sna.2015.04.031](https://doi.org/10.1016/j.sna.2015.04.031)
32. A. Sharaf, A. Gamal, M. Serry, High performance NEMS ultrahigh sensitive radiation sensor based on platinum nanorods capacitor, *IEEE Sensors 2013*, Baltimore, USA, 3–6 Nov 2013
33. C. Malatesta, F. Palmisano, L. Torsi, P.G. Zambonin, Glucose fast-response amperometric sensor based on glucose oxidase immobilized in an electropolymerized poly(o-phenylenediamine) film. *Anal. Chem.* **62(24)**, 2735 (1990)
34. B.J. White, H. James Harmon, Novel optical solid-state glucose sensor using immobilized glucose oxidase. *Biochem. Biophys. Res. Commun.* **296(5)**, 1069–1071 (2002)
35. S. Park, T.D. Chung, S.K. Kang, R. Jeong, H. Boo, H.C. Kim, Glucose sensor based on glucose oxidase immobilized by zirconium phosphate. *Anal. Sci.: Int. J. Jpn. Soc. Anal. Chem.* **20(12)**, 1635 (2004)
36. M. Mathew, N. Sandhyarani, A highly sensitive electrochemical glucose sensor structuring with nickel hydroxide and enzyme glucose oxidase. *Electrochim. Acta* **108**, 274–280 (2013)
37. S.M. Sze, K.K. Ng, *Physics of Semiconductor Device* (Wiley, New York, 2006)
38. M. Shaban, A.G.A. Hady, M. Serry, A New Sensor for Heavy Metals Detection in Aqueous Media, *IEEE Sensors J* **14(2)**, 436–441 (2014). [10.1109/JSEN.2013.2279916](https://doi.org/10.1109/JSEN.2013.2279916)

39. V. Yu, E. Whiteway, J. Maassen, M. Hilke, Raman spectroscopy of the internal strain of a graphene layer grown on copper tuned by chemical vapor deposition. *Phys. Rev. B* **84**(20), 205407 (2011)
40. UC Davis Organic Chem, http://chemwiki.ucdavis.edu/Organic_Chemistry/Organic_Chemistry_With_a_Biological_Emphasis/Chapter_03%3A_Conformations_and_Stereochemistry/Section_3.2%3A_Conformations_of_cyclic_organic_molecules. Accessed 31 Jan 2015
41. CSBSJU.edu, <http://employees.csbsju.edu/cschaller/Principles%20Chem/conformation/conf%20otherB.htm>. Accessed 1 Feb 2015
42. R.U. Lemieux, P. Chu, *Conformations and Relative Stabilities of Acetylated Sugars as Determined by Nuclear Magnetic Resonance Spectroscopy and Anomerization Equilibria*. Abstracts of Papers, (133rd National Meeting of the American Chemical Society, San Francisco, CA, American Chemical Society: Washington, DC, 1958, 31N)
43. F. Schmidt, O. Sczesny, C. Ruppei, V. Magori, Wireless interrogator system for SAW-identification marks and SAW-sensor components, in *IEEE International Frequency Control Symposium*, Honolulu, 1996

Design and Realization of a Planar Interdigital Microsensor for Biological Medium Characterization

T.-T. Ngo, A. Bourjilat, J. Claudel, D. Kourtiche and M. Nadi

Abstract In this work, we present the design of a planar interdigital microsensor for the characterization of biological mediums by impedance spectroscopy. We propose a theoretical optimization of the geometrical parameters of this sensor. The optimization allows to extend the measurement frequency range by reducing the polarization effect which is manifested by a double layer (DL). We present also a new method for a planar interdigital transducer to determine the parameters (relative permittivity, capacitance) of the double layer (DL) on the surface of the electrode loaded by a biological medium. The CoventorWare[®] software was used to simulate the model design of interdigital transducer in three dimensions (3D). The simulation results are coherent with the method proposed. Therefore, this method can be used to determine the parameters of double layers of a planar interdigital sensor in order to match its frequency band to the intended application.

1 Introduction

Public health problems related to the electromagnetic (EM) interactions with living matter as well as therapeutical or diagnostic aims based on these interactions could take benefit from bioimpedance spectroscopy for the determination of dielectric properties of biological tissues.

It is well known that the dielectric and conductive properties of biological medium depend on frequency. However, their determination is difficult for several reasons (heterogeneity and anisotropy of tissue, difficult access, ... etc.). Biofluids for example have very complex and difficult to determine electrical properties, because of their composition and their structure. Then, using bioimpedancemetry and an equivalent electric circuit we can deduce the conductivity and the permit-

T.-T. Ngo · A. Bourjilat · J. Claudel · D. Kourtiche (✉) · M. Nadi
Institut Jean Lamour, Université de Lorraine - CNRS,
UMR 7198 Vandœuvre-lès-Nancy, France
e-mail: djilali.kourtiche@univ-lorraine.fr

tivity of the medium. Consequently, the spectroscopy of bio-impedance allows us to obtain a data bank of the values of the specific conductivity and the permittivity of biologic tissues. The bio-impedance macroscopic measurement techniques were used to characterize several organs, to characterize nerve tissues [1]. Microscopic techniques were developed since the 90s for biological cell level for the blood and the erythrocytes [2], to study suspensions of cells in the culture [3], the culture of the dependent cells of anchoring [4], etc.

Numerous structures and design of microelectrodes were developed for microscopic spectroscopy of bio-impedance. Borkholder used planar electrodes by developing his own measurement system [5]. Heushkel measured electric impedances with electrodes designed to penetrate into an *in vitro* culture of neurons [6]. Popovtzer realized a device, including eight systems of three micrometric electrodes arranged at the bottom of micro-basins [7], etc. Since the early 70s, many researchers have studied and published on sensors with planar interdigital structure for various applications like surface acoustic wave devices (SAW) [8], the design of microwave filters [9], optically controlled microwave devices [10], etc. More recently, the planar interdigital sensors were used notably in biomedical applications such as: bio-impedance Spectroscopy [11–14] and impedimetric biosensing [15], to detect *Salmonella typhimurium* [16] or *Escherichia coli* O157:H7 in food samples [17], avian influenza virus H5N1 [18], to assess different chemicals related to food poisoning [19], to study the cellular activities of B16 melanoma cell line C57BL or the flow of a fluid [20], to detect and characterize cancer cells [21], to study the humidity of the skin and the detection of the humidity of environment [22], to improve the tanning process of sheep skin to produce better quality leather [23], to determine the conductivities of near-surface material [24], electroplate materials [25], etc.

The use of the interdigital coplanar sensors gives the advantage of fast measurement process and its compatibility for a continuous operation [26]. An additional advantage is that it is also non-destructive and non-intrusive; the tested samples are not destroyed. When an electric voltage is applied to the sensor loaded by a biological medium double layer (DL) appears at the interface between the electrodes and the medium. This result on an additional interface impedance that is necessary to reduce as much as possible. For this reason, the precise determination of double layer's parameters is important in order to allow us to optimize the geometric structure of the interdigital sensor and, thus, to reduce the interface impedance.

The geometry of a sensor is one among the parameters to optimize bio-impedance measurements. Pejic [27] pointed out that the optimized structure of a sensor is one of the most crucial steps in the realization of a bio-impedance measurement device. Pejic's experiments were performed to optimize electrode design for various applications. Igraja and Dias [28] have represented new analytical expressions for the capacitance between two comb electrodes of a periodic interdigital capacitive sensor based on conformal mapping techniques. The effect of the interdigitated electrode geometry (electrode width and spacing) and electro ceramic substrate thickness on the developed strain for bulk PZT substrates was modeled by Bowen [29]. They have described in detail the optimization of interdigitated electrodes for

piezoelectric actuators and active fibre composites. Alexander [21] have optimized an interdigital sensor for impedance based evaluation of HS 578T cancer cells. Wang et al. [30] have determined the sensitivity and frequency characteristics of coplanar electrical cell–substrate impedance sensors. All these microelectrodes optimizations were made for specific applications.

In this work, we present a new approach of physical and electrical modeling system of a planar interdigital microsensor. We propose a theoretical optimization of the sensor’s geometrical parameters by developing total impedance equations and modeling equivalent circuits. Furthermore, this work demonstrates a theoretical calculation to determine the relative permittivity, thickness and capacitance parameters of the double layer generated by the contact between the electrodes and the solutions. The electrical and physical models of an interdigital sensor were designed using ConvectorWare[®] software. In the following, we studied the influence of the biological medium’s physical properties on the frequency sensor response. Moreover, this research also describes the correlation between the design parameters and the frequency behavior in coplanar impedance sensors.

2 Theoretical Analysis and Optimization

2.1 Basic Concepts and Definitions of the Dielectric Material

Basically, the dielectric theory is explained starting from the concept of the electrical capacitor. In a capacitor, the electrical properties of the dielectric material are maintained between two planar parallels electrodes are characterized by the capacitance (C) and the conductance (G) corresponding (see Fig. 1). When an electric voltage is applied between the electrodes, the C and the G can be determined by the following equations:

$$C = A \cdot C_0 \text{ with } C_0 = \frac{\epsilon_0 \epsilon_r}{d} \tag{1}$$

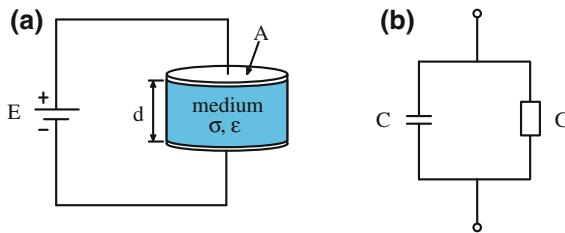


Fig. 1 **a** Dielectric biological medium between two metallic plates. **b** Equivalent circuit of a capacitor with a conductor

$$G = A \frac{\sigma}{d} \quad (2)$$

where, A is the surface of the planar electrodes (μm^2); d is the distance between the electrodes (μm); σ is the electrical conductivity of biological medium (S/m); ϵ_0 is the permittivity of vacuum and equal to $\epsilon_0 = 8.8542 \times 10^{-6}$ (pF/ μm^2); ϵ_r is the relative permittivity of biological medium; C_0 is the capacitance per unit area (pF/ μm^2).

It is well known that when a metal electrode is immersed into a biological medium, a double layer is formed at contact interface between electrode and biological medium. The determination of the parameters (relative permittivity, thickness) of double layer is necessary to obtain impedance measurement, which provides us with opportunity to calculate the relative permittivity and the electrical conductivity of biological medium. Furthermore, the capacitance per unit area (C_0) of the DL can be calculated by Eq. (1). According to Pajkossy [31] the capacitance per unit area C_0 of single crystal Pt(111) surface is similar to other metals, C_0 is approximately equal to 0.2 (pF/ μm^2).

In the work of Stern, the Gouy-Chapman model and the Helmholtz model are combined together [31–33]. Thus, the C_0 is the series combination of both capacitances ($C_{0,H}$ and $C_{0,G}$):

$$\frac{1}{C_0} = \frac{1}{C_{0,H}} + \frac{1}{C_{0,G}} \quad (3)$$

where, $C_{0,H}$ is the Helmholtz's capacitance per unit area (pF/ μm^2) and $C_{0,G}$ is the capacitance of Gouy-Chapman's model per unit area (pF/ μm^2). For most physiological systems, according to Borkholder [32], Bard and Faulkner [33], the value of $C_{0,H}$ is around 0.14 (pF/ μm^2) and $C_{0,G} = 0.07$ (pF/ μm^2). Hence, $C_0 = 0.047$ (pF/ μm^2).

2.2 Model of the Equivalent Electric Circuit

Figure 2 represents the schematic of the sensor's structure and its geometrical parameters. The equivalent electric circuit is adopted for the sensor immersed in a biological medium and is represented on Fig. 3.

Two metallic electrodes form the interdigital sensor with a comb shape, and each electrode has a width W (μm), a length L (mm) of electrodes and a distance between two consecutive electrodes S (μm). This sensor is deposited on a substrate.

The various components of biological impedance Z in this circuit is described by the electric components C_{sol} and R_{sol} . Where, the capacity of the solution is represented by the capacitance C_{sol} ; and the resistance R_{sol} describes the conductive properties of the solution under the influence of an electric field is described and is the resistance of the electrolyte solution.

Fig. 2 Geometrical structure of an interdigital sensor

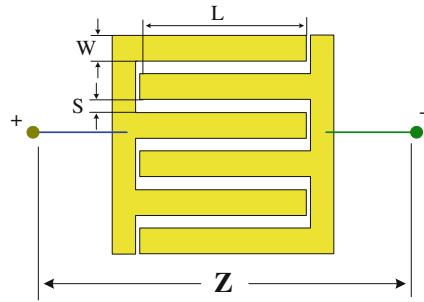
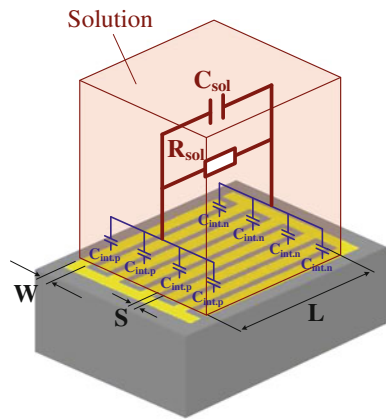


Fig. 3 Equivalent circuit model of an interdigital sensor. The C_{sol} , R_{sol} present the dielectric properties of the bio fluids, and $C_{int,p}$, $C_{int,n}$ indicate the properties of the double layer



According to Olthuis [34, 35], the R_{sol} is related to the conductivity σ_{sol} of the biological medium and the cell factor K_{cell} which depends completely on the geometry of the sensor according to the following formulas:

$$R_{sol} = \frac{K_{cell}}{\sigma_{sol}} \tag{4}$$

$$K_{cell} = \frac{2}{L(N - 1)} \cdot \frac{K(k)}{K(\sqrt{1 - k^2})} \tag{5}$$

where : σ_{sol} is the electric conductivity of the biological medium (S/m), N is the number of the electrodes of the sensor, L is the length of an electrode (mm), W is the width of an electrode (μm), S is the distance between two consecutive electrodes (μm), K_{cell} is the factor of cell (m^{-1}).

The function $K(k)$ is the complete elliptic integral of first kind given by the following formula:

$$K(k) = \int_0^1 \frac{1}{\sqrt{(1-t^2)(1-k^2t^2)}} dt \quad \text{where: } k = \cos\left(\frac{\pi}{2} \cdot \frac{W}{S+W}\right); \quad (6)$$

Let $\alpha = W/(S + W)$, α is the metallization ratio (for example $\alpha = 0.7$ means that 70 % metallization). Therefore, we have: $k = \cos\left(\frac{\pi}{2} \cdot \alpha\right)$.

2.3 Impedance Interface (Polarization Impedance)

In Fig. 3, the capacitance at the contact surface of each positive electrode with the biological medium is represented by the capacitance $C_{\text{int-p}}$; and the capacitance at the contact surface of a negative electrode with the solution is represented by the capacitance $C_{\text{int-n}}$. They are determined by:

$$C_{\text{int-p}} = C_{\text{int-n}} = A \cdot C_0 = LW \cdot C_0 \quad (7)$$

where, A is the surface of the each electrodes (μm^2); C_0 is the capacitance per unit area ($\text{pF}/\mu\text{m}^2$).

Since the number of negative electrodes and the number of positive electrodes are the same ($N/2$) in parallel, the total capacitance in the negative electrode and the positive electrode is calculated by:

$$\frac{N}{2}C_{\text{int-p}} = \frac{N}{2}C_{\text{int-n}} \quad (8)$$

Thus, the total capacitance at the contact surface of the sensor is determined by:

$$C_{\text{interface}} = \frac{N}{4}LWC_0 \quad (9)$$

The polarization appears at the contact surface between electrodes and solutions, it is a cause of measurement errors at low-frequency. The impedance of polarization is determined by the following expression:

$$Z_p = \frac{1}{j\omega C_{\text{interface}}} \quad (10)$$

2.4 Impedance of the Solution

We know that for a linear, homogeneous and isotropic material medium, the impedance depends not only on its electrical properties (conductivity and

permittivity), but also on the cell factor of the sensor K_{cell} [36, 37]. The impedance and the admittance are described by the following expressions:

$$\begin{cases} Z = \frac{K_{\text{cell}}}{\sigma_{\text{sol}} + j\omega\epsilon_0\epsilon_r} \\ Y = G + j\omega C \end{cases} \Rightarrow \begin{cases} G = \frac{\sigma}{K_{\text{cell}}} \\ C = \frac{\epsilon_0\epsilon_r}{K_{\text{cell}}} \end{cases} \quad (11)$$

where, j is the imaginary symbol, ω is the angular pulsation (rad/s), Z is the complex impedance (Ω), Y is the complex admittance (S), G is the conductance (S), C is the capacitance (F).

On the other hand, the total impedance and the total admittance in the equivalent electric circuit (see Fig. 3) are calculated by:

$$\begin{cases} Z = \frac{1}{G_{\text{sol}} + j\omega C_{\text{sol}}} + \frac{1}{j\omega C_{\text{interface}}} \\ Y = \frac{1}{Z} = G + j\omega C \end{cases} \quad (12)$$

By simplifying the Eq. (12), the capacitance C can be determined as presented below:

$$C = \frac{C_{\text{interface}}G_{\text{sol}}^2 + \omega^2 C_{\text{sol}}C_{\text{interface}}(C_{\text{sol}} + C_{\text{interface}})}{G_{\text{sol}}^2 + \omega^2(C_{\text{sol}} + C_{\text{interface}})^2} \quad (13)$$

From (13), where ω is approximately zero, the value of the total capacitance (C) can be determined by:

$$\lim_{\omega \rightarrow 0} C = C_{\text{interface}} \quad (14)$$

The Eq. (15) is the result of the substitution C from (11) and $C_{\text{interface}}$ from (9) in (14):

$$\frac{\epsilon_0\epsilon_{r,\text{low_frequency}}}{K_{\text{cell}}} = \frac{N}{4}LWC_0 \Rightarrow C_0 = \frac{4\epsilon_0\epsilon_{r,\text{low_frequency}}}{NLWK_{\text{cell}}} \quad (15)$$

From the Eq. (15), we observe that the value of C_0 depends not only on the relative permittivity of the low frequency $\epsilon_{r,\text{low_frequency}}$, but also depends on the sensor dimensions (N , L , W and K_{cell}). Therefore, the parameters of the double layer ($\epsilon_{r,\text{DL}}$ and d_{DL}) are determined according to Fig. 4.

The relative permittivity or dielectric constant of blood at low frequency is approximately equal to 5300 decreasing around 60 at high frequency [39]. Consequently, the capacitance per unit area C_0 is determined by formula (9). The parameters of the double layer and the capacitance per unit are indicated C_0C_0 in Table 1.

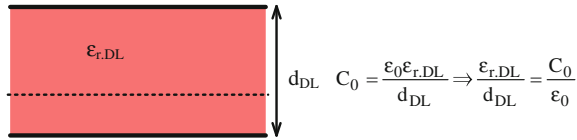


Fig. 4 Parameters of double-layer

Table 1 Parameters of interdigital sensors and DL

N	W (μm)	S (μm)	K_{cell} (m^{-1})	C_0 ($\text{pF}/\mu\text{m}^2$)	$\epsilon_r \cdot \text{DL}/d_{\text{DL}}$ (μm^{-1})
10	120	80	94.4502	8.3×10^{-4}	93.52
12	100	66.667	77.2774	1.0×10^{-3}	114.31
14	85.71	57.143	65.3886	1.2×10^{-3}	135.09
16	75	50	56.6701	1.4×10^{-3}	155.87
18	66.67	44.444	50.003	1.6×10^{-3}	176.66
20	60	40	44.74	1.7×10^{-3}	197.44
22	54.55	36.364	40.4786	1.9×10^{-3}	218.22
24	50	33.333	36.9588	2.1×10^{-3}	239
26	46.15	30.769	34.0021	2.3×10^{-3}	259.79
28	42.86	28.571	31.4834	2.5×10^{-3}	280.57
30	40	26.667	29.3121	2.7×10^{-3}	301.35
32	37.5	25	27.421	2.9×10^{-3}	322.14
34	35.29	23.529	25.7591	3.0×10^{-3}	342.92
36	33.33	22.222	24.2872	3.2×10^{-3}	363.7
38	31.58	21.053	22.9744	3.4×10^{-3}	384.49
40	30	20	21.8	3.6×10^{-3}	405
42	28.57	19.048	20.733	3.8×10^{-3}	426.05
44	27.27	18.182	19.7686	4.0×10^{-3}	446.84
46	26.09	17.391	18.89	4.1×10^{-3}	467.62
48	25	16.667	18.0862	4.3×10^{-3}	488.4
50	24	16	17.35	4.5×10^{-3}	509

2.5 The Cut-Off Frequency

The main objective of this work is the geometrical optimization of the sensor structure to widen the cut-off frequency. This frequency at which the impedance of the solution equals the interface impedance is given by [40]:

$$f_{\text{cut}} = \frac{1}{2\pi R_{\text{sol}} C_{\text{interface}}} \quad (16)$$

In this research, we use a square structure of $L \times L$. Figures 2 and 3 describe the structure of a planar interdigital sensor. From these figures, the total width of the structure is given by:

$$L = N(W + S) - S. \quad (17)$$

Because the dimension L is much larger than S , we assume the following approximation:

$$L \approx N(W + S) \Rightarrow N = \frac{L}{W + S} \quad (18)$$

By replacing R_{sol} from the Eq. (1) equation (4), the factor K_{cell} from (5), the capacitance $C_{interface}$ from (9), N from (18) and α , the equation of cut-off frequency (16) is thus rewritten as:

$$f_{cut} = \frac{\sigma}{\pi C_0} \cdot \frac{N - 1}{L \cdot \alpha} \cdot \frac{K(\sqrt{1 - k^2})}{K(k)} \quad (19)$$

2.6 Optimization of the Geometry of Electrodes

From the formula (19), the relation between the cut-off frequency and the metallization ratio α is presented in Fig. 5 with the calculated parameters as follows: $N = 20$, $L = 2$ mm, $\sigma = 0.7 \times 10^6$ (pS/ μ m).

We observe in Fig. 5, that the cut-off frequency of the sensor passes through a minimum for $\alpha = 0.6$ corresponding to the sensor with $N = 20$ electrodes. Using the

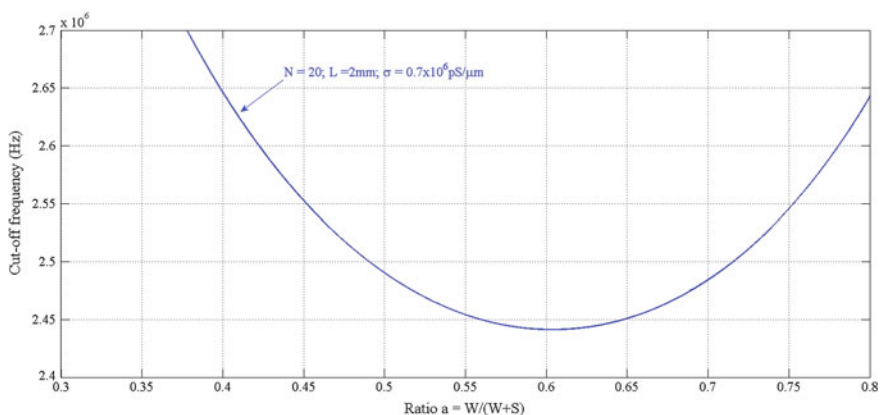


Fig. 5 Cut-off frequency of the sensor as a function of the metallization ratio α

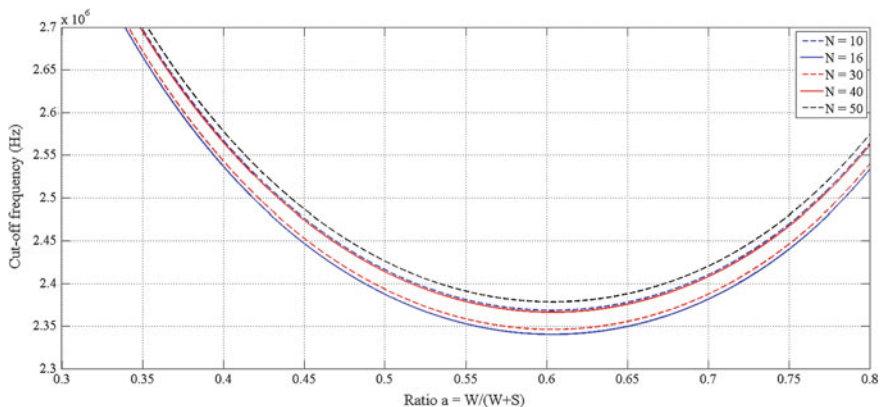


Fig. 6 Cut-off frequency of five different sensor electrodes ($N = 10, 16, 30, 40, 50$) as a function of the metallization ratio α

Table 2 Parameters of interdigital sensors and DL

N	L (mm)	C_0 (pF/ μm^2)
10	2	8.3×10^{-4}
16	2	1.4×10^{-3}
30	2	2.7×10^{-3}
40	2	3.6×10^{-3}
50	2	4.5×10^{-3}

relationship given above, we also study the sensors for different number of electrodes.

Figure 6 shows the cut-off frequency of different interdigitated electrodes as a function of the metallization ratio, with the calculated parameters given on Table 2.

According to Fig. 6, we see that in all cases, the number of sensor electrodes are different, the cut-off frequency always crosses through a minimum corresponding to $\alpha = 0.6$. From these results, we choose the metallization ratio $\alpha = W/(S + W) = 0.6$ as a rule to optimize the structure of the interdigitated electrodes sensor.

2.7 Optimization of the Thickness of the Biological Medium

One important parameter in bio-impedance measurement, is the thickness of the biological medium under test. Igreja and Dias [28] proposed a model for calculation of capacitance between electrodes in an interdigital sensor, based on conformal mapping techniques [41] (see Fig. 8).

where ϵ_r is the relative dielectric constant of the measured solution, $\epsilon_{r\text{-air}}$ is the relative dielectric constant of the air.

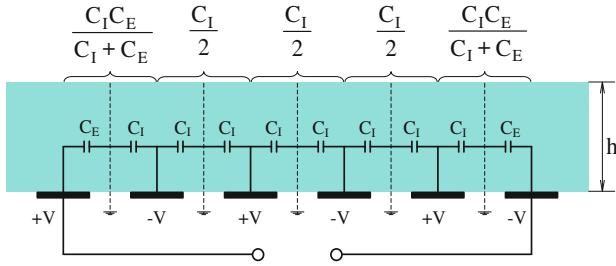


Fig. 7 Equivalent circuit for the evaluation of the capacitance with six electrodes [28]

The capacitance C_I in Fig. 7 is half the capacitance of one interior electrode relative to the ground potential and C_E is the capacitance of one outer electrode relative to the ground plane next to it. Table 3 describes the expressions used to calculate the capacitances C_I and C_E according to [25].

where,

$K(k)$ is the complete elliptic integral of first kind with modulus k

$sn(z, k)$ is the Jacobi elliptic function of modulus k

$v_2(0, q)$ and $v_3(0, q)$ are the Jacobi Theta functions

Based on the equivalent circuit of Fig. 8, where $N > 3$ one finds the total capacitance between the positive and negative electrodes by the following formula:

$$C_{total} = (N - 3) \frac{C_I}{2} + 2 \frac{C_I C_E}{C_I + C_E} \tag{20}$$

Table 3 Detailed equations needed for the calculation of C_I and C_E

Capacitance C_I	Capacitance C_E
$C_I = \epsilon_0 \epsilon_r \cdot L \cdot \frac{K(k_I)}{K(k_I')}$ $\begin{cases} k_I = t_2 \sqrt{\frac{t_4^2 - 1}{t_4^2 - t_2^2}} \\ k_I' = \sqrt{1 - k_I^2} \\ \begin{cases} t_2 = sn(z_2, k) \\ t_4 = \frac{1}{k} \end{cases} \\ \begin{cases} k = \left(\frac{v_2(0, q)}{v_3(0, q)}\right)^2 \\ z_2 = \alpha \cdot K(k) \end{cases} \\ \begin{cases} q = \exp(-4\pi r) \\ r = \frac{h}{\lambda} \\ \lambda = 2(W + S) \\ \alpha = \frac{W}{S + W} \end{cases} \end{cases}$	$C_E = \epsilon_0 \epsilon_r \cdot L \cdot \frac{K(k_E)}{K(k_E')}$ $\begin{cases} k_E = \frac{1}{t_3} \sqrt{\frac{t_4^2 - t_3^2}{t_4^2 - 1}} \\ k_E' = \sqrt{1 - k_E^2} \\ \begin{cases} t_3 = \cosh\left(\frac{\pi(1-\alpha)}{8F}\right) \\ t_4 = \cosh\left(\frac{\pi(1+\alpha)}{8F}\right) \end{cases} \end{cases}$

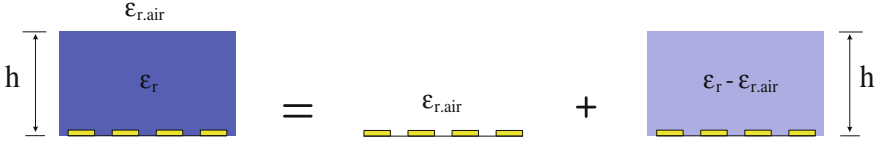


Fig. 8 Splitting of a half plane according to the partial capacitance technique

The capacitances C_I and C_E in Fig. 7, they can also be determined for a planar interdigital sensor having one or more layers (of different permittivities and thickness) on the top of the electrodes.

The capacitance of a sensor taking into account the different layers is the sum of the partial capacitances as follows:

$$C_{\text{total}} = C_{\text{air}} + C_h + C_s \quad (21)$$

where, C_{total} is the total capacitance of the upper half plane and C_h is the geometric capacitance of the measurement layer, which depends on its height h and on the particular electrode geometry and C_s is the capacitance of the substrate.

Using the equations in Table 3 and the technique of partial capacity, we obtain the total capacitances $C_{I\text{-total}}$ and $C_{E\text{-total}}$ by the following expressions:

$$\Rightarrow \begin{cases} C_{I\text{-total}} = \epsilon_0 \epsilon_{\text{air}} \cdot L \cdot \frac{K(k_{I\infty})}{K(k'_{I\infty})} + \epsilon_0 (\epsilon_r - \epsilon_{\text{air}}) \cdot L \cdot \frac{K(k_{I,h})}{K(k'_{I,h})} + \epsilon_0 \epsilon_s \cdot L \cdot \frac{K(k_{I\infty})}{K(k'_{I\infty})} \\ C_{E\text{-total}} = \epsilon_0 \epsilon_{\text{air}} \cdot L \cdot \frac{K(k_{E\infty})}{K(k'_{E\infty})} + \epsilon_0 (\epsilon_r - \epsilon_{\text{air}}) \cdot L \cdot \frac{K(k_{E,h})}{K(k'_{E,h})} + \epsilon_0 \epsilon_s \cdot L \cdot \frac{K(k_{E\infty})}{K(k'_{E\infty})} \end{cases}$$

with:
$$\begin{cases} k_{I\infty} = \sin\left(\frac{\pi}{2}\alpha\right) \\ k_{E\infty} = \frac{2\sqrt{\alpha}}{1+\alpha} \end{cases}$$

Finally, the total capacitance of the planar interdigital sensors is given by:

$$C_{\text{total}} = (N-3) \frac{C_{I\text{-total}}}{2} + 2 \frac{C_{I\text{-total}} \cdot C_{E\text{-total}}}{C_{I\text{-total}} + C_{E\text{-total}}} \quad (22)$$

As analyzed above, we apply the Eqs. (21) and (22) to optimize the thickness h of the biological medium for planar interdigital sensors with a glass substrate. The solution under test and glass substrate have the relative permittivities: $\epsilon_r = 80$ and $\epsilon_s = 5.4$, respectively.

Figure 9 shows the relationship between the total capacitance of the planar interdigital sensors and the thickness h of the biological medium by two sensors optimized: sensor 1 and sensor 2. According to this figure, we see that the values of the total capacitance C_{total} very greatly for the thickness $h < 100 \mu\text{m}$. Then, these values do not change for a thickness greater than $100 \mu\text{m}$.

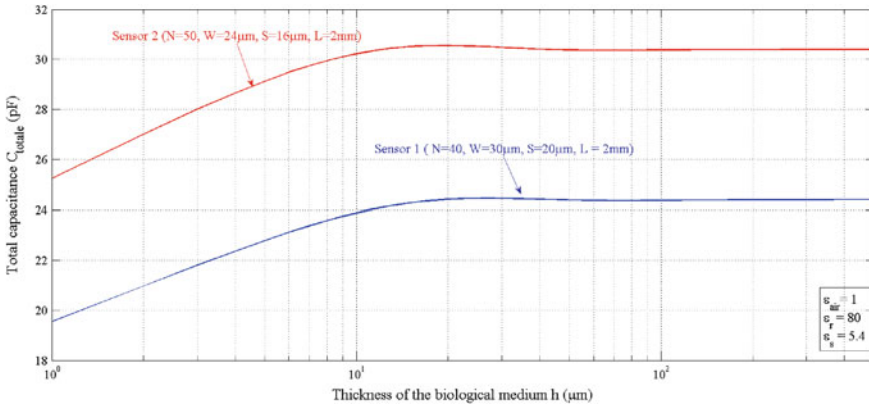


Fig. 9 The total capacitance as a function of the thickness of the biological medium

Figure 10 represents the relationship between the total capacitance of the sensor 1 and the thickness h of the biological medium by the two biological medium having different permittivities: $\epsilon_r = 80$ and $\epsilon_r = 84$.

According to this figure, we see that the values of the total capacitance C_{total} vary greatly for the thickness $h < 100 \mu\text{m}$. Then, again for the thickness $h > 100 \mu\text{m}$ these values are almost constant.

We can conclude, by analyzing Figs. 9 and 10, the thickness of the biological sample influences largely the results of the measured bioimpedance. Thus, when we measure the bio-impedance, it is necessary to have a medium thickness h greater than 100 μm

Consequently, we can choose the thickness of the biological sample as an optimization theory for the measuring bio-impedance

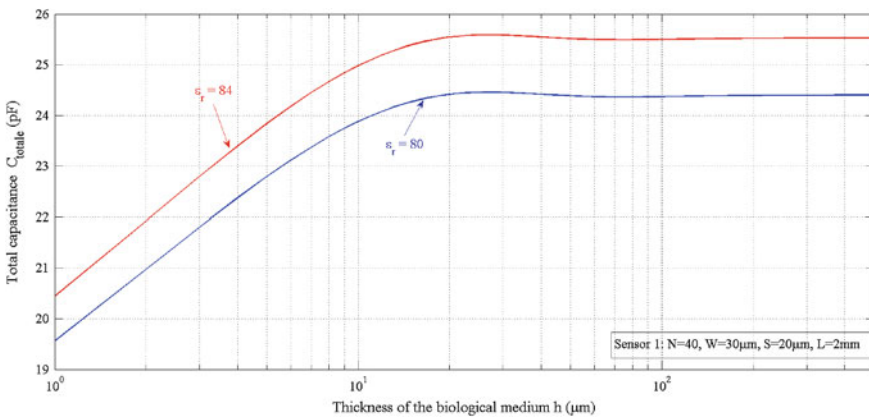


Fig. 10 Total capacitance as a function of the thickness of the biological medium

3 Simulation and the 3D Modelling of the System by Coventorware[®] Software

CoventorWare[®] is an integrated suite of software tools for designing and simulating MicroElectroMechanical Systems (MEMS) and microfluidics devices. CoventorWare supports two distinct design flows, as shown in Fig. 11, which may be used separately or in combination. The ARCHITECT module provides a unique system-level approach to MEMS design, whereas the DESIGNER and ANALYZER modules work together to provide a more conventional physical design flow. Both design flows require information about the fabrication process as a starting point, and this information is provided via a Process Editor and the Material Properties Database [42].

In this section, we describe the design of the physical model of the sensor loaded by a biological medium (for example the blood). We used the MEMS electro-quasistatic module proposed by the library of this software. In this simulation, we use the structure of the sensor at the micrometric scale. A top view is shown in Fig. 12.

3.1 Modeling of Substrate

The substrate is a glass layer of a $5000 \times 5000 \mu\text{m}$ square shape and a thickness of $1000 \mu\text{m}$.

The glass is very good insulator with a conductivity of approximately $10^{-17} \text{ S m}^{-1}$ and a permittivity very small around 5–7. Thus, we do not need to put an insulating layer between the substrate and the electrodes of the sensor.

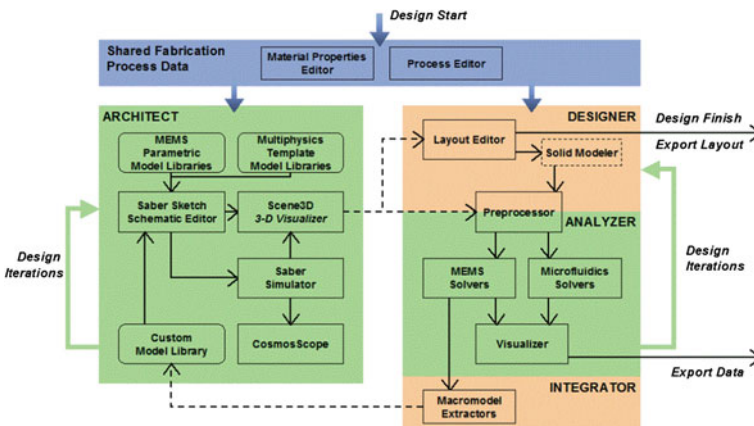
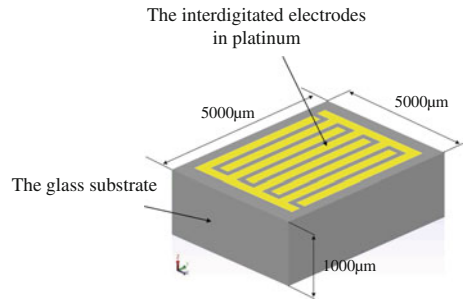


Fig. 11 Design flow [41]

Fig. 12 Model of a coplanar interdigitated electrode sensor



3.2 Modeling of Electrodes

Figure 12 describes the structure of the sensor. It is formed by two metallic electrodes in a comb shape. In the simulation, we chose the mask electrodes of platinum with a thickness of $1 \mu\text{m}$ deposited on the substrate. The total surface occupied by electrodes corresponds to that of a square with $L = 2000 \mu\text{m}$. The geometrical parameters of this sensor include the width of electrode W , the length of electrode L , the distance between two consecutive electrodes S and the number of electrodes N represented on Fig. 2. The platinum is one of the best materials to fabricate a sensor with interdigitated electrodes, its conductivity being of $9.66 \times 10^6 \text{ S/m}$.

3.3 Modeling of the Double Layer

As presented above, when electrodes in metal are loaded by a biological medium, a double layer is formed at their contact interface. In Fig. 3, $C_{\text{int-p}}$, $C_{\text{int-n}}$ model the properties of the phenomena of the double layer on the surface in contact between electrodes and biological medium. In Fig. 14, this double layer is presented by the layer 3.

The parameters (relative permittivity, thickness) of double layer are determined in a section above (see Table 1). For example, for the sensor forming $N = 50$ electrodes, the width of electrode $W = 24 \mu\text{m}$, the length of electrode $L = 2000 \mu\text{m}$, the distance between two consecutive electrodes $S = 16 \mu\text{m}$, from the report of choose $\epsilon_{\text{r-DL}}/d_{\text{DL}} = 509 \mu\text{m}^{-1}$, one can choose $\epsilon_{\text{r-DL}} = 590$ and $d_{\text{DL}} = 1 \mu\text{m}$. The choice of these values do not affect the results of the simulation because the ratio $\epsilon_{\text{r-DL}}/d_{\text{DL}} = 509 \mu\text{m}^{-1}$ is always constant.

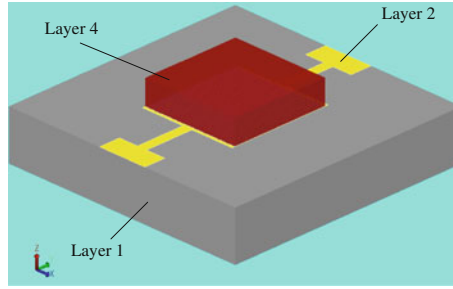


Fig. 13 The modeling 3D with CoventorWare[®]; the layer 1 indicates the glass substrate, the layer 2 represents the interdigitated electrodes in platinum, and the layer 4 represents the biological medium

3.4 Modeling of the Biological Medium

The layer 4 in Figs. 13 and 14 models the electric properties of the biological solution. The thickness of this layer is equal to 500 μm , it follows the theory of optimization in the section above (the thickness h of the biological solution must be greater than 100 μm). The values of the conductivity and permittivity of human tissue is taken from [38] or [39]. For example, the conductivity of the blood of 0.7 S/m; the relative permittivity of blood at low frequency is approximately equal to 5300 at high frequency and is 60 [38] in the frequency range 10^6 - 10^9 Hz.

3.5 Simulation and Results Obtained

3.5.1 Process Simulation

According to the simulation steps mentioned above, after choosing materials, designed 2D sensor geometry and created a 3D model, we make the meshing

Fig. 14 3D view, zoomed from Fig. 13, the layer 3 describes the double layer DL

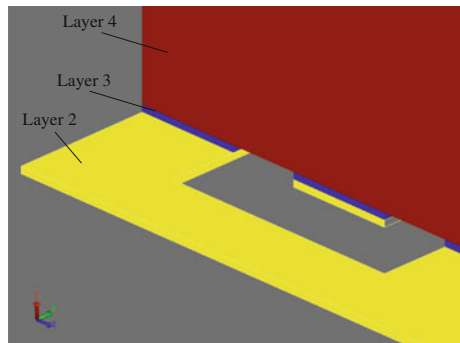
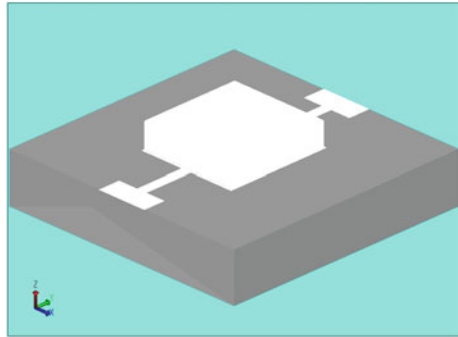


Fig. 15 3D view, the meshing of Manhattan bricks 1 μm



process. The meshing is created by using bricks of Manhattan of linear elements of 1 μm in the directions X, Y, Z. If the analysis of simulation does not converge, the mesh size is increased to 1 μm and the process of simulation starts. Figure 15 presents bricks of Manhattan of linear elements.

After meshing, a sinusoidal voltage 1 V is applied between the positive and negative electrodes. The frequency range of $10 \div 10^9$ Hz is used for the simulation.

As indicated in Fig. 11, from the analyzing by a simulation software, the available data are the results of capacitance C, conductance G between positive and negative electrodes, and the range of frequencies f. From these data, one can determine the measured quantities (the admittance Y, the impedance Z) following:

$$\begin{cases} \omega = 2\pi f \\ Y = G + j\omega C \\ Z = \frac{1}{Y} \end{cases} \quad (23)$$

From the impedance Z given in (23), the conductivity and the permittivity values of the biological research are calculated by the following expressions:

$$Z = \frac{K_{\text{cell}}}{\sigma + j\omega\epsilon_0\epsilon_r} \Rightarrow \sigma + j\omega\epsilon_0\epsilon_r = \frac{K_{\text{cell}}}{Z} \Rightarrow \begin{cases} \sigma = \text{Re}\left(\frac{K_{\text{cell}}}{Z}\right) \\ \epsilon_r = \frac{\text{Im}\left(\frac{K_{\text{cell}}}{Z}\right)}{\omega\epsilon_0} \end{cases} \quad (24)$$

where: j is the imaginary symbol, ω is the angular pulsation (rad/s), ϵ_0 is the permittivity of vacuum, ϵ_r is the relative permittivity of the biological medium, Z is the complex impedance (Ω); Y is the complex admittance (S), G is the conductance (S), C is the capacitance (F), K_{cell} is the cell factor of the sensor.

Table 4 Parameters of double layer

Authors	C_0 (pF/ μm^2)	$\epsilon_r \cdot d_{DL}/d_{DL}$ (μm^{-1})
Pajkossy [1]	0.2	22588
Borkholder [2], Bard and Faulkner [3]	0.047	5308
Our results	3.6×10^{-3}	405

3.6 Results

3.6.1 Determination of the Parameters of Double Layer

In the previous section, we have mentioned that the value of capacitance per unit area C_0 do not only depend on the relative permittivity of the medium, but also on the dimensions (geometry) of the sensor (N, L, W and K_{cell}).

According to Pajkossy [31], Borkholder [32] and Bard et Faulkner [33], the value of C_0 is constant and is presented in Table 1.

We choose different interdigitated electrodes sensor for simulations and comparisons with other authors. We choose an optimized sensor with $N = 40$, $W = 30 \mu\text{m}$, $= 20 \mu\text{m}$, $K_{cell} = 21.8 \text{ m}^{-1}$ and the value of capacitance per unit area $C_0 = 3.6 \times 10^{-3} \text{ pF}/\mu\text{m}$.

From the capacitance per unit area, we can determine the ratio between the relative permittivity and the thickness of double layer. This ratio is shown in Table 4.

The simulation for these three different cases are presented in Fig. 16.

Figure 16 shows the relative permittivity as a function of the frequency. In this figure, the curve of the relative permittivity is more similar to the curve obtained in [39]. The result of blood's relative permittivity is approximately equal to 5260 at low frequency and 65 at the high frequency. This confirms that the proposed

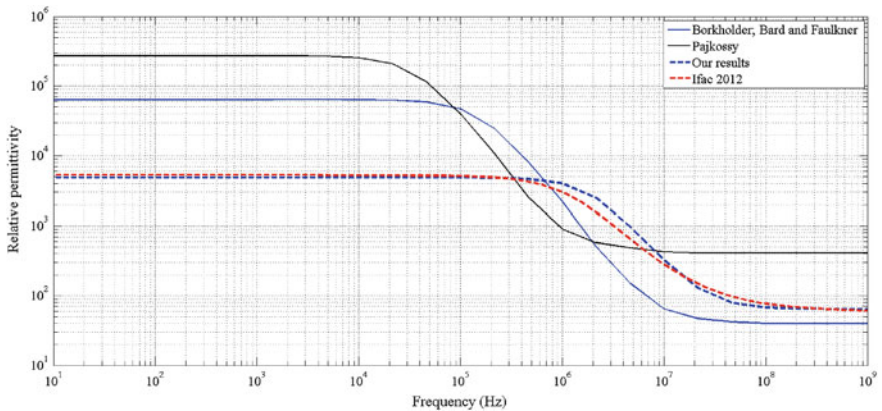


Fig. 16 Relative permittivity of blood as a function of the frequency

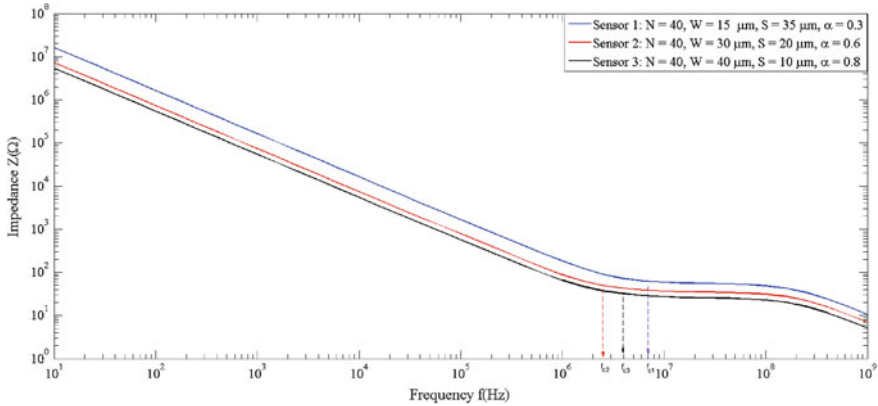


Fig. 17 Impedance as a function of the frequency

method to determine the parameters of the double layer of a planar interdigital sensor is correct.

3.6.2 Optimization of the Metallization Ratio

Figures 5 and 6 presented the relation between the cut-off frequency and the metallization ratio α . According to these figures, the cut-off frequency always crosses through a minimum corresponding to $\alpha = 0.6$ in all cases of the sensor’s different electrodes. Thus, the main result of this simulation is to check the metallization ratio. In the following we study the influence of this ratio by impedance spectroscopy.

A sinusoidal signal (1 volt) is applied between the terminals of interdigitated electrodes for 10 Hz to 1 GHz frequency range. We used the Manhattan mesh for this physical model with linear elements 10 microns of size in three directions (X, Y, and Z). The model is presented in Fig. 15.

In Fig. 17, we present the simulation results of the impedance as a function of the frequency for three types of sensors ($\alpha = 0.3$, $\alpha = 0.6$ and $\alpha = 0.8$). One must notice that the volume of the medium in all the simulation cases is the same. The geometrical parameters of the sensor used to make the simulation are given on Table 5.

The results indicated in Fig. 17 and Table 6 shows that the sensor 2 with a metal ratio of

$\alpha = 0.6$ has the lowest cutoff frequency confirm in also our theoretical approach.

Thickness of the Biological Medium Sample

Using bioimpedance spectroscopy we have determined the better thickness of the biological medium, which governs directly the quality of the measurement. From

Table 5 Simulation parameters of the interdigital sensor

Sensor	L (mm)	N	W (μm)	S (μm)	α	K_{cell} (m^{-1})	C_0 (pF/ μm^2)	$\epsilon_{\text{r,DL}}$	d_{DL} (μm)
1	2	40	15	35	0.3	35.8	4.37×10^{-3}	493.5	1
2	2	40	30	20	0.6	21.8	3.6×10^{-3}	405	1
3	2	40	40	10	0.8	15.1	3.9×10^{-3}	438.74	1

Table 6 Results of the simulation of the cut-off frequency for three cases

Sensor	L (mm)	N	W (μm)	S (μm)	α	f_{cut} (Hz)
1	2	40	15	35	0.3	7×10^6
2	2	40	30	20	0.6	2.5×10^6
3	2	40	40	10	0.8	4×10^6

analysis of Fig. 9 and Fig. 10, one can see, as previously shown theoretically, that the thickness h of the biological sample must be greater than $100 \mu\text{m}$.

In this section, we simulate an optimized sensor measuring a biological sample (blood) for various thicknesses. The thickness values of the biological sample under test are: 20, 40, 100, and $300 \mu\text{m}$ respectively. The sensor is formed by $N = 40$ electrodes; $\alpha = 0.6$; $L = 2 \text{ mm}$; $W = 30 \mu\text{m}$; $S = 20 \mu\text{m}$.

Figure 18 shows the relation between the measurement impedance and the thickness h of the biological sample. According to this figure, one can observe that the impedance decreases when the thickness h of the biological sample increases. However the impedance do not decrease and remains constant over $100 \mu\text{m}$.

Figure 19 shows the relation between the total capacitance and the thickness h of the biological sample for the same conditions as for Fig. 18. We can see that the total capacitance increases when the thickness h increases. And again, this increase stop for $100 \mu\text{m}$.

These results are entirely consistent with the proposed theory for choosing the best thickness of a biological medium sample to put on the sensor.

4 Design and Realization of Micro Sensors

The realization of our interdigital sensors, was made in association with and by the competence center MINALOR of the Institut Jean Lamour (IJL) of the University of Lorraine. To study empirically the various geometries of interdigitated structures, in order to verify the optimization theory developed, five geometries of different electrodes were realized. The geometric parameters of the sensor manufacturing are described in Table 7.

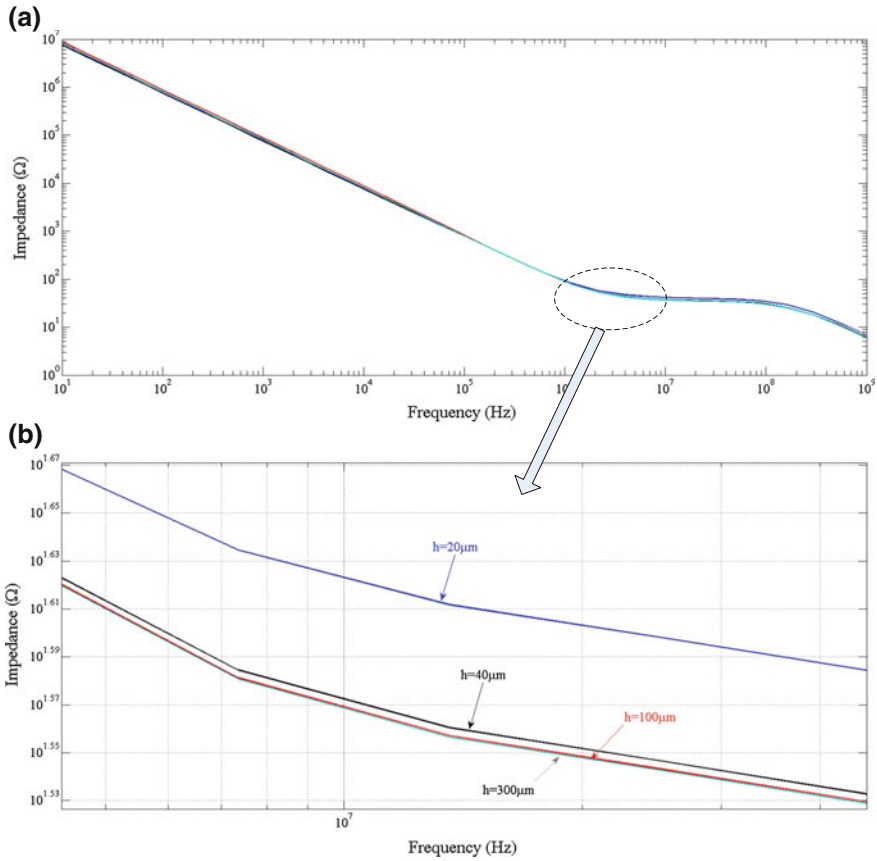


Fig. 18 **a** Impedance as a function of the frequency; **b** display zoomed in of (a)

4.1 Structuring of Layers and Masks Realization

The design is an important step in achieving our sensors. We define the necessary layers to complete the final system in three dimensions. They must also be compatible with available micro-manufacturing techniques.

The biological sample reservoir forms a square well (see Fig. 20) where a drop of biological sample for measure is deposited.

The realization of our sensors with interdigitate electrodes and their design using three layers (substrate, electrodes and reservoir) are presented on Fig. 21.

Once all the layers and geometrical sensor are defined, we realize the complete design of the sensor using CoventorWare[®]. The format “.GDS” is used as standard for the realization of masks.

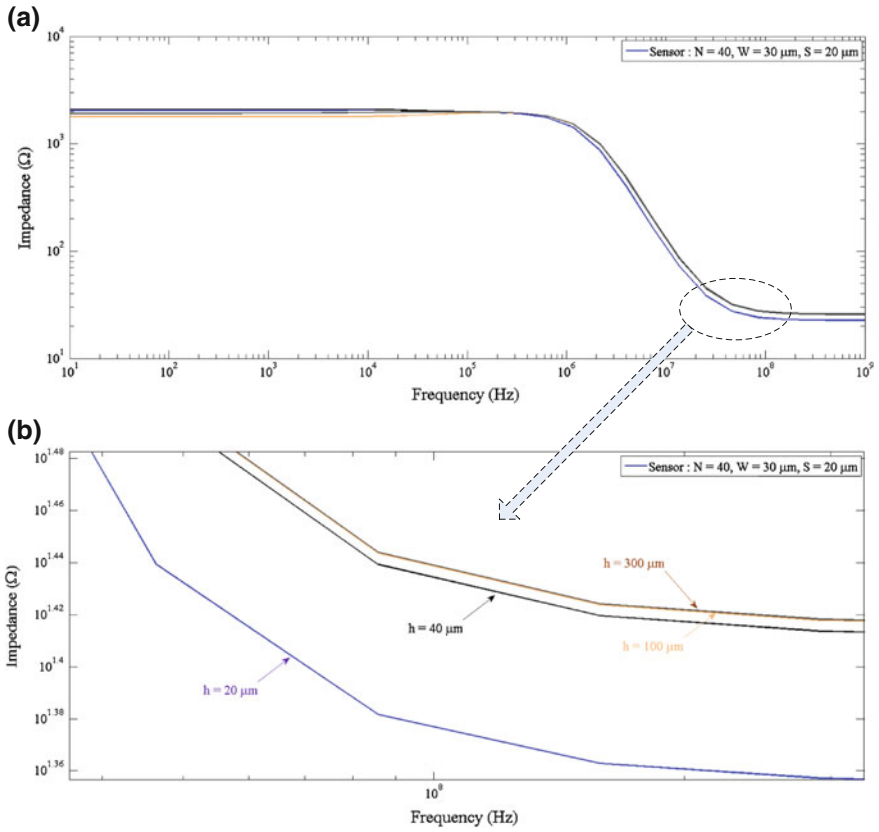


Fig. 19 a Impedance as a function of the frequency; b display zoomed in of (a)

Table 7 Parameters of the interdigital sensor manufacturing

Sensor	L (mm)	N	W (μm)	S (μm)	α	K_{cell} (m^{-1})
1	2	40	30	20	0.6	21.8
2	2	20	60	40	0.6	44.74
3	2	50	12	28	0.3	28.5
4	2	40	15	35	0.3	35.8
5	2	40	40	10	0.8	15.1

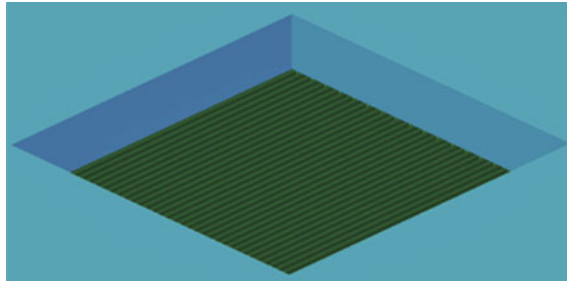


Fig. 20 Biological sample reservoir

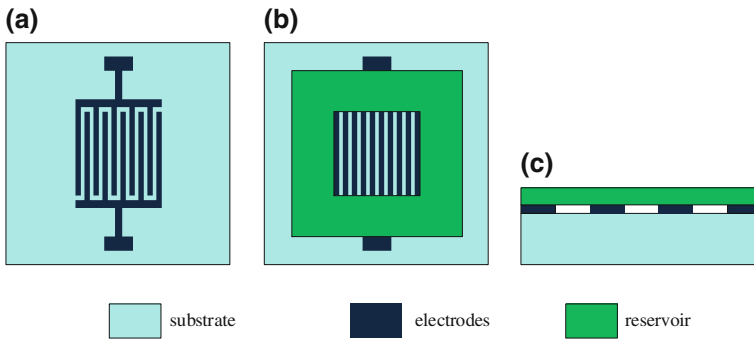


Fig. 21 Schematic representation of the layers. **a** The electrodes deposited on the substrate; **b** the reservoir layer deposited on the substrate carrying the electrodes; **c** the sensors consist of three layers

4.2 Manufacturing Process

Steps to fabricate a sensor are shown in Fig. 22:

- (a) The glass sample is first hand cleaned, with ultrasounds, hanging 10 min with a solution of NaOH, 10 min with a cleaner (RBS), 10 min with acetone then rinsed with isopropanol.
- (b) Deposit of a layer of catcher of tantalum about 10 nm then 150 nm of platinum by cathodic pulverizing.
- (c) Deposit of a layer of positive resin (S1813) by spreading with a spinner (SPIN COATING). With a positive resin, the parts exposed to UV radiation become more soluble and disappear during the development. The sample is placed on a heating plate to evaporate the solvent of the resin. We obtain a solid layer.
- (d) Exposure to the radiation UV
- (e) Development of the resin with a solvent (here the MF319). Only the parts of the resin which were not exposed to UV radiation resist the solvent. We obtain the negative of electrodes.

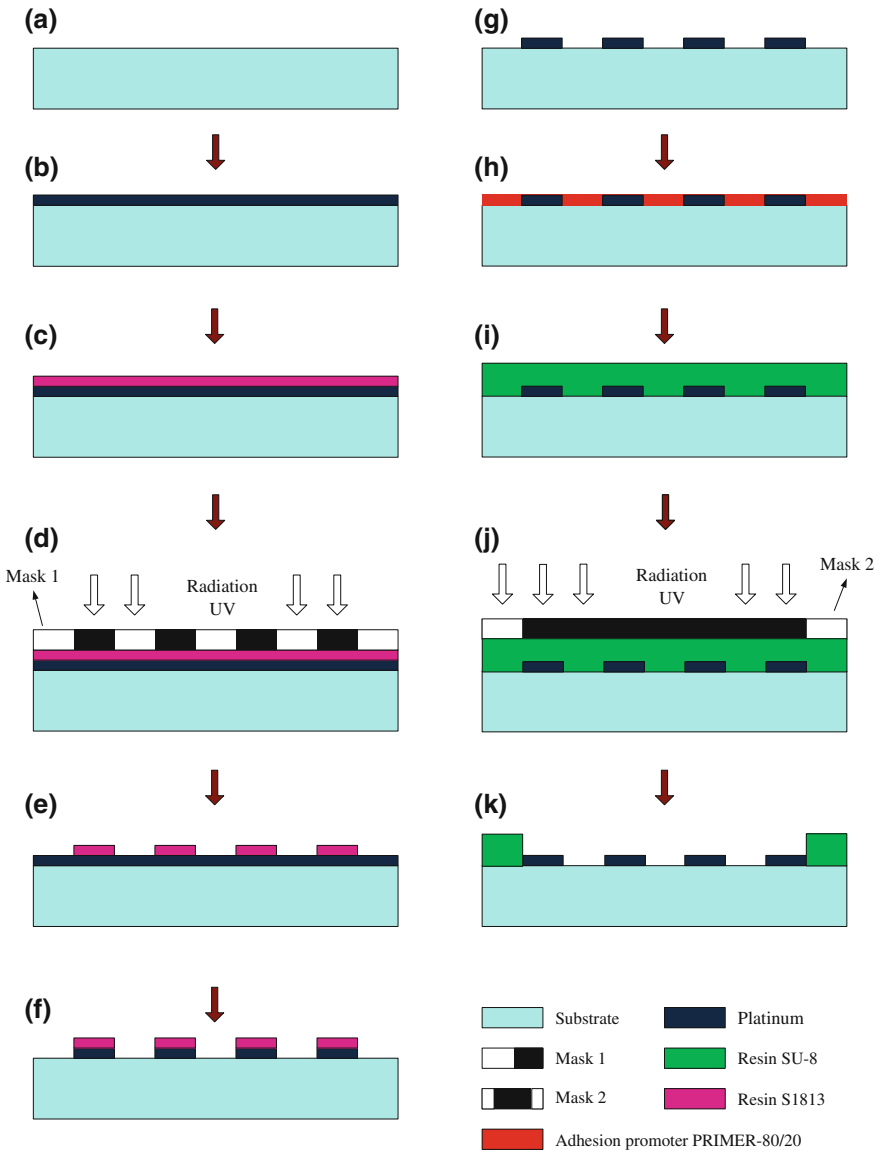


Fig. 22 Realization steps of our sensors. **a** Glass sample, **b** Deposition of the metal layer (150 nm platinum on 10nm Tantalum), **c** Deposit of a resin layer S1813, **d** Exposure to radiation UV, **e** Development of resin S1813, **f** Platinum etching, **g** Removal of the photosensitive resin, **h** Coating the adhesion promoter and evaporation, **i** Deposit of a resin layer SU-8, **j** Exposure to radiation UV, **k** Development of resin SU-8

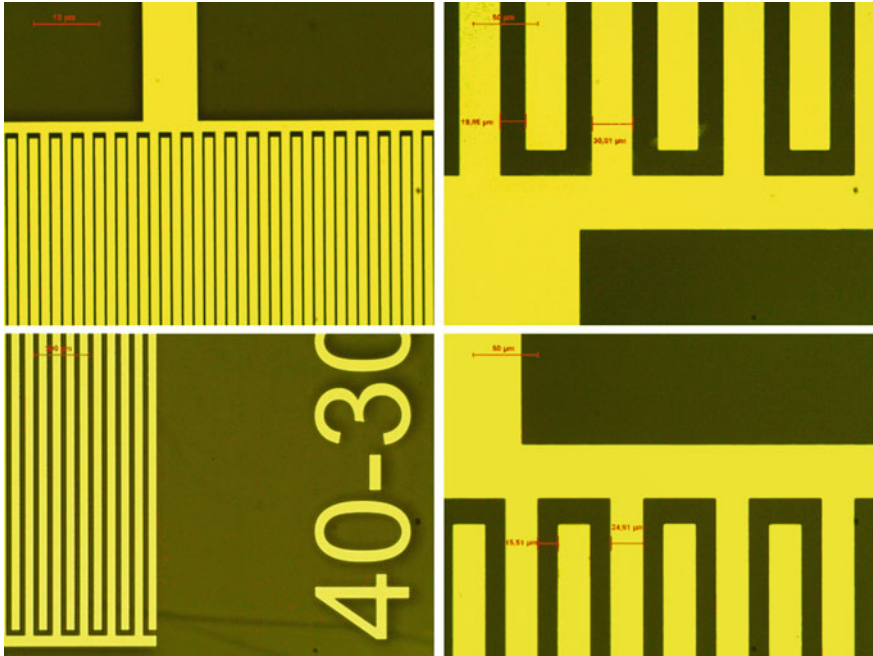


Fig. 23 Structures of the electrodes after the realization

- (f) The next step is the ion etching. The platinum electrodes are etched by an etching machine (Ionic beam etch – the IBE 4 Wave). A plasma is created, and the present ions in this plasma are accelerated towards the sample to come to pulverize the surface. The resin also is etched during the process, but its thickness is rather big to resist during the etching of the platinum.
- (g) After etching the rest of the resin (S1813) is removed with acetone.
- (h) Coating of the sample with an adhesion promoter (primer MMC 80/20). Once spread and evaporated on a heating plate, we can consider that the promoter does not form a layer unlike to a resin.
- (i) Depositing a layer of negative resin (SU-8) in the same way as in the step c). In the case of a positive resin, the part exposed to the radiation UV will become more resistant in solvents.
- (j) Exposure to the radiation UV
- (k) Development of the resin with a solvent (here the MF319). Only the parts of the resin which were not exposed to radiation UV resist the solvent. We obtain the negative of electrodes. After development of the resin we obtain the shape of reservoir.

Figures 23 and 24 present the results of the realization of our electrode sensors without reservoir.

Fig. 24 Image of the sensors after the realization without reservoir

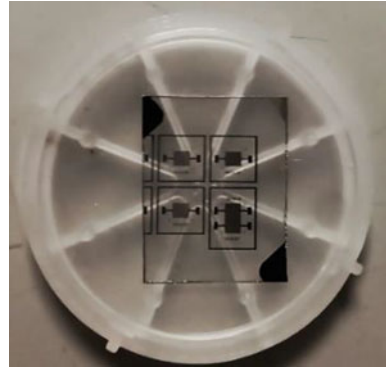
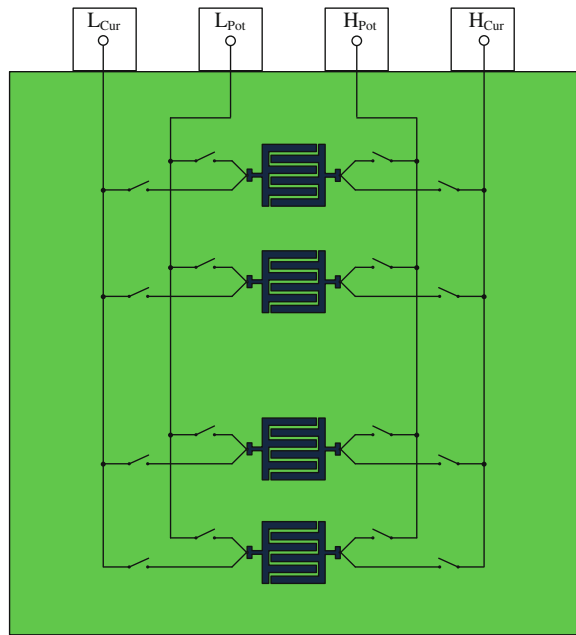


Fig. 25 Printed circuit board (PCB) to connect the sensor with a measuring instrument



We have designed a printed circuit board (PCB) to connect the sensor to the impedance meter (see Fig. 25). A four points method was used to make the impedance measurements. This method is used for the characterization of biological medium at frequencies below 100 MHz. It permits to eliminate the problems related to the impedance interface. This method requires the measurement of the current through the biofluids and the voltage at these terminals (Figs. 26 and 27).

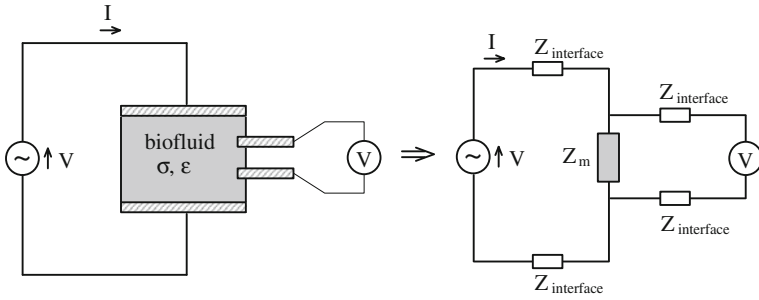
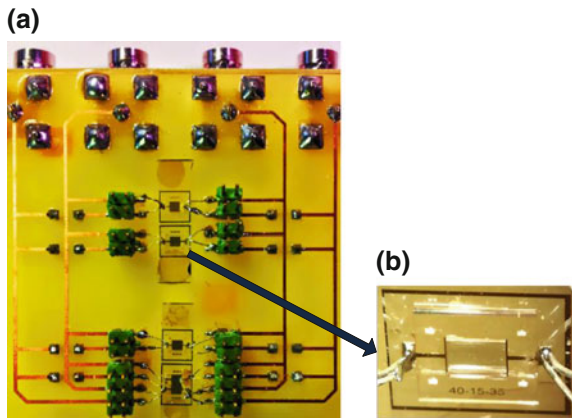


Fig. 26 The method of 4 points

Fig. 27 Photo of the micro-sensor (b) connected to the PCB (a)



5 Experimental Measurement

The experimental device consists on the following elements (Fig. 28):

- A drop of the sample solution with a conductivity of 12.88 mS/cm placed directly on the sensor (Figs. 29 and 30).
- A micropipette (Socorex Micropipette Acura 825) is used to add or remove the fluid volume.
- A thermometer to measure the ambient temperature.
- A microscope to observe the position of the liquid volume.
- A current amplifier HF2TA that converts 2 input currents to output voltages in a frequency range up to 50 MHz. This device is an active probe which can be conveniently placed close to the measurement setup. It supports most applications where a current must be converted to a voltage. The advanced design of the HF2TA ensures stability and a smooth operation over the entire frequency range. The HF2TA transimpedance current amplifier with the HF2 Series signal

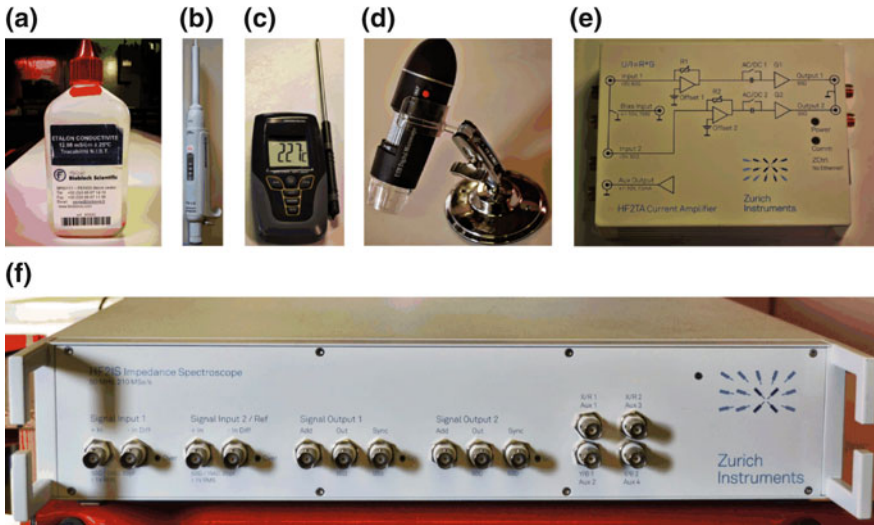


Fig. 28 Element of empirical measurement system: **a** the sample biofluids; **b** the micropipette; **c** the thermometer; **d** the microscope; **e** the current amplifier HF2TA; **f** the impedance spectroscopy HF2IS

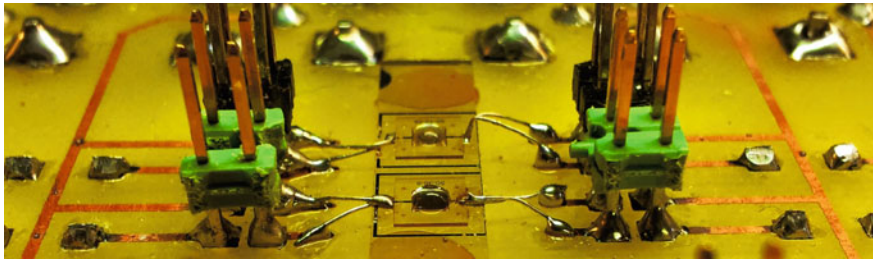


Fig. 29 A drop of the sample solution is placed directly on the sensor

analyzers allows for very high performance measurements and very low sensitivity to interferences.

- An impedance spectroscopy HF2IS covering a frequency range from 100 Hz to 10 MHz
- The biosensor with interdigitated electrodes.
- A computer for observation and data processing.

A sinusoidal signal (1 volt) is applied between the terminals of interdigitated electrodes and a frequency range of 10 Hz to 10 MHz is used for the experimental measurements.

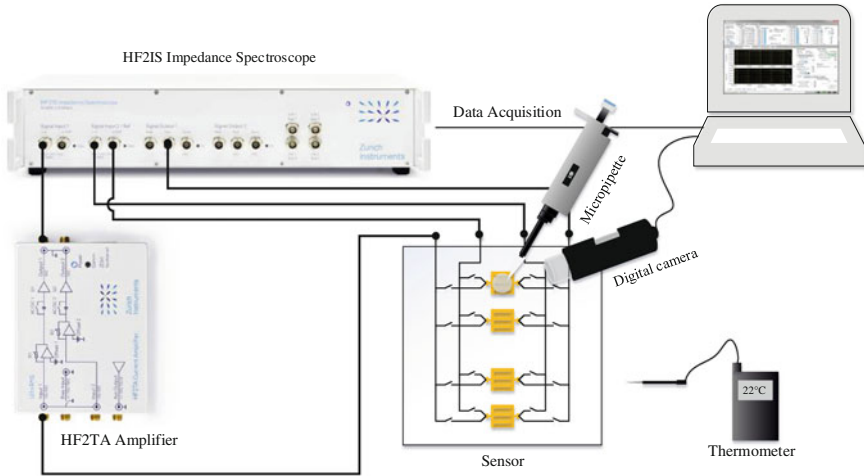


Fig. 30 Experimental set up for experimental measurements

In Fig. 31, we present the results of the impedance measurements as a function of the frequency for several types of sensors. The geometry of the sensor 1 is optimized, whereas the geometries of the sensor 2, 3, 4 and 5 are not optimized.

The results of experimental measurements indicated in Fig. 31 and Table 8 shows that the sensor 1 with a metal ratio of $\alpha = 0.6$ and the number of electrodes $N = 40$ has the lowest cutoff frequency. This confirms our theory and simulated results as presented above.

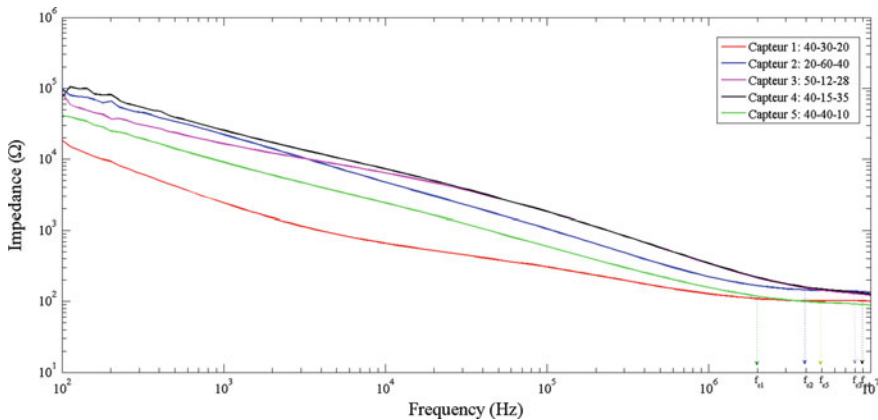


Fig. 31 Impedance amplitude as a function of the frequency

Table 8 Results of the experimental measurements

Sensor	L (mm)	N	W (μm)	S (μm)	α	f_{cut} (Hz)
1	2	40	30	20	0.6	1×10^6
2	2	20	60	40	0.6	4×10^6
3	2	50	12	28	0.3	8×10^6
4	2	40	15	35	0.3	9×10^6
5	2	40	40	10	0.8	5×10^6

6 Conclusion

In this work, we have proposed a new method to theoretically determine the parameters (relative permittivity, thickness and capacitance per unit area) of the double layer at the surface contact between the electrodes and the biological medium. Using an equivalent electrical circuit and the impedance formulae, we can estimate the capacitance per unit area C_0 according to the geometry (dimensions) of the sensor (N, L, W) and to the biological sample thickness. From this impedance we can deduce the values of the permittivity and the conductivity after having defined the cell factor K_{cell} .

We have described in detail the theoretical optimization method of the sensor's geometric parameters with interdigitated electrodes to widen the useful frequency band and decrease the impedance interfaces. The optimization results allow us to choose the sensor with interdigitated electrodes existing the parameters: $\alpha = 0.6$, $N = 40$, $L = 20$ mm.

On the other hand, the thickness of the biological medium also influences the process of measure bio-impedance. So, it is necessary to ensure that a thickness of the biological medium is greater than 100 μm according to our optimization theory.

These results were defined theoretically in the first part, checked by simulation using CoventorWare[®], and also verified by measurement with a home-made experimental set up. The results are in good agreement with these three approaches.

References

1. K.S. Cole, H.J. Curtis, Electric impedance of the squid giant axon during activity. *J. Gen. Physiol.* **22**(5), 649–670 (1939)
2. H. Fricke, S. Morse, The electric capacity of tumors of the breast. *J. Cancer Res.* **10**, 340–376 (1926)
3. H. P. Schwan, Electrical properties of tissue and cell suspensions. *Adv. Biol. Med. Phys.* **5**, 147–209 (1957)
4. I. Giaever, C. Keese, Micromotion of mammalian cells measured electrically. *Proc. Natl. Acad. Sci. USA* **88**(17), 7896–7900 (1991)
5. D.A. Borkholder, *Cell Based Biosensors Using Microelectrodes.pdf* (Stanford University, Stanford, 1998)

6. M. Heuschkel, M. Fejtl, A three-dimensional multi-electrode array for multi-site stimulation and recording in acute brain slices. *J. Neurosci. Methods* **114**(2), 135–148 (2002)
7. R. Popovtzer, T. Neufeld, Electrochemical detection of biological reactions using a novel nano-bio-chip array. *Sens. Actuators B Chem.* **119**(2), 664–672 (2006)
8. J.S. Wei, Distributed capacitance of and acoustic surface. *IEEE J. Quantum Electron.* **13**(4), 152–158 (1977)
9. G. Alley, Interdigital capacitors and their application to lumped-element microwave integrated circuits. *Microw. Theory Tech. IEEE Trans.* **18**, 1028–1033 (1970)
10. P.R. Herczfeld, Special issue on applications of lightwave technology to microwave devices. *IEEE-INST Electr. Electron. Eng. INC* **38**(5), 465–466 (1990)
11. M. Ibrahim, J. Claudel, D. Kourtiche, M. Nadi, Geometric parameters optimization of planar interdigitated electrodes for bioimpedance spectroscopy. *J. Electr. Bioimpedance* **4**(1), 13–22 (2013)
12. T.-T. Ngo, H. Shirzadfar, D. Kourtiche, M. Nadi, A planar interdigital sensor for bio-impedance measurement: theoretical analysis, optimization and simulation. *J. Nano-Electron. Phys.* **6**(1), 1–7 (2014)
13. T. Ngo, H. Shirzadfar, A. Bourjilat, D. Kourtiche, M. Nadi, A method to determine the parameters of the double layer of a planar interdigital sensor. www-ist.massey.ac.nz (2014), pp. 2–4
14. M. Ibrahim, J. Claudel, D. Kourtiche, Physical and electrical modeling of interdigitated electrode arrays for bioimpedance spectroscopy. in *New Developments and Applications in Sensing Technology* (2011), pp. 169–189
15. W. Laureyn, D. Nelis, P. Van Gerwen, Nanoscaled interdigitated titanium electrodes for impedimetric biosensing. *Sens. Actuators B* 360–370 (2000)
16. L. Yang, Y. Li, C.L. Griffis, M.G. Johnson, Interdigitated microelectrode (IME) impedance sensor for the detection of viable *Salmonella typhimurium*. *Biosens. Bioelectron.* **19**(10), 1139–1147 (2004)
17. M. Varshney, Y. Li, Interdigitated array microelectrode based impedance biosensor coupled with magnetic nanoparticle-antibody conjugates for detection of *Escherichia coli* O157:H7 in food samples. *Biosens. Bioelectron.* **22**(11), 2408–2414 (2007)
18. R. Wang, Y. Wang, K. Lassiter, Y. Li, B. Hargis, S. Tung, L. Berghman, W. Bottje, Interdigitated array microelectrode based impedance immunosensor for detection of avian influenza virus H5N1. *Talanta* **79**, 159–164 (2009)
19. A.R. Mohd Syaifudin, S.C. Mukhopadhyay, P.-L. Yu, H.-S.M.J., C.-H. Chuang, V.J.D., Y.-W. Huang, Measurements and performance evaluation of novel interdigital sensors for different chemicals related to food poisoning. *IEEE Sens. J.* **11**(11), 2957–2965 (2011)
20. M. Da Silva, T. Sühnel, E. Schleicher, R. Vaibar, Planar array sensor for high-speed component distribution imaging in fluid flow applications. *Sensors* **7**, 2445 (2007)
21. F. Alexander, D.T. Price, S. Bhansali, Optimization of interdigitated electrode (IDE) arrays for impedance based evaluation of Hs 578T cancer cells. *J. Phys: Conf. Ser.* **224**, 012134 (2010)
22. T. Huang, J. Chou, T. Sun, and S. Hsiung, A device for skin moisture and environment humidity detection. *Sens. Actuators B* **134**, 206–212 (2008)
23. V. Kasturi, S.C. Mukhopadhyay, Estimation of property of sheep skin to modify the tanning process using interdigital sensors. *Lecture Notes in Electrical Engineering*, vol. 21 LNEE, pp. 91–110 (2008)
24. M. Mukhopadhyay, S.C. Yamada, S. Iwahara, Evaluation of near- surface material properties using planar mesh type coils with post-processing from neural network model. *Int. J. Electromagn. Nondestructive Eval.* **23**, 181–188 (2002)
25. M.I.S.C. Mukhopadhyay, S. Yamada, Inspection of electroplated materials—performance comparison with planar meander and mesh type magnetic sensor. *Int. J. Appl. Electromagn. Mech.* **15**, 323–329 (2002)
26. A. Choi, J. Park, H. Jung, Solid-medium-integrated impedimetric biosensor for real-time monitoring of microorganisms. *Sens. Actuators B Chem.* **137**, 357–362 (2009)

27. B. Pejčić, R. De Marco, Impedance spectroscopy: Over 35 years of electrochemical sensor optimization. *Electrochim. Acta* **51**(28), 6217–6229 (2006)
28. R. Igreja, C.J. Dias, Analytical evaluation of the interdigital electrodes capacitance for a multi-layered structure. *Sens. Actuators A Phys.* **112**(2–3), 291–301 (2004)
29. C.R. Bowen, L.J. Nelson, R. Stevens, M.G. Cain, M. Stewart, Optimisation of interdigitated electrodes for piezoelectric actuators and active fibre composites. *J. Electroceramics* **16**(4), 263–269 (2006)
30. L. Wang, H. Wang, K. Mitchelson, Z. Yu, J. Cheng, Analysis of the sensitivity and frequency characteristics of coplanar electrical cell-substrate impedance sensors. *Biosens. Bioelectron.* **24**(1), 14–21 (2008)
31. T. Pajkossy, D.M. Kolb, Double layer capacitance of Pt(111) single crystal electrodes. *Electrochim. Acta* **46**(20–21), 3063–3071 (2001)
32. David A. Borkholder, *Cell Based Biosensors Using* (1998)
33. A. Bard, L. Faulkner, *Fundamentals and Applications* (1980)
34. R. Pradhan, A. Mitra, and S. Das, *Extended Stern Model* (2012), pp. 74–78
35. W. Olthuis, W. Streekstra, P. Bergveld, Theoretical and experimental determination of cell constants of planar-interdigitated electrolyte conductivity sensors. *Sens. Actuators B* **25**, 252–256 (1995)
36. B. Timmer, W. Sparreboom, W. Olthuis, P. Bergveld, A. van den Berg, Optimization of an electrolyte conductivity detector for measuring low ion concentrations. *Lab Chip* **2**(2), 121–124 (2002)
37. J.-F. Chateaux, *Conception et réalisation d'une cellule de caractérisation des tissus biologiques par spectroscopie de bioimpédance dans la gamme fréquentielle [100 Hz–1 MHz]. Application aux tissus osseux—Prise en compte de l'anisotropie* (Thèse de l'Université Henri Poincaré, Nancy I, 2000)
38. L. Bernard, Caractérisation électrique des tissus biologiques et calcul des phénomènes induits dans le corps humain par des champs électromagnétiques de fréquence inférieure au GHz ., Thèse de l'Ecole Centrale de Lyon, 2007
39. Ifac 2012, Calculation of the dielectric properties of body tissues in the frequency range 10 Hz–100 GHz. <http://niremf.ifac.cnr.it/tissprop/htmlclie/htmlclie/htmlclie.php>
40. O. Linderholm, Two-dimensional microimpedance imaging for cell culture monitoring, vol. 3604 (2006)
41. C. Veyres, V.F. Hanna, Extension of the application of conformal mapping techniques to coplanar lines with finite dimensions. *Int. J. Electron.* **48**(1), 47–56 (1980)
42. V. 2010, *Coventor Ware*[®] ANALYZER (2010)

Molecularly Imprinted Impedimetric Sensing of Phthalates: A Real-Time Assay Technique

A.I. Zia, Apeksha Rao and S.C. Mukhopadhyay

Abstract Phthalates are the most ubiquitous chemicals that are used as plasticizer in almost every plastic product manufacturing including food packaging, toys, and pharmaceutical consumables. The carcinogenic and teratogenic nature of these synthetic chemicals has been well cited in published research as a potential health threat for all living beings on earth. Contemporary phthalates detection techniques require high level of skills, expensive equipment and extended analysis time as compared to the rapid assay method presented in this chapter. A real-time, non-invasive detection of phthalates was performed by employing electrochemical impedance spectroscopy technique incorporating an enhanced penetration depth interdigital capacitive transducer. A research was conducted to investigate the application of pre-concentration extraction polymer with molecular imprinted recognition sites as an analyte sensitive coating for the sensor to introduce molecular selectivity for di (2-ethylhexyl) phthalate molecules. Self-assembled monolayer with embedded imprinted polymer was used to functionalize the sensing surface in order to capture phthalate molecules spiked in the water samples and commercial drinks. Equilibrium rebinding experiments were conducted to demonstrate the adsorption capabilities of the molecular imprinted polymer coating. Impedance spectra were obtained over a frequency range by applying frequency response analyzer (FRA) algorithm to observe impedance change that occurred for various concentrations of the analyte. Complex nonlinear least square (CNLS) curve fitting spectrum algorithm interpreted the experimentally obtained impedance spectra into electrochemical equivalent electric circuit and corresponding parameters. Analysis of the equivalent circuit was used to explain the kinetics of chemical bindings taking place at the electrode-electrolyte interface in the electrochemical cell in terms of electrical component parameters. The results from the proposed detection system were validated by high-performance liquid chromatography (HPLC-DAD).

A.I. Zia · A. Rao · S.C. Mukhopadhyay (✉)
School of Engineering and Advanced Technology, Massey University,
Palmerston North, New Zealand
e-mail: s.c.mukhopadhyay@massey.ac.nz

A.I. Zia
Department of Physics, COMSATS Institute of Information Technology, Islamabad, Pakistan

1 Background

Phthalates, the esters of 1-2-Benzenedicarboxylic acid, have been declared as ubiquitous environmental pollutants and endocrine disruptors by several health monitoring agencies all over the world for carcinogenic and teratogenic effects observed as reproductive and developmental defects in rodents [1, 2]. The ortho phthalate diesters are commercially manufactured by alcoholic esterification of phthalic anhydride. Among all synthetic phthalates, DEHP constitutes more than 80 % of the total phthalate production all over the world. The low-cost synthesis and mechanical strength induction capability to produce flexibility in Polyvinyl Chloride (PVC) products renders it a potential candidate for unlimited industrial applications. Published research concludes that phthalates pose highest toxicity and endocrine disruptive threat to the human race, especially to young children, infants, pregnant and nursing mothers [3]. Recent researches have suggested declining trend in the human reproductive hormonal levels, damage to sperm DNA and reduced sperm count in males [2]; whereas, elevated risk of altered breast development and breast cancer, premature puberty and prostate changes in females [4, 5] has also been indebted to its regular oral intake from different sources.

Phthalates with higher molecular weight i.e. DINP (Diisononyl phthalate) and DEHP are used as plasticizer in almost every plastic product including food and beverage packaging and even in the medical consumables. The phthalates with low molecular weight, such as diethyl phthalate (DEP) and dimethyl phthalate (DMP), are used in cosmetics, insecticides, paints and pharmaceutical applications [6] hence penetrating into human chemistry through inhalation and dermal absorption. Phthalates added as plasticizers in plastics; do not covalently bond to the molecular structure of the resulting product. Therefore, their potential for non-occupational exposure to the environment is high. They leach and migrate into packaged food and beverages, gas out in the atmosphere or enter directly into human body fluids through medical products [7]. Figure 1 provides an insight into the molecular structures of synthetic phthalates used as plasticizers and solvents in the industrial sector. In the recent years, the abundance of phthalates in our ecosystem has raised many public health concerns. These concerns transformed into alarming state especially after endocrine disrupting properties of these estrogenic compounds were highlighted by research [8]. The penetration of these teratogenic and carcinogenic compounds into the food chain, waste water, and human ecosystem occurs not only during their production phase but during their usage and even after their disposal via leaching, migration and volatilization. Their presence in the atmosphere has become so ubiquitous that even the best lab setup is unable to measure it below a concentration level of 2 parts per billion [9]. The extensive use of phthalates in medical products have paved their way to infuse directly into body fluids via medication and through the use of disposable medical plastic consumables in transfusion [10].

Human beings come in contact with phthalates by three major routes; Dermal, Inhalation and oral (dietary) intake [11]. The oral ingestion is the most efficient

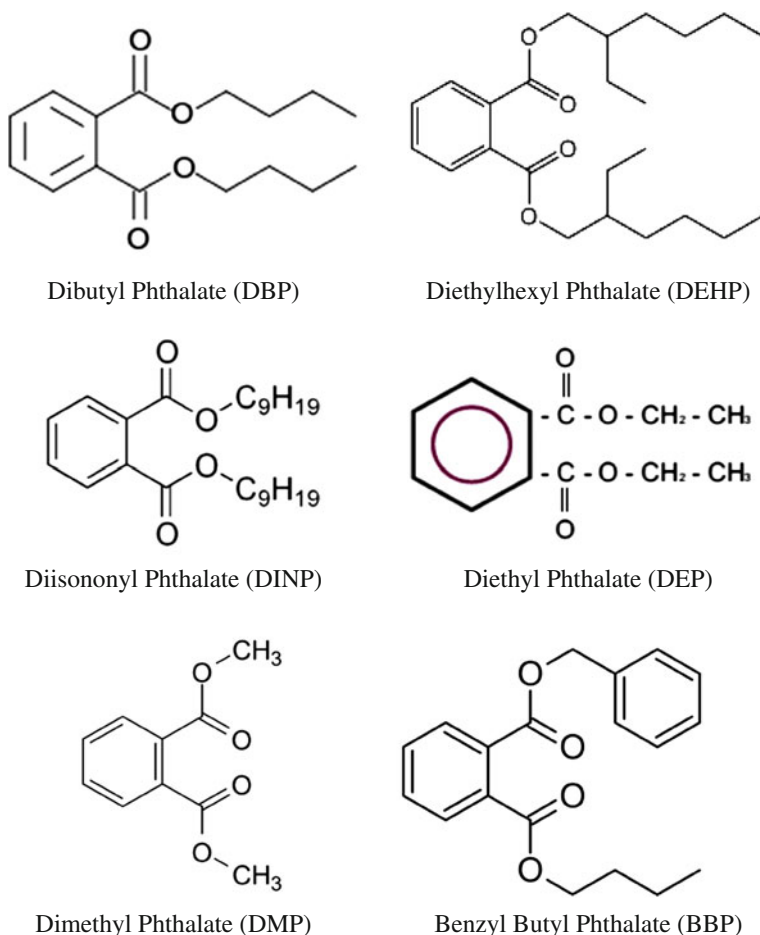


Fig. 1 Types of phthalates used in industrial sector as plasticizers

intake among all as it contributes the highest phthalate exposure rates to the human beings. [11]. Dietary exposures occur by accumulating phthalates either during the food processing and packaging from processing equipment or leaching into fatty foods, including dairy products, and from packaging during storage. Dairy products consumption by children per kilogram body weight is higher as compared to the adults that pose a greater risk of reproductive and developmental toxicities for young children [7]. Polymer toys softened with DINP were estimated exposures ranged from 5 to 44 $\mu\text{g}/\text{kg}$ body weight/day with 99th percentiles up to 183 $\mu\text{g}/\text{kg}$ body weight/day for infants via mouthing activities [8]. Leaching of phthalates into food from packaging [12]; from PET (PETE, polyethylene terephthalate) bottles

Table 1 Risk assessment for phthalate intake (mg/kg bodyweight/day) by world health agencies

Phthalate type	Risk assessment of phthalates			
	Country, region	Committee/year	mg/kg bodyweight/day	MRL ^a /TDI ^b /RfD ^c
DEHP	USA	US-EPA, 1993b	0.02	RfD
DEHP	USA	ATSDR, 2002	0.1	MRL
DEHP	Canada	Health Canada, 1994	0.044	TDI
DEHP	EU	CSTEE, 1998a, b	0.050	TDI
DINP	EU	CSTEE, 1998a, b	0.25	TDI
DEP	USA	ATSDR, 1995	7	MRL
DBP	USA	ATSDR, 2001	0.5	MRL
DBP	USA	US-EPA, 1990	0.1	RfD

^aminimal risk level

^btolerable daily intake

^creference dose levels

into beverages and mineral water [9] and from corks of glass bottles has been published [13]. United States Environmental Protection Agency has declared the limit of 6.0 µg/L as ‘safe intake’ limit for drinking water. The guideline for safe drinking water, published in a list of priority compounds, by World Health Organization (WHO) and European Union sets 8.0 µg/L as a maximum safe limit for DEHP presence in fresh and drinking water [14]. Wang et al. [15] experimentally demonstrated the phthalate concentration that leached into the orange juice from tetra pack plastic liner shoots to 110 times higher above the tolerable daily intake limit (TDI). Table 1 shows the risk assessment for phthalate intake (mg/kg bodyweight/day) declared by world health agencies.

2 International Context

In May 2011, Ministry of Health Taiwan reported the illegitimate addition of phthalates by a beverage company into its products to replace expensive palm oil. DEHP was added as a clouding agent in the juice drinks to provide a more appealing natural appearance to the juice products [16]. Later, on investigations, phthalates were found in 965 products classified as sports drinks, concentrated juices, tea drinks, jams and jellies, medicines and powdered foods supplements manufactured in Taiwan added at concentrations extremely dangerous for human health. Use of DEHP as plasticizers has been allowed in manufacturing of PVC food packaging disposable plastic products all over the world, but its use as a food additive in food products has never been legitimized due to the health risk involved. It is worth noting here that the maximal DEHP intake limit referred to as the reference dose (RfD), the minimal risk level (MRL), and the tolerable daily

intake (TDI) limit for DEHP by government agencies in the United States (US-EPA and ATSDR), Canada and European Union respectively, recommended a range of 0.02–0.06 mg/kgbw/day as “safe” for human consumption [6, 17]. Ingested DEHP is broken down into its metabolites by the human digestive system and is excreted in the urine. Long-time regular ingestion of DEHP with food at levels above the TDI can become a body burden and could create hormonal imbalance in the human body that may result in the decrease of male reproductive ability, and female precocious puberty, breast cancer and loss of gender uniqueness [5, 18–20]. This incident named as “Taiwan Food Scandal” raised public concerns about the potential adverse health outcomes from the raised exposure to DEHP and created a huge wave of suspicion for all packed beverages throughout the world. Importers demanded testing certifications from the manufacturing companies that caused massive workload on the test laboratories. Due to expensive and time-consuming testing, manufacturers had to face production loss and paid additional costs to get their products certified against phthalate tainting.

Phthalates’ detection and measurement are purely laboratory based procedures. The ubiquitous presence of this compound as a contaminant severely limits its minimal detection level. Even in most controlled laboratory setup it cannot generally be accurately quantified below about 2 ppb [21]. Gas chromatography (GC) is the most commonly used technique for detection and quantification of phthalates metabolites [22]. High-performance Liquid Chromatography (HPLC) is used to measure phthalate concentrations in blood plasma and urine sample at low detection limits [15, 23]. Chromatography technique is used to separate complex mixtures of organic compounds with each compound quantified by its particular detector. DEHP is measured using Electron Capture Detector (ECD) [22] and Flame Ionization Detector (FID) [24]. Liquid Chromatography (LC) coupled with mass spectrometry (MS) and ultraviolet (UV) detections are also a few commonly used techniques for detection of phthalates. Almost all contemporary analytical techniques described here are highly sensitive due to the requirement of measurement of trace levels of phthalates present in food and beverage samples. Unfortunately, on the other hand, these are time-consuming, expensive, complicated, produce laboratory waste, need the expertise of highly trained professionals in addition to the submission of samples to laboratories worth millions of dollars. Blood and urine are the most common matrices used for biomonitoring of phthalates, but the results of these bio-monitors do not provide the complete picture of phthalate intake, rather just provide the quantity of metabolites excreted, losing information about the amount of phthalate that has become the body burden. Therefore, it is necessary to have a rapid assay which may detect the quantity of phthalates present in food and beverages as initial intake via the oral route which is deemed to be the biggest source of human phthalate exposure due to the extensive use of plastics in our everyday lifestyle. The requirement of instant screening of a batch of products manufactured at an industrial setup still requires attention of the researchers to devise an assay which may be simple enough to be handled with minimal training needs and does not involve bulky and expensive support electronics.

3 Development of Smart Interdigital (ID) Sensors

Conventional ID capacitive sensors are structured as repeated patterns of single sensing and single excitation (working) finger-like electrode pairs fabricated on one side of solid substrate to achieve unique side access and non-invasive testing. Capacitive reactance is produced, as a function of analyte properties, consequent to the applied alternating electric field perturbations exposed as frequency sweep to the sensor. The penetration depth of the fringing electric field is a function of the spatial wavelength (distance between sensing and working electrode) of the thin film electrodes [25]. In situ testing capability, single side access, field penetration depth control, signal strength control, simplified modeling, and low cost renders planar ID capacitive sensors the most suitable candidate for chemical and biological sensing applications [26–28]. These type of sensors have already been used for hormone detection [29, 30], quality monitoring of dairy, meat and leather products [31–35] humidity sensors [36], chemical sensing [37], and position sensors [38]. Figure 2 displays the layout of conventional planar ID capacitive sensor.

3.1 Smart Sensor Design for ID Capacitive Sensors

In order to maintain system linearity and reversibility, very small amplitude perturbation is applied to the ID sensors therefore; the spatial wavelength has to be kept in the range of few microns, consequently limiting the penetration depth of the fringing electric field. The penetration depth of the fringing electric field was achieved by employing a smart design with multiple sensing electrodes between working electrodes. The design optimization and performance evaluation was carried out by finite element modeling (FEM) software COMSOL® Multiphysics using its AC/DC module in 3D quasi-static mode. The simulated mathematical model depicted that new sensor design is better as compared to the conventional sensor design with respect to size, design, performance, and sensitivity. The designs

Fig. 2 Conventional Planar Interdigital Capacitive Sensor configuration

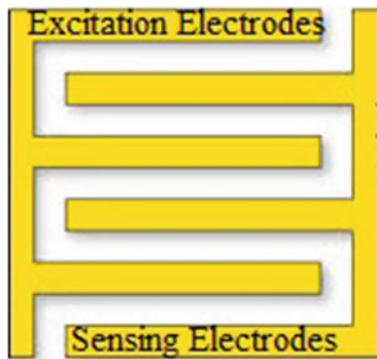
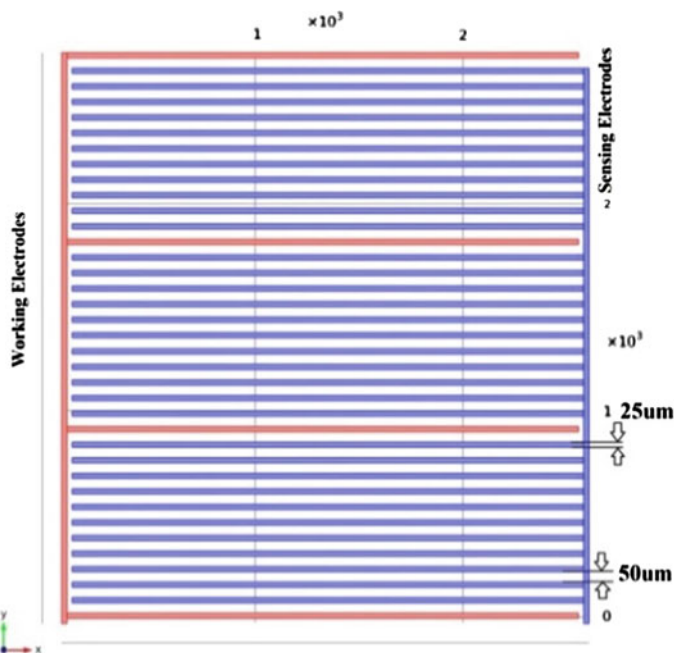


Table 2 FEM simulated capacitance and energy density values for two types of sensor geometries

Sensor type	V_{rms} (V)	Freq. (Hz)	Electrostatic energy density (J)		Capacitance (pF)	
			MilliQ ϵ_r = 80.1	DEHP ϵ_r = 5.1	MilliQ ϵ_r = 80.1	DEHP ϵ_r = 5.1
1-11-50	1	1000	6.9e-12	7.6e-13	13.94	1.52
1-5-50	1	1000	4.2e-12	4.9e-13	8.46	0.92

with eleven and five sensing electrodes owing pitch length (distance between two neighboring electrodes) set at 50 μm showed better sensitivity for the analyte in the simulation results. Table 2 FEM simulated capacitance and energy density values for two types of sensor geometries gives the FEM analysis results for the two types of sensors shows the sensor's geometric layout with multiple sensing electrodes in comparison to the conventional sensors as displayed in Fig. 2.

The new sensor was designed by keeping the substrate material and thickness, electrode material and thickness and effective sensing area constant. Design geometry drawn in eleven sensing electrodes between two working electrodes with pitch length set at 50 μm (Fig. 3). Sensing area was fixed to 2.5×2.5 mm, electrode area 25 $\mu\text{m} \times 2.425$ mm and electrode thickness to 520 nm was taken as standard.

**Fig. 3** New design Silicon substrate based ID sensor (1-11-50)

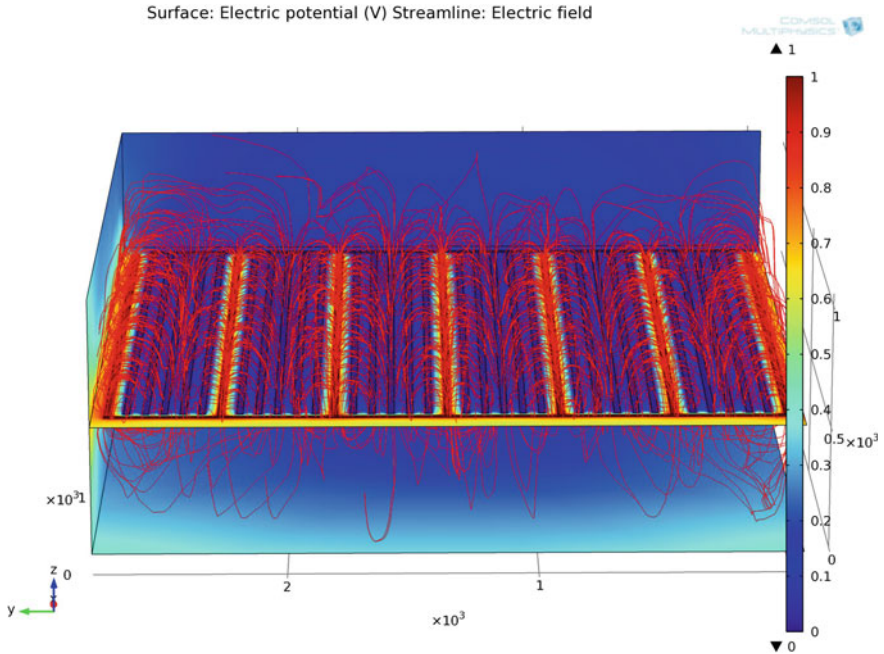


Fig. 4 Electric potential and field penetration depth for five sensing electrodes' sensor simulated by COMSOL FEM

COMSOL® Multiphysics software estimated an average penetration depth of 437.6 microns for eleven electrode design therefore it was selected for the fabrication. Figures 4 and 5 show the penetration depth of quasi-static electric field as theoretically calculated by FEM for proposed designs with five and eleven sensing electrodes. Detailed analysis and comparison results for the new smart model have been discussed elsewhere. [39–41].

4 Sensors' Fabrication

36 workable sensors were patterned and fabricated on a single crystal 4 in. (diameter) single crystal Silicon wafer (thickness 525 μm). Photolithography and plasma enhanced etching of photoresist were used to transfer sensors' patterned from soda lime mask over the native SiO_2 layer onto the wafer. A 20 nm DC magnetron sputtered seed layer of Chromium was used to provide better adhesion for gold electrodes on the substrate surface. Argon gas plasma DC magnetron sputtering was used to deposit 500 nm gold thin film to fabricate the new design of multiple sensing interdigital electrode structures. Gold has been the most preferred electrode material used for sensing applications for its excellent physicochemical

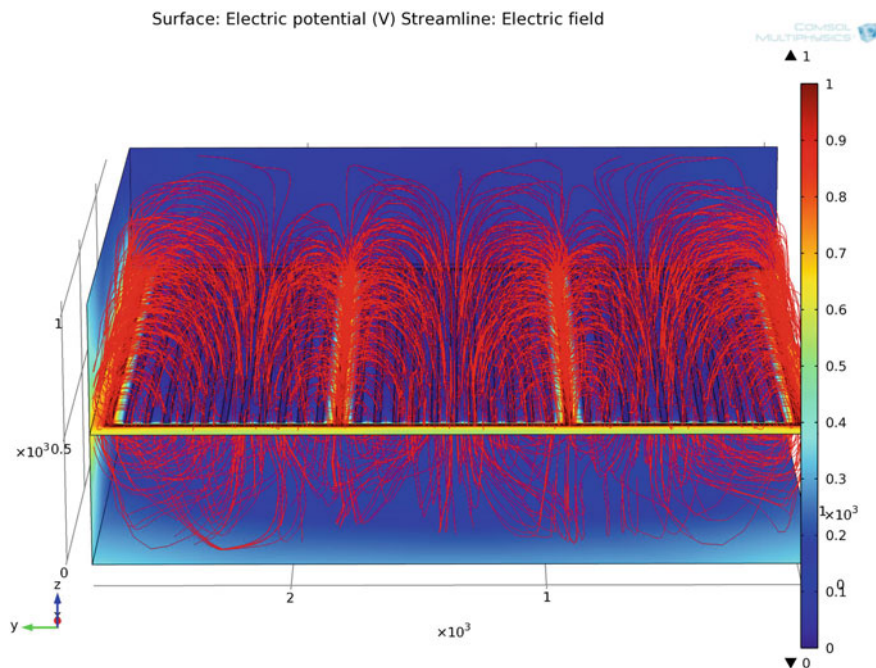


Fig. 5 Electric potential and field penetration depth for eleven sensing electrodes' sensor simulated by COMSOL FEM

stability, bio-affinity, low electrical resistivity and minimal oxidation [36]. After lift-off, the wafer was coated with a 1 μm layer of Parylene C in order to provide a uniform pinhole free layer of polymer on the sensor which enables it to withstand continuous exposure to air at high temperatures. It provides a protective layer of polymer to prevent thickening of silicon dioxide layer due to the further oxidation of silicon substrate at high temperatures. Plasma etching process was used to etch Parylene C from the connection pads and the sensing area in order to apply DEHP selective coating on the sensing surface (electrodes). Figure 6a displays sensors in fabricated wafer form and Fig. 6b displays individual sensor showing scale for sensors' dimension observation.

5 Sensor's Selectivity for DEHP

Molecular imprinted polymer (MIP) with DEHP recognition sites was used to introduce selectivity for the target molecule. Molecular imprinted polymers (MIPs) are specially synthesized polymerized materials having valuable molecular recognition capabilities for a particular molecule. These possess distinct cavities designed for a target molecule, privileged by unique advantages like high selectivity,

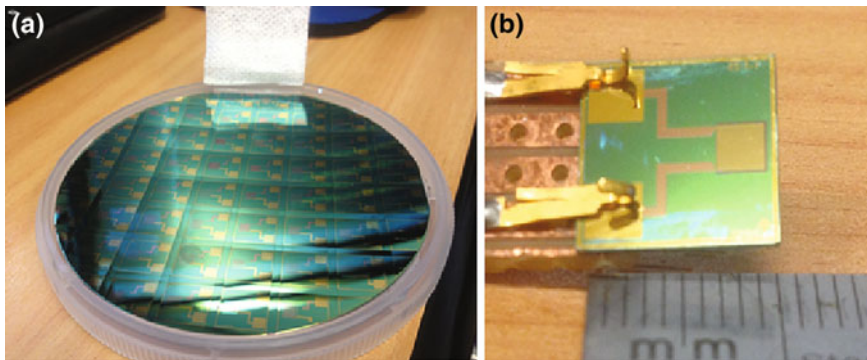


Fig. 6 **a** Fabricated wafer of ID thin film electrode sensors. **b** Individual sensor's design and connection pad

physiochemical stability, bonding interaction and explicit recognition of analyte with a unique quality of regeneration and rebinding. These polymers could be synthesized by applying a number of approaches like precipitation, bulk, suspension, swelling, miniemulsion and core-shell polymerizations depending on the application [37]. This molecular recognition selectivity has proved to be an attractive predominant advantage for separation and analyses of complicated samples and has been applied in several contexts e.g. solid phase extraction (SPE), chromatography, electro-chromatography, membrane filtration and sensing. It has obvious advantages over biological receptors and antibodies of number of target molecule capturing sites [38]. MIPs are intrinsically stable robust and reusable. The entrapment of target molecules is achieved by two established strategies using covalent or non-covalent interactions of the target molecule with the functional monomer. The non-covalent approach makes use of instinctive intermolecular forces present in the target and monomer molecule. These relatively weak forces could be hydrogen bonding, ion pair, dipole-dipole interactions or van der Waals forces between the monomer and the target molecule.

6 Experimental Setup

6.1 Materials

Di(2-ethylhexyl) phthalate (DEHP). N, N-methylene-bisacrylamide, methacrylamide, ammonium persulfate, Methanol, ethanol, acetonitrile, chloroform, dimethylformamide (DMF), dichloromethane and 3-aminopropyltriethoxysilane (APTES) were procured from Sigma-Aldrich, Germany. Deionized water MilliQ® was obtained from MILLIPORE water system (USA)- 18 MΩ cm. Gravimetrically prepared di (2-ethylhexyl) phthalate (DEHP) solution at a

concentration of 200 $\mu\text{g/mL}$ (200 ppm) in ethanol (99.5 %) purity was ordered and received from ChemService® USA. Other working samples of lower concentrations were achieved by serial dilution method in deionized water MilliQ®. Pure deionized water with a 200 ppm concentration of ethanol was used as control solution for the experiments. pH meter from IQ Scientific Instrument Inc. USA was used to measure pH levels of the test and control solutions. The device was calibrated with buffer solutions provided by the manufacturer.

6.2 *Synthesis of DEHP-Imprinted Polymer*

A solution of 2.5 ml DMF, 7.5 ml MilliQ water, 14.5 mmol meth acrylamide and 1 ml DEHP was prepared in an ice bath and functional monomer and template (DEHP) molecules were allowed to generate hydrogen bonds between DEHP and meth acrylamide (monomer) in the presence of nitrogen atmosphere. 5.3 mmol N, N-methylene-bisacrylamide (cross-linker) and 0.7 mmol ammonium persulfate (initiator) were added to the mixture and stirred until dissolved in the solution in a flask installed with a reflux condenser and a magnetic stirrer. The solution was kept at 50 °C for 6 h in order to complete the polymerization reaction. Figure 7 shows the MIP after polymerization. MIP was filtered, washed with deionized water and dried under nitrogen flow. MIP was ground and sieved to obtain 90 micron particle size. DEHP (template) was extracted out of the MIP powder encapsulated in 0.22 micron filter caplet by Soxhlet extraction in 12 h with methanol. MIP powder was dried under nitrogen at room temperature. Figure 8 shows the procedure of Soxhlet extraction.

A self-assembled monolayer of 3-aminopropyltriethoxysilane (APTES) was used to immobilize MIP functional coating on the sensing surface of the sensor by dip coating method. 2 g MIP powder was mixed with 2.5 ml APTES and 1.5 ml of DI water to prepare coating suspension. The sensor was dipped in the suspension and was withdrawn at a slow rate of 2.5 mm per min to achieve a uniform coating on the sensing surface. The dip coated sensor was dried for 18 h under nitrogen at room temperature prior to the adsorption investigation. Figure 9 shows the MIP synthesis process and Fig. 10 displays the magnified image from the confocal microscope of the MIP coated sensor showing porous surface of the molecular imprinted polymer embedded in APTES.

7 **Adsorption Studies of DEHP to MIP**

The extraction of adsorbed DEHP from the sensor's functionalized coating was carried out in an equal volume (2 ml) of dichloromethane by sonication process of 15 min at all instances. The solvent was evaporated and 50 μl dichloromethane was used for HPLC testing of the eluent. Luna C 18 column was used in

Fig. 7 DEHP imprinted polymer after polymerization

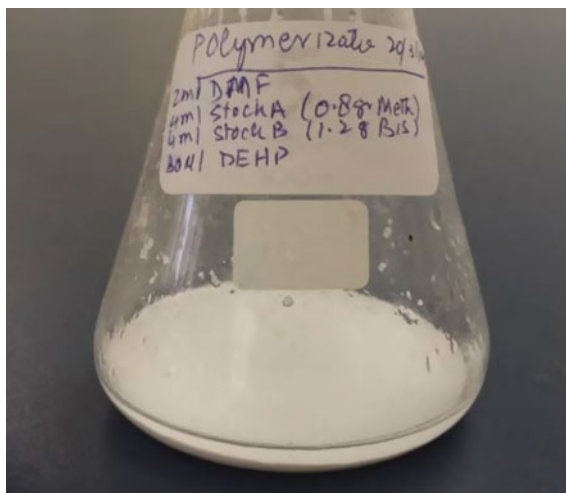


Fig. 8 Soxhlet extraction of the template (DEHP)



DIONEX HPLC system to test the samples at a wavelength of 224 nm for diode array detector (DAD) with a mobile phase of methanol/acetonitrile (1:9 v/v). The binding isotherms of DEHP to MIP were determined in the concentration range of 1–100 μgml^{-1} . The static adsorptions of MIP were calculated using following relation.

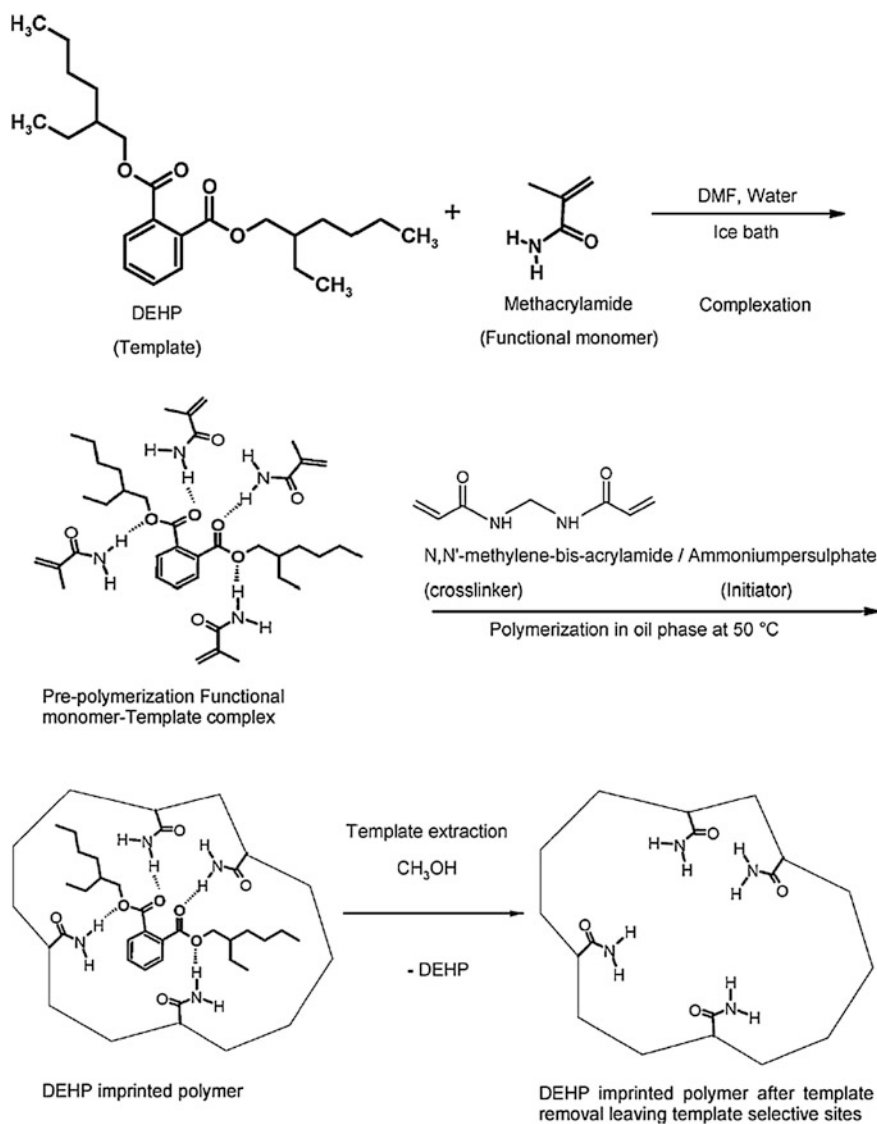
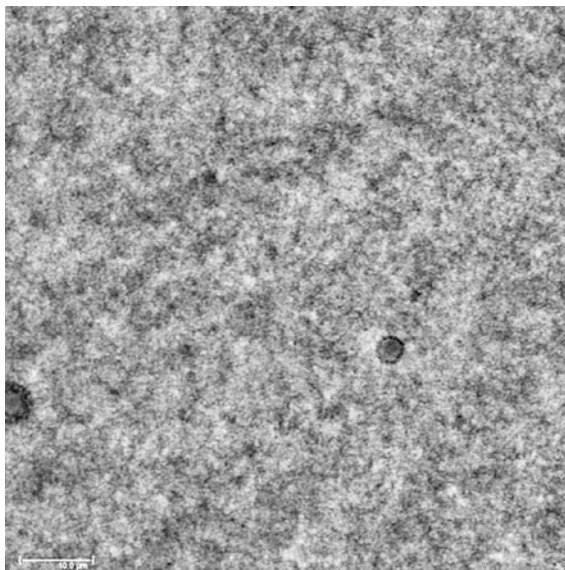


Fig. 9 Schematic diagram for MIP preparation [42]

$$Q = \frac{(C_i - C_f)V}{m} \quad (1)$$

Where Q (mg g^{-1}) is the mass of DEHP adsorbed per gram of MIP, C_i (mg l^{-1}) is the initial concentration of DEHP; C_f (mg l^{-1}) is final concentration of DEHP after adsorption. V (l) is the total volume of the adsorption mixture and m (g) is the mass of the polymer used.

Fig. 10 Confocal micrograph image of MIP coated sensor



7.1 Static Adsorption of DEHP to MIP

The isotherm for the static adsorption studies of DEHP to MIP is shown in Fig. 11. The plot depicts that the amount of DEHP bound to the polymer increases with the increase in concentration of the DEHP in the test samples below a concentration level of 50 mg l^{-1} (50 ppm). The polymer saturates as the concentration level increases above the said limit, and the curve becomes parallel to concentration axis. This is because the miniature size of the sensor allows very less MIP immobilized

Fig. 11 Static adsorption isotherm of DEHP to MIP

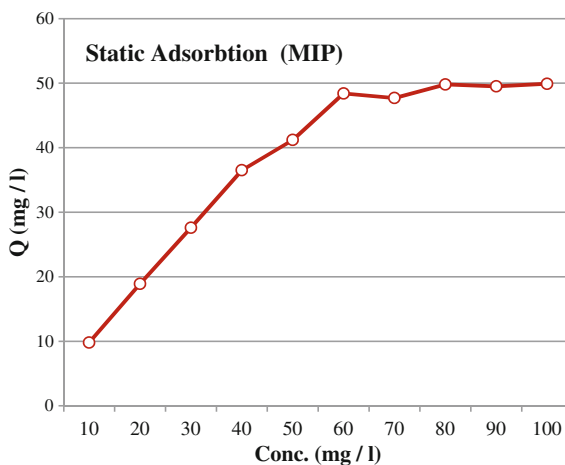
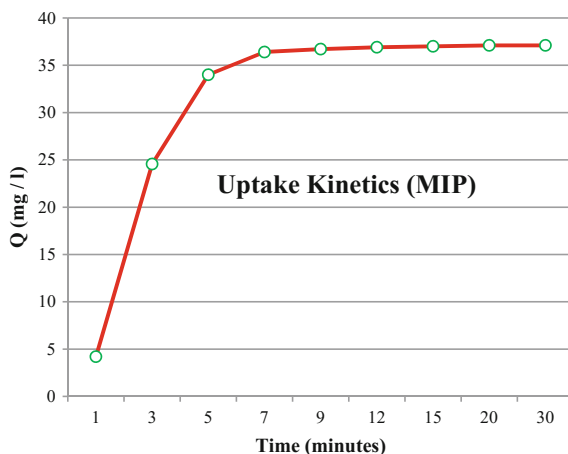


Fig. 12 Uptake kinetic study of DEHP to MIP



on the sensing surface. Since the targeted range of detection is lower to the saturation limit, therefore, it is acceptable.

7.2 Uptake Kinetics of DEHP to MIP

Figure 12 presents the plot for adsorption kinetics of DEHP to MIP. This study was helpful to determine the adsorption time required by DEHP present in the sample to get trapped at the molecular recognition sites in the MIP. The coated sensor dipped in 5 ml test solution with a concentration of $50 \mu\text{gml}^{-1}$. The concentration level was chosen in the light of static adsorption studies undertaken in Sect. 7.1. The results depicted that the molecularly imprinted polymer owns fast entrapment kinetics, and the binding equilibrium were reached in almost 7 min. The rapid absorption capability of the MIP is an advantage for using the polymer with electrochemical impedance spectroscopy where rapid impedance measurements are mandatory for non-stationary systems.

8 Electrochemical Impedance Spectroscopy Experiments

With an enormous research in the field of impedance measurements, the frequency response analyzer (FRA) has achieved a de facto standard for electrochemical impedance measurements. A dc potential overlaid by a small amplitude (5–15 mV) a sine wave applied to the excitation electrode and the consequent analysis of resulting a current made is commonly termed as FRA. Despite being highly sensitive, this method has a limitation of being viable only for stable and reversible systems in equilibrium [39]. The outcome of an impedance measurement is

represented as Bode and Nyquist (Cole-Cole) plot which is further analyzed on basis of Randle's equivalent circuit model in order to infer electrical equivalent of exchange and diffusion processes describing the system kinetics by complex nonlinear least square curve fitting (CNLS) of the experimental data. The algorithm performs statistical analysis to calculate the residual mean square $r_{amplitude}^2$ for experimentally observed values in measured spectra by complex nonlinear least square using following relation.

$$r_{amplitude}^2 = \sum_{i=1}^N \frac{(Z'_{iobs} - Z'_{icalc})^2 + (Z''_{iobs} - Z''_{icalc})^2}{Z'_{iobs}{}^2 + Z''_{iobs}{}^2} \quad (2)$$

where

Z'_{iobs} is the observed real impedance.

Z'_{icalc} is the calculated real impedance.

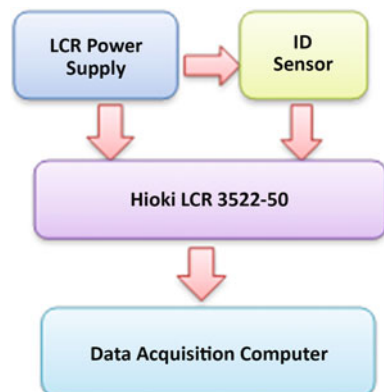
Z''_{iobs} is the observed imaginary impedance.

Z''_{icalc} is the calculated imaginary impedance.

$r_{amplitude}^2$ determines the deviation of the experimentally observed data from the optimal solution.

EIS experiments were carried out room temperature and at the slow mode of the Hioki hi precision 3522-50 LCR Hi Tester (Japan) to keep error rate of <0.05 % as specified by the manufacturer. A 1 Vrms constant voltage sinusoidal signal with a frequency sweep of 1 Hz to 10 kHz was applied to the sensing system. The data acquisition was made at 20 data points per decade on log scale that was written in an excel file by the automatic data acquisition algorithm. Reproducibility and reliability of the results were assured by averaging data from a set of three experiment carried out under same environmental conditions using temperature and humidity controls in the laboratory environment. Figure 13 shows the schematics for the impedance data acquisition system.

Fig. 13 Schematics of Laboratory set up for EIS experiments



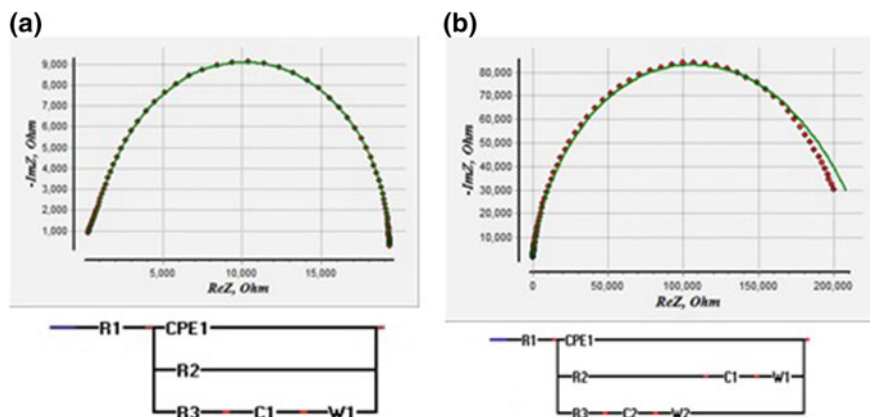


Fig. 14 **a** CNLS equivalent circuit for uncoated sensor. **b** CNLS equivalent circuit for MIP functionalized sensor

The sensor was tested in air under identical temperature (20 °C) and humidity (44 %) conditions before and after immobilization of selective MIP coating in order to investigate the effect of coating on the sensor.

The impedance data was analysed by CNLS algorithm to obtain the equivalent circuit for the system with and without coating. It should be noted that $r_{amplitude}^2$ for each fitting is of 1 the order of magnitude 10^{-4} achieved with 300 iterations. Figure 14a, b show the deduced equivalent circuit by CNLS algorithm without coating and with coating respectively.

On comparing the equivalent circuits, it is observed that coating has introduced two additional circuit components C2 and W2 in the equivalent circuit of MIP functionalized sensor. Table 3 and Table 4 show the values of the deduced circuit parameters. This is due to the fact that the self-assembled mono layer of APTES behaves as a dielectric layer introducing additional circuit capacitance, whereas, Warburg resistance is introduced due to the presence of non-conductive MIP coating on the sensing surface.

Table 3 Equivalent circuit parameters for the uncoated sensor

C1 (F)	R1 (Ohm)	R2 (Ohm)	R3 (Ohm)	W1 (Ohm)	CPE1
4.416E-10	2.39E-13	55058	3.25469	4.042E-14	3.261E-09
6.669E-10	2.236E-13	56898	4.25698	8.02E-14	1.503E-08
4.898E-10	1.241E-13	55078	1.9333	2.454E-15	6.967E-09

Table 4 Equivalent circuit parameters for sam-mip functionalized sensor

C1 (nF)	C2 (nF)	R1 (Ohm)	R2 (Ohm)	R3 (kOhm)	W1 (Ohm)	W2 (Ohm)	CPE1
1.07	1.28	1.39	6.33	24.0	1.15E-15	1.49E+06	2.93E-05
1.80	9.23	3.12	0.0217	4.99	2.19E-18	2.06E+06	4.40E-05

8.1 DEHP in Deionized Water Samples

Three different concentrations of DEHP; 1, 10, and 50 mgL⁻¹ (ppm) in deionized water were tested at initial temperature (20 °C) and humidity (44 %) conditions. The control solution was 18 MΩ cm deionized MilliQ water with pH 6.71. It was observed that the addition of DEHP in the working solutions did not alter the pH level and the average pH value measured was 6.52 at 20 °C. The sensor was profiled in the air before its exposure to the different DEHP concentrations to create an experimental reference curve for the sensor's performance. The immobilized MIP sensor was pipetted with 10 μl of MilliQ water, and the test was run to generate the control reference curve, later the MIP functionalized sensor was pipetted 10 μl 1 ppm solution on the sensing area. A 7 min time period was allowed to the polymer to entrap DEHP molecules from the test sample. The MIP was washed with acetone and rinsed with distilled water in order to remove excess / un-bound DEHP molecules, and the EIS testing was executed thrice under same initial temperature and humidity conditions. The MIP was sonicated in dichloro-methane for half an hour to remove the entrapped DEHP molecules and regenerate the functionalized MIP coating. The sensor surface was dried with nitrogen and profiled in the air in order to evaluate and ensure the presence of initial conditions for the EIS testing system before each run.

Each concentration was tested with the proposed system following the described procedural steps. Figure 15 shows the Nyquist plot for the experimentally obtained real and complex impedance. The control reference was plotted by executing experiment after pipetting 10 μl control solution on the MIP functionalized sensing area of the sensor. The decreasing diameter of the Nyquist plot indicates the increasing concentration of the phthalate in the sample.

It was observed that the sensor was sensitive to adsorbed phthalate molecules at low frequencies. The real part of impedance curve dominates due to the presence of ionic concentration in the sample. The diffusion of ions on the electrode surface is a slow kinetic process which is taking place at the low-frequency range, on the other hand the capacitive behavior of the sensor is observed at the relatively higher frequency range.

Figure 16 shows the HPLC chromatograph for eluent after testing each sample. A DEHP peak is observed at 6.91 min with few initial noise peaks. The noise observed before the appearance of the DEHP peak is predominantly due to the presence of traces of solvent in the eluent that appears even in the HPLC

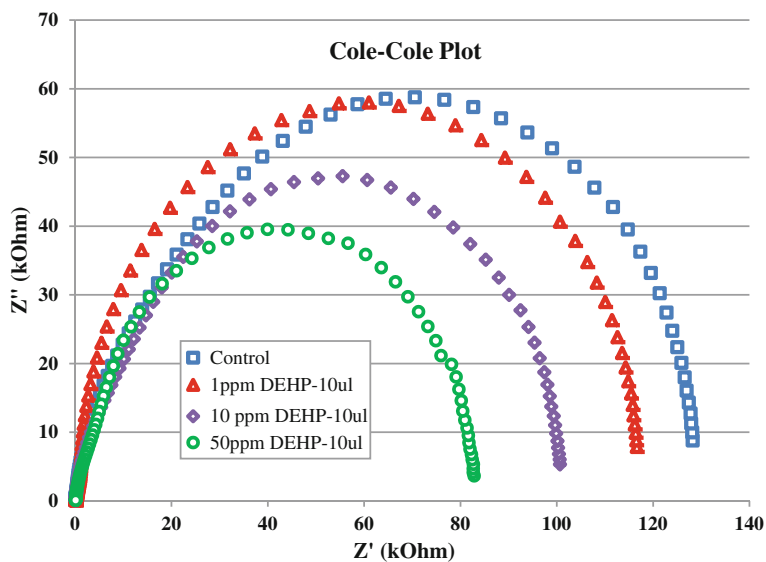


Fig. 15 Nyquist (Cole-Cole) Plot for selective detection of DEHP in DI water

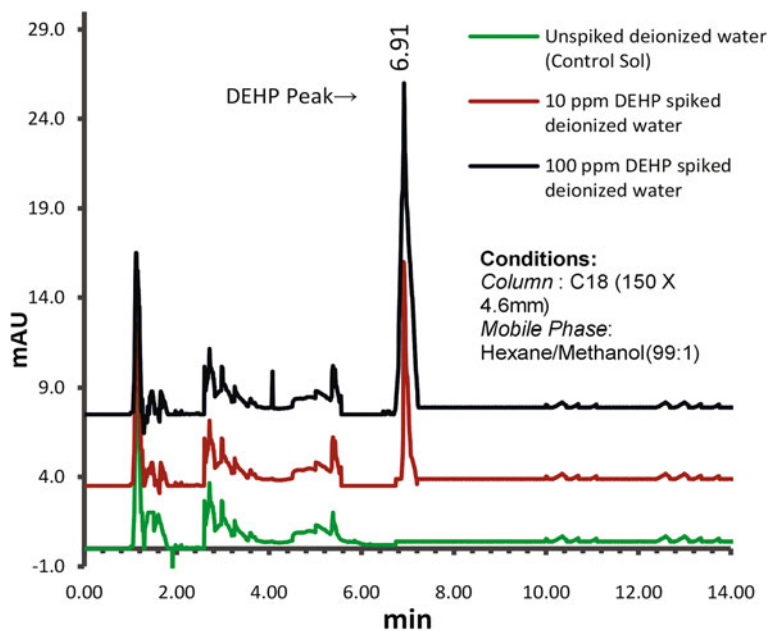


Fig. 16 HPLC-DAD for eluent from MIP tested 10 and 100 ppm DEHP in spiked DI water

chromatograph obtained for the control solution. The insolubility of DEHP in polar medium dictates the requirement for use of a solvent in the molecularly imprinted polymer.

9 DEHP in Energy Drink- MIP Coated Sensor

The energy drink (Lift Plus) sold in glass packaged bottles was selected for testing. Therefore, the possibility of addition of leached DEHP from the packaging was ruled out. The selected drink was spiked with DEHP at a 1, 5, 10 ppm concentration level. The spiked drink samples were tested using the MIP coated sensor.

The impedance spectra from the experimental results depicted that electrode and electrolyte are related by a mixed kinetic and diffusion processes at the electrode surface which causes a polarization at the interface. R_{ct} is, therefore, sometimes referred as polarization resistance, denoted as R_p , in EIS literature. The value of 'charge transfer resistance R_{ct} , or polarization resistance R_p ' can be calculated from bode or Nyquist plot. The rate of an electrochemical reaction can be strongly influenced by the diffusion of reactants towards, or away from the electrode-electrolyte interface. This situation can exist when the electrode is covered with adsorbed solution components or a selective coating. An addition element called Warburg impedance, Z_w , appears in series with resistance R_{ct} . Mathematically Warburg impedance is given by;

$$Z_w = \frac{w}{\sqrt{j\omega}} \quad (3)$$

Where, σ_w is called Warburg diffusion coefficient. It appears that the characteristic of the Warburg impedance is a straight line with a slope of 45° at a lower frequency. This refers to low-frequency diffusion control because the diffusion of reactants to the electrode surface is a slow-paced process which can happen at low frequencies only. At higher frequencies, however, the reactants do not have enough time to diffuse. The slope of this line gives Warburg diffusion coefficient. The Nyquist plot in Fig. 17 for the impedance data measured by the MIP functionalized sensor shows a diagonal line for diffusion process (Warburg impedance) at low frequencies. The charge transfer process at higher frequencies is illustrated by a single time constant semi-circle curve.

The change in impedance read by EIS system depicted that change of the concentration of the analyte in the spiked drink. The tail line with a semi-circular curve at 45° showed the presence of Warburg resistance of the equivalent circuit. The Warburg resistance showed the presence of the ions in the spiked samples that are attributed to the presence of electrolytes in the energy drink. The current flowing through the circuit due to conductive medium dictated the value of the resistance. The equivalent circuit parameters are shown in Table 5 evaluated for all three

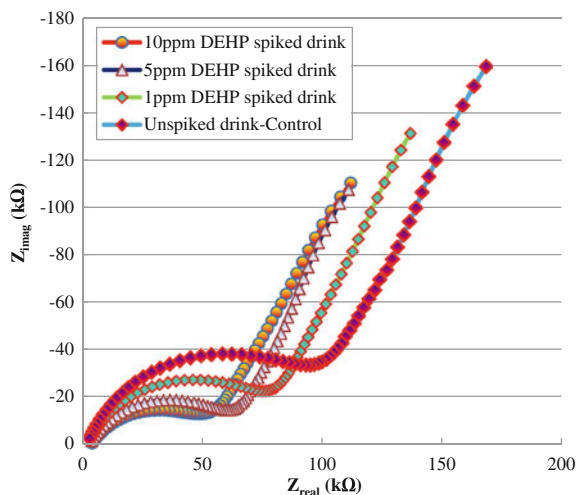


Fig. 17 Nyquist plot for Spiked DEHP energy drinks with MIP coated sensor

concentrations of the tainted drink. Figure 18 displays the equivalent circuit proposed by complex nonlinear least square curve fitting (CNLS) method. It was observed that the system pointed out an adsorption capacitance in series with the polarization resistance that appeared due to the presence of the selective polymer coating on sensing surface.

The results of the proposed system were validated by using HPLC analysis. The chromatogram shows DEHP peaks at 6.91 min in Fig. 19. The peaks before the DEHP peak were due to the presence of the other chemicals in the eluent which might get attached to the MIP due to its porous nature.

This problem can be overcome by increasing the density of the DEHP recognition sites in the MIP matrix by addition of template molecules. The quantity of the template compound added in the pre-polymerisation complex determines the density of the recognition sites formed in resulting MIP.

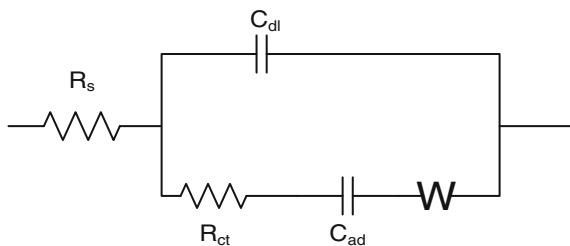
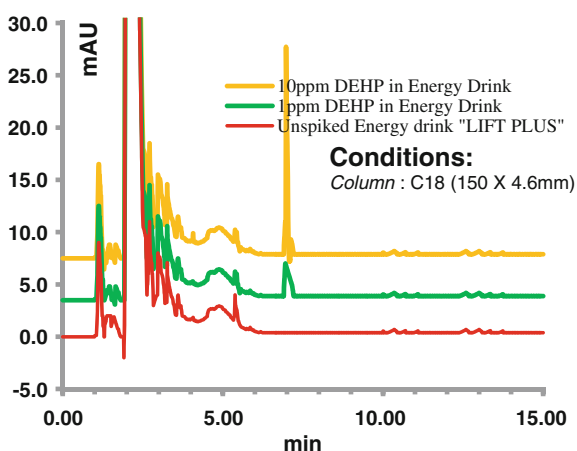
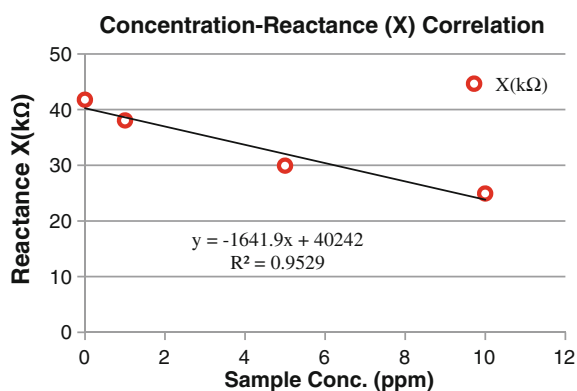


Fig. 18 Equivalent circuit for the electrochemical cell with MIP coated sensor

Table 5 Equivalent circuit parameters evaluated by CNLS fitting for DEHP detection in 'Lift Plus' drink by MIP functionalized sensor

Equation circuit parameters (unit)	DEHP spiked energy drink- MIP functionalized sensor		
	1 ppm	5 ppm	10 ppm
C_{ad} (F)	1.813E-07	1.359E-07	1.466E-07
R_s (Ω)	1.145E+02	1.33E+02	1.58E+02
R_{ct} (Ω)	8.2304E04	6.21E+04	5.57E+04
Z_w (Ω)	2.431E06	1.92E+06	1.64E+06
C_{dl} (F)	7.95E-09	8.79E-09	9.25E-09

Fig. 19 HPLC chromatogram showing the DEHP peaks in the eluent extracted out of the functionalized MIP**Fig. 20** Correlation of DEHP concentration to the reactance (X) read by the MIP coated sensor for the four concentrations of spiked drink samples

The imaginary reactance (X) read by the proposed smart system provided a good correlation for DEHP concentrations in the standard solutions of the spiked drink as read by HPLC system. Figure 20 shows a convincing correlation of 0.9529 that

shows the potential of the system to rapidly quantify the phthalate contents in beverages.

10 Conclusions

Real-time non-invasive selective detection of phthalates by EIS has been reported. The molecular imprinting technique has been used to introduce molecular recognition for the phthalate molecules in the test samples. A functional polymer with Bis (2-ethylhexyl) phthalate (DEHP) recognition sites has been polymerized. The polymer has been converted to micrometer size particles in order to embed the phthalate recognition sites into the self-assembled monolayer formed at the SiO₂ sensing surface for better adhesion of the functionalize coating on the sensing surface. HPLC has been used to study the adsorption capabilities and kinetic intake of the MIP in order to fine tune the experimental procedures and evaluate the performance of the proposed technique. Effects of the functionalized polymer coating on the smart sensor have been studied by complex nonlinear least square curve fitting to evaluate the performance of the proposed functionalized smart sensor. Various concentrations (1–200 ppm) of DEHP in deionized MilliQ water have been tested using the functional polymer to entrap the analyte. Impedance spectra have been obtained using EIS in order to determine sample conductance for evaluation of phthalate concentration in the solution. Experimental results comply with the fact that the immobilization of the functional polymer on sensor introduces selectivity for phthalates in the sensing system. The results were validated by testing the samples using High-Performance Liquid Chromatography (HPLC-DAD).

References

1. P. Foster, Disruption of reproductive development in male rat offspring following in utero exposure to phthalate esters. *Int. J. Androl.* **29**, 140–147 (2006)
2. J.D. Meeker, A.M. Calafat, R. Hauser, Urinary metabolites of di (2-ethylhexyl) phthalate are associated with decreased steroid hormone levels in adult men. *J. Androl.* **30**, 287 (2009)
3. J.A. Colacino, T.R. Harris, A. Schecter, Dietary intake is associated with phthalate body burden in a nationally representative sample. *Environ. Health Perspect.* **118**, 998 (2010)
4. L. López-Carrillo, R.U. Hernández-Ramírez, A.M. Calafat, L. Torres-Sánchez, M. Galván-Portillo, L.L. Needham et al., Exposure to phthalates and breast cancer risk in northern Mexico. *Environ. Health Perspect.* **118**, 539 (2010)
5. J.A. Colacino, A.S. Soliman, A.M. Calafat, M.S. Nahar, A. Van Zomeren-Dohm, A. Hablas et al., Exposure to phthalates among premenstrual girls from rural and urban Gharbiah, Egypt: a pilot exposure assessment study. *Environ. Health* **10**, 40 (2011)
6. U. Heudorf, V. Mersch-Sundermann, J. Angerer, Phthalates: toxicology and exposure. *Int. J. Hyg. Environ. Health* **210**, 623–634 (2007)

7. R. Hauser, S. Duty, L. Godfrey-Bailey, A.M. Calafat, Medications as a source of human exposure to phthalates. *Environ. Health Perspect.* **112**, 751 (2004)
8. S.H. Swan, Environmental phthalate exposure in relation to reproductive outcomes and other health endpoints in humans. *Environ. Res.* **108**, 177–184 (2008)
9. P. Montuori, E. Jover, M. Morgantini, J.M. Bayona, M. Triassi, Assessing human exposure to phthalic acid and phthalate esters from mineral water stored in polyethylene terephthalate and glass bottles. *Food Addit. Contam.* **25**, 511–518 (2008)
10. R. Green, R. Hauser, A.M. Calafat, J. Weuve, T. Schettler, S. Ringer et al., Use of di (2-ethylhexyl) phthalate-containing medical products and urinary levels of mono (2-ethylhexyl) phthalate in neonatal intensive care unit infants. *Environ. Health Perspect.* **113**, 1222 (2005)
11. V. Triantafyllou, K. Akrida-Demertzi, P. Demertzis, A study on the migration of organic pollutants from recycled paperboard packaging materials to solid food matrices. *Food Chem.* **101**, 1759–1768 (2007)
12. M.R. Lee, F.Y. Lai, J. Dou, K.L. Lin, L.W. Chung, Determination of trace leaching phthalate esters in water and urine from plastic containers by solid-phase microextraction and gas chromatography-mass spectrometry. *Anal. Lett.* **44**, 676–686 (2011)
13. R. Sendón, A. Sanches-Silva, J. Bustos, P. Martín, N. Martínez, M.E. Cirugeda, Detection of migration of phthalates from agglomerated cork stoppers using HPLC-MS/MS. *J. Sep. Sci.* **35**, 1319–1326 (2012)
14. Who, *WHO|Guidelines for Drinking-Water Quality*, 4th edn. (World Health Organization 2012-02-21 18:58:44, 2011)
15. Z. Guo, D. Wei, M. Wang, S. Wang, Determination of six phthalic acid esters in orange juice packaged by PVC bottle using SPE and HPLC-UV: application to the migration study. *J. Chromatogr. Sci.* **48**, 760–765 (2010)
16. J. Yang, R. Hauser, R.H. Goldman, Taiwan food scandal: the illegal use of phthalates as a clouding agent and their contribution to maternal exposure. *Food Chem. Toxicol.* **58**, 362–368 (2013)
17. A. Schecter, M. Lorber, Y. Guo, Q. Wu, S.H. Yun, K. Kannan et al., Phthalate concentrations and dietary exposure from food purchased in New York State. *Environ. Health Perspect.* **121**, 473 (2013)
18. L. Lopez-Carrillo, R.U. Hernandez-Ramirez, A.M. Calafat, L. Torres-Sanchez, M. Galvan-Portillo, L.L. Needham et al., Exposure to phthalates and breast cancer risk in Northern Mexico. *Environ. Health Perspect.* **118**, 539–544 (2010)
19. J.D. Meeker, A.M. Calafat, R. Hauser, Di (2-ethylhexyl) phthalate metabolites may alter thyroid hormone levels in men. *Environ. Health Perspect.* **115**, 1029 (2007)
20. H.M. Koch, R. Preuss, J. Angerer, Di (2-ethylhexyl) phthalate (DEHP): human metabolism and internal exposure—an update and latest results 1. *Int. J. Androl.* **29**, 155–165 (2006)
21. X.L. Cao, Determination of phthalates and adipate in bottled water by headspace solid-phase microextraction and gas chromatography/mass spectrometry. *J. Chromatogr. A* **1178**, 231–238 (2008)
22. A.D. LaFleur, K.A. Schug, A review of separation methods for the determination of estrogens and plastics-derived estrogen mimics from aqueous systems. *Anal. Chim. Acta* **696**, 6–26 (2011)
23. J. Li, Y. Cai, Y. Shi, S. Mou, G. Jiang, Analysis of phthalates via HPLC-UV in environmental water samples after concentration by solid-phase extraction using ionic liquid mixed hemimicelles. *Talanta* **74**, 498–504 (2008)
24. S. Hird, Mass Spectrometry in food safety: methods and protocols methods in molecular biology, vol. 747, ed. by J. Zweigenbaum. *Rapid Communications in Mass Spectrometry*, vol. 26 (Springer, New York, 2012), pp. 1162–1164 (ISBN: 978-61779-135-2 PRICE: \$139.00: 416 pp)
25. A.V. Mamishev, K. Sundara-Rajan, Y. Fumin, D. Yanqing, M. Zahn, Interdigital sensors and transducers. *Proc. IEEE* **92**, 808–845 (2004)

26. C. Berggren, B. Bjarnason, G. Johansson, Capacitive biosensors. *Electroanalysis* **13**, 173–180 (2001)
27. S.M. Radke, E.C. Alocilja, A microfabricated biosensor for detecting foodborne bioterrorism agents. *Sens. J. IEEE* **5**, 744–750 (2005)
28. W. Limbut, M. Hedström, P. Thavarungkul, P. Kanatharana, B. Mattiasson, Capacitive biosensor for detection of endotoxin. *Anal. Bioanal. Chem.* **389**, 517–525 (2007)
29. A.I. Zia, A. Mohd Syaifudin, S. Mukhopadhyay, P. Yu, I. Al-Bahadly, J. Kosel, et al., Sensor and instrumentation for progesterone detection, in *2012 IEEE International Instrumentation and Measurement Technology Conference (I2MTC)* (2012), pp. 1220–1225
30. A.Z.S.C. Mukhopadhyay, P.L. Yu, I.H. Al Bahadly, Ovarian hormone estrone glucuronide (E1G) quantification—Impedimetric electrochemical spectroscopy approach, in *2013 Seventh International Conference on Sensing Technology (ICST)* (2013), pp. 22–27
31. S. Mukhopadhyay, C. Gooneratne, G.S. Gupta, S. Yamada, Characterization and comparative evaluation of novel planar electromagnetic sensors. *IEEE Trans. Magn.* **41**, 3658–3660 (2005)
32. S.C. Mukhopadhyay, C.P. Gooneratne, G.S. Gupta, S.N. Demidenko, A low-cost sensing system for quality monitoring of dairy products. *IEEE Trans. Instrum. Meas.* **55**, 1331–1338 (2006)
33. S.C. Mukhopadhyay, C.P. Gooneratne, A novel planar-type biosensor for noninvasive meat inspection. *Sens. J. IEEE* **7**, 1340–1346 (2007)
34. S. Mukhopadhyay, S.D. Choudhury, T. Allsop, V. Kasturi, G. Norris, Assessment of pelt quality in leather making using a novel non-invasive sensing approach. *J. Biochem. Biophys. Methods* **70**, 809–815 (2008)
35. S.C. Mukhopadhyay, Planar electromagnetic sensors: characterization, applications and experimental results (Planare elektromagnetische Sensoren: Charakterisierung, Anwendungen und experimentelle Ergebnisse). *Tm-Technisches Messen* **74**, 290–297 (2007)
36. P. Fürjes, A. Kovács, C. Dúcsó, M. Ádám, B. Müller, U. Mescheder, Porous silicon-based humidity sensor with interdigital electrodes and internal heaters. *Sens. Actuators B: Chem.* **95**, 140–144 (2003)
37. M. Kitsara, D. Goustouridis, S. Chatzandroulis, M. Chatzichristidi, I. Raptis, T. Ganetsos et al., Single chip interdigitated electrode capacitive chemical sensor arrays. *Sens. Actuators B: Chem.* **127**, 186–192 (2007)
38. S. Yoshida, T. Gyoji, K. Toda, Position-sensitive photodetector using interdigital electrodes on Pb2CrO5 thin films. *Int. J. Electron. Theor. Exp.* **68**, 525–531 (1990)
39. A.I. Zia, M.S.A. Rahman, S. C. Mukhopadhyay, P.-L. Yu, I. Al-Bahadly, C.P. Gooneratne et al., Technique for rapid detection of phthalates in water and beverages. *J. Food Eng.* (2013)
40. A. Syaifudin, A.I. Zia, S. Mukhopadhyay, P. Yu, C.P. Gooneratne, J. Kosel, Improved detection limits of bacterial endotoxins using new type of planar interdigital sensors, in *Sensors, 2012* (IEEE, 2012), pp. 1–4
41. A.I. Zia, A.M. Syaifudin, S. Mukhopadhyay, P. Yu, I. Al-Bahadly, C.P. Gooneratne et al., Electrochemical impedance spectroscopy based MEMS sensors for phthalates detection in water and juices. *J. Phys: Conf. Ser.* **439**, 012026 (2013)
42. H. Shaikh, N. Memon, H. Khan, M. Bhangar, S. Nizamani, Preparation and characterization of molecularly imprinted polymer for di (2-ethylhexyl) phthalate: Application to sample clean-up prior to gas chromatographic determination. *J. Chromatogr. A* (2012)

Magnetic and Transport Properties of M-Cu (M = Co, Fe) Microwires

A. Zhukov, M. Ipatov, J.J. del Val, M. Ilyn, A. Granovsky
and V. Zhukova

Abstract We report on magnetic, transport and structural properties of $\text{Co}_x\text{-Cu}_{100-x}$ ($5 \leq x \leq 30$) and $\text{Fe}_{37}\text{Cu}_{63}$ glass-coated microwires prepared by the Taylor-Ulitovsky method. The objective of the reported work is to develop a novel functional materials exhibiting giant magnetoresistance (GMR). For Co-Cu microwires with $x = 5$ we observed the resistivity minimum at 40 K associated with the Kondo-like behaviour but magnetoresistance is small. For $x \geq 10$ magnetoresistance reaches 9 % at low temperatures. Temperature dependence of susceptibility shows considerable difference for $x > 10$ and $x \leq 10$ attributed to the presence of small Co grains embedded in the Cu matrix for $x \geq 10$. By X-ray diffraction we found, that the structure of $\text{Co}_x\text{-Cu}_{100-x}$ microwires for $x \geq 10$ is granular consisting of two phases: fcc Cu appearing in all the samples and fcc α -Co presented only in microwires with higher Co content. Structure of $\text{Fe}_{37}\text{Cu}_{63}$ microwires consists of Cu nanograins with average grain size of around 40 nm and α -Fe nanocrystals with average grain size ranging between 6 and 45 nm depending on samples geometry. These microwires also exhibit GMR (up to 7.5 % at 5 K).

A. Zhukov (✉) · M. Ipatov · J.J. del Val · V. Zhukova
Fac. Químicas, Dpto. Física de Materiales, UPV/EHU, P. Manuel de Lardizabal, 3,
20018 San Sebastian, Spain
e-mail: arkadi.joukov@ehu.eus

A. Zhukov · M. Ipatov · V. Zhukova
Dpto. Física Aplicada, EUPDS, UPV/EHU, San Sebastian, Spain

A. Zhukov
IKERBASQUE, Basque Foundation for Science, 48011 Bilbao, Spain

M. Ilyn
Center of Physics of Materials, CSIC-UPV/EHU, P. Manuel de Lardizabal, 5,
20018 San Sebastian, Spain

A. Granovsky
Faculty of Physics, Moscow State University, Moscow 119991, Russia

1 Introduction

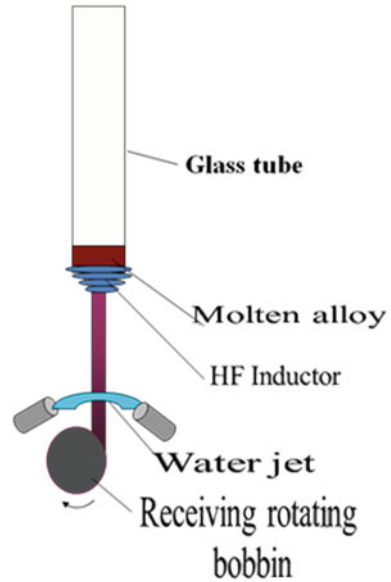
Thin metallic wire produced by rapid quenching technique attracted attention of researchers and engineers owing to excellent magnetic properties and inexpensive fabrication process. Recent industrial applications require miniaturization of the devices and sensors. Consequently considerable attention is paid to fabrication of novel magnetic materials with reduced dimensionality and simultaneously with improved magnetic properties [1, 2]. Particularly, studies of soft magnetic wires with reduced dimensionality and outstanding magnetic characteristics, such as melt extracted wires (typically with diameters of 40–50 μm) [3] and glass-coated microwires with even thinner diameters (between 1 and 40 μm) [4–7] recently attracted much attention. The advantage of the Taylor-Ulitovsky method allowing the fabrication of glass-coated metallic microwires consists of controllable fabrication of long (up to few km long continuous microwires), homogeneous, rather thin and composite wires. Glass-coated microwires produced by Taylor-Ulitovsky method with metallic nucleus of the order of 1–30 μm in diameter covered by an insulating glass coating (with thickness of 0.5–20 μm) are known along many years [8–11], but has been widely employed for fabrication of ferromagnetic amorphous microwires coated by glass only since middle of 90th [4–7]. The fabrication method denominated in most of modern publications as a modified Taylor-Ulitovsky and/or quenching-and-drawing method is actually well-known since 60th and well described in Russian in 60th [8–10] as well as in recent publications [7, 12].

In the laboratory process, an ingot containing few grams of the master alloy with the desired composition is placed into a Pyrex-like glass tube and within a high frequency inductor heater. The alloy is heated up to its melting point, forming a droplet. While the metal melts, the portion of the glass tube adjacent to the melting metal softens, enveloping the metal droplet. A glass capillary is then drawn from the softened glass portion and wound on a rotating coil. At suitable drawing conditions, the molten metal fills the glass capillary and a microwire is thus formed where the metal core is completely coated by a glass shell (see Fig. 1).

The microstructure of a microwire (and hence, its properties) depends mainly on the cooling rate. Chemical and metallurgical processes related with interaction of the ingot alloy and the glass, electromagnetic and electro-hydrodynamic phenomena in the system of inductor- ingot, thermal conditions of formation of cast microwire, parameters of the casting process and their limits affecting the casting rate and the diameter of a microwire were describe in details for non-magnetic microwires [8–10] and overviewed in relatively recent book [7, 12].

As mentioned above the great advantage of these microwires is that the obtained diameter could be significantly reduced as-compared with the case of conventional wires produced by in-rotating water method. Glass-coated microwires prepared from the alloys presenting deep eutectic on the phase diagrams can be prepared in amorphous state. Amorphous glass-coated microwires present few unusual and very attractive magnetic features, like magnetic bistability observed in Fe-rich compositions with positive magnetostriction constant and excellent soft magnetic

Fig. 1 Schematic picture of the fabrication process allowing preparation of glass-coated microwires (Reproduced from [13], Fig. 1)



properties and Giant magnetoimpedance effect in Co-rich compositions with vanishing magnetostriction constant [7].

In the case of glass-coated microwires, the fabrication process involves simultaneous solidification of metallic nucleus surrounded by the glass coating. This introduces an additional magnetoelastic contribution to the magnetic anisotropy acting as a new parameter determining the magnetization process [4, 5]. The origin of these additional stresses is determined by significant difference of the thermal expansion coefficients of the glass and the metal [4, 7, 12].

Recent studies demonstrated that essentially the same fabrication technique allows obtaining of microwires with granular structure exhibiting giant magneto-resistance (GMR) effect [7, 13, 14], Heusler-type microwires [14, 15] and microwires with magnetocaloric effect [15, 16]. In latter cases the composition of metallic nucleus was different from the case of amorphous magnetically soft microwires. Consequently studies of thin magnetic wires gain more and more attention.

In this book we are paying attention on overview of fabrication, magnetic properties and GMR effect in microwires with granular structure.

2 Motivation

Studies of various materials containing small nano-sized magnetic particles or grains or even magnetic impurities in non-magnetic matrix attracted great attention owing to a number of interesting properties, such as giant magnetoresistance (GMR) effect or Kondo effect [17–22]. Granular materials consisted of small grains

distributed inside a non-magnetic matrix exhibiting giant magnetoresistance (GMR) effect attracted considerable attention since beginning of 1990th [17, 19]. Mostly granular materials have been obtained in systems of immiscible elements (like Co-Co, Co-Ag...), when the structure consisting of small ferromagnetic grains embedded in paramagnetic matrix is formed. Like in the case of multilayered thin films, GMR effect has been attributed to spin-dependent scattering of conduction electrons within the magnetic granules as well as at the interfaces between magnetic and nonmagnetic regions [17, 19, 23]. Therefore, the size and the spatial distribution of nano-sized ferromagnetic grains (usually of Co or Fe) inside the metallic matrix (typically Cu, Ag, Au or Pt) are crucial for obtaining high GMR effect. On the other hand, if the size of magnetic grains is small and even if they can be considered as magnetic impurities, the scattering of conduction electrons in a metal due to magnetic impurities give rise to a Kondo effect [21, 22, 24]. Development of novel materials (like graphene) allows extending the systems where Kondo effect can be realized [24]. On the other hand, Kondo effect has become a key concept in condensed matter physics in understanding the behavior of metallic systems with strongly interacting electrons. Development of nano-scaled electronic devices requires the understanding and the control of electron behavior, in particular, of correlation effects at the atomic scale. The Kondo effect related to the resonant scattering of conductive electrons by quantum local centers is one of the key correlation effects in condensed matter physics.

In the case of immiscible alloys the nano-sized ferromagnetic grains randomly distributed in metallic matrix can be realized by the recrystallization of metastable alloys produced by various techniques. One of the common and the most convenient methods for obtaining such microstructure is a melt spinning technique involving rapid quenching from the melt [25–27].

As mentioned above during last years studies of composite microwires consisted of metallic nucleus surrounded by glass coating and prepared by rapid quenching Taylor-Ulitovsky technique attracted considerable attention [7]. Obtained by this method microwires consist of metallic nucleus surrounded by glass coating [28, 29]. Fe- and Co-based microwires containing metalloids (Si, B) obtaining by aforementioned technique in most of cases present amorphous structure and exhibit soft magnetic character [30–35]. But simultaneous rapid solidification of the composite wire consisting of metallic nucleus surrounded by the glass coating induces additional internal stresses. In fact it is well established that the strength of the internal stresses, σ , is related to the glass coating thickness through the difference in the thermal expansion coefficients of metallic nucleus and outer glass coating solidifying simultaneously. The estimated values of the internal stresses in these glass coated microwires arising from the difference in the thermal expansion coefficients of metallic nucleus and glass coating are of the order of 100–1000 MPa, depending strongly on the ratio between the glass coating thickness and metallic core diameter [33–36], increasing with the increasing of the glass coating thickness. These internal stresses can affect the crystallization process of amorphous microwires and the grain size of precipitating grains.

In this chapter we review results on preparation of glass-coated microwires from immisible elements exhibiting Kondo-like behaviour and GMR effect in $\text{Co}_x\text{-Cu}_{100-x}$ ($5 \leq x \leq 40$ at.%) and GMR effect in $\text{Cu}_{63}\text{Fe}_{37}$ microwires.

3 Experimental Details

We prepared a number of $\text{Co}_x\text{-Cu}_{100-x}$ ($5 \leq x \leq 40$ at.%) and $\text{Cu}_{63}\text{Fe}_{37}$ glass-coated microwires (typical total diameters, D , from few to $30 \mu\text{m}$) consisted of metallic nucleus (typical diameters, d , $9\text{--}20 \mu\text{m}$) covered by outer glass shell (typical thickness from $3 \mu\text{m}$ till $10 \mu\text{m}$) using the Taylor-Ulitovsky technique (see the scheme of fabrication process in Fig. 1) [4–7]. Within each composition of metallic nucleus we produced microwires with different ratio of metallic nucleus diameter, d , and total diameter, D , i.e. with different ratios $\rho = d/D$. This allowed us to control residual stresses, since the strength of internal stresses as described above is determined by the ratio ρ [4, 7].

Structure and phase composition have been checked using a BRUKER (D8 Advance) X-ray diffractometer with Cu K_α ($\lambda = 1.54 \text{ \AA}$) radiation.

We used PPMS device for measurements of magnetic and magneto-transport properties in the temperature range $5\text{--}300 \text{ K}$.

The magnetoresistance (MR) has been defined as:

$$\Delta R/R(\%) = (R(H) - R(0)) \times 100/R(0) \quad (1)$$

4 Co-Cu Microwires

For $\text{Co}_x\text{-Cu}_{100-x}$ microwires at $10 \leq x \leq 30$ we observed considerable MR effect (Fig. 2).

In the case of lowest Co content ($\text{Co}_5\text{Cu}_{95}$ microwires) the MR effect is much lower. We observed a well pronounced minimum on the temperature dependence of resistance, R , at about 40 K (Fig. 3), which should be attributed to Kondo-like behaviour. Few different mechanisms might be considered to explain an increase of the resistivity of a metallic microwire at low temperatures: magnetic Kondo effect, weak localization, enhanced electron-electron interaction, scattering of conduction electrons by structural two-level system (TLS) and scattering of strongly spin-polarized charge carriers on diluted magnetic moments [36–39]. Figure 4 shows that in the present case the temperature dependence of the resistivity below 40 K has a form typical for the Hamann model [40]. Furthermore, magnetic field sufficiently affects the logarithmic growth of resistivity making it much weaker.

Magnetic field significantly affects temperature dependence of resistivity, as shown in Fig. 4. MR is negative in this temperature range that also corresponds to

Fig. 2 $\Delta R/R(H)$ dependences for $\text{Co}_x\text{Cu}_{100-x}$ microwires with $x = 30$, $\rho = 0.612$ (a) and $x = 20$, $\rho = 0.649$ (b) and with $x = 5$, $\rho = 0.787$ (c) measured at different temperatures with maximum field of 50 kOe (Reproduced from [13], Fig. 2)

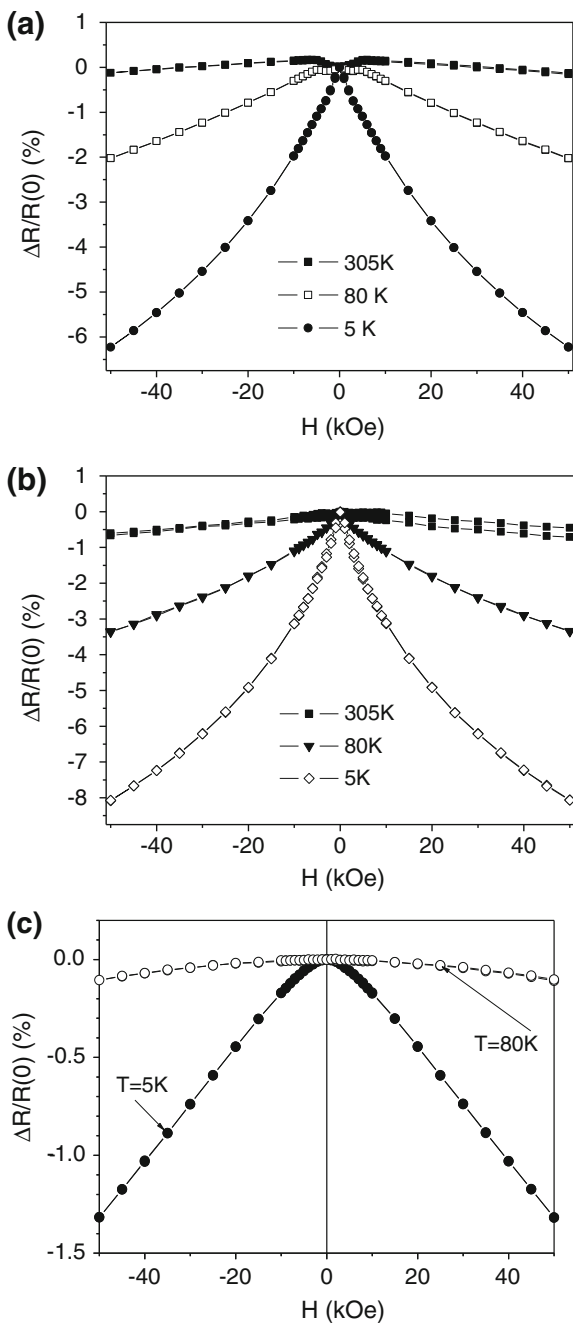


Fig. 3 Temperature dependences of resistivity $\text{Co}_5\text{Cu}_{95}$ sample (Reproduced from [13], Fig. 3)

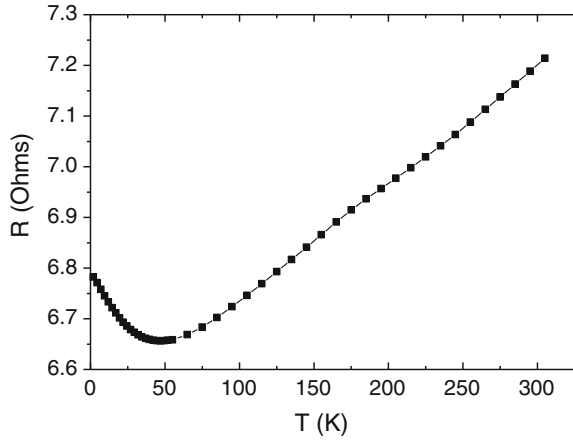
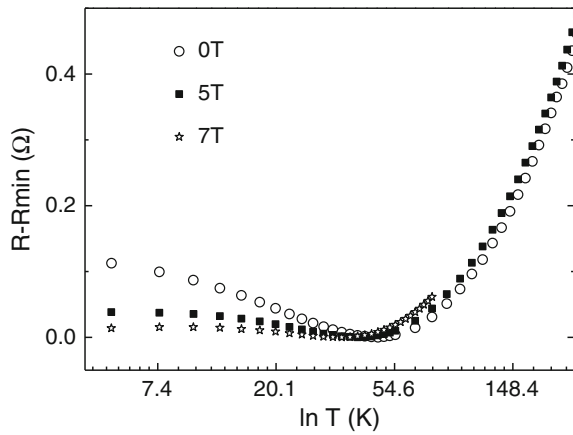


Fig. 4 Effect of magnetic field on temperature dependence of resistivity, R , of $\text{Co}_5\text{Cu}_{95}$ microwires (Reproduced from [13], Fig. 4)



suppression of Kondo effect in strong magnetic fields. On the other hand the resistivity minimum is not completely suppressed even at 7 T, the temperature of resistivity minimum is rather high for the diluted Kondo alloys, the concentration of randomly distributed Co ions in Cu matrix is not low (that can lead to interaction between magnetic ions and, consequently to partial suppression of Kondo effect). Therefore we cannot exclude the role of TLS mechanism.

Consequently, we assume that the most appropriate explanation of observed minimum on the temperature dependence of resistance, R , at about 40 K is the Kondo effect and/or TLS.

In fact, $\text{Co}_5\text{Cu}_{95}$ alloy is not a classical diluted Kondo system not only because of large Co single-ion concentration but also because a part of Co ions forms magnetic clusters and these clusters will create local magnetic fields and spin-polarization of current carriers [41]. The presence of such clusters can be considered from the magnetization measurements at different temperatures, exhibiting saturation at low temperatures (Fig. 5).

Fig. 5 Magnetization curves of $\text{Co}_5\text{Cu}_{95}$ microwires measured at different temperatures (Reproduced from [13], Fig. 5)

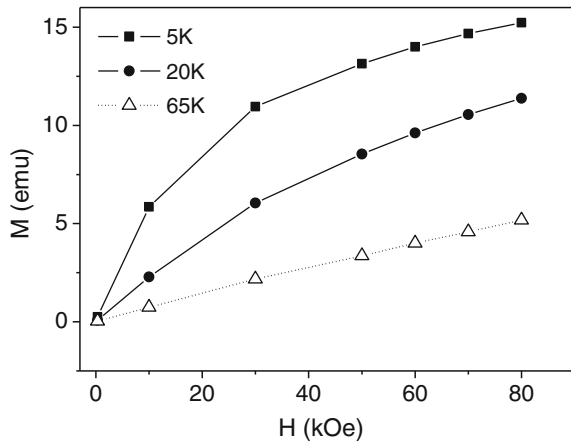
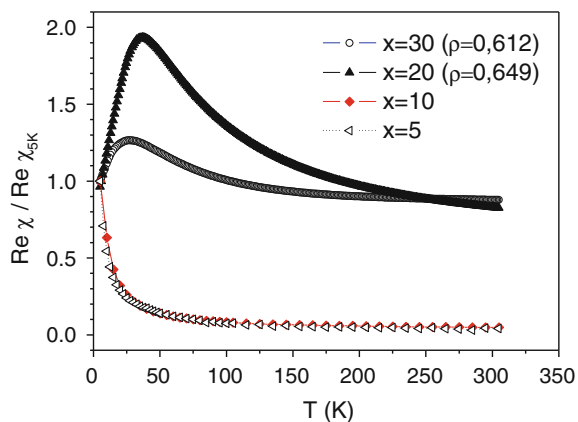


Figure 6 shows that in contrast to the samples with higher content of Co, $\text{Co}_5\text{Cu}_{95}$ and $\text{Co}_{10}\text{Cu}_{90}$ microwires do not present blocking temperature down to 5 K and do not present non vanishing susceptibility, χ , at higher temperature typical for multi-domain cobalt clusters. Apparently this interaction is strong enough in the sample with $x = 10$ to allow significant suppression of magnetic disorder in moderate fields giving rise to considerable negative magnetoresistance (see Fig. 2). Co clusters must be small enough to have a blocking temperature below 5 K, but their interaction is appreciable and affects M versus H curves at low temperatures.

At the same time the local fields of the clusters seem to be quite strong and cause the ordering of the moments of nearby Co atoms suppressing Kondo-type scattering (sample with $x = 10$ does not have minima at its temperature dependence of resistivity).

Interaction between the clusters in the $\text{Co}_5\text{Cu}_{95}$ sample is weaker, that results in very low magnetoresistance. Pronounced Kondo-type minima in resistivity shows

Fig. 6 AC-susceptibility measured for various $\text{Co}_x\text{Cu}_{100-x}$ microwires (Reproduced from [13], Fig. 6)



that considerable part of Co atoms is not magnetically ordered and therefore not affected by the local fields of clusters.

In order to analyse the origin of GMR effect we compared temperature dependence of $\Delta R/R$ and M^2 for $\text{Co}_{10}\text{Cu}_{90}$ with $\rho = 0.728$ and for $\text{Co}_{20}\text{Cu}_{80}$ microwire with $\rho \approx 0.7$ (see Fig. 7). We observed qualitative correlation for all temperature range.

X-ray diffraction (XRD) has been employed for structural studies. For $x \geq 5$ the structure of the metallic core is granular with two phases: the main one, *fcc* Cu (lattice parameter 3.61 Å), found in all samples and *fcc* α -Co (lattice parameter 3.54 Å) which presents in microwires with higher Co content. In $\text{Co}_5\text{Cu}_{95}$ sample Co atoms and ultra-small Co clusters are distributed within the Cu crystals (Fig. 8). The quantity and the crystallite size of the formed phases strongly depend on the geometry of the microwires. The residual concentration of Co dissolved in the Cu matrix and size of Co grains depend on the quenching rate and on internal stresses determined by the ρ -ratio. Consequently, strong internal stresses induced during the simultaneous rapid solidification of the thin metallic wire and glass coating layer affect magnetic properties and structure of glass coated microwires.

X-ray diffraction (XRD) results reveal that the structure of the metallic core in of $\text{Co}_x\text{-Cu}_{100-x}$ for $x \geq 10$ is granular with two phases: the main one, *fcc* Cu (lattice

Fig. 7 Temperature dependences of $\Delta R/R$ and M^2 for $\text{Co}_{10}\text{Cu}_{90}$ (a) and $\text{Co}_{20}\text{Cu}_{80}$ (b) microwires (Reproduced from [13], Fig. 7)

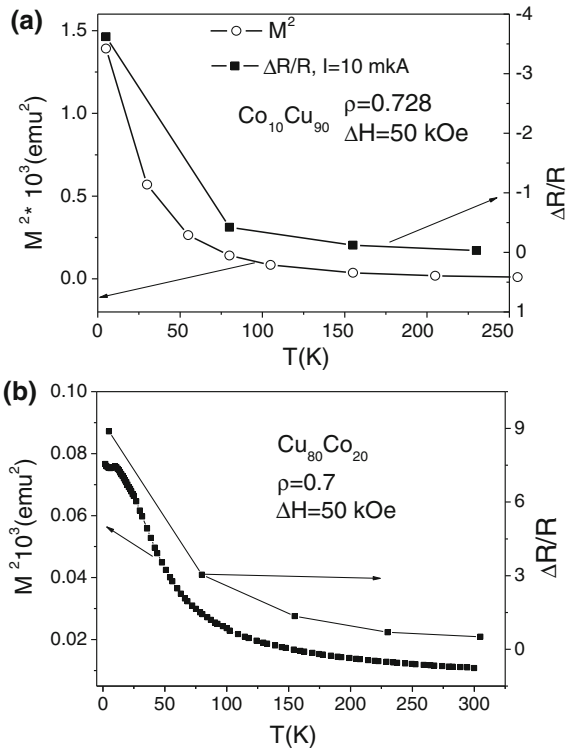
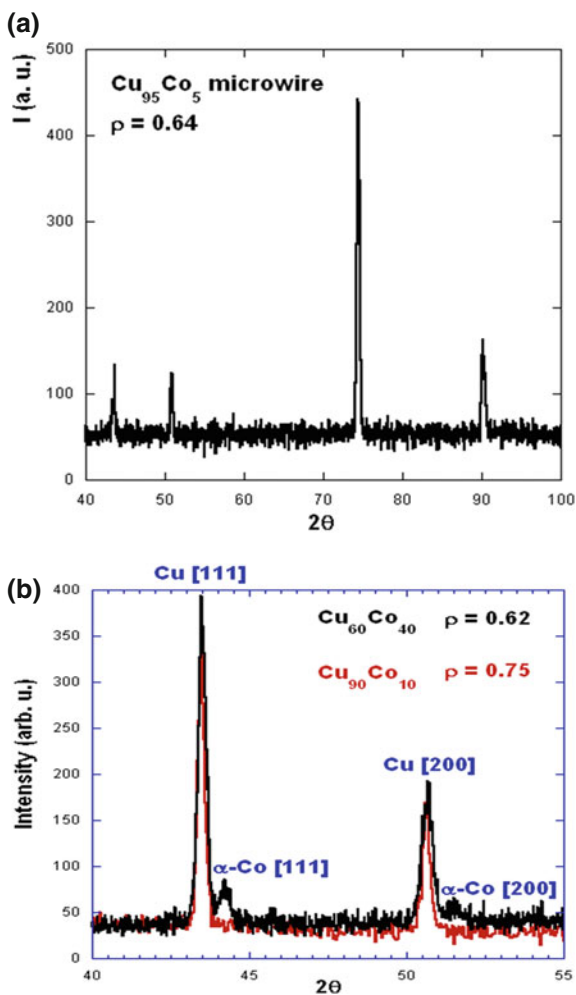


Fig. 8 XRD of $\text{Co}_5\text{Cu}_{95}$ microwire ($\rho = 0.64$) (a) and of $\text{Co}_{40}\text{Cu}_{60}$ ($\rho = 0.62$) and $\text{Co}_{10}\text{Cu}_{90}$ ($\rho = 0.75$) (b) measured at room temperatures (Reproduced from [13], Fig. 8)



parameter 3.61 \AA), found in all samples and *fcc* $\alpha\text{-Co}$ (lattice parameter 3.54 \AA) which presents in microwires with higher Co content. In the case of low Co content XRD indicates that Co atoms are distributed within the Cu crystals. The quantity and the crystallite size of the formed phases strongly depend on the geometry of the microwire.

Figure 8b shows XRD for $\text{Co}_{40}\text{Cu}_{60}$ and $\text{Co}_{10}\text{Cu}_{90}$ microwires. We can see that in microwires with $x = 40$ $\alpha\text{-Co}$ phase has been observed. At the same time we did not observe this phase in the sample with $x = 10$.

This is consistent with the Co-Cu equilibrium phase diagram and the method of microwires fabrication involving rapid quenching from the melt. Indeed, the Co-Cu phase diagram exhibits almost immiscibility, although at elevated temperature there is solubility of Co in Cu of about 13 at.%. Therefore we can

assume that rapid quenching results in quenching of high temperature structure consisting in supersaturated Co solution in Cu matrix.

Additionally, our data can be interpreted considering, that for $\text{Co}_5\text{Cu}_{95}$ sample Co atoms are distributed between the matrix and very small clusters (Fig. 8). For concentrations $x > 10$ partial coalescence of granules was observed. The anisotropic contribution to MR has been observed for $x \geq 30$, giving rise to non-monotonic magnetic field dependence of MR (Fig. 1b).

It is worth mentioning, that previously Kondo-like behaviour in Co-Cu system has been observed only in clusters consisting of a single Co atom and several Cu atoms fabricated by sophisticated technique using atomic manipulation with the microscope tip [41]. On the other hand previously resistivity minimum versus temperature has been observed in Co-Ag thin films prepared by electron gun evaporation under ultrahigh-vacuum conditions [42]. Like in our case, weak-localization effects have not been considered for interpretation of the observed resistivity minima because of low absolute values of the residual resistivity [42]. An interpretation associated with loose spins proposed by Slonczewski [43] and the decreasing of the spin-dependent scattering responsible for the GMR overwhelming an increasing spin fluctuation scattering have been also discussed, although further theoretical analysis is suggested for the case of the granular systems. On the other hand, the logarithmic temperature dependence of resistivity has been observed for the case of Au/Fe superlattices [21]. The authors considered two types of loose spins (within the non-magnetic spacer layer the “loose interfacial spins” comprising the ferromagnetic layers). But since magnetic field strongly affects the logarithmic temperature dependence of resistivity, Kondo-like scattering is considered for the interpretation of results. In the latter case the logarithmic temperature dependence of resistivity has been considered as an intrinsic of the multilayer samples, since similar dependence has been observed by the same authors in Al/Ni and Al/Ag multilayers with low thicknesses of layers (below 5 nm) [44].

On the other hand, quite recently for interpretation of temperature dependence of resistivity of nano-scale granular Aluminum films, with Al grains weakly coupled through thin Al oxide barriers it was suggested that small metallic grains weakly coupled to their environment can behave like magnetic impurities in a metallic matrix [45]. It is also pointed out, that the weak electron localization also results in a negative magneto-resistance if spin-orbit scattering is negligible.

Low interaction between the magnetic particles is proved by good correlation $\Delta R/R$ and M^2 for $\text{Co}_{10}\text{Cu}_{90}$ presented in Fig. 7a. Usually deviations from $\Delta R/R$ and M^2 correlation are interpreted as the existence of interaction among the magnetic particles [25, 46]. Some deviations from good correlation $\Delta R/R$ and M^2 observed for $\text{Co}_{20}\text{Cu}_{80}$ microwire might be related with more considerable interaction between the magnetic particles for this microwire with higher Co content.

Fabrication method involving rapid quenching from the melt of composite microwire and microstructure of studied $\text{Co}_5\text{Cu}_{95}$ microwires are quite different from that of thin films and multilayers studied before. The similarity might be originated by the existence of ultra-small Co grains and clusters distributed within the Cu

crystals, as observed by the X-ray diffraction (Fig. 7) and recently reported by us [47]. In this case similar results, as a pronounced minimum on the temperature dependence of resistance and considerable effect of magnetic field might be interpreted in similar way.

It is worth mentioning, that here we report on using of rather simple and fast (few meters per minute) preparation of the Co-Cu microwire, where local structure can be manipulated through the control of the internal stresses.

5 Fe-Cu Microwires

In the case of $\text{Fe}_{37}\text{Cu}_{63}$ microwires we observed three X-ray diffraction peaks are characteristic of the Cu phase (face centered cubic FCC, lattice parameter: 3.61 Å with atomic spacings of 2.09, 1.81 and 1.28 Å). The other two peaks are related to α -Fe phase (body centered cubic BCC, lattice parameter: 2.87 Å corresponding to atomic spacing of 2.03 and 1.43 Å). Note that the peak corresponding to 1.43 Å (α -Fe) is rather small and hardly observed.

The observed X-ray peaks have been identified by means of the Bragg's law, $2d \sin(\theta) = \lambda$, within an accuracy of 0.01 Å. The influence of the wire geometry on the X-ray patterns has been then studied. It is easy to see in Fig. 9a–d that with increasing the ratio ρ the intensity of X-ray peaks increases and its shape is more regular.

The structural information for the microwires is extracted once the crystalline peaks of each pattern are identified and the background contribution of the amorphous phase in the microwires (mainly from the glass coating) subtracted. An average grain size of the crystals formed in each case is derived from Scherrer's equation:

$$D = \frac{K \cdot \lambda}{\varepsilon \cdot \cos \theta_m} \quad (2)$$

where $2\theta_m$ is the scattering angle corresponding to maximum of the peak and ε is its half height width [48]. The parameter K is assumed to be around 0.9 (or almost 1) in most of cases [49].

Figure 10 shows the size of the Cu and α -Fe grains obtained for $\text{Cu}_{63}\text{Fe}_{37}$ microwires. As it is seen, Cu nano-grains with the average grain size of 40 nm are roughly independent of the sample geometry (represented by the ratio ρ), as found elsewhere [50]. On the other hand, the average size of Fe nanocrystals depends on the geometrical parameter varying between 6 and 45 nm, exhibiting a maximum at intermediate ρ ratio.

It should be indicated that X-ray diffraction allows estimating only the average grain size. The details of grain size morphology and grain size distribution might be obtained by means of high resolution SEM or TEM.

Fig. 9 XRD patterns for $\text{Fe}_{37}\text{Cu}_{63}$ microwires with different ρ values: 0.46 (a), 0.31 (b), 0.16 (c), 0.063 (d) (Reproduced from [55], Fig. 1)

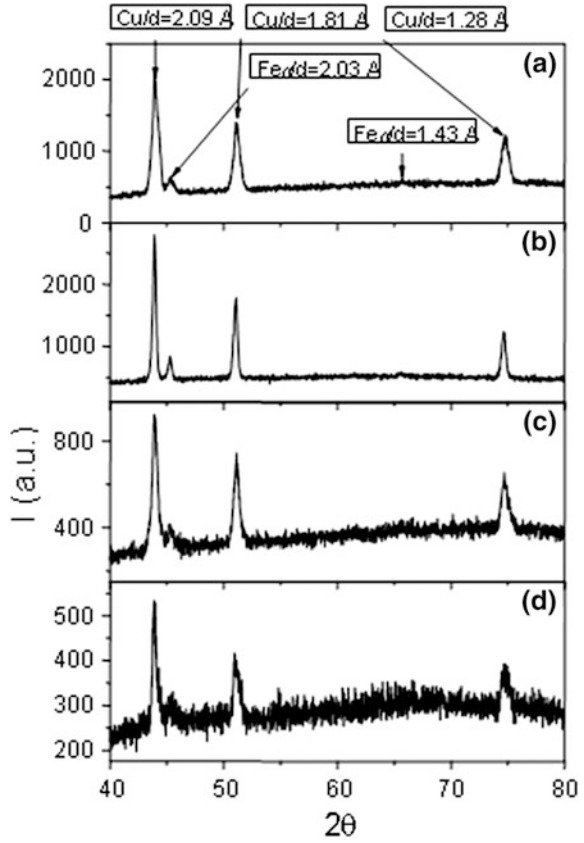
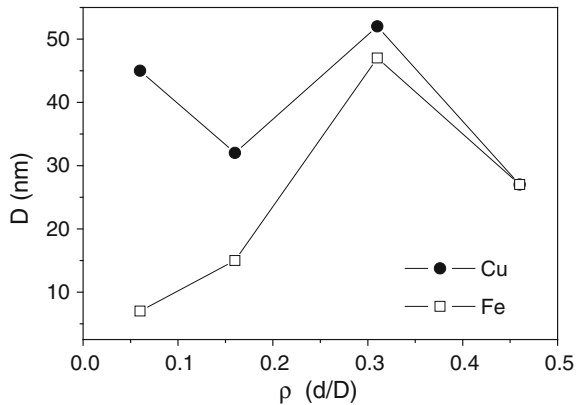


Fig. 10 Size of Cu and α -Fe crystallites plotted versus ρ ratio for $\text{Fe}_{37}\text{Cu}_{63}$ microwires (Reproduced from [55], Fig. 2)



Magnetization curves measured at different temperatures are shown in Fig. 11a, b. At room temperature the coercivity is of the order of 30 Oe. Significant dependence of the hysteresis loops on the geometrical parameter has been found.

All curves display both superparamagnetic and ferromagnetic features. A small hysteresis area of the measured loops and the absence of saturation indicate the presence of a superparamagnetic phase, especially significant for $\rho = 0.06$. The ferromagnetic behaviour is evidenced by the values of remanence and coercivity, which are indeed rather low. Such behaviour can be attributed to the combined superparamagnetic-ferromagnetic phases due to co-existence of the ferromagnetic and superparamagnetic particles. Such co-existence occurs due to a wide size distribution of Fe-grain and/or concentration distribution of Fe in Cu. At the same time, temperature dependences of the saturation magnetization, $M_s(T)$, shown in the inserts of Fig. 11a, b, exhibit decreasing with temperature but did not present well defined Curie temperature typical for ferromagnetic materials. This probably related with Fe nanocrystals size distribution and inhomogeneity of ferromagnetic phase.

The magnetization measured under applied magnetic field (FC) and without magnetic field (ZFC) exhibit significant difference (see Fig. 12). From the comparison between the two curves seen in Fig. 12a, b it is possible to roughly determine the average blocking temperature and distribution $f(TB)$ following a

Fig. 11 Hysteresis loop for the $Fe_{37}Cu_{63}$ as cast sample at different temperatures with different ratio ρ values **a** 0.46, **b** 0.063. Evolution of magnetization at saturation is shown at the *inset* (Reproduced from [55], Fig. 3)

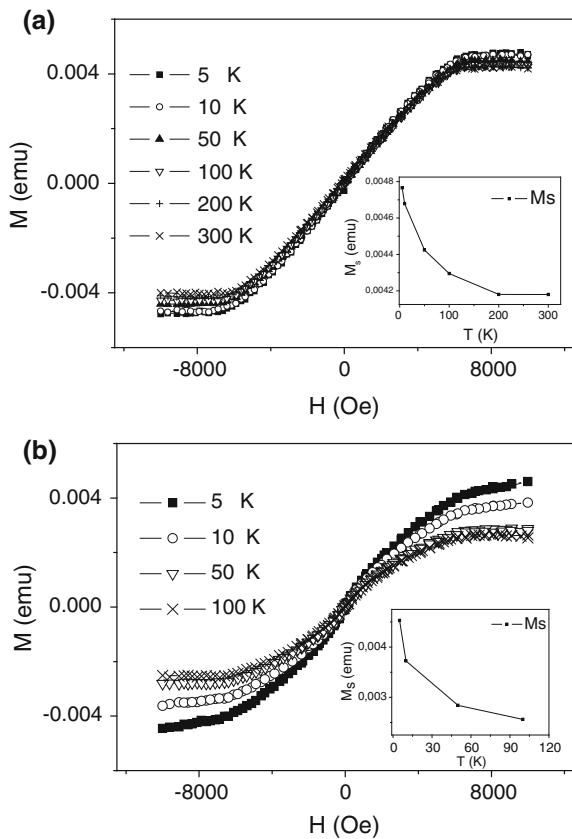
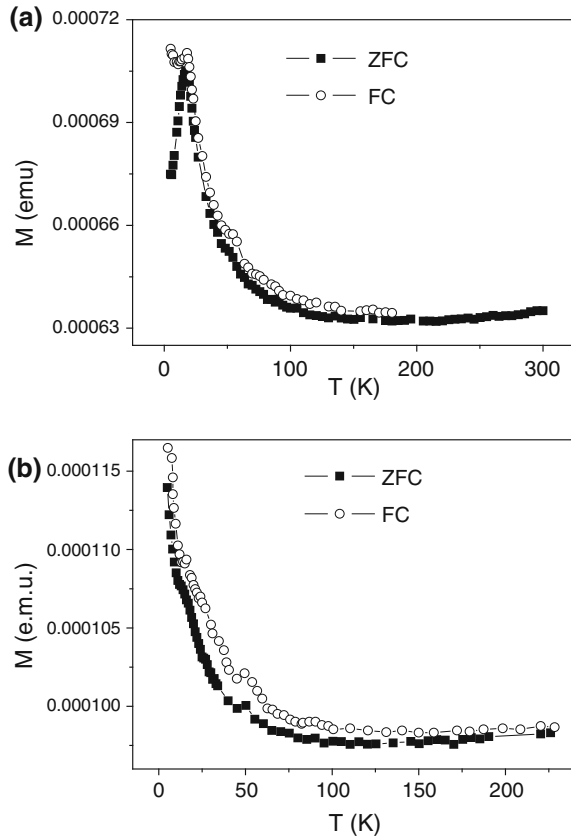


Fig. 12 Zero field cooled and field cooled curves for the $\text{Fe}_{37}\text{Cu}_{63}$ as cast measured at $H_{\text{DC}} = 100$ Oe up to 300 K with different ratio ρ values **a** 0.46, **b** 0.063 (Reproduced from [55], Fig. 4)



standard procedure [51]. The obtained $f(T_B) = \frac{d(M_{\text{ZFC}} - M_{\text{FC}})}{dT}$ confirms the inhomogeneous magnetic structure assumed by analysing the magnetization curves, consistent with previous works [52]. It follows from the analysis of Fig. 12a, corresponding to $\text{Fe}_{37}\text{Cu}_{63}$ microwires with the geometrical parameter $\rho = 0.46$, the existence of a large number of small particles with a diameter less than 30 nm and just a few large particles. On the other hand, for Fig. 12b ($\text{Fe}_{37}\text{Cu}_{63}$ microwires with a geometrical parameter $\rho = 0.06$) the estimated averaged crystal size is around 5 nm. ZFC/FC measurements performed on microwires with different geometrical parameters exhibit an intermediate behaviour. However, it is worth noting that ZFC/FC analysis in this case is only indicative, and it gives a rather rough perspective of the nanostructure. In fact, the observed ZFC/FC behaviour resembles the one expected for a rather narrow distribution of grain sizes. This apparently contradictory result was previously observed in several granular samples (see, for example, ref. 53). In fact dipolar interactions and magnetic cluster formation can lead to spurious structural data indirectly obtained from ZFC/FC curves, and thus such results are only valid when analysed together with direct structural data, such

as X-Ray diffraction and TEM analysis. Furthermore, it is worth noting that the FC curve displays an additional peak at lower temperature, indicating a more complex magnetic behaviour, probably a reentrant spin (or cluster) glass-like transition. This magnetic phase is usually present in complex granular systems, and can be related to both dipolar interactions and/or surface effects (see, for example, [54]). Although a careful analysis of this extra peak can lead to interesting results, it goes far beyond from the scope of the present chapter.

The behaviour of the main magnetic phase (α -Fe) is very important in this type of materials. Note that the content of α -Fe phase and the average grain size is lower for the sample $\text{Fe}_{37}\text{Cu}_{73}$ with $\rho = 0.063$. The obtained content of α -Fe phase varies around 1 % for $\rho = 0.06$, 8 % for $\rho = 0.16$ and $\rho = 0.31$, 7 % for $\rho = 0.46$, as was deduced from Fig. 1 and can be found elsewhere [50, 55]. It should be noted, that following the previously proposed scheme for these type of samples [56], the loops show a superparamagnetic character for $\rho = 0.063$ and a ferromagnetic one for $\rho = 0.46$. This ferromagnetic character could be related to the aforementioned higher content of α -Fe phase and larger average grain size for this sample and, in a certain way, there is a correlation between magnetic measurements and structural results.

It should be noted also that the field at which the saturation is roughly achieved is quite large (around 6 kOe) (see Fig. 11). But complete saturation of the sample with lowest ρ -ratio is not reached even at this magnetic field (Fig. 11b).

One of the possible explanations is that the axis of the microwires is the hard direction. But this assumption contradicts to the logics, since the demagnetizing factor of the sample with lowest ρ -value when applied magnetic field is along the microwire axis takes lowest values. Additionally, from the experimental data on Fe nanowires it is known that usually Fe nanowires have easy axis along the nanowire axis [57]. We assume that higher contribution of superparamagnetic behaviour of the thinnest microwire related also with the dependence of the structure on ρ -ratio can be attributed to the higher internal stresses induced by the difference in thermal expansion coefficients of simultaneously solidifying glass and metal [33–35]. In fact as mentioned above it is well established that the strength of the internal stresses, σ , is related to the glass coating thickness through the difference in the thermal expansion coefficients of metallic nucleus and outer glass coating solidifying simultaneously. These internal stresses can affect the grain size of Fe nano-grains precipitating during the devitrification of amorphous matrix [35, 36]. Such behaviour has been observed in Finemet-type microwires when the nanocrystallization process has been affected by the ρ -ratio. To explain this, it was suggested [35, 36], that the internal stresses in the metallic nucleus hinder the segregation of crystalline phases. It is also consistent with Fig. 10, where lowest Fe grain size is observed for the lowest ρ -ratio.

The MR effect in the range of 7 % has been also observed for $\rho = 0.46$ and $\rho = 0.31$ $\text{Fe}_{37}\text{Cu}_{73}$ glass coated microwires (Figs. 13, 14 respectively). The shape of magnetic field dependence is typical for the GMR effect, when resistance decreases with increasing magnetic field. Decreasing the temperature MR increases (from 0.05 % (300 K) up to 7.6 % (5 K) for the sample with $\rho = 0.31$ and from 1 % till

Fig. 13 Magnetoresistance of the as-cast $\text{Fe}_{37}\text{Cu}_{63}$ microwire with $\rho = 0.46$ measured at 5 and 300 K at magnetic field from -7 to 7 T (Reproduced from [55], Fig. 5)

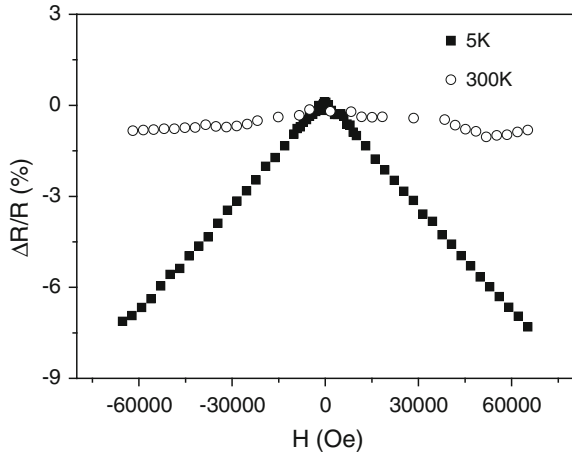
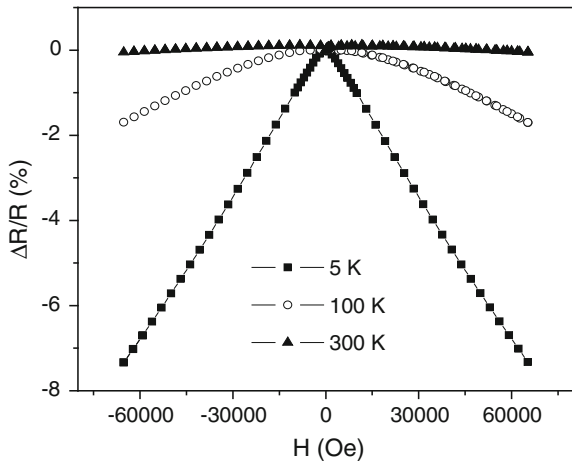


Fig. 14 Magnetoresistance of the as-prepared $\text{Fe}_{37}\text{Cu}_{63}$ microwire with $\rho = 0.31$ measured at 5, 100 and 300 K at magnetic field from -7 to 7 T (Reproduced from [55], Fig. 6)



7 % for the sample with $\rho = 0.46$). In most systems exhibiting GMR the GMR ratio increases decreasing the temperature [17, 18]. Usually this increase is attributed to the superparamagnetic origin of grains responsible for the GMR behaviour as well as related with temperature dependence of resistivity [17, 18].

The field dependent resistivity in granular materials is related to a spin-dependent scattering of conduction electrons within the magnetic particles as well as the interfaces between magnetic and non magnetic regions (however, it is assumed that the interfacial effect contributes to a dominant extent to GMR [17, 18, 58]). Because of the complex structure of the granular materials, the relationship between microstructure and GMR is still not fully understood.

In the case of glass-coated microwires the internal stresses induced mostly by the difference of thermal expansion coefficients of glass and metal are quite significant

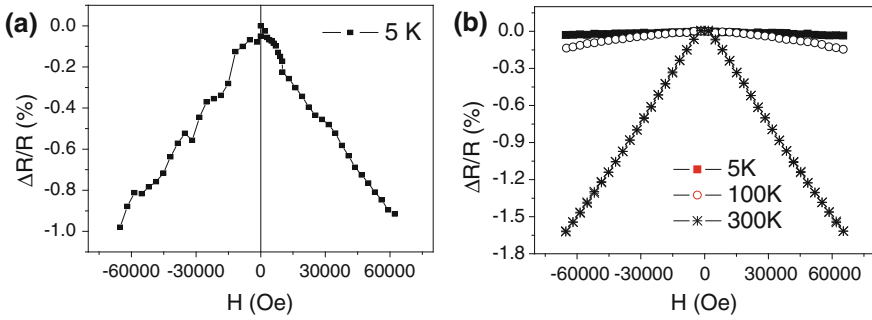


Fig. 15 Magnetoresistance of the as-prepared $\text{Cu}_{50}-(\text{Fe}_{69}\text{Si}_{10}\text{B}_{15}\text{C}_5)_{50}$ (a) and $\text{Cu}_{70}-(\text{Co}_{70}\text{Fe}_5\text{Si}_{10}\text{B}_{15})_{30}$ (b) microwires (b Reproduced from [61], Fig. 5)

[33–35]. Therefore studies of abovementioned composition with different geometry can be interesting in order to reveal the internal stress contribution in magnetic and magneto-transport properties. Similar studies in Co-Cu microwires allowed us to find that indeed crystalline structure and GMR effect is affected by the glass coating thickness and metallic nucleus diameter [58]. These internal stresses can affect the structure and magnetism of small Fe grains inside the Cu-matrix, as has been previously observed for the case of epitaxially grown Fe films on Cu(100), where bcc- and fcc-like structures were observed depending on the film thickness [59].

It is worth mentioning that similarly to Fe-Cu microwires we observed MR effect in $\text{Cu}_{50}-(\text{Fe}_{69}\text{Si}_{10}\text{B}_{15}\text{C}_5)_{50}$ and $\text{Cu}_{70}-(\text{Co}_{70}\text{Fe}_5\text{Si}_{10}\text{B}_{15})_{30}$ glass-coated microwires (see Fig. 15) [60, 61], although $\Delta R/R$ values were smaller (Fig. 15).

Similarly to the case of $\text{Fe}_{37}\text{Cu}_{63}$ microwires the structure of as-prepared $\text{Cu}_{50}-(\text{Fe}_{69}\text{Si}_{10}\text{B}_{15}\text{C}_5)_{50}$ and $\text{Cu}_{70}-(\text{Co}_{70}\text{Fe}_5\text{Si}_{10}\text{B}_{15})_{30}$ microwires consisted of small wither Fe or Co and Cu grains. But in these cases the presence of amorphous phase has been detected.

6 Conclusion

We observed GMR and Kondo-like behaviour in $\text{Co}_x\text{Cu}_{100-x}$ microwires prepared by the Taylor-Ulitovsky method. For $x = 5\%$ we observed resistivity minimum at 40 K. Magnetic field significantly affects temperature dependence of resistivity in $\text{Co}_5\text{Cu}_{95}$ microwires. Additionally in $\text{Co}_5\text{Cu}_{95}$ microwires by XRD we observed, that Co is distributed in the Cu- matrix. For $x > 10$ partial evidences of granular structure have been observed and GMR effect is considerable higher. ZFC and FC and χ (T) dependence show considerable difference for $x \geq 20\%$ at low temperatures, related with the presence of small Co grains embedded in the Cu matrix. Anisotropic MR is observed in $\text{Co}_x\text{Cu}_{100-x}$ microwires for $x \geq 30$. It is demonstrated that the local structure and magneto-transport properties can be manipulated through the control of the internal stresses. Similarly to Co-Cu microwires $\text{Fe}_{37}\text{Cu}_{63}$

microwires with granular structure have been produced by rapid quenching using Tailor-Ulitovsky method and characterized using X-ray diffraction and SQUID magnetometer technique. Structure of Fe₃₇Cu₆₃ microwires structure consists of Cu nanograins with average grain size of around 40 nm and α -Fe nanocrystals with average grain size ranging between 6 and 45 nm depending on samples geometry. The resulting content of α -Fe phases also strongly depends on the sample geometry. Magnetic characterization has been performed and it was found that the temperature dependence of magnetization (ZFC and FC curves) and hysteresis loops behaviour depend on geometrical parameters. Experimental data are interpreted assuming the mixed ferromagnetic-superparamagnetic behaviour of the fabricated samples. Significant Magnetoresistance (about 7 %) has been found in studied samples. The shape of observed dependences is typical for GMR effect.

References

1. M. Vazquez, H. Chiriac, A. Zhukov, L. Panina, T. Uchiyama, On the state-of-the-art in magnetic microwires and expected trends for scientific and technological studies. *Phys. Status Solidi A* **208**, 493–501 (2011)
2. J. González, A. Zhukov, Amorphous magnetic materials for sensors, in *Encyclopedia of Sensors*, ed. by C.A. Grimes, E.C. Dickey, M.V. Pishko, vol. 1 (American Scientific Publishers, Stevenson Ranch, 2006), pp. 79–103. ISBN:1-58883-056-X
3. V. Zhukova, A. Zhukov, V. Kraposhin, A. Prokoshin, J. Gonzalez, Magnetic properties and GMI of soft melt-extracted magnetic amorphous fibers. *Sens. Actuators, A* **106**, 225–229 (2003)
4. H. Chiriac, T.A. Ovari, Amorphous glass-covered magnetic wires: preparation, properties, applications. *Prog. Mater. Sci.* **40**, 333–407 (1997)
5. V. Zhukova, M. Ipatov, A. Zhukov, Thin magnetically soft wires for magnetic microsensors. *Sensors* **9**, 9216–9240 (2009)
6. M.-H. Phan, H.-X. Peng, Giant magnetoimpedance materials: fundamentals and applications. *Prog. Mater. Sci.* **53**, 323–420 (2008)
7. A. Zhukov, V. Zhukova, *Magnetic Properties and Applications of Ferromagnetic Microwires With Amorphous and Nanocrystalline Structure* (Nova Science Publishers, New York, 2009). ISBN:978-1-60741-770-5
8. A.V. Ulitovskii, N.M. Avernin, Method of fabrication of metallic microwire. USSR Patent, No. 161325. Bulletin No. 7, p. 14, 19 March 1964
9. A.V. Ulitovskii, I.M. Maianki, A.I. Avramenco, Method of continuous casting of glass coated microwire. USSR Patent, No. 128427. Bulletin No. 10, p. 14, 15 May 1960
10. E.Ya. Badinter, N.R. Berman, I.F. Drabenko, V.I. Zaborovskiy, Z.I. Zelikovskiy, V.G. Cheban, *Cast Microwires and Its Properties* (Shtinica, Kishinev, 1973)
11. L. Kraus, J. Schneider, H. Wiesner, Ferromagnetic resonance in amorphous alloys prepared by rapid quenching from the melt. *Czechoslovak J. Phys. B* **26**, 601–602 (1976)
12. V.S. Larin, A.V. Torcunov, A. Zhukov, J. González, M. Vazquez, L. Panina, Preparation and properties of glass-coated microwires. *J. Magn. Magn. Mater.* **249**(1–2), 39–45 (2002)
13. V. Zhukova, J.J. del Val, M. Ipatov, M. Ilyn, A. Granovskiy, A. Zhukov, Magnetic and transport properties of Co-Cu microwires, in *Proceedings of the 8th International Conference on Sensing Technology*, Liverpool, UK, pp. 332–337, 2–4 Sept 2014

14. A. Zhukov, C. Garcia, M. Ilyn, R. Varga, J.J. Del Val, A. Granovsky, V. Rodionova, M. Ipatov, V. Zhukova, Magnetic and transport properties of granular and Heusler-type glass-coated microwires. *J. Magn. Magn. Mater.* **324**, 3558–3562 (2012)
15. A. Zhukov, V. Rodionova, M. Ilyn, A.M. Aliev, R. Varga, S. Michalik, A. Aronin, G. Abrosimova, A. Kiselev, M. Ipatov, V. Zhukova, Magnetic properties and magnetocaloric effect in Heusler-type glass-coated NiMnGa microwires. *J. Alloy. Compd.* **575**, 73–79 (2013)
16. M.I. Ilyn, V. Zhukova, J.D. Santos, M.L. Sánchez, V.M. Prida, B. Hernando, V. Larin, J. González, A.M. Tishin, A. Zhukov, Magnetocaloric effect in nanogranular glass coated microwires. *Phys. Status Solidi A* **205**(6), 1378–1381 (2008)
17. A.E. Berkowitz, J.R. Mitchell, M.J. Carey, A.P. Young, S. Zhang, F.E. Spada, F.T. Parker, A. Hutten, G. Thomas, Giant magnetoresistance in heterogeneous Cu-Co alloys. *Phys. Rev. Lett.* **68**, 3745–3748 (1992)
18. J.Q. Xiao, J.S. Jiang, C.L. Chien, Giant magnetoresistance in nonmultilayer magnetic system. *Phys. Rev. Lett.* **68**, 3749–3752 (1992)
19. B. Gopalakrishnan, C. Stürgers, R. Montbrun, A. Singh, M. Uhlarz, H.V. Löhneysen, Electronic transport in magnetically ordered $Mn_5Si_3C_x$ films. *Phys. Rev. B* **77**, 104414 (2008)
20. A. Kawabata, Effects of tunneling on the properties of metallic fine particles. *J. Phys. Soc. Jpn.* **43**, 1491–1496 (1977)
21. H. Sato, Y. Kobayashi, Y. Aoki, K. Shintaku, Y. Hasaito, T. Shinjo, Kondo-like scattering correlated with the giant magnetoresistance in Au/Fe superlattices. *J. Phys. Soc. Jpn.* **62**, 3380–3383 (1993)
22. J.A. De Toro, J.P. Andres, J.A. Gonzalez, J.P. Goff, A.J. Barbero, J.M. Riveiro, The role of improved giant magnetoresistance in nanogranular Co/Ag: interparticle RKKY interactions. *Phys. Rev. B* **70**, 224412–224416 (2004)
23. M.N. Baibich, J.M. Broto, A. Fert, F. Nguyen Van Dau, F. Petron, P. Etienne, G. Creuzer, A. Friederich, J. Chazelas, Giant magnetoresistance of (001)Fe/(001)Cr magnetic superlattices. *Phys. Rev. Lett.* **61**, 2472–2475 (1998)
24. J.-H. Chen, L. Li, W.G. Cullen, E.D. Williams, M.S. Fuhrer, Tunable Kondo effect in graphene with defects. *Nat. Phys.* **7**, 535–538 (2011)
25. R.H. Yu, X.X. Zhang, J. Tejada, M. Knobel, P. Tiberto, P. Allia, Magnetic properties and giant magnetoresistance in melt-spun Co-Cu alloys. *J. Appl. Phys.* **78**, 392–397 (1995)
26. A. Zhukov, J. Gonzalez, V. Zhukova, Magnetoresistance in thin wires with granular structure. *J. Magn. Magn. Mater.* **294**, 165–173 (2005)
27. A. Zhukov, V. Zhukova, *Magnetic Sensors and Applications Based on Thin Magnetically Soft Wires with Tuneable Magnetic Properties* (International Frequency Sensor Association Publishing, Barcelona, 2013), p. 164p
28. H. Chiriac, T.A. Ovari, Gh Pop, Internal stress distribution in glass-covered amorphous magnetic wires. *Phys. Rev. B* **42**, 10105–10113 (1995)
29. M. Vázquez, J.M. García-Beneytez, J.M. García, J.P. Sinnecker, A. Zhukov, Giant magneto-impedance in heterogeneous microwires. *J. Appl. Phys.* **88**, 6501–6505 (2000)
30. A.P. Zhukov, The remagnetization process of bistable amorphous alloys. *Mater. Des.* **5**, 299–305 (1993)
31. A. Zhukov, M. Ipatov, M. Churyukanova, S. Kaloshkin, V. Zhukova, Giant magnetoimpedance in thin amorphous wires: from manipulation of magnetic field dependence to industrial applications. *J. Alloy Compd.* **586**, S279–S286 (2014)
32. T. Uchiyama, K. Mohri, S. Nakayama, Measurement of spontaneous oscillatory magnetic field of guinea-pig smooth muscle preparation using pico-tesla resolution amorphous wire magneto-impedance sensor. *IEEE Trans. Magn.* **47**, 3070–3073 (2011)
33. H. Chiriac, T.A. Ovari, A. Zhukov, Magnetoelastic anisotropy of amorphous microwires. *J. Magn. Magn. Mater.* **254–255**, 469–471 (2003)
34. A.S. Antonov, V.T. Borisov, O.V. Borisov, A.F. Prokoshin, N.A. Usov, Residual quenching stresses in glass-coated amorphous ferromagnetic microwires. *J. Phys. D Appl. Phys.* **33**, 1161–1168 (2000)

35. J. Gonzalez, A. Zhukov, V. Zhukova, A.F. Cobeño, J.M. Blanco, A.R. de Arellano-Lopez, S. Lopez-Pombero, J. Martinez-Fernandez, V. Larin, A. Torcunov, High coercivity of partially devitrified glass-coated finemet microwires: effect of geometry and thermal treatment. *IEEE Trans. Magn.* **36**(5), 3015–3017 (2000)
36. V. Zhukova, A.F. Cobeño, A. Zhukov, J.M. Blanco, V. Larin, J. Gonzalez, Coercivity of glass-coated Fe_{73.4-x}Cu₁Nb_{3.1}Si_{13.41+x}B_{9.1} (0<x<1.6) microwires. *Nanostruct. Mater.* **11** (8), 1319–1327 (1999)
37. A. Vedyayev, A. Granovsky, Electroresistivity of amorphous ferromagnetic alloys in the Ziman-Faber model. *Fiz. Met. Metalloved.* **63**, 1076–1082 (1987)
38. M. Csontos, T. Wojtowicz, X. Liu, M. Dobrowolska, B. Jankó, J.K. Furdyna, G. Mihály, Magnetic scattering of spin polarized carriers in (In, Mn)Sb dilute magnetic semiconductor. *Phys. Rev. Lett.* **95**, 227203–227204 (2005)
39. A. Granovsky, M. Ilyn, V. Zhukova, A. Zhukov, J. Gonzalez, Giant magnetoresistance of granular microwires: Spin-dependent scattering in intergranular spacers. *Phys. Solid State* **53**, 320–322 (2011)
40. D.R. Hamann, New solution for exchange scattering in dilute alloys. *Phys. Rev.* **158**, 570–580 (1967)
41. N. Néel, J. Kroger, R. Berndt, T.O. Wehling, A.I. Lichtenstein, M.I. Katsnelson, Controlling the Kondo effect in CoCun clusters atom by atom. *Phys. Rev. Lett* **101**, 266803–266804 (2008)
42. H. Sato, Y. Kobayashi, Y. Aoki, H. Yamamoto, Transport properties in granular Co-Ag alloys. *J. Phys.: Condens. Matter* **7**, 7053–7062 (1995)
43. J.C. Slonczewski, Origin of biquadratic exchange in magnetic multilayers. *J. Appl. Phys.* **73**, 5957–5962 (1993)
44. H. Sato, I. Sakamoto, C. Fiertz, Transport properties of Al/Ni and Al/Ag multilayer systems. *J. Phys.: Condens. Matter* **3**, 9067–9078 (1991)
45. N. Bachar, S. Lerer, S. Hacoen-Gourgy, B. Almog, G. Deutscher, Kondo-like behavior near the metal-to-insulator transition of nano-scale granular aluminum. arXiv: 1207.0970v1 [cond-mat.supr-con] 4 July 2012
46. I. Bakonyi, L. Peter, Electrodeposited multilayer films with giant magnetoresistance (GMR): progress and problems. *Prog. Mater. Sci.* **55**, 107–245 (2010)
47. V. Zhukova, C. Garcia, J.J. Del Val, M. Ilyn, A. Granovsky, A. Zhukov, Magnetic and transport properties of Co–Cu microwires with granular structure. *Thin Solid Films* **543**, 142–147 (2013)
48. R. Jenkins, R.L. Snyder, *Introduction to X-ray Powder Diffractometry* (Wiley, New York, 1996)
49. H.P. Klug, L.E. Alexander, *X-ray Diffraction Procedures for Polycrystalline and Amorphous Materials* (Wiley, New York, 1974)
50. J.J. Del Val, J. Gonzalez, A. Zhukov, Structural study of glass coated Cu-based microwires. *Phys. B* **299**, 242–250 (2001)
51. N. Peleg, S. Shtrikman, G. Gorodetsky, I. Felner, Magnetic study of particle distribution in granular Au-Co. *J. Magn. Magn. Mater.* **191**, 349–353 (1999)
52. A. Zhukov, J. González, M. Vázquez, V. Larin, A. Torcunov, Nanocrystalline and amorphous magnetic microwires, in *Encyclopedia of Nanoscience and Nanotechnology*, vol. 6 (American Scientific Publishers, Valencia, 2004), pp. 365–387
53. J.C. Denardin, A.L. Brandl, M. Knobel, P. Panissod, A.B. Pakhomov, H. Liu, X.X. Zhang, Thermoremanence and zero-field-cooled/field-cooled magnetization study of Cox(SiO₂)_{1-x} granular films. *Phys. Rev. B* **65**, 064422 (2002)
54. W.C. Nunes, E. De Biasi, C.T. Meneses, M. Knobel, H. Winnischofer, T.C.R. Rocha, D. Zanchet, Magnetic behavior of Ni nanoparticles with high disordered atomic structure. *Appl. Phys. Lett.* **92**, 183113 (2008)
55. A. Zhukov, C. Garcia, J.J. Del Val, J. Gonzalez, M. Knobel, D. Serantes, D. Baldomir, V. Zhukova, Studies of Fe–Cu microwires with nanogranular structure. *J. Phys.: Condens. Matter* **21**, 035301 (2009)

56. P. Allia, M. Knobel, P. Tiberto, F. Vinai, Magnetic properties and giant magnetoresistance of melt-spun granular $\text{Cu}_{100-x}\text{-Co}_x$ alloys. *Phys. Rev. B* **52**, 15398–15411 (1995)
57. P.M. Paulus, F. Luis, M. Kroll, G. Schmid, L.J. de Jongh, Low-temperature study of the magnetization reversal and magnetic anisotropy of Fe, Ni, and Co nanowires. *J. Magn. Magn. Mater.* **224**, 180–196 (2001)
58. M.N. Baibich, J.M. Broto, A. Fert, F. Nguyen Van Dau, F. Petron, P. Etienne, G. Creuzer, A. Friederich, J. Chazelas, Giant magnetoresistance of (001)Fe/(001)Cr magnetic superlattices. *Phys. Rev. Lett.* **61**, 2472–2475 (1988)
59. X.F. Jin, Morphology and magnetic structure of Fe/Cu(100). *J. Phys. D Appl. Phys.* **35**, 2332–2338 (2002)
60. A. Zhukov, C. García, V. Zhukova, V. Larin, J. González, J.J. del Val, M. Knobel, J.M. Blanco, Fabrication and magnetic properties of $\text{Cu}_{50}(\text{Fe}_{69}\text{Si}_{10}\text{B}_{16}\text{C}_5)_{50}$ thin microwires. *J. Non-Cryst. Solids* **353**, 922–924 (2007)
61. C. García, A. Zhukov, J. González, J.J. del Val, J.M. Blanco, M. Knobel, V. Zhukova, Fabrication, structural and magnetic characterization of thin microwires with novel composition $\text{Cu}_{70}(\text{Co}_{70}\text{Fe}_5\text{Si}_{10}\text{B}_{15})_{30}$. *J. Alloy. Compd.* **483**, 566–569 (2009)

Giant Magnetoimpedance Effect of Amorphous and Nanocrystalline Glass-Coated Microwires

A. Zhukov, A. Talaat, M. Ipatov, J.J. del Val, L. Gonzalez-Legarreta, B. Hernando and V. Zhukova

Abstract In this chapter we are reporting on correlation of Giant magnetoimpedance (GMI) effect and magnetic properties of amorphous and nanocrystalline Co-Fe rich glass-coated microwires. We measured the GMI magnetic field, frequency dependences and hysteresis loops of composite microwires produced by the Taylor-Ulitovsky technique. We observed that GMI effect and magnetic softness of glass-coated microwires produced by the Taylor-Ulitovsky technique can be tailored either controlling magnetoelastic anisotropy of as-prepared microwires or controlling their internal stresses and structure by heat treatment. High GMI effect has been observed in as-prepared and annealed Co-rich microwires. In the case of Fe-rich Finemet-type microwires we observed considerable magnetic softening of studied microwires after annealing. This magnetic softening correlates with the devitrification of amorphous samples. Amorphous Fe-rich microwires generally exhibited low GMI effect (GMI ratio below 5 %). Considerable enhancement of the GMI effect (GMI ratio up to 100 %) has been observed in heat treated microwires with nanocrystalline structure. The objective of this reported work is to develop magnetically soft thin wires for applications in magnetic field sensors.

A. Zhukov (✉) · A. Talaat · M. Ipatov · J.J. del Val · V. Zhukova
Department of Physics and Materials, Basque Country University, UPV/EHU,
San Sebastian, Spain
e-mail: arkadi.joukov@ehu.eus

A. Zhukov
IKERBASQUE, Basque Foundation for Science, Bilbao, Spain

L. Gonzalez-Legarreta · B. Hernando
Dpto de Física, Universidad de Oviedo, 33007 Oviedo, Spain

1 Introduction

Studies of Giant magnetoimpedance (GMI) effect attracted considerable during last two decades since its discovery in 1994 [1, 2]. It is worth mentioning that in fact GMI has been first reported in 1936 by Harrison et al. [3]. But intensive research of GMI effect in various materials began only after the publication in 1994 of a few papers on GMI effect in amorphous wires [4–8].

Phenomenologically, GMI effect consists of a large change of the impedance of a magnetically soft conductor under an applied magnetic field.

GMI effect is particularly interesting for magnetic sensors applications basically due to the extremely high magnetic field sensitivity suitable for low magnetic field detection [9, 10].

GMI effect has been successfully explained in the terms of classical electrodynamics through the influence of a magnetic field on the penetration depth of an electrical current flowing through the magnetically soft conductor [1, 2]. Cylindrical shape and high circumferential permeability observed in Co-rich amorphous wires with vanishing magnetostriction constant are quite favorable for achievement of high GMI effect [1, 2, 4].

The magnetic field dependence of impedance is intrinsically related to the magnetic anisotropy of magnetic materials [5, 7]. Magnetic materials with circumferential easy axis exhibit the maximum of the real component of wire impedance (and consequently of the GMI ratio) on magnetic field dependence. Although, magnetic materials with longitudinal easy axis present monotonic decay of the GMI ratio with increasing axial magnetic field, the maximum value of the GMI ratio corresponds to zero magnetic fields [5]. On the other hand, for optimization of the GMI effect, the magnetic anisotropy should be as small as possible.

The extremely high sensitivity of the GMI effect to even low magnetic field attracted a great interest in the field of applied magnetism, basically for applications for low magnetic field detection.

Usually, for the characterization of the GMI effect the magneto impedance ratio, $\Delta Z/Z$, is used. Aforementioned GMI ratio, $\Delta Z/Z$, is defined as:

$$\Delta Z/Z = [Z(H) - Z(H_{\max})]/Z(H_{\max}), \quad (1)$$

where H_{\max} is the applied axial DC-field with a maximum value up to a few kA/m.

Like the magnetic permeability, GMI effect has a tensor character [11–14]. From the point of view of industrial applications, the anti-symmetrical magnetic field dependence of the output voltage with a linear region obtained for pulsed GMI effect, that is based on the detection of the off-diagonal GMI component of amorphous wires is very suitable [5, 12]. Such pulsed scheme for GMI measurements results quite useful for real GMI sensors development [8].

The highest GMI effect is reported for the case of amorphous wires with high circumferential permeability [1, 2]. Moreover, after optimizing the magnetic anisotropy of Co-rich amorphous microwires a few researchers reported on an

achievement of about 600 % GMI ratio [15, 16]. The magnetic field dependence of the GMI ratio is mainly determined by the type of the magnetic anisotropy of the wire [5, 17]. Moreover, the AC and DC currents are the important parameters that affect the GMI effect. The main reason is that like magnetic permeability, GMI effect presents tensor character [13, 14]. The AC and DC currents flowing through the sample create a circumferential magnetic field. Additionally, the current produces Joule heating [18]. Depending on the frequency f of the driving AC current I_{ac} flowing through the sample, different GMI regimes can be considered:

1. At a low frequency range (1–10 kHz) the skin depth is usually larger than the radius or the sample (a rather weak skin effect). The impedance changes at these frequencies are of inductive character due to a circular magnetization process exclusively and might not be considered properly as the GMI effect.
2. At the frequency range from 10–100 kHz to 1–10 MHz (where the GMI effect has been first reported and described) the GMI originates basically from variations of the magnetic penetration depth due to strong changes of the effective magnetic permeability caused by a DC magnetic field [1, 2, 19]. It is widely believed that in this case both domain walls movement and magnetization rotation contribute to changes of the circular permeability and consequently to the skin effect.
3. For the MHz band frequencies (from 1–10 to 100–1000 MHz depending on the geometry of the sample), the GMI effect is also originated by the skin effect of the soft magnetic conductor, i.e. must be attributed to the GMI. But at these frequencies the domain walls are strongly damped. Therefore the magnetization rotation must be considered as responsible for the magnetic permeability change induced by an external magnetic field [1, 2, 19].
4. At GHz frequencies the magnetization rotation is strongly influenced by the gyromagnetic effect. With increasing the frequency the GMI peaks are shifted to higher magnetic fields values for being the sample magnetically saturated. At this frequency range, strong changes of the sample's impedance have been attributed to the ferromagnetic resonance (FMR) [20, 21].

It is also predicted that the diameter reduction must be associated with the increasing of the resonance frequency and therefore the increasing of the optimal GMI frequency range: a tradeoff between dimension and frequency is required in order to obtain a maximum effect [20].

Consequently, the major attention is recently focused on high frequencies (GHz range) GMI applications owing to the development of thin magnetically soft materials and the recent tendency in miniaturization of magnetic field sensors [7, 21].

Aforementioned GMI effect is considered as one of the most promising for applications in low magnetic field detection [8, 10, 22]. Magnetic sensors developed using amorphous wires with GMI effect allow achieving pT magnetic field sensitivity with low noise [22].

The aim of this chapter is to review recent efforts on the optimization of soft magnetic properties and GMI effect in amorphous and nanocrystalline glass-coated microwires fabricated by the Taylor-Ulitvosky technique.

2 Motivation

Nowadays, soft magnetic wires are considered as one of the most promising magnetic materials for industrial applications in various industrial sectors such as magnetic sensors, microelectronics, security, etc. [7, 9, 10, 19–22]. Extremely soft magnetic properties and Giant Magnetoimpedance effect are the features of magnetic wires that have been proposed for already existing and proposed industrial applications. Miniaturization of magnetic sensors requires reduction of the magnetic wires diameters. Thinnest magnetic wires can be produced using the Taylor-Ulitovsky method allowing the preparation of glass-coated microwires with metallic nucleus diameters from 0.05 to 50 μm coated by glass with a thickness ranging from 0.5 up to 30 μm . The fabrication method essentially consists in the melting of the metallic alloy ingot inside a glass tube and the rapid quenching from the melt of the metallic nucleus completely coated by the glass [4].

From the physical point of view, the interest in studying this kind of materials is related to its amorphous structure, therefore, such microwires are characterized by a low magnetic anisotropy (since the most important magneto-crystalline anisotropy is missing). Hence, their magnetic properties are determined mainly by the magnetoelastic and shape magnetic anisotropies. The latter can be significant if the microwire has thickest diameters (above 50 μm) in which the sample length affects their magnetic properties, particularly the hysteresis loop [4, 23]. Consequently, the main magnetoelastic anisotropy arises from the interaction of the local magnetic moments with the internal stresses induced during the microwire production, as well as from the difference between the thermal expansion coefficients of the metallic nucleus and the glass coating. Aforementioned magnetoelastic energy is given by:

$$K_{me} \approx 3/2 \lambda_s \sigma_i, \quad (2)$$

where λ_s is the saturation magnetostriction and σ_i is the internal stress. The magnetostriction constant depends mostly on the chemical composition and is vanishing in amorphous Fe-Co based alloys with Co/Fe \approx 70/5 [24–26].

The magnetic anisotropy of amorphous microwires in the absence of magnetocrystalline one has mostly a magnetoelastic origin, i.e., determined by the metallic nucleus composition and by the internal stresses [27–30]. The strength of internal stresses is mostly determined by the ratio, ρ , between the metallic nucleus diameter and total composite wire diameter, D ($\rho = d/D$). Such stresses arising during the simultaneous solidification of the composite wire originated from the

difference in thermal expansion coefficients of metallic alloy and glass coating [27–30] as has been above mentioned.

Consequently, the magnetic properties could be modified by either the heat treatment and/or chemical etching of the glass coating, or by selecting the adequate chemical composition of the metallic nucleus [4, 26].

On the other hand, it is well known that, the so-called “nanocrystalline materials”, that is, two-phase systems consisting of nano-sized grains randomly distributed in an amorphous matrix, attracted a great attention owing to extremely soft magnetic properties. These family of soft magnetic materials have been introduced in 1988, when Yoshizawa et al. [30], reported that the presence of small additions of Cu and Nb in certain Fe-Si-B alloys allows the creation of a two-phase material by the devitrification of the conventional amorphous alloy after adequate annealing (i.e., at temperatures between respective ones for the first and second crystallization processes) [30]. After crystallization, such material consists of small (around 10 nm grain size) nano-crystallites embedded in the residual amorphous matrix. In addition, the devitrification process of these amorphous alloys (with trademark FINEMET) leads to the possibility of obtaining rather different microstructures depending on the annealing parameters as well as on the chemical composition. These features are the basis to achieve the excellent soft magnetic properties indicated by a high value of permeability of about 10^5 , and correspondingly a low coercivity. Such soft magnetic character is thought to be originated because the magnetocrystalline anisotropy vanishes and a very small magnetostriction value results when the grain size approaches 10 nm [30–33]. As was theoretically estimated by Herzer [32, 33], the average anisotropy for randomly oriented α -Fe(Si) grains is negligibly small when grain diameter does not exceed about 10 nm. Thus, the resulting magnetic behavior can be well described with the random anisotropy model [32, 33]. According to this model, the low coercivity in the nanocrystalline state is ascribed to the small effective magnetic anisotropy K_{eff} around 10 J/m^3 .

GMI effect in amorphous microwires with positive magnetostriction constant exhibiting rectangular hysteresis loop is usually quite small because of their low initial permeability [34]. Recently, successful attempts for the improvement of GMI effect either by nanocrystallization of amorphous precursor or by induction of a transverse easy magnetization direction under special heat treatment (under stress and/or magnetic field) have been reported [34–38].

Meanwhile, substitution of Co-rich amorphous microwires by less expensive Fe-rich microwires can be essentially promising from industrial application’s point of view. Therefore, optimizing high GMI effect in Fe-rich glass-coated microwires is nowadays one of the major subjects of research.

In this chapter we present our last results on optimization of GMI effect in amorphous and nanocrystalline glass-coated microwires. This will help in improving the sensitivity of the magnetic sensors based on GMI effect.

3 Tuning of GMI Effect in Amorphous Glass-Coated Microwires

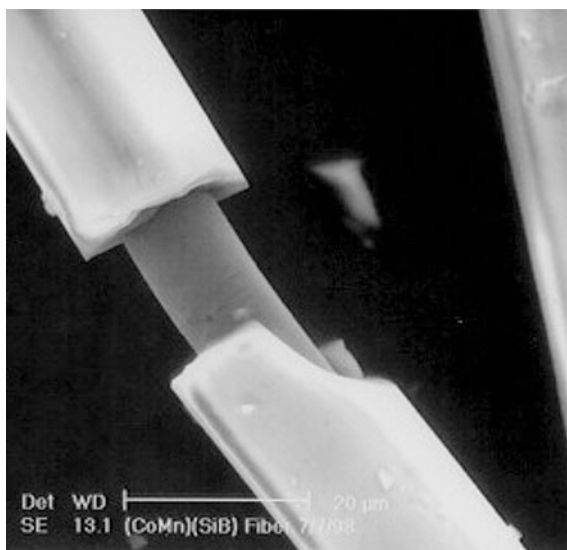
As mentioned above, the development of thin soft magnetic wires with amorphous and nanocrystalline structure is essential for the creation of magnetic sensors based on GMI effect. Therefore, the understanding of the main factors affecting magnetic properties of thin wires is of critical importance for the optimization of their magnetic properties.

The Taylor-Ulitovsky method allows producing of thinnest metallic wires (with typical diameters of the order of 1–30 μm) covered by an insulating glass coating [23, 26]. In fact, this method is known from many years [39–42], but since the 90s it has been widely employed for fabrication of ferromagnetic amorphous microwires coated by glass (see photo in Fig. 1). The fabrication method denominated in most of modern publications as a modified Taylor-Ulitovsky and/or quenching-and-drawing method is actually well-known since the 60s and well described in Russian in 60s [39–41] as well as in more recent publications [26, 42].

As described elsewhere the fabrication method consists of melting of an ingot containing a few grams of the master alloy with the desired composition placed into a Pyrex-like glass tube inside a high frequency inductor heater. Once the alloy is heated up to its melting point, forming a droplet and a glass capillary is then drawn from the softened glass portion and wound on a rotating spool. At suitable drawing conditions, the molten metal fills the glass capillary and a microwire is thus formed where the metal core is completely coated by the glass shell [4, 23, 26].

The microstructure of the microwire (and consequently its magnetic properties) depends mainly on the cooling rate. Chemical and metallurgical processes related to

Fig. 1 Micrograph of the glass-coated microwire. Reprinted with permission from [26] (Fig. 2)



the interaction of the ingot alloy and the glass, electromagnetic and electro-hydrodynamic phenomena in the system of inductor-ingot, thermal conditions of formation of cast microwire, casting process parameters and their limits affecting the casting rate and the diameter of the microwire were described in details for non-magnetic microwires [39–41] and overviewed in a relatively recent book [43]. From the point of view of magnetic properties of thin magnetic microwires and properties related to its surface layers (like is the case of GMI effect), the interfacial layer between the metallic nucleus and glass coating is especially relevant [43]. The features of the interfacial layer between the metallic nucleus and glass coating (its thickness, structure and physical properties) depend on the origin of the interfacial layer. Thus, the thickness of the interfacial layer might have from a few μm for the case of the formation of series of solid solutions or stable chemical compounds, to less than 0.1 μm in the case of the origin related to the uncompensated molecular forces on the interface between the glass and the metallic nucleus [43]. Recently an interfacial layer thickness for the case of Fe-rich microwires of about 0.5 μm has been reported [44].

The other source of instability of properties of as-prepared microwires is related to the gas content inside the microwire. The sources of the gas are: the atmosphere, gas impurities in the alloy and in the glass [43, 44].

The great advantage of these microwires is that the obtained diameter could be significantly reduced in comparison with the case of amorphous wires produced by the in-rotating water method. But their magnetic properties are also quite different from “thicker” amorphous wires. Thus although like in the case of “thicker wires” it was observed that Fe-rich compositions with positive magnetostriction constant show generally rectangular hysteresis loop, Co-rich negative magnetostrictive compositions present a completely different character of hysteresis loops. Co-rich microwires have almost non-hysteretic magnetization curves and glass coating removal results in the appearance of magnetic bistability [4, 23, 26, 43]. This is because the glass coating introduces additional internal stresses due to the difference between the thermal expansion coefficients of glass coating and metallic nucleus. Therefore, microwires of the same composition can show different magnetic properties arising from different magnetoelastic energy.

As already mentioned in the introduction, the GMI effect usually observed in soft magnetic materials phenomenologically consists of the change of the AC impedance, $Z = R + iX$ (where R is the real part, or resistance, and X is the imaginary part, or reactance), when submitted to an external magnetic field, H_0 . The GMI effect was well interpreted in terms of the classical skin effect in a magnetic conductor assuming the dependence of the penetration depth of the AC current flowing through the magnetically soft conductor on the DC applied magnetic field [1, 2].

The electrical impedance, Z , of a magnetic conductor in this case is given by [14–16]:

$$Z = R_{dc}krJ_0(kr)/2J_1(kr) \quad (3)$$

with $k = (1 + j)/\delta$, where J_0 and J_1 are the Bessel functions, r is the wire's radius and δ the penetration depth given by:

$$\delta = \sqrt{\pi\sigma\mu_\phi f} \quad (4)$$

where σ is the electrical conductivity, f the frequency of the current along the sample, and μ_ϕ the circular magnetic permeability assumed to be scalar. The DC applied magnetic field introduces significant changes in the circular permeability, μ_ϕ . Therefore, the penetration depth also changes through and finally results in a change of Z [1, 2].

In ferromagnetic materials with high circumferential anisotropy (the case of magnetic wires) the magnetic permeability possesses the tensor nature and the classic form of impedance definition is no valid. The relation between electric field (which determines the voltage) and the magnetic field (which determines the current) is defined through the surface impedance tensor [11, 12]

$$e = \hat{\zeta}h \quad \text{or} \quad \left\{ \begin{array}{l} e_z = \zeta_{zz}h_\phi - \zeta_{z\phi}h_z \\ e_\phi = \zeta_{\phi z}h_\phi - \zeta_{\phi\phi}h_z \end{array} \right\} \quad (5)$$

The circular magnetic fields h_ϕ is produced by the currents i_w running through the wire. At the wire surface $h_z = i/2\pi r$, where r is the wire radius. The longitudinal magnetic fields h_z is produced by the currents i_c running through the exciting coil, $h_z = N_1 i_c$, where N_1 is the exciting coil number of turns.

Various excitation and measurement methods are required to reveal the impedance matrix elements. The longitudinal and circumferential electrical field on the wire surface can be measured as voltage drop along the wire v_w and voltage induced in the pickup coil v_c wound on it [11, 12, 26, 45].

$$v_w \equiv e_z l_w = (\zeta_{zz}h_\phi - \zeta_{z\phi}h_z)l_w \quad (6)$$

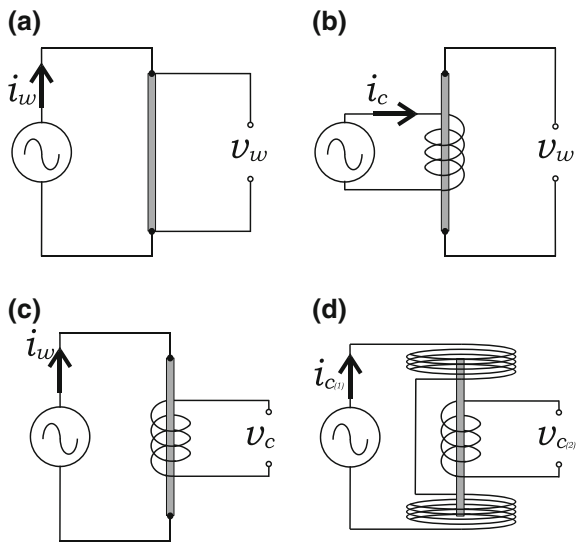
$$v_c \equiv e_\phi l_t = (\zeta_{\phi z}h_\phi - \zeta_{\phi\phi}h_z)l_t \quad (7)$$

where l_w is the wire length, $l_t = 2\pi r N_2$ the total length of the pickup coil turns N_2 wound directly on the wire.

The methods for revealing the different elements of impedance tensor are shown in Fig. 2. The longitudinal diagonal component ζ_{zz} is defined as the voltage drop along the wire and corresponds to impedance definition in classical model (Fig. 2a).

$$\zeta_{zz} \equiv \frac{v_w}{h_\phi l_w} = \left(\frac{2\pi a}{l_w} \right) \left(\frac{v_w}{i_w} \right) \quad (8)$$

Fig. 2 Methods for revealing the impedance matrix elements: **a** ζ_{zz} , **b** $\zeta_{z\phi}$, **c** $\zeta_{\phi z}$, **d** $\zeta_{\phi\phi}$. Reprinted with permission from [14] DOI 10.1002/pssa.200778133, Copyright © 2008 WILEY-VCH Verlag GmbH & Co. KGaA, Weinheim (Fig. 1)



The off-diagonal components $\zeta_{z\phi}$ and $\zeta_{\phi z}$ (Fig. 2b, c) and the circumferential diagonal component $\zeta_{\phi\phi}$ (Fig. 2d) arose from cross sectional magnetization process ($h_\phi \rightarrow m_z$ and $h_z \rightarrow m_\phi$) [11, 12, 26, 45].

From the point of view of industrial applications low hysteretic GMI effect with linear magnetic field dependence of the output signal are desirable [11, 12]. Anti-symmetrical magnetic field dependence of the output voltage with linear region has been obtained for a pulsed GMI effect based on the detection of the off-diagonal GMI component of amorphous wires [11, 12, 45]. Such pulsed scheme for GMI measurements resulted quite useful for real GMI sensors development [11, 12].

As mentioned above, the shape of magnetic field dependence of the GMI effect (including off-diagonal components) is intrinsically related to the magnetic anisotropy and the peculiar surface domain structure of amorphous wires [4, 5]. Magnetic anisotropy of amorphous microwires in the absence of magnetocrystalline anisotropy is determined mostly by the magnetoelastic contribution [4, 26]. As mentioned above, the internal stresses, σ_i , arising during simultaneous rapid quenching of metallic nucleus surrounding by the glass coating are the source of additional magnetoelastic anisotropy. The strength of such internal stresses can be controlled by the ρ -ratio. The strength of internal stresses increases with the decreasing of ρ -ratio (i.e., increases with the increasing of the glass volume) [27–29].

We measured magnetic field dependences of impedance, Z , and GMI ratio, $\Delta Z/Z$, for various as-prepared and annealed Co- and Fe-rich microwires.

A Schematic picture showing principles for revealing the impedance matrix elements: diagonal, ζ_{zz} , and off-diagonal, $\zeta_{z\phi}$, is shown in Fig. 3.

We used a specially designed micro-strip sample holder (see the image in Fig. 3b). The microwire was placed inside a sufficiently long solenoid that creates a

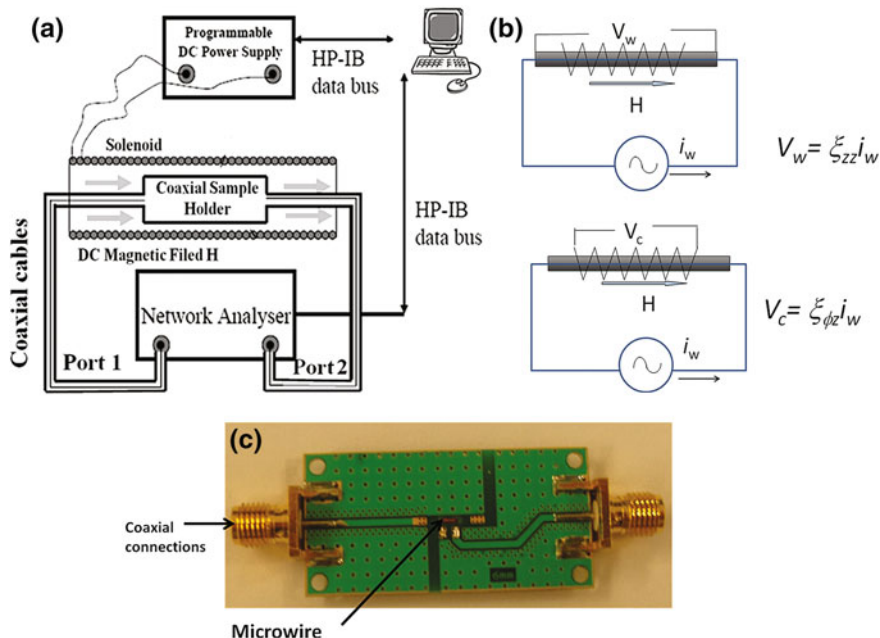


Fig. 3 Schematic picture of the experimental set-up for measurements of GMI effect (a), principles for revealing of the diagonal, ξ_{zz} , and off-diagonal, $\xi_{z\phi}$, impedance matrix elements (b) and the image of the micro-strip line (c). Reprinted with permission from [46], International Journal on Smart Sensing and Intelligent Systems, Copyright © 2014 (Fig. 3)

homogeneous magnetic field H . The sample impedance Z was measured using a vector network analyzer from the reflection coefficient S_{11} . The DC bias current I_B was applied to the sample through a bias-tee element. All experimental graphs show both ascending and descending branches of the field dependencies of the real part of impedance Z so that the magnetic hysteresis can be evaluated. More details on experimental technique can be found in Refs. [46–48].

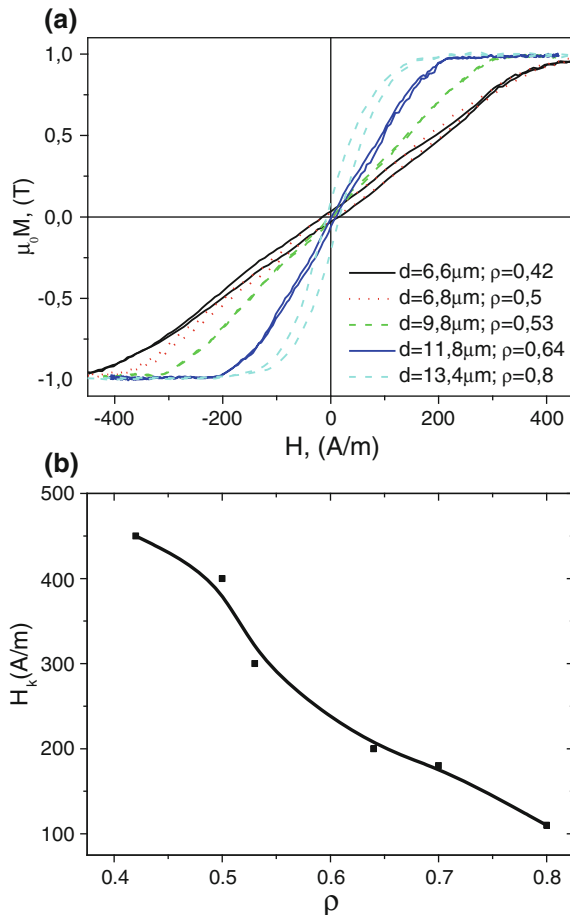
Below we overview a few recent results on GMI effect in microwires paying attention on its suitability for magnetic sensors applications.

It is worth mentioning, that usually the DC magnetic field that corresponds to the maximum GMI ratio, H_m , is attributed to the static magnetic anisotropy field, H_k . Consequently, the parameter ρ must be considered as one of the factors that affect both soft magnetic properties and GMI response.

Figure 4 shows the influence of the ρ -ratio on hysteresis loops and magnetic anisotropy field of $\text{Co}_{67.1}\text{Fe}_{3.8}\text{Ni}_{1.4}\text{Si}_{14.5}\text{B}_{11.5}$ microwires with the same composition of the metallic nucleus, but different ρ -ratio.

As can be appreciated, Co-rich microwire with appropriate geometry and composition present excellent magnetically soft properties with low coercivities (between 4 and 10 A/m) [4, 23, 26, 48]. Magnetic anisotropy field, H_k , is found to

Fig. 4 Hysteresis loops of $\text{Co}_{67.1}\text{Fe}_{3.8}\text{Ni}_{1.4}\text{Si}_{14.5}\text{B}_{11.5}\text{Mo}_{1.7}$ microwires with different geometry (a) and dependence of H_k on ρ -ratio (b). Reprinted with permission from [48], DOI: [10.1051/epjconf/20122900052](https://doi.org/10.1051/epjconf/20122900052), Owned by the authors, published by EDP Sciences, 2012 (Fig. 4)



be determined by the ρ -ratio, decreasing with ρ (Fig. 4b), as has been reported elsewhere [23, 26].

Consequently, one can expect that the ρ -ratio must affect the GMI effect of studied samples.

Figure 5 presents results on magnetic field dependences of ΔZZ measured in Co-rich microwire samples with different ρ -ratios.

Indeed both maximum values of the GMI ratio, ΔZZ_m , and the magnetic anisotropy field present a considerable dependence on the samples geometry. It is worth mentioning, that for microwires with the lowest glass coating thickness (largest ρ -ratio) a value of $\Delta ZZ_m \approx 600\%$ has been observed [23, 26]. Considering that the magnetoelastic energy, K_{me} , is determined by both internal, σ_i , and applied stresses, σ_a , the GMI effect has been measured under tensile stresses in various Co-rich microwires. Figure 6 presents tensile stress dependence measured in $\text{Co}_{67.05}\text{Fe}_{3.85}\text{Ni}_{1.4}\text{B}_{11.33}\text{Si}_{14.47}\text{Mo}_{1.69}$ and $\text{Co}_{68.5}\text{Mn}_{6.5}\text{Si}_{10}\text{B}_{15}$ microwires. It was

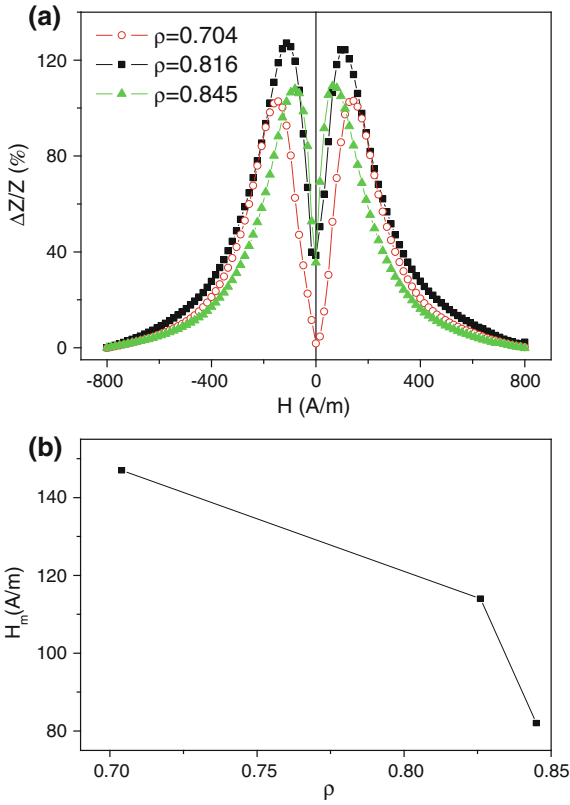


Fig. 5 Effect of ρ -ratio on GMI effect in $\text{Co}_{67.05}\text{Fe}_{3.85}\text{Ni}_{1.4}\text{B}_{11.33}\text{Si}_{14.47}\text{Mo}_{1.69}$ microwire samples with different ρ -ratios (a, b) and dependence of field of maximums on ρ -ratio (c). Reprinted with permission from Ref. [21] DOI 10.1007/s10948-012-1962-x, Copyright (2013) with permission from Springer (Fig. 6)

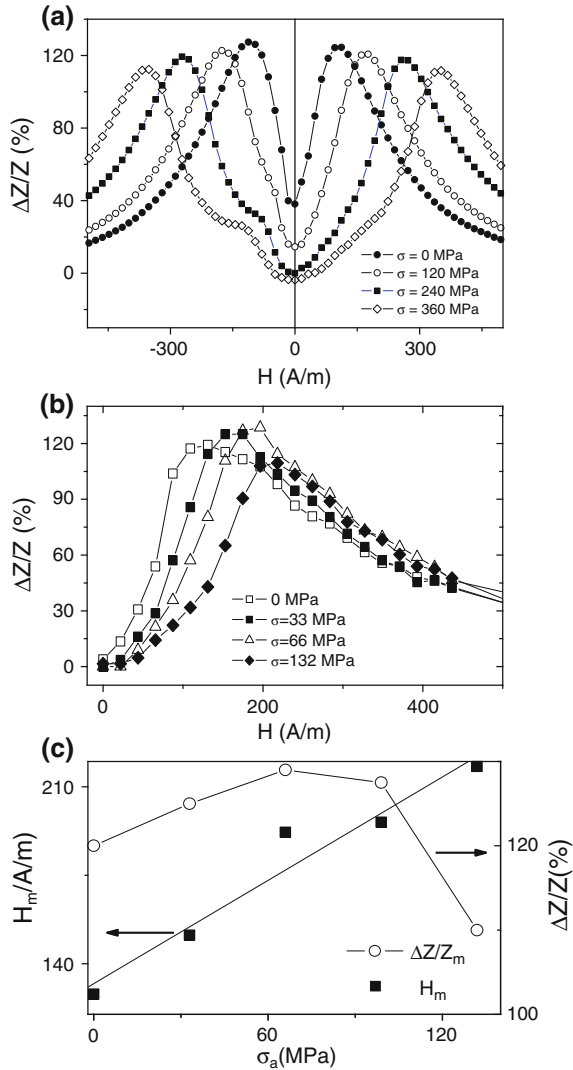
observed, that $\Delta Z/Z$ and H_m are quite sensitive to the application of external tensile stresses, σ_a : here the magnetic field, H_m corresponding to the maximum of $(\Delta Z/Z)$ shows a roughly linear increase with σ (Fig. 6c).

As mentioned above, the value of the DC axial field H_m , that corresponds to the maximum GMI ratio should be attributed to the static circular anisotropy field, H_k . This argument allows us to estimate the magnetostriction constant using the dependence $H_m(\sigma)$ presented in the Fig. 6c and the well known expression for the stress dependence of anisotropy field [23, 24, 49], given by

$$\lambda_s = (\mu_o M_s / 3)(dH_k / d\sigma), \quad (9)$$

where $\mu_o M_s$ is the saturation magnetization.

Fig. 6 $\Delta Z/Z(H)$ dependences of $\text{Co}_{67.05}\text{Fe}_{3.85}\text{Ni}_{1.4}\text{B}_{11.33}\text{Si}_{14.47}\text{Mo}_{1.69}$ (a) and $\text{Co}_{68.5}\text{Mn}_{6.5}\text{Si}_{10}\text{B}_{15}$ (b) amorphous microwires measured at different σ_a and $H_m(\sigma)$ dependence for $\text{Co}_{68.5}\text{Mn}_{6.5}\text{Si}_{10}\text{B}_{15}$ amorphous microwire (c). Reprinted with permission from Ref. [21] DOI 10.1007/s10948-012-1962-x, Copyright (2013) with permission from Springer (Fig. 7)



A comparison with the reported values measured from the stress dependence of initial magnetic susceptibility ($\lambda_{s,0} \approx -3 \times 10^{-7}$ for such composition) and the magnetostriction values measured in amorphous wires of similar compositions has been reported [49].

In fact, the tendency on the change of H_m under the application of tensile stresses (Fig. 6c) and the change of H_m and H_k with the decreasing of the ρ -ratio (Figs. 4, 5 and 6) is the same confirming then the effect of magnetoelastic anisotropy on hysteresis loops and GMI effect.

The $H_m(\sigma)$ dependence (see the Fig. 6c) exhibits a slope of around $0.7 \text{ A}/(\text{m} \times \text{MPa})$, that allows an estimation of the unstressed value of the saturation magnetostriction constant, $\lambda_{s,0}$. The estimated value for $\lambda_{s,0}$ was -2×10^{-7} , which is rather reasonable for the studied samples.

According to the usual definition, the complex impedance of a linear electronic element at the circular frequency ω is given by:

$$Z(\omega) = U_{ac}/I_{ac} = Z_1 + iZ_2, \quad (10)$$

where I_{ac} is the harmonic current with frequency ω flowing through the element and U_{ac} is the harmonic voltage of the same frequency, measured between its terminals [1, 2].

In fact as has been already mentioned, see for example [11], the Eq. (10) is not fully applicable to ferromagnetic conductors because usually such materials are not linear. This occurs because U_{ac} is generally not proportional to I_{ac} and it is not a harmonic function of time (it contains higher order harmonics) [11, 46].

Additionally, although widely used, the definition of the GMI ratio $\Delta Z/Z$, mentioned above, may be useful for quantifying the huge attained variations of impedance, but the information about the phase shift is lost; it depends on the ambiguously chosen H_0 max (although the sample might be apparently magnetically saturated it does not mean that GMI is also saturated). But in any case, most of published papers use $\Delta Z/Z$ or longitudinal impedance change when the frequency dependence of GMI effect is studied.

The magnetic field dependence of real part Z_1 of the longitudinal wire impedance Z_{zz} ($Z_{zz} = Z_1 + iZ_2$), measured up to 4 GHz in $\text{Co}_{66}\text{Cr}_{3.5}\text{Fe}_{3.5}\text{B}_{16}\text{Si}_{11}$, $\text{Co}_{67}\text{Fe}_{3.85}\text{Ni}_{1.45}\text{B}_{11.5}\text{Si}_{14.5}\text{Mo}_{1.7}$ and $\text{Co}_{67.71}\text{Fe}_{4.28}\text{Ni}_{1.57}\text{Si}_{11.24}\text{B}_{12.4}\text{Mo}_{1.25}\text{C}_{1.55}$ microwires is shown in Fig. 7. The general feature of this dependence is that the magnetic field value corresponding to the maximum impedance shifts to the higher field region with the increasing f . A high enough magnetic field sensitivity, i.e., GMI effect till GHz- range frequencies should be also underlined. On the other hand, if the maximum applied magnetic field is not high enough, impedance change induced by applied magnetic field at high frequencies starts to decrease at some frequency. For example, most of the microwires show the highest GMI ratio at frequencies between 100 and 300 MHz (see for example Fig. 8 for $\text{Co}_{66.87}\text{Fe}_{3.66}\text{C}_{0.98}\text{Si}_{11.47}\text{B}_{13.36}\text{Mo}_{1.52}$ microwires). Another interesting features observed in Fig. 8a, b are that the frequency dependence of maximum GMI ratio, $\Delta Z/Z_m(f)$, measured in microwires of the same composition with different diameters presents an optimum frequency (at which $\Delta Z/Z_m$ versus f exhibits the maximum) at different frequency values. Thus, for metallic nucleus diameters ranging between 8.5 and 9.0 μm , the optimal frequency is about 100 MHz, while for microwires with metallic nucleus diameters between 9 and 11.7 μm , the optimal frequency is about 200 MHz.

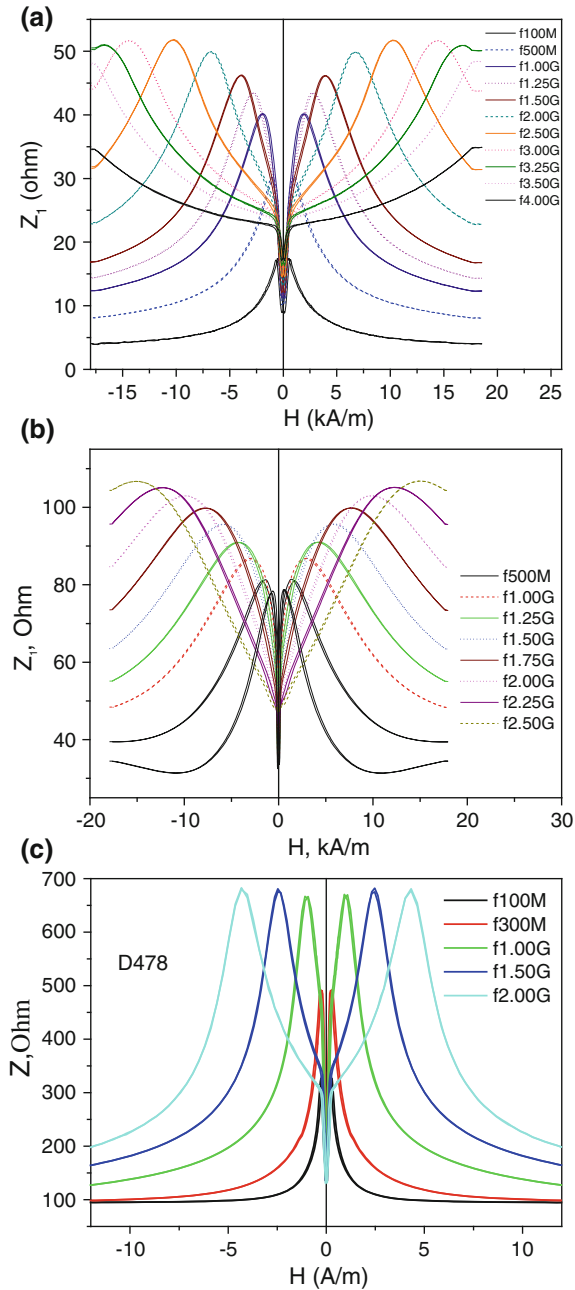


Fig. 7 $Z(H)$ dependences of $\text{Co}_{66}\text{Cr}_{3.5}\text{Fe}_{3.5}\text{B}_{16}\text{Si}_{11}$ (a) $\text{Co}_{67}\text{Fe}_{3.85}\text{Ni}_{1.45}\text{B}_{11.5}\text{Si}_{14.5}\text{Mo}_{1.7}$ (b) and $\text{Co}_{67.71}\text{Fe}_{4.28}\text{Ni}_{1.57}\text{Si}_{11.24}\text{B}_{12.4}\text{Mo}_{1.25}\text{C}_{1.55}$ (c) microwires measured at different frequencies. Reprinted with permission from [46], Copyright©2014, with permission from International Journal on Smart Sensing and Intelligent Systems, <http://www.s2is.org>, (Fig. 5)

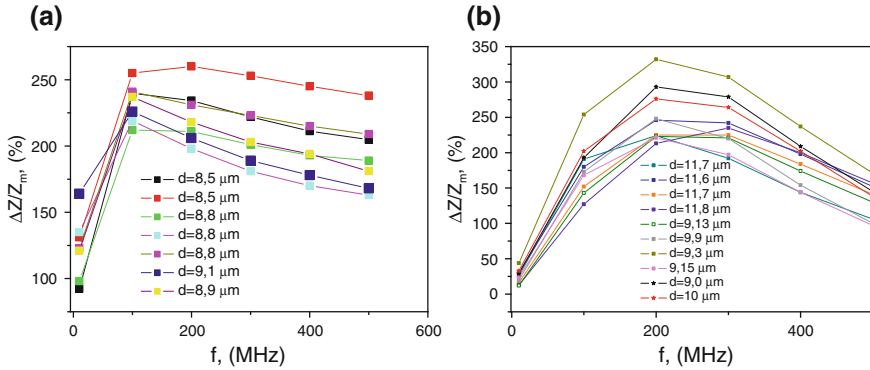


Fig. 8 Frequency dependence of ΔZZ_m in $\text{Co}_{66.87}\text{Fe}_{3.66}\text{C}_{0.98}\text{Si}_{11.47}\text{B}_{13.36}\text{Mo}_{1.52}$ microwires with different metallic nucleus diameters. Reprinted with permission from [7], Copyright (2014), with permission from Elsevier, doi:10.1016/j.jallcom.2012.10.082 (Fig. 5)

As regarding to the origin of the frequency dependence of H_m , observed in Fig. 8 for both microwires, there are different points of view. Experimentally, it has been observed that the magnetic field at which the maximum occurs considerably increases with the frequency (Fig. 7).

One possible explanation for this fact is that the magnetic domain structure and the anisotropy can be different near the surface. At higher frequencies the current flows closer to the surface, then the effective anisotropy field and dispersion can change with the frequency. Another reason might be connected with the frequency dependence of the domain wall permeability and aforementioned FMR contribution at higher frequencies.

The close analogy between the giant magnetoimpedance and ferromagnetic resonance has been previously reported elsewhere [20, 46, 50, 51]. Indeed the saturation magnetization M_s can be estimated from the equation:

$$M_s = 0.805 \times 10^{-9} df_0^2/dH \quad (11)$$

where f_0 is the resonant frequency and H is the applied magnetic field. This approach predicts the linear relation between the square of the resonance frequency as a function of the applied field, $f_0^2(H)$. The experimental data for GMI effect measured in $\text{Co}_{67.05}\text{Fe}_{3.85}\text{Ni}_{1.4}\text{B}_{11.33}\text{Si}_{14.47}\text{Mo}_{1.69}$ microwires fits well with the predicted linear dependence (see Fig. 9).

The saturation magnetization values, obtained from (11) give us quite reasonable values of about 0.5–0.53 MA/m. Consequently frequency dependence of GMI effect at GHz frequencies fits well with the ferromagnetic resonance behaviour, as has been previously reported elsewhere [46, 50, 51].

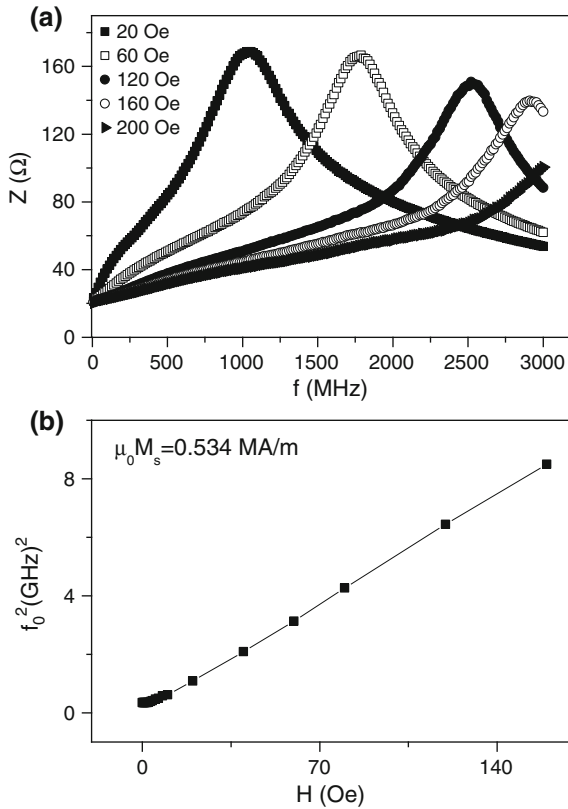


Fig. 9 Frequency dependence of GMI effect (a) and $f_0^2(H)$ dependence (b) measured for $\text{Co}_{67.05}\text{Fe}_{3.85}\text{Ni}_{1.4}\text{B}_{11.33}\text{Si}_{14.47}\text{Mo}_{1.69}$ microwires with $d \approx 21.4 \mu\text{m}$, $\rho \approx 0.816$. Reprinted with permission from Ref. [21] DOI 10.1007/s10948-012-1962-x, Copyright (2013) with permission from Springer (Fig. 4c, d)

4 Effect of Partial Crystallization and Nanocrystallization on Magnetic Properties and GMI

Although the crystallization of amorphous materials usually results in a degradation of their magnetic softness, in some cases the crystallization can improve its magnetically soft behaviour. This is the case of so-called “nanocrystalline” alloys obtained by suitable annealing of amorphous metals. These materials have been introduced in 1988 by Yoshizawa et al. [30], and later they have been intensively studied by a number of research groups [31–34]. As was mentioned in the introduction, the nanocrystalline structure of a partially crystalline amorphous precursor is observed particularly in Fe-Si-B alloys with small additions of Cu and Nb. Small additions of Cu and Nb allow inhibiting of the grains nucleation and decreasing of the grain growth rate [30–33]. The main interest in such nanocrystalline alloys is

related to extremely soft magnetic properties combined with a high saturation magnetization. Such soft magnetic character is thought to be originated because the magnetocrystalline anisotropy vanishes and the very small magnetostriction achieved value when the grain size approaches 10 nm [30–33].

Previously, a considerable magnetic softening and enhancement of GMI effect has been reported for Finemet-type ribbons, conventional wires [52] and glass-coated Finemet-type microwires [53–57]. But the most considerable improvement of GMI effect in the case of glass-coated microwires is reported quite recently [34–37].

As-prepared Finemet-type $\text{Fe}_{73.4}\text{Cu}_1\text{Nb}_{3.1}\text{Si}_x\text{B}_{22.5-x}$ ($x = 11.5, 13.5$ and 16.5) and $\text{Fe}_{73.4-x}\text{Cu}_1\text{Nb}_{3.1}\text{Si}_{13.4+x}\text{B}_{9.1}$ ($0 \leq x \leq 1.1$) microwires present rectangular bistable hysteresis loops similarly to other Fe-rich amorphous microwires [34–37]. For illustration in Fig. 10a we provide hysteresis loops of $\text{Fe}_{70.8}\text{Cu}_1\text{Nb}_{3.1}\text{Si}_{14.5}\text{B}_{10.6}$ microwires with different ρ -ratios ($\rho = 0.67$ and $\rho = 0.38$).

The coercivity, H_c , of as-prepared Finemet-type microwires depends on the ratio $\rho = d/D$ (Fig. 10b).

Fig. 10 Hysteresis loops (a) and $H_c(\rho)$ dependence (b) of $\text{Fe}_{70.8}\text{Cu}_1\text{Nb}_{3.1}\text{Si}_{14.5}\text{B}_{10.6}$ as-prepared microwires. Reprinted with permission from [57] Copyright © 2014, with permission from Springer DOI: [10.1007/s11664-014-3370-4](https://doi.org/10.1007/s11664-014-3370-4) (Fig. 5)

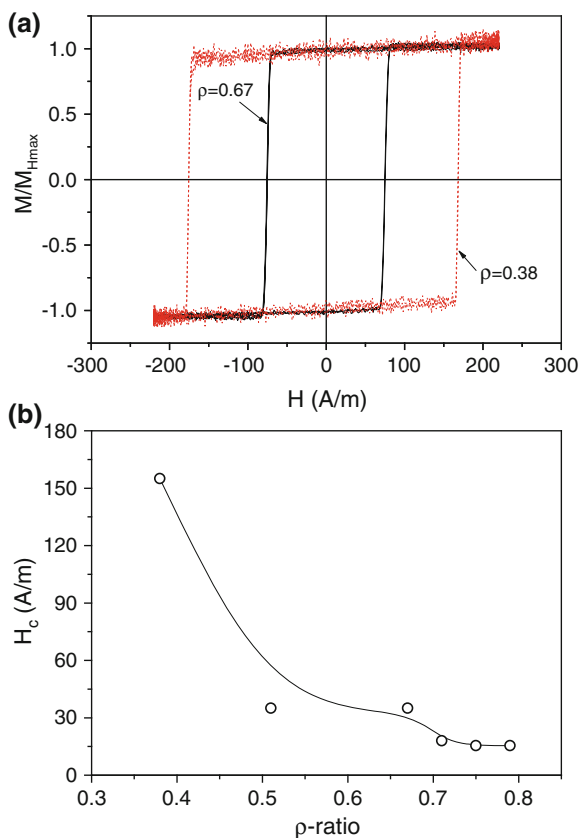


Figure 11a–c present XRD spectra of some selected as-prepared $\text{Fe}_{70.8}\text{Cu}_1\text{Nb}_{3.1}\text{Si}_{16}\text{B}_{9.1}$, $\text{Fe}_{70.8}\text{Cu}_1\text{Nb}_{3.1}\text{Si}_{14.5}\text{B}_{10.6}$ and $\text{Fe}_{73.8}\text{Cu}_1\text{Nb}_{3.1}\text{Si}_{13}\text{B}_{9.1}$ microwires.

The first two peaks of the XRD spectra between 10° and 30° correspond to the glass layer and the other peaks at above 40° are related to the metallic nucleus. All $\text{Fe}_{70.8}\text{Cu}_1\text{Nb}_{3.1}\text{Si}_{16}\text{B}_{9.1}$ and $\text{Fe}_{70.8}\text{Cu}_1\text{Nb}_{3.1}\text{Si}_{14.5}\text{B}_{10.6}$ samples present a completely amorphous structure (Fig. 11a, b).

But some of $\text{Fe}_{73.8}\text{Cu}_1\text{Nb}_{3.1}\text{Si}_{13}\text{B}_{9.1}$ microwires (see Fig. 11c) present a partially crystalline structure already in the as-prepared state.

Usually, the basic method to obtain a nanocrystalline structure from the amorphous state is achieving the crystallization of amorphous matrix by an appropriate heat treatment.

As-prepared samples have been annealed at different annealing temperatures, T_{ann} , at a fixed annealing time. Annealing results show considerable changes of the structure and magnetic properties.

Starting from T_{ann} ranging from 550 to 650 °C a main crystalline peak is appearing in the range between 42° and 45° which correspond to the existence of α -Fe (Si) BCC crystal structure [30–33], as well as another two weak peaks appearing in the range between 65° and 85° (Fig. 12a). However, in the case of the $\text{Fe}_{73.8}\text{Cu}_1\text{Nb}_{3.1}\text{Si}_{13}\text{B}_{9.1}$ microwire such crystalline peak has been observed in the as-prepared state (Fig. 11c) and, consequently after annealing (Fig. 12b). Increasing the annealing temperature, T_{ann} , this peak becomes higher and narrower which indicates an increase in both the bcc-Fe phase volume fraction and grain size growth, respectively.

The shape of the crystalline peak, particularly its width, contains useful information on the average grain size of the corresponding crystalline phase. Considering the main crystalline peak, by estimating the width of the peak, ϵ , as well as the crystallization angle, 2θ , then by substituting these parameters on the Debye-Scherrer equation (Eq. 12), one can obtain the value of the grain size (D).

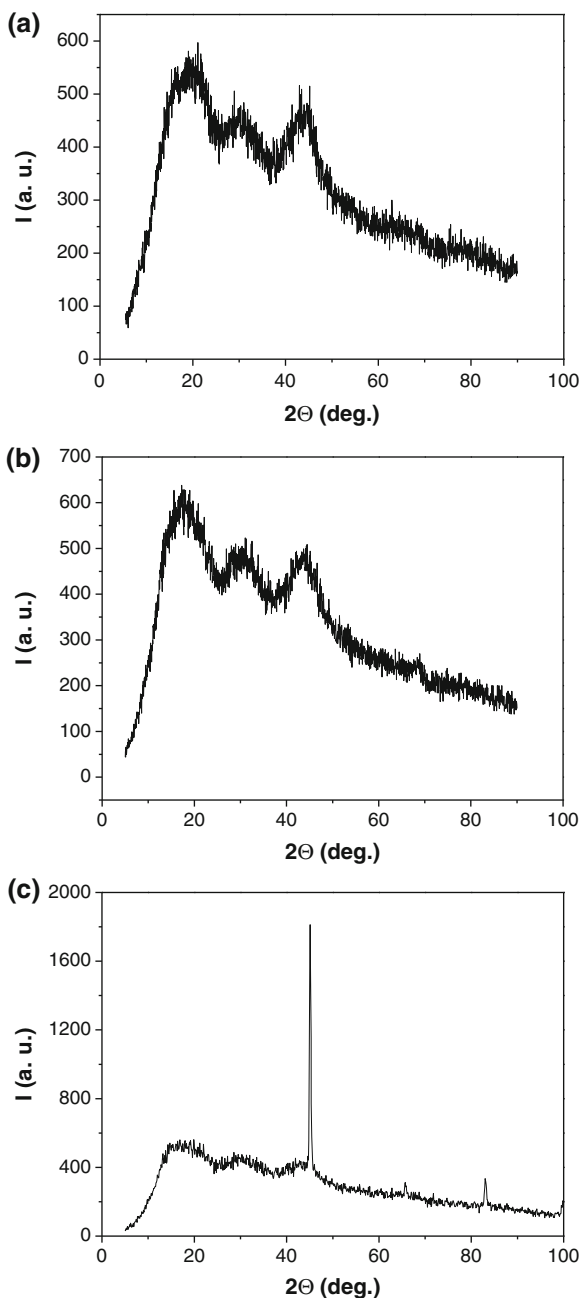
$$D = k\lambda / \epsilon \cos 2\theta \quad (12)$$

where, ϵ is the half height width of the crystalline peak and 2θ is the angular position of the maximum crystalline peak. We found that the average grain size in the range of 550 °C $\leq T_{\text{ann}} \leq 600$ °C is between 12 and 17 nm. By increasing at $T_{\text{ann}} \geq 650$ °C, D rapidly increases achieving values above 30 nm (see Fig. 13).

It is worth mentioning that not only the average grain size, but also the volume fraction of precipitating nanocrystalline phase affects the physical properties of devitrified materials [31, 32].

A strong dependence of magnetic properties on the sample's geometry in the as-prepared state has been observed for all compositions. Hysteresis loops (plotted as the normalized magnetization M/M_{Hmax} versus applied magnetic field H) of as-prepared microwires present rectangular shape typical for amorphous Fe-rich microwires (Figs. 10a and 14). As can be appreciated from Fig. 10b the coercivity,

Fig. 11 XRD patterns of as-prepared microwires: $\text{Fe}_{70.8}\text{Cu}_1\text{Nb}_{3.1}\text{Si}_{16}\text{B}_{9.1}$ with $\rho = 0.75$ (a), $\text{Fe}_{70.8}\text{Cu}_1\text{Nb}_{3.1}\text{Si}_{14.5}\text{B}_{10.6}$ with $\rho = 0.81$ (b) and $\text{Fe}_{73.8}\text{Cu}_1\text{Nb}_{3.1}\text{Si}_{13}\text{B}_{9.1}$ with $\rho = 0.6$ (c). Reprinted with permission from [57] Copyright © 2014, with permission from Springer DOI: [10.1007/s11664-014-3370-4](https://doi.org/10.1007/s11664-014-3370-4) (Fig. 1)



H_c is drastically affected by the ρ -ratio. Strong $H_c(\rho)$ dependence can be explained taking into account the influence of the internal stresses on the coercivity. As was mentioned above the strength of internal stresses is a function of ρ -ratio.

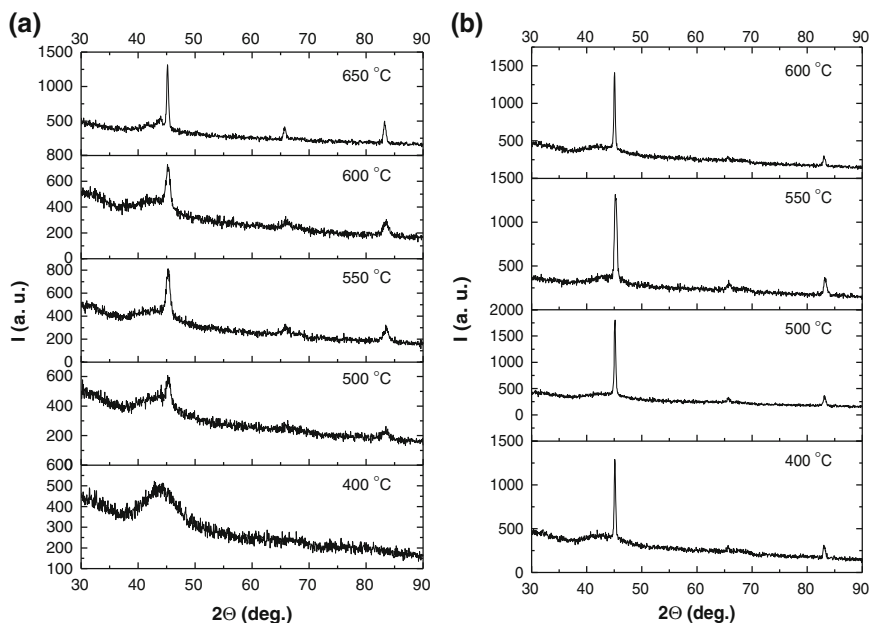


Fig. 12 XRD patterns of annealed microwires $\text{Fe}_{70.8}\text{Cu}_1\text{Nb}_{3.1}\text{Si}_{14.5}\text{B}_{10.6}$ with $\rho = 0.81$ (a) and $\text{Fe}_{73.8}\text{Cu}_1\text{Nb}_{3.1}\text{Si}_{13}\text{B}_{9.1}$ with $\rho = 0.6$ (b). Annealing temperatures are indicated within each pattern. (a) Reprinted with permission from [57] Copyright © 2014, with permission from Springer DOI: [10.1007/s11664-014-3370-4](https://doi.org/10.1007/s11664-014-3370-4) (Fig. 2)

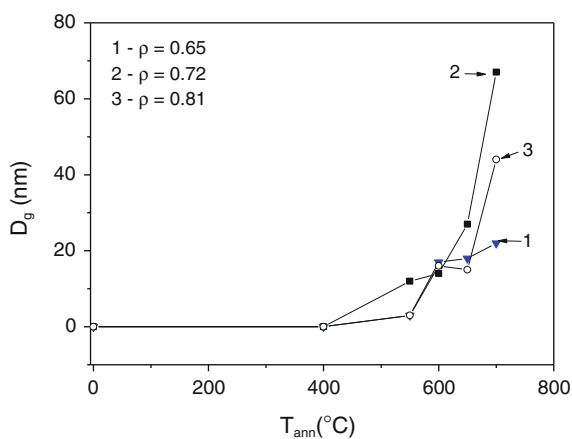
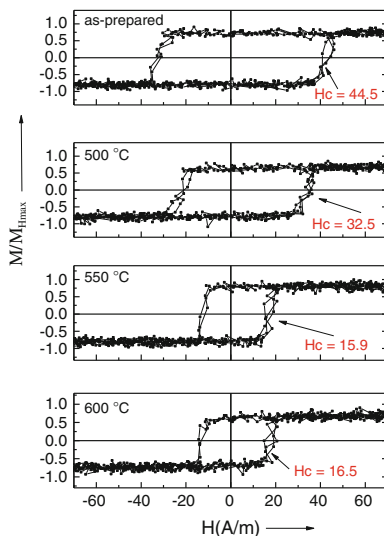


Fig. 13 Dependence of average grain size on annealing temperature for $\text{Fe}_{70.8}\text{Cu}_1\text{Nb}_{3.1}\text{Si}_{14.5}\text{B}_{10.6}$ microwires with various ρ -ratios. Reprinted with permission from [57] Copyright © 2014, with permission from Springer DOI: [10.1007/s11664-014-3370-4](https://doi.org/10.1007/s11664-014-3370-4) (Fig. 3)

Fig. 14 Hysteresis loops of as-prepared and annealed $\text{Fe}_{70.8}\text{Cu}_1\text{Nb}_{3.1}\text{Si}_{14.5}\text{B}_{10.6}$ microwires, with $\rho = 0.81$, at different temperatures measured at fixed magnetic field amplitude of 225 A/m. Reprinted with permission from [57] Copyright © 2014, with permission from Springer DOI: 10.1007/s11664-014-3370-4 (Fig. 6)



Hysteresis loops of as-prepared and annealed $\text{Fe}_{70.8}\text{Cu}_1\text{Nb}_{3.1}\text{Si}_{14.5}\text{B}_{10.6}$ microwires ($\rho = 0.81$) at different temperatures are presented in Fig. 14. It is worth mentioning, that the coercivity decreases upon increasing the annealing temperature, while the rectangular character of hysteresis loops is observed for all samples even annealed at below certain temperature.

In Fig. 15 we plotted the coercivity dependence on the annealing temperature for $\text{Fe}_{70.8}\text{Cu}_1\text{Nb}_{3.1}\text{Si}_{14.5}\text{B}_{10.6}$ glass-coated microwire with different ρ -ratio.

According to these data, a tendency towards decreasing H_c values is observed at the range of 500–550 °C. Above $T_{\text{ann}} \approx 600$ °C the magnetic bistability disappears (hysteresis loops cannot be considered perfectly rectangular). A similar behavior associated with the devitrification and magnetic softening has been previously reported in other Finemet-type microwires [53].

The dependence of the coercivity H_c on the metallic nucleus diameter (d), is in agreement with the previously reported dependence for Fe-Si-B-C amorphous microwires [26]. Hence, the coercivity increasing with the decreasing of the metallic nucleus diameter is interpreted as the interplay of internal stresses and demagnetizing factor.

It is worth mentioning that internal stresses induced by the glass coating affect not only magnetic properties of as-prepared microwires but also the nanocrystallization process. Thus, previously we have studied $H_c(T_{\text{ann}})$ dependences in microwires with rather different ρ -ratios and reported that the internal stresses induced by the glass coating affect the dependence of coercivity on the annealing temperature [56]. We have explained the considerable observed differences in $H_c(T_{\text{ann}})$ considering that internal stresses hinder the segregation of FeB phases responsible of the magnetic hardening.

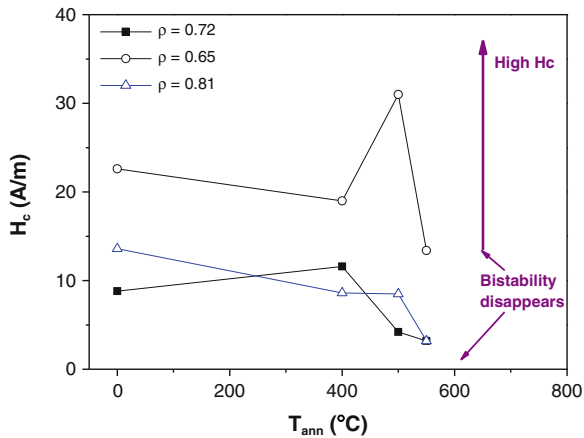


Fig. 15 Dependence of the coercivity, H_c , for the $\text{Fe}_{70.8}\text{Cu}_1\text{Nb}_{3.1}\text{Si}_{14.5}\text{B}_{10.6}$ glass-coated microwire with selected ρ -ratio on annealing temperature. Reprinted with permission from [57] Copyright © 2014, with permission from Springer DOI: [10.1007/s11664-014-3370-4](https://doi.org/10.1007/s11664-014-3370-4) (Fig. 7)

Consequently, a magnetic softening with the lowest value of coercivity and switching field is obtained in the samples treated at 500–600 °C, which could be ascribed to the fact that the first crystallization process has been developed leading to fine α -Fe (Si) nanocrystals with grain size around 10–20 nm (compare Figs. 12, 14 and 15). This behavior is similar to that one widely reported for FINEMET ribbons [30–33].

GMI ration has been measured in as-prepared and annealed samples. As it was expected, samples with amorphous structure in the as-prepared state exhibit a rather small GMI effect (below 5 % see Fig. 16) similar to other Fe-based glass-coated microwires with positive magnetostriction. In contrast, nanocrystalline $\text{Fe}_{70.8}\text{Cu}_1\text{Nb}_{3.1}\text{Si}_{14.5}\text{B}_{10.6}$ microwires annealed at 550 °C exhibit higher GMI effect ($\Delta Z/Z \approx 90$ %, see Fig. 16).

Indeed, like all Fe-based microwires, studied Fe-Cu-Nb-Si-B microwires exhibit a high positive magnetostriction. Consequently, the stress distribution arising from simultaneous rapid quenching of metallic nucleus inside the glass coating must result in a longitudinal magnetization easy axis [26]. The resulting domain structure (with a low circular magnetic permeability typical for magnetically bistable samples) usually exhibits a small GMI effect. Therefore, the GMI effect in the as-prepared FINEMET microwires with positive magnetostriction is low.

A noticeable change in the GMI has been observed after the appearance of nanocrystallites (Fig. 16). As discussed elsewhere, after the nanocrystallization the average magnetostriction constant takes nearly- zero values [31, 32] thanks to the control of the crystalline volume fraction:

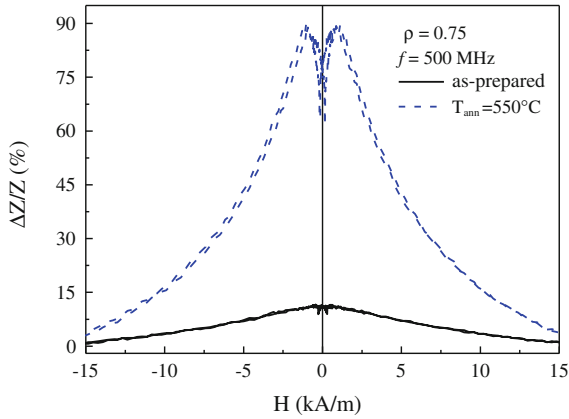


Fig. 16 Effect of annealing at 550 °C for 1 h on $\Delta Z/Z(H)$ dependence of $\text{Fe}_{70.8}\text{Cu}_1\text{Nb}_{3.1}\text{Si}_{16}\text{B}_{9.1}$ microwire with $\rho = 0.75$ measured at 500 MHz in comparison with the GMI response of the as-prepared sample. Reprinted with permission from [57] Copyright © 2014, with permission from Springer DOI: [10.1007/s11664-014-3370-4](https://doi.org/10.1007/s11664-014-3370-4) (Fig. 8)

$$\lambda_{s,\text{eff}} = V_{\text{cr}}\lambda_{s,\text{cr}} + (1 - V_{\text{cr}})\lambda_{s,\text{am}} \quad (13)$$

being $\lambda_{s,\text{eff}}$ the saturation magnetostriction coefficient and V_{cr} the crystalline volume fraction.

As discussed elsewhere, the GMI effect is affected by the magnetic anisotropy [5, 17]. Consequently, the shape of $\Delta Z/Z(H)$ dependence and maximum GMI ratio $\Delta Z/Z_{\text{max}}$ are considerably affected by annealing [17].

It should be noted that the GMI response is affected by the frequency and can be optimized choosing the appropriate driving frequency [26]. As was mentioned above, the variation of the skin effect of a magnetic conductor under an applied magnetic field is the main origin of the GMI effect [1, 2]. The skin depth, δ , of magnetic conductor is given by Eq. (4) being f the frequency of the current, σ the electrical conductivity of the material, and $\mu\phi$ the circular magnetic permeability as a parameters.

One of the conditions for the observation of the GMI effect is that the skin depth must be reduced below the wire radius. Despite this, the frequency at which the maximum GMI value is obtained depends strongly on the sample geometry, i.e., on the ρ -ratio [26].

Frequency dependences of $\Delta Z/Z_{\text{max}}$ obtained in $\text{Fe}_{70.8}\text{Cu}_1\text{Nb}_{3.1}\text{Si}_{16}\text{B}_{9.1}$ microwires with different ρ -ratios are displayed in Fig. 17. Similarly to amorphous Co-rich microwires one can conclude that $\Delta Z/Z$ and its frequency dependence are strongly affected by the magnetoelastic anisotropy determined by the ρ -ratio.

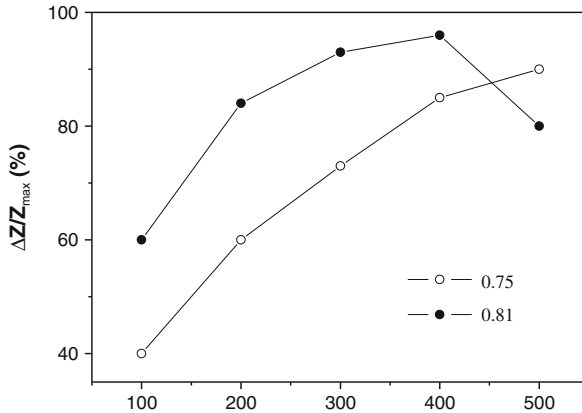


Fig. 17 Frequency dependence of $\text{Fe}_{70.8}\text{Cu}_1\text{Nb}_{3.1}\text{Si}_{16}\text{B}_{9.1}$ microwires annealed at $550\text{ }^\circ\text{C}$ with different geometric ratios ρ . Reprinted with permission from [57] Copyright © 2014, with permission from Springer DOI: [10.1007/s11664-014-3370-4](https://doi.org/10.1007/s11664-014-3370-4) (Fig. 9)

5 Conclusion

Studies of magnetic properties and GMI effect of amorphous Co-Fe rich microwires reveal that selecting its appropriate chemical composition and geometry they present GMI effect at GHz frequencies. Hysteresis loops and magnetic field dependences of GMI effect are affected by the magnetoelastic anisotropy. Features of high frequency GMI effect can be described using a FMR-like approximation.

Investigations of magnetic properties of Finemet-type Fe-Cu-Nb-Si-B microwires reveal that annealing considerably affects the hysteresis loops and GMI effect of this family of microwires. In as-prepared microwires, the reduction of the ρ -ratio results in the rise of coercivity. Magnetoelastic anisotropy affects soft magnetic properties of as-prepared FeCuNbSiB microwires. We observed magnetic softening and a considerable increasing of the GMI effect in Finemet-type FeCuNbSiB with nanocrystalline structure even in as-prepared microwires. After an adequate annealing of Finemet-type microwires we observed a GMI ratio of about 100 %. The nanocrystallization of FeCuNbSiB microwires is a key factor for the optimization of the GMI effect.

References

1. L.V. Panina, K. Mohri, Magneto-impedance effect in amorphous wires. *Appl. Phys. Lett.* **65**, 1189–1191 (1994)
2. R.S. Beach, A.E. Berkowitz, Giant magnetic-field dependent impedance of amorphous FeCoSiB wire. *Appl. Phys. Lett.* **64**(26), 3652 (1994)

3. E.P. Harrison, G.L. Turney, H. Rowe, H. Gollop, The electrical properties of high permeability wires carrying alternating current. *Proc. R. Soc. Lond. A* **157**, 451–479 (1936)
4. A. Zhukov, V. Zhukova, *Magnetic Sensors Based on Thin Magnetically Soft Wires with Tuneable Magnetic Properties and Its Applications*. International Frequency Sensor Association (IFSA) Publishing, Ronda de Ramon Otero Pedrayo, 42C, 1-5, 08860, Castelldefels (Barcelona), Spain (2014). ISBN-10: 84-617-1866-6
5. N.A. Usov, A.S. Antonov, A.N. Lagarkov, Theory of giant magneto-impedance effect in amorphous wires with different types of magnetic anisotropy. *J. Magn. Magn. Mater.* **8**, 159, 185 (1998)
6. P. Ciureanu, G. Rudkowska, L. Clime, A. Sklyuyev, A. Yelon, Anisotropy optimization of giant magnetoimpedance sensors. *J. Optoelectron. Adv. Mater.* **6**, 905–910 (2004)
7. A. Zhukov, M. Ipatov, M. Churyukanova, S. Kaloshkin, V. Zhukova, Giant magnetoimpedance in thin amorphous wires: from manipulation of magnetic field dependence to industrial applications. *J. Alloys Comp.* **586**(Suppl. 1), S279–S286 (2014). doi:[10.1016/j.jallcom.2012.10.082](https://doi.org/10.1016/j.jallcom.2012.10.082)
8. M.E. McHenry, M.A. Willard, D.E. Laughlin, Amorphous and nanocrystalline materials for applications as soft magnets. *Prog. Mater. Sci.* **44**, 291 (1999)
9. Y. Honkura, Development of amorphous wire type MI sensors for automobile use. *J. Magn. Magn. Mater.* **249**, 375–381 (2002)
10. K. Mohri, T. Uchiyama, L.P. Shen, C.M. Cai, L.V. Panina, Amorphous wire and CMOS IC-based sensitive micro-magnetic sensors (MI sensor and SI sensor) for intelligent measurements and controls. *J. Magn. Magn. Mater.* **249**, 351–356 (2002)
11. D.P. Makhnovskiy, L.V. Panina, D.J. Mapps, Field-dependent surface impedance tensor in amorphous wires with two types of magnetic anisotropy: helical and circumferential. *Phys. Rev. B* **63**, 1444241 (2001)
12. S.I. Sandacci, D.P. Makhnovskiy, L.V. Panina, K. Mohri, Y. Honkura, Off-diagonal impedance in amorphous wires and its application to linear magnetic sensors. *IEEE Trans. Magn.* **35**, 3505–3510 (2004)
13. P. Aragonese, A. Zhukov, J. Gonzalez, J.M. Blanco, L. Dominguez, Effect of AC driving current on magneto-impedance effect. *Sensors Actuators A* **81**(1–3), 86–90 (2000)
14. A. Zhukov, M. Ipatov, V. Zhukova, C. Garcia, J. Gonzalez, J.M. Blanco, Development of ultra-thin glass-coated amorphous microwires for HF magnetic sensor applications. *Phys. Stat. Sol. (A)* **205**(6), 1367–1372 (2008). doi:[10.1002/pssa.200778133](https://doi.org/10.1002/pssa.200778133)
15. K.R. Pirota, L. Kraus, H. Chiriac, M. Knobel, Magnetic properties and GMI in a CoFeSiB glass-covered microwire. *J. Magn. Magn. Mater.* **21**, L243–L247 (2000)
16. V. Zhukova, A. Chizhik, A. Zhukov, A. Torcunov, V. Larin, J. Gonzalez, Optimization of giant magneto-impedance in Co-rich amorphous microwires. *IEEE Trans. Magn.* **38**(5, Part I), 3090–3092 (2002)
17. J.M. Blanco, A. Zhukov, J. Gonzalez, Effect of tensile and torsion on GMI effect in amorphous wire. *J. Magn. Magn. Mater.* **196–197**, 377–379 (1999)
18. V. Zhukova, M. Ipatov, J. González, J.M. Blanco, A.P. Zhukov, Development of thin microwires with enhanced magnetic softness and GMI. *IEEE Trans. Magn.* **44**(Part 2), 3958–3961 (2008)
19. M.-H. Phan, H.-X. Peng, Giant magnetoimpedance materials: fundamentals and applications. *Prog. Mater. Sci.* **53**, 323–420 (2008)
20. D. Ménard, M. Britel, P. Ciureanu, A. Yelon, Giant magnetoimpedance in a cylindrical conductor. *J. Appl. Phys.* **84**, 2805–2814 (1998)
21. A. Zhukov, M. Ipatov, C. Garcia, M. Churyukanova, S. Kaloshkin, V. Zhukova, From manipulation of giant magnetoimpedance in thin wires to industrial applications. *J. Supercond. Nov. Magn.* **26**, 1045–1054 (2013)
22. T. Uchiyama, K. Mohri, Sh Nakayama, Measurement of spontaneous oscillatory magnetic field of Guinea-Pig smooth muscle preparation using pico-tesla resolution amorphous wire magneto-impedance sensor. *IEEE Trans. Magn.* **47**(10), 3070–3073 (2011)

23. V.S. Larin, A.V. Torcunov, A. Zhukov, J. González, M. Vazquez, L. Panina, Preparation and properties of glass-coated microwires. *J. Magn. Magn. Mater.* **249**(1-2), 39–45 (2002)
24. Y. Konno, K. Mohri, Magnetostriction measurements for amorphous wires. *IEEE Trans. Magn.* **25**, 3623–3625 (1989)
25. A. Zhukov, V. Zhukova, J.M. Blanco, A.F. Cobeño, M. Vazquez, J. Gonzalez, Magnetostriction in glass-coated magnetic microwires. *J. Magn. Magn. Mater.* **258–259**, 151–157 (2003)
26. V. Zhukova, M. Ipatov, A. Zhukov, Thin magnetically soft wires for magnetic microsensors. *Sensors* **9**, 9216–9240 (2009). doi:[10.3390/s91109216](https://doi.org/10.3390/s91109216)
27. J. Velázquez, M. Vazquez, A. Zhukov, Magnetoelastic anisotropy distribution in glass-coated microwires. *J. Mater. Res.* **11**, 2499–2505 (1996)
28. A.S. Antonov, V.T. Borisov, O.V. Borisov, A.F. Prokoshin, N.A. Usov, Residual quenching stresses in glass-coated amorphous ferromagnetic microwires. *J. Phys. D Appl. Phys.* **33**, 1161–1168 (2000)
29. H. Chiriac, T.-A. Ovari, A. Zhukov, Magnetoelastic anisotropy of amorphous microwires. *J. Magn. Magn. Mater.* **254–255**, 469–471 (2003)
30. Y. Yoshizawa, S. Oguma, K. Yamauchi, New Fe-based soft magnetic alloys composed of ultrafine grain structure. *J. Appl. Phys.* **64**, 6044 (1988)
31. Y. Yoshizawa, K. Yamauchi, Fe-based soft magnetic alloy composed of ultrafinegrain structure. *Mater. Trans. JIM* **31**, 307–314 (1990)
32. G. Herzer, Grain size dependence of coercivity and permeability in nanocrystalline ferromagnets. *IEEE Trans. Magn.* **26**, 1397–1402 (1990)
33. G. Herzer, Anisotropies in soft magnetic nanocrystalline alloys. *J. Magn. Magn. Mater.* **294**, 99–106 (2005)
34. A. Talaat, M. Ipatov, V. Zhukova, J.M. Blanco, M. Churyukanova, S. Kaloshkin, A. Zhukov, Giant magneto-impedance effect in thin Finemet nanocrystalline microwires. *Phys. Status Solidi C* **11**(5–6), 1120–1124 (2014)
35. A.P. Zhukov, A. Talaat, M. Ipatov, J.M. Blanco, L. Gonzalez-Legarreta, B. Hernando, V. Zhukova, Effect of nanocrystallization on magnetic properties and GMI effect of microwires. *IEEE Trans. Magn.* **50**(6), 2501905 (2014)
36. A. Zhukov, M. Ipatov, A. Talaat, M. Churyukanova, S. Kaloshkin, V. Zhukova, Giant magnetoimpedance in thin amorphous and nanocrystalline microwires. *Appl. Phys. A Mater. Sci. Process.* **115**, 547–553 (2014)
37. A. Talaat, V. Zhukova, M. Ipatov, J.J. del Val, L. Gonzalez-Legarreta, B. Hernando, J.M. Blanco, A. Zhukov, Effect of nanocrystallization on giant magnetoimpedance effect of Fe based microwires. *Intermetallics* **51**, 59–63 (2014)
38. A. Talaat, V. Zhukova, M. Ipatov, J.M. Blanco, L. Gonzalez-Legarreta, B. Hernando, J.J. del Val, J. Gonzalez, A. Zhukov, Optimization of the giant magnetoimpedance effect of Finemet-type microwires through the nanocrystallization. *J. Appl. Phys.* **115**, 17A313 (2014)
39. A.V. Ulitovski, N.M. Avernin, Method of fabrication of metallic microwire. Patent No 161325 (USSR), 19.03.64. Bulletin, No 7, p. 14
40. A.V. Ulitovsky, I.M. Maianski, A.I. Avramenco, Method of continuous casting of glass coated microwire. Patent No 128427 (USSR), 15.05.60. Bulletin, No 10, p. 14
41. E.Ya. Badinter, N.R. Berman, I.F. Drabenko, V.I. Zaborovsky, Z.I. Zelikovsky, V.G. Cheban, Cat microwires and its properties. Shtinica, Kishinev (1973)
42. L. Kraus, J. Schneider, H. Wiesner, Ferromagnetic resonance in amorphous alloys prepared by rapid quenching from the melt. *Czech J. Phys.* **26**(5), 601–602 (1976)
43. A. Zhukov, V. Zhukova, Magnetic properties and applications of ferromagnetic microwires with amorphous and nanocrystalline structure. Nova Science Publishers, New York (2009). ISBN:978-1-60741-770-5
44. A. Zhukov, E. Kostitsyna, E. Shuvaeva, S. Kaloshkin, M. Churyukanova, V. Sudarchikova, A. Talaat, V. Zhukova, Effect of composite origin on magnetic properties of glass-coated microwires. *Intermetallics* **44**, 88–93 (2014). doi:[10.1016/j.intermet.2013.08.014](https://doi.org/10.1016/j.intermet.2013.08.014)

45. A. Zhukov, A. Talaat, M. Ipatov, J.J. del Val, L. Gonzalez-Legarreta, B. Hernando, A. Chizhik, J.M. Blanco, V. Zhukova, Optimization of magnetic properties and giant magnetoimpedance effect in nanocrystalline microwires. *J. Supercond. Nov. Magn.* **28**, 813–822 (2015). doi:[10.1007/s10948-014-2654-5](https://doi.org/10.1007/s10948-014-2654-5)
46. A. Zhukov, A. Talaat, M. Ipatov, V. Zhukova, High frequency giant magnetoimpedance effect of amorphous microwires for magnetic sensors applications. *Int. J. Smart Sens. Intell. Syst.* (2014). In: Proceedings of the 8th international conference on sensing technology, 2–4 Sep 2014, Liverpool, UK, pp 624-629. <http://www.s2is.org>
47. M. Ipatov, V. Zhukova, A. Zhukov, J. Gonzalez, A. Zvezdin, Low-field hysteresis in the magnetoimpedance of amorphous microwires. *Phys. Rev. B* **81**, 134421 (2010)
48. A. Zhukov, M. Ipatov, V. Zhukova, Amorphous microwires with enhanced magnetic softness and GMI characteristics. *EPJ Web Conf.* **29**, 00052 (2012)
49. A.F. Cobeño, A. Zhukov, J.M. Blanco, J. Gonzalez, Giant magneto-impedance effect in CoMnSiB amorphous microwires. *J. Magn. Magn. Mater.* **234**, L359–L365 (2001)
50. C. García, A. Zhukov, V. Zhukova, M. Ipatov, J.M. Blanco, J. Gonzalez, Effect of tensile stresses on GMI of Co-rich amorphous microwires. *IEEE Trans. Magn.* **41**, 3688–3690 (2005)
51. A. Zhukov, A. Talaat, M. Ipatov, V. Zhukova, Tailoring of high frequency giant magnetoimpedance effect of amorphous Co-rich microwires. *IEEE Magn. Lett.* (2015) (accepted). doi:[10.1109/LMAG.2015.2397877](https://doi.org/10.1109/LMAG.2015.2397877)
52. H.Q. Guo, H. Kronmüller, T. Dragon, Z.H. Cheng, B.G. Shen, Influence of nanocrystallization on the evolution of domain patterns and the magnetoimpedance effect in amorphous $\text{Fe}_{73.5}\text{Cu}_1\text{Nb}_3\text{Si}_{13.5}\text{B}_9$ ribbons. *J. Appl. Phys.* **89**, 514 (2001)
53. J. Arcas, C. Gómez-Polo, A. Zhukov, M. Vázquez, V. Larin, A. Hernando, Magnetic properties of amorphous and devitrified FeSiBCuNb glass-coated microwires. *Nanostruct. Mater.* **7**(8), 823 (1996)
54. C. Dudek, A.L. Adenot-Engelvin, F. Bertin, O. Acher, J. Non-Cryst. Solids **353**, 925 (2007)
55. H. Chiriac, T.A. Ovari, C.S. Marinescu, Giant magneto-impedance effect in nanocrystalline glass-covered wires. *J. Appl. Phys.* **83**, 6584 (1998)
56. V. Zhukova, A.F. Cobeño, A. Zhukov, J.M. Blanco, V. Larin, J. Gonzalez, Coercivity of glass-coated $\text{Fe}_{73.4-x}\text{Cu}_1\text{Nb}_{3.1}\text{Si}_{13.4+x}\text{B}_{9.1}$ ($0 \leq x \leq 1.6$) microwires. *Nanostruct. Mater.* **11**(8), 1319–1327 (1999)
57. V. Zhukova, A. Talaat, M. Ipatov, J.J. del Val, L. Gonzalez-Legarreta, B. Hernando, A. Zhukov, Effect of nanocrystallization on magnetic properties and GMI effect of Fe-rich microwires. *J. Electron. Mater.* **43**(12) (2014). doi:[10.1007/s11664-014-3370-4](https://doi.org/10.1007/s11664-014-3370-4)

Aged Zirconia Electrochemical Oxygen Sensor Activation and Re-activation Using NEMCA

P. Shuk and R. Jantz

Abstract Zirconia electrochemical oxygen sensor is widely used today in different industrial power and chemicals production applications (O_2 -Analyzer) and transportation (λ sensor). Non-Faradaic Electrochemical Modification of Catalytic Activity (NEMCA) was invented in 80th and shown high efficiency in the catalytic activity and selectivity increase of the gas exposed electrodes. For the first time NEMCA was investigated for the activation and re-activation of the industrial potentiometric oxygen sensor based on stabilized zirconia solid electrolyte. Electrochemical promotion of O_2 -sensors with Pt-cermet electrodes aged in the field was significant with up to 5 times in the sensor's impedance reduction. Stability tests on the NEMCA activated O_2 -sensors were showing just a minor impedance increase after 2 weeks. Sensor response time was also reduced using NEMCA by $\sim 5\text{--}10\%$ with up to 3 times the sensor's signal noise reduction on the aged zirconia oxygen electrochemical cells.

1 Introduction

Electrochemical oxygen sensors based on the zirconia solid electrolytes widely used today in different industrial applications, i.e., power generation, petrochemical, incinerators, steelmaking, lime and cement kilns and for the controlling fuel/air ratio in the internal combustion engines (well known as λ sensor) were initially discovered early 60th by Möbius and Peters in Germany [1] and Weissbart and Ruka in USA [2]. Most industrial zirconia oxygen analysers are using electrochemical sensor with the solid electrolyte based on yttrium stabilized zirconium oxide working in the potentiometric mode [3–6]. After the exposure to the high temperature severe process environment these electrochemical zirconia oxygen sensors will be degrading after months or years in the service requiring more

P. Shuk (✉) · R. Jantz

Rosemount Analytical Inc, Emerson Process Management, Solon/Irvine, USA
e-mail: Pavel.Shuk@emerson.com

frequent sensor calibration and re-calibration or calibration gases validation and finally oxygen sensor replacement.

“Non-Faradaic Electrochemical Modification of Catalytic Activity (NEMCA), also known as Electrochemical Promotion Of Catalysis (EPOC) or In Situ Controlled Promotion” (ICP) was first discovered in 80th by Costantinos G. Vayenas and is used to increase the catalytic activity (up to 90 fold) and selectivity of the gas exposed electrodes on a solid electrolyte cell by applying direct current electric field to the electrochemical cell [7]. It was shown that electrochemistry can be used to activate and precisely tune heterogeneous catalytic processes with the catalyst supported by the ionic or mixed ionic-electronic conductors. These materials can act as reversible in situ promoter donors or poison acceptors to affect the catalytic activity and selectivity of the electrodes deposited on the solid electrolytes. This phenomenon was well documented and has been observed on the various metal electrode surfaces, e.g., Pt, Ni, Au and Pd supported by oxide ion (O^{2-}), sodium ion (Na^+) and proton (H^+) conductive solid electrolytes for the different catalytic reactions [8–14]. This electrochemical promotion was confirmed to be supported by the potential- or current-controlled electrocatalytic Faradaic introduction of the catalysis promoting species, e.g., O^{2-} , Na^+ or H^+ from the ionic conductive solid electrolyte to the catalyst/gas interface. This non-Faradaic activation of the heterogeneous catalytic reactions has shown to be very promising applications in the electrochemistry with several technological opportunities, particularly in the industrial catalyst products selectivity modification and in exhaust gas treatment [15].

In this work Non-Faradaic Electrochemical Modification of Catalytic Activity (NEMCA) known for the increasing the catalytic activity and selectivity of the gas exposed electrodes was for the first time investigated in new and ‘aged’ industrial O_2 -sensors electrochemical activation and re-activation affecting the sensor response, impedance and stability.

2 Experimental

Industrial zirconia potentiometric oxygen sensors (12 “aged” and 37 new cells) were evaluated on the impedance test rack as well in the 6888 O_2 Analyzer (Fig. 1) for the response, reproducibility and stability. After stabilizing the temperature at 736 °C the cell impedance was measured using Digital Multimeter Fluke 87 III (Fluke, WA) before and after NEMCA treatment. The impedance measurements of the selected “aged” O_2 cells were carried out using Solartron 1260 Frequency Analyzer (Solartron Analytical Corp, UK) in 0.1 Hz...10 MHz frequency range. Optimized ~ 1.5 V DC treatment was applied to the cell’s electrodes for 1, 3 or 5 min using Precision DC Source Model 2020B (Power Designs Inc., NY).

Test gas mixtures were prepared using calibrated EnviroNics 4000 mixing system (EnviroNics, Inc., CT, USA) and mixed oxygen concentrations were certified using a calibrated 6888 O_2 Analyzer (Rosemount Analytical Inc., OH, USA). The gas flow rate was kept constant at 2.5 L/min. The gas concentration was varied



Fig. 1 6888 O₂ Analyzer with Zirconia O₂-cell installed on the probe end

between 2 and 20 % O₂. Data acquisition system from National Instruments Inc. including signal conditioning module (SCXI-1000 + SCXI-1102 card) and the plug-in DAQ card (AT-MIO-16 XE-50) was used for the raw signal sensor data collection.

3 Results and Discussion

The ideal zirconia potentiometric O₂-sensor signal is logarithmically depending on the oxygen concentration in a wide oxygen concentration range (Fig. 2) according to the modified Nernstian equation:

$$E = Const + \frac{RT}{4F} \ln \frac{p(O_2)''_{process}}{p(O_2)'_{ref}}, \quad (1)$$

where R is universal gas constant, T is the sensor temperature in °K and F is the Faraday constant. In the industrial O₂-probe an additional constant related to the reference/process sides temperature deference and thermal junctions in the probe is included in the equation and should be calibrated out for the precise oxygen concentration measurements in the challenging combustion process environment.

6888 O₂ probe with optimized O₂-cell was showing minimal effect (<0.04 % O₂) of process temperature wide variation between 25 and 700 °C on the probe accuracy (Fig. 3) as well as good slope and constant reproducibility after many calibrations (Fig. 4). The “ideal” oxygen sensor in 6888 O₂ probe was replaced with the different new O₂-sensors as well as sensors exposed for years to severe combustion environment with the light, moderate and severe degradation on the impedance or response. As expected no significant NEMCA effect was observed on the new

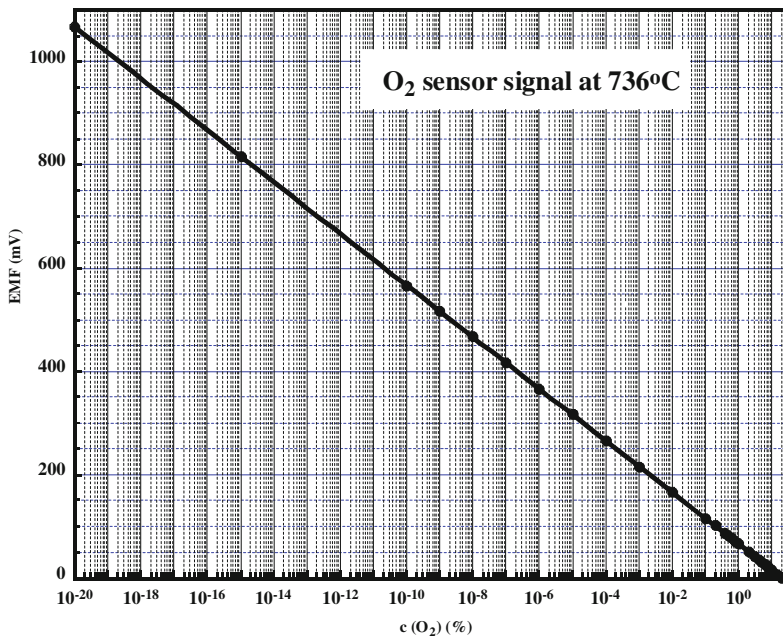


Fig. 2 O₂ sensor lineal dependence on logarithmic oxygen concentration

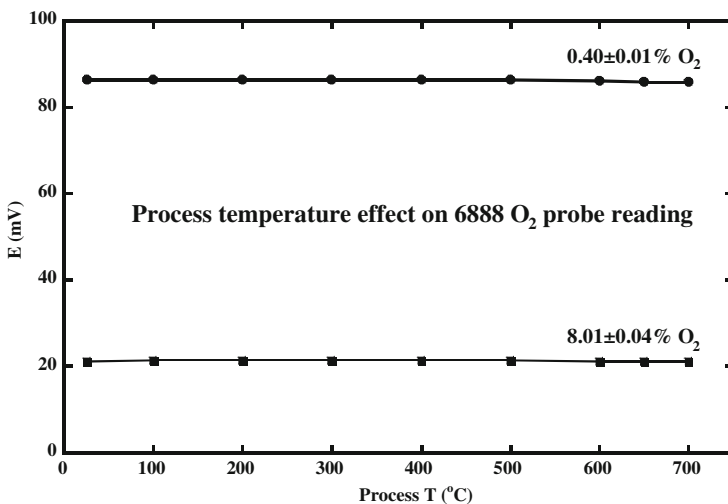


Fig. 3 Process temperature effect on 6888 O₂-probe performance at 0.40 and 8.0 % O₂

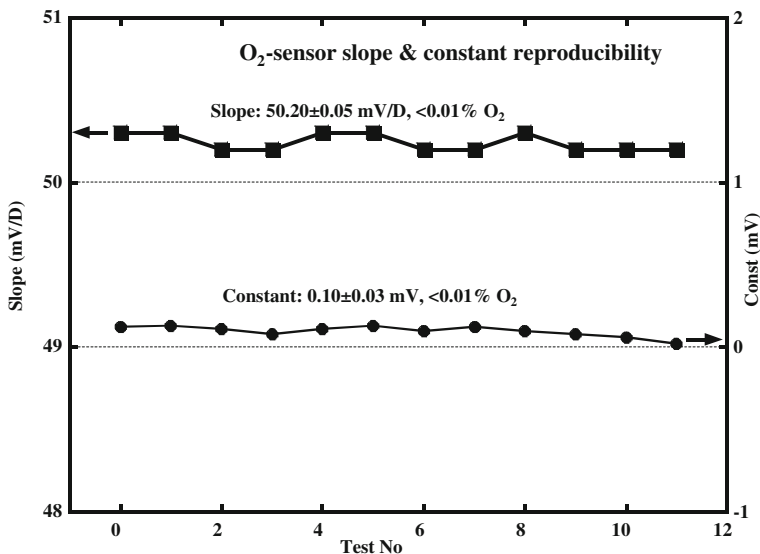


Fig. 4 O₂-sensor calibration slope and constant reproducibility at 736 °C

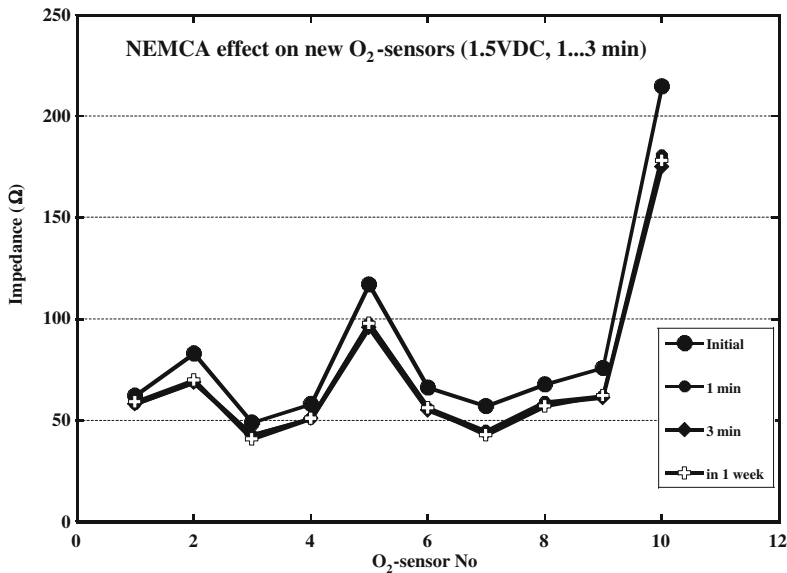


Fig. 5 NEMCA effect on new and ‘aged’ O₂-sensors at 736 °C

already chemically activated oxygen sensors with ~5...30 % impedance reduction of the selected oxygen sensors (Figs. 5 and 6).

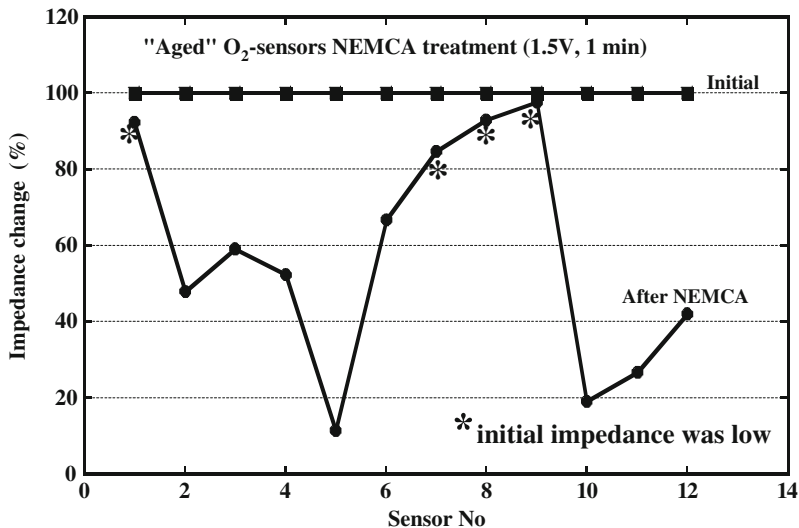


Fig. 6 NEMCA effect on new O₂-sensors at 736 °C

Short ~ 1 min NEMCA treatment was sufficient and the activation effect was quite permanent with the slight impedance degradation starting in ~2 weeks. NEMCA treatment on “aged” oxygen sensors exposed for 1–2 years to the combustion process flue gas was significantly increasing Pt-electrodes activity with up to 10 times the cell impedance reduction except for just slightly degraded low impedance (<100 Ω) O₂-sensors (Fig. 7).

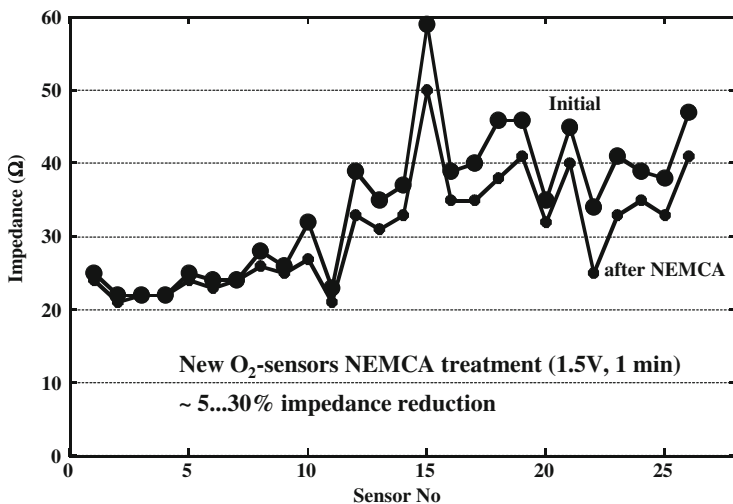


Fig. 7 NEMCA effect on “aged” O₂-sensors at 736 °C

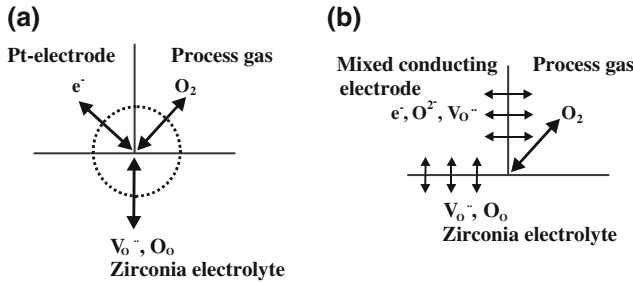
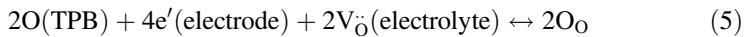


Fig. 8 Oxygen sensor electrochemical reaction schematically

The oxygen reaction in the electrochemical oxygen sensor (Fig. 8a) is taking place [16] on the triple phase boundary (TPB: electrode, electrolyte, and gas) where the oxygen molecules (O_2), electrons (e') and oxygen vacancies (V_{O}) are available and with the elemental steps of the reaction including molecular oxygen diffusion in the gas phase and absorption (2), diffusion and dissociation on the electrolyte/electrode surface (3), diffusion to TPB (4) and final oxygen electrochemical reaction (5):



By using mixed ionic-electronic conductive electrode or cermet electrode with electronic and ionic conductors, e.g., Pt-zirconia, the oxygen electrochemical reaction will be expanding to the electrode bulk (Fig. 8b) improving the electrode performance. We applied this mixed conductive electrode in our oxygen sensor NEMCA activation and re-activation investigation. The electrochemically active sites are assumed to be in the vicinity of the three-phase boundary [17] and NEMCA of the Pt- or Pt- cermet electrode most likely will be improving the critical electrochemical step of the oxygen reaction.

As it can be seen from Fig. 9 the NEMCA effect is quite permanent on the new O_2 -sensors with the impedance starting to increase in 1...2 weeks on the “aged” O_2 -sensors but still remaining 50...80 % smaller than the impedance of the sensors before the treatment.

The response time and stability of the oxygen sensor after the NEMCA treatment was slightly improved even on new already chemically activated sensors (Figs. 10 and 11) with very significant raw mV signal noise reduction from ± 0.6 to ± 0.2 mV at 2 % O_2 (Fig. 12) or ± 0.2 mV at 20 % O_2 (Fig. 13) increasing the signal/noise ratio from 40 to 240 at 2 % O_2 and from 1.4 to 3.5 at 20 % O_2 for the aged O_2 -

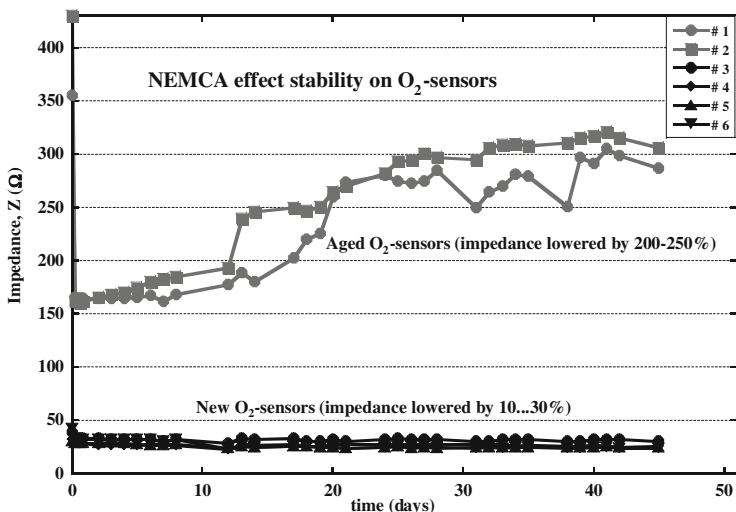


Fig. 9 O₂-sensors impedance stability after NEMCA treatment at 736 °C

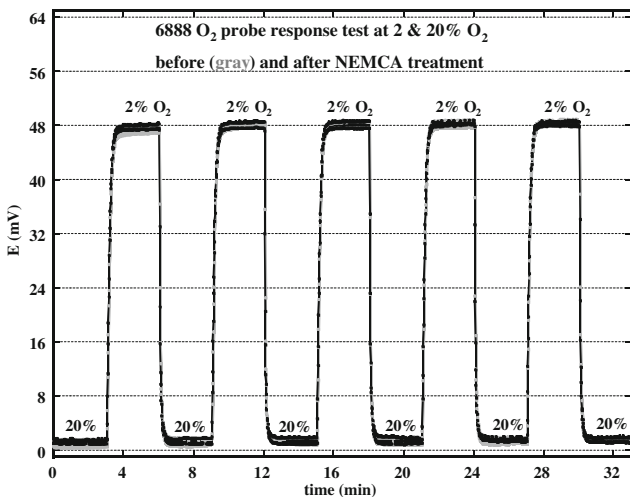


Fig. 10 NEMCA effect on “aged” O₂-sensor response to 2 and 20 % O₂ at 736 °C

sensors. Most likely it was attributed to the smooth electrochemical reaction path on the triple gas/electrode/electrolyte boundary after the NEMCA treatment “cleaning the electrode reaction zone” from the incomplete combustion products like carbon or carbon monoxide. The sensor reproducibility was highly improved from the initial ± 0.05 % O₂ to ± 0.01 % O₂ at ~ 2.0 % O₂ concentration after NEMCA treatment (Fig. 14). Finally “aged” O₂-sensor calibration slope value and

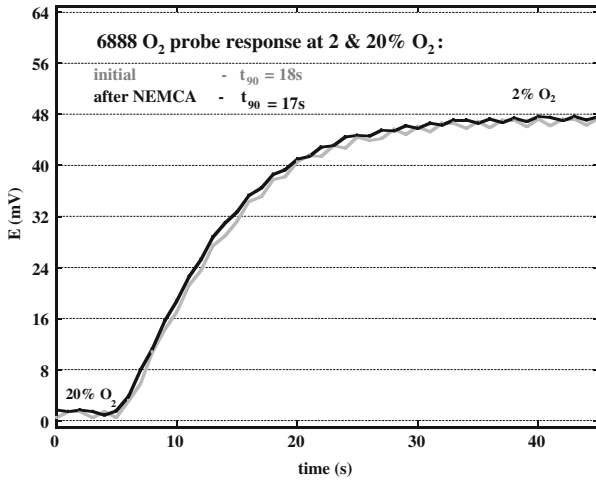


Fig. 11 NEMCA effect on new O₂-sensor response to 2 % O₂ at 736 °C

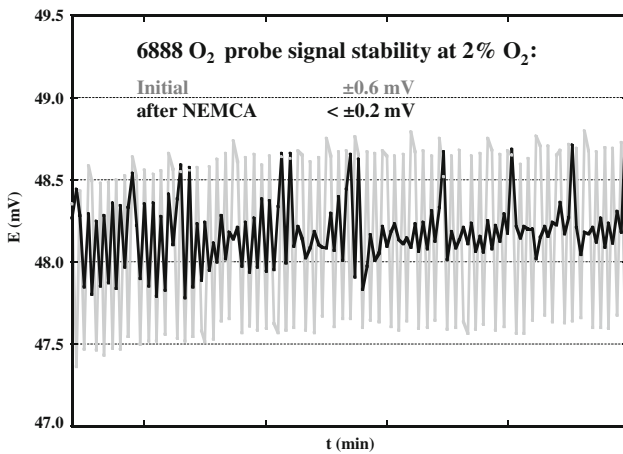


Fig. 12 NEMCA effect on the “aged” O₂-sensor mV raw signal noise at 2 % O₂

reproducibility were highly improved on the sensors exposed for years to the combustion environment (Fig. 15).

Further investigations on the NEMCA effect stability in the long term and this effect reliability on the zirconia oxygen sensors operating in severe combustion environment would be required to define the NEMCA application limits and perspective.

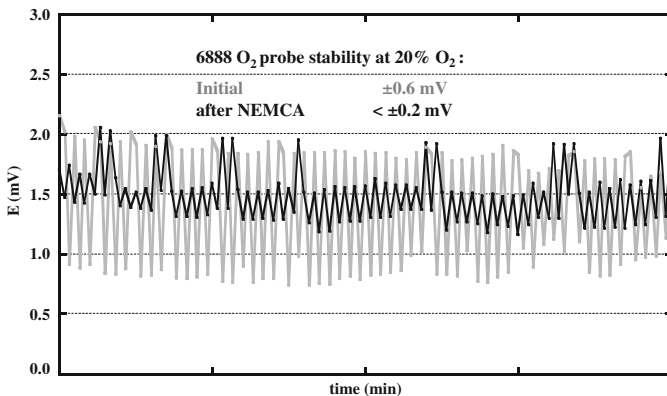


Fig. 13 NEMCA effect on the “aged” O₂-sensor mV raw signal noise at 20 % O₂

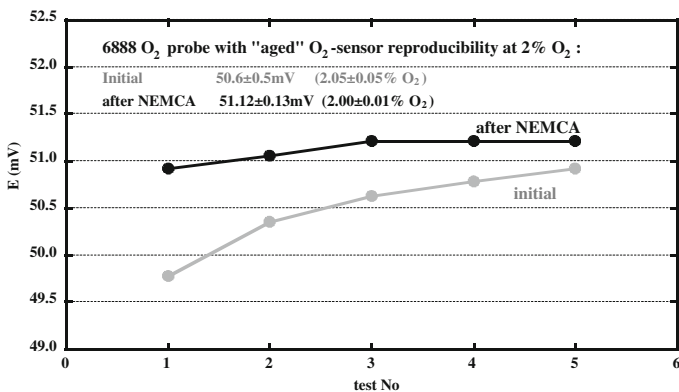


Fig. 14 NEMCA effect on the “aged” O₂-sensor reproducibility at 2 % O₂

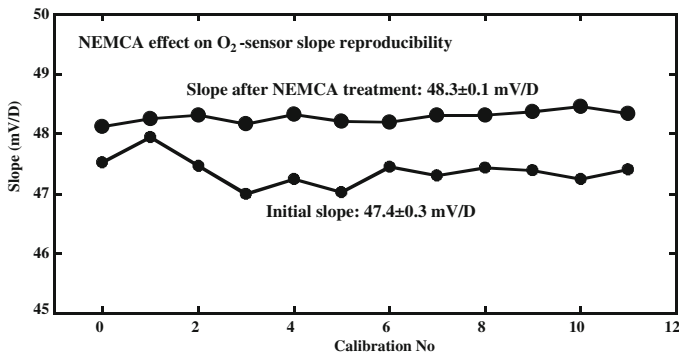


Fig. 15 NEMCA effect on the “aged” O₂-sensor slope reproducibility

4 Conclusion

Non-Faradaic Electrochemical Modification of Catalytic Activity (NEMCA) effect known for the increasing the catalytic activity/selectivity of the gas exposed electrodes was for the first time investigated on the potentiometric zirconia oxygen sensors. Electrochemical promotion on O₂-sensors with Pt-cermet electrodes was significant especially on the sensors aged in the field bringing up to 5 times sensor impedance reduction. The NEMCA effect was also notable on O₂-sensor raw signal reducing 90 % response time by 5–10 % and up to 3 times the signal noise of the aged oxygen sensors. Stability test on the NEMCA activated O₂-sensors was showing just a minor impedance increase after 2 weeks with the accelerated impedance degradation on the aged sensors.

Acknowledgment The authors would like to thank Rosemount Analytical Inc. for the research program support and Professor Costantinos G. Vayenas as well as Dr. Susanne Brosda for the sharing numerous NEMCA publications and NEMCA/EPOC/ICP knowledge.

References

1. H. Peters, H-H. Möbius, Procedure for the gas analysis at elevated temperatures using galvanic solid electrolyte elements, DD Patent 21673, Aug 1961
2. J. Weissbart, R. Ruka, Oxygen gauge. Rev. Sci. Instrum. **32**(5), 593–595 (1961)
3. H.-H. Möbius, Solid state electrochemical potentiometric sensors for gas analysis, in *Sensors a Comprehensive survey*, vol. 3, ed. by W. Göpel, J. Hesse, J.N. Zemel (VCH, New York, 1992), pp. 1105–1154
4. W.C. Maskell, Progress in the development of zirconia gas sensors. Solid State Ionics **134**(1–2), 43–50 (2000)
5. S. Zhuiykov, *Electrochemistry of zirconia gas sensors* (CRC Press, Boca Raton, 2008)
6. P. Shuk, Process zirconia oxygen analyzer: state of art. Tech. Mess. **77**(1), 19–23 (2010)
7. C.G. Vayenas, S. Bebelis, S. Neophytides, Non-Faradaic electrochemical modification of catalytic activity. J. Phys. Chem. **92**(18), 5083–5085 (1988)
8. C.G. Vayenas, S. Bebelis, S. Ladas, Dependence of catalytic rates on catalyst work function. Nature **343**(6259), 625–627 (1990)
9. Y. Jiang, I.V. Yentekakis, C.G. Vayenas, Methane to ethylene with 85 percent yield in a gas recycle electrocatalytic reactor-separator. Science **264**(5165), 1563–1566 (1994)
10. C.G. Vayenas, S.I. Bebelis, Electrocatalysis, catalysis and electrochemical promotion in solid electrolyte cells, in *Oxygen Ion and Mixed Conductors and their Technological Applications*, ed. by H.L. Tuller, J. Schoonman, I. Riess (Kluwer Academic, Dordrecht, 2000), pp. 123–164
11. C.G. Vayenas, S. Bebelis, C. Pliangos, S. Brosda, D. Tsiplakides, in *Electrochemical Activation of Catalysi. promotion. electrochemical promotion, and metal-support interactions*, (Kluwer Academic, New York, 2001)
12. C.G. Vayenas, A. Katsaounis, S. Brosda, A. Hammad, Electrochemical modification of catalytic activity, in *Handbook of Heterogeneous Catalysis*, vol. 8, ed. by G. Ertl, H. Knözinger, F. Schüth, J. Weitkamp (Wiley-VCH Publishers, Weinheim, 2007), pp. 1905–1935
13. A. Katsaounis, Electrochemical promotion of catalysis (EPOC) perspectives for application to gas emissions treatment. Glob. NEST **10**(2), 226–236 (2008)

14. C.G. Vayenas, C.G. Koutsodontis, Non-Faradaic electrochemical activation of catalysis. *J. Chem. Phys.* **128**(18), 1–13, 182506 (2008)
15. C.G. Vayenas, Bridging electrochemistry and heterogeneous catalysis. *J. Solid State Electrochem.* **15**(7–8), 1425–1435 (2011)
16. P. Shuk, E. Bailey, U. Guth, Zirconia oxygen sensor for the process application: state-of-the-art. *Sens. Transducers J.* **90**(4), 174–184 (2008)
17. K. Kinoshita, *Electrochemical oxygen technology* (Wiley, New York, 1992)

A New Scheme for Determination of Respiration Rate in Human Being Using MEMS Based Capacitive Pressure Sensor

Madhurima Chattopadhyay and Deborshi Chakraborty

Abstract Monitoring respiration rate in everyday life enables an early detection of the diseases and disorders that can suddenly appear as a life threatening episode. Respiratory Rate (RR) is defined as the number of breaths per minute and is a very important physiological parameter to be monitored in people both in healthy and critical condition, as it gives meaningful information regarding their respiratory system performance as well as condition. A typical RR for adult human being at rest is 12–20 and its corresponding frequency is 0.2 Hz approximately. During recovery from surgical anesthesia, a μ -opioid agonists used for pain control can slow down RR leading to bradypnea ($RR < 12$) or even apnea (cessation of respiration for an indeterminate period), while airway obstructions like asthma, emphysema and COPD. In all these cases long term monitoring can extend the capabilities of healthcare providers but only constraint lies with the performance reliability along with the economic barrier. In this chapter, a MEMS based capacitive nasal sensor system for measuring Respiration Rate (RR) of human being is developed. In order to develop such system, two identical arrays of diaphragms based MEMS capacitive nasal sensors are designed and virtually fabricated. A proposed schematic of the system consists of signal conditioning circuitry alongwith the sensors, is described here. In this proposed scheme, the two identical sensor arrays are mounted below Right Nostril (RN) and Left Nostril (LN), in such a way that the nasal airflow during inspiration and expiration impinge on the sensor diaphragms. Due to nasal airflow, the designed square diaphragm of the sensor is being deflected and thus induces a corresponding change in the original capacitance value. This change in capacitance value is be detected by a CMOS based clocked capacitance-to-voltage converter. The capacitive type MEMS sensors often suffer from stray and standing capacitive effect, in order to nullify this precision interface with MEMS capacitive pressure sensor, followed by an amplifier and a differential cyclic ADC is implemented to digitize the pressure information. The designed MEMS based capacitive nasal sensors is capable of identifying normal RR

M. Chattopadhyay (✉) · D. Chakraborty
Heritage Institute of Technology, Kolkata, India
e-mail: madhurima02@gmail.com

(18.5 ± 1.5 bpm) of human being. The design of sensors and its characteristics analysis are performed on a FEA/BEA based virtual simulation platform.

1 Introduction

Respiration monitoring is vital for diagnosis of many diseases related to the functioning of the heart and lungs. As found in statistical study that nearly 5 % of the total human population suffers from respiration illnesses such as Sleep Apnea Syndrome (SAS) and about 30 % of people in their seventies are reported to have a respiratory diseases in industrially developed countries, hence effective methods for monitoring respiration are essential. According to the World Health Organization (WHO), the top five respiratory diseases account for 17.4 % of all deaths and 13.3 % of all Disability-Adjusted Life Years (DALYs) [1]. Lower respiratory tract infections, Chronic Obstructive Pulmonary Disease (COPD), tuberculosis and lung cancer are each among the 10 leading causes of death worldwide. As respiration rate is a crucial sign, it is essential to record RR regularly in both emergency and clinical situations. In a clinical setting, respiration monitoring is useful for detecting pulmonary disease, heart failure, anxiety disorders, and sleep disorders. Unfortunately, reliable methods of respiration monitoring hardly exist for home and ambulatory monitoring [2]. Some conditions, like chronic obstructive pulmonary disorders, are difficult to diagnose acutely in the clinic so a reliable device that could monitor a person chronically at home or in ambulatory situations would enhance the capabilities of medicine to diagnose and monitor disease.

Since respiration is one of the most important signals among vital signs [3], there have been many studies on measuring and monitoring respiration signals while minimizing discomfort [4, 5], including noncontact sensing methods for measuring respiration. Noncontact sensing method is valuable because it neither confines nor inhibits the subject with cables, and it does not cause discomfort or skin irritation from electrodes or straps. This makes the sensors more attractive for long-term continuous respiration monitoring. Since the patient does not feel the measurement, the patient is less likely to alter his/her respiration during measurement, as commonly occurs during face-mask respiration measurements. Additionally, there are no surface loading effects that might reduce the accuracy of the measurement. The RR is defined as the number of breaths per minute and the typical RR at resting is 12 of a healthy person with a frequency of 0.2 Hz [6]. It has been noticed very often that there is a sudden degradation in RR leading to bradypnea ($RR < 12$) while recovering from surgical anesthesia due to μ -opioid agonists used for pain control. Similar may happen in case of apnea (cessation of respiration for an indeterminate period) [7]. In contrast, the increase in RR causing tachypnea ($RR > 30$) which may arise as a result of airway obstructions like asthma, emphysema and COPD [8]. Thus to diagnose different kinds of respiratory diseases, RR measurement becomes clinically very important. The methods commonly used

for measuring RR are visual observation, impedance pneumography, acoustic sensing, fiber optic sensing, Respiratory Inductance Plethysmograph (RIP) and Nasal Prongs (NP) [9]. Inductive plethysmography uses an inductive sensor that is a wire configured in a sinusoidal arrangement that wraps completely around the circumference of the chest or abdomen. This sinusoidal patterned inductive sensor measures changes of inductance in the wire, where these inductance changes are directly related to the shape changes of the sensor and torso caused by respiration. Piezoresistive sensors are usually conductive elastic coatings [10] or knitted conductive yarn that changes their resistance when stretched. A piezoresistive sensor is usually made in the form of a rectangular strip whose longer dimensions run laterally across the chest or abdomen [11]. The final sensing method commonly fabricated and used for respiration monitoring is the piezoelectric sensor. The piezoelectric sensor, for example, is found in the Pneumotrace II belt and is made by UFI [12]. This sensor generates a small voltage when the belt stretches due to changes in circumference of the chest or abdomen. The most popular methods that are applied to home and ambulatory monitoring utilize a belt or sensor integrated into a garment. Now, whereas respiration belts are commercially available, garments are most commonly found only in a prototype form and have yet to find widespread commercialization. However, due to very sensitive patients' movements and high cost, these methods find limited use in the clinical settings [13]. Earlier, Siivola [14], Choi and Jiang [15] used Poly Vinyl Di Fluoride (PVDF) to record respiration and cardiac action in human beings. In 2008, J.H. Oum et al. reported a non contact type capacitive sensor for determination of the heart rate and respiration rate [16]. Different materials have been studied as a diaphragm material for such capacitive sensors and it has been reported that Polysilicon is working efficiently as diaphragm material for a wide variety of applications [17]

In our present study, MEMS based capacitive respiration rate sensor is designed in FEA/BEA based virtual design simulation platform. The characteristics analysis of the designed sensor is also computed in the same simulation software. The characteristics plots obtained from the sensor are compared with 'Gold standard' RIP and NP methods. The schematic diagram of a Positive Airway (PA) respirator using the developed MEMS capacitive pressure is shown by Fig. 1.

2 Motivation

Respiration monitoring is among the most important elements of assessing the physiological state. Given that nearly 5 % of the total human population suffers from respiration illnesses such as Sleep Apnea Syndrome (SAS) and about 30 % of people in their seventies are reported to have a respiration disease in industrially developed countries [18, 19], effective methods for monitoring respiration is essential. Lower respiratory tract infections, Chronic Obstructive Pulmonary Disease (COPD), tuberculosis and lung cancer are each among the 10 leading causes of death worldwide. Respiration rates are recorded regularly in both

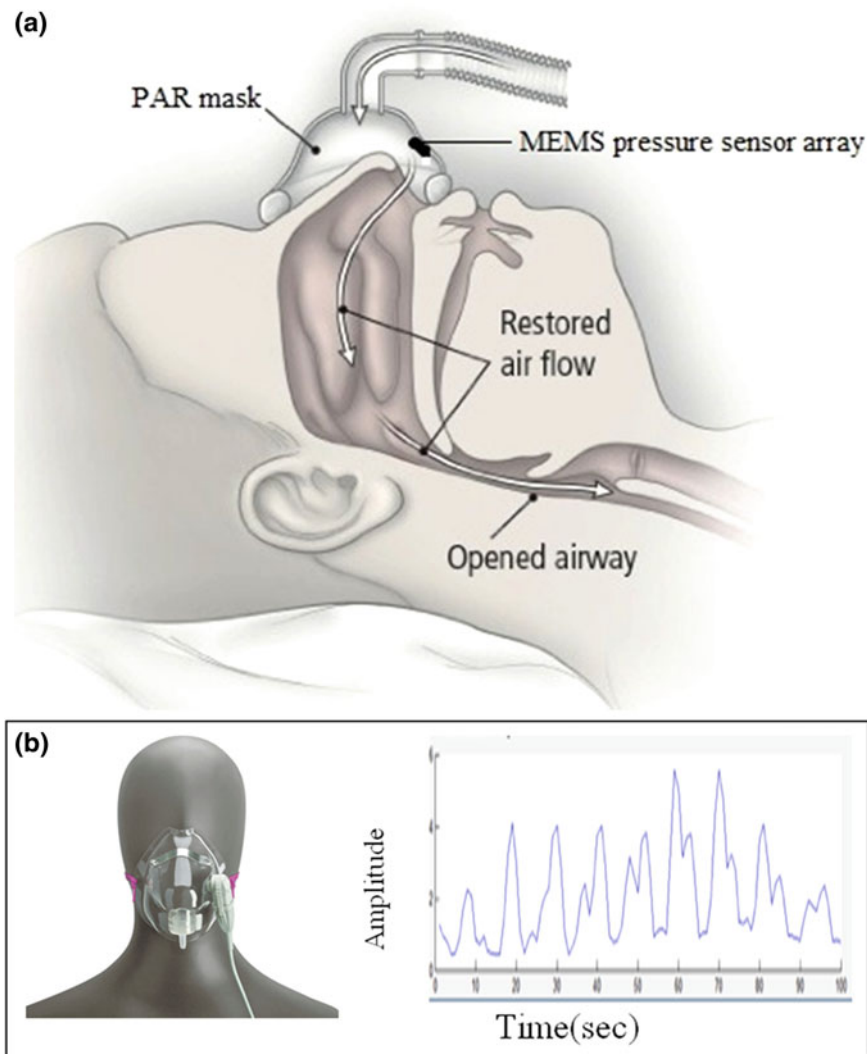


Fig. 1 a and b Schematic of the process for the respiration rate (RR) measurement

emergency and clinical situations because several levels of physiological condition can be obtained by measuring respiration rates. The first and foremost level is to assess whether the subject is breathing or not. Second, respiratory rate and pattern are indicators of respiratory physiology and an irregular pulse rate can indicate cardiac abnormality. Third, the increased rate of due to apnea events indicates the level of tissue hypoxia associated with sleep apnea [21]. Fourth, changes in respiratory rates can indicate the sympathetic and parasympathetic responses to trauma [22]. The shapes of the respiration signatures could potentially be used as an

additional diagnostic tool, including correlating the amount of motion with respiratory effort in the area of abdomen and chest. Since a respiration is one of the most important signals among vital signs [23], there have been many studies on measuring and monitoring respiration signals while minimizing discomfort [24], including noncontact sensing methods for measuring respiration. Noncontact sensing method is advantageous because it neither confines nor inhibits the subject with cables, and it does not cause discomfort or skin irritation from electrodes or straps [20]. This makes the sensors more attractive for long-term continuous respiration monitoring. Since the patient does not feel the measurement, the patient is less likely to alter his/her respiration during measurement, as commonly occurs during face-mask respiration measurements. Additionally, there are no surface loading effects that might reduce the accuracy of the measurement. There have been several studies on noncontact respiration measurement methods through the observation of body surface movement changes with respiration. For example, T. Kondo et al. has employed a laser sensor to measure anteroposterior chest wall motion during respiration [25]. The laser monitor measures the distance between the chest wall and the sensor, and obtains a respiratory waveform by plotting the change in distance over time. In addition, an adaptation of the Doppler radar is used to measure respiration, where the change in linear motion on the subject's chest is directed by the RADAR [26]. As found in literature a study performed by Hirooki Aoki et al. [27] on application of near-infrared multiple slit-light pattern to measure respiration. In this method, motion-image analysis is performed by observing the shift length of multiple-slit pattern light projected on the thoracic abdominal part of sleeping subject. These examples of noncontact respiratory measurement do not require resistance to respiration nor tactile stimuli, ensuring a non invasive means of measuring respiration that does not alter the respiratory pattern. Thus keeping this in view we have developed a non contact MEMS based respiration rate sensor for detection of the normal and abnormal breathing rates in human.

3 Sensor Design

Figure 2 illustrates the innovative design of the square diaphragm based MEMS capacitive pressure sensor for determination of the respiration rate (RR) [2]. As shown in the Fig. 2, this capacitive pressure sensor consists of a pair of plates (one fixed plate and one moving plate). The diaphragm, the moving plate and the fixed plate are all in square shape to maintain mirror symmetry for the stresses at the edges where the diaphragm is clamped. This fixed plate caps the moving plate inside of a sealed cavity in order to develop a parallel plate capacitor.

As the diaphragm deflects under a pressure load, the moving plate of the capacitor experiences the same amount of deflection from the centre of the diaphragm. Thus a diaphragm deflection is readily converted to a capacitance change. For square diaphragm with a small deflection at any point (x,y) is given by [3]:

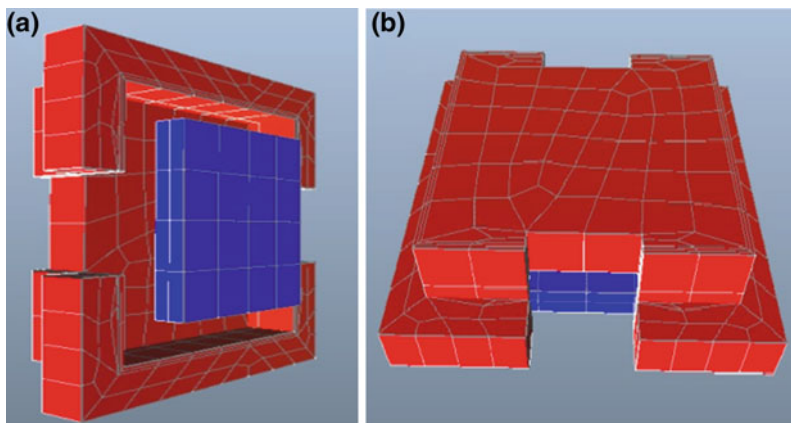


Fig. 2 3D view of the designed respiratory sensor. **a** Top view and **b** Side view

$$w(x, y) = \frac{49Pa^4(x^2 - a^2)(y^2 - a^2)}{2304D} \quad (1)$$

Here, 'a' is the half side length of the diaphragm and maximum deflection occurs at the centre ($x = 0, y = 0$) is given by

$$w_o = \frac{0.216Pa^4}{Eh^3} \quad (2)$$

and the capacitance is given as:

$$C = \iint \frac{\epsilon dx dy}{d - w(x, y)} \quad (3)$$

Here, in this present simulation platform Eq. (3) is solved numerically.

For a small deflection, the analytical deflection of the capacitance can be derived by expanding the denominator of Eq. (3) in the Taylor's series expansion as given below:

$$C = \frac{\epsilon}{d} \iint \left\{ 1 + \frac{w(x, y)}{d} + \frac{w^2(x, y)}{2d^2} \right\} dx dy \quad (4)$$

Since it is a small deflection case the higher order terms in the expression can be neglected and the Eq. (4) reduces to:

$$C = \frac{\epsilon}{d} \iint \left\{ 1 + \frac{w(x, y)}{d} \right\} dx dy \quad (5)$$

Integrating Eq. (5) and using the value of $w(x,y)$ from Eq. (1) we get,

$$C = C_0 \left(1 + \frac{12.5Pa^4}{2025dD} \right) \quad (6)$$

Here, in this simulation platform Eq. (6) is solved numerically.

Where, C_0 is the zero pressure capacitance and is given by,

$$C_0 = \frac{\epsilon 4a^2}{d} \quad (7)$$

The term sensitivity of a capacitive type pressure sensor can be defined as,

$$S_A = \frac{dC}{dP} \quad (8)$$

Thus, sensitivity is obtained in this work by differentiating Eq. (6) w.r.t. pressure (P) and can be expressed as

$$S_A = \frac{49\epsilon a^6}{2025d^2D} \quad (9)$$

4 Virtual Sensor Fabrication

The virtual fabrication steps for the designed sensor in FEA/BEA based virtual simulation software is provided by twenty different steps below in Fig. 3.

In Step 1, we have chosen Si Czochralski (100) as a substrate material with thickness of 10 μm as shown in Fig. 3. A thin layer of SiO_2 is deposited over the substrate in Step 2. The thickness of this conformal layer is of 1000 nm. For lithography purpose, a photo resist (PR-AZ5214) is deposited via spin coating technique having thickness of 300 nm on top of SiO_2 in Step 3.

The corresponding mask required for this UV Lithography is shown in Fig. 4 as Layer 1 (Step 4). Now partial Etching of SiO_2 layer is carried out with Wet BOE in Step 5. The deposited photoresist PR-AZ5214 is removed using wet etching (Step 6).

In order to form the fixed plate of the sensor, P Implant (P-ion) is doped with a junction depth of 1000 nm Step 7). Henceforth wet etching is carried out for removing SiO_2 (Fig. 3 (Step 8)).

Here we have chosen PSG (Phosphosilicate Glass) as a sacrificial layer to form the desired space between the two plates of the capacitor. Thus a thin layer of PSG (Phosphosilicate Glass) is deposited on the fixed plate of the sensor capacitor via LPCVD (Fig. 3 (Step 9)). Once the sacrificial layer thickness 2000 nm (Conformal) is formed, the photo resist (PR-AZ5214) is again deposited (Fig. 3 (Step 10)).

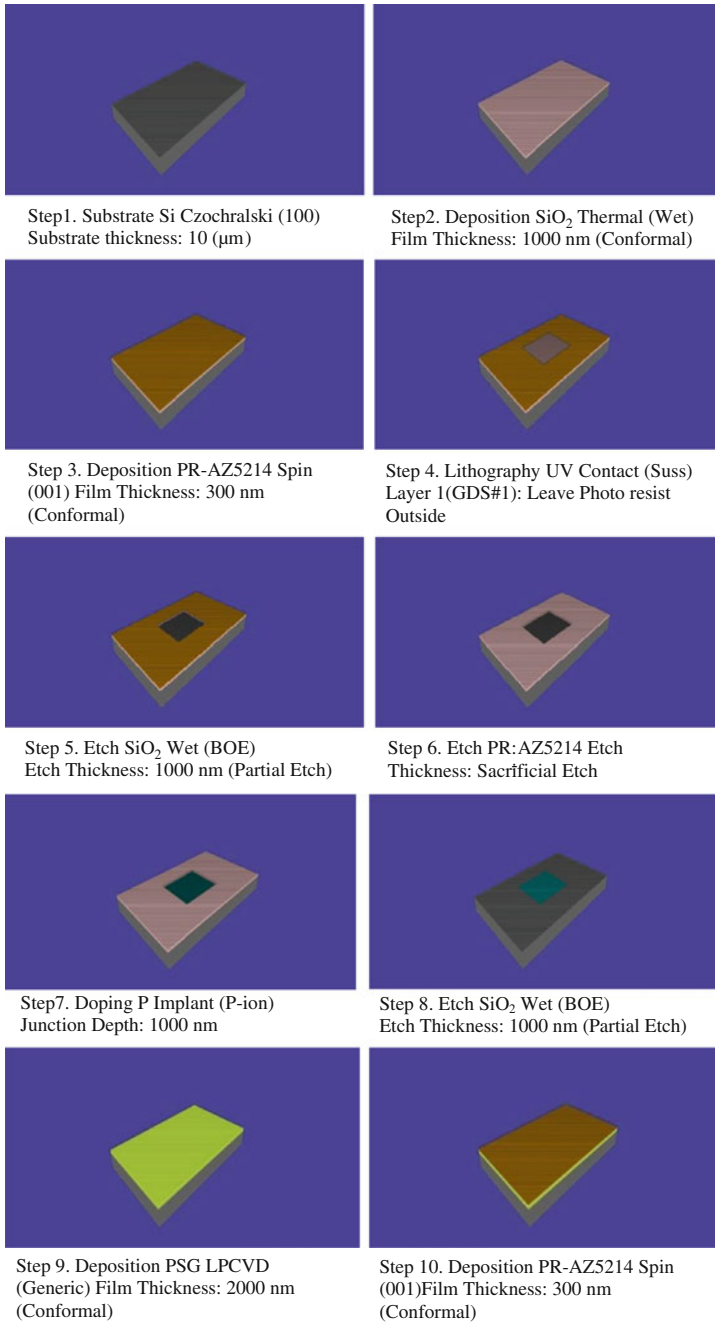


Fig. 3 Views of the virtually fabricated sensor with the above mentioned steps

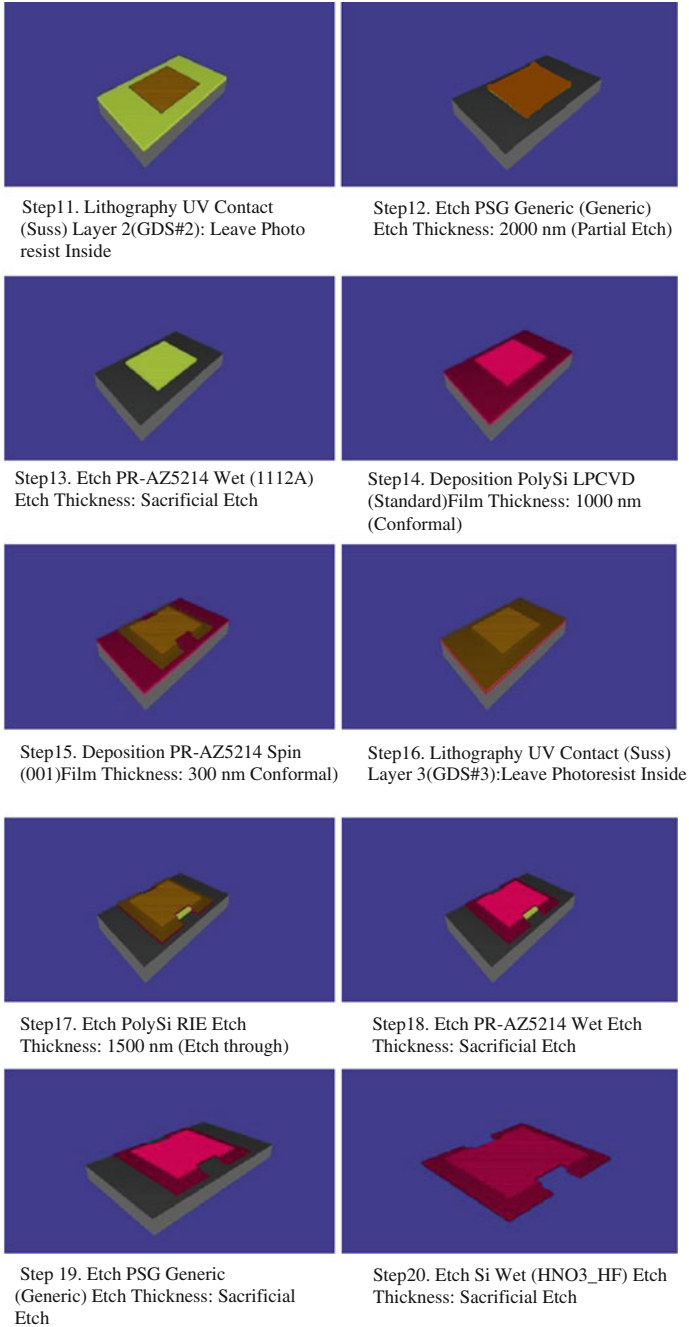


Fig. 3 (continued)

Subsequently, to generate the sensor's upper movable plate, lithography with UV Contact is performed with Mask Layer 2 (Fig. 3 (Step 11)). As we have applied negative resist, the side walls are removed leaving behind the middle portion where the mask is placed.

Now PolySi is deposited by LPCVD of thickness 1000 nm (Conformal) in order to form upper movable diaphragm (Fig. 3 (Step 14)). Moreover to achieve the desired shape, Mask Layer 3 is placed over the layer of PolySi and UV Lithography is performed (Fig. 3 (Step 16)). Reactive Ion Etching (RIE) using C_{12} is applied to remove the extra deposited layers of PolySi from the side surfaces (Fig. 3 (Step 17)). Subsequently, photoresist PR-AZ5214 is removed by Wet Etching (Fig. 3 (Step 18)).

The required gapping between the two plates is hence achieved by etching out the PSG layer. Simultaneously, the photo resist is also removed as etch PSG Generic (Fig. 3 (Step 19)).

Finally, sacrificial Si is removed through wet (HNO_3_HF) Etching (Fig. 3 (Step 20)). The designed mask layers for virtual fabrication of the sensor are shown by Figs. 4 and 5. Figure 5 shows the detail mask layout for the sensors that is to be printed during the real time fabrication of the sensor array. It consists of 1000 sensors connected in parallel so to obtain an enhanced output of the total capacitance in the nanofarad order.

5 Measurement Circuit

The measurement circuit designed for sensing a change in capacitance is shown in Fig. 6, which is clocked by two signals presented as clock1 and clock2 by Fig. 7.

The operation begins as clock1 goes high and switches Q_1 ON, thus allowing the reference capacitor (C_{ref}) to charge by the power supply. The charging current passes through the transistor Q_3 which is mirrored in Q_2 this drives the output buffer Q_5 . The voltage across this reference capacitor appears across the sensor

Fig. 4 Design of the mask layers in the simulation platform

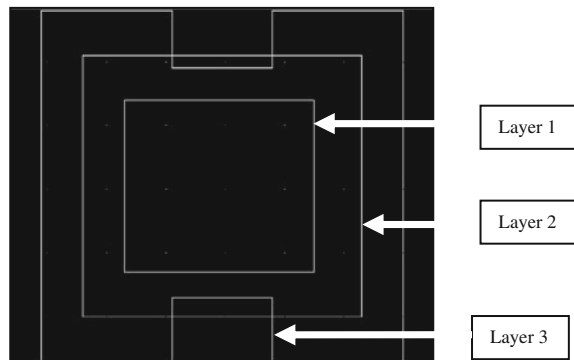


Fig. 5 Design layout of the mask for sensor array fabrication

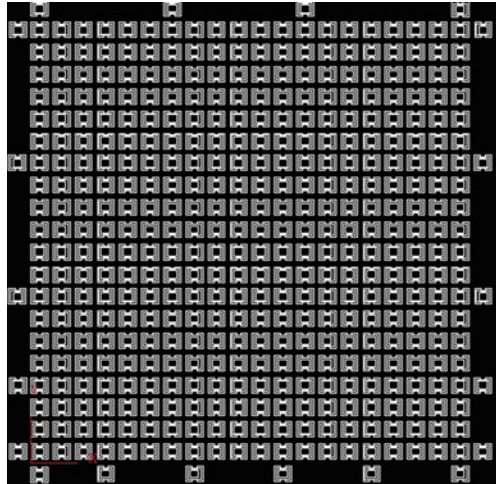


Fig. 6 Capacitance measurement circuit

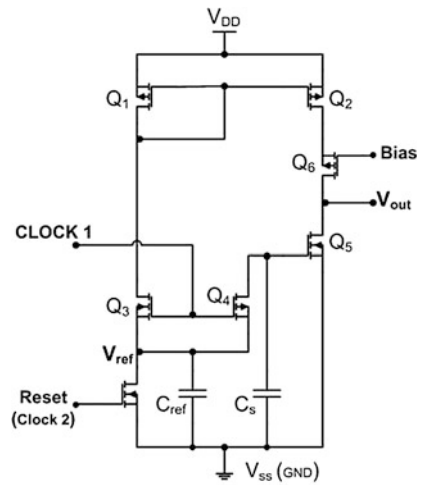


Fig. 7 Clock scheme for the measurement circuit

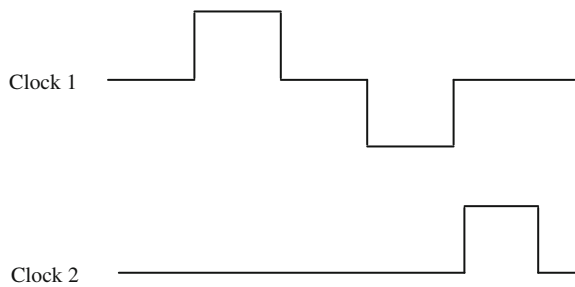


Fig. 8 Analogy to eliminate stray capacitance

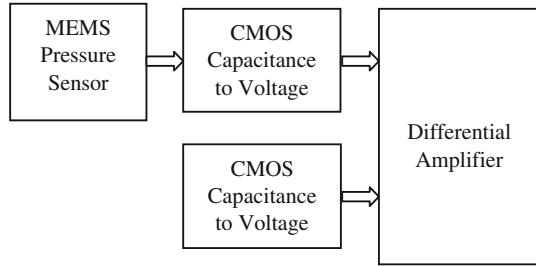
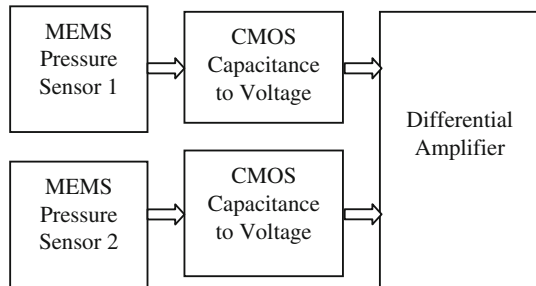


Fig. 9 Analogy to eliminate standing capacitance



capacitance and its associated strays when clock1 goes low. The circuit is reset by triggering Q_7 , when clock2 goes high.

To eliminate the effect of stray capacitances, an identical second, circuit is employed (Fig. 8). Which circuit is kept not connected to the MEMS pressure sensor, and thus the output of the circuit is proportional only to the stray capacitance associated with the reference capacitor and the along associated CMOS transistors. The outputs from both the circuits are subtracted using a differential amplifier.

If both circuits are identical and are well matched then the stray capacitances should be identical, and are eliminated by the differential amplifier leaving an output which only comprises of the sensor capacitance. This configuration is shown in Fig. 9.

Another, potentially more useful configuration is to connect a sensor to both of the circuits connected to the differential amplifier [4]. In this case, not only is the effect of stray capacitance subtracted at the output, but also the standing sensor capacitance. This configuration is beneficial as it allows the circuit gain to be increased thus allowing small capacitance changes to be measured more accurately. The differential approach is also beneficial for eliminating temperature effects [5].

6 Circuit Analysis

A simplified analysis of the circuit shown in Fig. 6 can be carried out using circuit shown in Fig. 10.

The circuit shown in Fig. 10 is valid if transistor Q_1 has minimum impedance and Q_5 has very large impedance [6].

The current through the CMOS transistor is given by Eq. 10 if the channel modulation effect is neglected.

$$I_1 = \frac{1}{2} \mu_n C_{ox} \left(\frac{W}{L} \right)_1 (V_{DD} - V_t)^2 \tag{10}$$

where μ_n is the mobility of the charge carriers in the channel, C_{ox} is the gate capacitance per unit area and W/L are the dimensions of the gate [28].

The current flowing through Q_1 charges the reference capacitor C_{ref} . The relation between charging current I_1 to the potential V_{ref} across the capacitor is given by Eqs. 11 and 12.

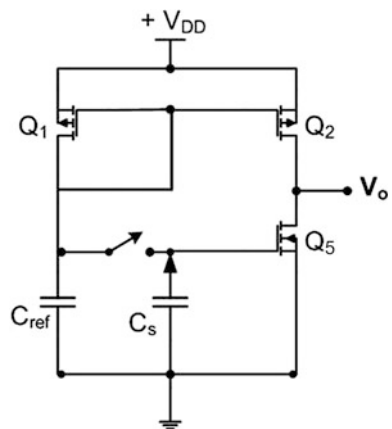
$$V_{ref} = \frac{1}{C_{ref}} \int_0^t I_1 dt \tag{11}$$

$$V_{ref} = \frac{1}{2C_{ref}} \mu_n C_{ox} \left(\frac{W}{L} \right)_1 (V_{DD} - V_t)^2 t \tag{12}$$

The total amount of charge stored in the reference capacitor is given by Eq. 13

$$Q_{ref} = \frac{1}{2} \mu_n C_{ox} \left(\frac{W}{L} \right)_1 (V_{DD} - V_t)^2 t \tag{13}$$

Fig. 10 Simplified capacitance to voltage converter



The charge Q_{ref} stored in reference capacitor is transferred to the capacitive sensor C_s when the CMOS transistor Q_4 (Fig. 6) is turned on by negative going clock1. The final output voltage is given by Eq. 14.

$$V_o = \frac{1}{2C_s} \mu_n C_{\text{ox}} \left(\frac{W}{L} \right)_1 (V_{\text{DD}} - V_t)^2 t \quad (14)$$

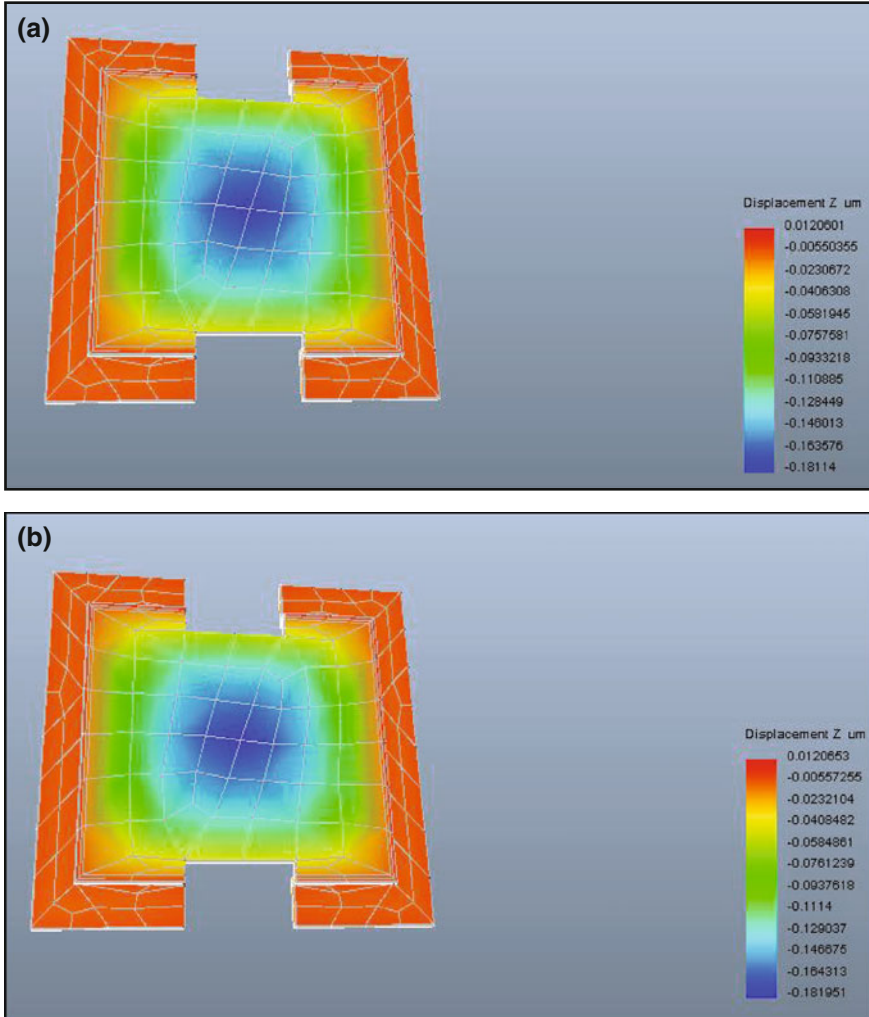


Fig. 11 Simulated view of the diaphragm displacement with applied pressure of **a** 0.3 kPa. **b** 2 kPa

7 Results and Discussions

The pressure range during exhalation for a healthy human being varies from 0.3 to 2 kPa [8]. Therefore pressure range mentioned before is applied on the diaphragm of the designed sensor. Corresponding deflection of the diaphragm for a minimum and maximum pressure of that specified pressure range if given in Fig. 11a, b and its corresponding plot for the whole pressure range is shown in Fig. 12.

The change in capacitance (μF) with applied pressure of 0.3–2 kPa for a potential of 1 Volt applied between the plates is shown in Fig. 13. It gives a linear response for the exhaled pressure range. In order to detect the exhalation rate, the corresponding movement of the diaphragm due to the applied pressure, induces a change in the capacitance between the plates with respect to time. As a result, the dynamic response of the designed sensor is obtained for the range of the exhaled pressure which is represented in Fig. 14. It is observed that the pattern obtained

Fig. 12 Plot of deflection of the diaphragm corresponding to the pressure (0.2–2.2 kPa)

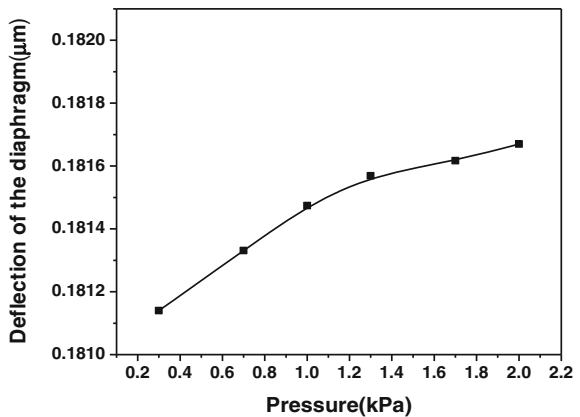


Fig. 13 Plot of change in capacitance (μF) versus pressure (kPa)

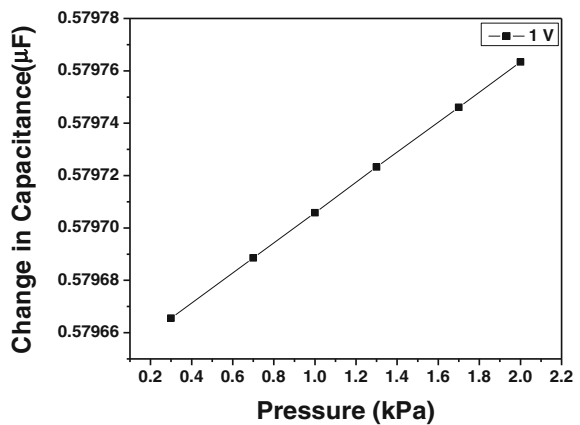
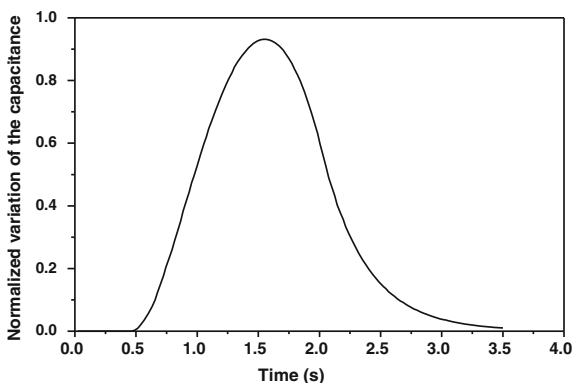


Fig. 14 Dynamic response of the diaphragm



from the response validate with the normal breathing rate (18.5 ± 1.5 bpm) of the human being [9].

8 Conclusion

In this present study we have restricted our work to simulation only where we have verified the simulation studies with the actual exhaled pressure. During verification, the nature of the dynamic response is showing a confirmation with the actual nature of the normal breathing pattern, a more detailed study on different RR (number of breaths per minute (bpm)) corresponding to tachypnea (34.5 ± 4 bpm), and bradypnea (10.5 ± 2.2 bpm) will be performed. Once the simulation study will be satisfied, a real time implementation of this system will be developed with required associated signal conditioning circuitry. After real time fabrication of MEMS sensor

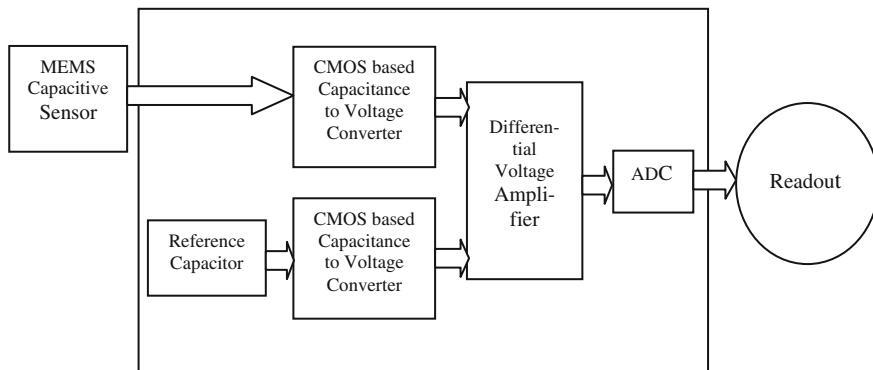


Fig. 15 Block diagram of the electronic system design architecture of the MEMS capacitive type nasal exhalation sensor

array, we will be able to verify the system with different subjects. The main challenge of this work is to nullify the stray and standing capacitance to correct output voltage generated from the change in capacitance due to breathing activity. The detail circuit diagram required for this purpose is also discussed in this chapter.

The Fig. 15 presents overall block diagram of the electronic system design architecture for the signal processing of the sensor. A fully differential architecture is chosen for the interface electronics to suppress common-mode disturbances. A CMOS transistor based correlated-double-sampling (CDS) capacitance-to-voltage converter is designed for a precision interface with a MEMS capacitive pressure sensor, followed by an amplifier and a differential cyclic ADC to digitize the pressure information.

The obtained output in the form of voltage is calibrated with the respiration rate pressure and is stored for the further analysis.

Acknowledgments Author Madurima Chattopadhyay likes to acknowledge Department of Science and Technology, Govt. of India for financial support from the First Track Young Scientist scheme to carry out the research work. The authors also acknowledge Heritage Institute of Technology for providing the lab infrastructure and Mr Debjyoti Chowdhury for experimenting the CMOS measurement circuitry.

References

1. J. Milic-Emili, Recent advances in clinical assessment of control of breathing. *Lung* **160**, 1–17 (1982)
2. D. Moffett, S. Moffett, C. Schauf, *Human Physiology*, 2nd edn, Ch. 13 and 16. (Wm. C. Brown Publishers, Dubuque, 1993)
3. I. Prkic et al., Pontine μ -opioid receptors mediate bradypnea caused by intravenous remifentanyl infusions at clinically relevant concentrations in dogs. *J. Neurophysiol.* **108**, 2430–2441 (2012)
4. S.S. Weigt, M. Abrazado, E.C. Kleerup, D.P. Tashkin, C.B. Cooper, Time course and degree of hyperinflation with metronomepaced tachypnea in COPD patients. *COPD* **5**(5), 298–304 (2008). doi: [10.1080/15412550802363428](https://doi.org/10.1080/15412550802363428)
5. M. Folke, L. Cernerud, M. Ekstrom, B. Hok, Critical review of non-invasive respiratory monitoring in medical care. *Med. Biol. Eng. Comput.* **41**, 377–383 (2003)
6. R. Farre, J.M. Montserrat, D. Navajas, Noninvasive monitoring of respiratory mechanics during sleep. *Eur. Respir. J.* **24**, 1052–1060 (2004)
7. H. Kawai, The piezoelectricity of polyvinylidene fluoride. *J. Appl. Phys.* **8**, 73–77 (1969)
8. J. Siivola, New non-invasive piezoelectric transducer for recording of respiration, heart rate and body movements. *Med. Bio. Eng. Comp.* **27**, 423–424 (1989)
9. S. Choi, Z. Jiang, A novel wearable sensor device with conductive fabric and PVDF film for monitoring cardiorespiratory signals. *Sens. Actuators A* **128**, 317–326 (2006)
10. J.H. Oum, S.E. Lee, D.-W. Kim, S. Hong, Non-contact heartbeat and respiration detector using capacitive sensor with Colpitts oscillator. *Electron. Lett.* **44**(2) (2008)
11. S.H. Nam, T.G. Yim, C.Y. Ryu, S.C. Shin, J.H. Kang, S. Kim, The preliminary study of unobtrusive respiratory monitoring for e-health, in *Proceedings of IEEE 27th Annual Conference on Engineering and Medical Biology*, Shanghai, China, 1–4 Sep 2005
12. P. Varady, T. Micsik, S. Benedek, Z. Benyó, A novel method for the detection of apnea and hypopnea events in respiration signals. *IEEE Trans. Biomed. Eng.* **49**, 936–942 (2002)

13. M. Coyle, Ambulatory cardiopulmonary data capture, in *Proceedings of 2nd Annual International IEEE-EMBS Conference Microtechnologies in Medicine and Biology*, Madison, WI, May 2002, pp. 297–300
14. World Health Organization, *WHO strategy for prevention and control of chronic respiratory diseases*. www.WHO/MNC/CRA/02.1
15. H. Saito, M. Nishimura, E. Shibuya, H. Makita, I. Tsujino, K. Miyamoto, Y. Kawakami, Tissue hypoxia in sleep apnea syndrome assessed by uric acid and adenosine. *Chest* **122**(5), 1686–1694 (2002)
16. P. Fathizadeh, W.C. Shoemaker, C.C.J. Wo, J. Colombo, Autonomic activity in trauma patients based on variability of heart rate and respiratory rate. *Crit. Care Med.* **32**(6), 1420–1421 (2004)
17. Joanna Briggs Institute, *Vital Sign*, vol. 3, no. 3, 1999
18. T. Kondo, T. Uhlig, P. Pemberton, P.D. Sly, Laser monitoring of chest wall displacement. *Eur. Respir. J.* **10**, 1865–1869 (1997)
19. Y. Xiao, C. Li, J. Lin, A portable noncontact heartbeat and respiration monitoring system using 5-GHz radar. *IEEE Sens. J* **7**(7) (2007)
20. M. Uenoyama, T. Matsui, K. Yamada, S. Suzuki, B. Takase, S. Suzuki, M. Ishihara, M. Kawakami, Non-contact respiratory monitoring system using a ceiling-attached microwave antenna. *Med. Bio. Eng. Comput.* **44**, 835–840 (2006)
21. A.D. Droitcoour, Non-contact measurement of heart and respiration rates with a single-chip microwave Doppler radar. Ph.D. dissertation, Stanford University, Stanford, CA, June 2006
22. H. Aoki, K. Koshiji, Non-contact respiration monitoring method for screening sleep respiratory disturbance using slit light pattern projection, in *IFMBE Proceedings of World Congress Medical Physics and Biomedical Engineering*, vol. 2, Track 06 (2006)
23. S.D. Min, D.J. Yoon, S.W. Yoon, Y.H. Yun, M. Lee, A study on a non-contacting respiration signal monitoring system using Doppler ultrasound. *Med. Bio. Eng. Comput.* **45**(11), 1113–1119 (2007)
24. P. Corbishley, E. Rodríguez-Villegas, Breathing detection: towards a miniaturized, wearable, battery-operated monitoring system. *IEEE Trans. Biomed. Eng.* **55**(1) 2008
25. A. Sharma, Modelling of a pull-in voltage and touch point pressure for MEMS capacitive transducers with square diaphragm. Ph.D. thesis, Kurukshetra University, Kurukshetra, July 2008
26. Roopa et al., Identification of different respiratory rate by a piezo polymer based nasal sensor. *IEEE xplore*. ISBN:978-1-4673-4642-9/13
27. J. Milic-Emili, Recent advances in clinical assessment of control of breathing. *Lung* **160**, 1–17
28. H. Kawai, Charge-Based capacitive sensor array for CMOS-based laboratory-on-chip applications. **8**(4) (2008)

Monitoring of the Lung Fluid Movement and Estimation of Lung Area Using Electrical Impedance Tomography

Deborshi Chakraborty and Madhurima Chattopadhyay

Abstract It is very essential to visualise the internal condition of human body not only for studying the anatomy and physiology, but also for diagnosing a disease. Physicians always try to analyze an organ or body part in order to study its physiological and anatomical status for understanding and/or treating its illness. Thus, it is always requisite to introduce the diagnostic tool called medical imaging. The period of medical imaging started in 1895, when Roentgen discovered the powerful invisible rays called X-rays. Gradually the medical imaging introduced X-Ray CT, Gamma Camera, Positron emission tomography (PET), Single-Photon Emission Computed Tomography (SPECT), Magnetic Resonance Imaging (MRI), and Ultra SonoGraphy (USG). Recently, medical imaging field is more advanced with comparatively newer tomographic imaging modalities like Electrical Impedance Tomography (EIT), Diffuse Optical Tomography (DOT), Optical Coherence Tomography (OCT), and Photoacoustic Tomography (PAT). The EIT has been extensively researched in different fields of science and engineering due to its several advantages. In correlation with the application of the EIT in the medical field, thoracic electrical impedance tomography (EIT) is used to diagnose patients suffering from the acute respiratory distress syndrome (ARDS) for monitoring their conditions ranging from dynamic shifting of body fluids to lung aeration, right at the bedside. Moreover, EIT-derived numeric parameters would help the physician to evaluate the state of the lung of a patient under observation. Thus, here we have performed a Finite Element Method based simulation study for monitoring the condition of lungs and heart of ARDS patients. Therefore, a finite element method (FEM) model of human thorax in three dimensional platform with FEM Multiphysics software is created and tested with new ventilation indices regarding their ability to quantitatively describe structural changes in the lung due to the gravitationally dependent lung

D. Chakraborty

Department of Instrumentation Science, Jadavpur University, Kolkata, India
e-mail: dcphy123@gmail.com

M. Chattopadhyay (✉)

Department of Applied Electronics and Instrumentation Engineering,
Heritage Institute of Technology, Kolkata, India
e-mail: madhurima02@gmail.com

collapse. Additionally, analysis is made to find the electrode pairs capable of separating the lung and heart activity when a particular amount of constant current is injected through them, are also carried out. Finally, a real time EIT system using 16 Ag-AgCl electrodes are developed to get the image of human thorax. The data are collected using the adjacent current injection technique and are plotted using FEM Multiphysics software. The reconstructed FEM images using the forward solver of EIT method shows the approximate area of the thorax (lungs, heart etc.) under observation. This chapter will present a brief overview on application of EIT for monitoring of the lung fluid movement and estimation of lung area in a human being alongwith physical and mathematical aspect with a goal to achieve a system having higher potential to cater medical challenges in lung oriented diseases.

1 Introduction

Physicians have always been interested to visualize interior body parts for treating the illness which insisted them to search for a diagnostic tool called medical imaging. It was the year 1895, when Roentgen discovered X-rays which were unexpectedly found in his laboratory to be useful for visualizing the tissue contrast on photography plates called planar radiography. After that the medical imaging field introduced X-Ray Computed Tomography (X-Ray CT), Gamma Camera, Positron emission tomography (PET), Single-Photon Emission Computed Tomography (SPECT), Magnetic Resonance Imaging (MRI) and Ultra SonoGraphy (USG). In recent age, medical imaging field is enriched with comparatively newer tomographic imaging modalities with electric current and light signals. The computed tomography that uses the electric signal is called Electrical Impedance Tomography (EIT) whereas the other tomographic methods make use of light signal can be found in form of Diffuse Optical Tomography (DOT), Optical Coherence Tomography (OCT), PhotoAcoustic Tomography (PAT), and others [1]. The EIT has been extensively researched in different field of science and engineering for more than three decades due to its several advantages over other tomographic imaging modalities. As a very fast, low-cost, radiation free, nonionizing, non-invasive, portable tomographic imaging technique, EIT is studied and applied over a wide field of applications which are discussed below.

Electrical impedance tomography (EIT) is a medical imaging technique in which an image of the conductivity or permittivity of a body part is inferred from surface electrical measurements. The invention of EIT as a medical imaging technique is usually attributed to John G. Webster and a publication in 1978 [2], although the first practical realisation of a medical EIT system was detailed in 1984 due to the work of David C. Barber and Brian H. Brown [3]. Typically, conducting electrodes are attached on the skin of the subject and small alternating currents are applied to some or all of the electrodes. The resulting electrical potentials are measured, and the process may be repeated for numerous different configurations of applied current.

EIT has the potential to be of clinical value and plays an important role in diagnosis and monitoring of a number of disease conditions, from the detection of breast cancer [4] to monitoring brain function [5] and possibly stroke. However, it has yet to be routinely used as a tool in everyday clinical practice. A technique that does not use ionizing radiation and in principle, is safe and cheap would be of great value. At present, EIT does not have the spatial resolution of other methods like MRI or computer tomography (CT). Its key advantage is its temporal resolution, which is in the order of milliseconds.

It is worth considering the basic physical properties of the human tissues through EIT images. Bio-impedance of a human body produces a great deal of information about the changes of the body during different kinds of activities. For example, the measured impedance is dependent on the amount of water in the body. This kind of information would be very useful in case of athletes. The measurement of bio-impedance is not just limited to tissue water. It includes the characterization and identification of cells based on their impedance, which differs between cells based on the size, orientation, and membrane thickness, among other factors. This phenomenon has been exploited in EIT, where the impedance information is used to form images of the contents of the human body. In EIT, it is possible to inject a range of currents at different frequencies. Different physiological mechanisms can be identified depending on the chosen frequency range, such as the identification of blood volume changes [6, 7].

Tissue consists of cells and membranes that are thin but have a high resistivity as well as electrically behave as small capacitors. The impedance of biological tissues comprises two components, resistance and reactance. The conductivity characteristics of body fluids provide the resistive component, whereas the cell membranes acting as imperfect capacitors, contribute a frequency-dependence and the results are dependent only on liquids outside the cells. The medical use of EIT is based around imaging these impedance properties. The biological tissue impedance measurements can be made over a range of low (20 Hz) to high (1 MHz) frequencies. During measurement using high frequencies, the current passes right through these capacitors, and the result is dependent on tissue and liquids both inside and outside the cells. At low frequencies, current flow impedes the cell membrane and this bio-impedance can therefore, be used to measure volumes, shapes, or the electrical properties of the tissues [8]. Another consideration, which has yet to be fully addressed in EIT, is the anisotropic nature of human tissue. The work described here makes a number of assumptions, one of which is that the object to be reconstructed is isotropic in nature. This assumption is probably incorrect, but as yet there is limited research on this in EIT and related fields.

Though EIT was first developed for nonclinical applications, the first clinical images obtained using EIT were produced by the Sheffield group [9]. They developed a system that used the electrical impedance of various tissues within the human body to produce tomographic image maps of the resistivity distribution. This was termed applied potential tomography (APT). However, the common term that most people use today is EIT. The Sheffield group produced the first images of pulmonary function using a simple back-projection algorithm to reconstruct the

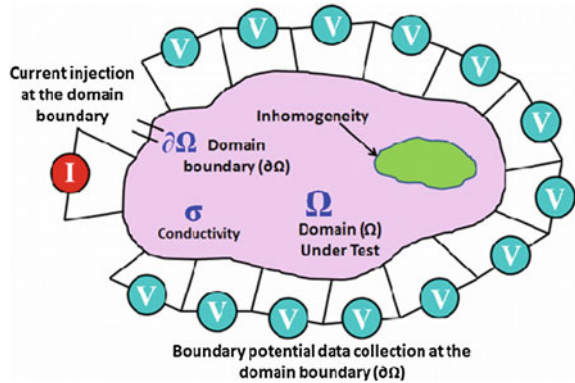
images. There are groups still today those perform clinical studies based on this system. The Sheffield group also produced an algorithm based on the filter back-projection method used in X-ray CT imaging. The Sheffield Algorithm, as it came to be known [9], produces images in a two-dimensional (2D) plane. Later Metherall [10] from the same group produced the first three-dimensional (3D) EIT image that used a sensitivity approach.

It was not until recently that EIT research groups began to use other methods implemented in the Electrical Impedance and Diffuse Optical Reconstruction Software project (EIDORS) set up by Lionheart [11]. However the progress toward EIT being adopted as a clinical tool is slow, as there are many technical problems that need to be addressed.

The key goal of EIT is to produce images that are physiologically useful. EIT is capable of creating two types of images. The first is known as difference imaging, where a change in ratio or percentage represents some physiological parameter like blood volume or cell size. The Sheffield group produced the first lung images using this method. The images are obtained by measuring two data sets at different time or frequencies at the boundary of the object, which is then subtracted and divided by a reference data set. The resultant reconstruction produces the difference images. The second is known as absolute imaging, which produces an image of the absolute conductivity or permittivity. This absolute method of imaging is technically more difficult than the difference method, as the contact impedance of the electrodes cannot be accurately characterized when making clinical measurements. The current is applied using current sources, either a single current source switched between electrodes using a multiplexor or a system of voltage-to-current converters, one for each electrode, each controlled by a digital to analog converter is used. The measurements again may be taken either by a single voltage measurement circuit multiplexed over the electrodes or a separate circuit for each electrode. Earlier systems typically used an analog demodulation circuit to convert the alternating voltage to a direct current level then an analog to digital converter. The voltages measured are then passed to a computer to perform the reconstruction and display of the image [12–17].

Till date, Electrical Impedance Tomography (EIT) [18–21] has been researched extensively in the medical field [5, 22, 23] as well as in other areas like industrial process control [17], chemical engineering [24], geotechnical research [25] and biotechnology [26] due to its several advantages [27–29] over other computed tomographic techniques [30]. Practical phantoms [19, 31–33] with surface electrodes [34–36] are used to assess the performance of EIT systems for their validation, calibration and comparison purposes. In EIT, the impedance images are reconstructed from the surface potentials developed by a constant current signal injected to the boundary ($\delta\Omega$) of the domain (Ω) to be imaged (Fig. 1). The sensitivity, spatial resolution and distinguishability of an EIT system depends on the current injection techniques applied for boundary data generation. Different current injection methods called current injection patterns [37, 38] have their own sensitivity to the different inhomogeneity positions in the domain under test.

Fig. 1 Explanation of EIT principle



In this due relation, the estimation of the spatial conductivity distribution in a thorax cross section is carried out by thoracic electrical impedance tomography (EIT) as it is a non-invasive technique [39, 40]. In this procedure, the electrodes are equidistantly attached to the patient's skin around the thorax. During a measurement, adjacent electrodes are fed with a small alternating currents and the potentials at the remaining electrodes are measured (i.e., adjacent drive/adjacent receive). Then, reconstructed images with this data visualize the change in conductivity of the specific area of interest [41]. In recent years, EIT is used to monitor a variety of clinical problems such as respiratory failure, cardiac volume changes, gastric emptying, and head imaging [42]. In spite of low spatial resolution (about one tenth of the thorax diameter), but due to its non-invasiveness and high temporal resolution it seems to be particularly useful for the bedside monitoring of patients suffering from the acute respiratory distress syndrome (ARDS) [43]. ARDS is a life-threatening state of the lung characterized by atelectasis (i.e., lung collapse) and pulmonary edema (i.e., water in the lung) and thus, variations of the conductivity distribution in the thorax. ARDS patients have to be mechanically ventilated with higher oxygen concentrations and changing pressure levels resulting in dynamic shifts of body fluids and lung aeration. For visualizing those shifts, EIT is well suited in providing an instantaneous feedback to the medical staff [44, 45]. In order to achieve maximum benefit, further investigations are to be carried out to process the fast sequence of EIT images (up to 50 images/s) and also the way out for the extraction and quantification of the underlying physiological information. The attending physician should be able to immediately recognize ventilation changes in the lung resulting from, e.g., new ventilator settings. EIT-derived numeric parameters could be able to evaluate the objective more precisely in comparison with the visual observations of the EIT images (subtle changes are simply hard to detect). Additionally, EIT-based trend can analyze different kinds of diseases with the help of numeric parameters. Therefore, we first created a two dimensional finite element model of the human thorax and divided the lung into three coronal layers. Then, we altered the fluid contents of the dorsal layers close to the back in order to simulate lung collapse of increasing severity. Later the thorax model from two dimensional

platform is transformed to three dimensional platform for the analysis. After reconstruction, we looked at different methods to quantify the given ventilation changes and compared them with the actual modifications made in the thorax model. From this EIT based reconstructed images, an approximate determination of the lung area is obtained.

Finally, as EIT seems also to be capable of distinguishing between heart and lung related changes of the conductivity in the thorax [46], we examined which current-injection and voltage measurement electrode pairs are best suited for a proper separation between lung and heart activity. Hence, we calculated the average current density for the different tissues and compared them based on the position of the current injection. In this chapter a brief descriptions on the physical and mathematical aspects of the EIT technology along with its potentials and challenges in the field of thorax imaging of humans are discussed.

2 Motivation

Monitoring lung function with EIT is particularly helpful because lung tissue resistivity is five times higher when compared to most other soft tissues within the thorax. The results obtained by this method have absolutely in high contrast with the lungs condition in general. In addition, the resistivity of the lung increases and decreases several-fold between inspiration and expiration which explains why monitoring the respiratory cycle is currently the most promising clinical application of functional EIT since mechanical ventilation frequently results in Ventilator-associated lung injury (VALI). In 1990 at Rensselaer Polytechnic Institute, the feasibility of EIT for lung imaging was first demonstrated using the NOSER algorithm [47]. During critical illness or anesthesia, functional EIT can resolve the changes in the distribution of lung volumes between dependent and non-dependent lung regions that can able to assist in adjusting ventilator settings to provide lung protective ventilation to patients [48].

By using the information determined by functional EIT (f-EIT), most EIT studies have focused on monitoring regional lung function. However, absolute EIT (a-EIT) also has the growing edge potential to become a clinically useful tool for lung imaging, as this approach would allow to bring a direct distinction between lung conditions which result from regions with lower resistivity (e.g. hemothorax, pleural effusion, atelectasis, lung edema) and those with higher resistivity (e.g. pneumothorax, emphysema) [49, 50].

In this work, we investigate the lung fluid movement related with the activities of the lungs using simulation as well as real time sensors utilizing the principle of EIT. This basic study will provide an introductory idea of imaging of human thorax by EIT technique with the use of low cost hardware components.

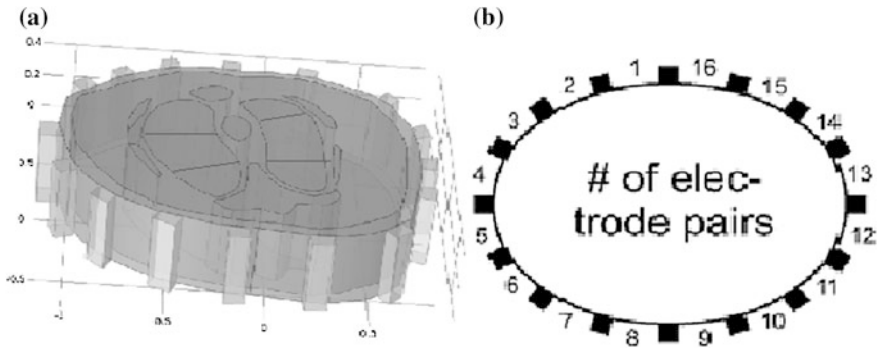


Fig. 2 **a** Electrode placement (considering the diameter of the thorax \sim 12 cm horizontally) and **b** numbering of electrode pairs

3 Methods

An adequate geometric model of the human thorax is designed with realistic values of the electrical properties of biological tissue for the proper assessment of lung collapse. Thus, a correct geometric dimension of the model (shown in Fig. 2a) from real CT images of a human male is designed in the Multiphysics software platform. During the mesh generation, necessary simplifications and conditions are made is similar to the ones described in [51]. The resulting mesh consisted of 454,847 first-order triangular elements are created with FEM based Multiphysics software. In total, five different types of tissue are being modelled with electrical properties taken from the literature: muscle, heart, bones (spinal column, ribs, and sternum), fat, and lung (shown in Table 1). The currents of 10 mA @200 kHz (as frequencies between 20 and 200 kHz are widely used for thoracic single-frequency EIT) are injected across the electrode pair. In order to simulate patient breathing, conductivity and relative permittivity of the lung are varied between deflated and inflated lung as given in the article “Dielectric properties of body tissue” [52]. Visceral

Table 1 Electrical properties of the modeled tissues between 20 and 200 khz [52]

Tissue	Conductivity (S/m)	Relative permittivity
Lung* (deflated)	0.26197	8531.40
Lung (inflated)	0.10265	4272.50
Heart*	0.19543	16982.00
Bone* (cortial)	0.02064	264.19
Fat*	0.02424	172.42
Muscle*	0.35182	10094.00
Body fluid	1.50000	98.56
Blood	0.70080	5197.70

(Asterisk-Marked (*) properties were used for the simulation of the reference state)

movements (i.e., geometric changes) during a breath cycle are not considered as it has been reported to have a rather low influence for state-differential reconstruction algorithms [53].

Patients suffering from acute respiratory failure are usually treated in supine position. Due to the weight of its upper parts, the lung tends to collapse in the lower parts first (commonly termed as gravitationally dependent collapse). Therefore, we divided the lung into three coronal layers and modelled different amounts of lung collapse by subsequently replacing the bottommost layers with collapsed lung tissue (Fig. 2a) without any breathing activity. The electrical properties of the collapsed areas (0.6 S/m, 1000) were assumed to be a mixture of deflated lung tissue and well-conducting body fluid [54].

This straightforward simplification should be sufficient, as mainly the missing ventilation of the collapsed lung tissue will influence the reconstructed images of conductivity change. Figure 2 provides the detailed overview of the electrode placement and numbering of adjacent electrode pairs. For the simulation of the heart activity, variation of its electrical properties between “normal” heart and blood-filled heart (a mixture of blood and heart properties: 0.45 S/m, 11,000 as given in Table 1) are considered. As before, to obtain qualitative character, the geometric changes during a breath cycle are omitted.

(i) Mathematical Model

For a known conductivity, a relationship can be established between the electrical conductivity (σ) and spatial potential (Φ), to calculate the nodal potential [55]. Electro-dynamics of EIT is governed by a nonlinear partial differential equation, called the governing equation of EIT [55], is given by,

$$\nabla \cdot \sigma \nabla \Phi = 0 \quad (1)$$

The potential field inside of the conductor having no internal electrical sources or sinks, must satisfy the Eq. (1). To solve this equation, the following boundary conditions are to be known

Dirichlet Boundary Condition:

$$\Phi = \Phi_i \quad (2)$$

Where, $i = 1 \dots N$, are the measured potentials on the electrodes.

Neumann Boundary Condition:

$$\int_{\partial\Omega} \sigma \frac{\partial\Phi}{\partial\eta} = \begin{cases} +I \\ -I \\ 0 \end{cases} \quad (3)$$

Here, $+I$ is for source electrode, $-I$ is for sink electrode and 0 otherwise. $\partial\Phi$ is the boundary and η is the outward normal vector to the electrode surface. In this chapter, forward problem solver algorithm is used. The description of this problem is discussed below.

Forward Problem:

A relation can be obtained between the voltage measurements made on the boundary ($\partial\Omega$) and the domain conductivity can be found [52, 53] as,

$$\Phi = K\sigma \quad (4)$$

Where σ is a vector of conductivity values, Φ is the vector of voltage measurements and K is the transformation matrix relating Φ to σ .

If K and σ are known, Eq. (1) can be solved numerically using FEM to calculate the nodal potentials of the domain for the known conductivity (σ). It is known as the “forward problem”.

Thus, for a known value of a constant current, the nodal potentials within the phantom area are computed using the forward solver problem of EIT [56, 55]. The value of the conductivity and permittivity of the blood, body fluids etc. of the designed FEM model are obtained from Luepschen et al. [57].

(ii) Implementation of the proposed model in FEM based Multiphysics Simulation Platform

The FEM based modelling approach used for the models can be represented in Fig. 3 as:

Step 1: Choosing the design module from the Model Library

This step includes the selection of space dimensions (2D and 3D), physics module (AC/DC, Electrostatics etc.) and selection of study type i.e. stationary, transient, frequency etc., as per our requirement for the analysis.

Step 2: Specification of the sensor geometrical parameters to draw/design the sensor

In this step the selection of dimensions of the sensor in SI/CGS unit i.e. m/cm is done along with the selection of angular dimensions in degree or radian.

Step 3: Initialization of the electrical properties of the domain/boundary

It includes the setting of the conductivity, permittivity of different objects (here the objects are the lungs at different conditions, heart, blood, fat, bones etc., as mentioned in Table 1) under consideration which helps for computation of AC/DC and electrostatic study.

Step 4: Setting up the boundary conditions

This includes setting up the value of the potential on the electrode array surrounding the thorax.

Step 5: Mesh generation

It includes the generation of mesh for the constructed thorax model. Here triangular type user defined meshing is applied. If the mesh generation is successful on the model then it jumps to the analysis module otherwise the different boundary conditions and geometries are varied to obtain successful computation of the mesh over the considered model.

Step 6. Solving and finding the field distribution

Here, the forward model of the EIT is solved after the successful mesh generation to generate the characteristic plots.

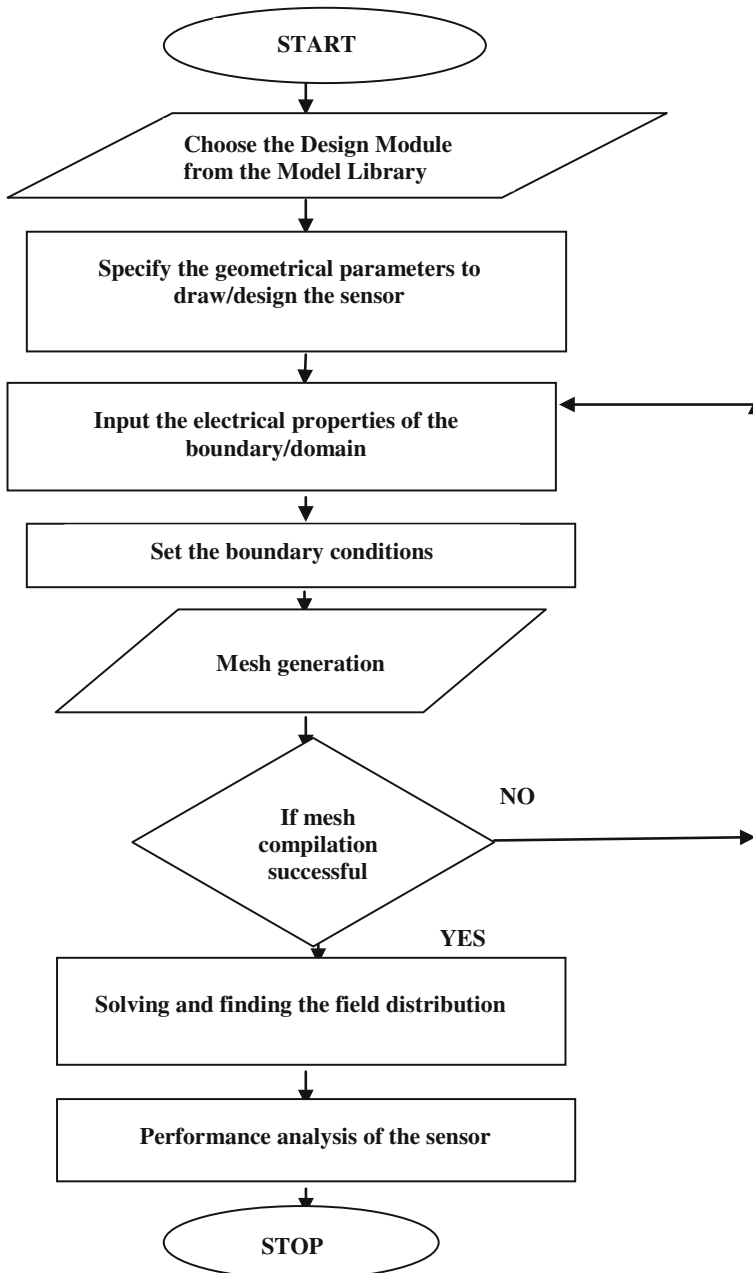


Fig. 3 Flowchart showing the steps for modelling the sensor in FEM based Multiphysics software

Step 7: Performance analysis of the sensor

The study of the sensor with the 2D and 3D group plots are done to virtually optimize the sensor.

(iii) Impedance Measurement Methodology:

In EIT a low frequency constant sinusoidal current through the electrodes (called current electrodes) is injected to the domain under test. The boundary potentials are measured on the electrodes called voltage electrodes. The method or pattern in which the current is injected to the object under imaging is called the current pattern or current injection protocol. The existing famous four different current injection protocols as reported by the researchers. Here, the injection pattern i.e. the adjacent method which is used in this analysis is discussed below. In general, to avoid the contact impedance problem the differential potentials are measured across the different electrodes excluding the current electrodes.

(a) Adjacent method

The adjacent or neighbouring current injection method was suggested by Brown and Segar [58]. In this protocol, the current is applied through neighbouring or adjacent electrodes and the voltage is measured successively from all other adjacent electrode pairs excluding the pairs containing one or both the current electrodes. Figure 4 illustrates the neighbouring method for a 16-electrode EIT system with a circular domain under test (within a cylindrical volume conductor) surrounded by 16 surface electrodes denoted as the electrode-1 through electrode-16 ($E_1, E_2, E_3, E_4, E_5, E_6, E_7, E_8, E_9, E_{10}, E_{11}, E_{12}, E_{13}, E_{14}, E_{15}$ and E_{16}). In neighbouring method, for the first current projection (P1), the current is injected through electrode-1 (E_1) and electrode-2 (E_2) and the differential potentials ($V_d: V_1, V_2, V_3 \dots V_{13}$) are measured successively with 13 electrode pairs E_3-E_4, E_4-E_5, \dots and $E_{15}-E_{16}$ (Fig. 4a). Hence the first current projection yields 13 differential voltage data viz. V_1 or V_{3-4} (measured between E_3 and E_4), V_2 or V_{4-5} (measured between E_4 and

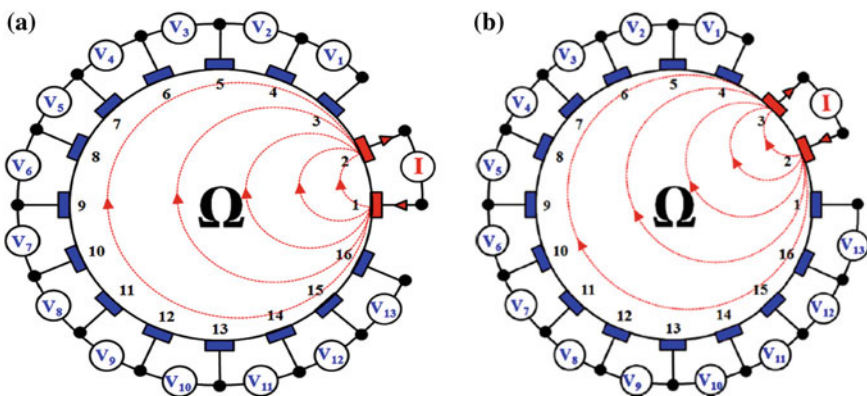


Fig. 4 Neighbouring or adjacent current method of boundary potential data collection illustrated for a cylindrical volume conductor and 16 equally spaced electrodes: **a** projection-1 (P1), **b** projection-2 (P2)

E_5)... and V_{13} or V_{15-16} (measured between E_{15} and E_{16}). The 13 differential voltage data obtained in this process are assumed to represent the impedance between the equipotential lines intersecting their corresponding measurement electrodes and are all independent to each other [59]. In neighbouring method, the current density is, of course, the highest between the current electrodes (E_1 and E_2 for the projection-1), decreasing rapidly as a function of distance [59]. In current projection-2 (P_2), the set of other 13 differential voltage measurements is obtained by feeding the current through electrodes 2 (E_2) and 3 (E_3) as shown in Fig. 4b. Therefore, in this current projection, the current is injected through electrodes 2 (E_2) and 3 (E_3) and the differential potentials (V_d : $V_1, V_2, V_3, \dots, V_{13}$) are measured successively with 13 electrode pairs E_4-E_5, E_5-E_6, \dots and $E_{16}-E_1$.

Hence the second current projection (P_2) yields 13 differential voltage data viz. V_1 or V_{4-5} (measured between E_4 and E_5), V_2 or V_{5-6} (measured between E_5 and E_6),... and V_{13} or V_{16-1} (measured between E_{16} and E_1) as shown in Fig. 4b. Similarly, in current projection-16 (P_{16}), another set of 13 differential voltage measurements is obtained with a current injection through electrodes 16 (E_{16}) and 1 (E_1). Therefore, in this current projection, the current is injected through electrodes 16 (E_{16}) and 1 (E_1) and the differential potentials (V_d : $V_1, V_2, V_3, \dots, V_{13}$) are measured successively with 13 electrode pairs E_2-E_3, E_3-E_4, \dots and $E_{14}-E_{15}$. Hence the P_{16} yields 13 differential voltage data viz. V_1 or V_{2-3} (measured between E_2 and E_3), V_2 or V_{3-4} (measured between E_3 and E_4),... and V_{13} or V_{14-15} (measured between E_{14} and E_{15}). Therefore, for a 16-electrode system, the neighbouring current injection method yields 16 current projections ($P_1, P_2, P_3, \dots, P_{15}$ and P_{16}) each of which will produce 13 differential voltage data. Therefore, in neighbouring method, a complete scan on a 16-electrode EIT system yields $16 \times 13 = 208$ V measurements are made. But, due to the reciprocity [38], the measurements made on the boundary yield identical voltage data in which the current electrodes and voltage electrodes are interchanged [38]. Thus we obtain, 104 data are independent to each other among the 208 differential voltage measurements only. In the neighbouring method, the measured voltage is only about 2.5 % opposite electrode pairs and becomes maximum for the adjacent electrode pairs [59].

(iv) Finite Element Method:

The finite element method (FEM) is a numerical technique for finding approximate solutions to partial differential equations (PDE) and their systems, as well as (less often) integral equations.

In simple terms, FEM is a method for dividing up a very complicated problem into small elements that can be solved in relation to each other.

The solution approach is based on eliminating the spatial derivatives from the PDE. This approximates the PDE with

- a system of algebraic equations for steady state problems,
- a system of ordinary differential equations for transient problems.

These equation systems are linear if the underlying PDE is linear, and vice versa.

As EIT contributes to a non linear inverse problem in which the electrical conductivity distribution across a closed domain (Ω) of interest inside a volume

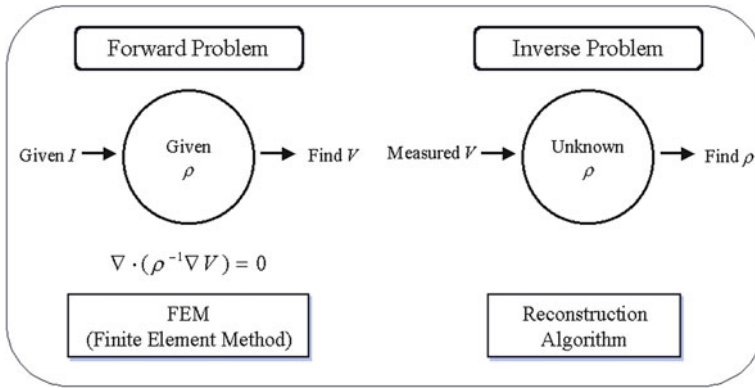


Fig. 5 Forward versus inverse problem of electrical impedance tomography

conductor is reconstructed from the surface potentials measured at the domain boundary ($\delta\Omega$) (shown in Fig. 1). This problem is solved in FEM in two ways, the forward problem and the next is the inverse problem.

The forward problem calculates the voltages on the electrodes by using the injected current and assumed resistivity distribution whereas the inverse problem reconstructs the resistivity distribution by using the voltage measurements on the electrodes. The pictorial representation of these two problems is presented in Fig. 5.

(v) Meshing:

A polygonal or polyhedral mesh that approximates a geometric domain is generated during the mesh generation. The term “grid generation” is often used interchangeably. Typical uses are for rendering to a computer screen or for physical simulation such as finite element analysis. In the analysis explained in this chapter, a physics controlled mesh of triangular type is generated over the entire geometry under consideration and is then solved in a FEM based Multiphysics simulation platform.

(vi) Field Simulation:

The FEM Multiphysics software is used to simulate the models. Simulations are conducted similar to the measuring procedure of the EIT system. For each physiological state of the lung, 16 simulations are to be carried out to account for all current-injection positions while determining the voltages between the remaining 13 electrode pairs. Hence, voltages distributions are determined for each state of the lung (shown in Fig. 2).

(vii) Image Reconstruction and Processing:

State-differential EIT images were reconstructed from the simulated 208 voltages using the forward algorithm [17] and the boundary conditions as discussed in Sect. 3i [60]. The reconstructed images represent the conductivity changes based on either the breathing or the heartbeat activity. In order to quantify dorsoventral as well as lateral shifts of the ventilation distributions resulting from different amounts of lung collapse are studied [59].

4 Experimental Setup

For the real time analysis, a 16 electrodes array of Ag-AgCl is developed for imaging of the human thorax. The electrodes are circular with a diameter of about 2.5 cm. The electrodes are placed equidistantly with spacing of 3 cm. This spacing is adjustable as per the size of the thorax of the objective (photography of these electrodes along with their arrangements is shown in Fig. 6).

The real time data using the electrode array were obtained along a single plane of the human thorax. A current of 10 mA, 20–200 kHz is injected across the electrodes using adjacent current injection protocol. The boundaries are obtained manually and are recorded and fed into FEM based Multiphysics software to generate the voltage density plots shown in the Fig. 20. The figure shows that the reconstructed images using forward solver of EIT of human thorax in a single plane is obtained successfully. From the plots, approximate area coverage of the lungs as well as the human thorax is estimated for analysis.

(i) Associated Circuitry

The proposed block diagram of the 16 electrode based EIT system is shown in Fig. 7 alongwith its associated circuitry. It consists of a phantom under test, a voltage control current source (VCCS) for injection of current across the boundary of the phantom, a multiplexer for controlling the electrodes pair for injection of current and collection of the boundary potentials and a data acquisition system to store the data connected with a PC for its image reconstruction and analysis.

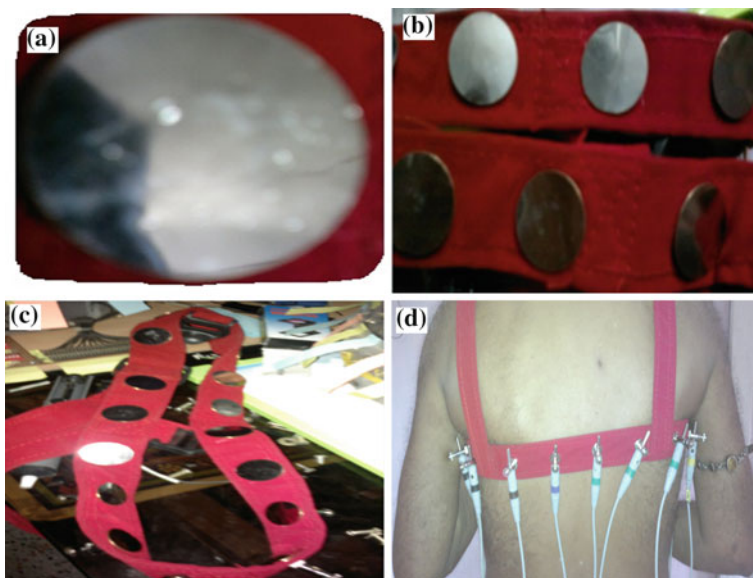


Fig. 6 Photograph of **a** Single Ag-AgCl electrode, **b**, **c** showing the arrangement of the 16 electrodes in the array belt and **d** objective wearing the belt for imaging of the thorax

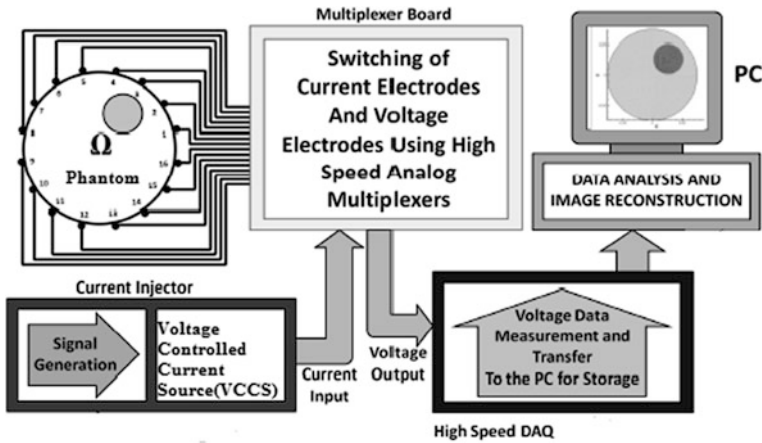


Fig. 7 Proposed block diagram of an EIT system with associated circuitry

(a) EIT Instrumentation

EIT instrumentation is required to inject a constant current to the phantom boundary and measure the boundary potentials developed at the surface electrodes. The EIT instrumentation comprised of a constant current injector (CCI), automatic electrode switching module (ESM), signal conditioner module (SCM) and a data acquisition system (DAS) is used for boundary data collection. The block diagram of each part is shown in Fig. 8.

The developed experimental set up has 16 electrodes, a constant current supply, analog multiplexers, differential amplifiers and a data acquisition system for the boundary voltage measurements from the electrodes paced across the phantom under observation.

(b) Constant Current Injector (CCI)

In the present study, the constant current injector of this circuit is designed by using IC chip XTR 111(Texas Instruments). It is a precision voltage to current converter designed for the standard 0–20 mA to 4–20 mA and can source up to

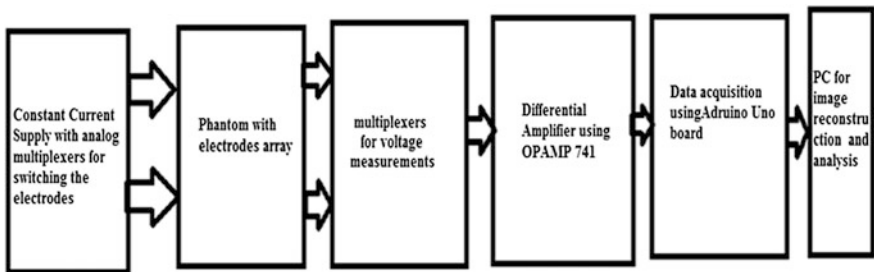
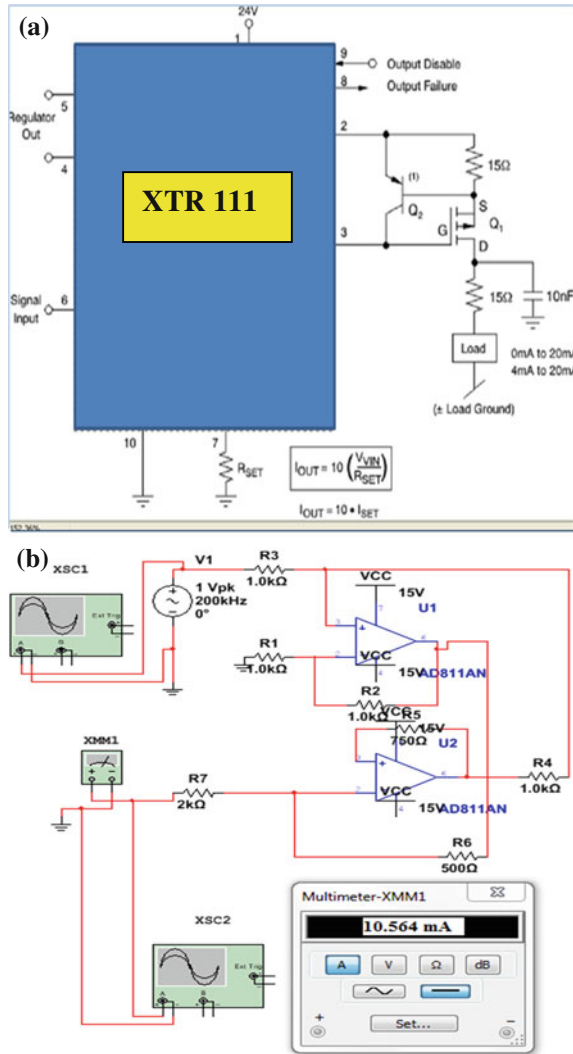


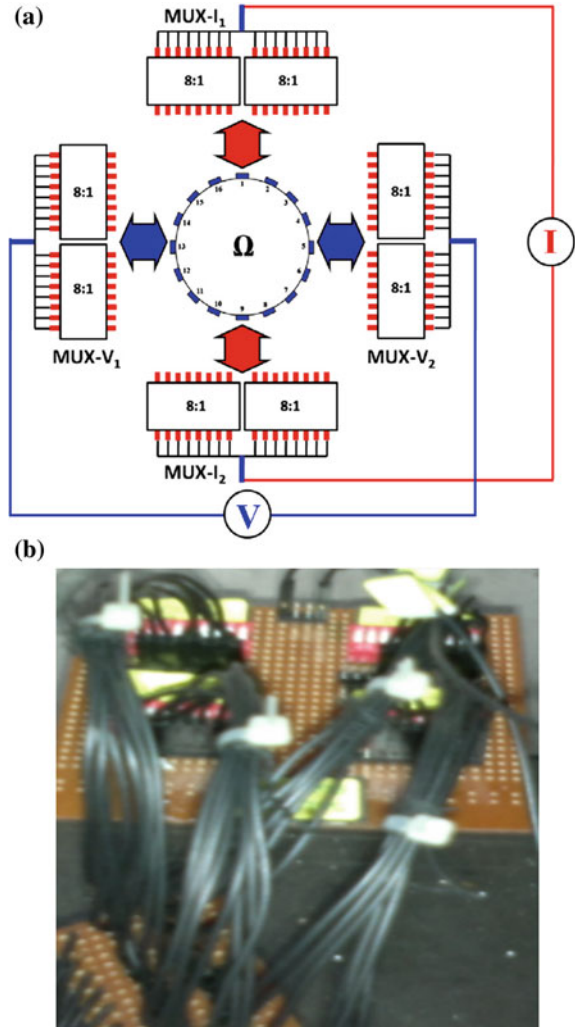
Fig. 8 Block diagram of the 16 electrodes based EIT system

Fig. 9 Constant current sources using **a** XTR 111(for real time implementation), **b** Simulation based designed of modified Howland circuit using operational amplifier AD811



36 mA. The ratio between input voltage and output current is set by the single resistance R_{SET} . The circuit (in Fig. 9a) can also be modified for the voltage output. The other important details of this chip are provided in the datasheet mentioned in the references [61]. Finally we have designed a modified Howland constant current generator which is basically a VCCS (Fig. 9b) and it is fed by the VCO. VCCS is developed with two AD 811 ICs (Analog Devices Inc. USA) [62]. AD 811 is a high speed wideband current feedback operational amplifier which is suitably used in modified Howland current source with a feedback resistor [61]. A MULTISIM 12.0 based simulation study for the modified Howland circuit is also performed using two AD811 operational. For a voltage of 1 Vp-p, 200 kHz sine wave input from a

Fig. 10 Multiplexers for injecting current and measuring voltages using DIP switches **a** Block diagram and **b** real time implemented circuit



signal generator VCCS provides an approximate 10.564 mA as a constant current output.

(c) Electrode Switching Module (ESM)

Single Pole Single Throw (SPST) slide actuated DIP switch-based multiplexers is used for electrode switching module (Fig. 10) which is operated manually for injecting current and measuring the voltage.

The DIP switches with gold plated slide type having 50 m Ω contact resistance and 1000 M Ω insulation resistance with a mechanical life of 2000 operation are used (Fig. 10). Two 8-point SPST DIP switches are used to form a 16:1 multiplexer (MUX I₁) and another two 8-point SPST DIP switches from another pair of 16:1

multiplexer (MUX I₂). For current switching operation, the input side all the inputs of first MUX I₁ are shorted and connected to one terminal of the current source and its outputs are connected to all the 16 electrodes in the phantom.

Similar, arrangements are made to connect other terminal of the current source to the electrodes.

(d) Data Acquisition System

ARDUINO UNO board based data acquisition system is developed using USB port [63]. ATmega 328 microcontroller within the board allows handling 6 analog inputs and 14 digital inputs. The transmission/reception of data from the board can be controlled by writing high level language programs within its software consol.

As the negative voltage data are not displayed, so parallel connections are made with the four inputs coming from the differential amplifier constructed using operational amplifier IC 741. The four inputs are then passed through current inverter circuits and then the outputs from the inverter circuit are connected to the four analog inputs of another ARDUINO board. The voltage data are saved in a.txt file for further analysis. The details specifications of this board are provided in a data sheet [63].

(e) Data Collection

The 16 Ag-AgCl electrodes are placed on phantom (thorax) equidistantly. The different parts inside the phantom conduct differently due to their varying value of the permittivity in presence of the applied current. Following the neighbouring pattern current injection protocol constant current of 10 mA is applied across two electrodes at a time (but current can also be applied through opposite, cross and adaptive method [64]). For example, in a set of 16 electrodes the current is applied between electrode pair 1–16 and the voltage is measured between 2–3, 3–4 and so on (excluding source pair electrodes). Thus the first 13 readings are obtained. The current source is then shifted to pair 1–2, 2–3...etc. and the procedure is repeated to get the next set of 13 readings [64]. Then, the voltage difference is measured between adjacent electrodes [64]. After taking all the voltage set readings finite element method is used for reconstruction of images.

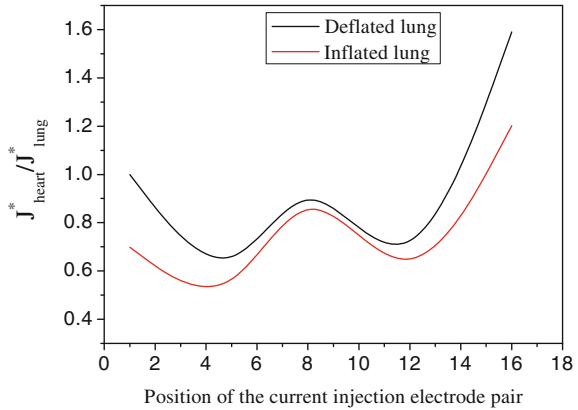
5 Results and Discussions

(i) Determination of Heart Activity

The amount of current through the different tissues is obviously influenced by the position of the current-injection electrode pair. Electrode pair #5 will lead to a greater amount of current flowing through the (right) lung, whereas injection through electrode pair #16 maximizes the current flow in the heart and it is easily be visualize from the plot of the ratio of the current density of heart to that of the lungs as shown in Fig. 11.

The corresponding current density images of the FEM simulations are provided in Fig. 12. The qualitative results for the best electrode pairs to measure the heart activity is additionally backed up by looking at the voltage changes at the boundary.

Fig. 11 Plot of current densities of heart and lungs J^*_{heart} and J^*_{lung} versus the position of the current injection electrode pair



Especially, when using the identified optimal current-injection electrodes as receiver electrodes (e.g., current-injection pair: #16, receive pair: #8), SNR is maximized (here, the lung activity is regarded as “noise”).

From the Fig. 11, it is seen that depending on the position of the current-injection electrode pair, the amount of current through heart and lung varies. For the detection of the heart activity, electrode pairs #1, #8, #9, #15, and #16 provide the best chances for the observation.

(ii) Determination of Lung Collapse and Lung Area:

From the Fig. 13 it is seen that the different amount of collapsed lung area which is determined by forward solver algorithm.

The voltage distribution plots as of the lungs in Fig. 13 shows that the collapse of different layers of the lungs starting from the lowermost part.

From these figures approximate determination of the lung area can also be estimated, which can provide an overview condition of the lungs to the physician.

(iii) Simulated and Real time studies of the designed electrode array:

We have implemented a real time 16 Ag-AgCl electrode belt for monitoring the physiological conditions of the humans. The diameter of the electrode is 2.5 cm and the thickness is 0.1 cm.

First, we have developed a design model of the electrode in FEM Multiphysics based simulation platform (shown in Fig. 14). Then, we have considered two electrodes of the same dimension and material to be placed on the two surface of a cubical block (shown in Fig. 15). The block is assumed to be the skin of the human body. The permittivity of the box i.e. considered human skin is taken from [65]. Then we have applied two different voltages 8×10^{-6} V and 12×10^{-6} V on two faces of the block. The designed model is solved with 10,742 normal size triangular meshing elements. After the successful computation of the mesh, following analysis is performed.

It is seen from the Figs. 16 and 17 that the pickup voltages within the electrodes remains almost constant value.

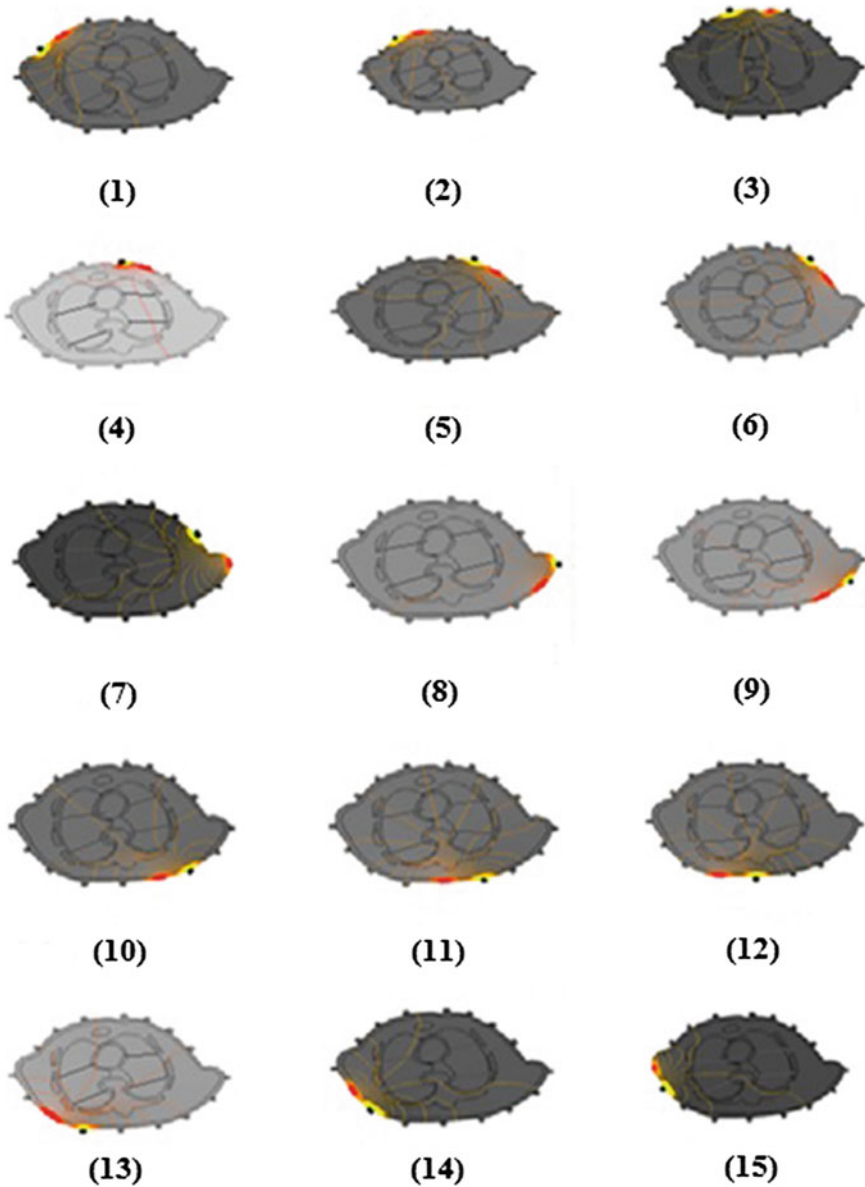


Fig. 12 Current density distribution and potential isolines plots from the FEM based simulation study for different current-injection positions

Analysis of the resistive losses inside the electrode shows that there is a very little variation of the resistive loss within the material. Thus the signal obtained from the electrode will be of full strength value (shown in Fig. 18).

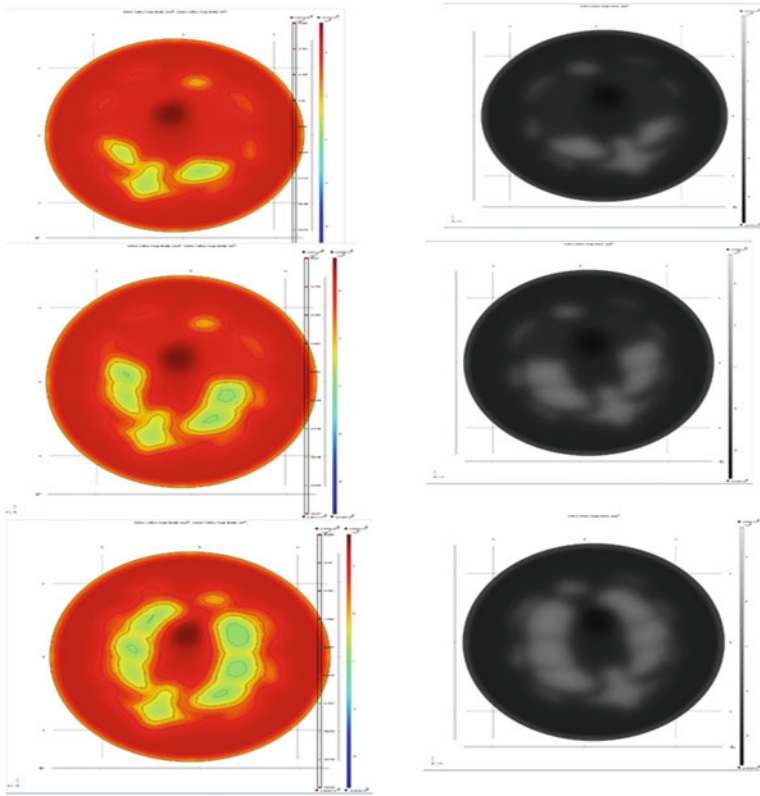


Fig. 13 Reconstructed differential EIT images for different amounts of collapsed lung with forward solver algorithm

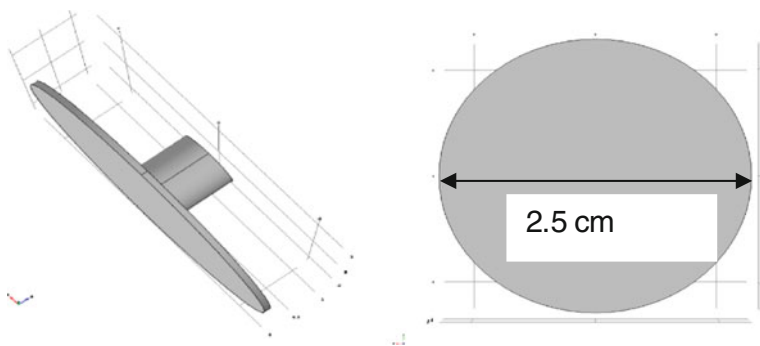


Fig. 14 Photograph of the constructed Ag-AgCl electrode

Fig. 15 Photograph of the two electrodes placed on a block (considered as human skin)

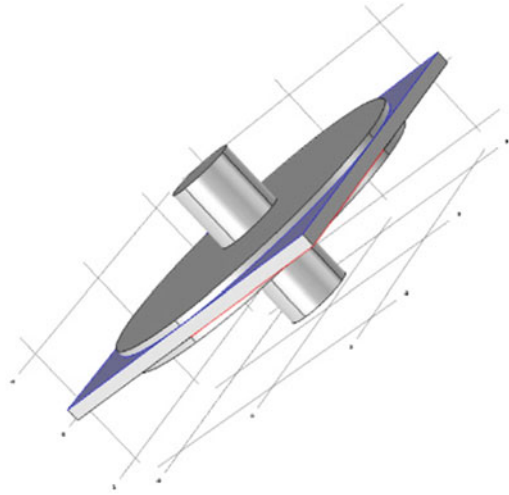


Fig. 16 Photograph of the variation of voltage on the two electrodes if the pickup voltages from the skin are 8×10^{-6} and 12×10^{-6} V

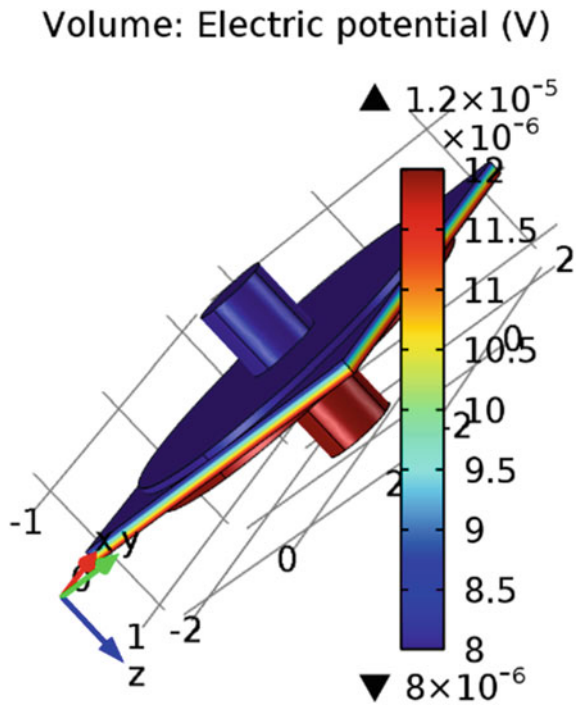
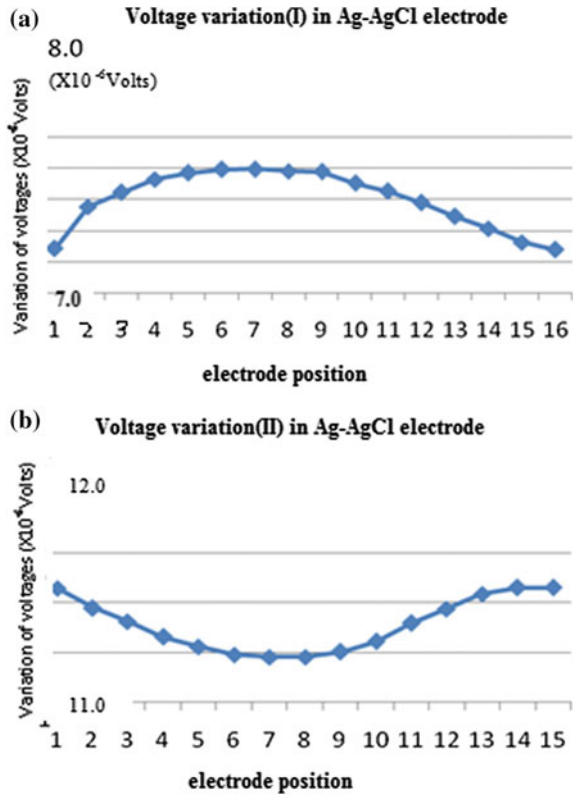


Fig. 17 Plot of variation of pick up voltages within the electrodes with **a** voltage at the skin surface 8×10^{-6} V and **b** voltage at the skin surface 12×10^{-6} V



In order to establish such a system, a 16 electrodes array of Ag-AgCl has been developed for imaging of the human thorax. These electrodes are round shaped with dimension of 2.5 cm. and are placed 3 cm apart. The total arrangement of the electrodes and the photography of the other accessories of the system are provided in Fig. 19. It should be noted that the spacing is adaptable with the perimeter of the thorax under test.

The real time data using the electrode array were obtained along a single plane of the human thorax. A current of 10 mA, 20–200 kHz is injected across the electrodes using adjacent current injection protocol. The boundaries were obtained manually and were recorded and fed into FEM based Multiphysics software to obtain the voltage density plots shown in the Fig. 20. This figure shows that the reconstructed images using forward solver of EIT of human thorax in a single plane is obtained successfully. From the plots approximate area coverage of the lungs as well as the human thorax is estimated for analysis.

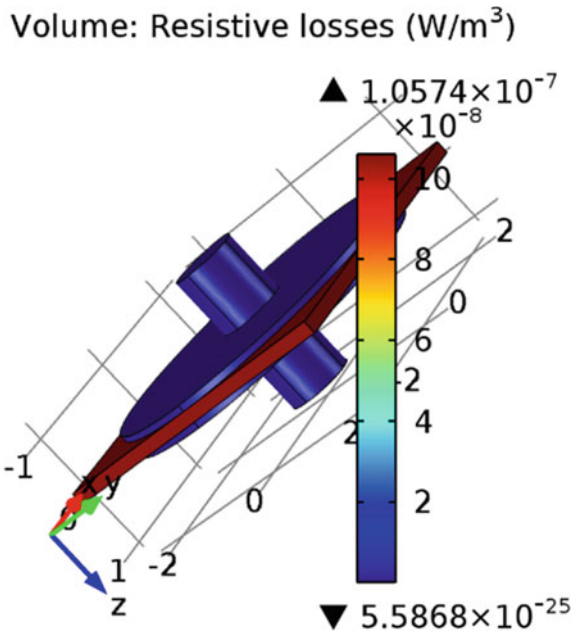


Fig. 18 Photograph showing the variation of resistive loss (W/m^3) within the electrode material

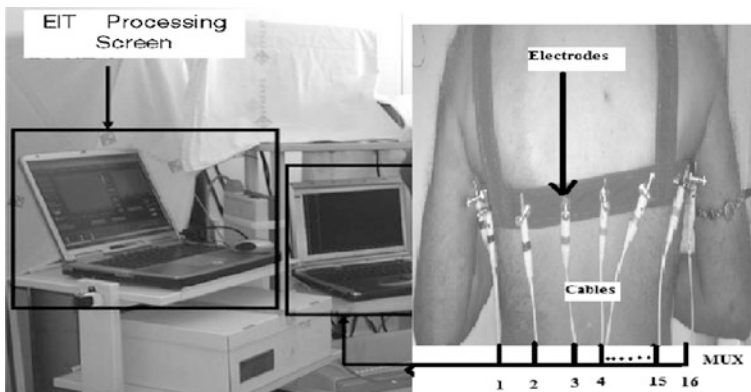


Fig. 19 Photograph of a objective wearing the belt along with computer for processing the data for imaging of the thorax

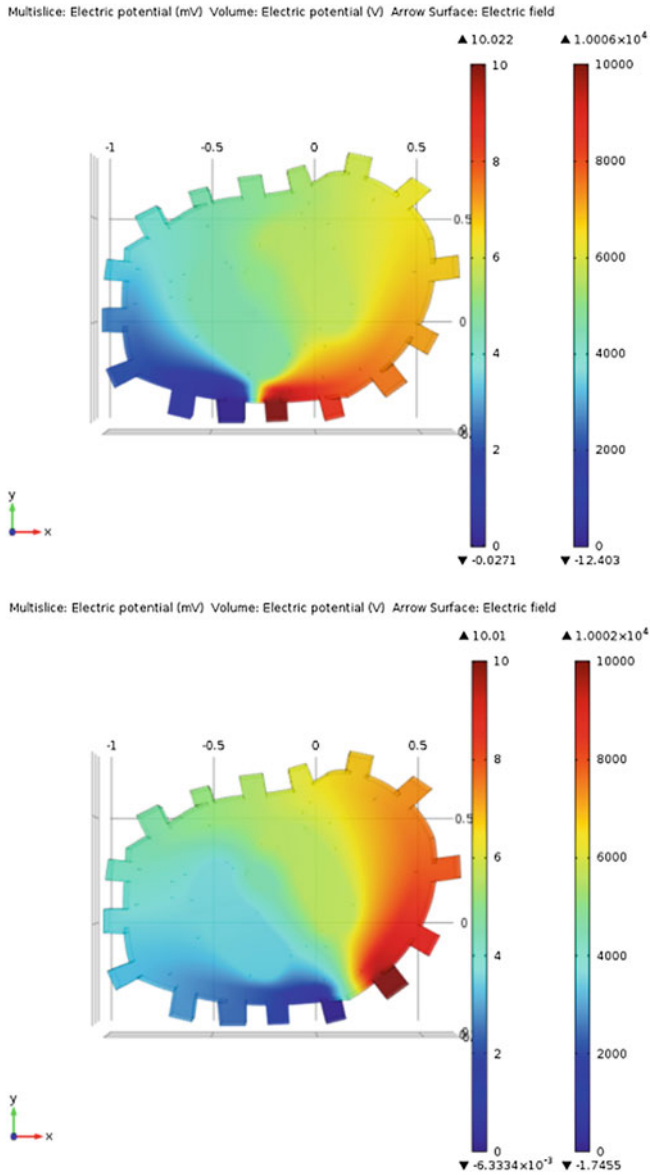


Fig. 20 Voltage density plots of the data obtained from the real time imaging of the thorax using adjacent protocol type current (10 mA, 20–200 kHz) injection pattern

6 Conclusions

Lung condition of a subject under diagnosis can be imaged by conventional radiographic, x ray computed tomography, or magnetic resonance imaging (MRI) techniques, but there are situations where it would be desirable to have portable means of imaging regional lung ventilation which could, if necessary generate repeated images with time. Being inexpensive, relatively portable and having high temporal resolution, EIT is suited for this application, but significant challenges, off course remains.

The most viable areas of research for EIT corresponds to lung imaging as it is most widely recognized (Barber 2005). In the past and present years the EIT have been applied for imaging of a large numbers of medical conditions in the thoracic region, with a varieties of techniques, algorithms and devices. The studies conducted here have exclusively use circular electrode configurations, but the conditions have been varied considerably. The diagnosis of human in such conditions like pulmonary embolism (PE) (Leathard et al. 1994), emphysema (Harris et al. 1987; Eyuboglu et al. in 1995), bronchial carcinoma (Holder and Temple in 1993; Morice et al. 1993; Shrinkarenko et al. 1997), and chronic obstructive pulmonary disease (COPD) (Eyubouglu et al. 1995, Von Noordergraaf et al. 1998), among others are very much important [66]. Subjects in these studies were under spontaneous or mechanically ventilated, depending on the study [67].

Specifically, for the patients under mechanical ventilation, pioneering work performed by a close collaboration between clinicians and EIT experts shows the viability of the use of EIT for establishing the best ventilator regime to be used by the critically ill patients at the bedside. In this work, real time data using the electrode array are obtained along a single plane of the human thorax. A current of 10 mA, 20–200 kHz are injected across the electrodes using adjacent current injection protocol. The boundaries are obtained manually and are recorded and fed into FEM based Multiphysics software to obtain the voltage density plots shown in the Fig. 11, 12 and 13. The Figs. (12, 13 and 19), shows that the reconstructed images using forward solver of EIT of human thorax in a single plane is obtained successfully. From the plots approximate area coverage of the lungs as well as the human thorax is estimated for analysis.

The most interested area of research for EIT lung imaging has been neonatal lung formation, owing to the fact of non-invasiveness, radiation free are preferred in the application. The detection of PE and COPD diseases can be estimated by monitoring the blood volume in the thorax and is also being one intense topic for study, as the conductivity of the blood is 6.7 mS/cm which is approximately three times that of inter thoracic tissues. As a result, due to the pulsatile flow of the blood through the thorax, the image quality will be a change in conductivity due to replacement of tissue by blood (vice versa). This may be relatively large in cardiac ventricles but may be smaller in the peripheral lung fields. When a blood clot is present in the lung, the lung beyond the clot is not perfuse and under favourable circumstances, this may be imaged as a gated volume image of the lung, and PE can

be diagnose if the ventilation image of the same region shows the normal ventilation.

Research is ongoing in this very promising field. It is hence, fitting the lung imaging is possibly the only application of EIT to enjoy a linear reconstruction algorithm developed from the consensus of the most EIT group in the world, which can be modified to suit the specific applications. Moreover, a lung EIT is used as testing ground of new reconstruction algorithm, where the efficacy of a novel reconstruction algorithm in preserving the sharp conductivity boundaries was proven via in vivo thoracic measurements. EIT of the lungs is obviously close to becoming, a clinical reality.

References

1. T. Kanti Bera, J. Nagaraju, *Electrical Impedance Tomography (EIT): a harmless imaging modality*, ed. by S. Singh, K. Shukhla, R. Srivastava. Research Developments in Computer Vision and Image Processing (IGI Global Publisher, 2013)
2. D.C. Barber, B.H. Brown, Applied Potential Tomography. *J. Phys. E: Sci. Instrum.* **17**(9), 723–733K (1984)
3. R.P. Henderson, J.G. Webster, An impedance camera for spatially specific measurements of the thorax. *IEEE Trans. Biomed. Eng.* **25**(3), 250–254I (1978)
4. V.A. Cherepenin, A.Y. Karpov, A.V. Korjnevsky, V.N. Kornienko, Y.S. Kultiasov et al., Three-dimensional EIT imaging of breast tissues: system design and clinical testing. *IEEE Trans. Med. Imaging* **21**(6), 662–667 (2002)
5. A.P. Bagshaw, A.D. Liston, R.H. Bayford, A. Tizzard, A.P. Gibson et al., Validation of reconstruction algorithms for electrical impedance tomography of human brain function. *NeuroImage* **20**, 752–764 (2003)
6. A. Vonk-Noordegraaf, A. Janse, J.T. Marcus, J.G.F. Bronzwaer, P.E. Postmus et al., Determination of stroke volume by means of electrical impedance tomography. *Physiol. Meas.* **21**, 285–293 (2000)
7. J.R. Pere, J. Rosell, R. Bragos, O. Casas, *Electrical Bioimpedance Methods, Applications to Medicine and Biotechnology*, vol. 873 (Ann. N.Y. Acad. Sci, New York, 1999)
8. L.A. Geddes, L.E. Baker, The specific resistance of biological materials: a compendium of data for the biomedical engineer and physiologist. *Med. Biol. Eng.* **5**, 271–293 (1967)
9. B.H. Brown, A.D. Seager, The sheffield data collection system. *Clin. Phys. Physiol. Meas.* (Suppl. A) **8**, 91–97 (1987)
10. P. Metherall, D.C. Barber, R.H. Smallwood, B.H. Brown, Three-dimensional electrical impedance tomography. *Nature* **380**, 509–512 (1996)
11. N. Polydorides, W.R.B. Lionheart, A Matlab toolkit for three-dimensional electrical impedance tomography: a contribution to the Electrical Impedance and Diffuse Optical Reconstruction Software project. *Meas. Sci. Technol.* **13**, 1871–1883 (2002)
12. D.S. Holder, *Electrical Impedance Tomography: Methods, History and Applications*, Institute of Physics, 2004. ISBN 0-7503-0952-0
13. Draeger medical, Technical Data for Pulmo Vista 500, http://www.draeger.com/media/10/08/96/10089606/rsp_pulmovista_500_pi_9066475_en.pdf. Accessed 17 June 2011
14. M.S. Beck, R. Williams, *Process Tomography: Principles, Techniques and Applications*, Butterworth-Heinemann (19 July 1995). ISBN 0-7506-0744-0
15. P.D. Ledger, hp-Finite element discretisation of the electrical impedance tomography problem. *Comput. Methods Appl. Mech. Eng.* **225–228**(1), 54–176 (2012)

16. J.J. Cilliers, W. Xie, S.J. Neethling, E.W. Randall, A.J. Wilkinson, Electrical resistance tomography using a bi-directional current pulse technique 31 May 2001
17. Prof. J. Greene 'EEE485F Systematic Electronic Design course notes' Department of Electrical Engineering, University of Cape Town
18. J.G. Webster, *Electrical Impedance Tomography, Adam Hilger Series of Biomedical Engineering* (Adam Hilger, New York, USA, 1990)
19. D.S. Holder, Y. Hanquan, A. Rao, Some practical biological phantoms for calibrating multifrequency electrical impedance tomography. *Physiol. Meas.* **17**, A167–A177 (1996)
20. T.K. Bera, J. Nagaraju, A study of practical biological phantoms with simple instrumentation for electrical impedance tomography (EIT). In: *Proceedings of IEEE International Instrumentation and Measurement Technology Conference (I2MTC2009)*, Singapore, 5–7th May 2009, pp. 511–516
21. T.K. Bera, J. Nagaraju, Studying the boundary data profile of a practical phantom for medical electrical impedance tomography with different electrode geometries, ed. by O. Dössel, W.C. Schlegel, editors. *Proceedings of the World Congress on Medical Physics and Biomedical Engineering—2009*, Munich, Germany, WC, 7–12 Sept 2009, pp. 925–929 (IFMBE proceedings 25/II; 2009.)
22. L. Fabrizi, A. McEwan, T. Oh, E.J. Woo, D.S. Holder, An electrode addressing protocol for imaging brain function with electrical impedance tomography using a 16-channel semi-parallel system. *Physiol. Meas.* S85–S101 (2009)
23. D.S. Holder, *Clinical and physiological applications of electrical impedance tomography*, 1st ed., Taylor & Francis, 1 July 1993
24. F. Dickin, M. Wang, Electrical resistance tomography for process applications. *Meas. Sci. Technol.* **7**, 247 (1996)
25. D.R. Stephenson, T.L. Rodgers, R. Manna, T.A. Yorkb, Application of three-dimensional electrical impedance tomography to investigate fluid mixing in a stirred vessel. In: *13th European Conference on Mixing*, London, 14–17 April 2009
26. C.J. Kotre, Subsurface electrical impedance imaging: measurement strategy, image reconstruction and in vivo results, *Physiol. Meas.* **17**, A197–A204 (1996) (Printed in the UK)
27. P. Linderholm, L. Marescot, M.H. Loke, P. Renaud, Cell culture imaging using microimpedance tomography, *IEEE Trans. Biomed. Eng.* **55**(1) (2008)
28. R.H. Bayford, Bioimpedance tomography (electrical impedance tomography). *Annu. Rev. Biomed. Eng.* **8**, 63–91 (2006)
29. C.W.L. Denyer, *Electronics for real-time and three-dimensional electrical impedance tomographs*. Ph.D. thesis. Oxford Brookes University, Jan 1996
30. M. Peter, *Three dimensional electrical impedance tomography of the human thorax*. Ph.D. thesis. University of Sheffield, Jan 1998
31. J.T. Bushberg, J.A. Seibert, E.M. Leidholdt Jr., J.M. Boone, *The essential Physics of Medical Imaging*, 2nd ed., (Lippincott Williams & Wilkins, 2001)
32. T.K. Bera, J. Nagaraju, A stainless steel electrode phantom to study the forward problem of electrical impedance tomography (EIT). *Sens. Trans. J.* **104**(5), 33–40 (2009)
33. T.K. Bera, J. Nagaraju, Resistivity imaging of a reconfigurable phantom with circular inhomogeneities in 2D-electrical impedance tomography. *Measurement* **44**(3), 518–526 (2011)
34. T.K. Bera, J. Nagaraju, A reconfigurable practical phantom for studying the 2-D electrical impedance tomography (EIT) using a FEM based forward solver. In: *10th International Conference on Biomedical Applications of Electrical Impedance Tomography (EIT 2009)*, School of Mathematics, The University of Manchester, UK, 16–19th June 2009
35. J.G. Webster, *Medical instrumentation: principle and design* (Wiley, Hoboken, 1995)
36. T.K. Bera, J. Nagaraju, A simple instrumentation calibration technique for electrical impedance tomography (EIT) using A 16 electrode phantom. In: *Proceedings of the Fifth Annual IEEE Conference on Automation Science and Engineering (IEEE CASE 2009)*, Bangalore, pp. 347–52. doi:10.1109/COASE.2009.5234117. Accessed 22–25 Aug (2009)

37. D. Holder, *Electrical Impedance Tomography: Methods, History and Applications* (Series in medical physics and biomedical engineering Institute of Physics Publishing Ltd., 2005)
38. J. Malmivuo, R. Plonsey, *Bioelectromagnetism: Principles and Applications of Bioelectric and Biomagnetic Fields* (Oxford University Press, New York, Oxford, 1995) (Chapter 26, Section 26.2.1)
39. M.T. Erwati, N. Farrukh, Applications of electrical impedance tomography for imaging in biomedical and material technology, in *Proceedings of 2009 IEEE Students Conference on Research and Development (SCoReD 2009)*, UPM Serdang, Malaysia, 16–18 Nov 2009
40. S. Kumar, S. Anand, A. Sengupta, Impedence based image reconstruction of the field distribution inside the closed phantom using finite element method, (IJCNS) Int. J. Comput. Netw. Secur. **2**(7) (2010)
41. J.G. Webster, *Medical Instrumentation Application and Design*, 3rd edn. (Wiley India, 2007)
42. B.H. Brown, Electrical impedance tomography (EIT): a review. J. Med. Eng. Technol. **27**, 97–108 (2003)
43. H. Luepschen, T. Meier, M. Grossherr, T. Leibecke, J. Karsten, S. Leonhardt, Protective ventilation using electrical impedance tomography. Physiol. Meas. **28**, S247–S260 (2007)
44. J.A. Victorino et al., Imbalances in regional lung ventilation—A validation study on electrical impedance tomography. Am. J. Respir. Crit. Care Med. **169**, 791–800 (2004)
45. T. Meier, H. Luepschen, J. Karsten, T. Leibecke, M. Grossherr, H.Gehring, S. Leonhardt, Assessment of regional lung recruitment and derecruitment during a PEEP trial based on electrical impedance tomography. Intensive Care Med. July 25, 2007. (Epub ahead of print)
46. H. Smith et al., Electrical impedance tomography to measure pulmonary perfusion: Is the reproducibility high enough for clinical practice? Am. J. Respir. Crit. Care Med. **24**(2), 491–499 (2003)
47. M. Cheney, D. Isaacson, J.C. Newell, S. Simske, J. Goble, NOSER: an algorithm for solving the inverse conductivity problem. Int. J. Imaging Syst. Technol. **2**(2), 66–75 (1990)
48. I. Frerichs, J. Scholz, N. Weiler, *Yearbook of Intensive Care and Emergency Medicine*. Yearbook of Intensive Care and Emergency Medicine 2006. (Springer, Berlin, 2006). pp. 437–447. doi:10.1007/3-540-33396-7_40.ISBN978-3-540-30155-4
49. T. Luecke, F. Corradi, P. Pelosi, Lung imaging for titration of mechanical ventilation. Curr. Opin. Anaesth. **25**(2), 131–140 (2012)
50. E.L. Costa, R.G. Lima, M.B. Amato, Electrical impedance tomography. Curr. Opin. Crit. Care **15**(1), 18–24 (2009)
51. O.A. Mohammed, F.G. Uler, Detailed 2-D and 3-D finite element modeling of the human body for the evaluation of defibrillation fields. IEEE Trans. Magn. **29**(2), 1403–1406 (1993)
52. Institute for Applied Physics, *Italian National Research Council*, “Dielectric properties of body tissue,” (2007), <http://niremf.ifac.cnr.it/tissprop>
53. A. Adler, R. Guardo, Y. Berthiaume, Impedance imaging of lung ventilation: Do we need to account for chest expansion? IEEE Trans. Biomed. Eng. **43**, 414–420 (1996)
54. A. Boyle, A. Adler, W.R.B. Lionheart, Shape deformation in two-dimensional electrical impedance tomography. IEEE Trans. Med. Imaging **31**(12) (2012)
55. T.K. Bera, J. Nagaraju, A FEM-Based forward solver for studying the forward problem of electrical impedance tomography (EIT) with a practical biological phantom, in *Proceeding of 2009 IEEE International Advance Computing Conference (IACC 2009)*, Patiala, India, 6–7 March 2009
56. P. Ghaderi Daneshmand, R. Jafari A 3D hybrid BE–FE solution to the forward problem of electrical impedance tomography. Eng. Anal. Bound. Elem. **37**(4), 757–764 (2013)
57. H. Luepschen et al., Modeling of fluid shifts in human thorax for electrical impedance tomography. IEEE Trans. Magn. **44**(6) (2008)
58. B.H. Brown, A.D. Segar, The Sheffield data collection system. Clin. Phys. Physiol. Meas. (Suppl. A) **8**, 91–97 (1987)
59. J.G. Webster, *Electrical impedance tomography, Adam Hilger series of biomedical engineering* (Adam Hilger, New York (USA), 1990)

60. D.C. Barber, A.D. Seagar, Fast reconstruction of resistance images. *Clin. Phys. Physiol. Meas.* (Suppl. A), **8**, 47–54 (1987)
61. Data Sheet, AD811—High Performance Video Op Amp, Analog Devices, Inc., www.analog.com/static/imported-files/data_sheets/AD811.pdf
62. Data Sheet, XTR 111, Precision voltage to current converter, Texas Instruments., www.ti.com/cn/lit/gpn/xtr111
63. Data Sheet, ADRUINO UNO with AT mega 328 MC., www.atmel.com/.../atmel-8271-8-bit-avr-microcontroller-atmega48a-48...
64. T.K. Bera, J. Nagaraju, Studying the resistivity imaging of chicken tissue phantoms with different current patterns in Electrical Impedance Tomography(EIT). *Measurement* (2012). doi:10.1016/j.measurement.2012.01.002
65. N.M. Tamyis, D.K. Ghodgaonkar, M. Nasir, T.W. Tin Wui, Dielectric properties of human skin in vivo in the frequency range 20–38 GHz for 42 Healthy volunteers, [http://www.ursi.org/Proceedings/ProcGA05/pdf/KP.45\(0850\).pdf](http://www.ursi.org/Proceedings/ProcGA05/pdf/KP.45(0850).pdf)
66. J.D. Bronzino, D.R. Peterson, *Biomedical Signals, Imaging, and Informatics*, Fourth Edition, Chapter:15, (CRC Press, 2014), pp. 15–14
67. M. Anuloi, J. Brorzuino, D.R. Peterson, *Medical Imaging: Principles and Practices* (CRC Press, 2012), pp. 8–13, 8–14

Activity and Anomaly Detection in Smart Home: A Survey

U.A.B.U.A. Bakar, Hemant Ghayvat, S.F. Hasanm
and S.C. Mukhopadhyay

Abstract Activity recognition is a popular research area with a number of applications, particularly in the smart home environment. The unique features of smart home sensors have challenged traditional data analysis methods. However, the recognition of anomalous activities is still immature in the smart home when compared with other domains such as computer security, manufacturing defect detection, medical image processing, etc. This chapter reviews smart home's dense sensing approaches, an extensive review from sensors, data, analysis, algorithms, prompting reminder system, to the recent development of anomaly activity detection.

1 Introduction

Increasing demand for independent living lifestyle has motivated the research and development of smart home's monitoring technologies. The term "smart" in smart home defines the ability of household to monitor occupancy's activities and providing them necessary supports. This is to assist their daily activities, including spotting potential unsafe activities, such as falling or reminding their forgotten activity. The other similar names been used for the smart home are home monitoring, home automation, assistive living system and intelligent home. In the last few years, most of the smart home research projects were focusing on behaviour understanding or activity classifications from sensory reading. Recently, more attention is given on anomaly activity detection, activity prediction, incorporating contextual aspects including temporal, spatial and health status, concept drift, irregular behaviour adaptive learning and online data.

U.A.B.U.A.Bakar · H. Ghayvat · S.F. Hasanm · S.C. Mukhopadhyay (✉)
School of Engineering and Advanced Technology, Massey University,
Palmerston North, New Zealand
e-mail: S.C.Mukhopadhyay@massey.ac.nz

The rest of the book chapter is organized as follows: Sect. 1 initiated research motivation, Sect. 2 described in brief about smart home's sensors, Sect. 3 presented sensors data's features, Sect. 4 given the details of data analysis processes, Sect. 5 explained approaches in algorithms, Sect. 6 exhibited recent ongoing researchers and Sect. 7 summarized the chapter with conclusion.

2 Research Motivation

The increasing trend of independent living, also by the elderly and disability patients, the issue of world aging populations and the aggregate of people who diagnosed with dementia have motivated the ongoing research on smart home's monitoring system and technologies.

It is well reported that there is an increasing trend of people who chosen to live at home alone and independent [1–7]. The similar trend by the elderly and disability patients whose preferences were to stay independently at home without accompanying by any caregiver. This is due to the privacy concern of living with caregiver, the high cost of hiring home nurses and issue of nurses shortage [8]. Statistics has shown a sharp increasing figure of alone living people, by 80 % in 15 years, from 153 million in 1996 to 277 million people in 2011 [9]. It is also reported by United Nations, Department of Economic and Social Affairs (DESA), the aging world population is made up of increasing 10 % aged 60 + people and anticipated to be doubled by the year 2050 [10]. Further, world widely 18 million people have been diagnosed with dementia and the figure is expected to reach 35 million by 2050 [11]. In New Zealand, reported by the Government statistics, one-person households are estimated to be the quickest-rising household type. one person household supposed to increase by 240,000 from 363,000 in 2006 at 23 % to 602,000 in 2031 at 29 % [12]. Euromonitor a research firm estimates that the world will add up 48 m new alone household by 2020, a sharp increase of 20 %, as shown in Fig. 1.

However, the raising concerns are that the people who are living alone are most likely to get depression and at the higher risk of mental and physical disorder [13–15]. According to the news from The New Zealand Herald March 2013, a 37-year-old woman, Kirstine Hill, lay dead in her Hastings home for up to three weeks before her death was revealed. Police got her body in the kitchen of her semi-detached flat. A neighbour said afterward: “Like most people live here, we keep to ourselves” [12, 16].

It is impossible to cease every unfortunate event from happening at home, especially for independent home alone occupancies. However, prevention measures could be early established through the home monitoring system, to forecast the most likely unlikely activities, such as accidents and suicides, which are rare and anomalies. Smart Home's monitoring system has the capability to percept and understands occupancy's daily activities, according to the occupancy's actions,

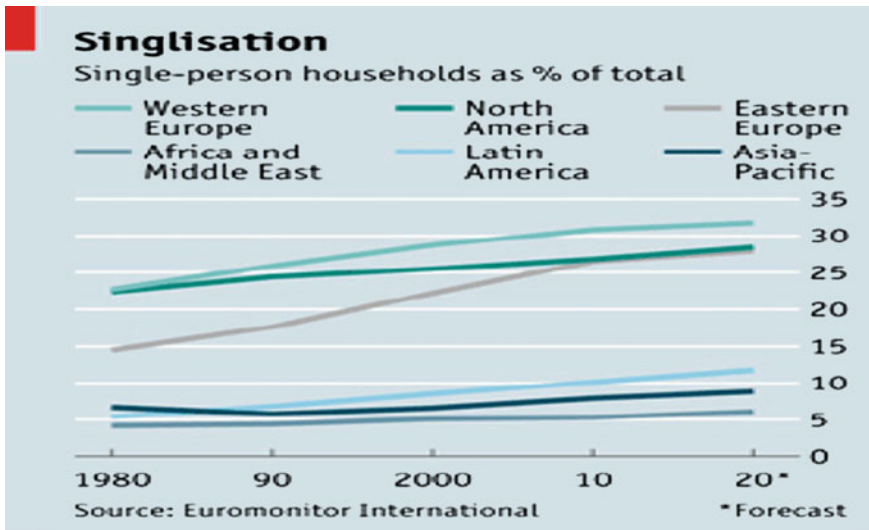


Fig. 1 Euromonitor, a research firm, forecasts that the world will add up 48 m new alone household by 2020, a sharp increase of 20 % [178]

movements and interactions with household’s objects. The system generates activity patterns that are demonstrating the wellness’s status of an occupancy, and forecasting occupancy’s future behaviours. In any foreseen ill-fated events or health related issues detected or forecasted, such information is sent to the caregiver to alert and prevent hazardous activities from happening [17–29].

Presently there are quite numbers of the smart home project being established world widely. The researchers and developers are ranged from in lab-prototypes to industrial commercials. Examples are the AHRI (Aware Home Research Initiative) at Georgia Institute of Technology [30], CASAS (The Center for Advanced Studies in Adaptive Systems) at Washington State University [31], AgingMo at University of Missouri [32], PlaceLab at MIT [33] and Smart home Lab at Iowa State University [34]. These smart home project technologies monitor occupancy’s daily living activities, enhancing comfort and deploying heterogeneous sensors for better percepts daily activity’s contextual aspects. Obtrusive camera sensors are included in their project as well. Nevertheless, they are relatively few numbers of households chosen to install and apply smart home’s monitoring system. The main reasons have been the complexity of the requirements and installation processes, costs and privacy obtrusiveness related issues [35–59].

In smart home’s monitoring system, sensors have played an important role in observing and understanding occupancy’s daily activities. In the next section, smart home’s sensors will be reviewed accordingly.

3 Smart Home Sensors

A sensor is a small node and inexpensive device that reasonably use to sense occupancy's activity, movements or health status. These "biological measures" from occupancy are then transformed into electrical signals, digitalized from analog and eventually send to the end point microcontroller for data processing purposes.

A smart home is equipped with sensors to perceive, monitor and understand occupancy's daily activities. The sensors are equipped around the household with uniquely identified identity (ID), together with time-stamp to indicate and record of occupancy's activity. The sensors are equipped in both modes, wired and wireless and communicating with ZigBee and WiFi protocols. The sensors equipped in a smart home are ranged from the camera, microphone, body-worn sensors, temperature sensors, pressure sensors and motion detectors. These sensors could broadly categorized into two groups, obtrusive type visual sensing [60] and none-obtrusive type dense sensing [61]. The latter approach is popular than the former, due to the reason as the name implied, the occurrence of such sensing devices do not intrude user's privacy and could be attached to any household object without the burden to remind the user to wear and carry them everywhere. The PIR sensors, motion detectors, door/window entry point sensors, electric usage power sensors and pressure sensors are an example of nonintrusive sensors. And as opposing to these, body worn sensors [62], cameras and microphones [63] are examples of obtrusive sensors. These none-obtrusive type dense sensing paradigm is practically cheap, reliable, readily available and could be deployed in large quantities [64, 65–92].

The device installation process is fairly easy that could be done by the by the informal caregiver or even by occupancy themselves. The sensors are scattered in such a manner so that system get every essential value from every corner of the ambient environment which is applicable to wellness determination of an individual who stays there. Figures 2, 3 and 4 show the sensor units placement to the smart home, these sensing units transmit their data through RF module XBee series-2 end-device to XBee Coordinator connected (XBee coordinator connected to laptop through USB connection) to home gateway server laptop. The data from local MySQL server is raw data, from this raw data information is extracted through software. The software is designed according to the individual requirement of data extraction. The Visual Studio C# graphical user interface is designed to upload raw data to MySQL server. From local server that data will be analysed and uploaded to the website with the help of internet [93–96].

All these raw sensing data received by local home gateway server is analysed via data mining and machine learning algorithms to generate the wellness information and pattern. In the succeeding, section will review the sensory reading's data, the features and characteristics (Fig. 5).



Fig. 2 PIR sensor placed at front door [179]

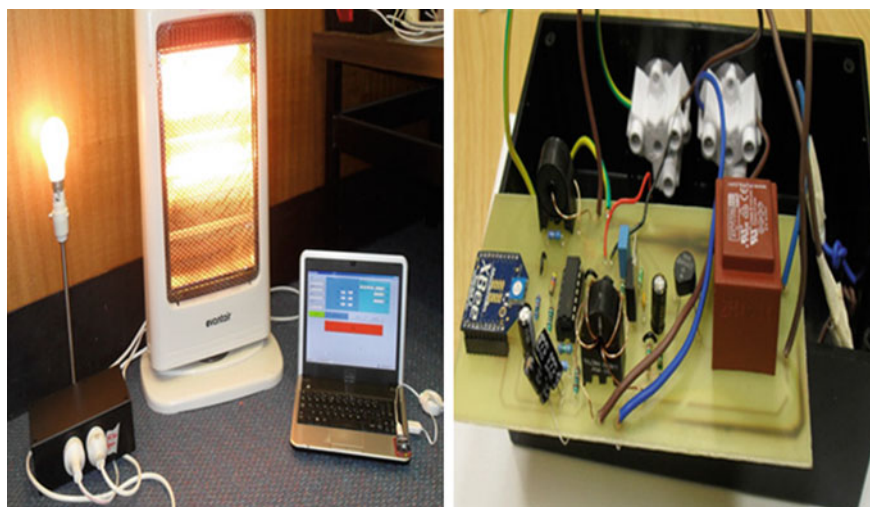


Fig. 3 Intelligent building—smart power management and WSN [93]

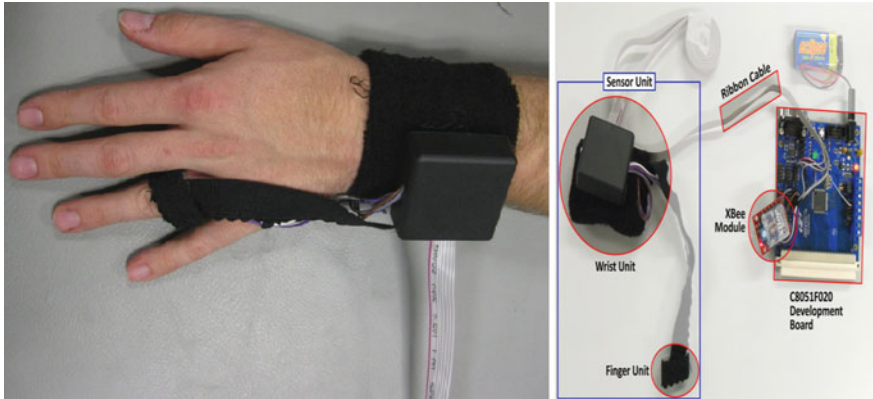


Fig. 4 Wireless sensors network based physiological parameters measurement [94]

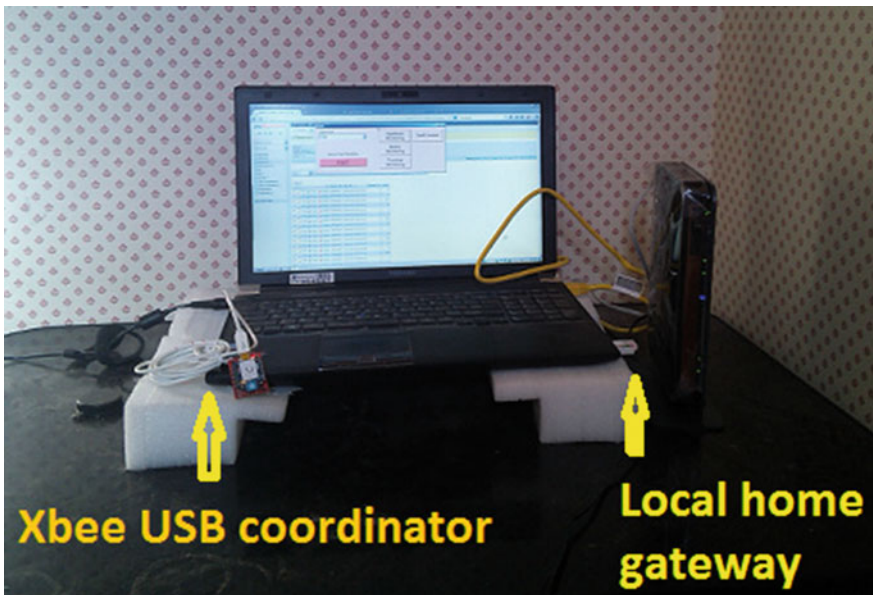
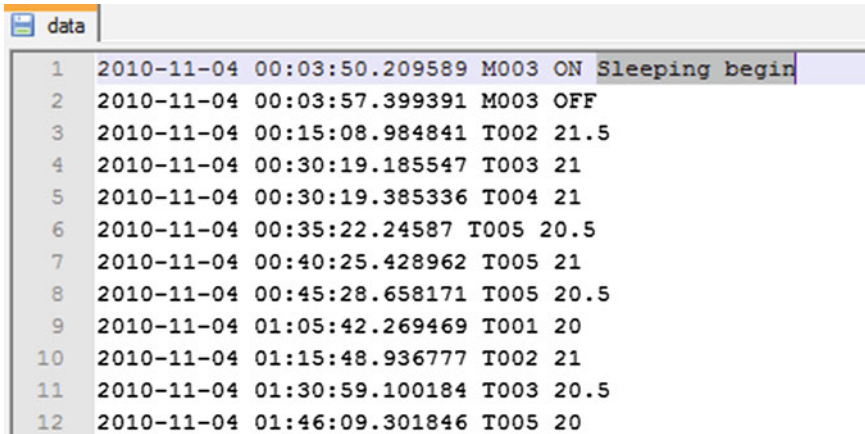


Fig. 5 Local home gateway server [96]

4 Sensory Data

The smart home generated sensory reading's data is naturally noisy, in large volume and multidimensional, temporal ordered, ununiformed and in unending sequence. These unique features have challenged the traditional data analysis methods as far as impossible to process these data manually. The unlikely situation might come



	date				
1	2010-11-04	00:03:50.209589	M003	ON	Sleeping begin
2	2010-11-04	00:03:57.399391	M003	OFF	
3	2010-11-04	00:15:08.984841	T002	21.5	
4	2010-11-04	00:30:19.185547	T003	21	
5	2010-11-04	00:30:19.385336	T004	21	
6	2010-11-04	00:35:22.24587	T005	20.5	
7	2010-11-04	00:40:25.428962	T005	21	
8	2010-11-04	00:45:28.658171	T005	20.5	
9	2010-11-04	01:05:42.269469	T001	20	
10	2010-11-04	01:15:48.936777	T002	21	
11	2010-11-04	01:30:59.100184	T003	20.5	
12	2010-11-04	01:46:09.301846	T005	20	

Fig. 6 Example of multidimensional sensory data with features of date, time, and sensor’s location based ID and annotated activity label gathered by CASAS dataset [31]

about when the sensor reading is imprecise and failed, these could cause the generated data to be noisy, redundant and the having missing values. The ununiformed and unending sensory data is also needed to be handled on the fly as the streaming data. The temporal ordered sensory data isn’t really in time series form. While the time series data has uniformed time intervals, the smart home generated sensory reading data appeared to be in ununiformed time interval. As the sensors are being activated contextually random when the occupancy is carrying out their non-deterministic daily activities. These have caused the start time and end time of each sensor’s activation to be anonymous and uncertain in values. The Fig. 6 below shows an example of sensory reading generated data taken from CASAS dataset [31] with several features such as date, time, sensor ID, sensor status and activity label. Nonetheless, the raw data provided by the sensory readings are often useless and require further analysis.

5 Data Analysis

Occupancy activity is complex and goal-oriented. The activity could be as simple as the single goal of sequential collection events, and could be as complex as multiple goal non-sequential collection of events. Concurrent and Interleaved activities are in the category of complex activity. The example in concurrent activities, a professor in his activity of attending a lecture theatre would pass by the printer room to print lecture notes. Here, the two goals in an activity are attending lecture theatre and print lecture notes. An example of interleaved activity is, when the phone is ringing while a person is cooking in the kitchen. The person has to “pause” her cooking activity and pick the phone calls, and then “resume” the cooking activity [97].

Due to the temporal-ordered nature of sensory data, activity classification problem possessed the same challenge of Sequence Classification problem (SC). Sequence Classification (SC) technique is mature in many domains such as analysing genomic data (e.g. to understand function of different genes and proteins), time series data (e.g. gesture and motion recognition) and text data (e.g. for information retrieval). There are basically three general types sequence classification strategies: (1) Feature-Based (e.g. k-gram, pattern-based feature selection), (2) Sequence Distance-Based (e.g. using “distance function” to measure similarity between sequence together with existing classification techniques, KNN, SVM) and (3) Model-Based (e.g. Naïve Bayes, Markov Model, HMM). However, to extract feature from sequential data is non-trivial, because basically there are no explicit features in the sequential data and difficult to transform sequence into a set of the feature even by using many available feature selection methods. Further, in sequence classification, it is desirable to predict the sequence of the label (e.g. using HMM and CRF) than the single class label (e.g. using Naïve Bayes) [98].

Sensory data is analysed at two levels, lower sensory level and higher activity level [99]. The former lower level analysis is to extract (classify) activities from sensory readings and the later higher level analysis is to analysed the extracted activity labels for further decision-making processes. In low level analysis, depending on the availability of data instance (annotated data), supervised learning is used to learn the model of the data instance, well known as activity recognition (AR) process and unsupervised learning is used to discover activity labels without the presence of data instance, popularly known as activity discovery (AD) process. Once activity labels are known, at higher level analysis, these activity labels are reused for further analysed for potential hazardous activities (anomaly) detection or as prompting reminder system.

i. Low-level sensory data analysis

Occupancy’s activities are not directly observed, only observation from sensors, to understand occupancy’s daily activities, observations made by low-level sensory data is needed to be classified as activities. However, beforehand of getting into the classification process, the raw data gathered from low-level sensors is required to go through several data analysis phases such as pre-processing, segmentation and feature extraction. Referring to the Fig. 7 below, the data gathered from acquisition phase is sent to pre-processing phase for filtering noises, redundancies and missing values. Subsequently, as the data is arriving in unending nonuniformed temporal ordered, the segmentation phase is applied to divide and conquer the whole arriving dataset. An example of segmentation technique is fixed length sliding window. Several data segmentation strategies were compared in [100]. Each segmented data’s size is still large, and multidimensional (contains many attributes). Moreover, it is infeasible to classify the whole dataset into activities, as this would slow down the classification process. Successively, feature extraction [101] phase is implemented to reduce the data dimensionality through selecting only significant data dimension (attribute) for the later classification phase. The PCA (Principle Component Analysis) is an example of feature extraction method that selecting only higher correlated features from a particular dataset. Alternatively, data characterization

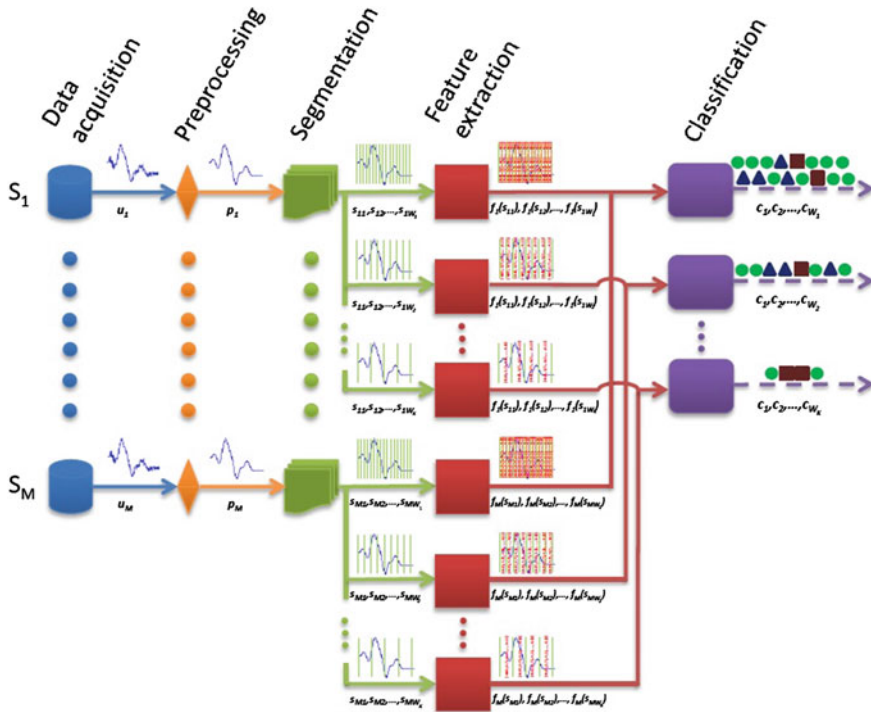


Fig. 7 Low-level data analysis process [180]

(e.g. clustering) could be a potential strategy to reduce data dimensionality, as data with similar characteristic are group together before taken into the classification process. In complement to this, the data representation is also a key strategy for organizing data effectively before getting into activity classification process, and several data representation strategies were compared in [102]. Eventually, pre-processed, segmented and feature extracted data is sent to the classification phase [103–115].

Classification phase is the process of understanding occupancy’s activity from sensory generated data. It encompasses (1) activity recognition (AR) process and (2) activity pattern discovery (AD) process [116, 117]. All the previously pre-processed, segmented and feature extracted data is presented and given to the classifier (learning system) in the form of “token”, as an abstraction of sensor properties. Ranges of techniques could be used for activity classification, these including statistics, data mining, machine learning, ontologies, information theory and more. In machine learning paradigm, activity classification is developing a model by a training set of extracted features instances. During the testing phase, the unseen instances (from time window) is used to evaluate the built model [101].

Occupancy activity is complex and goal-oriented. The activity could be as simple as the single goal of sequential collection events, and could be as complex as

multiple goal non-sequential collection of events. Concurrent and Interleaved activities are in the category of complex activity. The example in concurrent activities, a professor in his activity of attending a lecture theatre would pass by the printer room to print lecture notes. Here, the two goals in an activity are attending lecture theatre and print lecture notes. An example of interleaved activity is, when the phone is ringing while a person is cooking in the kitchen. The person has to “pause” her cooking activity and pick the phone calls, and then “resume” the cooking activity [97].

Depending on the availability of data instance, as a sample (annotations), activity classification (modelling) could be divided into supervised activity recognition (AR) and unsupervised activity discovery (AD).

a. Activity Recognition (AR)

Activity recognition (AR) is the process of mapping predefined activity classes to the sensory reading generated data [117]; it is a Supervised Learning approach. The main purpose of classification is to identify occupancy activities in the household from temporal-ordered motion sensors. The algorithm could range from Decision Tree (DT), Neural Network (NN), Instance-Based learner (IB), Support Vector Machine (SVM). The algorithm differ in how the classifier handles the data, either the class labels have discrete or continuous values, whether there is any error or missing values in the data, how much data is available for training and how to represent the classifier output [118].

b. Activity Discovery (AD)

Activity Discovery (AD) [117, 118] is the data analysis process of discovering knowledge or desired data pattern by finding the frequency of data co-occurrence in generated sensory reading. It is an Unsupervised Learning approach. An example is association rule mining (ARM) analysis. If there are strong correlations between the co-occurrence of data (multiple attributes data), then these data could be represented in IF-THEN rules. Activity Discovery (AD) possessed the challenge of sequence mining or searching frequent sequence from temporal ordered sensory data. An example of sequence mining is the Episode Discovery (ED) Algorithm [119] and Greedy Search by [117]. Episodic discovery [119] moves a predefined size of the window across sensory data to collect potentially interested sequences. Later, MDL (Minimum Description Length principle) is applied to evaluated the sequences (or episodes) based on their frequency of occurrence, length or periodicity. Greedy Search [117] is used to find a potential sequence (i.e. sensor’s events) that best compressed the input dataset (remove redundancy). The searching strategy is by searching the sequence ordered by length, due to the reason given that the size of the potential sequence is exponential the size of input data.

ii. Higher level activity data analysis

The eventuality output of low-level data analysis is occupancy’s activities or labels, such as sleeping, eating, showering, entering or leaving home. These different activity labels could be further analyse from high-level context, for more information about occupancy’s model of lifestyle (living habit). Particularly in analysing occupancy’s anomaly activities and prompting useful information to the caregiver. Occupancy’s anomaly activities are unsafe activities such falling,

suffering a stroke or unconscious at home. A prompting system could use this observation to prompt alert to the next of keen or a remote caregiver for further assistance. Also, a prompting could be used as a reminder system [120–125].

a. Anomaly detection

Besides behaviour modelling, detecting **behaviour changes** (anomaly detection) is another crucial and challenging task. **Anomaly detection** is the process of detecting behavioural “changes” of occupancy’s usual lifestyle pattern, and the concern has been unusual data is very rarely seen to be modelled as abnormal behaviour for classification. And this has possessed the challenge of 1-class classification problem rather than the traditional 2-class (binary) classification problem. The detecting of changes could involve the changes in different contextual aspects, such as spatial (location), temporal (time and duration), time’s order, activity’s order, health’s status and more. In essence, behaviour detection is the challenge of modelling occupancy’s behaviour from sensory data and anomaly detection is the challenge of how to detect changes of usual behaviour that also possessed the challenge (creativity) of behaviour modelling technique that could to effectively capture usual lifestyle’s pattern (attributes) for changes (anomaly) detection.

There are basically two ways to detect behavioural changes, **Profiling** and **Discriminating**. **Profiling** is modelling normal behaviour and considering any incoming new input that doesn’t match this model (the deviation) as an anomaly. **Discriminating** is learning anomaly data from historical data and searching for a similar pattern from incoming new input data to consider anomaly. **Profiling** strategy is more realistic as anomaly data is rarely seen (scarcity) in real life, to provide learning sample instances for the classifier [126].

Anomaly detection is still at infancy in smart home and much more mature in other domains such as intrusion detection, fraud detection, medical, industrial defect detection, image processing, text data and more. Ranges of machine learning techniques been used for anomaly detection, such as classification (neural network, Bayesian, SVM, rule based), nearest neighbour (density based), clustering, statistical (parametric: Gaussian, Regression, non-parametric: Histogram, Kernel function), information theory, spectral and more. In smart home domain, the detection of changes (anomaly) been majorly used for elderly’s safety alert and assistive technology for cognitive impairment such as dementia patients [127].

There are basically three ways to decide for anomaly data. (1) Point anomaly, (2) Contextual anomaly and (3) Collective anomaly. First, point anomaly is the simplest and most popular approach to decide anomaly through a predefined threshold value. Whenever an incoming data instance is exceeding the normal data’s threshold value, then it is an anomaly. Example, a money transaction that beyond the limit of normal range expenditure. Second, the contextual anomaly is making a decision based on the contextual aspect (e.g. temporal and spatial) of the data. Example, a money transaction of \$1000 for shopping is normal in the context of seasonal celebration but otherwise if it happened on the weekly basis context. Third, collective anomaly, the data instance would only be an anomaly in a collection but may not be anomaly by individually themselves. Example sequence of actions from user’s activity in the computer: [buffer-overflow, ssh, ftp]. These

actions would not be anomaly individually, but otherwise when the actions are existing together in a form of sequence collections, and is representing web-based attack of copying file to remote destination via FTP protocol. The output of anomaly detection is either in a score unit (threshold's numerical value) or a label as a categorical unit, e.g. normal or abnormal [127].

b. Prompting System

Further, the eventual of activity labels from classification's output and spotted anomalous activities could be integrated and reuse with the decision-making process to build a complete system for prompting or a reminder. A prompting system is a systematic system taken input from classified activity labels, look for differences between expected and observed activities and reasons about "whether", "how" and "when" to prompt reminder to the caregiver (OT—Occupational therapists, medical staff, neighbours or family). Also could be prompting information to the occupancy themselves, to assist their daily livings. An example, the authors [128] have integrated activity classification and decision making with artificial intelligence for prompting system.

The Markov decision process (MDP) and (POMDP) models are two most successive models been used in data-driven approaches for prompting system. Example MDP is used in [129] for scheduling and [130, 131] for task assistance for daily activities. POMDP is used in [132] together with integrated high-level knowledge from the psychological analysis.

In knowledge-driven approaches, ontologies been mainly used conceptually representing (model) sensors, temporal-spatial contexts, activity labels for different purpose such as data integration, interoperation, sharing, context management and decision making support [133–134].

Besides activity labels, domain knowledge plays an important role as an input to a prompting system. Example in automated health monitoring system, Patel et al. [135] system estimating Parkinson's disease patient symptom's severity by automating the health assessment process, through comparing perception from accelerometer sensor with assessment criteria provided by domain expert for activity profiling [61]. More works on prompting system are [136–137].

iii. Other challenges: Adaptive, Trend and Concept Drift

Besides low level and high level data analysis, due to non-deterministic and of occupancy's activities, to understand accurately occupancy's activities has possessed the next challenged of adaptability of activity modelling technique to the irregularity of occupancy's behaviours pattern. E.g. an occupancy may wake up late in the morning or cleaning the household at a different time than the regular habit. The failing of adapting may result in system prompting false warning alarm for anomaly activities. Example works are [138, 139].

Another advantage of having temporally ordered criteria in sensory data are that the temporal component could be used for analysing trend. Trend is a kind pattern that tells the "concept drift" [140, 141] of the data, indicating how the data changes over time: either steadily increasing, decreasing, cyclic or remain fairly stable.

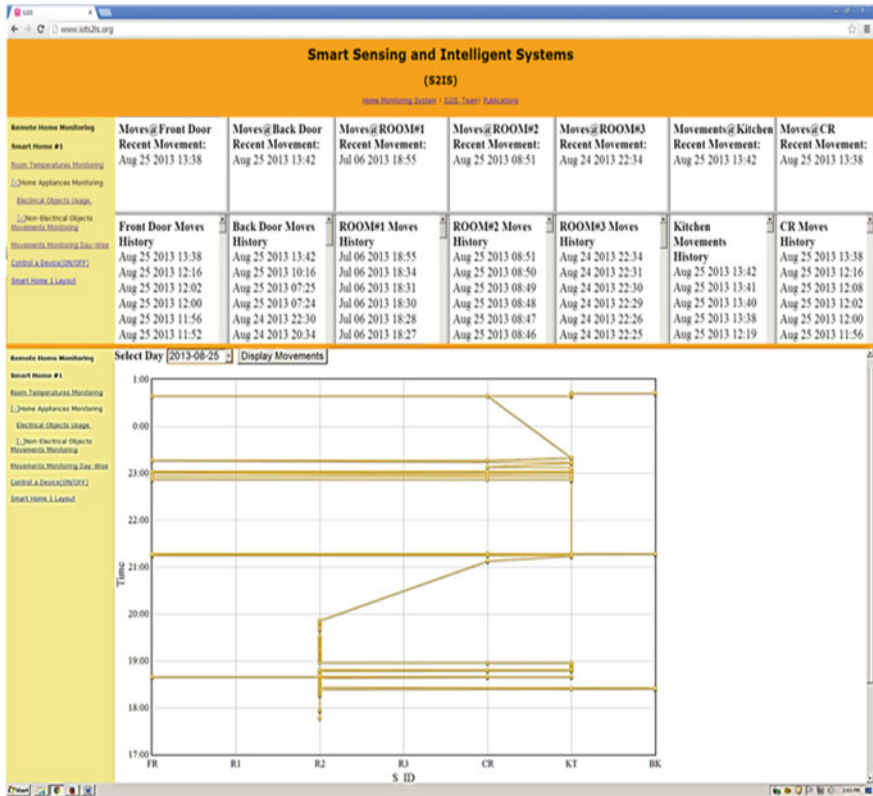


Fig. 8 Online smart home monitoring website [93]

At present, data analysis works have given most attention toward “health monitoring” and “activity recognition” and less attention has been given to activity prediction and online data processing (data stream) [142]. Figure 8 shows an example of web-based smart home monitoring system [93].

The subsequent section will review the algorithms used for data analysis.

6 Algorithms for Data Analysis

Anomaly data analysis is the process of finding a pattern that do not conform to the existing normal activities patterns or is referring to detecting of changes in occupancy’s activity’s routine. The main approaches to detect anomaly are classification based, clustering based and statistical based. Mainly researches been done were on inactive periods of time [143], falls [144] and identifying a disease [145–146].

Traditional activity classification (modelling) techniques could also detect anomaly activities. The anomaly activity is identified as a new activity that deviate from norm (or known as outlier). And the techniques could range from rule-based reasoning [147–152], probabilistic model [150], data mining [151, 152], sensor network based decision support [153] and video-based monitoring [154]. Nonetheless, such approach is limited of detecting an only “ongoing” event, without the capability of detecting future anomalies ahead (predicting future event). In due course, a health monitoring system fails to detect a sudden attack of sickness and only notify a doctor when the disease is attained her mature state [155].

Anomaly detection based on clustering approach could generally be categorized into three method. (1) Group Cluster, (2) Near Cluster Centroid and (3) Small/Sparse Cluster. In the first approach Group Cluster, normal data (profile) belong to the group cluster, and any clusters that do not fit into this group cluster is treated as anomaly. This approach has the advantage of could be implemented by any clustering algorithm. The second approach Near Cluster Centroid is similar to the Group Cluster approach, with an extra computation of “score” to determine the “distance” between normal (profile) group and anomaly group. The third approach Small/Sparse Cluster used “cluster’s size” and “threshold value” are used to determine anomaly. A cluster group is an anomaly when the cluster size is below the determined threshold value [102].

Modelling occupancy’s daily lifestyle (activity modelling/activity recognition) approaches could generally be classified into two main categories based on the sensor type (data input). The first is Visual Sensing paradigm, exploiting computer vision techniques; example is pattern recognition. The second is Sensor Network that take advantage of unobtrusive sensors that could attach to either to the actor (wearable sensors) or to the environment (dense sensing).

Dense sensing paradigm has gained the most attention by smart home projects due to the reason that it is unobtrusive, easy to install, low power and low cost. Dense sensing paradigm could further be categorized into two main divisions, data-driven and knowledge-driven.

A data-driven approach is the method of modelling occupant behaviour directly from the gathered raw data through observation sensors. The generative way of data-driven approach build a complete description of the sensory input data through statistical probabilistic distribution and discriminative tactic of data-driven approach mapping input (data) to output (activity labelling process). Although these approaches found to be effective in dealing with noise and uncertainty of sensory data, however, the disadvantages has been data scarcity (or cold start problem) due to the requirement of training large datasets and the difficulties of applying this method on individual occupant basis. Also, the drawback of the generative probabilistic method has been a static model and subjective to the configuration.

Logical formalism method has been the alternative to overcome the cold start problem. Example are event calculus, lattice theory and ontology modelling. “Activity model” being created in this way doesn’t require a large amount of observation data and training process. Nonetheless, the drawback has been logical

Table 1 General categorial of anomaly detection techniques

Algorithm	Pros	Cons	Reference
Classification (Supervised)	• Could measure model’s accuracy through confusion matrix	• Needs data instance for training • Human’ biased problem in labelling data	[143]
			[181]
Clustering based (Unsupervised)	• Do not need data instance as a sample	• Performance depends on the assumption about data distribution • Not optimized for anomaly detection [146]	[182]
			[183]
Statistical based (Unsupervised)	• Do not need data instance as a sample	• Performance depends on the assumption about data distribution • Not optimized for anomaly detection [146]	[184]
			[185]

formalism method is not suitable to deal with noisy and uncertain sensory data gathered from smart home. Alternatively fuzzy logic approach was used.

Table 1 presents the main types of anomaly detection techniques and Table 2 represents the traditional activity classification approaches that also been used as anomaly detection.

Table 2 Traditional activity classification (modelling) approaches [60]

	Knowledge-driven approach (KDA)			Data-driven approaches (DDA)	Discriminative
	Mining-based	Logic-based	Ontology-bbased	Generative	
Model type	HMM, DBN, SVM, CRF, NN	Logical formula, e.g. plans, lattices, event trees	HMM, DBN, SVM, CRF, NN	Naïve Bayes, HMM, LDS, DBNs	NN, SVM, CRF, Decision Tree
Modelling mechanism	Information retrieval and analysis	Formal knowledge modelling	(un)supervised learning from datasets	(un)supervised learning from datasets	(un)supervised learning from datasets
Activity recognition method	Generative or discriminative methods	Logical inference e.g. deduction, induction	Generative or discriminative methods	Probabilistic classification	(un)supervised learning from datasets
Advantages	No “Cold Start” problem, using multiple data sources.	No, “Cold Start” problem, clear semantics on modelling and inference	Shared terms, interoperability and reusability	Modelling uncertainty, temporal information	Modelling uncertainty, temporal information, Heuristics
Disadvantages	The same problem as DDA	Weak in handling uncertainty and scalability	The same problem as DDA	“Cold start” problem, lack of reusability and scalability	“Cold start” problem, Lack of reusability and scalability

7 Recent and Ongoing Method on Anomaly Detection

There are ranges of techniques been used for anomaly detection, these include statistical: Histogram, GMM, probabilistic: HMM, Machine Learning: Feed forward, Recurrent Neural Network, Fuzzy System, Support Vector Machine (SVM), One Class Support Vector Machine (OCSVM), Support Vector Data Description (SVDD), Data mining: clustering, association rules, FCM clustering, K-means, agglomerative hierarchical clustering [102].

There were various approaches in the past to detect anomaly activities of occupancy in the smart home domain. The techniques could range from how activities are extracted from sensory data, how to model normal data (profiling) when anomaly activity samples are rarely seen from historical data and how to capture activity's duration. Most of the authors claimed that occupancy's activities follow some "regular pattern" that could be learned from probabilistic models. Cardinaux et al. (2008) [126] proposed individual profiling strategy with Gaussian Mixture Model (GMM) to form normal data. This approach is better than previously Histogram techniques [156–158] due to the reason that GMM could captured attribute's dependency. Example: When capturing both attributes of time and duration, an activity of watching TV at 8 am (time) for 5 h (duration) could be an anomaly. Behaviours were extracted by the author from the sensors through Rule-Based algorithm, e.g., <time-in, time-out, duration>. Some authors claimed that Hidden Markov Model is the best suit noisy domain for smart home. Instead of using GMM, Monekosso et al. (2009) [159] employed HMM as general profiling strategy by inputting clusters of "daily activity routines" into the model. They claimed that their way of unsupervised activity extraction strategy was better than traditional supervised method. Mori et al. (2007) [160] chosen to detail the individual profiling strategy by profiling each activity's frequency of occurrence (how much the activity label occurred at a certain time) through probabilistic density model. SDLE and SDEM algorithm used by outlier detection engine SmartSifter were used here for this purpose and activities were extracted through HMM and Segmentation, in which later the alpha values were group into k-means clusters to form labels. Nevertheless, their approaches were judged by several authors for the incapacity of accurately measure anomaly behaviour because same activities have different activity's duration. Example, a collection of temporal ordered sensor events: "door", "fridge", "sink", "bench", "fridge", "door" may represent the activity of preparing cereal. However, same event collection may represent the activity of making toast if take into considering the activity's duration. Because the duration of making toast is longer than preparing cereal. Kang et al. (2010) [161] had clarified that H-HMM (Hierarchical Hidden Markov Model) is better than any traditional flat—HMM when considering the aspect of capturing activity's duration. The authors assumed that sub-activities in the lower hierarchical level should last shorter than the coverage top main-activities (overlapping time zone), because the main activity is formed by the combination of sub-activities. However, Chung and Liu (2008) [162] went further into considering the contextual aspect of hierarchical

structure through HC-HMM (Hierarchical Context - HMM), and employed three HMM (λ_{SC} , λ_{BR} , λ_{TR}) at different contextual later to reason activities. The authors considering three contextual aspects of spatial, temporal and their novel work on activity context. D-HMM is used to capture activity duration. Duong et al. (2005) [163] uniquely develop their own duration model with discrete Coxian distribution and claimed that their technique is better in computation time and generalization of error in comparing to any classical method by explicitly modelling the duration, which used “multinomial distribution” and required large number of parameters for learning (training and classification). Luhr et al. (2004) claimed that classical way of using HMM as prediction model to detect anomaly activity have failed to detect similar activity sequences. Especially when the activity duration is lesser than or greater than the normally observed duration. Hung et al. (2010) [164] combined the advantages of HMM in handling sequential data and discriminative model of SVM to detect anomaly activities.

Forkan et al. [155] had pointed two disadvantages of traditional anomaly detection system. First, the incapacity of predicting future trends (anomaly ahead) that causing the failure of detecting disease’s sudden attack and the second, the incorporating of single context for decision making had caused high false alarm rate. Patient’s sickness could not attained during the mature state and the observation of diseases e.g. diabetes must incorporating others context besides the sugar level. Consequently, the authors have developed an “integrated system” by using HMM and Fuzzy Logic to detect “multiple contextual activities” and “predict” the outcome by combining all the information. In monitoring daily routine, the authors have used Gaussian Mixture Model and incorporating health status as context by correlating the status with daily activities. The system could detect anomalies in activity, location, routine (collective anomaly) and changes of health status changes respectively. The eventual result is analysed again by sending the result to the Fuzzy Rule model for final prediction. The authors used two approaches for detecting anomalies, depending on the availability of anomaly data instance as a sample for training. The first approach, the 1-class HMM is employed when anomaly data instance is unavailable, and the whole data set is used as normal data (Profile). A threshold value is defined to decide normal- anomaly boundary. During the testing phase, the log joins probability “ $\log P(O | \lambda)$ ” is used as an evaluation measure, by comparing this value with a predefined threshold value to alert anomaly. The second approach, both normal and anomaly data instances are used to model two hidden states HMM (2-HMM). During the testing phase, Viterbi algorithm [165] is used to find the best hidden state configuration that represent the “predicted” two hidden states, to define which activities are anomaly from the incoming, unseen testing data set.

Wong et al. [166] hypothesized that the best way to capture profile data is to define the most likely and most frequent place, i.e. region occupancy that the occupant could be there for particular his/her activity and the most frequent visited place to detect occupant’s motion, i.e. Concurrency hotspot. The behavioural model is captured based on the histogram of 30 min chunk per day (24 h), producing a

total of 48 histograms per day. The anomaly (behavioural changes) is detected based on the changes of daily histogram through Euclidean distance.

Ordenez et al. [167] used Bayesian Statistic to model the distribution of the next features and estimated three probabilistic features: the sensor activation likelihood (SAL), sensor sequence likelihood (SSL) and sensor event-duration likelihood (SDL) in wireless sensor network domain. Anomaly is detected based on the changes of health status context.

Novaik et al. [168] simply used Self-Organizing Map (SOM) to cluster and modeling activities. After the training process, any activities that deviate (not fitting) from this cluster group is considered as anomalous.

Song et al. [169] claimed that main challenging aspect to detect anomaly activities from sequential data (i.e. temporal ordered) is that the anomaly data instance is scarce, from that have caused the data distribution to be in “1-class” distribution naturally. The “1-class” distribution machine learning, is the technique of using training data collected from only 1-class distribution and to predict whether the given unseen new data sample is drawn from the same distribution. The second challenge is that the difficulties of capturing the “dependency structure” in the sequential data [170]. As a solution, the authors have proposed 1-class Classification with Support Vector Machine (SVM) and at the same time capturing the dependency structure of the data with CRF (Conditional Random Field). 1-class SVM is done by making the solution space of 1-class data distribution as tight as possible.

Novaik et al. [99] applied Self-Organizing Map (SOM) as unsupervised classification approach to model activities and Markov Model to predict next potential activity. Changes in daily activity patterns are detected as anomalies, and could broadly categorized into three types: anomalies due to long periods of inactivity, lacking activity and the unusual presence of activity.

Khan et al. [171] had proposed three distinct approaches of Hidden Markov Model (HMM) to detect unusual temporal events from the sensor network. The first two approaches used log-likelihood threshold to detect the deviation of anomaly events from normal when the first approach modelled separately each event with HMM and the second approach modelled the whole dataset with 1-class HMM. The third approach modelled the normal events with 1-class HMM and build anomaly event model through approximation by varying the covariance of the observation anomaly events. Anomaly detection is conducted during the testing phase.

Aztiria et al. [172] developed a system that could identify possible “shift” of profile data. A “shift” or known as “concept drift” is the change detected, when comparing occupancy’s new activities with the recorded frequent activities represented from the profile data. The modification steps required to turn the frequent activity to newly observed activity were used as a measurement metric to decide whether the newly observed activity is to be classified as anomaly.

Hoque and Stankovic [173] have asserted the reasons of false alarm (false positive) in anomaly detection was caused by (1) the ignoring of correlation

(dependency) between activity and day [174] to better understand the trend of change and (2) the lack of “semantic rule” to filter false positive through defining logical deviations of regular activities. The authors considered both threshold based point anomaly and collective based anomaly detection. They reasoned that each independent activity instance would not be sufficient for anomaly classification without considering the same instances that existed in different days. They defined features for activity instances in different days, combine them and develop a profile model for normal activities. Any deviation from these profile models is to be considered as anomaly activities. Features are the relative order of activities or causal relationship. E.g. Drinking is happened before/after/during Eating. The authors have also included social and healthy norms that defined by an expert as the contextual aspect of anomaly detection. Example doesn't brush teeth in a day and doesn't wash hands before and after a meal is against the social and healthy norms. Also, the system is capable of getting feedback from occupancy and experts to define new semantic rules.

Alam et al. [175] had argued the limitation of Allen's temporal logic, which could relate event's duration (e.g. the duration of event A is larger/smaller/equal to event B) but without the capability of relating event duration's explicit numerical value. They had proposed temporal prediction algorithm based on Gaussian distribution and claimed that had successfully validate the previous authors' assumption about event duration could be modelled in Gaussian distribution. They predicting an event interval's duration through approximating user's activity's ending time (duration) from Gaussian distribution's mean and standard deviation values: $(\mu + 2\sigma)$.

Shin et al. [138] build 1-class SVDD (Support Vector Data Descriptor) [176] that inspired by SVM (Support Vector Machine). They used PIR (Passive Infra-Red) sensors to track the “mobility” of 9 elderly occupants. Tracking the “changes” in motion sensors by measuring: (1) how many times (the percentage) the motion sensors were triggered and (2) how often (the frequency) an occupancy is moving between two sensors. The authors build 24 SVDD for 24 h tracking per day.

However, Wong et al. [166] pointed that this system would often generate a false alarm for anomaly detection due to the reason that occupancy's activity pattern is irregular. Such as waking up late in the morning or performing usual activities during different times in the day.

Weisenberg et al. [177] detects anomaly pure from sensory level data, from sensor's timestamp and interval of inactivity. The system doesn't know anything about occupant's activities e.g. Sleeping, Cooking, enter Home, etc. Table 3 represents the different algorithms applicable for anomaly detection in a smart home.

Table 3 Algorithms used for anomaly detection

Algorithm	Pros	Cons	References
Histogram	<ul style="list-style-type: none"> • Could know the frequency of occurrence • Could know the location (where) frequently data occurred 	<ul style="list-style-type: none"> • Capturing independent data • Independent data assumption • Could not capture data dependency structure • Could not relating two data attributes 	[156–158, 186]
Gaussian mixture model	<ul style="list-style-type: none"> • Could relate two data attributes for activity classification (modelling) 	<ul style="list-style-type: none"> • Reducing the matching times and eventually improve the detection efficiency 	[126]
Hidden Markov model	<ul style="list-style-type: none"> • Simple • Handling sequential data. An efficient model for learning sequential data • Having temporal dependency structure [187, 188] • A statistical model that is handling noisy data 	<ul style="list-style-type: none"> • The generative model that is having “Cold start” problem • Need a full description of the big data • Requiring lots of trainings • Not fully capturing dependency structure of the data: a conditionally independent assumption • Supervised Learning. Requires human intervention that may cause label biased problem 	[155, 162, 163, 189]
Conditional random field	<ul style="list-style-type: none"> • The discriminative model that have no “Cold start” problem • Could capture long range dependency data structure • A statistical model that is handling noisy data 	<ul style="list-style-type: none"> • Expensive training cost when capturing long-range dependency data structure. Also a “Cold start” problem • Supervised Learning. Requires human intervention that may cause label biased problem • Requiring 1-class CRF for anomaly detection when anomaly data instance is rare or unavailable 	[169, 190]
Artificial neural network	<ul style="list-style-type: none"> • Being able to add new rules, by “adapting” its hidden layer to hold new information • One of the best approach for the typical problem of neural network 	<ul style="list-style-type: none"> • Could adapt new rules through hidden layer but could not incorporate user for adding new rules • Complex network architecture • Human unable to read and understand the logic and rules lays inside the neuron’s complex structure • Feed-Forward Neural Network (FNN) doesn’t capture data dependency structure 	[191–192]
Support vector machine	<ul style="list-style-type: none"> • SVMs provide a good out-of-sample generalization data linearly separable 	<ul style="list-style-type: none"> • Requiring 1-class SVM for anomaly detection when anomaly data instance is rare or unavailable 	[138, 193, 194]

(continued)

Table 3 (continued)

Algorithm	Pros	Cons	References
Semantic rule	<ul style="list-style-type: none"> • Could reduce false positive rate • Human readable logic rules 	<ul style="list-style-type: none"> • Not handling noisy data 	[195]
Binary dis/similarity measure functions	<ul style="list-style-type: none"> • Easy to compute the differences with function formulas 	<ul style="list-style-type: none"> • Handling is only binary data • Work quite well at analysing low binary level sensory data but not high-level activity data • Could not know detail “that” type of activity is an anomaly, “when” and “where” these anomalies had happened 	[196–204]

8 Conclusion

This survey has shown the greatest contribution of dense sensing paradigm monitoring system. Insight into the details of the architecture of dense sensing paradigm monitoring system. Including state-of-the-art works on sensors, data extraction, low and high-level analysis of algorithms and the strategies of detecting anomalies.

References

1. M. Marmot, Fair society, healthy lives, in *Inequalities in Health: Concepts, Measures, and Ethics*, (New York: Oxford University Press, 2013), p. 282
2. S. Häfner et al., To live alone and to be depressed, an alarming combination for the renin–angiotensin–aldosterone-system (RAAS). *Psychoneuroendocrinology* **37**(2), 230–237 (2012)
3. K. Kinsella, J. Beard, R. Suzman, Can populations age better, not just live longer? *Generations* **37**(1), 19–26 (2013)
4. K. Raworth, A safe and just space for humanity: can we live within the doughnut. *Oxfam Policy Pract. Clim. Change Resilience* **8**(1), 1–26 (2012)
5. TIME—Living alone—solitary living. <http://content.time.com/time/magazine/article/0,9171,2108055,00.html>
6. T. Guardian, The rise of solo living. <http://www.theguardian.com/lifeandstyle/2012/mar/30/the-rise-of-solo-living>
7. System, q., Living independently
8. S. Simoens, M. Villeneuve, J. Hurst, *Tackling Nurse Shortages in OECD Countries* (2005)
9. Living alone statistic. <http://www.statisticbrain.com/living-alone-statistics/>
10. G.K. Heilig, *World Urbanization Prospects: The 2011 Revision* (United Nations, Department of Economic and Social Affairs (DESA), Population Division, Population Estimates and Projections Section, New York, 2012)
11. J. Bates, J. Boote, C. Beverley, Psychosocial interventions for people with a milder dementing illness: a systematic review. *J. Adv. Nurs.* **45**(6), 644–658 (2004)
12. New Zealand government statistic. http://www.stats.govt.nz/browse_for_stats/population/estimates_and_p

13. I. Graham et al., European guidelines on cardiovascular disease prevention in clinical practice: executive summary fourth joint task force of the European Society of cardiology and other societies on cardiovascular disease prevention in clinical practice (constituted by representatives of nine societies and by invited experts). *Eur. Heart J.* **28**(19), 2375–2414 (2007)
14. R.B. Singh et al., Effect of an Indo-Mediterranean diet on progression of coronary artery disease in high risk patients (Indo-Mediterranean diet heart study): a randomised single-blind trial. *Lancet* **360**(9344), 1455–1461 (2002)
15. H.F. Raymond et al., The role of individual and neighborhood factors: HIV acquisition risk among high-risk populations in San Francisco. *AIDS Behav.* **18**(2), 346–356 (2014)
16. How does someone die alone
17. S. Luhr et al., Duration abnormality detection in sequences of human activity. Technical report, Department of Computing, Curtin University of Technology (2004)
18. F. Rivera-illingworth, V. Callaghan, H. Hagra, Towards the detection of temporal behavioural patterns in intelligent environments, in *2nd IET International Conference on Intelligent Environments, IE 06 (IET, 2006)*
19. M. Klein, A. Schmidt, R. Lauer, Ontology-centred design of an ambient middleware for assisted living: the case of soprano, in *Towards Ambient Intelligence: Methods for Cooperating Ensembles in Ubiquitous Environments (AIM-CU), 30th Annual German Conference on Artificial Intelligence (KI 2007)* (Osnabrück, 2007)
20. L. Chen et al., *Semantic Smart Homes: Towards Knowledge Rich Assisted Living Environments*. Intelligent Patient Management (Springer, 2009), p. 279–296
21. T.B.T. Truong et al., Alert management for home healthcare based on home automation analysis, in *Engineering in Medicine and Biology Society (EMBC), 2010 Annual International Conference of the IEEE (IEEE, 2010)*
22. M. Rudary, S. Singh, M.E. Pollack, Adaptive cognitive orthotics: combining reinforcement learning and constraint-based temporal reasoning, in *Proceedings of the Twenty-First International Conference on Machine Learning (ACM, 2004)*
23. M.-A. Dragan, I. Mocanu, Human activity recognition in smart environments, in *2013 19th International Conference on Control Systems and Computer Science (CSCS)* (IEEE, 2013)
24. B.D. Carolis, S. Ferilli, D. Redavid, Incremental Learning of Daily Routines as Workflows in a Smart Home Environment. *ACM Trans. Interact. Intell. Syst.* **4**(4), 20 (2015)
25. A. Sarkar, Hidden Markov mined activity model for human activity recognition. *Int. J. Distrib. Sens. Netw.* **2014** (2014)
26. G. Krempf et al., Open challenges for data stream mining research. *ACM SIGKDD Explor. Newsl.* **16**(1), 1–10 (2014)
27. L.G. Fahad, S.F. Tahir, M. Rajarajan, Activity recognition in smart homes using clustering based classification, in *2014 22nd International Conference on Pattern Recognition (ICPR)* (IEEE, 2014)
28. J. Wan, M.J. O’Grady, G.M. O’Hare, Dynamic Sensor Event Segmentation for Real-Time Activity Recognition in a Smart Home Context. *Personal and Ubiquitous Computing*, **19**(2), 1–15 (2014)
29. E. Nazerfard, D.J. Cook, CRAFFT: an activity prediction model based on Bayesian networks. *J. Ambient Intell. Humanized Comput.* 1–13 (2014)
30. C. Bell et al. Examining social media use among older adults, in *Proceedings of the 24th ACM Conference on Hypertext and Social Media (ACM, 2013)*
31. CASAS dataset. <https://wsucasas.wordpress.com/datasets/>
32. M.J. Rantz et al., Initiative to test a multidisciplinary model with advanced practice nurses to reduce avoidable hospitalizations among nursing facility residents. *J. Nurs. Care Qual.* **29**(1), 1–8 (2014)
33. M.R. Alam, M.B.I. Reaz, M.A.M. Ali, A review of smart homes—past, present, and future. *IEEE Trans. Syst. Man Cybern. Part C Appl. Rev* **42**(6), 1190–1203 (2012)
34. H.-I. Yang et al., A framework for service morphing and heterogeneous service discovery in smart environments, in *Impact Analysis of Solutions for Chronic Disease Prevention and Management* (Springer, 2012), p. 9–17

35. S. Mahmoud, A. Lotfi, C. Langensiepen, Behavioural pattern identification and prediction in intelligent environments. *Appl. Soft Comput.* **13**(4), 1813–1822 (2013)
36. S. Zhang, S.I. McClean, B.W. Scotney, Probabilistic learning from incomplete data for recognition of activities of daily living in smart homes. *IEEE Trans. Inf. Technol. Biomed.* **16**(3), 454–462 (2012)
37. S. Dernbach et al., Simple and complex activity recognition through smart phones, in *2012 8th International Conference on Intelligent Environments (IE)* (IEEE, 2012)
38. T. Gu et al., A pattern mining approach to sensor-based human activity recognition. *IEEE Trans. Knowl. Data Eng.* **23**(9), 1359–1372 (2011)
39. P. Rashidi, D.J. Cook, Mining sensor streams for discovering human activity patterns over time, in *2010 IEEE 10th International Conference on Data Mining (ICDM)* (IEEE, 2010)
40. S.-H. Park et al., *Forecasting Change Directions for Financial Time Series Using Hidden Markov Model*. Rough Sets and Knowledge Technology (Springer, 2009), p. 184–191
41. T. Van Kasteren et al., Accurate activity recognition in a home setting, in *Proceedings of the 10th International Conference on Ubiquitous Computing* (ACM, 2008)
42. F.J.P. Otte, B.R. Saurer, W. Stork, *Unsupervised Learning in Ambient Assisted Living for Pattern and Anomaly Detection: A Survey*. Evolving Ambient Intelligence (Springer, 2013), p. 44–53
43. K.F. Li, Smart home technology for telemedicine and emergency management. *J. Ambient Intell. Humaniz. Comput.* **4**(5), 535–546 (2013)
44. L. Atallah, G.-Z. Yang, The use of pervasive sensing for behaviour profiling—a survey. *Pervasive Mob. Comput.* **5**(5), 447–464 (2009)
45. P. Rashidi, D.J. Cook, Adapting to resident preferences in smart environments, in *AAAI Workshop on Preference Handling* (2008)
46. M. Usman et al., Wireless smart home sensor networks: mobile agent based anomaly detection, in *Ubiquitous Intelligence and Computing and 9th International Conference on Autonomic & Trusted Computing (UIC/ATC)* (IEEE, 2012)
47. A. Lotfi et al., Smart homes for the elderly dementia sufferers: identification and prediction of abnormal behaviour. *J. Ambient Intell. Humaniz. Comput.* **3**(3), 205–218 (2012)
48. F. Rivera-Illingworth, V. Callaghan, H. Hagrais, Detection of normal and novel behaviours in ubiquitous domestic environments. *Comput. J.* **53**(2), 142–151 (2010)
49. T. Mori et al., Anomaly detection and life pattern estimation for the elderly based on categorization of accumulated data, in *AIP Conference Proceedings-American Institute of Physics* (2011)
50. Z. Liao, Y. Yu, B. Chen, Anomaly detection in GPS data based on visual analytics, in *2010 IEEE Symposium on Visual Analytics Science and Technology (VAST)* (IEEE, 2010)
51. E. Serral, P. Valderas, V. Pelechano, *Supporting Runtime System Evolution to Adapt to User Behaviour*. Advanced Information Systems Engineering (Springer, 2010)
52. V. Jakkula, D.J. Cook, Anomaly detection using temporal data mining in a smart home environment. *Methods Inf. Med.* **47**(1), 70–75 (2008)
53. D.J. Hill, B.S. Minsker, E. Amir, Real-time Bayesian anomaly detection for environmental sensor data, in *Proceedings of the Congress-International Association for Hydraulic Research* (Citeseer, 2007)
54. P. Cuddihy et al., Algorithm to automatically detect abnormally long periods of inactivity in a home, in *Proceedings of the 1st ACM SIGMOBILE international workshop on Systems and networking support for healthcare and assisted living environments* (ACM, 2007)
55. D. Zhang et al., Semi-supervised adapted hmms for unusual event detection, in *IEEE Computer Society Conference on Computer Vision and Pattern Recognition, 2005. CVPR 2005* (IEEE, 2005)
56. M.-L. Shyu et al., *A novel anomaly detection scheme based on principal component classifier* (DTIC Document, 2003)
57. J. Loane et al., Interpreting presence sensor data and looking for similarities between homes using cluster analysis, in *2011 5th International Conference on Pervasive Computing Technologies for Healthcare (PervasiveHealth)* (IEEE, 2011)

58. H.-H. Hsu, K.-C. Lu, M. Takizawa, Abnormal behavior detection with fuzzy clustering for elderly care, in *2010 International Computer Symposium (ICS)* (IEEE, 2010)
59. T. Barger et al., Objective remote assessment of activities of daily living: Analysis of meal preparation patterns. Poster presentation, Medical Automation Research Center, University of Virginia Health System (2002)
60. R. Poppe, A survey on vision-based human action recognition. *Image Vis. Comput.* **28**(6), 976–990 (2010)
61. L. Chen et al., Sensor-based activity recognition. *IEEE Trans. Syst. Man Cybern. Part C Appl. Rev.* **42**(6), 790–808 (2012)
62. B. Kaluza, M. Gams. An approach to analysis of daily living dynamics in *Proceedings of the World Congress on Engineering and Computer Science* (2010)
63. T. Choudhury et al., Towards activity databases: using sensors and statistical models to summarize people's lives. *IEEE Data Eng. Bull.* **29**(1), 49–58 (2006)
64. D.H. Wilson, C. Atkeson, *Simultaneous tracking and activity recognition (STAR) using many anonymous, binary sensors*. Pervasive Computing (Springer, 2005), p. 62–79
65. N.K. Suryadevara, S.C. Mukhopadhyay, *Smart Homes: Design, Implementation and Issues*, vol. 14. (Springer, 2015)
66. N. Suryadevara, S. Mukhopadhyay, L. Barrack, Towards a smart non-invasive fluid loss measurement system. *J. Med. Syst.* **39**(4), 1–10 (2015)
67. H. Ghayvat, S.C. Mukhopadhyay, X. Gui, *Sensing Technologies for Intelligent Environments: A Review*. Intelligent Environmental Sensing, (Springer, 2015), p. 1–31
68. N.K. Suryadevara et al., WSN-based smart sensors and actuator for power management in intelligent buildings. *IEEE Trans. Mechatron. (Early Access Article)* **10** (2014)
69. N. Suryadevara, S. Mukhopadhyay, *Determination of Wellness of an Elderly in an Ambient Assisted Living Environment* (2014)
70. N. Suryadevara, S. Kelly, S. Mukhopadhyay, *Ambient Assisted Living Environment Towards Internet of Things Using Multifarious Sensors Integrated with XBee Platform*. Internet of Things, (Springer, 2014), p. 217–231
71. S.C. Mukhopadhyay, N. Suryadevara, *Internet of Things: Challenges and Opportunities* (Springer, 2014)
72. S. Mukhopadhyay, N. Suryadevara, Homes for assisted living: smart sensors, instrumentation, energy, control and communication perspective, in *Proceedings of IEEE International Conference on Control, Instrumentation, Energy & Communication (CIEC)*,(Kolkata-India, 2014)
73. S. Mukhopadhyay, O.A. Postolache, *Are Technologically Assisted Homes Safer for the Elderly*, Smart Sensors, Measurement and Instrumentation, vol. 2. Pervasive and Mobile Sensing and Computing for Healthcare (Springer 2014)
74. N. Suryadevara et al., Forecasting the behavior of an elderly using wireless sensors data in a smart home. *Eng. Appl. Artif. Intell.* **26**(10), 2641–2652 (2013)
75. Suryadevara, N., et al. Reliable measurement of wireless sensor network data for forecasting wellness of elderly at smart home, in *2013 IEEE International Instrumentation and Measurement Technology Conference (I2MTC)* (IEEE, 2013)
76. N. Suryadevara et al. Ambient assisted living framework for elderly wellness determination through wireless sensor scalar data, in *2013 Seventh International Conference on Sensing Technology (ICST)* (IEEE, 2013)
77. Y.-X. Lai et al. Ubiquitous motion sensing service using wearable shoe module and mobile device, in *2013 IEEE International Instrumentation and Measurement Technology Conference (I2MTC)* (IEEE, 2013)
78. S.D.T. Kelly, N.K. Suryadevara, S.C. Mukhopadhyay, Towards the implementation of IoT for environmental condition monitoring in homes. *IEEE Sens. J.* **13**(10), 3846–3853 (2013)
79. JA Nazabal et al., Accessing KNX devices using USB/KNX interfaces for remote monitoring and storing sensor data. *Int. J. Smart Home* **7**(2), 105–110 (2013)
80. H.W. Guesgen, Sensors for smart home, in *Human Behavior Recognition Technologies: Intelligent Applications for Monitoring and Security*, IGI Global (2013)

81. N. Suryadevara, M. Quazi, S.C. Mukhopadhyay, Intelligent sensing systems for measuring wellness indices of the daily activities for the elderly, in *2012 8th International Conference on Intelligent Environments (IE)* (IEEE, 2012)
82. N. Suryadevara et al., *Sensor data fusion to determine wellness of an elderly in intelligent home monitoring environment*, in *2012 IEEE International Instrumentation and Measurement Technology Conference (I2MTC)* (IEEE, 2012)
83. N. Suryadevara et al., Wireless sensors network based safe home to care elderly people: behaviour detection. *Sens. Actuators A* **186**, 277–283 (2012)
84. N. Suryadevara, S. Mukhopadhyay, R. Rayudu, Applying SARIMA time series to forecast sleeping activity for wellness model of elderly monitoring in smart home, in *2012 Sixth International Conference on Sensing Technology (ICST)* (IEEE, 2012)
85. S. Kelly, N. Suryadevara, S. Mukhopadhyay, *Integration of Zigbee-IPv6 Networks for Smart Home Sensor Data Transmission to Augment Internet of Things* (IB2COM, Australia, 2012), p. 44–49
86. A. Gaddam, S.C. Mukhopadhyay, G. Sen Gupta, Elder care based on cognitive sensor network. *IEEE Sens. J.* **11**(3), 574–581 (2011)
87. S.C. Mukhopadhyay, A. Gaddam, G.S. Gupta, Wireless sensors for home monitoring—a review. *Recent Pat. Electr. Electron. Eng. (Formerly Recent Patents on Electrical Engineering)* **1**(1), 32–39 (2008)
88. S. Bhardwaj et al., Ubiquitous healthcare data analysis and monitoring using multiple wireless sensors for elderly person. *Sens. Transducer J.* **90**, 87–99 (2008)
89. Suryadevara, N. and S. Mukhopadhyay, *Internet of Things: A Review and Future Perspective*
90. A. Nag, S.C. Mukhopadhyay, Smart home: recognition of activities of elderly for 24/7; Coverage issues, in *Proceedings of the 2014 International Conference on Sensing Technology, Liverpool, UK*
91. Internet of things: challenges and opportunities. <http://www.europeanbusinessreview.com/?p=5049>
92. S. Mukhopadhyay, *Wearable Sensors for Human Activity Monitoring: A Review* (2015)
93. K. Malhi et al., A Zigbee-based wearable physiological parameters monitoring system. *IEEE Sens. J.* **12**(3), 423–430 (2012)
94. N.K. Suryadevara, S.C. Mukhopadhyay, Wireless sensor network based home monitoring system for wellness determination of elderly. *IEEE Sens. J.* **12**(6), 1965–1972 (2012)
95. S.D.T. Kelly, N. Suryadevara, S.C. Mukhopadhyay, Towards the implementation of IoT for environmental condition monitoring in homes. *IEEE Sens. J.* **13**(10), 3846–3853 (2013)
96. H. Ghayvat et al., WSN- and IOT-based smart homes and their extension to smart buildings. *Sensors* **15**(5), 10350–10379 (2015)
97. D.H. Hu, Q. Yang, CIGAR: concurrent and interleaving goal and activity recognition, in *AAAI* (2008)
98. Z. Xing, J. Pei, E. Keogh, A brief survey on sequence classification. *ACM SIGKDD Explor. Newsl.* **12**(1), 40–48 (2010)
99. M. Novak, M. Binias, F. Jakab, Unobtrusive anomaly detection in presence of elderly in a smart-home environment, in *ELEKTRO, 2012* (IEEE 2012)
100. S.-L. Chua, *Thesis—Behaviour Recognition in Smart Home* (2012)
101. O.D. Lara, M.A. Labrador, A survey on human activity recognition using wearable sensors. *IEEE Commun. Surv. Tutor.* **15**(3), 1192–1209 (2013)
102. S.M. Mahmoud, *Thesis—Identification and Prediction of Abnormal Behaviour Activities of Daily Living in Intelligent Environments* (2012)
103. K. Matsuoka et al., Smart House monitoring living behaviors for finding un-usual conditions. *Procee ROBOMECH* **4**, 1–4
104. B. Yao et al. A Type-2 Fuzzy Logic based system for linguistic summarization of video monitoring in indoor intelligent environments, in *2014 IEEE International Conference on Fuzzy Systems (FUZZ-IEEE)* (IEEE, 2014)
105. S.M. Mahmoud, A. Lotfi, C. Langensiepen, User activities outlier detection system using principal component analysis and fuzzy rule-based system, in *Proceedings of the 5th*

- International Conference on Pervasive Technologies Related to Assistive Environments* (ACM, 2012)
106. H. Medjahed et al., Human activities of daily living recognition using fuzzy logic for elderly home monitoring, in *IEEE International Conference on Fuzzy Systems, 2009. FUZZ-IEEE 2009*. (IEEE, 2009)
 107. G. Stefanos, A.B. Hamza, Cluster pca for outliers detection in high-dimensional data, in *IEEE International Conference on Systems, Man and Cybernetics, 2007. ISIC* (IEEE, 2007)
 108. T. Martin et al., Fuzzy ambient intelligence for next generation telecare, in *2006 IEEE International Conference on Fuzzy Systems* (IEEE, 2006)
 109. M.D. Lee, M.A. Butavicius, E. Rachel, Reilly. An empirical evaluation of Chernoff faces, star glyphs, and spatial visualizations for binary data. *APVis* **3**, 1–10
 110. R. Helaoui, M. Niepert, H. Stuckenschmidt, Recognizing interleaved and concurrent activities: A statistical-relational approach, in *2011 IEEE International Conference on Pervasive Computing and Communications (PerCom)* (IEEE, 2011)
 111. N. Lesh, M.J. Zaki, M. Ogihara, Mining features for sequence classification, in *Proceedings of the fifth ACM SIGKDD International Conference on Knowledge Discovery and Data Mining* (ACM, 1999)
 112. V. Guralnik, K.Z. Haigh, Learning models of human behaviour with sequential patterns, in *Proceedings of the AAAI-02 workshop "Automation as Caregiver"* (2002)
 113. M. Markou, S. Singh, Novelty detection: a review—part 1: statistical approaches. *Sig. Process.* **83**(12), 2481–2497 (2003)
 114. M. Markou, S. Singh, Novelty detection: a review—part 2: neural network based approaches. *Sig. Process.* **83**(12), 2499–2521 (2003)
 115. X. Xu, T. Xie, *A Reinforcement Learning Approach for Host-Based Intrusion Detection Using Sequences of System Calls*. *Advances in Intelligent Computing* (Springer, 2005), p. 995–1003
 116. E. Kim, S. Helal, D. Cook, Human activity recognition and pattern discovery. *IEEE Pervasive Comput.* **9**(1), 48–53 (2010)
 117. D.J. Cook et al., CASAS: a smart home in a box. *Computer* **46**(7), 26–33 (2013)
 118. D.J. Cook, Making sense of sensor data. *IEEE Pervasive Comput.* **6**(2), 105–108 (2007)
 119. E.O. Heierman III, D.J. Cook, Improving home automation by discovering regularly occurring device usage patterns, in *Third IEEE International Conference on Data Mining, 2003. ICDM 2003* (IEEE, 2003)
 120. T. Lane, C.E. Brodley, Temporal sequence learning and data reduction for anomaly detection. *ACM Trans. Inf. Syst. Secur. (TISSEC)* **2**(3), 295–331 (1999)
 121. T. Lane, C.E. Brodley, Approaches to Online Learning and Concept Drift for User Identification in Computer Security, in *KDD* (1998)
 122. T. Lane, C.E. Brodley, An application of machine learning to anomaly detection, in *Proceedings of the 20th National Information Systems Security Conference* (Baltimore, USA, 1997)
 123. T. Lane, C.E. Brodley, Detecting the abnormal: Machine learning in computer security. *ECE Technical reports* (1997), p. 74
 124. T. Lane, C.E. Brodley, Sequence matching and learning in anomaly detection for computer security, in *AAAI Workshop: AI Approaches to Fraud Detection and Risk Management* (1997)
 125. D.J. Patterson et al., Fine-grained activity recognition by aggregating abstract object usage, in *Ninth IEEE International Symposium on Wearable Computers, 2005* (IEEE, 2005)
 126. F. Cardinaux et al., Modelling of behavioural patterns for abnormality detection in the context of lifestyle reassurance, in *Progress in Pattern Recognition, Image Analysis and Applications* (Springer, 2008), p. 243–251
 127. V. Chandola, A. Banerjee, V. Kumar, Anomaly detection: A survey. *ACM Comput. Surv. (CSUR)* **41**(3), 15 (2009)
 128. J. Modayil et al., Integrating sensing and cueing for more effective activity reminders, in *AAAI Fall Symposium: AI in Eldercare: New Solutions to Old Problems* (2008)

129. M.E. Pollack et al., Autominder: An intelligent cognitive orthotic system for people with memory impairment. *Robot. Autonom. Syst.* **44**(3), 273–282 (2003)
130. P. Kan et al., The development of an adaptive upper-limb stroke rehabilitation robotic system. *J. Neuroeng. Rehabil.* **8**(1), 1–18 (2011)
131. J. Hoey et al., Automated handwashing assistance for persons with dementia using video and a partially observable markov decision process. *Comput. Vis. Image Underst.* **114**(5), 503–519 (2010)
132. J. Hoey et al., Rapid specification and automated generation of prompting systems to assist people with dementia. *Pervasive Mob. Comput.* **7**(3), 299–318 (2011)
133. F. Latfi, B. Lefebvre, C. Descheneaux, Ontology-based management of the telehealth smart home, dedicated to elderly in loss of cognitive autonomy, in *OWLED (2007)*
134. L. Chen, C. Nugent, Ontology-based activity recognition in intelligent pervasive environments. *Int. J Web Inf. Syst.* **5**(4), 410–430 (2009)
135. S. Patel et al., Monitoring motor fluctuations in patients with Parkinson’s disease using wearable sensors. *IEEE Trans. Inf. Technol. Biomed.* **13**(6), 864–873 (2009)
136. B. Das, D.J. Cook, Data mining challenges in automated prompting systems, in *Proceedings of 2011 International Conference on Intelligent User Interfaces Workshop on Interaction with Smart Objects* (2011)
137. K.Z. Haigh, H. Yanco, Automation as caregiver: A survey of issues and technologies, in *AAAI-02 Workshop on Automation as Caregiver: The Role of Intelligent Technology in Elder Care* (2002)
138. J.H. Shin, B. Lee, K.S. Park, Detection of abnormal living patterns for elderly living alone using support vector data description. *IEEE Trans. Inf. Technol. Biomed.* **15**(3), 438–448 (2011)
139. P. Rashidi, D.J. Cook, Keeping the resident in the loop: Adapting the smart home to the user. *IEEE Trans. Syst. Man Cybern. Part A Syst. Humans* **39**(5), 949–959 (2009)
140. I. Žliobaitė, Learning Under Concept Drift: An Overview. arXiv preprint arXiv:1010.4784 , 1–36 (2010)
141. I. Žliobaitė, Learning under concept drift: an overview. Overview. Technical report, Vilnius University, 2009 techniques, related areas, applications Subjects: Artificial Intelligence (2009)
142. B. Das et al., Automated prompting in a smart home environment, in *2010 IEEE International Conference on Data Mining Workshops (ICDMW)* (IEEE, 2010)
143. R.M. Pulsford et al., Actigraph accelerometer-defined boundaries for sedentary behaviour and physical activity intensities in 7 year old children. *PLoS ONE* **6**(8), e21822 (2011)
144. S. Abbate et al., A smartphone-based fall detection system. *Pervasive Mob. Comput.* **8**(6), 883–899 (2012)
145. F. Albinali, M.S. Goodwin, S. Intille, Detecting stereotypical motor movements in the classroom using accelerometry and pattern recognition algorithms. *Pervasive Mob. Comput.* **8**(1), 103–114 (2012)
146. J.L.C. Candás et al., An automatic data mining method to detect abnormal human behaviour using physical activity measurements. *Pervasive Mob. Comput.* **15**, 228–241 (2014)
147. F. Paganelli, D. Giuli, An ontology-based system for context-aware and configurable services to support home-based continuous care. *IEEE Trans. Inf. Technol. Biomed.* **15**(2), 324–333 (2011)
148. Y. Oh, J. Han, W. Woo, A context management architecture for large-scale smart environments. *IEEE Commun. Mag.* **48**(3), 118–126 (2010)
149. A. Mileo, D. Merico, R. Bisiani, Support for context-aware monitoring in home healthcare. *J. Ambient Intell. Smart Environ.* **2**(1), 49–66 (2010)
150. F. Ongenae et al., A probabilistic ontology-based platform for self-learning context-aware healthcare applications. *Expert Syst. Appl.* **40**(18), 7629–7646 (2013)
151. C.-H. Lee, J.C.-Y. Chen, V.S. Tseng, A novel data mining mechanism considering bio-signal and environmental data with applications on asthma monitoring. *Comput. Methods Programs Biomed.* **101**(1), 44–61 (2011)

152. T.C. Panagiotakopoulos et al., A contextual data mining approach toward assisting the treatment of anxiety disorders. *IEEE Trans. Inf. Technol. Biomed.* **14**(3), 567–581 (2010)
153. T. Taleb et al., ANGELAH: a framework for assisting elders at home. *IEEE J. Sel. Areas Commun.* **27**(4), 480–494 (2009)
154. Y. Zhu, N.M. Nayak, A.K. Roy-Chowdhury, Context-aware activity recognition and anomaly detection in video. *IEEE J. Sel. Top. Signal Process.* **7**(1), 91–101 (2013)
155. A.R.M. Forkan et al., A context-aware approach for long-term behavioural change detection and abnormality prediction in ambient assisted living. *Pattern Recogn.* **48**(3), 628–641 (2015)
156. G. Virone et al., Behavioral patterns of older adults in assisted living. *IEEE Trans. Inf. Technol. Biomed.* **12**(3), 387–398 (2008)
157. V. Patterson, Home Telehealth: Connecting Care Within The Community. *Ulster Med. J.* **76**(1), 60 (2007)
158. G. Virone, N. Noury, J. Demongeot, A system for automatic measurement of circadian activity deviations in telemedicine. *IEEE Trans. Biomed. Eng.* **49**(12), 1463–1469 (2002)
159. D.N. Monekosso, P. Remagnino, *Anomalous behavior detection: Supporting independent living*. *Intelligent Environments* (2009), p. 33–48
160. T. Mori et al., Typical behavior patterns extraction and anomaly detection algorithm based on accumulated home sensor data, in *Future Generation Communication and Networking (FGCN 2007)* (IEEE, 2007)
161. W. Kang, D. Shin, D. Shin, Detecting and predicting of abnormal behavior using hierarchical markov model in smart home network, in *2010 IEEE 17th International Conference on Industrial Engineering and Engineering Management (IE&EM)* (IEEE, 2010)
162. P.-C. Chung, C.-D. Liu, A daily behavior enabled hidden Markov model for human behavior understanding. *Pattern Recogn.* **41**(5), 1572–1580 (2008)
163. T.V. Duong et al., Activity recognition and abnormality detection with the switching hidden semi-markov model, in *IEEE Computer Society Conference on Computer Vision and Pattern Recognition, 2005. CVPR 2005* (IEEE, 2005)
164. Y.-X. Hung et al., Abnormality detection for improving elder’s daily life independent, in *Aging Friendly Technology for Health and Independence* (Springer, 2010), p. 186–194
165. G.D. Forney Jr, The viterbi algorithm. *Proc. IEEE* **61**(3), 268–278 (1973)
166. K.B.-Y. Wong, T. Zhang, H. Aghajan, *Data Fusion with a Dense Sensor Network for Anomaly Detection in Smart Homes*. *Human Behavior Understanding in Networked Sensing* (Springer, 2014), p. 211–237
167. F.J. Ordóñez, P. de Toledo, A. Sanchis, *Sensor-Based Bayesian Detection of Anomalous Living Patterns in a Home Setting*. *Personal and Ubiquitous Computing* (2014), p. 1–12
168. M. Novák, F. Jakab, L. Lain, *Anomaly Detection in User Daily Patterns in Smart-Home Environment*
169. Y. Song et al., One-class conditional random fields for sequential anomaly detection, in *Proceedings of the Twenty-Third international joint conference on Artificial Intelligence* (AAAI Press, 2013)
170. A. Quattoni et al., Hidden conditional random fields. *IEEE Trans. Pattern Anal. Mach. Intell.* **10**, 1848–1852 (2007)
171. S.S. Khan et al., Towards the detection of unusual temporal events during activities using hmms, in *Proceedings of the 2012 ACM Conference on Ubiquitous Computing* (ACM, 2012)
172. A. Aztiria, G. Farhadi, H. Aghajan, *User Behavior Shift Detection in Intelligent Environments*. *Ambient Assisted Living and Home Care* (Springer, 2012), p. 90–97
173. E. Hoque, J. Stankovic, Semantic anomaly detection in daily activities, in *Proceedings of the 2012 ACM Conference on Ubiquitous Computing* (ACM, 2012)
174. Y. Han et al., A framework for supervising lifestyle diseases using long-term activity monitoring. *Sensors* **12**(5), 5363–5379 (2012)
175. M. Alam, M. Reaz, H. Husain, Temporal modeling and its application for anomaly detection in smart homes. *Int. J. Phys. Sci.* **6**(31), 7233–7241 (2011)
176. D.M. Tax, R.P. Duin, Support vector data description. *Mach. Learn.* **54**(1), 45–66 (2004)

177. J. Weisenberg, P. Cuddihy, V. Rajiv, Augmenting motion sensing to improve detection of periods of unusual inactivity, in *Proceedings of the 2nd International Workshop on Systems and Networking Support for Health Care and Assisted Living Environments* (ACM, 2008)
178. Economist. Singlisation. <http://www.economist.com/node/21560844>
179. H. Ghayvat et al., *Sharing Research Experiences of Wsn Based Smart Home*
180. O. Banos et al., Window size impact in human activity recognition. *Sensors* **14**(4), 6474–6499 (2014)
181. W.A. Khan et al., Healthcare standards based sensory data exchange for Home Healthcare Monitoring System, in *Engineering in Medicine and Biology Society (EMBC), 2012 Annual International Conference of the IEEE* (IEEE, 2012)
182. M.-S. Lee et al., Unsupervised clustering for abnormality detection based on the tri-axial accelerometer, in *ICCAS-SICE, 2009* (IEEE, 2009)
183. N. Eagle, A.S. Pentland, Eigenbehaviors: Identifying structure in routine. *Behav. Ecol. Sociobiol.* **63**(7), 1057–1066 (2009)
184. N.H. Chehade et al., Detecting stumbles with a single accelerometer, in *Engineering in Medicine and Biology Society (EMBC), 2012 Annual International Conference of the IEEE* (IEEE, 2012)
185. Y.-S. Lee, W.-Y. Chung, Automated abnormal behavior detection for ubiquitous healthcare application in daytime and nighttime, in *2012 IEEE-EMBS International Conference on Biomedical and Health Informatics (BHI)* (IEEE, 2012)
186. M.T. Hagh, N. Ghadimi, *Multisignal Histogram-Based Islanding Detection Using Neuro-Fuzzy Algorithm*. Complexity (2014)
187. J.-F. Mari, F. Le Ber, Temporal and spatial data mining with second-order hidden markov models. *Soft. Comput.* **10**(5), 406–414 (2006)
188. L. Rabiner, A tutorial on hidden Markov models and selected applications in speech recognition. *Proc. IEEE* **77**(2), 257–286 (1989)
189. T. Van Kasteren, G. Englebienne, B.J. Kröse, An activity monitoring system for elderly care using generative and discriminative models. *Pers. Ubiquit. Comput.* **14**(6), 489–498 (2010)
190. K.K. Gupta, B. Nath, K. Ramamohanarao, Conditional random fields for intrusion detection, in *21st International Conference on Advanced Information Networking and Applications Workshops, 2007, AINAW'07* (IEEE, 2007)
191. T.-H.T. Hou, W.-L. Liu, L. Lin, Intelligent remote monitoring and diagnosis of manufacturing processes using an integrated approach of neural networks and rough sets. *J. Intell. Manuf.* **14**(2), 239–253 (2003)
192. F. Rivera-illingworth, V. Callaghan, H. Hagrais, A connectionist embedded agent approach for abnormal behaviour detection in intelligent health care environments, in *2004 IEEE International Conference on Systems, Man and Cybernetics* (IEEE, 2004)
193. V.R. Jakkula, D.J. Cook, Detecting anomalous sensor events in smart home data for enhancing the living experience. *Artif. intell. Smarter Living* **11**, 07 (2011)
194. J. Yin, Q. Yang, J.J. Pan, Sensor-based abnormal human-activity detection. *IEEE Trans. Knowl. Data Eng.* **20**(8), 1082–1090 (2008)
195. P. Barsocchi et al., *Monitoring Elderly Behavior via Indoor Position-Based Stigmergy*. Pervasive and Mobile Computing (2015)
196. P. Rashidi et al., Discovering activities to recognize and track in a smart environment. *IEEE Trans. Knowl. Data Eng.* **23**(4), 527–539 (2011)
197. L. Ye et al., Anomaly event detection in temporal sensor network data of intelligent environments, in *2010 2nd International Conference on Computer Engineering and Technology (ICCET)* (IEEE, 2010)
198. Q. Yan, S. Xia, Y. Shi, An anomaly detection approach based on symbolic similarity, in *Control and Decision Conference (CCDC), 2010 Chinese* (IEEE, 2010)
199. K. Park et al., Abnormal human behavioral pattern detection in assisted living environments, in *Proceedings of the 3rd International Conference on Pervasive Technologies Related to Assistive Environments* (ACM, 2010)

200. V. Jakkula, D. Cook, Outlier detection in smart environment structured power datasets, in *2010 Sixth International Conference on Intelligent Environments (IE)* (IEEE, 2010)
201. A. Huang, Similarity measures for text document clustering, in *Proceedings of the sixth new zealand computer science research student conference (NZCSRSC2008)* (Christchurch, New Zealand, 2008)
202. A. Sharma, A.K. Pujari, K.K. Paliwal, Intrusion detection using text processing techniques with a kernel based similarity measure. *Comput. Secur.* **26**(7), 488–495 (2007)
203. S.-H. Cha, S. Yoon, C.C. Tappert, On binary similarity measures for handwritten character recognition, in *Eighth International Conference on Document Analysis and Recognition, 2005. Proceedings* (IEEE, 2005)
204. Z. Erlich, R. Gelbard, I. Spiegler, Data mining by means of binary representation: a model for similarity and clustering. *Inf. Syst. Front.* **4**(2), 187–197 (2002)

Real-Time Monitoring of Meat Drying Process Using Electromagnetic Wave Sensors

Magomed Muradov, Jeff Cullen and Alex Mason

Abstract There are currently limited options for the meat producers for monitoring the water content of their products as they are processed or cured. Most existing methodologies are destructive, or require the use of probes which touch or penetrate the meat and lead to issues of contamination and damage. Thus, the aim of this investigation is to use an electromagnetic (EM) wave sensor to monitor the meat drying process and determine its suitability as a non-destructive and non-contact technique. The sensor has been modelled using High Frequency Structure Simulation Software (HFSS) and then constructed. Experimental work was conducted involving measurement of meat weight and EM signature (namely the S_{11} parameter in the frequency range 1–6 GHz) over a period of approximately 1 week, with measurements recorded every hour. The change in EM signature and weight loss has been analysed and correlations drawn from the resultant data. The results demonstrate a strong relationship between the S_{11} measurement and weight loss of the meat sample ($R^2 = 0.8973$), and it is proposed that this could be used as the basis for future industrial application for measuring meat products during drying processes, such as those used in curing.

Keywords Dry-curing · Electromagnetic wave · Non-invasive · Sensor · Real-time meat analysis

1 Introduction

Products of certified high quality are increasingly sought by both consumers and manufacturers [1]. Products in the meat industry are no exception to this rule [2, 3], although it is a challenging task since the product exhibits considerable variability as a result of the natural raw material [4]. Meat curing is the process by which food

M. Muradov · J. Cullen · A. Mason (✉)
School of Built Environment, Liverpool John Moores University, Liverpool, UK
e-mail: A.Mason1@ljmu.ac.uk

products are preserved and flavoured, typically through the addition of salts, nitrates, nitrites or sugars and perhaps in combination with other cooking or smoking processes. In some countries, such products have lost favour due to widespread use of mechanical refrigeration systems which means that fresh meat produce can be readily purchased in local stores and supermarkets, and indeed very few people can remember a time before refrigeration or when salt was regularly used to preserve meat [5].

However, across much of Europe (e.g. Spain, France and Germany) cured meat products have retained a place in the consumer market, and so the industry is interested to find ways of improving the process. Despite curing being used as early as 1300 BC in China, there are few techniques for monitoring the curing process with producers typically relying upon “rule of thumb” methods or crude measurements such as product weight or solidity. While fresh meat products have benefitted from the advent of sensor systems, with near-infrared and x-ray based techniques being the most prevalent for applications such as meat composition monitoring,¹ sorting² and foreign object detection (i.e. detection of metal, plastic and bone shards), these technologies have made little impact on monitoring of cured meat production. Thus there is heavy reliance upon the experience of key workers within the industry which leads to problems of consistency if the instincts or opinions of those workers vary [6].

Electromagnetic (EM) sensors, namely those which operate at radio or microwave frequencies, are widely used in a variety of industrial sectors. Examples include, civil engineering materials analysis [7], timber imaging [8], chemical processing [9–11] and medicine [12–15]. However, there has yet to be a significant impact of these sensors in the food industry, with the majority of such technology there being centred on cooking or sterilisation. However, the authors have demonstrated the first potentially non-invasive solution for measurement of *water holding capacity* [16] and *water activity* [17] in meat products based on EM wave sensors operating at microwave frequencies, and so there is the belief that further benefits could be brought to the cured meat industry; this belief is supported by other authors in the field [18]. The particular benefit of the technology is its non-invasive nature, which, in contrast with current techniques, holds the potential to eliminate fears over instrumentation contributing to food contamination which has disastrous consequences for consumers and suppliers. Thus the purpose of this study is to demonstrate the potential for EM wave sensors in monitoring cured meat products.

¹The “Spektron” device launched recently by Prediktor (<http://www.prediktor.no>) is a good example of an online system designed for this function.

²Tomra (<http://www.tomra.com/>) have the “ODENBERG QVision 500” sensor system for online monitoring and sorting of meat products on the basis of bulk fat content.

2 Meat Curing

Meat curing is the application of salt, colour fixing ingredients, and seasoning in order to impart unique properties to the end product [19]. Some techniques involve adding sugar, nitrite, nitrate and sometimes phosphates and ascorbates to meats for preservation, colour development, and flavour enhancement [20]. The functions of the most popular ingredients used in curing are as follows.

Salt:

- Provides a characteristic flavour to impart a cured meat taste.
- Acts as a preservative through growth inhibition and destruction of microorganisms.
- Enhances the transport of other cure ingredients throughout the muscle by osmotic movement of salt itself.
- Dehydrates meat tissue to reduce bacterial growth.

Sugar:

- Provides a characteristic flavour to impart a cured meat taste.
- Counteracts the harshness of salt.
- Provides an energy source for microorganisms which convert nitrate to nitrite during a long term cure.
- Provides a surface colour characteristic of aged ham if caramelized sugar is used.

Nitrates and nitrites:

- Contribute to the characteristic cured flavour.
- Contribute the characteristic reddish-pink colour of cured meat.
- Prevent growth of a food poisoning microorganism known as *Clostridium botulinum* which can occur in foods that require heat processing.
- Retard the development of oxidative rancidity and rancid taste.
- Prevent warmed-over flavour in reheated products.

Curing materials may be in either dry or liquid form. They will be applied either to the surface of meat or into it by some injection method. The oldest method of curing is dry cure in which the curing ingredients are rubbed on the surface of the meat. The dry sugar cure method can be used under wider temperature variations and will have less spoilage problems under unfavourable curing conditions [19]. A simple and time-tested dry-curing formula for pork (i.e. ham) based products requires the following ingredients:

- 8 lbs salt
- 3 lbs sugar
- 2 oz. sodium nitrate
- 1/2 oz. sodium nitrite



Fig. 1 Traditional ham curing process in Spain

The length of curing is typically seven days per inch of thickness. For instance, if a ham joint weighs 12–14 lbs and measures 5 inches at its thickest point, then it should be cured for 35 days. A two-inch thick belly should cure in 14 days. Another important consideration is to be sure the cure is rubbed into the aitch bone joint and hock end of the ham to avoid bone sour. The temperature range should be high enough for the meat to cure properly and dry, but low enough so harmful bacteria and mould doesn't grow. Ideal temperatures for dry-curing are between 10–15 °C [19]. Examples of cured meat products during production are illustrated in Fig. 1.

3 Planar Electromagnetic Wave Sensor

For the purposes of this work a patch type EM wave sensor is utilised; it's simple and well understood design allows for accurate prediction of sensor performance based up on preliminary models created using Ansys HFSS electromagnetic wave simulation software. The physical model is illustrated in Fig. 2.

The sensor consists of 4 key parts; (1) active radiating element, (2) ground plane, (3) substrate and (4) the feed. The dimensions of the sensor illustrated in Fig. 2 allow the sensor to resonate at approximately 2 GHz when not in contact with any material. The radiating element and ground plane are copper based conductors, while the substrate material is FR4 with dielectric constant of 4.4 and loss tangent

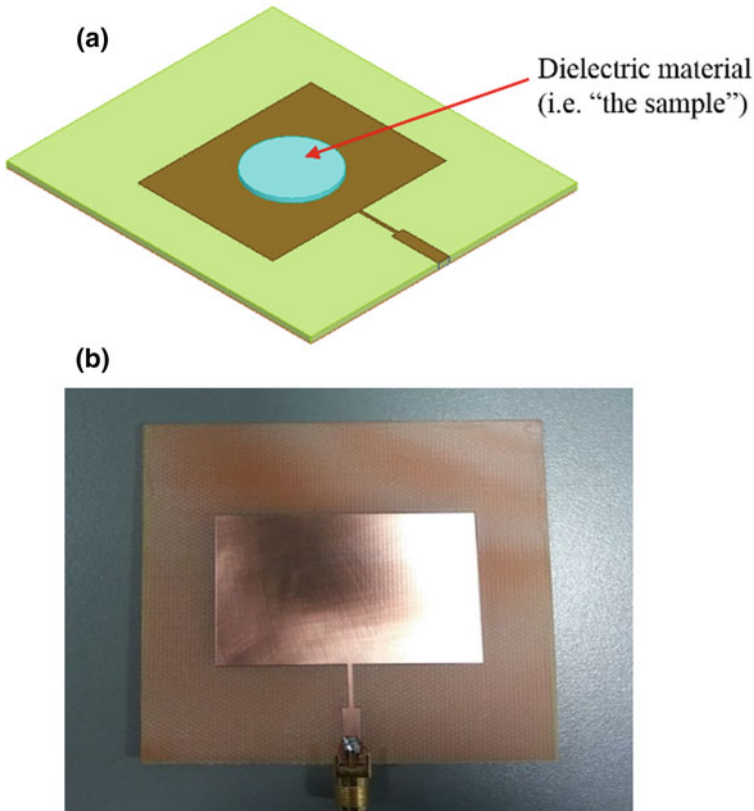


Fig. 2 **a** Model of patch type electromagnetic wave sensor, designed to operate at approx. 2 GHz and **b** the constructed sensor

of 0.021. The modelled return loss was in good agreement with the physical measurement, as indicated in Fig. 3.

The sensor model, depicted in Figs. 2a and 4(a), includes a cylindrical dielectric material which represents a water volume in this work. As this volume was increased, the sensor was parametrically modelled to understand the relationship between the return loss and water volume. As expected, the sensor response changes with the increasing water volume, likely as a result of the changing dielectric constant (ϵ_r) directly above the radiating element; it is on this basis that the sensor was selected for use in monitoring meat during the curing process.

Generally speaking, sensors of this nature offer a good number of benefits, including being low profile, conformable to planar and non-planar surfaces, simple and cheap to fabricate using modern printed-circuit technology, mechanically robust when mounted on rigid surfaces and very flexible in terms of resonant frequency, polarisation, pattern, and impedance [21]. Furthermore, such sensors

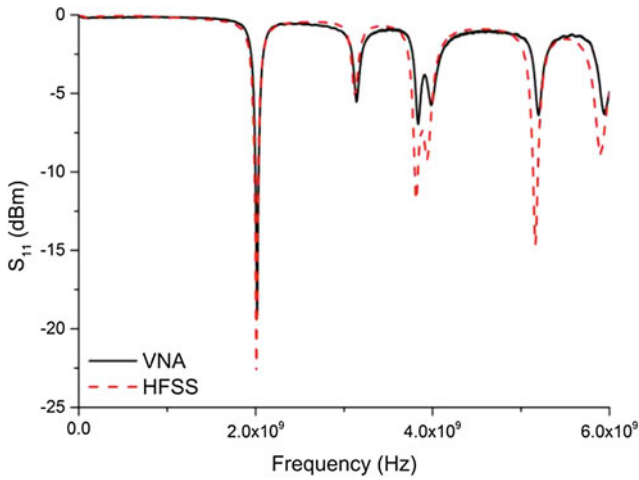


Fig. 3 Demonstrating the modelled and measured sensor return loss through modelling in Ansys HFSS and real-world measurement respectively

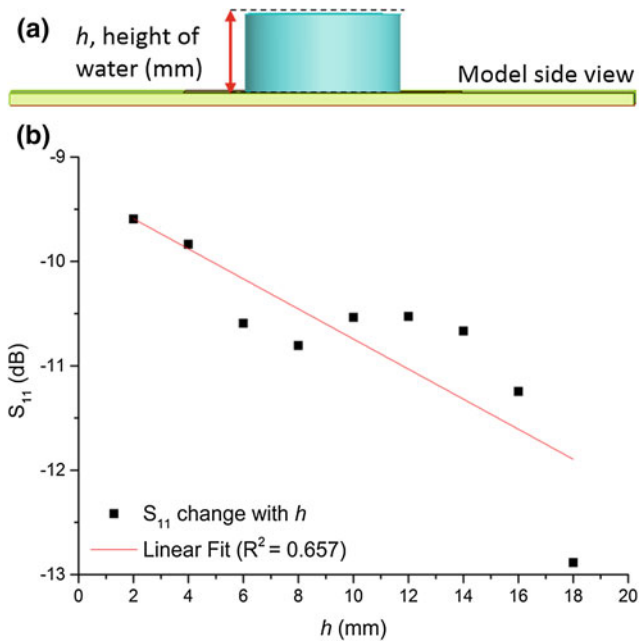


Fig. 4 a Model of sensor with variable water volume and **b** parametric analysis result with correlation between sensor return loss and water volume ($R^2 = 0.657$)

provide good depth of penetration (>100 mm) a relatively low power (<1 mW), which is important given that rapid drying of meat products occurs on surfaces exposed to the atmosphere.

4 Experimental Setup

Pork loin steaks were acquired from a local supermarket, and stored at 5 °C. Rather than salting the meat at this stage, it was the intention to let the meat dry naturally to determine the sensor response in the unsalted condition.

The meat samples were cut into approximately $70 \times 50 \times 15$ mm pieces and placed on top of a bespoke water run-off system, designed for rapid removal drips from the meat which would otherwise skew weight measurements. Such issues would not exist with products during real production as invariably they are hung to dry. The meat was situated on top of a set of digital scales so that weight of the sample could be continuously recorded during the drying process. This arrangement was placed within a refrigerator which was set to approx. 5 °C, ± 2 °C. Temperature was monitored throughout the experimental procedure.

To promote air circulation and water loss, a fan was fixed inside the fridge. The fan was connected to power supply via a relay (see Fig. 5) which is used to switch off the fan while the measurements are taken. The purpose of this is to avoid incorrect weight measurements as the scale is sensitive to small changes in air pressure. The scale was zeroed once the sensor and water runoff system were fixed to it, and before placing the meat sample.

Once the meat was in place, the sensor (described in Sect. 3) was positioned on top of the sample and fixed in place. A conformal polypropylene based spray coating was applied to the sensor (both radiating and ground planes) to eliminate issues with corrosion which could cause damage to both the meat sample and the sensor.

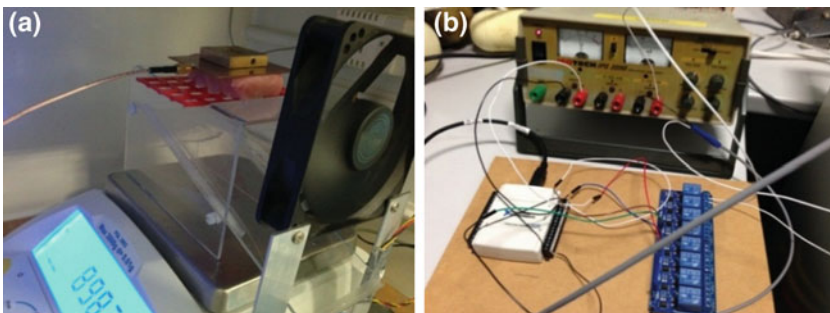


Fig. 5 **a** Experimental setup inside the refrigerator, showing the water run-off system, digital scales, meat sample, sensor and fan system used to promote rapid drying and reduce water residue; **b** the relay system for controlling fan via LabView

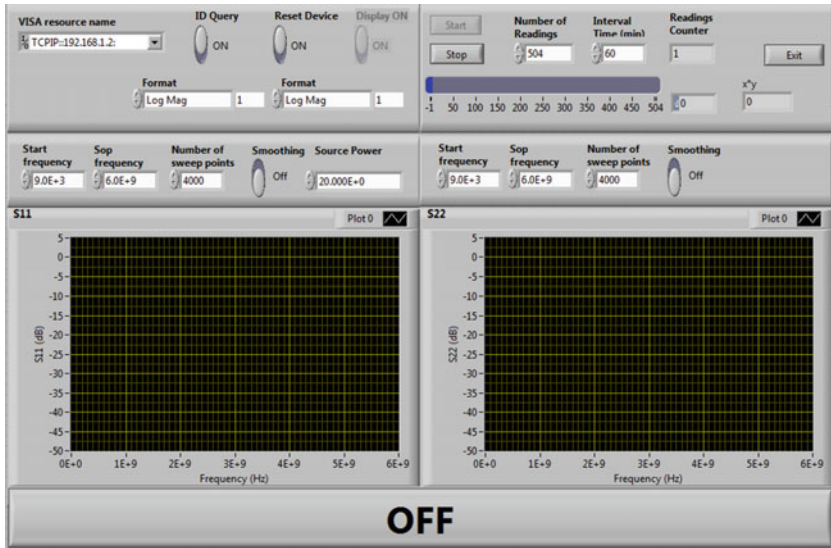


Fig. 6 LabView interface utilised for continuous automated measurements over the experimental period

The sensor was connected to a Vector Network Analyser (VNA, model Rohde and Schwarz ZVL13), which in turn was connected to a desktop computer running a bespoke LabView interface (see Fig. 6) for continuous capture of S-Parameters (namely S_{11}). Two identical systems were utilised in order to facilitate multiple measurements and repetitions of the experimental work, which was conducted over a period of 28 days.

Measurement from the patch sensor was provided by using the S_{11} -parameter from the VNA since the sensor is single port structure. Data acquisition (i.e. S_{11} , temperature and weight) took place once per hour over a period of 6.5 days; at this point typically the loin samples have lost >40 % of their original weight through shedding of loosely bound and immobilised water, and the experiment may be halted. Weight and S_{11} measurement were then correlated to determine the relationship between weight loss of the meat and change in EM signature from the sensor.

5 Results

Figure 7 shows the S_{11} measurements, i.e. S_{11} of sample of pork loin steak. The measurements shown in this figure were taken every hour (i.e. 24 times per day) over a period of 6.5 days. Measurements of the weight loss of the sample also were

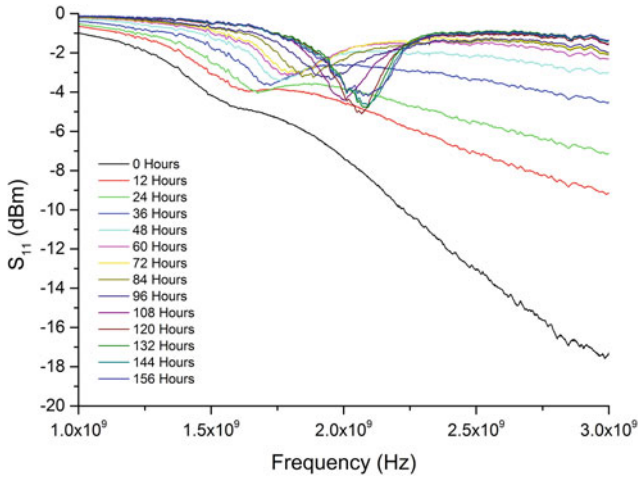


Fig. 7 Readings from the electromagnetic wave sensor; measurements were taken once per hour in the frequency range 1–6 GHz, but for clarity data from 1 to 3 GHz is presented, with measurements from 12 h intervals over a 6.5 day period

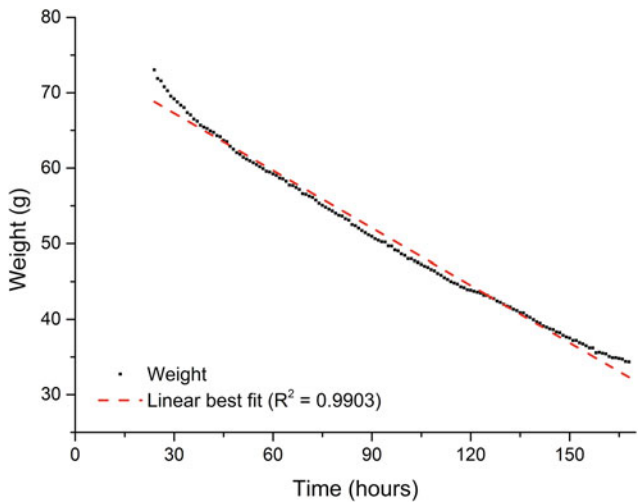


Fig. 8 Typical weight loss of loin samples over a 7 day period. In this time frame, water lost from the meat, which is inferred via weight loss, tends to follow a linear model very closely, as demonstrated here with $R^2 = 0.9903$

taken at the same time during the week, with Fig. 8 illustrating the typical loss experienced.

It can be seen in Fig. 7 that there is a noticeable change in EM signature. The change is thought to be caused by the decreasing amount of water in the meat

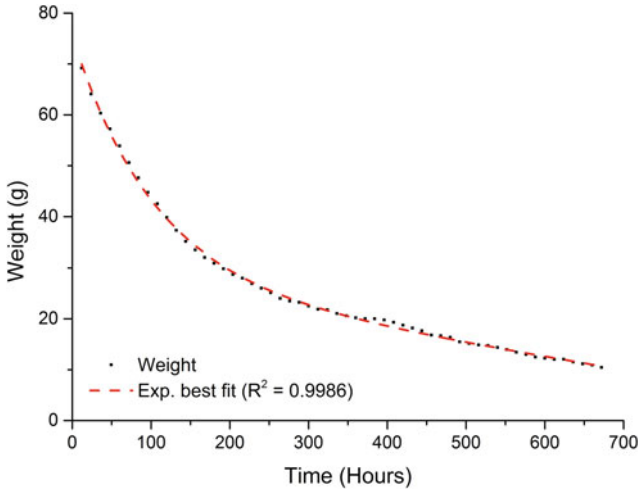


Fig. 9 Typical weight loss of loin samples over a 28 day period. In this extended time period, the loss of weight is best modelled exponentially as demonstrated here with $R^2 = 0.9986$

sample, which would have a significant impact on its dielectric properties. The change which occurs is present quite broadly within the measured spectra, particularly due to the broadband nature of the sensor used. The largest change in sensor output is experienced at approximately 3 GHz, although the smaller changes that occur in the 1–2 GHz region are highly repeatable. This is advantageous as it gives a great deal of choice in designing relevant electronics to replace the VNA should a commercialisation route be taken at some later stage.

Figure 8 shows that the sample weight loss in our experimental environment can typically be represented by a linear model; the model used here results in $R^2 > 0.99$ demonstrating a good fit. Experience shows that a linear model does not fit well if the experimental work is conducted for longer than a 7 day period; after this the rate of water loss slows dramatically and an exponential model provides a better fit, an example of which is shown in Fig. 9.

Figure 10 shows a comparison between weight and S_{11} at 1.5 GHz. The results are normalised to give a percentage change based on the range of values yielded during the experiment to enable a reasonable direct comparison. It is notable that the change in S_{11} parameter is non-linear, and the largest change in sensor output occurs in the early stages of the experiment. This is also demonstrated through the raw data output illustrated in Fig. 7.

Despite the non-linear response of the sensor, it is possible to correlate the change in sensor output to the loss of weight experienced, as proven in Fig. 11, and a linear fitting model yields $R^2 = 0.8973$. While this does indicate some potential

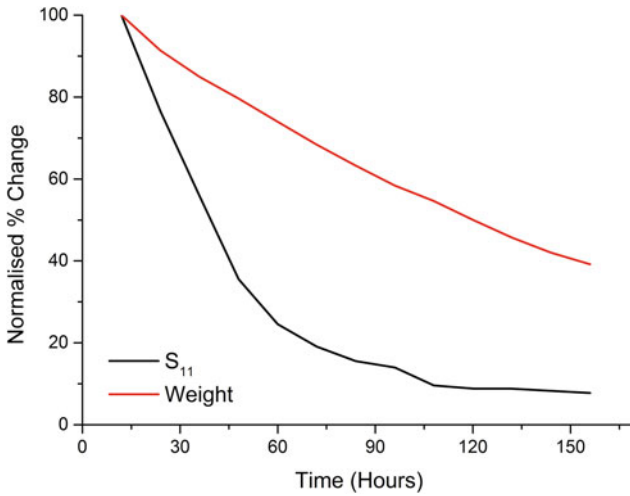


Fig. 10 Comparison with weight and measured S₁₁ at 1.5 GHz

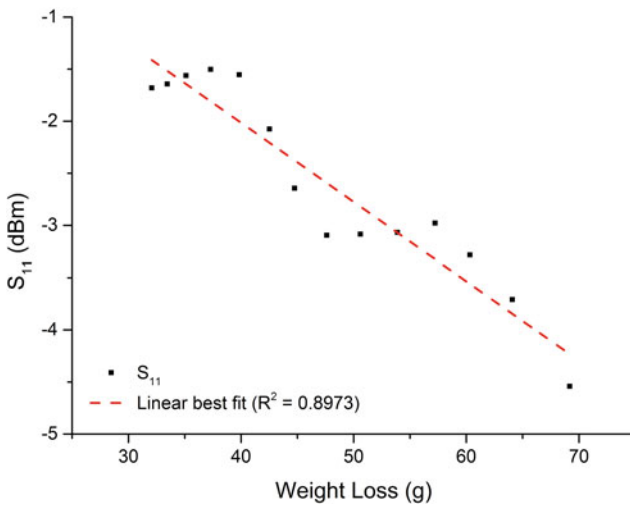


Fig. 11 Correlation of weight loss and S₁₁ at 1.5 GHz, with R² = 0.8973

for error or inaccuracy from the sensor, it is certainly a good step in demonstrating the capability of electromagnetic wave sensors at the low GHz frequencies for monitoring the moisture content of curing meat.

6 Conclusion

The purpose of this work was to demonstrate the capability of electromagnetic wave sensors operating at low GHz frequencies for monitoring the meat curing process. Through a methodology, developed in partnership with experts from the Norwegian food industry, this work has taken a valuable first step in demonstrating the capability of the sensor technology. In particular, the results demonstrate a clear correlation ($R^2 = 0.8973$) between the weight lost by meat samples, with weight lost being equated to water loss, and the S_{11} output of the sensor utilised.

The ability of this sensor system to monitor the water content of cured meat could have huge implications for the meat industry, who currently lack appropriate tools for inspection of products *in situ* during the processing stages. While there have been significant improvements over recent years with the introduction of x-ray scanners, near-infrared and optical systems, they currently do not provide the opportunity for continuous monitoring of water content, perhaps due to cost, safety or practicality. Alternative testing methods tend to be destructive, either through the use of invasive probes, which pose a contamination risk, or the sampling of meat for short time-based studies. Since the water content of meat has impact on the saleable value in addition to its quality and shelf-life, the availability of tools to monitor water content, and perhaps more importantly, the loss of water, is certainly desirable.

While this is an issue that is present across the meat industry (i.e. not only the cured meat sector), the reliance on “rule of thumb” or processing techniques passed on through family generations precludes advancement which could improve the sustainability of cured meat production. In particular it is suggested by some in the industry that significant savings in time and energy could be made through knowing at which stage in the curing process a product is. Given that the curing process could well be taking place over days, weeks or even months, knowing whether a product is ready earlier than expected allows it to be shipped for sale and the precious temperature and humidity controlled environments can be utilised effectively for new product. Such information could be derived from knowing the product water content.

There is still considerable work to be conducted in this area, particularly to prove the technology in a real-world scenario. Working with partners in Norway and Spain, the authors plan to do just that and test the technology on a range of meat products, particularly lamb and pork. Given the success so far at relatively low GHz frequencies, the outlook for the future is optimistic as the electronics to generate EM waves at these frequencies is abundant. This means that the technology could be made portable and be presented in a number of different forms for instantaneous and continuous monitoring purposes across the industrial and research domains.

Acknowledgments The authors thank Chechen Ministry of Education and Science and Chechen Government for their support during the PhD research. Furthermore, the authors thank the members of the INFORMED EUREKA project consortium for their continued support of LJMU researchers in this application of their sensor technology.

References

1. W. Verbeke, Consumer attitudes and communication challenges for agro-food technologies. *Agro Food Ind. Hi-Tech* **22**(5), 34–36 (2011)
2. W. Verbeke, L. Van Wezemael, M.D. de Barcellos, J.O. Kügler, J.-F. Hocquette, Ø. Ueland, K.G. Grunert, European beef consumers' interest in a beef eating-quality guarantee Insights from a qualitative study in four EU countries. *Appetite* **54**(2), 289–296 (2010)
3. K.G. Grunert, Future trends and consumer lifestyles with regard to meat consumption. *Meat Sci.* **74**(1), 149–160 (2006)
4. J.L. Damez, S. Clerjon, Quantifying and predicting meat and meat products quality attributes using electromagnetic waves: an overview. *Meat Sci.* **95**(4), 879–896 (2013)
5. G. Rentfrow, R. Chaplin, S.P. Suman, Technology of dry-cured ham production: Science enhancing art
6. SWISS MEAT, Production of Meat Specialties (2014), <http://www.schweizerfleisch.ch/en/swiss-meat/handling/production-of-meat-specialties/>. Accessed: 18 May 2014
7. M. Adous, P. Quéffélec, L. Laguerre, Coaxial/cylindrical transition line for broadband permittivity measurement of civil engineering materials. *Meas. Sci. Technol.* **17**(8), 2241–2246 (2006)
8. B. Goy, P. Martin, J.-M. Leban, The measurement of wood density by microwave sensor. *Holz als Roh- und Werkst.* **50**(4), 163–166 (1992)
9. L. Gradinarsky, H. Brage, B. Lagerholm, I.N. Björn, S. Folestad, In situ monitoring and control of moisture content in pharmaceutical powder processes using an open-ended coaxial probe. *Meas. Sci. Technol.* **17**(7), 1847–1853 (2006)
10. O. Korostynska, A. Mason, M. Ortoneda-Pedrola, A. Al-Shamma'a, Electromagnetic wave sensing of NO₃ and COD concentrations for real-time environmental and industrial monitoring. *Sens. Actuat. B Chem.* **198**, 49–54 (2014)
11. O. Korostynska, M. Ortoneda-Pedrola, a Mason, a I. Al-Shamma'a, Flexible electromagnetic wave sensor operating at GHz frequencies for instantaneous concentration measurements of NaCl, KCl, MnCl₂ and CuCl solutions. *Meas. Sci. Technol.* **25**(6), 065105 (2014)
12. A.I. Al-Shamma'a, O. Korostynska, A. Mason, Microwave sensors for the non-invasive monitoring of industrial and medical applications. *Sens. Rev.* **34**, 182–191 (2014)
13. M.F. J.H. Goh, A. Mason, O. Korostynska, A.I. Al-Shamma'a, P. Browning, Real-time monitoring of bodily fluids using a novel electromagnetic wave sensor. *J. Public Heal. Front.* **2** (4) 201–206 (2013)
14. A. Mason, O. Korostynska, M. Ortoneda-Pedrola, A. Shaw, A. Al-Shamma'a, A resonant co-planar sensor at microwave frequencies for biomedical applications. *Sens. Actuat. A Phys.* **202**, 170–175 (2013)
15. J.H. Goh, A. Mason, M. Field, P. Browning, A. Al-Shamma'a, Using a microwave sensor as an online indicator of neurological impairment during surgical procedures. *Key Eng. Mater.* **543**, 368–372 (2013)
16. A.I. Al-Shamma'a, B.M. Abdullah, J.D. Cullen, O. Korostynska, A. Mason, Assessing water-holding capacity (WHC) of meat using microwave spectroscopy. *Sens. Technol. Curr. Status Futur. Trends I*, **7**, 117–140 (2014)
17. A.I. Al-Shamma'a, S.G. Bjarnadottir, K. Lunde, O. Alvseike, A. Mason, Assessing quality parameters in dry-cured ham using microwave spectroscopy. *Meat Sci* (in-Press, 2015)
18. S. Clerjon, J.L. Damez, Microwave sensing for an objective evaluation of meat ageing. *J. Food Eng.* **94**(3–4), 379–389 (2009)
19. F. Ray, Meat curing. Oklahoma State University (2014), <http://pods.dasnr.okstate.edu/docushare/dsweb/Get/Document-2055/ANSI-3994web.pdf>. Accessed 19 May 2014
20. N.G. Marriott, P.P. Graham, V.C. Extension, *Some Solutions to Difficulties of Home-curing Pork*. Virginia Cooperative Extension (2000)
21. B.A. Constantine, *Antennas Theory. Analysis and Design*, 3rd edn. (Wiley, Hoboken, 2005)

An Improved Fusion Algorithm For Estimating Speed From Smartphone's Ins/Gps Sensors

Arijit Chowdhury, Avik Ghose, Tapas Chakravarty
and P. Balamuralidhar

Abstract In recent times, number of researchers have investigated vehicle tracking applications by fusing the measurements done by accelerometers (as part of Inertial Navigation System-INS) and Global Positioning System (GPS). Since smartphones contain both the set of sensors, there exists a high degree of interest in utilizing personal phones for such tracking applications. However, mobile phone sensors have limitations in measurement accuracy and reliability. Usually, sudden changes in vehicle speed are not always captured well by GPS. Accelerometers, on the other hand, suffer from multiple noise sources. In this chapter, we investigate the noise performance of a few smartphone based accelerometers. Then, we apply the said noise analysis for improving the estimation of the speed of moving vehicle, as captured by GPS. A number of experiments were carried out to capture the vehicle's position and speed from OBD2 (On Board Diagnosis V2), GPS as well as 3-axes accelerometer. We also demonstrate a method by which the phone's orientation is compensated for while calculating speed from the measured acceleration. Further, a new method of INS/GPS fusion is proposed which enhances the accuracy of speed estimation. It is envisaged that with increasing estimation accuracy, the application of multi-sensor fusion in autonomous vehicles will be greatly enhanced.

Keywords GPS · Allan variance · OBD2 · Speed correction · Accelerometer · SCA

A. Chowdhury · A. Ghose · T. Chakravarty (✉)
TCS Innovation Labs, Tata Consultancy Services, Kolkata, India
e-mail: tapas.ieee@gmail.com

A. Chowdhury
e-mail: arijit.chowdhury2@tcs.com

A. Ghose
e-mail: avik.ghose@tcs.com

P. Balamuralidhar
TCS Innovation Labs, Tata Consultancy Services, Bangalore, India
e-mail: balamurali.p@tcs.com

1 Introduction

A vehicle navigational framework that combines GPS and INS measurements is gaining much importance and has become an important field of study. The performance of low cost GPS receiver together with low cost INS (or alternatively, inertial measurement unit -IMU) is therefore very important from navigational perspective [1, 2]. Detailed performance analyses of such sensors are likely to throw up new approaches that will greatly enhance the estimation accuracy in futuristic vehicles including the autonomous ones. Different sensors have different pros and cons. Also as mentioned by Gupta [2], for different conditions of use, the sensor measurement accuracy varies. Therefore in order to achieve precision, we need to “experimentally validate the estimates against high accuracy vehicle state estimators” [2]. However, GPS systems can fail in a few common locations (namely urban canyons, actual canyons, or forested road areas) due to non-availability of satellite signal or due to multi-path errors [2]. For such cases, one can fuse accelerometer measurements with GPS to derive accuracy.

Personally owned Smartphones are becoming the most popular choice in deploying sensors like accelerometers and gyroscopes, not just for the purpose of navigation but also for the purpose of introducing ‘driving style’ related applications. If personal phones can be utilized for accurate speed estimation, new solutions can be introduced to serve the consumers better. Also, such data can be used as the basis for sending feedback signals directed towards vehicle control and guidance [3]. Accelerometers are generally used to identify aggressiveness in driving [4, 5]. On the other hand, smartphones have an added advantage in being able to process the captured data and transmit them over communication network [6]. Two recent works on similar lines are related to the smartphone based sensing for identifying aggressive driving behaviour [7, 8]. Keeping the above stated synergy in mind, we decided to carry out extensive experiments using smartphones and data logging tools for the purpose of investigating the accuracy and reliability of vehicle speed estimation, in a moving vehicle. It is believed that significantly improved speed estimation accuracy under varying conditions, particularly for congested city drive, will make autonomous vehicles more reliable.

In this paper, we propose an approach to mitigate the issue of estimating the true speed of a moving vehicle, using primarily smartphone accelerometers. It is known that the accelerometers suffer from multiple noise effects. The noise level and the type may vary from phone to phone. In order to test the variability, authors have used Allan Variance method [9, 10] to estimate and compensate for the noise present in accelerometers. Authors compare different smartphone models in terms of the noise performance of their integrated accelerometers. After suitable compensation, the measured acceleration values are integrated to obtain the speed of the moving vehicle. These speed values are fused with GPS speed measurements to obtain robust overall speed estimation. Generally, Kalman filter is a popular choice for such sensor fusion. Kalman filter implementation is done for measurement i.e. pseudo-range and Doppler [2]. Kalman filter applications on measured data require

robust model and works towards correcting speed in real-time. Here GPS plays a major role [2], as GPS measured speed “corrects the inertial estimate periodically”. Apart from Kalman, Monte Carlo based statistical filtering is also used in vehicle tracking and navigation application [11]. Such filtering is also known as particle filtering method. They are also used for vehicle trajectory generation [12]. Some available solutions use Sequential Importance Resampling (SIS) which assumes state dynamics and measurement functions to be known [13].

In this paper, we present a novel data driven approach that is computationally efficient and uses less resources. The purpose of this method (named Slope Check Algorithm -SCA) is to fuse GPS and accelerometer data appropriately so that the accuracy of speed estimation is greatly improved. Towards such objective, the GPS based speed measurements, at every ‘ n ’ sec interval, are used to correct the speed estimation obtained from acceleration measurements (at higher sampling rate). A new empirical fusion method of forward and backward speed estimation is proposed. It is seen that the proposed approach significantly improves the speed estimation. For comparison purposes, we have utilized the OBD2 based speed measurement (denoted by v_{OBD}) as the true measure of the vehicle speed.

2 Motivation

Rapid progress in sensor technology has made it possible to deploy both INS and GPS receivers in modern day cars. GPS is primarily used for navigational purposes; thus in most cases, 1–5 s sampling interval for GPS data is deemed adequate. Also recreational (mobile phone based) and professional GPS units have different purposes and different levels of accuracy [14]. Low cost GPS loses accuracy if sampling rate is above 1 Hz.

A GPS measurement provides both the position and the speed of car, together with an accuracy measure (usually called Horizontal Accuracy). Such speed measurements can also be used for assessing the driving skills of the driver. But those applications usually require speed measurements at higher sampling rate. Thus, if acceleration (at higher resolution) can be fused with sparse measurement of GPS speed, it will enable a wide range of applications to be deployed in GPS-INS system; implemented through a distributed server-client application. As modern day smartphones include both INS and GPS and can communicate with a remote server, hence they can be used as internet connected sensors [6]. In this work, we primarily deal with acceleration-GPS fusion to obtain speed at higher resolution. Towards achieving that goal, noise analysis on smartphone based accelerometer is done. Then a fusion algorithm is proposed which reduces the effects of noisy measurements present in acceleration data and gives output speed at higher rate.

Table 1 Summary of different errors

Error type	Description	Effect on speed
Bias	Constant bias ε in present in accelerometer's output signal	A linearly growing speed error
Temperature effects	Temperature dependent residual bias	Any residual bias causes an error in speed which grows linearly with time
Calibration	Deterministic errors in scale factors, alignments	Speed changes proportional to the time rate and duration of acceleration
Bias instability	Bias fluctuations, which can be modelled as a bias random walk	A second-order random walk in speed
White noise	White noise with standard deviation (σ)	A first-order random walk

3 Accelerometer Noise Analysis

In this section, the different types of noise errors impacting an accelerometer measurement are investigated. An important concern regarding the noise effect is that they impact the speed evaluation vide the integration process. Thus it is important to know the difference in noise level and type of noise present in different smartphones. This will enable us to judge compatibility and accuracy across different smartphones.

A. Constant bias

The offset of the output value from the true value is called bias of an accelerometer (in m/s^2). A constant bias error of ε , when integrated to get speed, causes an error which grows proportionally with time. The total error in speed estimation is $e(t) = 0.5.\varepsilon.t$, where t is the time of integration [10].

B. White Noise/Velocity Random Walk

Accelerometer output generally contains some amount of white noise. Integration of the white noise produces a random walk with variance proportional to \sqrt{t} . Hence, white noise creates a velocity random walk [10]. This is measured in $m/s/\sqrt{s}$.

C. Rate Ramp

This is a deterministic error. Slow monotonic change of output over time is Rate Ramp. It can be described as: $w(t) = R.t$, where R is the slope of the ramp. This creates a line of slope +1 in Allan Deviation (AD) plot [9, 10]. R is the value of Allan Deviation at time = $\sqrt{2}$.

Other errors are briefly summarized in Table 1 [10].

4 Allan Deviation Results for Different Phones

In this section we present the results on Allan Variance method applied to different phones. These phones have different accelerometer makes; in addition, they may be embedded differently in each smartphone. Thus, the Allan Variance method is applied on different phones to measure their noise characteristics.

Allan Variance is a time domain signal analysis technique that can be used on any signal to determine the character of noise in the system. Allan Variance is measured as a function of averaging time.

Hence Allan Variance calculation gives [t,AD(t)] pair where t = averaging time. AD(t) is the value of Allan deviation = $\sqrt{\text{Allan variance}}$. The technique to calculate AD is given in [9, 10] and for the sake of completion, we reproduce it, as below.

1. Divide a sequence of data it into sequence of length t. There must be enough data for at least 10 such sequences. Hence it is good practice to log data for a long time. This will enable user to detect different type of noise (if present) in signal.
2. The data in each bin is averaged to obtain a series of averages (a(t)₁, a(t)₂, ..., a(t)_n), where n is the number of bins.
3. The Allan Variance is then calculated using Eq. (1)

$$AVAR(t) = \frac{1}{2 * (n - 1)} \sum_i (a(t)_{i+1} - a(t)_i)^2 \tag{1}$$

Allan Deviation, denoted by AD(t) is given in (2)

$$AD(t) = \sigma(t) = \sqrt{AVAR(t)} \tag{2}$$

Then [t, AD(t)] pair is plotted in a log-log plot for identifying different noises. In the log-log scale plot, the different slope sections identify different types of noise which are orthogonal in nature. The process identification is followed by computing the numerical parameters directly from the AD plot [9, 10]. A typical plot of Allan deviation shows different errors in different sections of ‘t’. The slope of the line indicates type of noise and parameters of different noise can be computed from the AD curve. Value of different noise parameters can be calculated easily from the curve. Table 2 of reference [10] gives comprehensive steps to calculate different error terms (Fig. 1).

The error modelling, discussed as above, is now tested on different smartphones (iphone5, google nexus, LG nexus S and Samsung galaxy note 2). Results and plot for these 4 types of smartphones are presented in Figs. 2, 3, 4 and 5 and Table 2 and 3 respectively.

Table 2 White noise variance for different phones

Accelerometers	x axis	y axis	z axis
Google nexus	0.019	0.018	0.02
iphone 5	0.0029	0.0031	0.003
Lg nexus	0.002	0.0018	0.0031
Note 2	0.0016	0.0017	0.0025

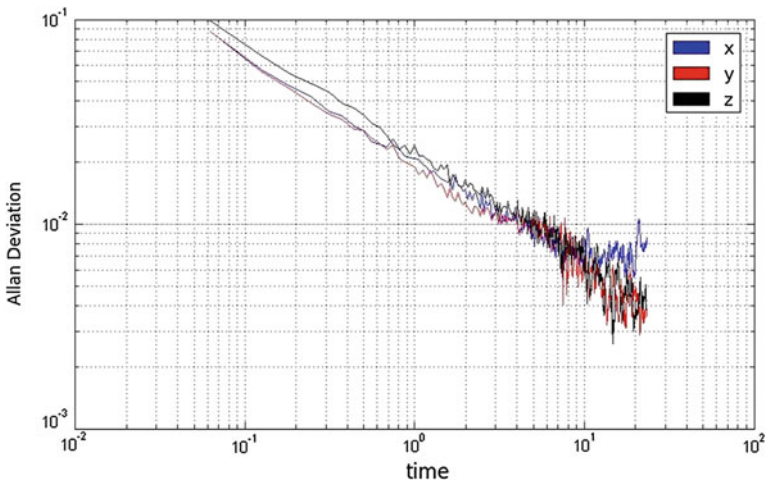


Fig. 1 Allan deviation plot for Samsung Google Nexus for all 3 axes

The analysis of the Samsung Google Nexus AD plot (as shown in Fig. 1) displays the presence of white noise for all three axes and additionally a bias instability for X axis. The value of white noise variance is the value at $t = 1$ on the approximate line with slope $-1/2$. Clearly for x, y, z axis the value of σ at $t = 1$ are 0.019, 0.018, 0.02 respectively. Hence, these are the standard deviation of white noises for the given axis. The values of different types of error coefficient can be calculated as indicated in Table 2. Only for the X axis, the Allan deviation curve shows a flat portion from $t = 7$ to 25 s. Hence bias instability for X axis $BX = 0.0065/0.664 = 0.0098$.

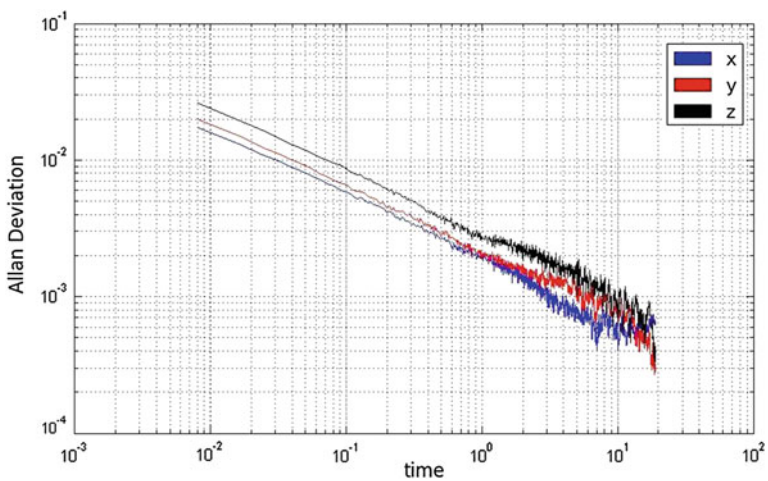


Fig. 2 Allan deviation plot for Samsung Galaxy Note 2

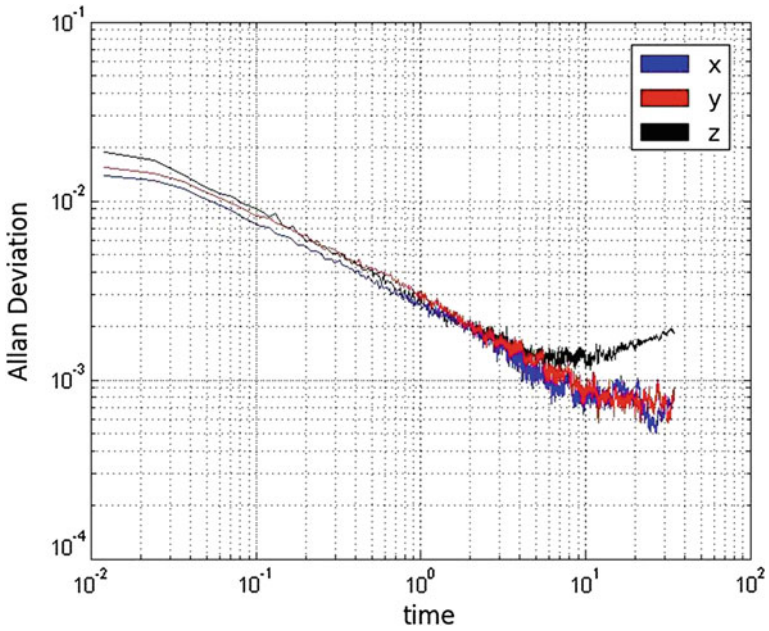


Fig. 3 Allan deviation plot for iPhone 5

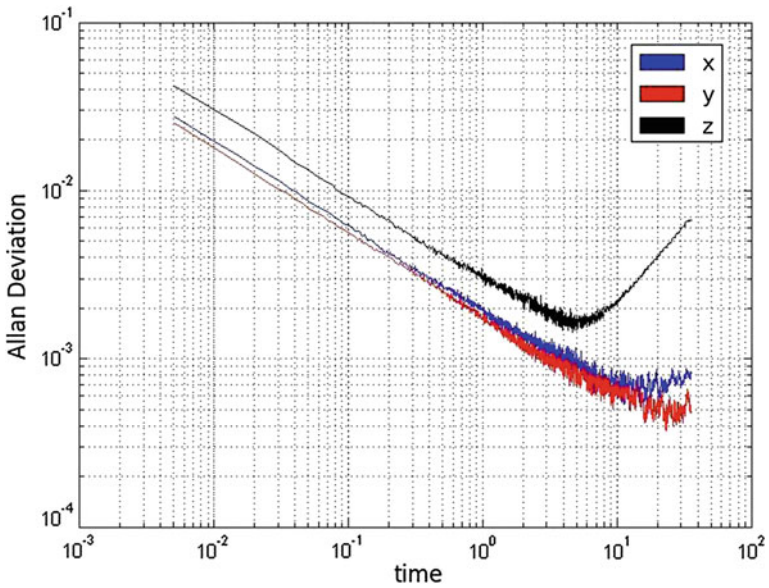


Fig. 4 Allan deviation plot for LG Nexus



Fig. 5 Experimental set-up displaying Bluetooth OBDII device and Tab as data logger

For Samsung Note 2, the Allan deviation plot is shown in Fig. 2. Bias instability (portion with slope = 0 in time zone 7–10 s.) is present in the X axis only with value $B_x = 0.0006/0.664 = 0.0009$, which is 10 times smaller than Samsung Google Nexus (refer Fig. 2). Thus, it is seen that the accelerometer performance in Samsung Note 2 is better than Samsung Google Nexus phone. Similar comparisons can be made from Allan deviation plots to obtain noise characteristics and determine different noise coefficients (as listed in Table 3 and 4).

Allan deviation plot for iPhone 5 is given in Fig. 3. The plot shows the presence of white noise and bias instability (flat region in the AD curve) on each the axis. The curve of Z-axial accelerometer in iphone plot (Fig. 3) indicates a correlated noise and/or sinusoidal noise in time interval 10–36 s. All the noise parameters found with method described in this note using Table 2 are summarized in Table 3.

AD curve for LG Nexus in Fig. 4 shows presence of white noise for all 3 axes, bias instability for X axis only. Presence of Rate Ramp is observed only in case of LG nexus (Fig. 4) for Z axis in the region $t = 5-40$ s. (slope of AD curve in Fig. 4 is +1) and measurement for this noise can be measured by fitting a straight line through the slope and reading value at $t = \sqrt{2}$. Hence for that Rate ramp $RZ = \sigma(\sqrt{2}) = 0.0004$. White noise parameters for LG nexus are summarized in Table 3.

Now from the presented AD figures the white noise parameter ($m/s/\sqrt{s}$) of these 4 phones are given in Table 2.

In Table 3 bias instability (in m/s^2) for different phones is consolidated.

Table 3 Bias instability for different phones

Accelerometers	x axis	y axis	z axis
Google nexus	0.0098	NA	NA
Iphone 5	0.0012	0.0012	0.0018
Lg nexus	0.0012	NA	NA
Note 2	0.0009	NA	NA

Table 4 Sample data from experimental setup

GPS time	GPS speed (m/s)	Horizontal dilution of precision	G(x)	G(y)	G(z)	Speed (OBD) (km/h)
Fri Mar 21 09:45:15 GMT + 05:30 2014	1.68	12	0.995988	-2.43251	11.79863	11
Fri Mar 21 09:45:16 GMT + 05:30 2014	2.28	8	0.287304	-0.14365	8.255207	12
Fri Mar 21 09:45:17 GMT + 05:30 2014	2.59	12	-0.99599	-2.48039	11.18571	15
Fri Mar 21 09:45:18 GMT + 05:30 2014	2.74	12	0.986411	-0.43096	10.92714	17

5 Experimental Setup and Speed Calculations

Our work is based on experiment conducted over 2 months. As experimental set-up Samsung Galaxy Note 2 and Kiwi Bluetooth OBD2 device is used. Entire setup is presented on Fig. 5. Kiwi Bluetooth connects through the on board diagnostic port (OBD2/CAN) in cars [15]. The data is logged using Torque Pro Android App which is used to log the OBD2 speed along with GPS measurements [16]. In this case, the OBD2 based speed of vehicle is collected at 1 Hz sampling rate and the accelerations are also logged using the smartphone at 1 Hz sampling rate. The experimental setup is activated when vehicle starts moving.

Data collection is done in Kolkata, India. For data collection phone is kept at constant position although this may not be possible in real life scenario. Thus the need for orientation correction for acceleration is needed. This setup is used for ongoing works related to GPS speed and accuracy also [17]. To validate our approach, we logged GPS data at different rates and then fused with acceleration data to obtain speed at acceleration sampling rate (i.e. 1 Hz). These fused speeds are then compared with OBD speed. OBD speed is taken as true speed of the vehicle. Accuracy of fused speed is measured by its deviation from true OBD speed. Data are collected in csv format. A sample data is given in Table 4.

In the given sample, GPS is collected at 1 Hz rate. For the experimental purpose, GPS sampling rate can be configured at less than 1 Hz. (for e.g. 1 sample every t seconds $t = 2, 3, 4, \dots$). Our algorithm fuses accelerometer data at F_{s_A} Hz to GPS speed at $F_{s_{GPS}}$ Hz to obtain fused speed output at F_{s_A} Hz. In the context of this paper $F_{s_A} = 1$. The phone (shown in Fig. 5) is harnessed in a fixed orientation, yet

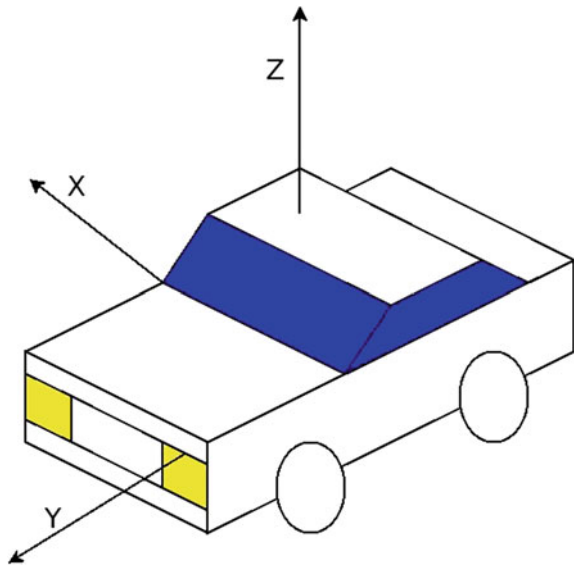
there is a small tilt of the axes of measurement. Moreover, car vibrations continue to affect the phone and hence it is necessary to measure and intermittently compensate for this tilt. The orientation measurement and correction scheme is discussed in Sect. 5.1.

5.1 Orientation Correction Calculations

The accelerations reported by the phone sensors are provided in phone coordinate system and they need to be rotated to vehicular coordinate system before further analysis [18, 19]. Hence, the phone orientation needs to be derived. However, the phone inertial sensors are noisy and an accurate stable value of orientation is not derived directly from them [20]. Hence, some corrective measures need to be applied. It is known that the directional component of the GPS measurement or the bearing is quite accurate. Similarly, while using accelerometers, the gravity vector can give accurate direction of the normal reaction force. If ‘GPS bearing’ and ‘gravity’ are orthogonal, they can be combined to provide the vehicle coordinate system where the positive ‘Y’ axis is given by the direction of vehicle movement and the positive ‘Z’ is given by the normal reaction on the vehicle. This is depicted in Fig. 6.

To achieve this rotation, a quaternion rotation matrix is created using the above mentioned axes and the accelerometer space upgraded to homogeneous coordinate system $[x, y, z, 1]$, is multiplied to the same to achieve the rotation. However due to sensor noise, the rotation matrix itself becomes noisy, making the measurements

Fig. 6 Vehicle coordinate system



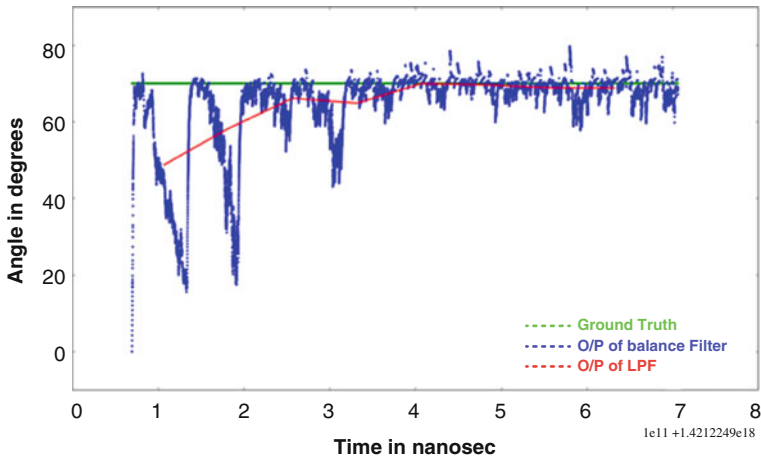


Fig. 7 Orientation values after applying our algorithm (in red)

unstable. To achieve stability in the system the orientation values need to be corrected. We have used the balance filter [21] to correct orientation. Additionally, a smoothing algorithm is developed—based on sub-sampling followed by low-pass filtering to achieve smoother results for trajectories as shown in results section. The orientation experiment was conducted by keeping the phone static in a fixed known azimuth angle for 10 min and studying the values obtained from the filter. The phone used for experimentation was a LG Nexus 5. The second experiment involved a ‘Z’ like trajectory with two 90° turns.

For orientation related experiment described as above, it is seen that after applying the balance filter the orientation values converge to the ground-truth value of orientation in a specified amount of time. Further smoothing can be done by applying a low-pass filter to remove the high-frequency jitter. This is shown in Fig. 7.

The mean and standard deviation of original and filtered output is shown in Table 5.

Further, in Fig. 8, we show a trajectory which forms a Z, and show how our algorithm is able to smooth out the orientation values.

The stability achieved in orientation deduction using the balance filter implies that further processing on the same can be applied and the solution may be used for a better GPS-INS fusion by using the accelerometer data only along the vehicle major axis for velocity estimate. Using this technique, the tilt in the phone was

Table 5 Mean and standard deviation of original and filtered signal

Signal type	Mean	Standard deviation
Original	64.68	10.80
Balanced filter output	64.04	11.31
Our algorithm	67.89	6.04

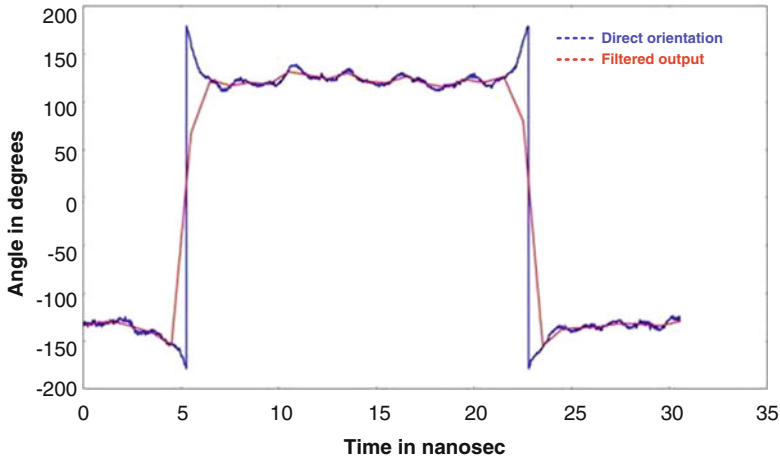


Fig. 8 Orientation value after applying our algorithm

identified on a second-by-second basis. It was seen that the tilt of the phone with respect to Z axis ranges from 5.8° to 6.2° .

5.2 Speed Calculations

For the above mentioned experimental setup, we define,

$n = 1/F_{s_{GPS}}$, delay between 2 consecutive GPS data in seconds

$N = n \cdot F_{s_A}$ No of speeds calculated from accelerometer and GPS data

From GPS we speed values: v_1, v_{N+1} , and so on. Then using the GPS and accelerometer fusion algorithm, we calculate v_1, v_2, \dots, v_{N+1} that is we compute speeds at finer resolution ($1/F_{s_A}$ seconds apart). The speed computation is described as below.

For purpose of analysis, we consider that the overall trip is segmented where the j th segment corresponds to the journey between two consecutive GPS speed measurements, $v_{(j-1)N+1}$ and v_{jN+1} . Then the speed is calculated by application of Eq. 1.

$$v(t_2) = v(t_1) + \int_{t_1}^{t_2} a(t).dt \tag{1}$$

Where $a(t)$ denotes acceleration at time t , $v(t_1)$ is the initial speed.

For forward speed correction, we use the initial speed value as $v_{(j-1)N+1}$ and continue to compute the speeds at subsequent time samples using the measured acceleration at that time sample.

Thus, we calculate v_2, v_3, \dots, v_N . These are forward speed (*F speed*) as shown in Eq. 2.

$$\hat{v}((j-1)N+i) = \hat{v}((j-1)N+i-1) + \int_{(j-1)N+i-1}^{(j-1)N+i} a.(t)dt \quad (2)$$

Now time reversal is applied whereby the initial speed considered is v_{jN+1} and intermittent speed values are computed backwards in time, as shown in Eq. 3.

$$\hat{v}(N-i) = \hat{v}(N-i+1) - \int_{N-i}^{N-i+1} a.(t)dt \quad (3)$$

Using Eq. (3) we calculate $\hat{v}_2, \hat{v}_3, \dots, \hat{v}_N$, called backward speed (*B speed*). Throughout this paper v_i denotes F speed and \hat{v}_i denotes B speed.

Once these basic calculations are done for a segment, the proposed SCA is applied to obtain a major improvement in speed estimation as compared to the one illustrated in [22].

5.3 Slope check algorithm (SCA)

For each segment, we have two GPS speed measurements at n (sec) intervals; hence we can calculate speed change in kmph/s as slope

$$S_j = (v_{(j-1)N+1} - v_{jN+1})/n$$

Thus for each segment we calculate the slope value in kmph/s. These are then categorized as follows.

- Case I: If $S_j > 4$ kmph/s—categorized as increasing
- Case II: If $S_j < -4$ kmph/s—categorized as decreasing
- Case III: Else – categorized as average

Hence for any segment there are 3 possibility categories: Increasing (denoted by I), Decreasing (denoted by D) and Average (denoted by A). For a given segment we categorize the slope of that segment as well as the previous segment. Now in speed correction flow occurs as follows:

For 1st segment we choose CaseDefault.

For j -th segment ($j > 1$)

If ($\text{slope}_{j-1} = I$ AND ($S_{j-1} = A$ OR $S_{j-1} = D$)) :

Choose caseMax.

If ($\text{slope}_{j-1} = D$ AND ($S_{j-1} = A$ OR $S_{j-1} = I$)) :

Choose caseMin.

Else

Choose CaseDefault.

The Slope Check Algorithm flowchart is given in Fig. 9.

The three conditions namely CaseMax, CaseMin and CaseDefault are described in detail in 5.3.a-c.

5.3.1 CaseDefault

In default mode we take weighted average of the F speed and B speed (which are calculated using Eqs. 2 and 3) to infer speed estimate FB speed (referred as Forward-Backward speed) of the vehicle. In default mode, let v_i denotes F speed, \hat{v}_i denotes B speed for the i th estimate (in a segment). Then the i th speed estimate (denoted by \bar{v}_i) is calculated using Eq. 4.

$$\bar{v}_i = \frac{(N - i + 1)v_i + (i - 1)\hat{v}_i}{N}, \quad 1 \leq i \leq N + 1 \tag{4}$$

Fig. 9 Slope check algorithm flow chart

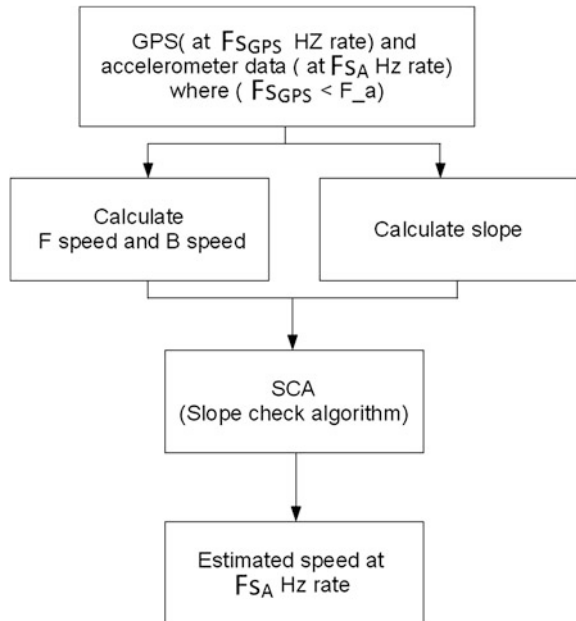


Table 6 Sample data from experimental setup

Time instance in a segment	Weight for F speed	Weight for B speed
1	1	0
2	0.9	0.1
3	0.8	0.2
4	0.7	0.3
5	0.6	0.4
6	0.5	0.5
7	0.4	0.6
8	0.3	0.7
9	0.2	0.8
10	0.1	0.9
11	0	1

Table 7 Experimental results comparing SCA with default result ($F_{sA} = 1$)

Algorithm used	r.m.s. error (m/s)	Maximum absolute error (m/s)
SCA (for N = 5, $F_{sA} = 1$)	0.79	4.91
Simple averaging (N = 5)	1.03	6.27
SCA (for N = 8)	1.15	6.57
Simple averaging (N = 8)	1.59	8.02
SCA (for N = 10)	1.39	8.45
Simple averaging (N = 10)	1.90	10.03

For each segment, these weights are dependent on N. Table 6 illustrates example of weights for N = 10.

At the time instance when GPS reading (time instance 1, 11 in Table 7) is done, the output speed is same as the measured GPS speed. The intermittent values are inferred based on slope check algorithm Default Case as shown in Table 6.

5.3.2 CaseMax

Output FB speed (i.e. ith speed) estimate is given by Eq. 5

$$\bar{v}_i = \max\{v_i, \hat{v}_i\}, \quad 1 < i < N + 1 \tag{5}$$

5.3.3 CaseMin

Output FB speed (i.e. i th speed) estimate is given by Eq. 6

$$\bar{v}_i = \min\{v_i, \hat{v}_i\}, \quad 1 < i < N + 1 \quad (6)$$

The implementation can be configured to use different values of N . For our purpose $N = 5$ was used. The experimental results are given in Sect. 6. Analysis of obtained speed is compared to OBD speed of the car in order to determine accuracy of the speed estimation.

6 Experimental Results

Once the data is collected, the acceleration measurements are compensated for orientation and noise corrections. Subsequently SCA is applied on the compensated acceleration data to estimate the speed. In our previous work [22] the estimation method offers reasonably good accuracy. But that approach relies on simple averaging of F speed and B speed. Now SCA is applied to improve the estimation further. As reference, we reproduce the result (Fig. 10) given in [22].

Further improvements are achieved by using slope SCA. It is observed that there is a decrease in speed estimate error when the SCA dependant FB speed is compared with OBD speed. Table 7 gives the r.m.s and maximum absolute error for slope check algorithm and simple averaging method.

The results in Table 7 indicates that for identical GPS sampling rate, SCA consistently performs better. Also, if we want to keep a fixed threshold for r.m.s. error, GPS sampling rate can be made lower by use of SCA. SCA with $N = 10$ gives

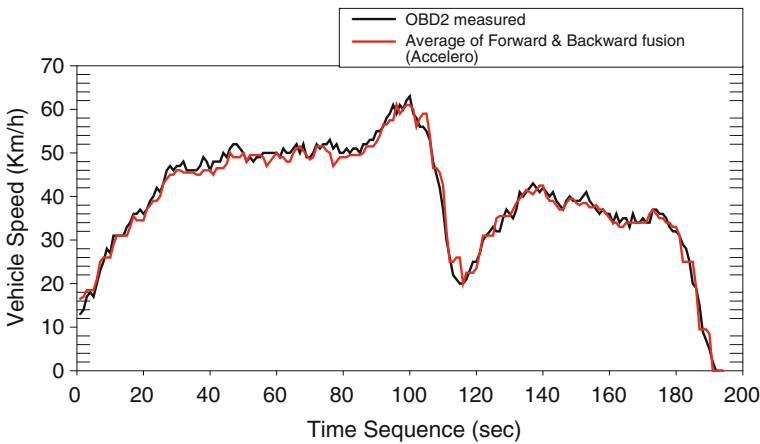


Fig. 10 Estimated speed using INS/GPS simple average and compared with OBD2 speed

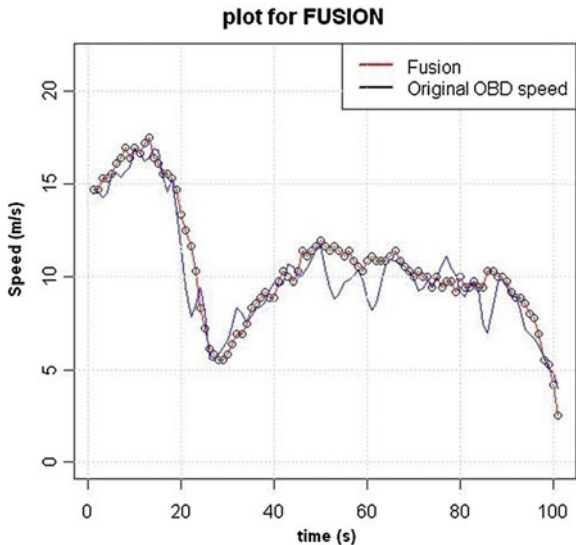


Fig. 11 Estimated speed using INS/GPS fusion (SCA) and compared with OBD2 speed

better result than simple averaging for $N = 8$. Thus SCA can replace simple averaging as a better alternative. Figure 11 displays SCA output (i.e. FB speed) and OBD speed comparison for $N = 8$.

As expected, the derived speed follows the OBD speed but with occasional high error peaks. Further investigation is done on error analysis as well as the fusion time interval n .

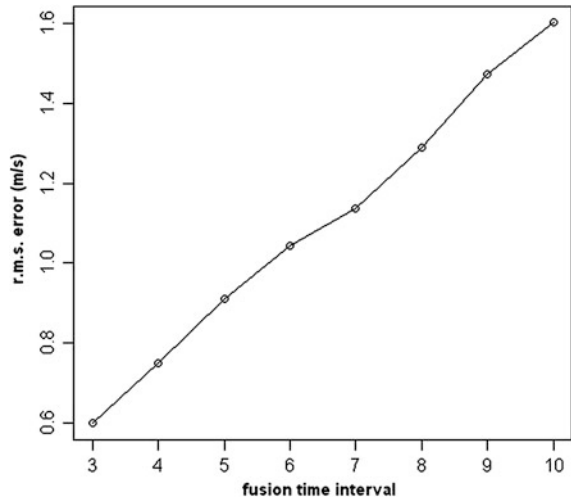
$$e_i = \overline{v_i} - v_{\text{OBD}} \tag{7}$$

The error analysis is carried out only for those segments of journey that represent a moving vehicle. Results for the error analysis are shown in Table 8.

Table 8 Experimental results for error with varying fusion time interval

Fusion Interval (s)	rms error (m/s)	Mean(error) (m/s)	Standard deviation(error) (m/s)
3	0.59	-0.16	0.58
4	0.74	-0.16	0.73
5	0.9	-0.21	0.88
6	1.04	-0.27	1.0
7	1.13	-0.22	1.12
8	1.29	-0.27	1.26
9	1.47	-0.29	1.44
10	1.6	-0.40	1.55

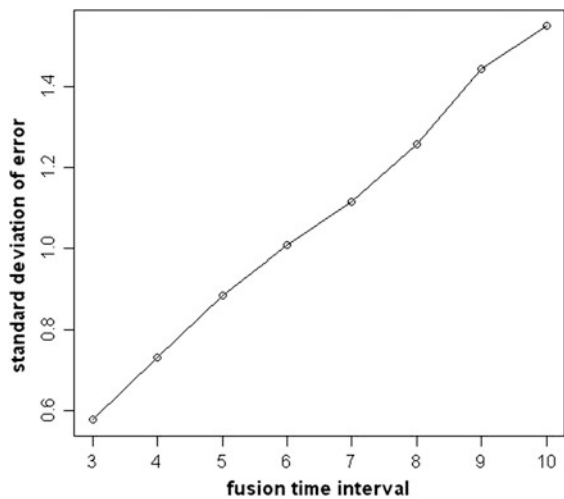
Fig. 12 Rms error variation with fusion time interval



From Table 8 it is quite clear that increase in time gap (i.e. fusion time interval) increases the estimate error. But such increase in both r.m.s error and standard deviation of error is linear with the fusion time interval. Figures 12 and 13 displays the variation of r.m.s error and standard deviation of error with respect to fusion time interval.

Additionally the pdf plot for the estimate error shows that though the spread of the error curve vary with change in fusion time interval but nature of pdf curve is similar. Figure 14 displays obtained result for a journey. All statistical analysis is done using R tool [23].

Fig. 13 Standard deviation of error variation with fusion time interval



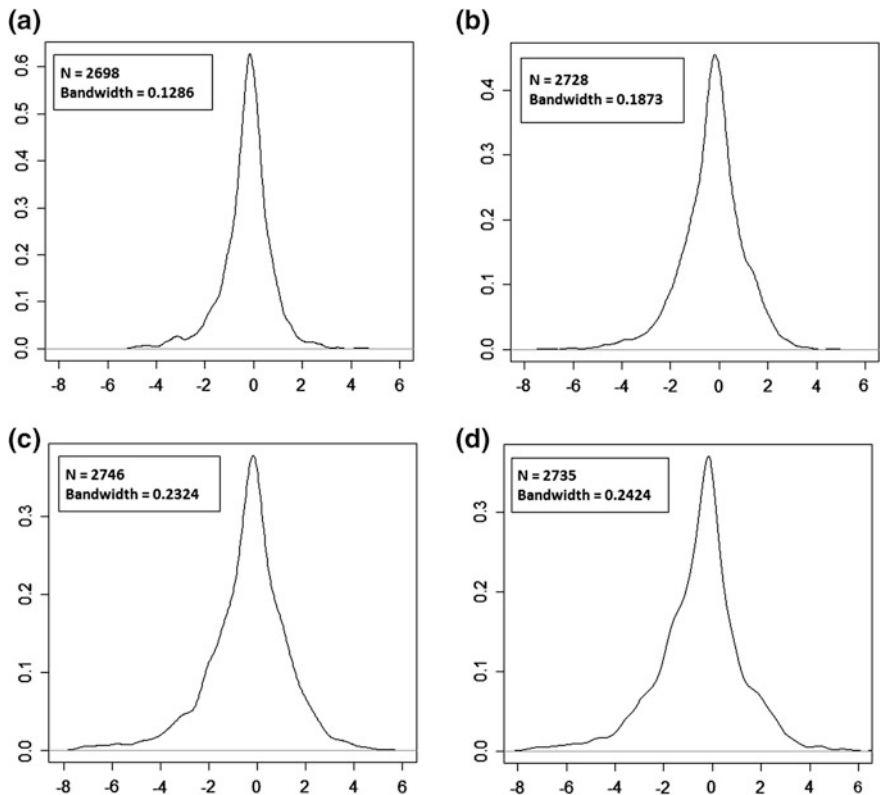


Fig. 14 Plots of probability distribution of error in speed for different fusion intervals. **a** N = 5; **b** N = 7; **c** N = 9; **d** N = 10

The above analysis shows that for a desired level of accuracy, the fusion time interval can be suitably chosen by scaling the error measurements done at one fusion interval. To obtain the range of the estimated error, the 5th and the 95th percentile of the error is computed for different values of n (fusion time delay). Table 9 displays the relevant percentile values.

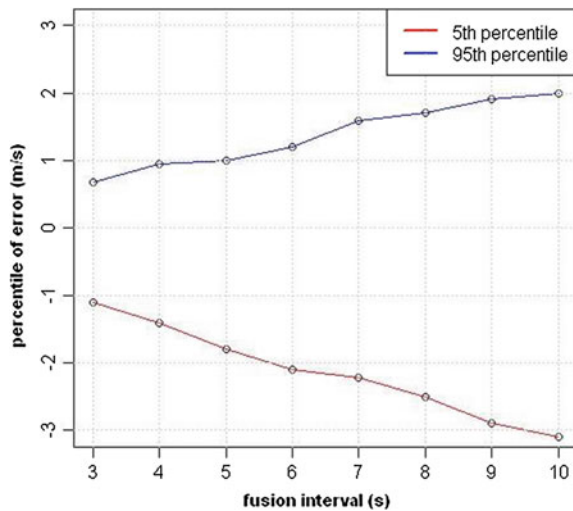
It can be seen that the percentile error varies linearly with fusion interval. It is very important to observe the variation of 5th and 95th (shown in Fig. 15) percentile.

From Fig. 15, the linear variation of error with fusion interval is approximately established. Hence error can be characterize as $O(n)$, where n denotes fusion interval. Also as it observed that mean of GPS speed is less than that of OBD speed. Hence errors for fusion speed (SCA) have a nonzero mean but that is expected as SCA corrects speed using GPS speed. GPS speed has nonzero mean for GPS speed error (defined as GPS speed—OBD speed).

Table 9 Experimental results for percentile of error

Fusion Interval (s)	5th percentile (m/s)	95th percentile (m/s)
3	-1.1	0.68
4	-1.4	0.95
5	-1.8	1.0
6	-2.1	1.2
7	-2.21	1.58
8	-2.5	1.7
9	-2.9	1.9
10	-3.1	2.0

Fig. 15 Plots of 5th and 95th percentile of error in speed for different fusion intervals



7 Conclusion

Smartphone market is increasing at a rapid pace. With technological progress the usage of smartphones in large scale sensor deployment and analysis is gaining much prominence. Phone based sensors like accelerometers and GPS can be easily deployed in vehicle tracking solutions; however, such solutions are affected by the professed lack of measurement accuracy as compared to professional grade units. A GPS based speed estimation method requires high sampling rate, to obtain accuracy. Thus, for a typical long duration vehicle trip, the power consumption will be heavy. Accelerometer based speed estimation can become a much preferred method provided the sensor errors are properly compensated for. In this paper, we attempt to analyze a few categories of smartphones (as sensor and computation units) from the perspective of noise. Further, we apply an innovative fusion algorithm (SCA) to get a much better estimate of vehicle speed using primarily

accelerometer measurements. Also using statistical analysis it is verified that error grows linearly with fusion interval. Thus tuning of fusion interval to contain error within a predefined limit can be very useful. Use of such adaptive scheme can empower higher accuracy at low power rate and cost. Also tracking speed of a vehicle in a zone where GPS is not available (like tunnel or a shadow zone) is possible. Thus SCA with a configurable fusion interval can serve as an improved tool for calculating car speed with an acceptable accuracy. SCA will generate output speed from a non-uniform GPS sampling, thus eliminating the need for a fixed GPS sampling rate algorithm. SCA is easily adaptable for such purpose.

References

1. M.S. Grewal, L.R. Weill, A.P. Andrews, *Global positioning Systems, Inertial Navigation, and Integration* (Wiley, New Jersey, 2007)
2. V. Gupta, Vehicle localization using low-accuracy GPS, IMU and map aided vision, Doctoral Thesis, The Pennsylvania State University (2009)
3. R.D. Martini, GPS/INS sensing coordination for vehicle state identification and road grade positioning, Doctoral thesis. The Pennsylvania State University (2006)
4. T. Chakravarty, A. Ghose, C. Bhaumik, A. Chowdhury, MobiDriveScore-a system for mobile sensor based driving analysis: A risk assessment model for improving one's driving, in *7th International Conference on Sensing Technology (ICST)*, pp. 338–344 (2013)
5. T. Toledo, O. Musicant, T. Lotan, In-vehicle data recorders for monitoring and feedback on drivers behavior. *Trans. Res. Part C: Emerg Technol* **16**(3), 320–331 (2008)
6. A. Ghose, P. Biswas, C. Bhaumik, M. Sharma, A. Pal, A. Jha, Road condition monitoring and alert application: using in-vehicle smartphone as internet-connected sensor, in *2012 IEEE International Conference Proceedings of Pervasive Computing and Communications Workshops (PERCOM Workshops)*, pp. 489–491 (2012)
7. J.H. Hong, B. Margines, A.K. Dey, A smartphone-based sensing platform to model aggressive driving behaviors, in *ACM Conference on Human-Computer Interaction (CHI)* (Toronto, Canada, 2014)
8. R. Vaiana, T. Iuele, V. Astarita, M.V. Caruso, A. Tassitani, C. Zaffino, V.P. Giofrè, Driving behavior and traffic safety: An acceleration-based safety evaluation procedure for smartphones. *Mod. Appl. Sci.* **8**(1), 88–96 (2014)
9. O.J. Woodman, An introduction to inertial navigation, University of Cambridge, Computer Laboratory, Technical Report UCAMCL-TR-696, 14, 15, 2007, <http://www.cl.cam.ac.uk/techreports/UCAM-CL-TR-696.pdf>
10. X. Zhang, Y. Li, P. Mumford, C. Rizos, Allan variance analysis on error characters of MEMS inertial sensors for an FPGA-based GPS/INS System, in *Proceedings of the International Symposium on GPS/GNSS* (2008)
11. F. Gustafsson, F. Gunnarsson, N. Bergman, U. Forssell, J. Jansson, R. Karlsson, P. J. Nordlund, Particle filters for positioning, navigation, and tracking. *Signal Process. IEEE Trans.* **50**(2), 425–437 (2002)
12. M. Roth, F. Gustafsson, U. Orguner, On-road trajectory generation from GPS data: a particle filtering/smoothing application, in *IEEE 2012 15th International Conference Information Fusion (FUSION)*, (2012), pp. 779–786
13. M.S. Arulampalam, S. Maskell, N. Gordon, T. Clapp, A tutorial on particle filters for online nonlinear/non-Gaussian Bayesian tracking. *Signal Process. IEEE Trans.* **50**(2), 174–188 (2002)

14. Timble Navigation Ltd., Differentiating between recreational and professional grade GPS receivers, (Whitepaper), www.timble.com (2006), <http://www.clintoncountyohgis.org/Metadata/Difference%20between%20recreational%20and%20professional%20grade%20gps%20receivers.pdf>
15. <http://www.plxdevices.com/>
16. <https://play.google.com/store/apps/>
17. A. Chowdhury, T. Chakravarty, P. Balamuralidhar, Estimating true speed of moving vehicle using smartphone-based GPS measurement, in *IEEE International Conference on Systems, Man and Cybernetics (SMC)* (IEEE, 2014), pp. 3348–3353
18. Z. Hui, C. Wei, Z. Huan-Tao, L. Qiang, Research on calibration method for the installation error of three-axis acceleration sensor. *Int J Mech. Mechatron. Eng. IJMME-IJENS* **11**(04), 6–11 (2011)
19. B.T. Sutcliffe, Coordinate systems and transformations, in *Handbook of Molecular Physics and Quantum Chemistry*, vol. 1 (2003)
20. H. Hou, *Modeling Inertial Sensors Errors Using Allan Variance* (Department of Geomatics Engineering, University of Calgary, 2004)
21. S. Colton, F.R.C. Mentor, The balance filter, Presentation (Massachusetts Institute of Technology, 2007), <http://burt.googlecode.com/svn-history/r121/trunk/Hardware/Sensors/filter.pdf>
22. A. Chowdhury, T. Chakravarty, P. Balamuralidhar, A novel approach to improve vehicle speed estimation using smartphone's INS/GPS sensors, in *International Conference on Sensing Technology (ICST)* (Liverpool, UK, 2014)
23. <http://www.r-project.org/>

Monitoring Water in Treatment and Distribution System

Joyanta Kumar Roy and Subhas Chandra Mukhopadhyay

Abstract This chapter reviewed and explained the importance of water quality monitoring and its technology from generation to the distribution. The authors are reporting a SCADA based intelligence sensing system which is utilising the Internet of Things to improve easy access to monitor water quality, treatment process and plant health in real time. Internet of Things, a new era of computing technology and a smart connect, machine to machine, machine to infrastructure, machine to environment an intelligent system which can talk each other, make operational functions in universal network in the cloud. Continuous surveillance of potable water quality during production and delivery, what is happening in a plant and information required to apply needs in the water distribution network requires huge connection infrastructure and its availability with time. IoT is the solution of these problems of platform. In North 24 parganas Arsenic area water supply scheme uses Internet of Things 1st time in India to access water quality information, plant information, and water supply information globally anywhere in the earth having the network of internet. This paper describes how IoT works in a water treatment process, production and distribution in a scalable way. This will be the convergence of consumer, business and industrial internet considering environmental impacts. This will be the way to get the information in your pocket. This chapter also describes how SCADA works with IoT to assist in the production of potable safe drinking water. The case study describes the functionalities of Supervisory Control and Data Acquisition System (SCADA) and Internet of Things (IoT) system installed which proves its sustainability for last 10 years. It helps to minimize the cost of production, smooth delivery and maximize water quality to help rural people from menace of various water contaminations like Arsenic threat. This chapter also described the features of future water monitoring through indigenously developed sensors.

J.K. Roy (✉)

MCKV Institute of Engineering, West Bengal, India
e-mail: jkroy.cal51@gmail.com

S.C. Mukhopadhyay

Massey University, Palmerston North, New Zealand
e-mail: S.C.Mukhopadhyay@massey.ac.nz

1 Introduction

Water is very important component of life, on an average; the body of an adult human being contains 60 % water. Most of the water in the human body is contained inside our cells. In fact, our billions of cells must have water to live. The most of the diseases are water borne. The waterborne disease is reserved largely for infections that predominantly are transmitted through contact with or consumption of disease infected water. Many of the Protozoa infections, parasitic infections, Bacterial infections and viral infections are water waterborne. This overall Bacteriological contamination play a vital role in Nation's health. Beside the bacteriological contamination our natural resources of water are being continuously contaminated by industrial waste. One of the Millennium Development Goals is to improve access to safe water defined as engine for socio-economic growth. Therefore in this contest the importance of information on water resources systems is very valued and cannot be overestimated the environmental status of our world as well as in the socio-economic development process of nations. Access to clean water for drinking and sanitary purposes is a precondition for human health and well-being. Unpolluted water is also essential for ecosystems. Plants and animals in lakes, rivers and seas react to changes in their environment caused by changes in chemical water quality and physical disturbance of their habitat.

According to the European Environment Agency (EEA), "the pollution can take many forms and have different effects:

Faecal contamination: The common source is sewage. It makes water unsafe and aesthetically for human consumption and recreational activities, such as swimming, boating or fishing. Many organic pollutants, including sewage effluent and farm and food processing wastes consume huge oxygen, suffocating the aquatic life. Ultimately these contaminations affect groundwater resources used for drinking water purposes.

Nutrients: Nitrates and phosphates, from farm fertilizers to household detergents can over fertilize, the water causing the growth of large mats of algae; some of which can be toxic. When the algae die, they sink to the bottom, decompose, consume oxygen and damage ecosystems.

Pesticides and veterinary medicines from farmland and some industrial chemicals can threaten wildlife and human health. Some of these damage the hormonal systems of fish, causing 'feminisation' (endocrine disruption).

Metals, such as zinc, lead, chromium, mercury and cadmium are extremely toxic. Copper complexes are less toxic, and cobalt and ferrous complexes are only weak toxicants. Concentrations of cyanides in waters intended for human use, including complex forms, are strictly limited because of their high toxicity.

Arsenic contamination of ground water may occur in two ways: anthropogenic activities and aquifer naturally contain. Ground water contamination cross the permissible limit of WHO (0.01 mg/l), excess arsenic has been detected in tube well/hand pump drinking water supply in many country about 200 million people

under risk. Arsenic found in widely the earth's crust, it's mostly in organic, inorganic and gas form. Organic arsenic abundantly found in sea food, it's not harmful and Inorganic arsenic that is found in ground water is harmful to health because it's stored in the body, thus adversely affecting multiple organ systems and form many diseases sometimes cancer leads to death. Consuming arsenic contaminated water is slowly leads to death.

Organic micro-pollutants, such as pharmaceuticals, hormones and chemical substances used in products and households can also threaten health.

Chlorinated hydrocarbons exist in the natural systems, several of which are highly toxic to humans. These molecules persist in the environment for a longer time, and threaten to contaminate aquatic and soil systems.

There are two sources of natural water i.e., Ground water and Surface water. Normally we abducted water from ground by hand or motor operated pump. The major water supply is taken from ground in India; Major possible pollutants in ground water are Faecal Coliform, Nutrients, Pesticides and veterinary medicines, Organic micro-pollutants, Arsenic and Fluoride contaminations.

The production of Arsenic free drinking water for the large community in the wide rural areas of West Bengal is a great challenge to the water sector industries. The Arsenic treat for today's world is becoming an epidemic and its intensity will reach its highest extent in near future. Due to the pressure of increasingly high population rate in India, it has become a basic need to regulate the usage of precious purified water in our community. Indian government along with the State Govt. has taken needful steps to prevent this problem. The underground-water is the natural source of water but due to excessive pumping out the Arsenic contamination is taking place due to excessive reduction of partial pressure in the underground water level. Moreover, the surface water is not able to penetrate through the land-bed to reach up to the under-ground water level to balance the deficiency of water quantity. India is a country abounds with rivers enriching the large population by its natural river water resource. River water is much safer from than the underground water from today's world scenario. Contamination of Arsenic has a minute chance in this water source. Regardless of these facts, the other chemical contamination has also very minimum chance to have. So, Government had taken a first step to implement the water treatment plant supported by distributed SCADA control system at Mongol Pandey water Treatment Plant, situated at the bank of river Ganges, at the favourable location of Barrackpore, North 24 Paraganas and W.B. Now almost all the new water supply systems are coming with water monitoring based on SCADA system.

2 Review on Water Monitoring, SCADA and IoT in Water Sector

Temido et al., in the year 2014, introduced an idea of value creation for the water sector companies using SCADA applications and Smart Metering Systems for the companies. Information technology (IT) application is also applied for the

implementation of the SCADA system for the operating and maintenance of the whole system. The cost benefit was also an important aspect of this system. The two CBA (Cost benefit analysis) models have been developed in this work having potentially advanced utilizations towards the society [1]. G. Williams et al., in the year 2014, analysed SCADA for understanding the contribution of Hydraulic Pressure for failure analysis in main trunk pipeline for urban sub-network. Failure analysis using frequency analysis technique was the main theme of this research work. The pump off- peak (POP) failure was characterized by high speed, predominantly off peak pumping etc. The data failure recording option is available with the SCADA system for forensic investigation [2]. Dorin Adrian Rusua et al., in the year 2013, used a novel technique for Anomaly detection system (ADS) for SCADA system based on systematic approach of pattern based technique. The technique uses graphical interface technique for model based SCADA topology and some auto generated ADS rules. The technique (system) they have used is user-friendly for anomaly detection in the SCADA network [3]. Adrian Gligor et al., in 2012, developed an oriented SCADA system to facilitate the business intelligence in any production sector (like water treatment plant etc.) by the economical respect. The author have done some analysis regarding various aspects of the SCADA system like safety, implementation, design the system etc. For that purpose, the service oriented Architecture (SOA) has been used [4]. Rezaul K. Chowdhury et al., in 2013, introduced Informatics, Logistics and Governance in Water Treatment plant using SCADA Architecture with Artificial Neural Network (ANN) in water treatment problems to make the system intelligent. They also proposed a SCADA system diagram for water treatment plant. They also proposed an idea of water governance using which the business intelligence can be achieved in water sector for public interest [5]. Maria Muntean et al., in 2011 used knowledge discovery in a SCADA system Database using data mining technique in for performance evaluation for better functionality of the whole process plant. The main purpose of this work was to analyse the classifier that is best suited to the data set provided by SCADA system. Discarding normal values and transmitting warning messages as the anomaly value by the classifier was the theme of the system [6]. Oladipupo Bello et al., in the year 2014, used fuzzy logic for the development of dynamic modelling and predictive control for coagulation chemical dosing for water treatment plants. Fuzzy model predictive control (FMPC) strategy has been proposed in regulating the dosing treatment. MIMO processes for linearized Takagi–Sugeno (T–S) fuzzy model technique have been implemented [7].

Shri Prabir Kumar Dutta discussed his view over SCADA system for business intelligence in water treatment plants first time in India. Arsenic contamination in drinking water was a major problem for most of the rural areas in west Bengal. Portable drinking water production plant for rural areas in North 24 Paraganas (at Mongol Pandey water Treatment Plant) has been developed under this mission. The treatment plant has 7.5 MGD capacity, two Booster Stations and fourteen overhead reservoirs distributed over 7.4 million people covering 369 sq. km area. The SCADA system has good amount of plant running data for technical analysis purposes [8]. R. Wang et al., in the year 2014, analysed Water hammer assessment techniques for

water distribution Systems for the mass community to protect valuable life and wealth that can be destructed by this problem. The business intelligence is one of its sole aspects to calculate the water hazards due to five different reasons discussed in this paper. Pipe rupture risk factors have been analysed for maximum water pressure, maximum vacuum, maximum vapour volume, and maximum transient force by the knowledge of hydraulic transient flow analysis [9]. The application of automation in modified SCADA system had empowered the overall plant efficiency and surveillance the functionality of the plant for the Great lakes-upper Mississippi River to provide service for the public health and Environmental aspects [10].

By definition the Internet of Things (IoT) is a concept and a paradigm that considers pervasive presence in the environment of a variety of things/objects that through wireless and wired connections and unique addressing schemes are able to interact with each other and cooperate with other things/objects to create new applications/services and reach common goals [11, 12]. In the smart world environment the goal of the Internet of Things is to enable things to be connected anytime, anyplace, with anything and anyone ideally using any path/network and any service [11, 12]. Internet of Things is a revolution of the Internet application. Objects in the cloud of internet make themselves recognizable and they have their own intelligence by making or enabling context related decisions through communicating information about themselves. They access information that has been aggregated by other things, or they are the components of complex services and systems. This transformation is happens with the emergence of cloud computing capabilities and techniques and the transition of the Internet towards IPv6 with an almost unlimited addressing capacity. The revolution is all emerging technologies developing in all areas of electronic products like sensors, transmitters, and communication devices have the facilities of inbuilt internet capability and have smart function to talk each other.

Now we are making real from the imagination talking about creation of Smart Planet to make Green environment, trying to make smart cities with connected communities, applying smart energy system in electrical grids, implementing Smart homes and building, improving electric mobility through Smart Transport, creating Smart Industry for flawless efficient production, applying Smart Health Care system with target goal of Smart living. All these application requires IoT technology which makes the thing real (Fig. 1). All the devices, equipment, ubiquitous, equipment for wellness, military whatever the available electronic novelties and research appliances will be IPV6 enabled can talk each other, data mobility worldwide through high speed internet and our twentieth century expectation is everything is available in hand.

Dr. Ovidiu Vermesan et al. [11], in the year of 2013 written a book on “Internet of Things- Converging technology for Smart Environment and Integrated Eco System”, Published by River Publishers Series in communications, IERC Book open access, 2013, TP- 343. In this book the vast idea on Internet of things can be gained and its different application sides are also depicted [11]. Dr. Ovidiu Vermesan et al., in the year of 2014, written another book on “Internet of Things- From research and innovation to Market Deployment”, Published by River



Fig. 1 IoT enabled green world

Publishers Series in communications, IERC Book open access, 2014, TP- 143. From this book the idea on Internet of things in the market deployment to different plant automation techniques are discussed [12]. Shri Prabir Kumar Dutta discussed his view over SCADA system for business intelligence in water treatment plants first time in India. Arsenic contamination in drinking water was a major problem for most of the rural areas in west Bengal. Portable drinking water production plant for rural areas in North 24 Paraganas (at Mongal Pandey water Treatment Plant) has been developed under this mission. The treatment plant has 7.5 MGD capacity, two Booster Stations and fourteen overhead reservoirs distributed over 7.4 million people covering 369 sq. km area. The SCADA system has good amount of plant running data for technical analysis purposes [13]. Dave Evans, in the year 2011, written a book on “The Internet of Things How the Next Evolution of the Internet Is Changing Everything”, published by Cisco Internet Business Solutions Group (IBSG) [14]. K. Karimi, in the year 2012 has written the book on “What the Internet

of Things (IOT) Needs to Become a Reality”, Tp. 16, 2012. In this book the basic idea along with the application criteria of the IOT model can be achieved [15]. Joseph Bradley et al., in the year 2014 implemented the idea on “Internet of Everything: A \$4.6 Trillion Public-Sector Opportunity” [16]. Simon Bunn, in the year 2007 discussed on “Closing the Loop in Water Supply Optimization” [17]. Merchant et al. [18], in the year 2014, proposed an Analytics driven water management system for Bangalore city. His is an ongoing project for the minimization of the complexity in instrumentation and control mechanism in water sector. They have developed new software using customizable key performance indicator (KPI) to implement the business intelligence which has great importance in the water sector to handle different problem situations. The software developed for this purpose is Smart, reliable and easy to use by the plant officials. The business level optimization was also a great achievement of this system minimizing different losses like energy loss, produced water loss etc. which helps to build the business intelligence in a productive way. The Minneapolis Province of USA [19] has utilized SCADA technology [13, 20, 21] for real time energy usage that can be connected with other system parameters like storage levels of water and he intake volume. The essence of this system is to have an efficient control using minimum staff support. Vlastimir Nikolić et al., in 2010, implemented a new idea of intelligent decision making system based on Fuzzy controller [22] for waste water treatment plant using SCADA system. The main emphasis was given by the authors on the development of remote monitoring and controlling of systems for wastewater treatment and its improvement. The development of RTU module for this type of systems has been discussed with its intelligent attributes [13].

3 Motivation

Most of the water treatment and supply plants use the conventional methods for treatment of water. From raw water suction to the filtration using rapid gravity filter bed and distribution to the community through high speed pumping systems, which require lots of attention regarding production, distribution and water quality. The status of pumping machineries, plant and process parameters for entire water distribution network require continuous surveillance which are not possible with human intervention considering large inspection area of production and distribution zone. Most of the conventional water treatment plant do not have any surveillance system for monitoring plant and process parameters on-line. They suffer from production target as well as in quality too. Similarly most of modern treatment plant having Plant wise SCADA, do not have any monitoring system for distributed remote Booster stations or overhead reservoirs, therefore they are facing problems in managing the flawless distribution to keep water quality well as per standard specified by ISO/WHO. These water treatment plant and distribution systems also have minimum monitoring facilities, which are local panel based system. The operators are used to visit monitoring equipment location and take data into log book.

The water treatment plant machineries are distributed in vast areas. Simultaneous measurement of water monitoring data is physically impossible. Therefore use of online water monitoring equipment along with distributed SCADA system are the perfect choice to integrate all distributed Plant and Process system under single umbrella which give on-line pictures of water quality trends, health of the pumping machineries and also support as useful tool to the engineers. Therefore sustainable water supply system has been established. Now days various on-line smart measuring system for on-line water quality parameters are available. Some of them can measure water quality in continuous real time, some are using sampling method. These equipment can give water quality data on demand. Each water treatment plant has a water testing laboratories for routine testing of water quality at various locations from source to destination. There laboratories are well equipped with all test equipment for the measurement of different water quality parameters as per Table 1. But these laboratories do not have facilities to publish on-line Water quality data. Plant engineers are also interested to monitor laboratory and plant data in real time at their office which is far off from the treatment plant. This is important requirement for operational and maintenance aspect for smooth supply of safe drinking water to the consumer. The laboratory normally test some parameters daily, some parameters weekly and some parameters on monthly basis. Normally one or two water samples are taken from various locations of water resources within the plant in routine manner. This procedure does not ensure variance of water quality with variation of time and water flow. In this chapter, some aspect of distributed SCADA system with IoT and business intelligence has been discussed.

4 SCADA System in Mangal Pandey Water Treatment Plant, India

4.1 Description of Hardware Infrastructure:

The Distributed SCADA system is installed and commissioned in 2003 in Mangal Pandey water Treatment plant, Barrackpore. It has two Boosting stations, one at Madavpur with aerial distance 11 km and other at Naksa with aerial distance of 26 km from Barrackpore, N24 Parganas [8]. These two Boosting stations are getting water supply from the Mangal Pandey Water Treatment Plant and are delivering potable water to 15 nos. overhead reservoirs at various locations. These OHRs are supplying water under gravity flow to the population through house to house connection system. Each of the Boosting Stations and OHRs have Remote Terminal Unit (RTU), which is PLC based Data Acquisition system with built in Radio based data telemetry connected in a dedicated wireless network.

Table 1 Plant and process parameters and its measuring systems for SCADA

Sl no	Location	Parameter	Unit	Equipment used
1	Raw water Pump house	<i>Plant parameter:</i> a. Raw water pump status (on-off-standby) b. Raw water Header water flow c. Raw water delivery pressure <i>Process parameter:</i> a. Raw water pH b. Raw water turbidity c. Raw water pump house operation time	Logical M ³ / hour kg/cm ² NPU Hour	Electrical contacts with opto electronic isolators Electromagnetic flow meter Smart pressure transmitter Smart pH transmitter Insertion type smart Turbidity analyser Virtual timer
2	Clari-flocculator	a. Bridge drive motor b. Mixture motors c. Flow to clariflocculator 1 and 2	Logical Logical M ³ / hour	Electrical contacts with opto electronic isolators Ultrasonic open channel flow meter
3	Filter house	<i>Process parameter:</i> a. Filter bed operation (Running-shot off—stand by) b. Flow through filter c. Loss of head d. Flow meter for back wash e. Backwash overhead reservoir level	Logical M ³ / hour Metre M ³ / hour Metre	Virtual sensor Open channel flow meter with capacitive transducer Differential pressure transmitter Electromagnetic type of flow meter Ultrasonic non- contact level transmitter
4	Sludge pump house	a. Sludge water level b. Sludge mixing motor status c. Sludge pump house operation time	Metre Logical Hour	Ultrasonic non-contact level transmitter Electrical contacts with opto-electronic isolators Virtual clock
5	Compressor room	a. Compressor and blower status	Logical	Electrical contacts with opto-electronic isolators
6	Chemical house	a. Chemical dosing pumps b. Coagulant dosing status c. Pre chlorination and post chlorination status	Logical Logical Logical	Electrical contacts with opto-electronic isolators Electrical contacts with opto-electronic isolators Electrical contacts with opto-electronic isolators
7	Sub station	a. Incoming feeder voltage (3 phase) b. Plant feeder voltage(3 phase) c. Plant feeder current(3 phase) d. Power factor e. Frequency f. Active power	KV V A Theta Hz KW	Potential transformer Potential transformer Current transformer Multi parameter transmitter Multi parameter transmitter

(continued)

Table 1 (continued)

Sl no	Location	Parameter	Unit	Equipment used
		g. Reactive power h. Energy consumption	KW KWH	
8	Booster pumping station(2 numbers)	a. Inflow b. Outflow c. Level d. Pump status e. Pump operating hours f. Pump status	M ³ /hour Metre Logical Hours Logical	Electromagnetic flow transmitter Ultrasonic non-contact level transmitter Electrical contacts with opto-electronic isolators Virtual timer Electrical contacts with opto-electronic isolators
9	Overhead reservoir	a. Residual chlorination pump status b. Residual chlorine value of OHR water c. Water input to the OHR d. Water level in OHR	Logical mg/l M ³ /hour Metre	Electrical contacts with opto-electronic isolators Residual chlorine analyser Electromagnetic flow meter Ultrasonic non-contact level transmitter

The electronic field equipment like sensors and actuators are installed at various point of interest at treatment plant, Booster stations and OHRs. The central monitoring room is equipped with HMI SCADA Server, Data Server and Web Servers with redundant system. These servers are connected with PLC based Remote Terminal Units located at different sections of the treatment plant, boosting stations and OHRs through communicating network. The local area network of inside central monitoring station is copper with speed 100/10 mbps. All RTUs within the treatment plant are connected with HMI servers through Optical fibre network with 1Gbps speed. The RTUs of remote boosting stations and OHRs are connected through smart cognitive radios. Field RTUs have opto-isolated inputs and outputs, which are connected with various smart metering system for monitoring plant and process parameters as a whole. The plant and process parameters available through SCADA for smart management of water supply scheme are described in Table 1.

The field units such as various on-line process parameter measuring transmitters, which are installed in the process and connected to the PLC based data acquisition system as shown in the schematic diagram (Fig. 2). Each field unit have Analogue inputs/outputs and Digital inputs/outputs called IO modules of PLC as shown in Fig. 3. The digital inputs are sensing the status of pump motors and other electrical actuators (ON/OFF, Stand by and Fault). Analogue inputs are measuring process parameters like pH, Turbidity, etc. in terms of 4–20 mA DC current from transmitters, which are digitized with 16 BIT resolution and sent to MTU through optical fibre network. HMI server is collecting these raw data for processing and broadcasting in the network for display, logging etc. A typical construction of RTU panel and brief technical specification has been shown in Figs. 2 and 3. The electrical

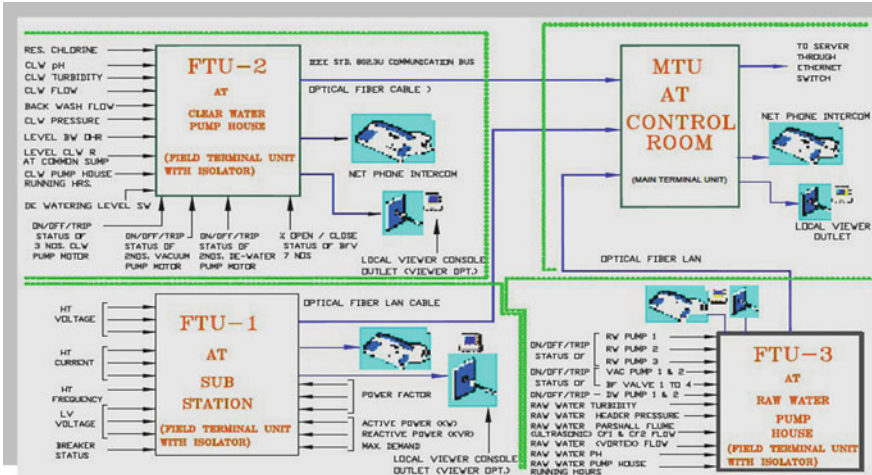


Fig. 2 Part of the schematic diagram of plant-wise interconnected RTUs

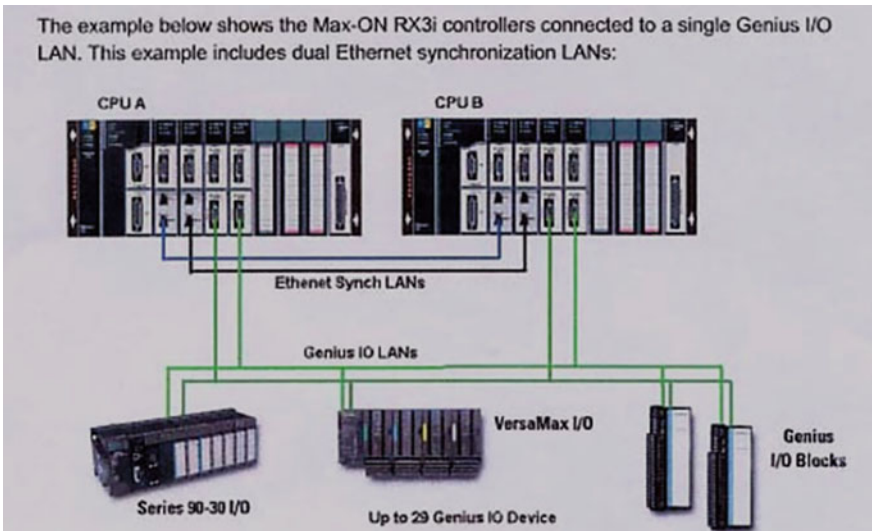


Fig. 3 Example schematic of PLC based SCADA hardware

status of pump motor and other actuators are collected from isolated contact of individual circuits through Opt-isolated digital interfaces.

The fault status are collected from fault sensing relays. The substation parameters are collected from multi parameters electrical transducers installed at Sub

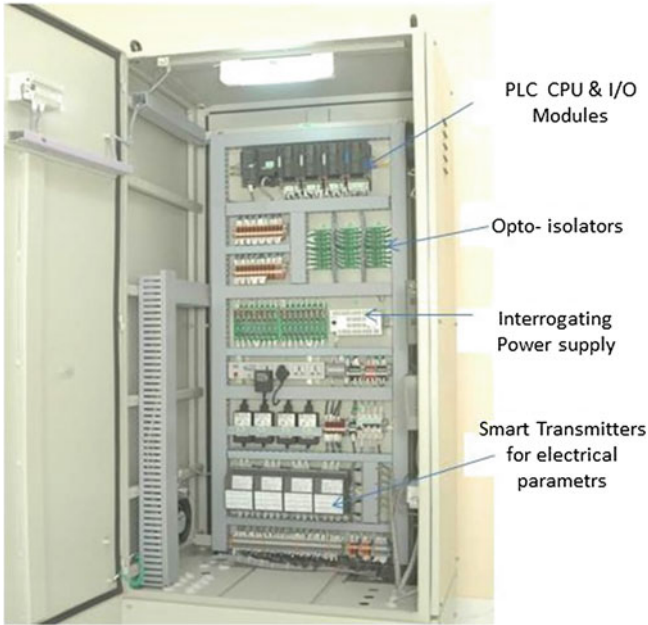


Fig. 4 Example schematic of PLC based SCADA hardware

Station. The Field terminal units are floor standing panel consisted of Genius I/O panel with mixed signal I/O modules.

The Digital and Analogue Inputs and outputs are connected to Genius I/O LAN or GE Fanuc make Versamax CPU and I/O modules (Fig. 4). The LAN communication module with 10/100 Mbps speed has been used for data communication with Master Terminal Unit. The optically isolated fiber cables are connected in Ring topology. These FTU panels are power by uninterrupted Power supply of 230 V, AC, 50 Hz with ± 1 % stability. The UPS system has 7 days energy storage for backup power such that all SCADA system components, Field control and measuring instruments will get uninterrupted power for data acquisition. The RTU at different OHR sites are PLC and Radio based telemetering unit. They are used to control and monitoring of Chlorine gas injection system, to measure water inflow to the reservoir and outflow to the distribution to the consumers. The OHR sites do not have any HMI monitoring for visualization. But the visualization can be available by use of Laptop computer having SCADA runtime software if connected in the LAN output of the radio system. This facility has been found very useful for maintenance purpose during fault detection of on-line water analyzer or any field transmitters and actuators. All smart on-line transmitters are HART protocol activated and can also be calibrated through PC using HART software.

4.2 Computer and Software Infrastructure:

The application software was developed for the proprietary requirement of water treatment and its distribution called Water Management System (WMS) as shown in Fig. 5.

The WMS is concerned to make decision through monitoring of health status of distributed plant machineries, water demand, water quality and other process conditions.

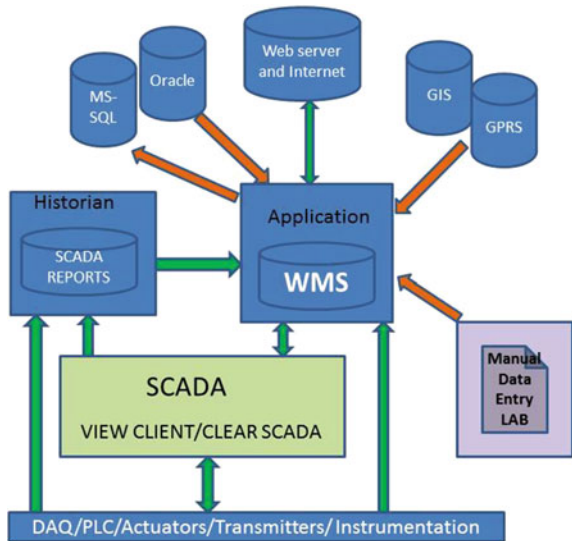
The HMI server is running with SCADA software “CIMPLICITY” of GE Fanuc Intelligent systems, configured similar to Clear SCADA software of Schneider Electric Co. There are two HMI servers are working in redundant mode with RAID 2 configuration, such that any failure in hardware or software of one server could trigger other server bouncelessly and the system runs almost without failure.

There are two database servers running with redundant mode in the network. The operating systems of these data base server are Microsoft SQL 2010. The raw data with tie stamped from all over the system are stored in these servers in continuous manner (24 × 7).

The entire system has power backup designed to sustain for 7 days considering catastrophic failure of power in a plant. This water monitoring system has two SCADA viewer are running thin client viewer mode. The plant operators, chemist and plant engineers are using these viewing systems for water monitoring at central SCADA room. The schematic diagram of the distributed SCADA system is shown in Fig. 6. A view of control room for central monitoring of water is shown in Fig. 7.

LMS software is called software for laboratory data management was developed for making laboratory data according to Public Health Engineering requirement.

Fig. 5 Schematic of water management system



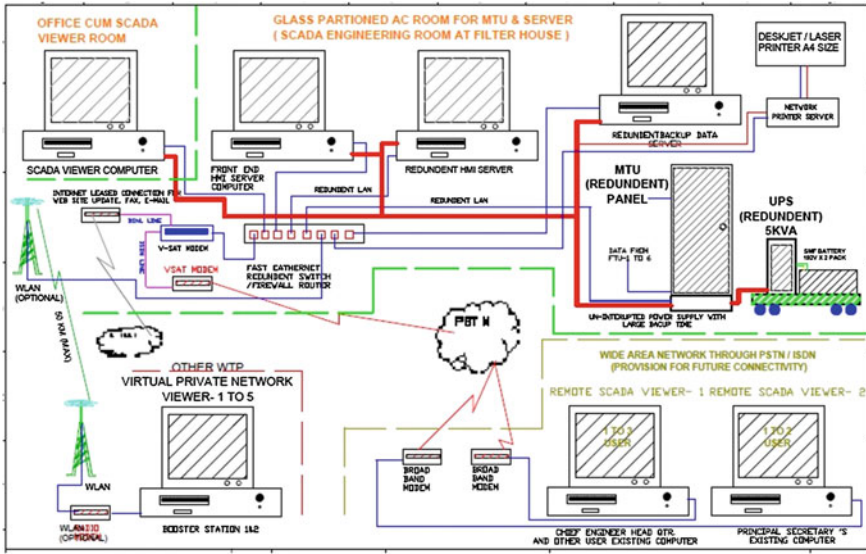


Fig. 6 Schematic diagram of distributed SCADA system



Fig. 7 SCADA room at Mongol Pandey water treatment plant

This is running in the SCADA network. The laboratory water test data regularly feed to the LMS, Data server stores laboratory data (offline) and SCADA data (online) with time stamped. Water monitoring data as well as plant data are available in various approved table format according to quarry set in the WMS.

The SCADA software is built in Historian so quick trend or configured trend of all plant, process parameters are available in viewer machines as well in the entire network. The WMS is at Centre of the software system which interact with HMI, field equipment also interact with World Wide Web (WWW) through web server and public IP.

Some preapproved configured water monitoring quarry based data in tabular format is available through password protected web page, which are accessible anywhere any place through internet.

The system is also activated with GIS and SMS server such that the system is synchronized with world standard time and WMS can generate mobile alert through SMS to the operation and maintenance engineer during any undesired event in the plant or process.

The Central SCADA Room is situated in the first floor of filter House where all local RTUs through optical fiber and remote RTUs through wireless radios are integrated through a three layer smart network switch and fire wall. The firewall is used to save the important database of SCADA server from external hacking. Firewall also prevents unauthorized access or to get information from SCADA through network. The HMI server collects field raw data and displays those data in various interacting graphical pages. HMI server also sends those field data to the data base server which logs data in its memory. The HMI server with data base server can generate customized report, as for example residual chlorine status of all 15 Over head reservoirs and treatment plant or water level status of 15 overhead reservoirs.

A CISCO security management system is also implemented to save system from external cyber threat. Air conditioning system works day and night to control environmental temperature and humidity of the control room. This will keep the system healthy and protect the system from mal-functioning. There is a redundant web server installed to broadcast all consolidated report generated by the data server. The web server is broadcasting plant and OHR data through lease Internet facility through BSNL service provider.

The website of Mongol Pandey water treatment plant has dynamic web pages which are Java enabled. Through this dynamic pages, online SCADA can be viewed at anywhere any place by any remote computer through Internet. The wireless backbone created between Mongol Pandey water treatment plant with Booster Station-1 and Booster Station-2 through Smart Cognitive Radio fitted on the self-supported towers.

At OHR site, Radio transmitters are mounted over the OHR top dome. All the radio transmitters are mounted with maintaining line of sight. The voice over IP telephony (VOIP) systems are also established between water treatment plant, Booster Stations and OHRs. All plant operators can talk each other can manage centrally from the control room of the treatment plant through this VOIP system.

Figure 8 depicts the distribution of water supply through pipe lines under North 24 Pgs W/S having distributed SCADA facilities. IoT network were established using Smart cognitive radios installed at the OHR roof tops and self-supported



Fig. 8 IoT network in north 24 Pgs Arsenic area water supply scheme

towers communicating each other through powerful wireless backbone. A typical installation of communication radio and self-supported tower (Base Station) at Naksa, N24 pgs, WB (Booster Station-2) is shown in Fig. 9.

The wireless network used point to point to multi point Topologies. The Radio uses NLOS urban coverage with OFDM technologies 5xGHz extended frequency range and support for 4.9 GHz. It is having +29 dBm aggregated output power and 2×2 MIMO with software. The radio uses for data and VOIP for telephonic



Fig. 9 Typical installation of radio base station at Naksa, N24 Pgs



Fig. 10 Typical line of site alignment of SCADA radios

communication uses EION Trust link technologies with user friendly web based GUI. The radio systems are used advanced OFDM and MIMO technologies to deliver breakthrough performance in the unlicensed band. It supports IPV6 and can handle the extreme backhaul loads that originate from today’s 4G/LTE based network. MS angle structure based self-supported towers erected at each locations of interest. The height of towers are ranging from 18 to 28 m depends on the sea level height to match line of sight. Figure 10 shows such typical installation of radios and alignment of radio. Table 2 describes hybrid network structures are used in the present water monitoring system.

5 The Monitoring and Visualization of Treatment Process and Water Quality

The goal of the project is to monitor all plant and process parameters including distribution under a single roof. Therefore graphical interface units for each treatment and distribution zones are separated for detail monitoring and designed into graphical pages. There are two home pages, 1st one is home page for water supply scheme through which all different OHRs, Booster station and central treatment plant can be navigated. 2nd home page is for treatment plant only, through which different sections like substation, raw water pump house, clear water pump house,

Table 2 Nature of communication network used

SI no.	Network level	Equipment used	Types of network	Speed
1	Ground level	Monitoring equipment and PLC Base	Flow wise LAN made of ORC and copper	10/100 MBPS (plant)
2	WTP level	SCADA interconnected RTUs	Optical fibre network	100/1000 MBPS (control room)
3	OHR and booster station	Interconnected RTUs	MAN radio operated	1–2 MBPS
4	Connected other WTP	Interconnected SCADA	MAN radio operated	1–2 MBPS
5	Internet	WWW	Internet lease line	2 MBPS raw

filter house, sludge pump house, chemical house, clear water pump house can be navigated. The short description of major SCADA pages are as follows.

5.1 Sub-station Monitoring

The Sub-station has two large transformer dedicated solely for use by treatment plant. One transformer is working and other is stand by. The transformer power rating is 500 KVA. The input supply is dedicated supply of 11 kV, 50 Hz incomer. The transformer output voltage 433 V. The vacuum circuit breaker and air circuit breakers are used to engage and de-engage the transformer from the circuit. Figure 11 is the SCADA page for Sub Station Monitoring. There are various power sensors are installed in the power circuit to monitor all necessary electrical parameters like, Incoming three phase voltages, Power line voltages, load currents, Frequency, Power factor, Quality factor, KVA, KW, KVAR energy consumption and phase voltage.

The substation is built in power protection system using latest micro controller based protection relays, Very good electrical earthing, protective devices are also installed to protect the substation from accidental damage due to lightning discharge. The substation provides power to the different pumping houses, filter beds and all equipment distributed in the plant, lighting systems etc. However SCADA and WMS infrastructure need uninterrupted smooth harmonics free stabilized power therefore separate on line UPS with sufficient power back up is used for individual installations at different houses. The SCADA is also monitoring all parameters related to the health of the UPS supply and records data for future health prediction.

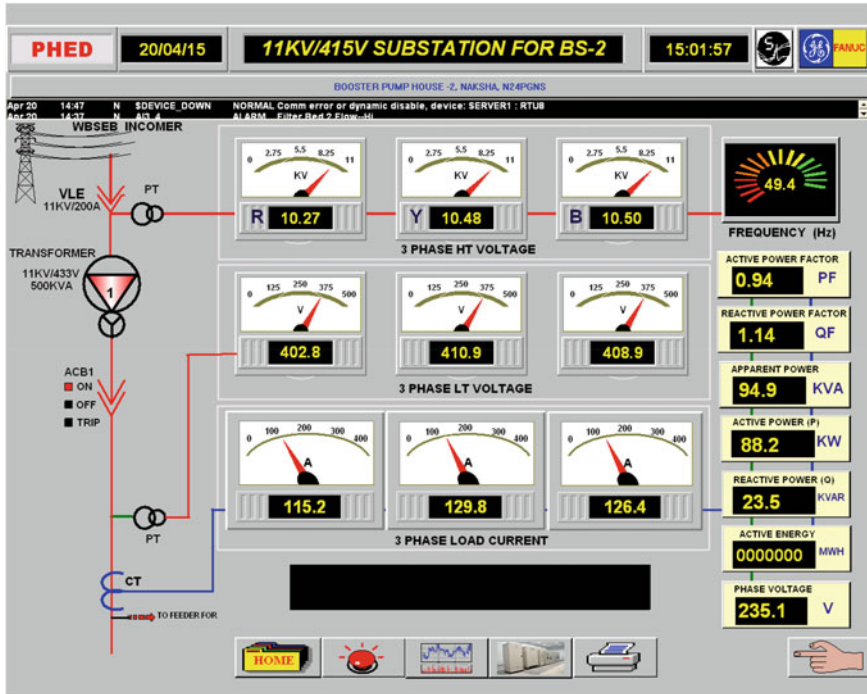


Fig. 11 Typical Substation electrical parameter monitoring

5.2 Clariflocculator Zone and Water Quality Online

The Clariflocculator (Fig. 12) plays a vital in water treatment process. The clariflocculator is a combination of flocculation and clarification in a single tank. It has two concentric tanks where inner tank serves as a flocculation basin and the outer tank as a clarifier. The water enters the flocculator and motor operated flocculator paddles enhance the flocculation. The water flows rapidly upwards in the clarifier zone.

The clarified liquid is discharged over a peripheral launder. The deposited sludge at the bottom of clarified zone is raked by motor operated bridge scraper moved to the central weir from where it is routed to the sludge chamber. Monitoring the health of clariflocculator is very important. The problem is wired cable routing to the clariflocculator system is difficult. As the all machineries are fitted over rotating bridge of the clariflocculator therefore the RTU for monitoring status of clariflocculator is built in wireless.

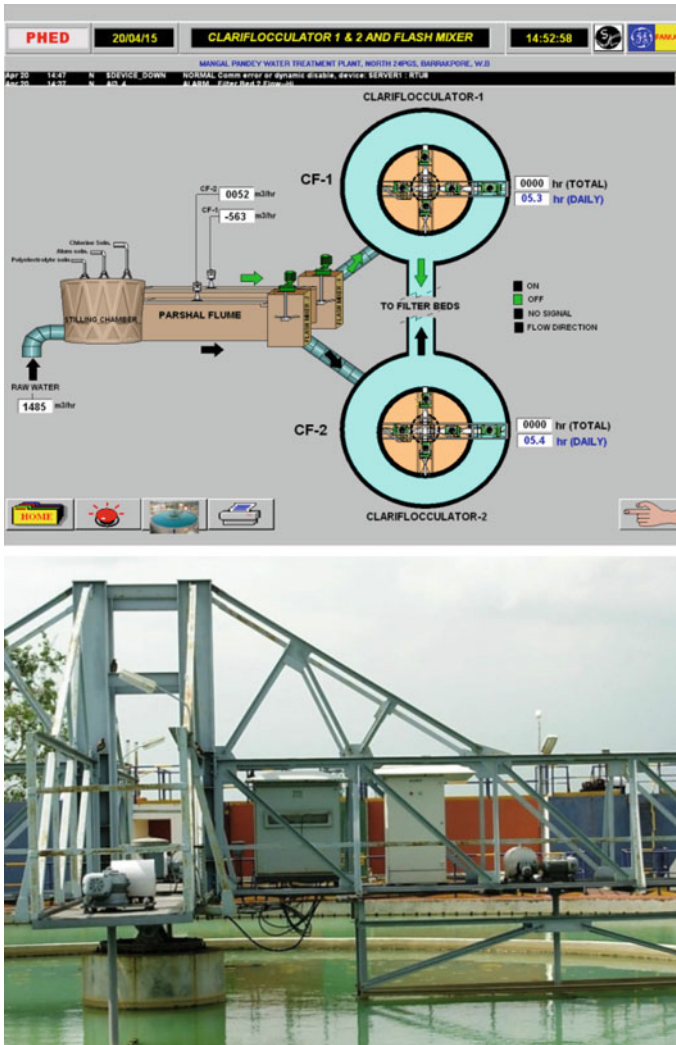


Fig. 12 Clariflocculator monitoring

5.3 Monitoring Filter Beds and Monitoring Filtration Process

The rapid gravity filter bed is type of filter used in large capacity water filtration system. The filter bed uses relatively coarse sand and other granular media to remove impurities that has been trapped in a floc through flocculation process in a clariflocculator. There are ten filter rapid gravity sand filter beds engaged to filter clarified water to potable drinking water. These filter beds are automatic and

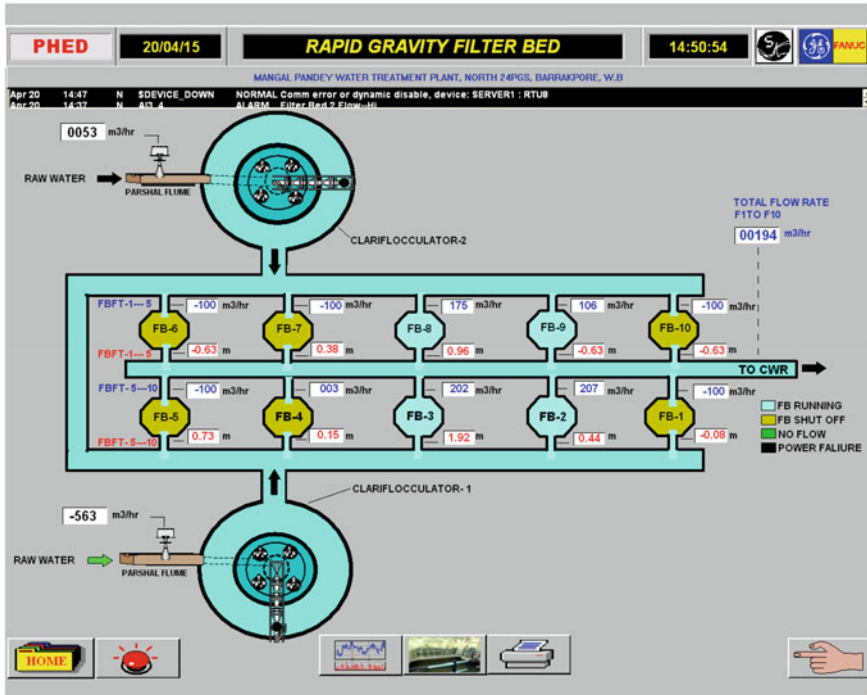


Fig. 13 Filter bed monitoring

pneumatically controlled. There are several sensors for monitoring loss of head in the filter bed, Filter bed out flow and different digital sensors to monitor filter bed through SCADA system.

When loss of head is high above the normal working limit, there is backwash system which activated the cleaning of filter bed through scouring of air from filter bed bottom, which clean the filter bed material thoroughly and increase production. Figure 13 is the GIU page of HMI SCADA through which the operator can monitor all the parameters and can log the values of the parameter with respect of time. The trends of all parameters during filter operation are also available in the central monitoring system. Through this SCADA page one can also monitor the alum chlorine and poly electrolyte dosing during filtration process.

6 Monitoring of Different Pump Houses

6.1 Raw Water Pump House

The raw water is abducted from river Hooghly through three vertical pumps installed at Raw Water Pump house. Two pumps run normally and one kept as

stand by. The discharged water from pumps passes through the common header, where a smart pressure transmitter is monitoring raw water discharge pressure. Smart pH transmitter, smart electromagnetic flow meter and online smart turbidity analysers are installed in the pipe line of raw water and connected to the I/O ports of PLC based remote terminal unit. The raw water pump status, working hours of pumps and other online water quality parameters are available in RAW water SCADA page GIU of HMI viewer.

6.2 Clear Water Pump House

The chlorine is added in the form of chlorinated water at two places during water treatment. Pre chlorination at stilling chamber and post chlorination at clear water tank are the normal practise for disinfection process. The filtered water from filter house collected at ground based clear water tank. There are five high speed water pumps are in Clear water pump house. Normally four pumps are operating through common header and one pump is kept as stand by. The pressure transmitter at discharge point measures clear water delivery pressure and one magnetic flow meter is measuring the amount of water flow to the consumer. The SCADA is monitoring the pump operating status, pH value of potable drinking water, turbidity and many more. One ultrasonic water level transmitter is installed at Clear water reservoir to measure water level in the tank. There is a roof top water reservoir for storing filtered water for back wash. The entire backwash process water level in the backwash reservoir are monitoring through clear water SCADA page (Fig. 14).

6.3 Sludge Pump House

A sludge pump house is big underground reservoir where sludge from clarifloculator and Filter house are settled and collected through pipe lines. There are two submersible sludge pump and four submersible mixer pumps are installed. Sludge pumps push sludge from the sludge tank to the sludge pond. Here one non-contact ultrasonic level transmitter is measuring sludge level in the tank. The local RTU connected with these physical devices and send data to the SCADA for monitoring and control. The sludge pumps are controlled through SCADA system.

7 Monitoring of Chemical House and Compressure Room

The chemical house of treatment plant is responsible feeding coagulant to raw water and making chlorinated water for pre and post chlorination. There are two poly electrolyte storage tank with mixer and three alum solution tanks with mixer driven

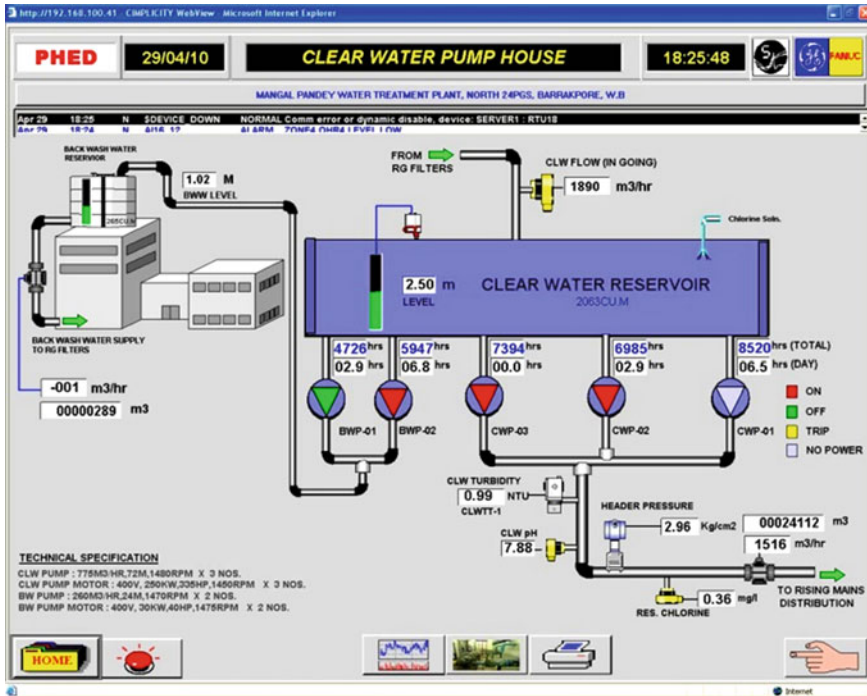


Fig. 14 Clear water pumps house monitoring

electrically. There are six dosing pumps for dosing the coagulant to the raw water. Four pumps out of which six are running for the purpose and rest are kept hot stand by. The chlorination unit mix chlorine gas with water and feed to the clear water tank and raw water at Parshal flume water channel. Here SCADA monitors (Fig. 15) the dosing pump, mixer motors and chlorination unit as well as residual chlorine analyser on line in real time basis. The SCADA also monitors the working status of Compressor and blowers.

8 Monitoring Water Overhead Reservoirs

This project has 16 nos. overhead reservoirs which are distributed throughout the action area of the water supply scheme. There are two Booster stations are working in between two points of water mains such that booster station re-boost the water to the distribution keeping water pressure sufficient to reach overhead reservoir.

We monitor residual chlorine level in Over Head Reservoir and also monitor incoming water flow out going water flow and water level in the OHR. Electromagnetic Flow meters are used for water flow measurement. The ultrasonic

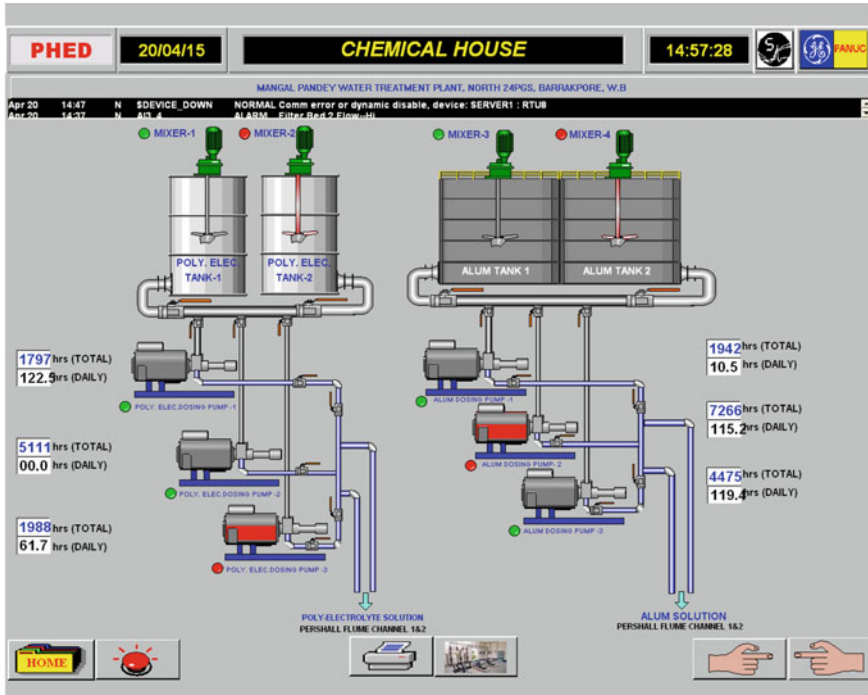


Fig. 15 Chemical house status monitoring

level transmitters are used for OHR water level measurement. The SCADA pages for individual OHRs are created for monitoring centrally. A sample SCADA page of one OHR zone is shown in Fig. 16.

9 Future Water Monitoring Through Indigenously Developed Sensor

In recent times, with the rapid development of agriculture and industry, the excessive discharge of waste water has led to a massive degradation of the quality water in different parts of the world. This has not only caused numerous death of aquatic life and increased outbreak of water-related diseases but also changing the ecological balance of the world.

There is a need of development of new methods of detection of nutrients and pollutants in water at real-time. The current monitoring techniques used are mainly laboratory based and rely on the results of some chemical reactions. For a long-term real-time application the chemical reaction based detection is undesirable as the performance degrades over time. Moreover, with the new regulations the available

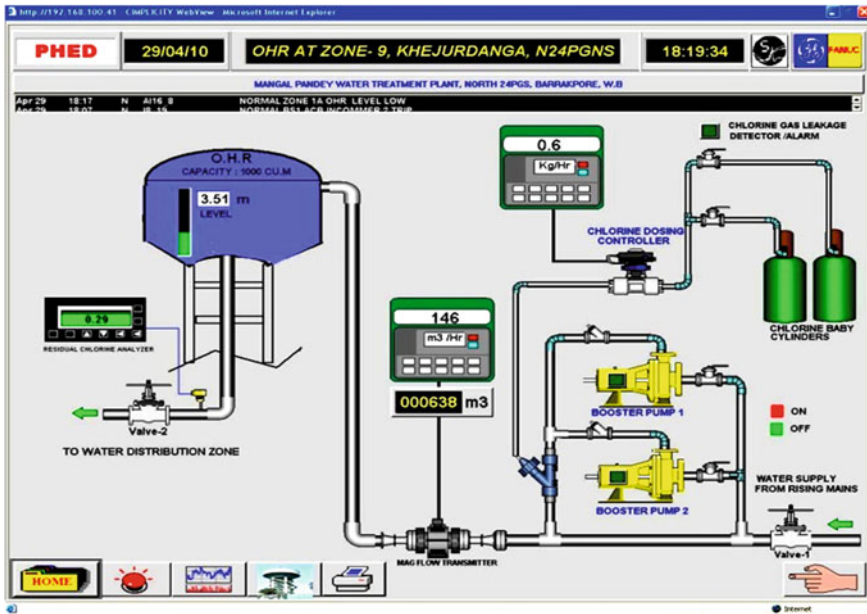
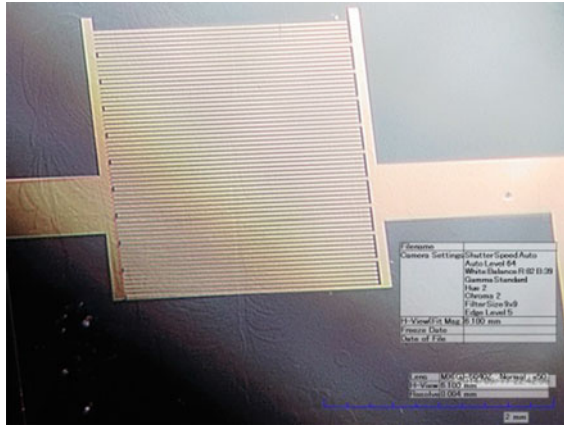


Fig. 16 Remote OHR monitoring

systems may not be suitable in near future to determine the amount of nutrients and pollutants in water relative to allowable levels. Environmental pollution is a huge concern of our society so the emphasis on the monitoring of environment has become very important in recent times. Water is the most important natural resources and getting polluted due to farming, industrial discharge and other reasons. It is very important to monitor water at different points, especially at the different meeting points of rivers and lakes of the country so that a thorough understanding of the relationship between soil, ground and surface water is possible. The continuous monitoring of the constituents of water will enable to determine the sensitivity of the hydrologic system to change of environmental parameters. There is a need of a water monitoring system with wide ranges of water parameters, smart and robust sensors, frequent data input and consequent analysis. This will provide to develop a relationship between water quality and environmental parameters including sources of pollution. This will help to different councils to have a better understanding of the conditions of water and track the sources of pollution.

For now and future, there is a need of development of an integrated framework of water monitoring system based on smart sensors and sensor network. The complete system may consist of three parts: The first part consists of integration of available sensors and development of smart high-performance of novel sensors. There is a need of development of novel sensors as the available sensors are not suitable for continuous monitoring of water under harsh condition. The second part

Fig. 17 Interdigital sensor [32]

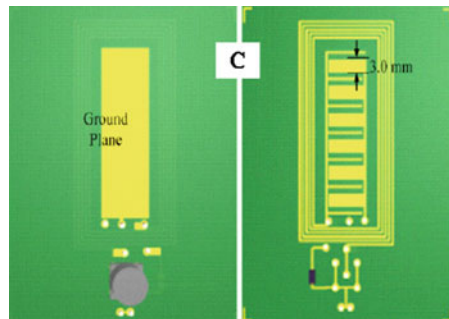


is the development of combination of energy harvesting techniques such as solar, wind and hydel to obtain energy to supply the sensors for normal operation and communication. The third part is the integration of the sensors to wireless sensor nodes, collection of data, storage and putting the data in a website using Internet of Things techniques. This will provide an easy access to the concerned authority as well as some part of it may be available to general public to know the changes of water parameters over time due to environmental changes.

The water parameters considered are: temperature, humidity, pH, conductance, rain-fall, light-intensity, turbidity, nitrate, phosphate, bio-toxin, BOD, COD, TOC, nitrogen, phosphorus, potassium etc. Novel types of sensors and sensing system will be designed and developed to measure different parameters to qualify and quantify water. The working knowledge of the development of high performance planar electromagnetic sensors to determine the nitrate levels in water as well other parameters may be exploited to develop new sensors [23–37].

Figure 17 shows the interdigital sensor used for detection of contamination in water and Fig. 18 shows the planar electromagnetic sensors developed to detect nitrate contamination in water [23, 30]. The planar electromagnetic sensor consists of interdigital part at the center and surrounded by meander coils at periphery.

Fig. 18 Planar electromagnetic sensor [25]



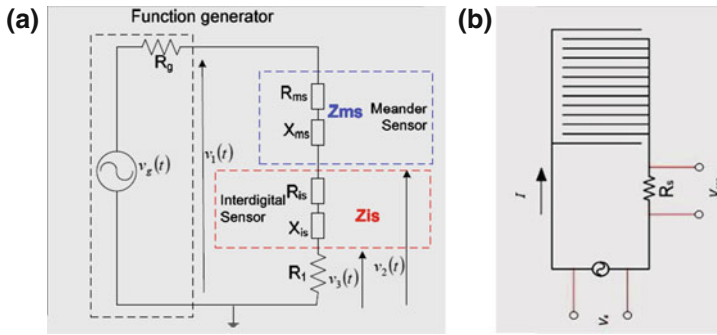


Fig. 19 Meander and interdigital sensing part of planar electromagnetic sensor. **a** Equivalent circuit of meander coil of planar electromagnetic sensor [23]. **b**. Equivalent circuit of the interdigital sensing part of planar electromagnetic sensor [30]

The meander coil produced magnetic field and the inter-digital produced electric field between the electrodes. An alternating perturbation of required frequency is supplied to the sensor. The produced electromagnetic field extrudes useful information from the sample under test. The impedance of the sensor is measured to determine the level of contamination. Figure 19 shows the equivalent circuit of the planar electromagnetic sensor. The components of impedances are measured for the concentration of contamination levels (Fig. 20)

Using electromagnetic sensor, water from different sources was tested to determine the concentration of sodium nitrate in it. The graph given below in Fig. 21 shows the amount of increase in sensitivity of the nitrate sensor to the increase in the concentration of sodium nitrate. It can be seen from the graph that the sensitivity increases linearly with the increase in the amount of sodium nitrate.

The Nyquist plot is given in Fig. 20 shows that the rate of change of the real part of impedance to the imaginary part of impedance at different frequencies as a function of contamination water from different sources.

Fig. 20 Sensitivity of SCS3 with sodium nitrate concentration

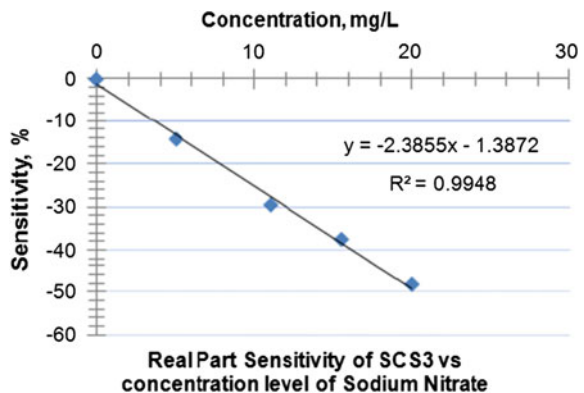
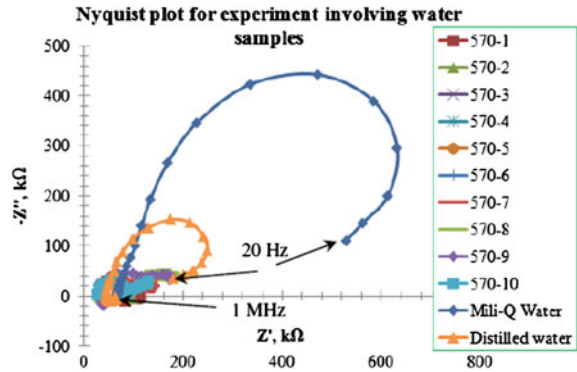


Fig. 21 The Nyquist plot



The biggest challenge of development of sensors for remote monitoring is the supply of power. Due to the non-availability of electricity, sensors will rely on batteries. The sensors especially the sensor nodes used in wireless sensor network need continuous supply of power.

The battery has limited amount of energy storage which will get depleted with use. This means that the primary or disposable batteries are not the viable option for the sensor nodes. The energy of the batteries should be replenished before it gets completely depleted. This tells that the rechargeable batteries along with some energy harvesting techniques are the only viable options. Energy harvesting is defined as the process of collecting energy from the surrounding environment and converting it into electricity. The energy harvesting techniques are gaining interest as a future next-generation energy source as they have the following advantages:

- i. Long lasting operability,
- ii. No chemical disposal,
- iii. Cost saving,
- iv. Maintenance free,
- v. No charging points,
- vi. Inaccessible sites operability,
- vii. Flexibility,
- viii. Environmentally friendly,
- ix. Applications otherwise impossible.

Though different techniques are explored separately but the amount of energy available from one type of sources may be limited. So it may be a good idea to combine a few sources together to form a hybrid harvesting of energy. In the current project the combination of solar, wind and hydel (stream of river) will be exploited. The sensors will be located at different points distributed over a wide region of monitoring area. The fusion of sensors data are done at the wireless sensor node.

The nodes are connected wirelessly with the central coordinator located at a distant point. The collected data from different nodes are stored in a computer. The data will be analysed and then the useful data are uploaded in a website for remote access.

10 Conclusion

This chapter has detailed need of monitoring water quality and different sensors associated with water quality monitoring. A case study of water treatment plant and details of different sub-system associated with it has been described. There is a need of development of new sensors and extension of real-time monitoring through Internet of Things for monitoring of water quality in current times as well for the future generations.

References

1. J. Temido, J. Sousa, R. Malheiro, SCADA and smart metering systems in water companies. A perspective based on the value creation analysis. 12th International Conference on Computing and Control for the Water Industry, CCWI2013. *Procedia Engineering*, vol. 70, pp. 1629–1638 (2014), <http://dx.doi.org/10.1016/j.proeng.2014.02.180>
2. G. Williams, G. Kuczera, Analyzing SCADA to understand the contribution of hydraulic pressures to trunk-main failure. 16th Water Distribution System Analysis Conference, WDSA2014—Urban Water Hydro informatics and Strategic Planning. *Procedia Engineering*, vol. 89, pp. 1452–1459 (2014), <http://dx.doi.org/10.1016/j.proeng.2014.11.472>
3. D.A. Rusua, B. Gengeb, C. Siaterlis, SPEAR: A systematic approach for connection pattern-based anomaly detection in SCADA systems. The 7th International Conference Interdisciplinarity in Engineering, INTER-ENG 2013, 10–11 Oct 2013, Petru Maior University of Tirgu Mures, Romania. *Procedia Engineering*, vol. 12, pp. 168–173 (2014)
4. A. Gligor, T. Turc, Development of a service oriented SCADA system. International Conference Emerging Markets Queries in Finance and Business, Petru Maior University of Tirgu-Mures, ROMANIA, 24–27th Oct 2012. *Procedia Economics and Finance*, vol. 3, pp. 256–261 (2012), [http://dx.doi.org/10.1016/S2212-5671\(12\)00149-9](http://dx.doi.org/10.1016/S2212-5671(12)00149-9)
5. R.K. Chowdhury, W. El-Shorbagy, *Informatics, logistics and governance in water treatment processes*. Department of Civil and Environmental Engineering, United Arab Emirates University, Al Ain, United Arab Emirates, ISBN 978-953-51-0928-0, Published: 16 January 2013 under CC BY 3.0 license. © The Author(s), doi:[10.5772/54386](https://doi.org/10.5772/54386)
6. M. Muntean, H. Valean, C. Rotar, M. Risteiu, *Knowledge discovery in a SCADA system, DATABASE*. *Acta Universitatis Apulensis* (2011), pp. 37–54. ISSN 1582-5329
7. O. Bello, Y. Hamam, K. Djouani, Fuzzy dynamic modelling and predictive control of a coagulation Chemical dosing unit for water treatment plants. *J. Electr. Syst. Inf. Technol.* **1**, 129–143 (2014), <http://dx.doi.org/10.1016/j.jesit.2014.08.001>
8. S.P. Kumar Dutta, SCADA system for north 24 pgs arsenic areas: Rural water supply scheme at Mongal Pandey water treatment plant-first time in India. *J. IPHE India* **8**(2), 24–31 (2007)

9. R. Wang, Z. Wang, X. Wang, H. Yang, J. Sun, Water hammer assessment techniques for water distribution Systems. 12th International Conference on Computing and Control for the Water Industry, CCWI2013. Procedia Engineering, vol. 70, pp. 1717–1725 (2014), doi:10.1016/j.proeng.2014.02.189
10. Recommended standards for water Works, A report of water supply committee of the great lakes—Upper Mississippi river Board of State of Provincial public health & environmental managers. Health Research Inc., Health Education Services Division (2003)
11. O. Vermesan, P. Friess, *Internet of Things- Converging Technology for Smart Environment and Integrated Eco System*. River Publishers Series in Communications, IERC Book open access, TP- 343 (2013)
12. O. Vermesan, P. Friess, *Internet of Things- From research and innovation to Market Deployment*. River Publishers Series in communications, IERC Book open access, TP-143 (2014), http://www.internet-of-things-research.eu/pdf/IERC_Cluster_Book_2014_Ch.3_SRIA_WEB.pdf
13. The fundamentals of SCADA. ©2004 Bentley Systems, Incorporated. All rights reserved, ftp://ftp2.bentley.com/dist/collateral/whitepaper/fundscada_whitepaper.pdf
14. D. Evans, *The Internet of Things How the Next Evolution of the Internet Is Changing Everything*. Cisco Internet Business Solutions Group (IBSG), Tp. 11 (2011)
15. K. Karimi, *What the Internet of Things (IoT) Needs to Become a Reality*. Tp. 16 (2012), http://cache.freescale.com/files/32bit/doc/white_paper/INTOTHNGSWP.pdf
16. J. Bradley, C. Reberger, A. Dixit, V. Gupta, Internet of everything: A \$4.6 trillion public-sector opportunity. <http://globenewswire.com/news-release/2014/04/16/627796/10077088/en/iTalk-to-Launch-Medical-Marijuana-M2M-Enterprise-Solution.html>
17. S. Bunn, Closing the Loop in water supply optimisation. <http://www.schneider-electric.co.uk/documents/support/white-papers/energy-optimisation-software-for-drinking-water.pdf>
18. A. Merchant, M.S. Mohan Kumar, P.N. Ravindra, P. Vyas, U. Manohar, Analytics driven water management system for Bangalore city. 12th International Conference on Computing and Control for the Water Industry, CCWI2013. Procedia Engineering vol. 70, pp. 1137–1146 (2014). doi: 10.1016/j.proeng.2014.02.126
19. Minneapolis water Works uses SCADA system, <http://www.epa.gov/safewater>, <http://www.awwa.org>, <http://www.health.state.mn.us/divs/eh/water>
20. S.J. Sosik, SCADA systems in wastewater treatment, <http://www.process-logic.com/content/images/SCADA.pdf>
21. Water and Wastewater Secure Power Solutions. http://www.schneider-electric.com/solutions/au/en/med/44855164/application/pdf/1736_www-brochurev2-998-1152943_gma_us_x1a_verb.pdf
22. V. Nikolić, Ž. Čojbašić, I. Ćirić, E. Petrović, *Intelligent Decision Making in Waste Water Treatment Plant SCADA System*. Facta Universitatis Series: Automatic Control and Robotics, vol. 9, No 1, pp. 69–77 (2010)
23. M. A. Yunus, S.C. Mukhopadhyay, Novel planar electromagnetic sensors for detection of nitrates and contamination in natural water sources. *IEEE Sens. J.* **11**(6), pp. 1440–1447 (2011)
24. M.A. Yunus, S.C. Mukhopadhyay, Development of planar electromagnetic sensors for measurement and monitoring of environmental parameters. *Meas. Sci. Technol.* **22**, 025107 (9 pp), (2011), doi:10.1088/0957-0233/22/2/025107
25. M.A. Yunus, S.C. Mukhopadhyay, S. Ibrahim, Planar electromagnetic sensors based estimation of nitrates contamination in water sources using independent component analysis. *IEEE Sens. J.* **12**(6), 2024–2033 (2012)
26. M.A. Md Yunus, S.C. Mukhopadhyay, A. Punchihewa, Application of independent component analysis for estimating nitrate contamination in natural water sources using planar electromagnetic sensor, in *Proceedings of the 2011 International Conference on Sensing Technology, ICST 2011*, 28 Nov–1 Dec 2011, Palmerston North, New Zealand, pp. 564–569 (2011). ISBN 978-1-4577-0167-2

27. M.A. Md Yunus, S.C. Mukhopadhyay, A new method for monitoring ammonium nitrate contamination in natural water sources based on independent component analysis, in *Proceedings of the 2011 IEEE Sensors conference*, 29–31 Oct 2011, pp. 1066–1031. IEEE catalog Number CFP11SEN-CDR, ISBN Number 978-1-4244-9288-6
28. S.C. Mukhopadhyay, in *Smart Sensors, Measurement and Instrumentation*, vol. 3, ed. by J.A. Jiang. Wireless Sensor Networks and Ecological Monitoring (Springer, Dordrecht, 2013). ISBN 978-3-642-36364-1
29. S.C. Mukhopadhyay, A. Mason, *Smart Sensors, Measurement and Instrumentation*. Smart Sensors for Real-Time Water Quality Monitoring, vol. 4 (Springer, Dordrecht, 2013). ISBN 978-3-642-37005-2-1
30. A.I. Zia, M.S. Abdul Rahman, S.C. Mukhopadhyay, P.-L. Yu, I.H. Al-Bahadly, C. P. Gooneratne, J. Kosel, T.-S. Liao, Technique for rapid detection of phthalates in water and beverages. *J. Food Eng.* **116**, 515–523 (2013)
31. M.S.A. Rahman, S.C. Mukhopadhyay, P.L. Yu, J. Goicoechea, I.R. Matias, C.P. Gooneratne, J. Kosel, Detection of bacterial endotoxin in food: New planar interdigital sensors based approach. *J. Food Eng.* **114**, 346–360 (2013), (<http://dx.doi.org/10.1016/j.jfoodeng.2012.08.026>)
32. M.S. Abdul Rahman, S.C. Mukhopadhyay, P.L. Yu, C.H. Chuang, M. Haji-Sheikh, Measurements and performance evaluation of novel interdigital sensors for different chemicals related to food poisoning. *IEEE Sens. J.* **11**(11), 2957–2965 (2011)
33. M.A. Md Yunus, S.C. Mukhopadhyay, M.S.A Rahman, N.S. Zuhidin, S. Ibrahim, The selection of novel planar electromagnetic sensors for the application of nitrate contamination detection, in *Smart Sensors, Measurement and Instrumentation*, vol. 4, ed. by S.C. Mukhopadhyay and A. Mason. Smart Sensors for Real-Time Water Quality Monitoring (Springer, Dordrecht, 2013), pp. 171–195. ISBN 978-3-642-37005-2-1
34. M.A. Md Yunus, S.C. Mukhopadhyay, A. PUNCHIHewa and S. Ibrahim, The effect of temperature factor on the detection of nitrate based on planar electromagnetic sensor and independent component analysis, in *Smart Sensing Technology for Agricultural and Environmental Monitoring*, vol. 146, ed. by S.C. Mukhopadhyay. Lecture Notes in Electrical Engineering. (Springer, Dordrecht, 2012), pp. 103–118. ISBN 978-3-642-27637-8
35. M.A. Md Yunus, S.C. Mukhopadhyay, Design and application of low cost system based on planar electromagnetic sensors and impedance spectroscopy for monitoring of nitrate contamination in natural water sources, in *Lecture Notes on Impedance Spectroscopy, Measurement, Modeling and Applications*, vol. 2, ed. by O. Kanoun. (CRC Press, Taylor and Francis group, Boca Raton), pp. 83–102. ISBN 978-0-415-69838-2
36. G.M. Mendez, M.A.M. Yunus, S.C. Mukhopadhyay, A WiFi based smart wireless sensor network for monitoring an agricultural environment, in *Proceedings of IEEE I2MTC 2012 conference*, IEEE Catalog number CFP12MT-CDR, 13–16 May 2012, Graz, Austria, pp. 2640–2645. ISBN 978-1-4577-1771-0
37. M. Haefke, S.C. Mukhopadhyay, H. Ewald, A zigbee based smart sensing platform for monitoring environmental parameters, in *Proceedings of IEEE I2MTC 2011 conference*, IEEE Catalog number CFP11MT-CDR, 10–12 May 2011, Hangzhou, China, pp. 1549–1556. ISBN 978-1-4244-7934-4

An Application of the Frame Theory for Signature Extraction in the Analysis of 3D Point Clouds

F. Martino, C. Patruno, R. Marani and E. Stella

Abstract In this work a novel way for the recognition and classification of objects inside a scene, inspired by the well-known frame theory, is described. First of all, three-dimensional (3D) point clouds have been obtained using a laser triangulation system of high resolution, in order to achieve low noise datasets for the method validation. Once specific areas are extracted following a novel autonomous algorithm, a fit of the second order is defined on these acquired samples to find local curvatures. Such information is compared to the words of a precomputed dictionary made of curvatures, which constitutes the frame basis. The results of the comparison give evidence to the presence of particular objects in the scene under investigation. As a matter of fact, introducing a threshold value ζ , similarities can be found and thus objects can be recognized. Specifically, the final results state the effectiveness of the method to distinguish objects having different surface properties. Moreover, the agreement of results is proven despite of the contribution of the measurement noise which produces outlier points.

1 Introduction

One of the most important open-problems for the interpretation of 3D models is the object recognition. Although some relevant progresses in this way have been made in Literature, nowadays it is still widely acknowledged that, in actual contexts, occlusions and noise increase the complexity of the task of object recognition [1]. Moreover the scene understanding becomes more difficult especially for complex-shaped objects with ambiguous geometries [2]. At the current state of the art, algorithms could be divided in methods based on the interpretation of global or local features [3].

F. Martino (✉) · C. Patruno · R. Marani · E. Stella
National Research Council of Italy (CNR), Institute of Intelligent Systems
for Automation (ISSIA), Bari, Italy
e-mail: fabio.martino1969@gmail.com

A global method defines features referenced to a new coordinate system, centred on the object under analysis. Then, a parametric function defined in the new system of coordinates is created to represent the object properties. As an example, the 3D Generalized Cylinder (GC) can be used for the exhaustive approximation of the shapes of the objects [4]. However, this methodology operates on intensity images, and is not suitable for the investigation of complex 3D point clouds, where samples are expressed in terms of spatial coordinates. At the same time, super-quadratics [5] are simple formulation often used to represent the shape of objects. Unfortunately, only a small number of shapes can be represented by means of this formulation. As a consequence, the analysis of intricate scenes requires high computational costs, since objects have to be segmented preliminary. Finally also the Gauss Map method [6] falls in the category of global methods. This latter gives good results independently of translations and perspective deformations, but, on the other hand, leads to errors when occlusions emerge.

Local methods exploit the segmentation of the initial model to find different objects which are then described by features. An example of local descriptor is in the Normal Aligned Radial Feature (NARF) [7]. It is based on the extraction of edges which are then classified in two categories of background/occluded regions, in order to understand the properties of the scene. This approach gives optimal results, when the edge extraction process is robust enough against 3D measurement noise [8].

As stated before, the problem of object recognition in a complex environment is one of the most relevant tasks in robotics, as it could be linked to the Visual Odometry, i.e. the estimation of motion of autonomous vehicles [9]. In fact, considering a couple of images acquired by a sensor mounted on a mobile robot in two consecutive time instants, it is possible to find and link distinguishable features, i.e. signatures. Then, the robot movement in the environment can be estimated defining the roto-translation matrices that express the relative motion experienced by the robot between the two considered frames [10]. In this context, the basic techniques for the analysis of two-dimensional images are the Scale Invariant Feature Transform (SIFT) [11] and the Speeded Up Robust Feature (SURF) [12]. In the case of intensity images, it is important to notice that it is necessary to perform complex camera calibrations to compute the robot movements in world coordinates, given the information on the pixel displacements. On the contrary, such calibrations are unnecessary when 3D images are used, as the displacement information is implicitly comprised within the point cloud.

In this work, 3D datasets are processed using the frame theory for the definition of local surface descriptors. As a first step a triangulation-based laser scanner assisted by a high definition camera is used to obtain the 3D point clouds. Each returned measurement has information about the distances of the target from the camera. Then, a group of points belonging to a spherical volume with fixed radius is extracted from those points of the dataset that show the highest informative contributions. Points are processed to define a least square (LS) fit on a quadratic function, used to obtain the curvature information which are compared with those of a predefined vocabulary. Curvatures are reported to the frame, which is a

non-orthonormal but complete basis of an equivalent space (dictionary). The dictionary is defined by means of precomputed Gaussian and mean curvatures of artificially generated surfaces, having properties similar to those of the actual surfaces. The weights of the curvature representation on the basis are the surface signatures, which describe the surface properties of the considered object. The Chapter is organized as follows: in Sect. 2 the frame theory is briefly described with reference to the problem of interest; Sect. 3 shows the steps which lead to the generation of the frame, whereas Sect. 4 reports the preliminary steps required for the analysis of real datasets, while Sect. 5 includes the description of a novel algorithm for the extraction of meaningful points. Section 6 highlights the final results concerning the use of the proposed model for the recognition of simple objects. Final conclusion and remarks are in Sect. 6.

2 Mathematical Framework

The presented method analyses 3D data to find the object properties in terms of a projection on an equivalent space, following the well-known frame theory [13]. The following paragraphs summarize the theory of frames and give the processing steps that produce the scene understanding and the recognition of objects.

2.1 Frame Definition

The frame theory aims to represent an input f , belonging to a generic Hilbert space H , in an equivalent space, which can also show higher dimensions.

A family F of functions φ_j ($j = 1, \dots, l$) is a *frame*, if two bounds $A > 0$ and $B < \infty$ exist, i.e. for any input f belonging to H :

$$A\|f\|^2 \leq \sum_{\varphi_j \in F} f \cdot \varphi_j \leq B\|f\|^2 \quad (1)$$

Note that the functions φ_j are often addressed as *atoms*. In the case $A = B$ the frame is named as *tight* and the previous relation becomes:

$$\sum_{\varphi_j \in F} f \cdot \varphi_j = A\|f\|^2 \quad (2)$$

Orthonormal bases are a subset of the tight frames where $A = 1$. In this case, the relationship can be rewritten as:

$$f = \sum_{j=1}^l c_j \cdot \varphi_j \quad (3)$$

In general, a frame is a non-orthonormal but complete basis of a space where a generic input f can be represented. In this case the representation is expressed by the entries of the coefficient vectors c_j which are in general not unique. These coefficients are the signature of the input on the equivalent space defined by the frames.

The application of this theory to the field of image understanding has three relevant aspects that should be underlined:

- Which is the informative content of the input f and how is it related to the image?
- How f can be expressed as a linear expansion of frame function φ_j ?
- How a set of φ_j , defined as $F = [\varphi_1, \varphi_2, \dots, \varphi_n]$ where $F: \mathbb{R}^n \rightarrow \mathbb{R}^l$ could be classified as a Frame?

Given the definition of the set F , Eq. (1) can be rewritten, obtaining:

$$A\|f\|^2 \leq \|fF\|^2 \leq B\|f\|^2 \quad (4)$$

After simple algebra, the formulation is:

$$Af^T f \leq f^T F^T F f \leq Bf^T f \Leftrightarrow A \leq \frac{(f^T F^T F f)}{f^T f} \leq B \quad (5)$$

The central term is known as the Rayleigh quotient of the matrix. In [13] the quantities A and B are estimated respectively as the minimum and the maximum eigenvalues of the Rayleigh quotient (λ_{min} and λ_{max} , respectively). Thus, accordingly to the frame theory, the matrix F can be effectively considered as a frame if it satisfies a fundamental condition: the eigenvalues of the matrix $F \cdot F^T$ have to be positive, comparable to the order of magnitude of the entries of the input vector (further evidence will be provided in the following paragraphs).

Finally, the generic input vector can be expressed as a linear expansion of the frame vector:

$$f = \sum_{i=1}^l c_i \Phi_i \quad (6)$$

where:

$$\Phi_i = \frac{1}{(F^T F)} \varphi_i \quad (7)$$

As already stated, the frame expansion of the input vector produces a not-unique representation since the vectors in the frame are not linearly independent.

Consequently, the coefficients have to be determined choosing a specific solution, which is often the one showing the minimum norm.

2.2 Input Vector Selection

Once the mathematical aspects of the frame theory are described, it is necessary to select the input vector that will be processed to define the signature c . In the case of analysis of 3D point clouds, the vector f is defined equal to α , whose entries are an ordered set of couples of Gaussian and mean curvatures, computed punctually over a grid resampling the input surface.

Considering a generic point p of the input differentiable surface S , we define the two principal curvatures, i.e. the maximum and the minimum curvatures (k_r and k_r' , respectively). In particular the input data is made up by the product of the principal curvatures (Gaussian curvature, K) and their mean value (mean curvature, H). With reference to Fig. 1 [14] these terms are linked to the maximum and minimum radii of a curve passing through p and belonging to the surface S . In a 2D space the curvatures are proportional to the inverse of the radius of the osculating circle which passes through the point p and makes a good approximation of the tangent curve c .

It is worth noticing that elementary surfaces, such as planes, cylinders and spheres, have elementary curvature values, which are reported in Table 1.

In a more quantitative way, given the differentiable surface $z = f(x,y)$, where x and y are the independent variables belonging to \mathbb{R} , the Gaussian and the mean curvatures are defined as:

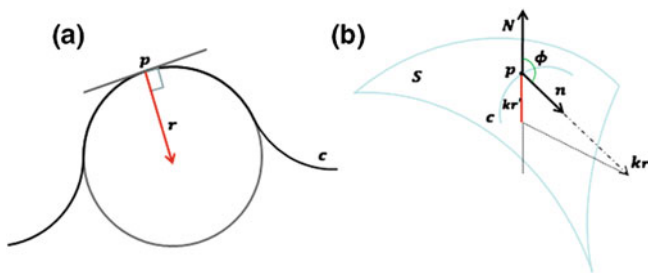


Fig. 1 **a** Geometrical radius of the osculating circle passing through the point p and **b** representation of the curvature of a generic surface with respect to a curve passing through the point p and the normal vector N

Table 1 Gaussian and mean curvatures of common surfaces

Surfaces	K	H
Plane	0	0
Cylinder	0	$1/2r$
Sphere	$1/r^2$	$1/r$

$$K = \frac{f_{xx}f_{yy} - f_{xy}^2}{(1 + f_x^2 + f_y^2)^2} \quad (8)$$

$$H = \frac{(1 + f_x^2)f_{yy} - 2f_x f_y f_{xy} + (1 + f_y^2)f_{xx}}{2(1 + f_x^2 + f_y^2)^2} \quad (9)$$

where:

$$f_x = \frac{df(x,y)}{dx} f_y = \frac{df(x,y)}{dy} f_{xx} = \frac{df_x(x,y)}{dx} \quad (10)$$

$$f_{xy} = \frac{df_x(x,y)}{dy} f_{yy} = \frac{df_y(x,y)}{dy} \quad (11)$$

For further details the reader can refer to Ref. [14].

It is fundamental to observe that the local curvatures have been chosen as the input feature for the frame development, since these are perspective invariant, in accordance with the *theorema egregium*. It states that Gaussian curvature values are only ascribable to the properties of the object surface, regardless of the observer point of view. In actual contexts, also mean curvatures have the same property, since wrapped surfaces can be observed in a one-shot acquisition from a single point of view. As a consequence, perspective ambiguities due to the possible existence of negative values of the mean curvature are practically avoided. By this way, the method can overcome one of the most relevant problems in object recognition and modelling, i.e. the perspective deformation of scenes when the same environment is acquired in two consecutive time instants from different points of view [15].

After the definition of the input vector, the output, i.e. the patch signature c , can be obtained following:

$$F \cdot c = \alpha \rightarrow c = F^* \cdot \alpha \quad (12)$$

where F^* is the pseudo-inverse of the Frame F .

3 Frame Generation

In this Chapter, we create a model of generic indoor environments in terms of a combination of quadratic surfaces, taking advantages of the frame theory. In particular, we have chosen the paraboloid (see Fig. 2), for its properties:

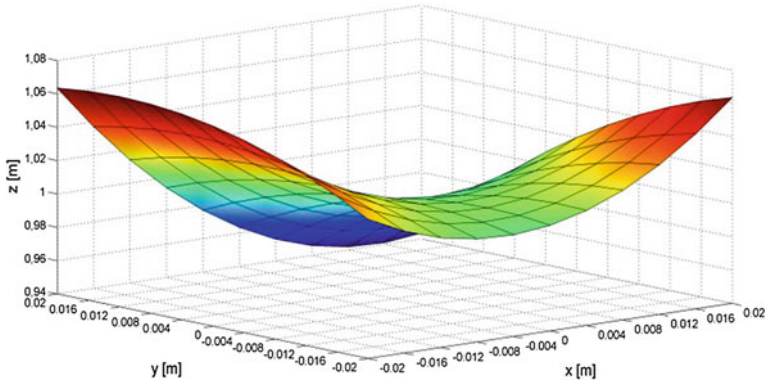


Fig. 2 Surface of a paraboloid in the 3D space

- Best candidate to represent many different basic surfaces, such as cylinders, spheres and planes;
- Robust to occlusion problem.

The initial analytical formulation is the following:

$$z = ax^2 + by^2 + cx + dy + exy + f \tag{13}$$

where, changing the values assumed by the coefficients in Eq. (13), the generic paraboloid can be classified as hyperbolic or elliptic.

The generation of the vocabulary, i.e. the frame, is the preliminary step of the whole processing. As explained before, curvatures can be easily computed using Eqs. (8) and (9). By imposing that the two independent variables x and y can span in a square domain having side length of 40 mm by steps of 4 mm, several synthetic paraboloids have been created by varying the values of the coefficients in Eq. (13), keeping the parameters in the range boundaries reported in Table 2. These limits have been chosen in order to create realistic paraboloids, similar to those that can be found in actual scenes. The span of the coefficients within the bounds determines the set of paraboloids which will be the starting point for the frame generation, mediated by the computation of the curvatures.

Table 2 Admissible ranges of paraboloid parameters

Parameter	Minimum value	Maximum value
a	-100	100
b	-100	100
c	-1	1
d	-1	1
e	-100	100
f	-0.02	0.02

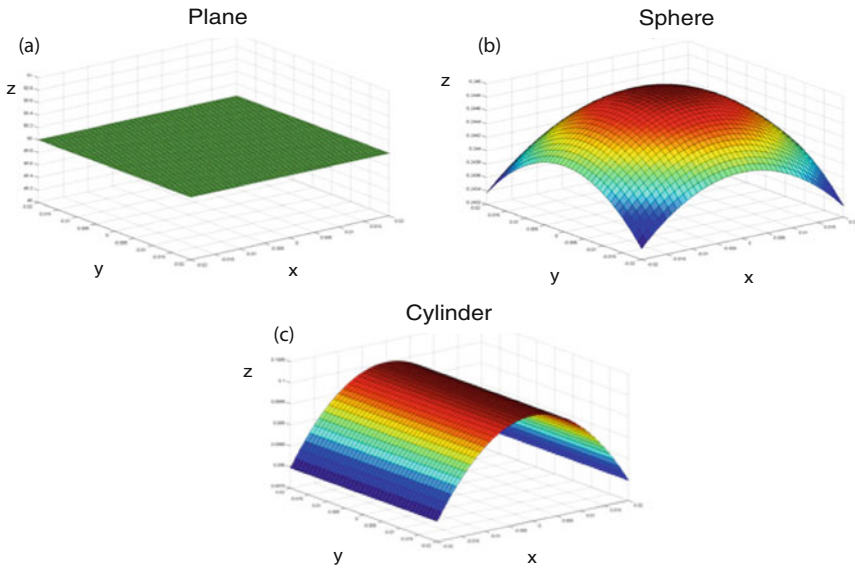


Fig. 3 Three examples of surfaces derived by varying the coefficients of the paraboloid: **a** plane, **b** sphere and **c** cylinder

In Fig. 3 some examples of paraboloids of different shapes obtained by changing the coefficients of Eq. (13) are shown.

Given the set of generated surfaces, a selection of paraboloids was executed. In fact using the information linked to the sensor depth of field, only those quadrics inscribed in a sphere of diameter equal to $\sqrt{3}$ times the patch size (40 mm of side) are kept in the frame generation. In this way, the artificially created surfaces constitute a good set of atoms where real surfaces can be decomposed.

Then, Gaussian and mean curvatures are punctually extracted for each point of the planar grid, using the analytical expression of the partial derivatives:

$$f_x = 2ax + c + ey \quad (14)$$

$$f_y = 2by + d + ex \quad (15)$$

$$f_{xx} = 2a \quad (16)$$

$$f_{yy} = 2b \quad (17)$$

$$f_{xy} = e \quad (18)$$

For each point described by discrete values of x and y , two curvatures are determined, thus leading to two matrices, K and H (Gaussian and mean curvature matrices, respectively), of size equal to 11×11 . The two matrices are reshaped

columnwise generating two column arrays of 121 elements each, which are then mixed to produce the specific atom φ_j of the frame (column vector of 242 entries). The computation of the atoms is repeated for all the synthetic paraboloids. Atoms are then placed side by side, thus giving the final frame candidate for the specific problem.

The frame is finally tested determining whether the smallest eigenvalue of the product $F \cdot F^T$ vanishes. Substantially, a threshold on the smallest accepted value, connected to the size of the square domain used to create the paraboloids, is imposed equal to 2.5×10^{-4} .

4 Processing of Real Data

The presented analysis has been used to discriminate several objects, finding common properties among real acquisitions. In particular, different basic objects, such as plane, sphere and cylinders, have been acquired under altered conditions, residing in different relative displacements and orientations.

3D point clouds are acquired using a triangulation-based laser scanner having resolution of 2×10^{-5} m. Figure 4 reports an example of real dataset, where a sphere is displayed. It is important to underline that the heights are oriented oppositely with reference to the vertical axis, and therefore heights are developed along the negative part of the z -axis.

As an example, Fig. 5 displays the extracted points, taken from the sphere in Fig. 4, and the corresponding quadratic surface, result of a least square fitting. Following the proposed algorithm, the patch is then used to compute the Gaussian and mean curvatures on a sampling grid centred on the specific reference point set.

The use of a fitted surface introduces two important advantages. First of all, measurement errors are implicitly compensated by the least square process. Then,

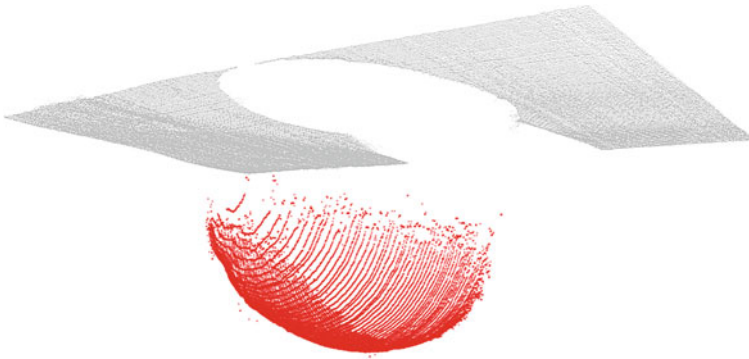
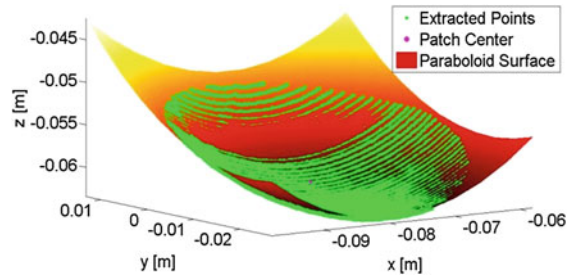


Fig. 4 Example of real data: acquisition of a sphere. *Red dots* represent the set of points used for the signature extraction

Fig. 5 Approximation of a quadratic surface for the extracted real data



possible occlusions are avoided, since continuous surfaces always result from the non-linear least square fit.

5 Patch Extraction

In the previous paragraph, points of interest are picked from the point cloud, searching for those regions that show the main contribution of information (in the case of the sphere, the whole curved surface). This task can be performed automatically, finding the edge of the objects and then extracting the most meaningful regions around the selected edges. Here signatures can be used to connect different regions, then used to label a specific point.

In practice, the initial point cloud is first investigated to delete the outliers, due to the presence of secondary reflections which create artifacts in the final acquisitions. In this case outliers are removed exploiting the dataset statistics [16]. Since the cloud of points is dense of vertices, it is possible to assume that a point is an outlier when a spherical region centered in that point includes a number of vertices lower than the one below the statistics. Equivalently, the acquired samples are clustered and then processed to find those poor sets whose size is lower than a threshold. Given the resolution of the sensor and the size of the clusters, the threshold has been set to 15.

Then the point cloud is processed to get a complete model, where information about point normals are added. Results on the analysis of an actual point cloud returned by scanning a cylindrical-shaped object are reported in Fig. 6.

After the outlier removal, points are ordered to produce a triangular surface mesh. Results are displayed in Fig. 7 where triangular elements are clearly visible.

Triangles are then analyzed in order to determine the ones that show at least one of the following properties:

1. The half-perimeter is almost equal to the sum of two sides;
2. One of the sides has length higher than a threshold

The vertices that belongs to the triangles which satisfy one of the two conditions are candidate object edges. These candidates are further tested analysing the angles

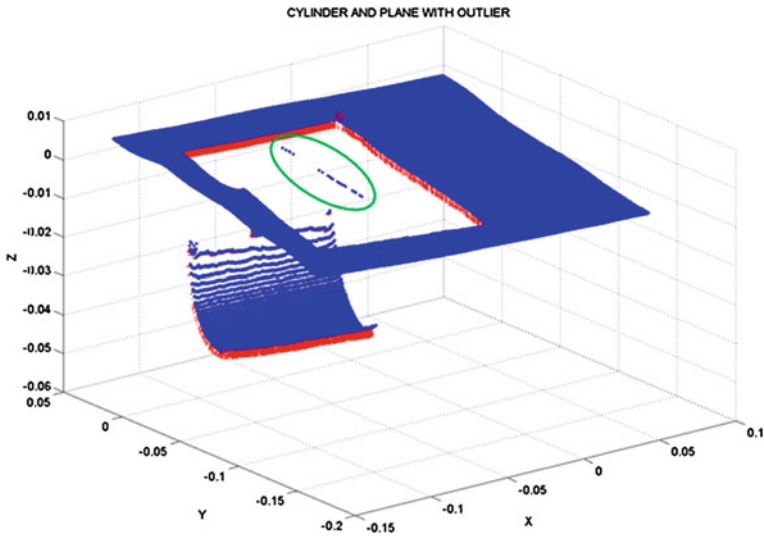


Fig. 6 Acquired point cloud (blue dots) and point normals (red vectors). Outliers are included in the green circle. All measurement units are in meters

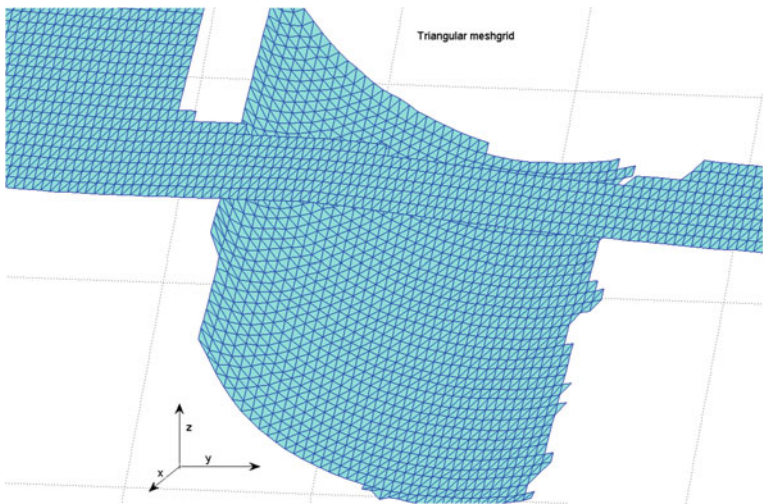


Fig. 7 Magnified view of the triangular mesh generated starting from the points in Fig. 6

comprised by the normal of the considered triangle and the normal of the adjacent triangles, having one side in common. The considered angles are labelled as ρ , τ and ω in Fig. 8. If one of the resulting angles is higher than a threshold, chosen close to 75° , the vertex is finally labeled as an edge.

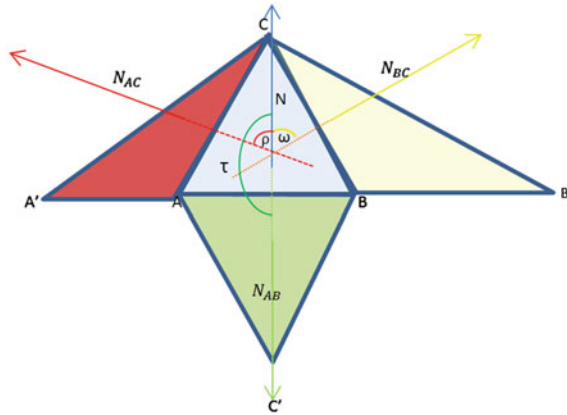


Fig. 8 Geometric scheme for the normal analysis of the triangle ABC . A , B and C are the three points which belong to the point cloud, while A' , B' and C' are three points that connects the adjacent triangles, used in the normal comparison

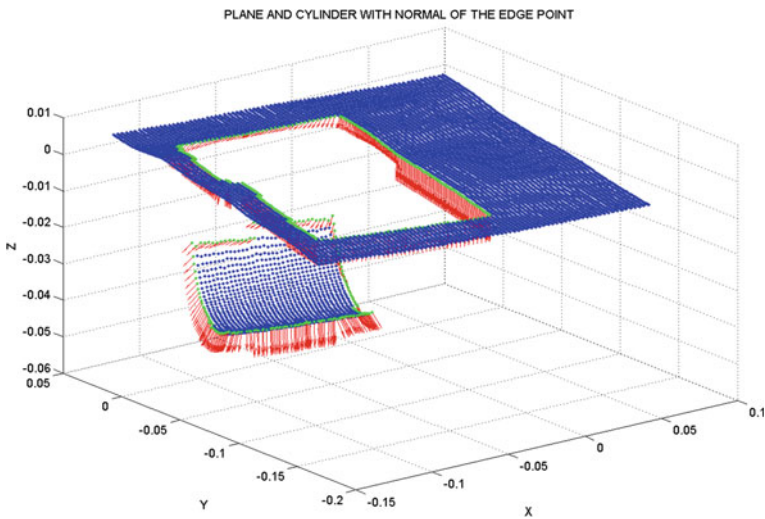


Fig. 9 Green points are candidate edges for the proposed point clouds, since they satisfy conditions (1) and (2). Red arrows are the normals compared for the study of the angle condition. All measurement units are in meters

The results of this processing are shown in Fig. 9 where candidate edges are highlighted, and corresponding point normals are displayed by the red arrows. In this case, it is worth underlying that point normals are directly obtained as the average value of the normals of the six triangles that include the specific vertex

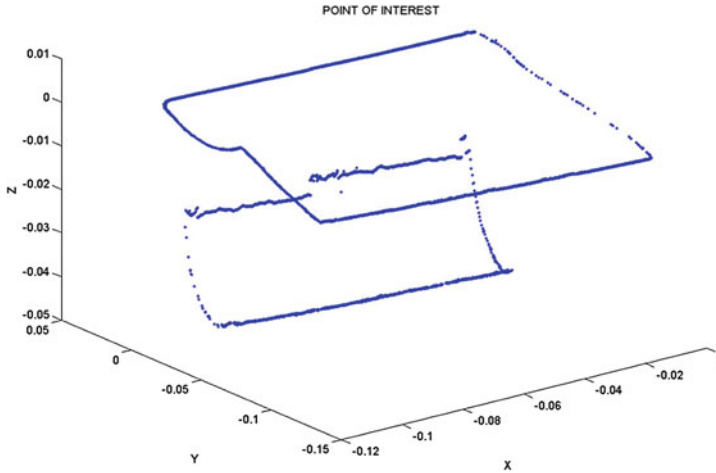


Fig. 10 Points of interest obtained considering the three conditions for the edge selection. Measurement units are expressed in meters

under analysis. On the other hand, patch normals are easily derived as the unit vector describing the plane which includes the three triangle vertices.

The threshold process returns the results in Fig. 10, where the points of interest are shown in the 3D space.

When the point of interest are found, it is possible to proceed with the detection of those points that are characteristics of the object under analysis. In other words, the goal of this processing is the recognition of the centre of the patch highlighted in Fig. 5. This patch will be the starting point for the processing described previously. For these reason, each point of interest is further investigated to find four more patches.

As a first step, we consider the maximum and minimum curvatures computed considering the spherical neighbour of the point of interest. At the same time, also the two directions of the two curvature terms are found. Then, the four novel points are determined by finding the vertices which belong to the two directions and have distance from the starting point of interest equal to the diameter of the sphere used for the curvature computation. Results are reported in Fig. 11, where the purple dot represents the starting point and the green dots are the four novel vertices where signatures can be computed.

Figure 11 clearly demonstrates that the automatic method for the patch extraction recognizes the four novel points around the initial one which belong to different surfaces, specifically one of the cylinder and the remaining of the background plane. The patches can be thus built around the detected points and then translated in terms of signatures defined in the frame basis.

Moreover, with reference to Fig. 11b, it could be observed that the two curvature directions (red dotted lines) cross void regions, due to the presence of occlusions. As a consequence, it is possible that any point of the dataset intercepts the two

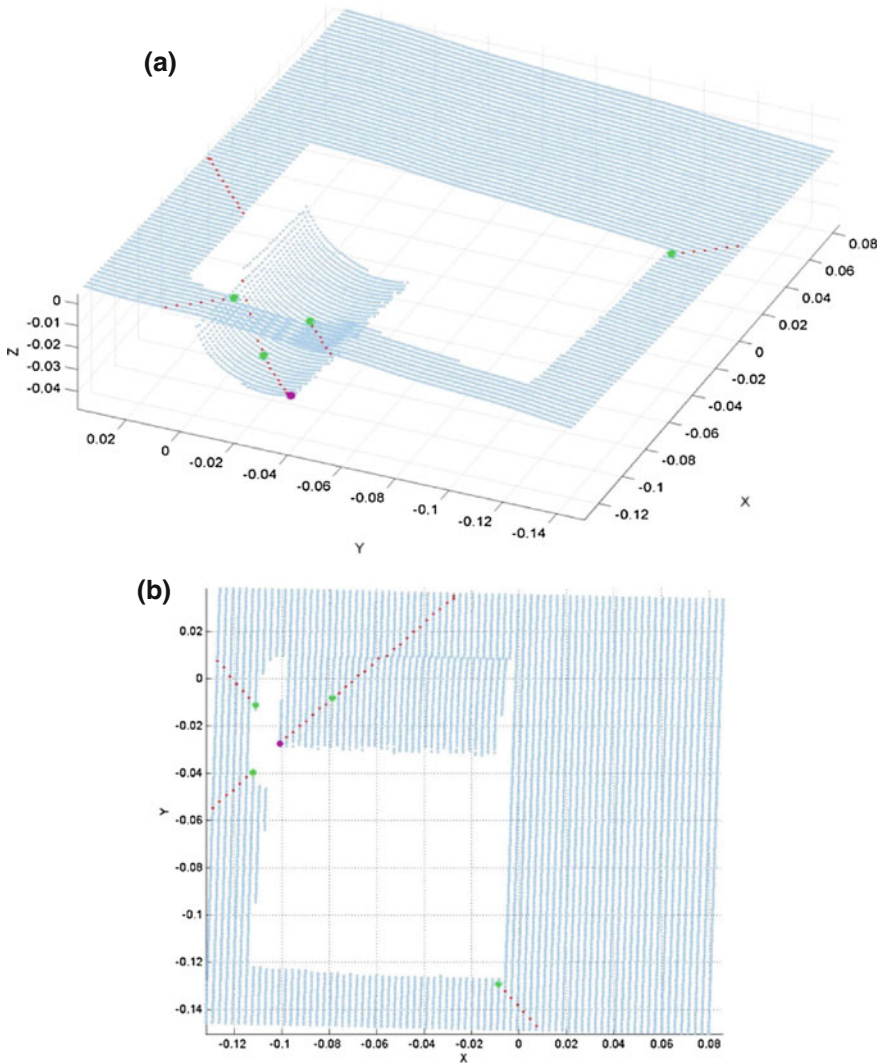
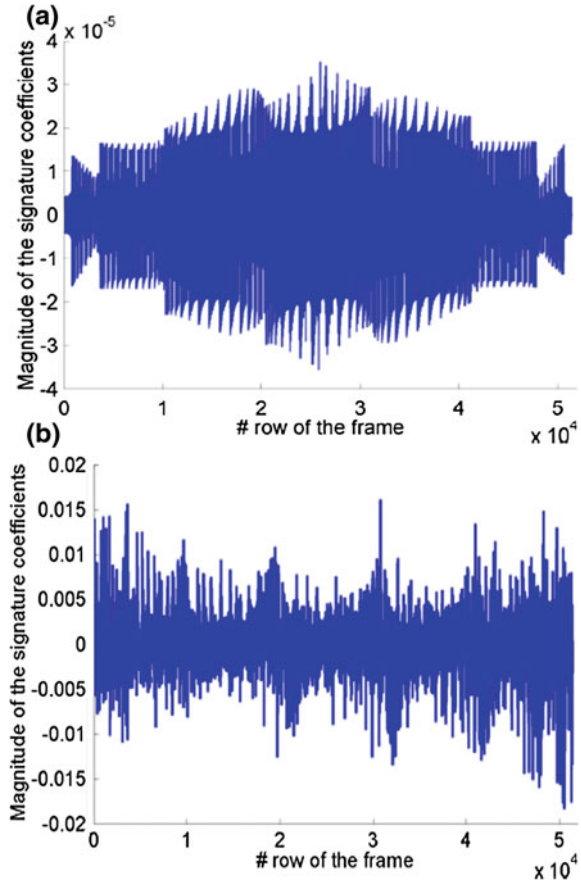


Fig. 11 Computation of the points of interest (*green dots*) given by the intersection of the two curvature directions (*red dotted lines*) reported on the point cloud (*blue dots*). The purple point is the starting vertex, edge of the considered cylindrical object. **a** 3D and **b** 2D sight of the dataset. All measurement units are in meters

curvature directions at the fixed required distance. In this case the method considers the first point belonging to the curvature directions, closer to the previously set distance from the initial starting point.

Fig. 12 Example of signature vectors extracted from a planar (a) and cylindrical (b) surface



6 Final Results

Knowing the definition of the signature, a comparison among local signatures belonging to several real objects acquired by means of a triangulation-based laser scanner can be performed.

As shown previously, when the algorithm of edge extraction determines the starting interest points, the computation of curvatures allows the determination of four further points of interest, centre of the patches used for the signature evaluation. Considering two patches lying on a plane or a cylinder, the corresponding signatures, referred in the novel frame space, show the profiles reported in Fig. 12a and b, respectively.

When signatures have to be compared, it is useful to define a specific metrics. In this case, the dot product of the two signature vectors is exploited to compute the distance between the two signature vectors under investigation.

$$\text{dot}(c_1, c_2) = \|c_1\| * \|c_2\| \cos \theta \quad (19)$$

$$\zeta = \cos \theta = \frac{|\text{dot}(v_1, v_2)|}{\|c_1\| * \|c_2\|} \quad (20)$$

The ζ term can also be interpreted as a confidence level bounded between 0 and 1. In this case, the following classification can be defined:

- $\zeta \geq 0.9$: optimal similarity;
- $0.5 \leq \zeta < 0.9$: good similarity;
- $0 \leq \zeta < 0.5$: dissimilarity.

Almost seventy experiments have been performed to prove the ability of the method to classify objects, e.g. planes, spheres and cylinders. For the sake of simplicity, only twenty acquisitions are reported in this paper.

Table 3 lists the most relevant acquisitions performed for the model validation and the corresponding numbers used as reference in the following lines. Specifically, the first three acquisitions are derived from the inspection of three horizontal planes, of two different materials (one of plastic and two of aluminium). The acquisitions from 4 to 7 are obtained by tilting the plastic plane, following directions which are expressed by the normal vectors n_i . Acquisitions 8 and 9 are obtained by scanning different cylinders with comparable radii (r_8 and r_9), whereas

Table 3 List of objects used for the model validation

# acq	Kind of surface	Object property
1	Horizontal plane 1	Plastic medium
2	Horizontal plane 2	Aluminium
3	Horizontal plane 3	Aluminium
4	Tilted plane 1	$\mathbf{n}_4 = [0.781, -0.499, -0.375]$
5	Tilted plane 2	$\mathbf{n}_5 = [-0.507, -0.028, -0.862]$
6	Tilted plane 3	$\mathbf{n}_6 = [-0.381, -0.334, -0.862]$
7	Tilted plane 4	$\mathbf{n}_7 = [-0.435, 0.268, -0.860]$
8	Cylinder 1	$r_8 = 24.27$ mm
9	Cylinder 2	$r_9 = 38.27$ mm
10	Sphere 1	$r_{10} = 18.85$ mm
11	Sphere 2	$r_{11} = 34.42$ mm
12	Sphere 3	$r_{12} = 29.70$ mm
13	Sphere 4	$r_{13} = 27.25$ mm
14	Sphere 5	$r_{14} = 14.15$ mm
15	Sphere 6	$r_{15} = 20.5$ mm
16	Sphere 2	$r_{16} = r_{11}$
17	Sphere 7	$r_{17} = 35.12$ mm
18	Sphere 6	$r_{18} = r_{15}$
19	Sphere 5	$r_{19} = r_{14}$
20	Irregular surface	–

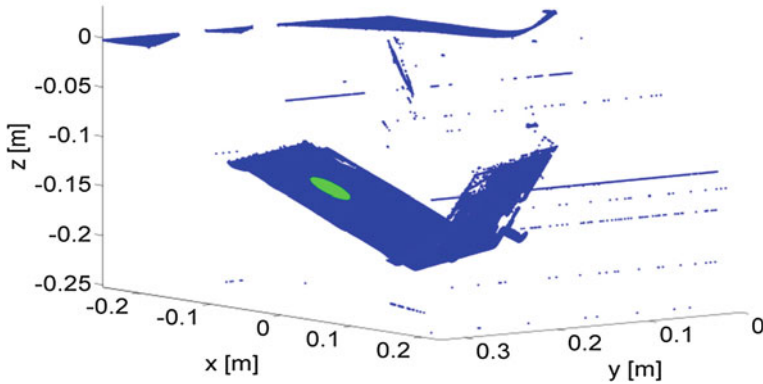


Fig. 13 Point cloud related to acquisition 5 (blue dots) and corresponding extracted patch used for the computation of the signature vector (green dots)

the acquisitions from 10 to 19 are related to the acquisition of seven spheres having different radius r_k ($k = 10, \dots, 19$). Acquisitions 16, 18 and 19 are redundant, since these are obtained by applying rigid displacements to the spheres of acquisition 11, 14 and 15, respectively. Finally, acquisition 20 is performed on an irregular surface.

Figure 13 reports an example of acquisition performed on a tilted plane (acquisition 5, tilted plane 2), whereas green dots belong to the patch obtained following the automatic method described in the previous paragraph. In this case it is possible to notice the noise contribution which induces the presence of cloud outliers, which can lead to processing errors.

Table 4 reports the ζ value obtained comparing the signature vector of the object in acquisition 5 with the remaining examples. The confidence values in bold are the ones that confers the best results, accordingly with the aforementioned classification. Quantitatively, some ζ values are very close to the unity, regardless of the tilt experienced by the planar regions. These results are strictly connected to the

Table 4 Comparison of signature vectors with the one related to the target in acquisition 5 (tilted plane 2)

# acq	ζ value	# acq	ζ value
1	0.9996	11	0.1207
2	0.9996	12	0.1687
3	0.9996	13	0.0107
4	0.9667	14	0.0174
5	–	15	0.0955
6	0.9997	16	0.1954
7	0.9945	17	0.1855
8	0.2615	18	0.0692
9	0.1036	19	0.0066
10	0.0795	20	0.2438

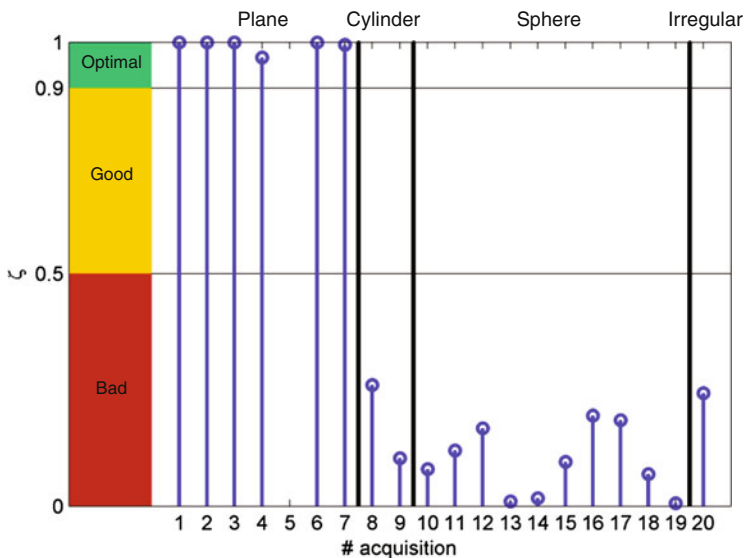


Fig. 14 Stem diagram representation of the results presented in Table 4, obtained by the comparison of acquisition 5 with the remaining datasets

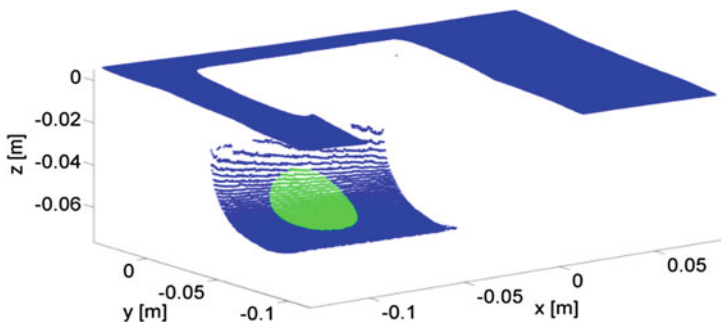


Fig. 15 Point cloud of acquisition 8 (blue dots) and points considered for the signature definition (green dots)

theorema egregium, which states that results are independent of the point of view of the observer, or, equivalently, of the tilt experienced by the target.

The results in Table 4 are also presented in the stem diagram of Fig. 14.

Figure 15 reports the dataset related to acquisition 8, where a cylinder is scanned by the laser profilometer.

The results of the comparison of signatures with the one produced by the analysis of the cylindrical target are expressed in Table 5, where the term ζ is shown. Also in this case bold values are those that indicate the best matching of signatures. Despite the previous case, only one value passes the confidence check,

Table 5 Comparison of signature vectors with the one related to the target in acquisition 8 (cylinder 1)

# acq	ζ value	# acq	ζ value
1	0.2710	11	0.0146
2	0.2727	12	0.0182
3	0.2727	13	0.0484
4	0.3062	14	0.0024
5	0.26154	15	0.0114
6	0.2719	16	0.0230
7	0.3052	17	0.0012
8	–	18	0.0156
9	0.5951	19	0.0025
10	0.0005	20	0.0731

i.e., the one related to the comparison with the other cylinder. Here the bold value is not “optimal” but only “good”, since cylinders have slightly different radii. As the curvatures are dependent on the inverse of the radius of the cylinder section, signatures are implicitly different and thus the method does not converge to the recognition of the same object in the two datasets, as required. On the contrary, the other ζ values are much more different than the previous one, since different kinds of surfaces are compared.

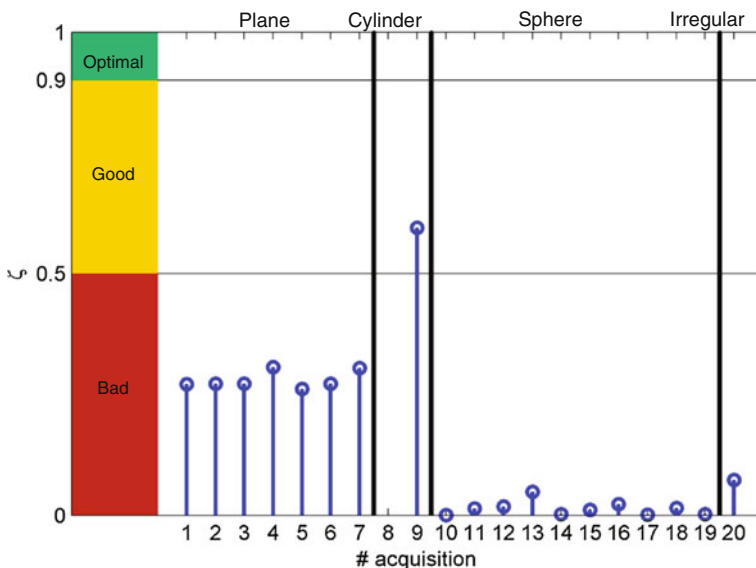


Fig. 16 Stem diagram representation of the result of the signature comparison with the one produced by the cylinder 1 (acquisition 8)

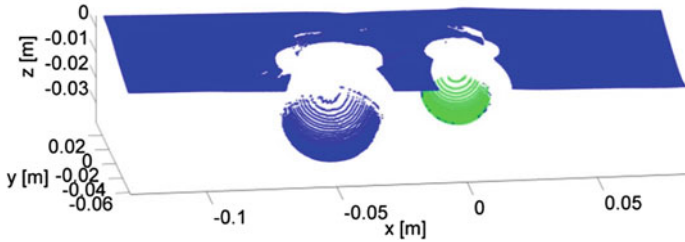


Fig. 17 Point cloud obtained by the inspection of spheres 5 (green dots) and 6 (blue dots), modelled in acquisitions 14 and 15, respectively

Table 6 Comparison of signature vectors with the one related to the target in acquisition 14 (sphere 5)

# acq	ζ value	# acq	ζ value
1	0.0170	11	0.0308
2	0.0170	12	0.0012
3	0.0173	13	0.0478
4	0.0164	14	–
5	0.0174	15	0.3034
6	0.0172	16	0.0003
7	0.0175	17	0.0011
8	0.0021	18	0.1959
9	0.0013	19	0.6935
10	0.2306	20	0.0391

Table 5 produces the results in Fig. 16, where the stem diagram related to the signature comparison with the one produced by the cylinder is presented.

Finally, the comparison of signatures has been performed with reference to acquisition 14, where a 28 mm diameter sphere is investigated. The corresponding point cloud is reported in Fig. 17 (blue dots refer to the sphere of acquisition 15, whereas green dots are those of acquisition 14). It is important to notice that also in this case, the method for the patch extraction has produced the correct results in an automatic way (see how green dots are characteristics of the spherical surface). Following the procedure already described for the previous cases of study, corresponding results of signature comparison are reported in Table 6.

Also the results in Table 5 prove the capability of the proposed method to recognize the sphere 5 in the other measurements. As for the analysis of cylinders, the highest value, marked in bold, is obtained for acquisition 19, which is performed on the same object, but under different conditions. Once again, the comparison with the other spheres produces low similarity since input data are in inverse proportion with the radius. Consequently, different radii create dissimilarities among spheres. The stem diagram in Fig. 18 gives further evidence to the presented results.

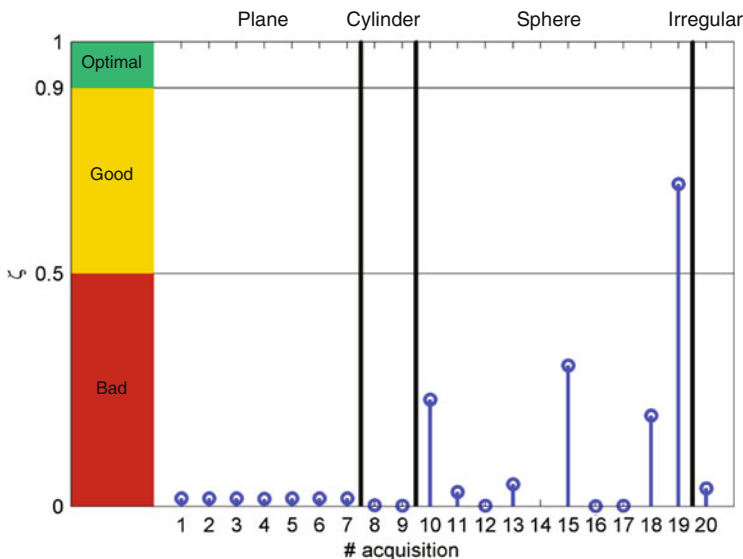


Fig. 18 Stem diagram representation of the result of the signature comparison with the one produced by the sphere 5 (acquisition 14)

7 Conclusions and Future Work

In this Chapter, we have described and tested a method for object detection in actual datasets. The method is implicitly unaffected by perspective deformations because it exploits the properties of the Gaussian and mean curvatures to produce robust signatures, in accordance with the frame theory. A frame, namely a basis made of linearly dependent elements, is created by inspecting the curvatures of parametric synthetic surfaces. Real datasets are processed to find local signatures, made by decomposing the curvatures of a fitting paraboloids in terms of a weighted summation of the frame entries. The final results confirm that the method is able to recognize elementary objects among several primitives, i.e. planes, cylinders and spheres, despite of the noise which produces outliers in the measurements. This work constitutes the fundamental basis for several applications in the field of robotics. As an example the motion estimation of autonomous vehicles through the pose estimation of recognized objects can be envisaged. In this context, the use of the algorithm for the detection of points of interests will give more consistency and reliability to the proposed method for its actual implementation on mobile vehicles.

Acknowledgement This work was funded within the CNR-ISSIA project MASSIME —“Mechatronic innovative safety systems (wired and wireless) for railway, aerospace and robotic applications”.

References

1. F. Dell'acqua, R. Fisher, Reconstruction of planar surfaces behind occlusion in range images. *IEEE Trans. Pattern Anal. Mach. Intell.* **24**(4), 569–575 (2002)
2. R. Benlamri, Curved shapes construction for object recognition. in *Proceedings IEEE Geometric Modeling and Processing (GMP)* (2002), pp. 197–204
3. H. Delingette, M. Hebert, K. Ikeuchi, A spherical representation for the recognition of curved objects, in *Proceedings IEEE Computer Vision* (1993), pp. 103–112
4. A.D. Gross, T. Boult, An algorithm to recover Generalized Cylinders from a single intensity view. *IEEE Trans. Robot. Autom.* **2**, 790–795 (1990)
5. A.P. Pentland, Perceptual organization and the representation of natural form. *Artif. Intell.* **28** (3), 293–331 (1986)
6. K. Ikeuchi, K.S. Hong, Determining linear shape change: toward automatic generation of object recognition program, in *Proceedings IEEE Computer Vision and Pattern Recognition (CVPR)* (1989), pp. 450–457
7. B. Stader, R.B. Rusu, K. Konolige, W. Bugar, Point feature extraction on 3D range scans taking into account object boundaries *IEEE Trans. Robot. Autom.* **121**, 2601–2608 (2011)
8. M. Oshima, Y. Shirai, Object recognition using three-dimensional information. *IEEE Trans. Pattern Anal. Mach. Intell.* **PAMI-5**(4), 353–361 (1983)
9. F. Fraundorfer, D. Scaramuzza, Visual odometry part II: matching, robustness, optimization and applications. *IEEE Trans. Robot. Autom. Mag.* **19**(2), 78–90 (2012)
10. D. Scaramuzza, F. Fraundorfer, Visual odometry part I: the first 30 years and fundamental. *IEEE Trans. Robot. Autom. Mag.* **18**(4), 80–92 (2011)
11. P. Scovanner, S. Ali, M. Shah, A 3-Dimensional SIFT Descriptor and its application to Action recognition, in *Proceedings 15th International Conference on Multimedia* (2007), pp. 357–360
12. E. Oyallon, J. Rabin, An analysis and implementation of the SURF method, and its comparison to SIFT. *Image Process. Line* **18**, 1–31 (2013)
13. E. Stella, *Novel Perspective on Automatic classification of Defects*, (Institute on Intelligent Systems for Automation, National Research Council, Bari, Italy, 2008). Report RI-ISSIA/CNR 04-2008, July 2008
14. M.P. Do Carmo, *Differential Geometry of Curves and Surfaces* (Prentice Hall, New Jersey, 1976), pp. 162–164
15. A. Pogorelov, *Geometry* (Mir Publishers, Moscow, 1987), pp. 175–184
16. R.B. Rusu, Z.C. Marton, N. Blodow, M. Dolha, M. Beetz, Towards 3D Point cloud based object maps for household environments. *Robot. Auton. Syst.* **56**(11), 927–941 (2008)

Design of Self-generating Component Powered by Magnetic Energy Harvesting—Magnetic Field Alarm

K. Tashiro, A. Ikegami, S. Shimada, H. Kojima and H. Wakiwaka

Abstract A design of self-generating component powered by magnetic energy harvesting is presented. In order to demonstrate the devices, a magnetic field alarm is developed. It consists of an energy harvesting module, Cockcroft-Walton circuit and piezo buzzer. The energy harvesting module is composed of coil and magnetic flux concentration core. It can generate 200 μW from an environmental magnetic field of 200 μT at 60 Hz. The Cockcroft-Walton circuit can convert the AC voltage to a suitable DC voltage for the piezo buzzer. This alarm can notice not only the magnetic field level defined by ICNIRP2010 but also the existence of magnetic field energy to be harvested. For the further developments, theoretical estimations for harvesting energy, effective permeability and optimum load condition are also discussed.

Keywords Magnetic energy harvesting · Self-generating component · Magnetic field alarm · Cockcroft-Walton circuit · Effective permeability

1 Introduction

Magnetic field is a reusable energy source to be used for both energy harvesting and wireless power transmission applications. Because electrical appliances are usually powered by electric wire, the well-known component of environmental magnetic fields is 50 or 60 Hz. In previous report, energy harvesting of 6.32 mW from a uniform magnetic field of 21.2 μT at 60 Hz, and activating a wireless sensor node have been demonstrated [1]. For energy management systems, some researcher's proposed a battery-free real-time current-waveform sensor powered by magnetic field around ac power line [2, 3]. Because the output voltage of an energy harvesting module for environmental electromagnetic field is ac signal, rectifier and

K. Tashiro (✉) · A. Ikegami · S. Shimada · H. Kojima · H. Wakiwaka
Spin Device Technology Center (SDTC), Shinshu University, Wakasato 4-17-1, Nagano,
Japan
e-mail: tashiro@shinshu-u.ac.jp

signal conditioning circuits should be installed for the energy source of wireless sensor nodes [4–6]. With a Cockcroft-Walton circuit (CW circuit) [7, 8] and storage capacitor [9], magnetic energy harvesting of 17 mJ from electrical appliances have been also demonstrated [10]. It may enough energy to activate a wireless sensor node, and “one-shot” signal. It was also mentioned the benefit of magnetic flux concentration core [11]. The theoretical design have revealed that the harvesting power is proportional to the fifth power of the outer diameter [12]. For example, air-cored Brooks coil of 280 mm in outer diameter demonstrated the energy harvesting of 562 mW from a magnetic field of 200 μT at 60 Hz. In contrast, the estimated power becomes 100 kW when the outer diameter is 3.6 m. It could be used for wireless power transmission application with a room-sized or building-sized coil system for producing a uniform magnetic field.

From the view point of the effect on humans, ICNIRP2010 provides a guideline for an acceptable electromagnetic field level [13]. At the power-line frequency of 50/60 Hz, an acceptable level in a public space is 200 μT . The motivation of this study is to notice and use this magnetic field. Compared with other reusable energy sources, such as light, thermal or vibration energy, human cannot notice the existence of magnetic field by own five senses.

This chapter presents a design of magnetic field alarm which does not require an external battery, and the size is limited to 50 mm \times 50 mm \times 50 mm. Figure 1 shows schematic diagram of the magnetic field alarm. It consists of an energy harvesting module, CW circuit, and piezo buzzer. It is an demonstration of “self-generating component” powered by magnetic energy harvesting. From the data sheets of the piezo buzzer sold in market, a special loud buzzer that functions at very low voltage was selected whose minimum operating voltage and current are as low as 0.7 V_{dc} and 0.3 mA (SC 0715 BL, Sonitron), respectively.

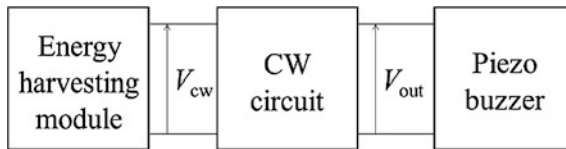


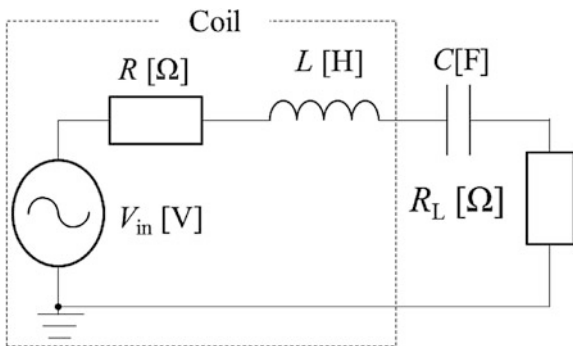
Fig. 1 Schematic diagram of the magnetic field alarm. It is an example of self-generating component powered by magnetic energy harvesting

2 Energy Harvesting Module

2.1 Equivalent Circuit

Figure 2 shows the equivalent circuit of the energy harvesting module. Based on the Faraday’s law of induction and Thevenin’s theorem, the amplitude of the voltage source V_{in} [V] can be expressed by:

Fig. 2 Equivalent circuit of the energy harvesting module



$$V_{in} = 2\pi^2 f n a^2 \mu_{\text{eff}} \mu_0 H_{\text{ext}} [v], \quad (1)$$

where f [Hz] is the frequency of the magnetic field, n [turn] is the number of coil windings, a [m] is the mean radius of the coil, μ_{eff} is the effective permeability of magnetic flux concentration core, μ_0 is the permeability of vacuum, and $\mu_0 \times \mu_{\text{eff}} \times H_{\text{ext}}$ [T] is the mean flux density crossing with the mean cross section of the coil. The magnetic flange can concentrate the environmental magnetic field to the core, which improves the effective permeability. The effective permeability is defined by:

$$\mu_{\text{eff}} = \frac{V_{in}}{V_{\text{air}}}, \quad (2)$$

where V_{air} is the induced voltage of the coil without the core. The impedance of this circuit can be expressed by:

$$Z = (R + R_L) + j\left(\omega L - \frac{1}{\omega C}\right) [\Omega]. \quad (3)$$

When the imaginary part is negligible, the impedance becomes minimum. Using the maximum power transfer theorem, load R_L should be the same as the coil resistance. The output voltage can be used for calculating the harvesting energy:

$$W = \frac{V_{\text{out}}^2}{R} = \frac{V_{in}^2}{4R} [W]. \quad (4)$$

If the diameter and total length of the core are fixed, the harvested energy is limited. Figure 3 shows an example of energy harvesting modules as a function of the coil length. The magnetic flux concentration cores were made of PC permalloy. The total length is 45 mm, outer diameter is 20 mm, inner diameter is 10 mm, and the diameter of the wire is 0.2 mm. The values of number of coil windings are 500, 1500, 3500 and 4300 for 5, 15, 35 and 43 mm in coil length, respectively.

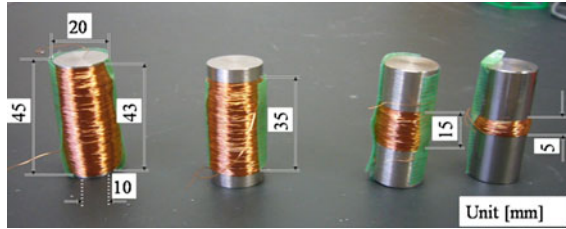


Fig. 3 An example of energy harvesting modules as a function of the coil length. Magnetic flux concentration cores were made of PC permalloy

2.2 Primary Design

Figure 4 shows the induced voltage as a function of coil length. The calculated results by FEM (JMAG-Designer Ver.12) are also plotted. When the coil length was larger than half of length of the core, the value of induced voltage converged. An increase in the coil length produces an increase in the number of coil windings and an decrease in the flange length. Although the induced voltage is proportional to the number of coil windings, an decrease in the flange length limits the induced voltage because of an decrease in the effective permeability. Figure 5 shows the harvested energy as a function of the coil length. When the coil length was larger than half of length of the core, the value of induced voltage converged. Although an CW circuit can convert to a suitable DC output voltage, the input voltage should be larger than 0.1 V. From several considerations, final design of the energy harvesting module was defined.

Fig. 4 Induced voltage as a function of coil length, as a parameter of magnetic field strength. The frequency of magnetic field was 60 Hz

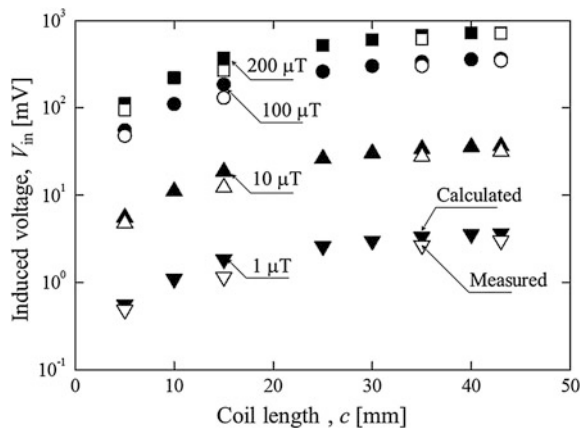
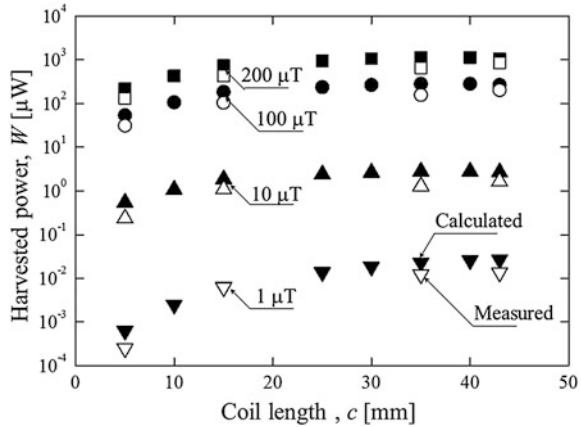


Fig. 5 Harvested power as a function of coil length, as a parameter of magnetic field strength. The frequency of magnetic field was 60 Hz



2.3 Final Design

Figure 6 shows the energy harvesting module for the magnetic field alarm. It consists of a coil and magnetic flux concentration core made of iron. The core has 10 mm in inner diameter, 20 mm in outer diameter, 0.5 mm in magnetic flange length, and 30 mm in coil length, respectively. The number of coil windings is 7000 with the wire of 0.12 mm in diameter. The measured resistance and inductance were 515 Ω and 2.04 H, respectively. The estimated value of induced voltage was 0.1 V when a magnetic field of 200 μT at 60 Hz crossed to the coil without the core.

Figure 7 shows the experimental setup for evaluation of the energy harvesting module. The energy harvesting module was placed inside an Simple-Box-9 coil system (SB9). SB9 can generate a uniform magnetic field. SB9 was composed of nine square coils connected in series, the ratio of the coil windings is 2:1:1:1:1:1:1:1:2, and the distance was 1/4 side length of the coil. When the side length of the square coil is d [m], it can generate $4.762/d$ [μT/A] [14]. The fabricated SB9 has 0.1 m in the side length, which can generate 190.5 μT/A because the number of windings is 4 times as 8:4:4:4:4:4:4:4:8.

Fig. 6 Energy harvesting module for magnetic field alarm. The magnetic flux concentration core was made of iron, whose flange length was 0.5 mm

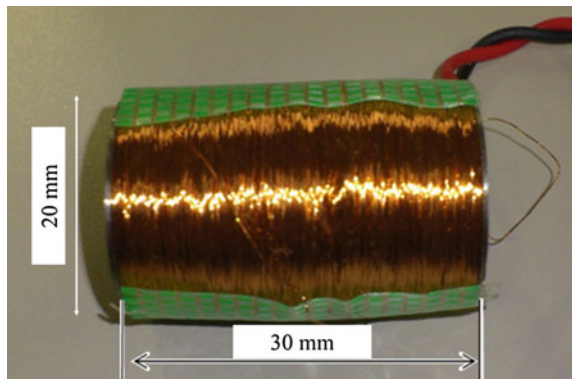


Fig. 7 Experimental setup for evaluation of the energy harvesting module

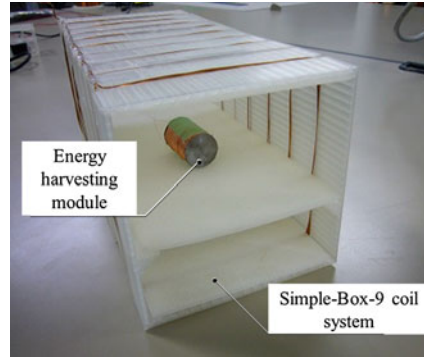


Fig. 8 Induced voltage of the energy harvesting module as a function of magnetic field strength. The frequency of magnetic field was 60 Hz

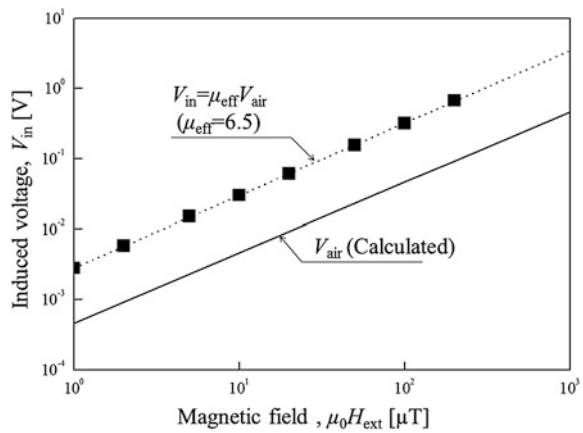


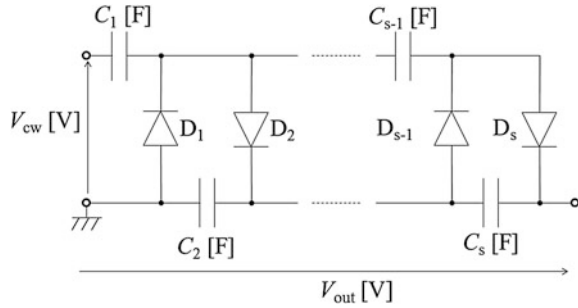
Figure 8 shows the induced voltage of the energy harvesting module as a function of the magnetic field of 60 Hz. Solid line represents the estimated value of the induced voltage without the core, plots represent the experimental results, respectively. When the magnetic field was 200 μT , the induced voltage was 668 mV. The estimated effective permeability and harvesting energy of this module are 6.5 and 200 μW , respectively.

3 Magnetic Field Alarm

3.1 CW Circuit

In order to activate the piezo buzzer, the required output voltage should be larger than 1.5 V. To provide the suitable voltage, design of the CW circuit was considered. Figure 9 shows the CW circuit. For reducing the losses at the circuit, low-voltage driven diodes and low-ESR (equivalent-series resistance) capacitors

Fig. 9 Schematic design of CW circuit



should be used. Here, low-voltage-driving Schottky diodes (1N5818, ST Microelectronics corp.) and capacitors of 10 μ F (1HEC-FS100 M, Toushin Kougyou) were used. The building block of the CW circuit consists of two diodes and two capacitors, and can provide twice value of dc output voltage. In an ideal CW circuit, the number of building block, or number of steps, can make the multiple the value of the dc output voltage. However, the losses in the CW circuit make the value low. The output voltage of the CW circuit can expressed by:

$$V_{out} = \sqrt{2}\alpha s V_{cw} [V], \tag{5}$$

where $\sqrt{2}V_{cw}$ is the peak value of the input voltage to the CW circuit, s is the number of steps and α is the ratio compared with the ideal value. When there are no losses in the circuit, the value of α is 1.

3.2 Experimental Confirmation

Figure 10 shows the schematic design of the experimental setup for evaluation of the CW circuit. The output voltage was measured with a TRUE RMS MULTIMETER (Digital tester 187, FLUKE). Figure 11 shows the measured output

Fig. 10 Experimental setup for evaluation of the CW circuit

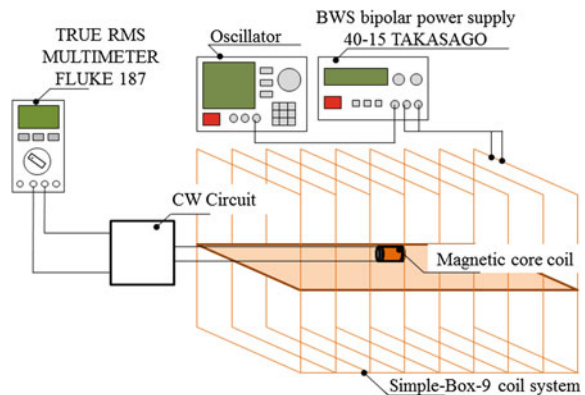
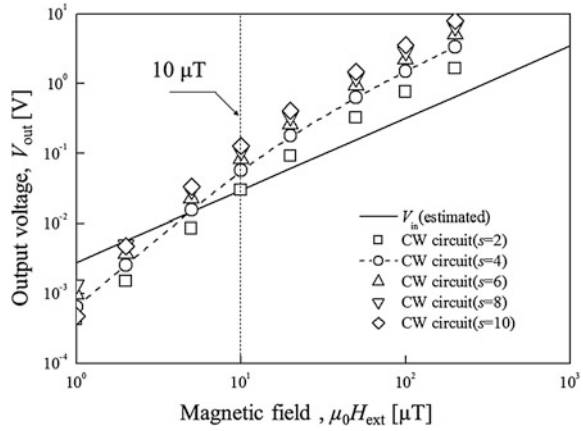
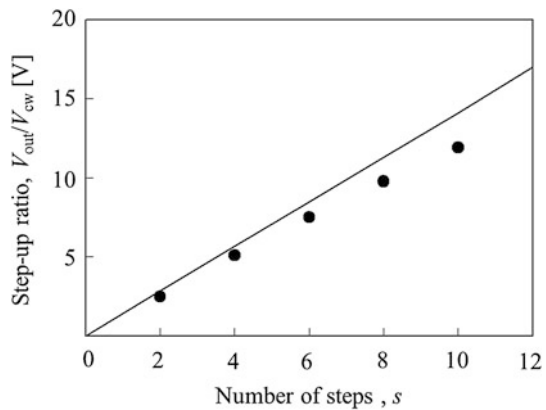


Fig. 11 Output voltage of the CW circuit as a function of magnetic field strength. The frequency of magnetic field was 60 Hz



voltage as a function of the magnetic field, as a parameter of the number of steps. It was found that all CW circuit provided the amplified dc output voltage when the magnetic field was larger than $10 \mu T$. If the magnetic field was larger than $100 \mu T$, the output voltage was larger than $1.5 V$ when the number of steps was larger than 4. Figure 12 shows the ratio of V_{out}/V_{cw} as a function of the number of steps. The magnetic field was $200 \mu T$ at 60 Hz. From the estimations, ideal step-up ratios, V_{out}/V_{cw} , are 2.83, 5.66, 8.49, 11.3 and 14.1, respectively. However, the measured step-up ratios are 2.47, 5.08, 7.5, 9.76 and 11.9, respectively. Although an increase in the number of steps produces an increase in the output voltage, it also produces an increase in the energy loss at the circuit. When the number of steps was 4, the maximum value of α was obtained. From the consideration mentioned above, the number of step was designed as 4 for the magnetic field alarm.

Fig. 12 Measured ratios, V_{out}/V_{cw} and α , as a function of the number of steps in the CW circuit. Magnetic field was $200 \mu T$ at 60 Hz



3.3 Magnetic Field Alarm

Figure 13 shows the magnetic field alarm. All of the parts were contained inside a cubic case made by an 3D printer (MakerBot replicator 2), and the size of the alarm is 50 mm × 50 mm × 50 mm. In order to check the operation, it was placed inside the SB9. When the magnetic field of 60 Hz was larger than 100 μT, the alarm started to sound a buzzer. Figure 14 shows the measured output voltage as a function of magnetic field. When the alarm sounded a buzzer, the voltage drop at the buzzer was about 0.5 V. This alarm can notice the existence of environmental magnetic field without any external battery.

Fig. 13 Magnetic field alarm

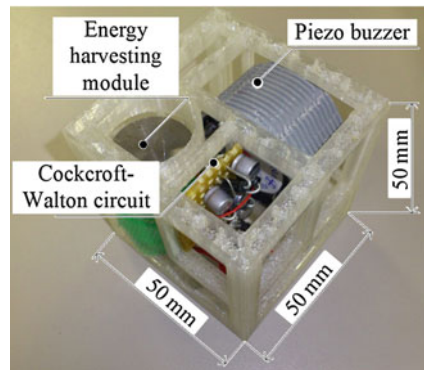
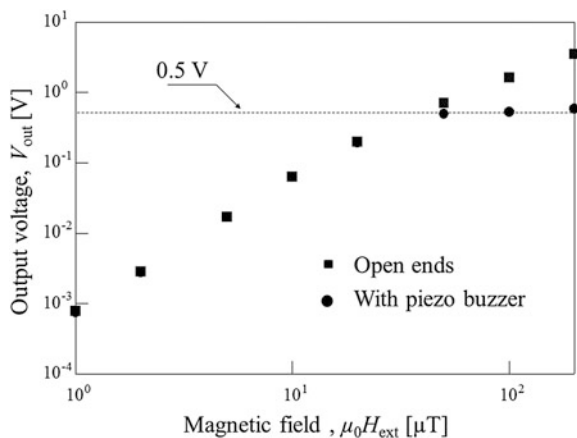


Fig. 14 Measured output voltage as a function of magnetic field strength. The frequency of magnetic field was 60 Hz



4 Discussion

4.1 Harvesting Power

As mentioned before, the harvesting energy is proportional to the square of the magnetic flux density. Substituting Eq. (1) into Eq. (4):

$$W = \frac{\pi^4 f^2 n^2 d^4}{R} \times \mu_{\text{eff}} \times (\mu_0 H_{\text{ext}})^2 [\text{W}]. \quad (6)$$

Fortunately, the harvesting energy is also proportional to the square of the effective permeability. However, the effective permeability is defined by the shape of the magnetic core due to the demagnetizing field. In other words, the effective permeability is finite value even if the magnetic material has infinity permeability. It should be also noted that the inductance of the core is not negligible in general. When a suitable resonant capacitor is inserted, the impedance becomes minimum because the imaginary part is negligible. To provide a resonance frequency at f [Hz], the resonant capacitor C [F] can be chosen from:

$$f = \frac{1}{2\pi\sqrt{LC}} [\text{Hz}]. \quad (7)$$

Here, the limitation of harvesting energy defined by the coil size is considered. In general, the values of the inductance and resistance for a coil were given as:

$$L = P_0 a n^2 [\text{H}], \quad (8)$$

$$R = \frac{2\pi a n \rho}{A} [\Omega], \quad (9)$$

where ρ [$\Omega \cdot \text{m}$] is the resistivity of copper at room temperature and A [m^2] is the cross sectional area of the winding. P_0 [H/m] is the coil coefficient defined by the coil shape. For example, the value of P_0 for an ideal solenoid coil with finite length is determined by the product of the circular constant π , permeability of vacuum in H/m, length to diameter ratio of the coil, and the Nagaoka coefficient. If the ratio of coil length, inner diameter and outer diameter are constant, the value of P_0 becomes constant. A Brooks coil is a circular coil with a square cross section, and the ratio of the coil length, inner diameter, and outer diameter is 1:2:4 [15]. Because of the constraint shape, it is known that the value of P_0 is constant as 1.6994×10^{-8} H/m. The air-core coil is Brooks coil having the spacing factor β :

$$\beta = \frac{c^2}{nA}, \quad (10)$$

where, c [m] is the length, $2c$ [m] is the inner diameter, $4c$ [m] is the outer diameter, c^2 [m²] is the cross section and $3c/2$ [m] is the mean radius of Brooks coil. Without considering a wire insulator, an ideal lamination factor corresponds to $\beta = 1$. Substituting Eqs. (9) and (10) into Eq. (6) gives:

$$W = \frac{27\pi^3\beta f^2}{16\rho} c^5 \times \mu_{\text{eff}}^2 \times (\mu_0 H_{\text{ext}})^2 [\text{W}]. \tag{11}$$

It can be seen that the harvesting energy does not depend on the number of windings. In contrast, the harvesting energy is proportional to the fifth power of c . This means that the harvesting energy has strongly depended on the coil size.

Figure 15 shows the estimated energy as a function of the outer diameter of a Brooks coil [12]. In this estimation, the spacing factor is $\beta = 0.737$, the resistivity is $\rho = 1.78 \times 10^{-8} \Omega\cdot\text{m}$, and the frequency is $f = 60$ Hz. The line represents the air-core coil, and the dash and dotted line represent the coil with a magnetic core having an effective permeability of 10 and 100, respectively.

The required outer diameter of an air-core coil for harvesting 1 W is larger than 300 mm. If it can be designed the harvesting module with an effective permeability of 100, the required diameter becomes 50 mm. Unfortunately, the theoretical design revealed that the estimated power is negligible if the outer diameter is less than 10 mm. In contrast, if it can be prepared a relatively large air-core module, the estimated energy is enough in typical applications related with wireless power transfer. For example, the estimated power becomes 100 kW when the diameter is larger than 3.2 m.

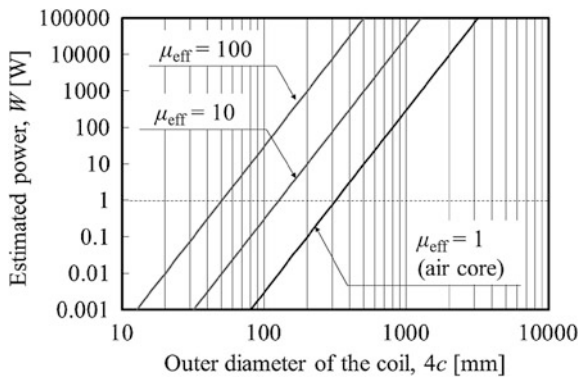


Fig. 15 Estimated harvesting power as a function of outer diameter of the Brooks coil, as a parameter of the effective permeability, μ_{eff} . Where, $\beta = 0.737$, $\rho = 1.78 \times 10^{-8} \Omega\cdot\text{m}$, $f = 60$ Hz and $\mu_0 H = 200 \mu\text{T}$

4.2 Effective Permeability

It is well known that the demagnetizing factor strongly depends on the core shape which defines the effective permeability. Because exact calculation of the demagnetization factor for ellipsoidal bodies exists [16], it is widely used for the estimation of the effective permeability for ellipsoidal core or relatively long rod core. Unfortunately, this estimation is not acceptable for the magnetic flux concentration core. The shape of the flange part, or magnetic flux concentration part, is a relatively long cylinder. And the cross section of the flange part is larger than that of the coil winding part. Several researchers related to magnetic sensor have proposed an approximation for this core [17, 18]. However, it cannot take into account the flange part length. Here, an approximation is mentioned below, which could be acceptable when the ratio of the length to diameter was less than 2.25.

Figure 16 shows the magnetic flux concentration cores. The material of the cores is PC Permalloy. Compared with a conventional rod-shaped core, a magnetic concentration core can provide an amplification of an external magnetic field to the coil. Table 1 shows the specifications of the cores. In order to evaluate the effective permeability, coil were wound around the coil winding part. The shape of coil was Brooks coil whose length, inner and outer diameter were 5, 10 and 20 mm, respectively. The number of coil turns was 500 with a wire of 0.2 mm in diameter. The effective permeability, μ_{eff} , is defined by the ratio of the mean magnetic field inside the core, B_{coil} [T], to the external magnetic field, $\mu_0 H_{\text{ext}}$ [T]:

$$\mu_{\text{eff}} = \frac{B_{\text{coil}}}{\mu_0 H_{\text{ext}}} = \frac{V_{\text{in}}}{V_{\text{air}}}, \tag{12}$$

Fig. 16 Magnetic flux concentration cores

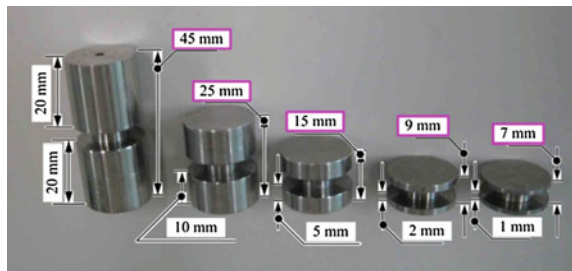


Table 1 Specifications of the magnetic flux concentration cores

Property	Value
Coil length, c [mm]	5
Inner diameter, d [mm]	10
Outer diameter, D [mm]	20
Flange length, δ [mm]	1, 2, 5, 10, 20
Material	PC Permalloy (Nilaco Inc.)

where V_{in} [V] and V_{air} [V] represent the induced voltage of the coil with or without the core, respectively. If the shape of the core is a conventional rod or plate, the value of μ_{eff} is defined by

$$\mu_{\text{eff}} = \frac{B_{\text{coil}}}{\mu_0 H_{\text{ext}}} = \frac{\mu_r}{1 + (\mu_r - 1)N}, \quad (13a)$$

where, μ_r is the relative permeability of the core, N is the demagnetizing factor of the core. The value of N can be expressed using the aspect ratio, m :

$$m = \frac{L}{D}, \quad (13b)$$

where L and D are the outer length and diameter of the core, respectively. The value of N can be roughly estimated by using the demagnetizing factor of the ellipsoidal bodies [19] as

$$\left\{ \begin{array}{ll} N = \frac{1}{1 - m^2} \left[1 - \frac{m}{\sqrt{1 - m^2}} \arccos m \right] & (m < 1), \\ N = \frac{1}{3} & (m = 1), \\ N = \frac{1}{m^2 - 1} \left[\frac{m}{\sqrt{m^2 - 1}} \operatorname{arccosh} m - 1 \right] & (m > 1), \\ N = \frac{1}{m^2} (\ln 2m - 1) & (m > 12). \end{array} \right. \quad (14)$$

It is easy to understand that the value of μ_{eff} strongly depends on the value of N . In other words, the value of μ_{eff} is defined by the inverse value of N when the value of μ_r for the core is relatively large:

$$\mu_{\text{eff}} = \frac{1}{\frac{1}{\mu_r} + (1 - \frac{1}{\mu_r})N} \cong \frac{1}{N}. \quad (15)$$

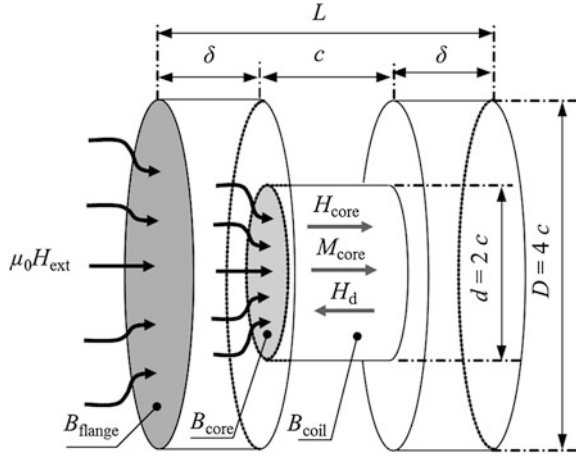
Figure 17 shows the schematic design of the concentration core. In order to improve the performance of induction magnetometer, several researchers also proposed similar core shape.

From Eq. (12), it could be expressed by following equations:

$$\mu_{\text{eff}} = \frac{B_{\text{flange}}}{\mu_0 H_{\text{ext}}} \times \frac{B_{\text{coil}}}{B_{\text{flange}}}, \quad (16)$$

$$B_{\text{core}} = \frac{\pi(D/2)^2}{\pi(d/2)^2} \times B_{\text{flange}} = \left(\frac{D}{d} \right)^2 B_{\text{flange}} [\text{T}], \quad (17)$$

Fig. 17 Schematic design of the magnetic concentration core



$$B_{\text{coil}} = B_{\text{core}} - \mu_0 H_d [\text{T}], \quad (18)$$

where H_d [A/m] and B_{coil} [T] are the demagnetizing field and mean magnetic flux density in the coil winding part, B_{flange} [T] and B_{core} [T] are the magnetic flux density at the connection surfaces of flange part, respectively. It is based on the conservation of the magnetic flux. In other words, all magnetic flux passes between the end and coil winding part. If the value of μ_r is relatively large, the first term of right side in Eq. (16) can be expressed by

$$\frac{B_{\text{flange}}}{\mu_0 H_{\text{ext}}} = \frac{\mu_r}{1 + (\mu_r - 1)N_{\text{flange}}} \cong \frac{1}{N_{\text{flange}}}. \quad (19)$$

Where N_{flange} is the demagnetizing factor of the end part. Relationship between demagnetizing field and magnetic flux density of the core can be summarized by following equations:

$$H_d = N_{\text{core}} M_{\text{core}} [\text{A/m}], \quad (20)$$

$$B_{\text{core}} = \mu_0 H_{\text{core}} + \mu_0 M_{\text{core}} [\text{T}], \quad (21)$$

$$\mu_r = B_{\text{core}} / \mu_0 H_{\text{core}}, \quad (22)$$

where N_{core} , M_{core} [A/m] are the demagnetizing factor and magnetization of the coil winding part, respectively. From Eqs. (18), (20), (21) and (22), the magnetic flux density of the coil winding part is expressed by

$$B_{\text{coil}} = \left[\left(1 - N_{\text{core}} + \frac{N_{\text{core}}}{\mu_r} \right) \right] B_{\text{core}} [\text{T}] \quad (23)$$

When the relative permeability is relatively high, the ratio of the B_{coil}/B_{core} can be expressed by

$$\frac{B_{coil}}{B_{core}} = \left[\left(1 - N_{core} + \frac{N_{core}}{\mu_r} \right) \right] \cong (1 - N_{core}). \tag{24}$$

From Eq. (17), the ratio of the B_{coil}/B_{flange} and μ_{eff} can be expressed by:

$$\frac{B_{coil}}{B_{flange}} = (1 - N_{core}) \times \left(\frac{D}{d} \right)^2, \tag{25}$$

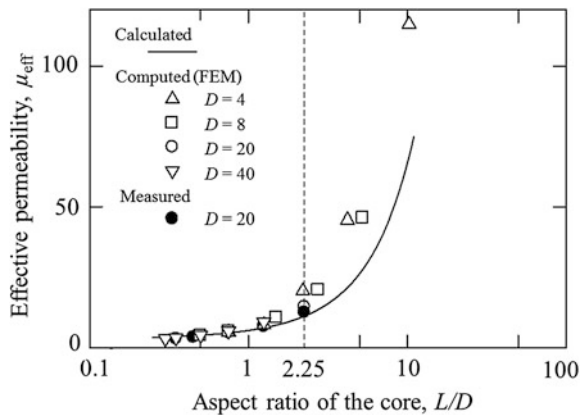
$$\mu_{eff} = \frac{1 - N_{core}}{N_{flange}} \times \left(\frac{D}{d} \right)^2. \tag{26}$$

For the calculation of both N_{core} and N_{flange} , demagnetizing factor of the ellipsoidal bodies, Eq. (14), could be used. The value of m was (l/d) for N_{core} , and (δ/D) for N_{flange} , respectively. Although this equation is theoretically expressed, it is not agreed with both the numerical and experimental results. According to several researchers, a correction term related to the aspect ratio are usually taken into account. From the several considerations, the final is expressed as:

$$\mu_{eff} = \frac{1 - N_{core}}{N_{flange}} \times \left(\frac{d}{l} \right) \times \left(\frac{D}{d} \right)^2. \tag{27}$$

Figure 18 shows the value of μ_{eff} as a function of the value of L/D . Filled plots represent the measured results, and line represents the calculation results from Eq. (27). Open plots represent the FEM analysis results with JMAG-Designer Ver. 12.0.2. In the experimental results, V_{in} [V] was the induced voltage of the coil measured with a lock-in amplifier (5610B, NF corp.), V_{air} [V] was calculated from

Fig. 18 Effective permeability as a function of the aspect ratio



Faraday’s law of induction, f [Hz] was the frequency ($= 60$ Hz) and $\mu_0 H_{ext}$ [T] was the external magnetic flux density ($= 1 \mu\text{T}$). Although the ratio of a coil part length, coil part diameter and flange diameter was fixed to 1:2:4, several similar models were tested for the FEM analysis. From experimental results, the validity of the proposed approximation was successfully confirmed. The relative values of estimation error were less than 10 %. The FEM analysis also indicated that proposed approximation could be acceptable when the L/D was less than 2.25.

4.3 Optimum Load

For energy harvesting devices, power conversion is a key point. CW circuit is a good power converter which has both rectifier and step-up voltage functions. If the voltage drop in the diode is zero, it is an ideal power converter.

Figure 19 shows a CW circuit for considering the maximum power transfer condition. Where R_L [Ω] is the load, V_{in} [V] and R [Ω] are AC the voltage source and its resistance, respectively. The CW circuit converts an AC voltage of V_{cw_in} [V] to an DC voltage of V_{cw_out} [V]. If there is no power loss in CW circuit, the input power is consumed at both the source resistance and load. According to the power transfer theorem, the power consumption of both resistance. In other words, the value of V_{cw_in} should be the half value of V_{in} . The output voltage and power consumption of both resistors are expressed by:

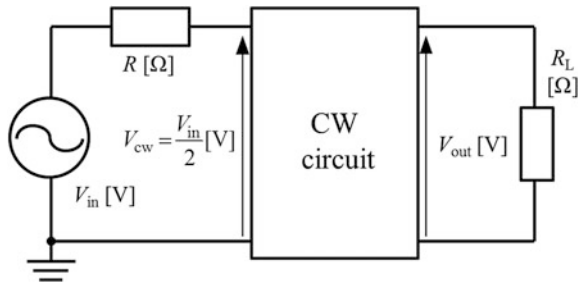
$$V_{out} = \sqrt{2}sV_{cw} = \frac{\sqrt{2}}{2}sV_{in}[\text{V}], \tag{28}$$

$$W_1 = \frac{V_{in}^2}{4R}[\text{W}], \tag{29}$$

$$W_2 = \frac{V_{out}^2}{R_L} = \frac{2s^2V_{in}^2}{4R_L}[\text{W}]. \tag{30}$$

Because of $W_1 = W_2$, the optimum load is expressed by:

Fig. 19 CW circuit for considering the maximum power transfer condition



$$R_L = 2s^2R[\Omega]. \tag{31}$$

This equation is also acceptable for a conventional full wave rectifier ($s = 2$). If the voltage drop in diodes is negligible, the value of V_{cw-out} and W_2 are $\sqrt{2} V_{cw-out}$ and $2V_{cw-out}^2/R_L$, respectively. According to the Eq. (31), the value of optimum load is $R_L = 8R$. At the condition, the energy consumption of both resistor is as same as $V_{cw-out}^2/4R_L = V_{in}^2/4R_L$.

Because magnetic energy harvesting module consists of the coil, the effect of the inductance should be taken into account. Figure 20 shows the equivalent circuits of the magnetic energy harvesting components for considering the maximum power transfer condition. When the reluctance is negligible compared with the resistance, the equivalent circuit can be drawn as (a). In general case, both the resistance and inductance should be taken into account to the equivalent circuit. When the target frequency is fixed, the use of a suitable resonant capacitor is well known as (b). If the capacitor is not connected, the equivalent circuit is drawn as (c).

Table 2 shows an example of the parameters for a circuit simulator LTSpice (Linear Technology Inc.). In the CW circuit, the voltage drops in the diodes are set to be zero. The values of load for the number of steps are calculated from Eq. (31). Figure 21 shows the comparison of the theoretical and simulated results. The

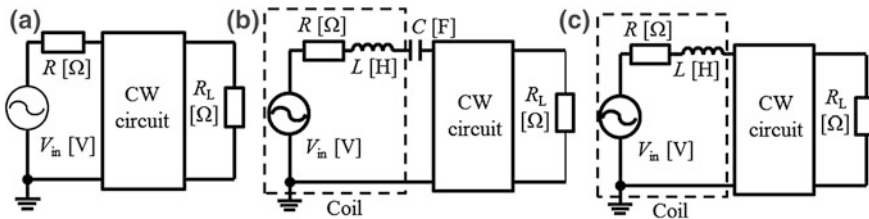
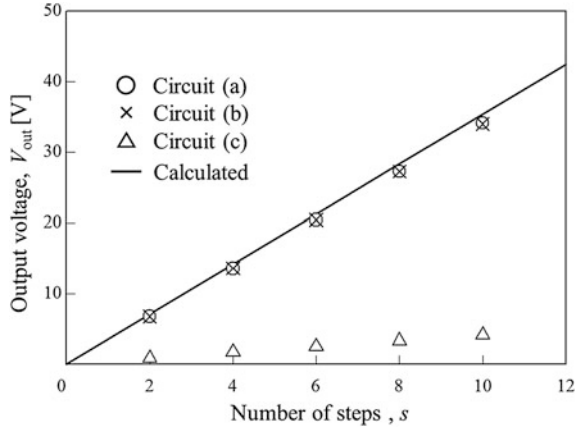


Fig. 20 Equivalent circuits of the magnetic energy harvesting component for considering the maximum power transfer condition: **a** the inductance of the coil is negligible, **b** a resonant capacitor for the inductance of the coil is inserted, **c** the resonant capacitor is not connected although the coil has both the resistance and inductance

Table 2 Parameters for the equivalent circuits

Parameter	Value				
Resistance, R [Ω]	1060				
Inductance, L [H]	60.4				
Frequency, f [Hz]	60				
Resonant capacitor, C [μ F]	0.117				
Input voltage, V_{in} [V]	5				
Capacitors in CW circuit, $C_1 \sim C_s$ [μ F]	47				
Number of steps in CW circuit, s	2	4	6	8	10
Load, R_L [k Ω]	8.480	33.92	76.32	135.7	212.0

Fig. 21 Comparison of V_{out} as a function of s . The parameters of the circuit element are summarized in Table 2. Line represents the calculated value from the Eq. (28)



theoretical estimation was acceptable when the reluctance in the magnetic energy harvesting module is negligible as (a) and (b).

Although the voltage drops in the diodes are not negligible, the theoretical estimation is acceptable for the practical use. In order to confirm the validity, an experiment was conducted as follows.

Figure 22 shows a magnetic energy harvesting module which used in this experiment. The parameters are the same as summarized in Table 2. For a magnetic field of $90 \mu\text{T}$ at 60 Hz, this module can harvest of 100 mW. The CW circuits were composed of low-voltage-driving Schottky diodes (1N5818, ST Microelectronics corp.) and capacitors of $47 \mu\text{F}$. The magnetic field of 60 Hz was generated by an SB9 whose side length of the square coil was 2 m. In order to compare with the calculated results, the generating magnetic field was controlled to which the induced voltage of the coil was 5 V. The optimum load were experimentally

Fig. 22 Magnetic energy harvesting module with an air-core Brooks coil and resonant capacitor. The number of coil windings is 18395 turn

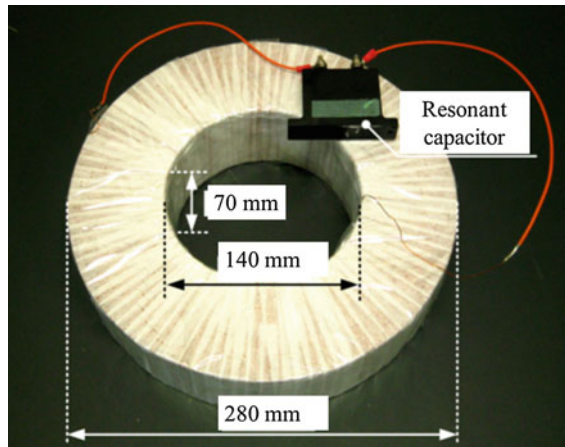
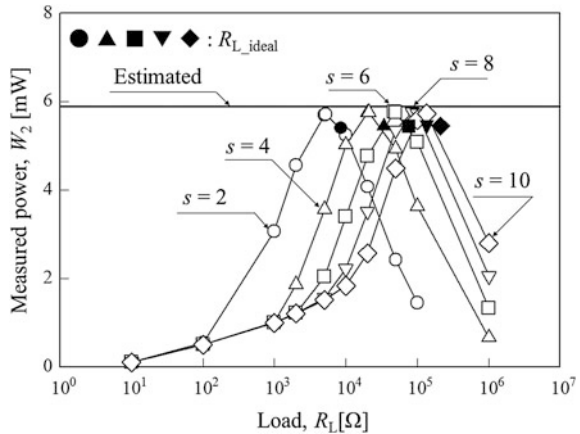


Fig. 23 Measured power as a function of the connected load



investigated by measuring the output voltage when the dummy loads were connected. The values of measured power were calculated from the values of the output voltage and load’s resistance.

Figure 23 shows the measured power as a function of the connected load. Bold line represents the maximum power consumption estimated by Eq. (29). The filled plots represent the values of optimum load, R_{L_ideal} , which are expressed by Eq. (31). The values of R_{L_ideal} were acceptable, and the maximum relative error was 40 %. The maximum values of measured power were good in agreement with the values estimated by Eq. (29).

5 Conclusion

Design of self-generating component powered by magnetic energy harvesting was presented. A design of magnetic field alarm powered by an energy harvesting module was described in the Sect. 2 and 3. With a help of the FEM analysis and experimental confirmation, it was successfully demonstrated. For the further developments of other self-generating components, several tips were discussed in the Sect. 4. Although the harvesting power is limited by the size of the coil, the use of the magnetic flux concentration core could reduce the required size. Approximation of the effective permeability may help the theoretical design of the core whose aspect ratio, L/D is less than 2.25. According to the maximum power transfer theorem, the design of optimum load was also explained.

Acknowledgements This work was supported in part by JSPS KAKENHI, Scientific Research (C), Grant Number 25502001, 2013–2015.

References

1. K. Tashiro, H. Wakiwaka, S. Inoue, Y. Uchiyama, Energy Harvesting of Magnetic Power-Line Noise. *IEEE Trans. Magn.* **47**, 4441–4444 (2011)
2. S. Takahashi, N. Yoshida, K. Maruhashi M. Fukaishi, Real-time current-waveform sensor with plugless energy harvesting from AC power lines for home/building energy-management systems, in *2011 IEEE International Solid-State Circuits Conference* (2011), pp. 220–222
3. N.M. Roscoe, M.D. Judd, Harvesting energy from magnetic fields to power condition monitoring sensors. *IEEE Sens. J.* **13**, 2263–2270 (2013)
4. R.J.M. Vuller, R. van Schaijk, I. Doms, C. Van Hoof, R. Merten, Micropower energy harvesting. *Solid State Electron.* **53**, 684–693 (2009)
5. A. Harb, Energy harvesting: state-of-the-art. *Renewable Energy* **36**, 2641–2654 (2011)
6. R.J. Vyas, B.B. Cook, Y. Kawahara, M.M. Tenzeris, E-WEHP: a batteryless embedded sensor-platform wirelessly powered from ambient Digital-TV signals. *IEEE Trans. Microw. Theory Tech.* **41**, 2491–2505 (2013)
7. K. Tashiro, H. Wakiwaka, Y. Uchiyama G. Hattori, *Design of AC–DC Converter for Magnetic Energy Harvesting Device*. Sensing technology: current status and future trends I, smart sensors, measurement and instrumentation, vol. 7 (Springer, Dordrecht, 2014), pp. 297–308
8. K. Tashiro, H. Wakiwaka, Y. Uchiyama, Loss measurement in power conditioning module for power-line magnetic noise energy harvesting device. *J. Japan Soc. Appl. Electromagnet. Mechan.* **20**, 440–445 (2012)
9. K. Tashiro, H. Wakiwaka, Y. Uchiyama, Consideration of energy storage circuits for magnetic energy harvesting. *J. Japan Soc. Appl. Electromagnet. Mech.* **21**, 308–313 (2013)
10. K. Tashiro, H. Wakiwaka, S. Shimada, Demonstration of magnetic energy harvesting from electrical appliances. *J. Energy Power Eng.* **8**, 568–572 (2014)
11. K. Tashiro, G. Hattori, H. Wakiwaka, Magnetic flux concentration methods for magnetic energy harvesting module. *EPJ Web Conf.* **40**, 06011 (2013)
12. K. Tashiro, H. Wakiwaka, Y. Uchiyama, Theoretical design of energy harvesting module or wireless power transmission receiver using magnetic field of 0.2 mT at 60 Hz. *J. Energy Power Eng.* **7**, 740–745 (2013)
13. ICNIRP : Guideline for limiting exposure to time-varying electric and magnetic fields (1 Hz to 100 kHz), *Health Phys.* **99**(6), 818–836 (2010)
14. K. Tashiro, A. Matsuoka, H. Wakiwaka, Simple-Box-9 coil system: a novel approach to design of a square coil system for producing uniform magnetic fields. *Mater. Sci. Forum* **670**, 275–283 (2011)
15. F.W. Grover, *Inductance Calculations, Dover Phoenix Editions* (2004), pp. 94–113
16. J.A. Osborn, Demagnetizing factors of the general ellipsoid. *Phys. Rev.* **67**, 351–357 (1945)
17. C. Coillot, J. Moutoussamy, P. Leroy, G. Chanteur, A. Roux, Improvements on the design of search coil magnetometer for space experiments. *Sensor Letters* **5**, 167–170 (2007)
18. E. Paperno, A. Grosz, A miniature and ultralow power search coil optimized for a 20 mHz to 2 kHz frequency range. *J. Appl. Phys.* **105**, 07E708 (2009)
19. D.-X. Chen, E. Pardo, A. Sanchez, Fluxmetric and magnetometric demagnetizing factors for cylinders. *J. Magn. Magn. Mater.* **306**, 135–146 (2006)